# ERTS-1
# A NEW WINDOW ON OUR PLANET

GEOLOGICAL SURVEY PROFESSIONAL PAPER 929

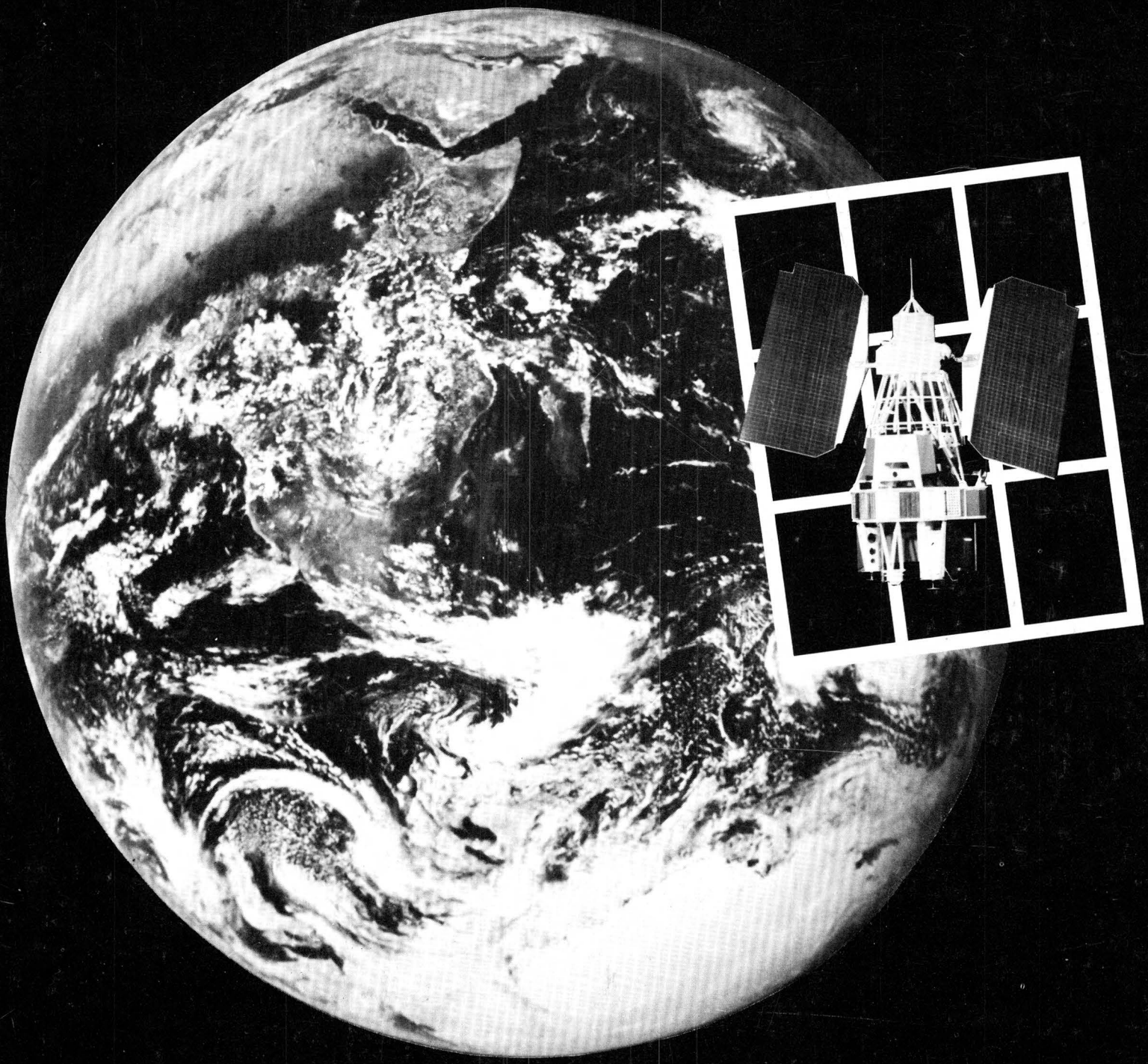

# ERTS-1
# A NEW WINDOW ON OUR PLANET

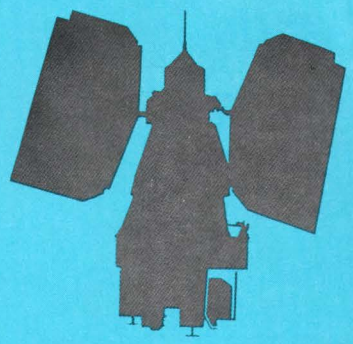

RICHARD S. WILLIAMS, JR., and WILLIAM D. CARTER, EDITORS

GEOLOGICAL SURVEY PROFESSIONAL PAPER 929

*Cooperating Organizations:*

*U.S. Department of the Interior:*
- *Geological Survey*
- *Bureau of Land Management*
- *Bureau of Reclamation*
- *Bureau of Mines*
- *Fish and Wildlife Service*
- *National Park Service*

*University of Tennessee*
*Environmental Research Institute of Michigan*
*U.S. Army Corps of Engineers*
*The American University*
*Jet Propulsion Laboratory (California Institute of Technology)*
*University of Minnesota*
*National Oceanic and Atmospheric Administration*
*University of Alabama*
*California State University*
*Wyoming Geological Survey*

*Cover photography of the Earth taken from* Apollo *(72–HC–928) courtesy of National Aeronautics and Space Administration*

UNITED STATES GOVERNMENT PRINTING OFFICE, WASHINGTON : 1976

UNITED STATES DEPARTMENT OF THE INTERIOR

THOMAS S. KLEPPE, SECRETARY

GEOLOGICAL SURVEY

V. E. McKELVEY, DIRECTOR

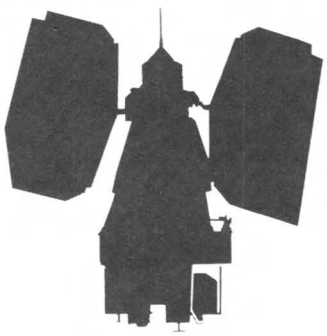

For sale by the Superintendent of Documents,
U.S. Government Printing Office
Washington, D.C. 20402–$13 (paper cover)
Stock Number 024–001–02757–7
Catalog Number I 19.16:929

Library of Congress catalog-card No. 75–37451

# FOREWORD

The launch, on July 23, 1972, of the first Earth Resources Technology Satellite (ERTS–1) by the National Aeronautics and Space Administration and the subsequent launch of ERTS–2 (Landsat–2) on January 22, 1975, were major steps forward in extending man's ability to inventory the Earth's resources and to evaluate objectively his impact upon the environment.

The ERTS spacecraft represent the first step in merging space and remote-sensing technologies into a system for inventorying and managing the Earth's resources. This development is a good example of applying the scientific and technological methodology gained from the Nation's space program to the solution of global environmental, natural-resource, food, and energy problems. Evidence in hand strongly suggests that the ERTS spacecraft are central to one of the largest and most significant earth-science experiments ever undertaken.

Examples presented in this book demonstrate ERTS' vast potential for inventorying resources, monitoring environmental conditions, and measuring changes. Such information is essential for the full evaluation of the Federal lands and determining their future use, as well as for improved planning of overall land use throughout the United States and the world.

More than being merely another scientific experiment, this undertaking is a multinational, multidisciplinary experiment on a global scale. Approximately 100 nations are participating, and it is believed that the program will contribute materially to achievement of an objective basis for setting interrelated resource, environmental, and social priorities for much of the world.

Data from U.S. Earth resources survey satellites are of help to all nations in coping with natural resource and environmental problems. This is so because we have only rudimentary knowledge of our resources. Even more limited is our knowledge of the effect of development and consumption of these resources on the long-term future of our planet. Thus, we are restricted in our ability to make the decisions necessary for the wisest possible utilization and conservation of the resources upon which we depend for our very existence.

The Government of the United States hopes and believes that by working together with other nations we will be able to develop cooperative programs in remote sensing. The development of these programs will allow the diffusion of knowledge gained from remote sensor technology, such as ERTS, by making data available and providing for the education and training of technicians in this field, and also through the user assistance necessary to convert imagery, photographs, and other data into useful information for resource inventory and survey purposes. Typical repetitive information already available relates to such disciplines as geology, hydrology, geography, cartography, agriculture and rangeland management, forestry, and land use mapping and planning.

Original electronic signals of data acquired with ERTS are being converted by NASA to photographic-type images, that in turn are being processed at the EROS Data Center, Sioux Falls, South Dakota. The Center, thus, is a key installation serving as an international repository for processing, interpreting, and disseminating thousands of images per year of a wide variety of land and water features of the world. These images are being provided to all users, domestic and foreign, at nominal cost. The data are particularly useful for those who are involved in urban and suburban planning, zoning, construction, and similar activities, as they provide unique tools in helping to arrive at wise land- and water-use decisions.

A number of formal scientific experiments have been completed or are in progress within the Department of the Interior that have demonstrated contributions from space technology to resource assessments. Ten bureaus of the Department have roles in the ERTS project: the Bureaus of Indian Affairs, Land Management, Mines, Outdoor Recreation, and Reclamation and the Fish and Wildlife Service, the Bonneville Power Administration, the National Park Service, Office of Trust Territories, and the Geological Survey.

Nearly all of these participating bureaus are represented in the many papers included in this book. I encourage you, whether you be a scientist, resource manager, educator, or layman from the United States or from another country, to review these examples of this exciting and totally new technology which has been developed for the benefit of all the world's peoples. I think that you will agree with me that we have made a fine start in the effective and beneficial use of "space" for all mankind.

V. E. McKelvey

V. E. McKelvey,

Director, U.S. Geological Survey

# PREFACE

Discovery, or the possibility of it, is that which whets, stimulates, and hopefully satisfies the cravings of scientists, inventors, and explorers. The hope of discovery pushed Ericson and Columbus west across the Atlantic against the odds that their frail crafts would perish by storm or "fall off the edge of the Earth." The desire for discovery encouraged Lewis and Clark, Powell, Hayden, and others to explore our western plains, mountains, river canyons, and mineral and water resources against the many odds of traversing unknown areas. Lt. Maury, working against tradition and inertia in the U.S. Navy, laboriously compiled the many bits of wind, current, and sea-state information contained in the logs of sailing ship captains to chart the ocean currents and winds. Such audacious, and to some, revolutionary, discoveries also inspired man to learn to fly and eventually project himself into space.

At this time, man has already landed on and begun exploration of the Moon. During the progress of the Mercury, Gemini, and Apollo programs, our astronauts began to carry cameras and took many photographs of the Earth from space. These photographs immediately interested earth-bound scientists involved in important projects of mapping the geology, hydrology, agriculture, and other environmental phenomena of the Earth.

The NASA Earth Resources Survey Program was born in 1964 as a handful of scientists representing a few scientific disciplines from major U.S. Government agencies. The program gradually grew to include scientists from all earth-resource disciplines in industry, university, and state organizations. Through cooperative information exchange and training, scientists from all over the world became interested and involved. These scientists studied various types of remotely sensed data from aircraft and spacecraft to develop specifications for an Earth Resources Technology Satellite (ERTS–1). Six hundred proposals were submitted to NASA to analyze ERTS–1 data. More than 320 experiments, representing multidisciplinary and multinational interests, were selected to give the first satellite as broad a test as possible. Of the 81 experiments submitted to NASA by scientists of the various bureaus within the U.S. Department of the Interior, 45 were ultimately selected and made.

In our capacity as research scientists within the EROS Program, it was our responsibility to not only carry out our own ERTS investigations in Iceland and South America, respectively, but to coordinate, review, and document, for the U.S. Geological Survey and NASA, the U.S. Department of the Interior results of the ERTS experiment. As experimental findings flowed through our hands from Interior scientists to NASA, it became increasingly clear that these results would be of interest to earth scientists throughout the world, especially those in developing nations, who are just beginning to explore potential applications of satellite data.

While the results presented herein are but a small sampling of the work currently in progress around the world, we believe that they are representative of the capabilities that are fast becoming available to earth scientists and resource managers, not only in the U.S. Department of the Interior but in other domestic and foreign organizations as well. We hope that this publication will inspire others to similar investigations and that universities and high schools will find this book helpful in their earth-science curricula. To aid in this objective the EROS Program has available for purchase 35-mm slides of selected ERTS images printed in this book and, of course, all the original image data as well. Slide set E–1–30–35 may be purchased from the EROS Data Center, Sioux Falls, South Dakota

57198. We also hope that the book will help national decisionmakers, as well as taxpayers, realize the value of expenditures, past and future, that are made for programs such as ERTS.

In nearly every respect ERTS–1 is an exceptional and unique satellite and may very well represent the most important accomplishment yet of our space program in terms of benefits to our Nation, to other nations, and hence to all people of the world. ERTS, like its equally inexpensive sister satellites, the civilian weather satellites (NOAA and Nimbus), was designed so that its data would serve a large number of users within the United States and throughout the world. For the first time in the history of the U.S. space program, with the exception of some civilian meteorological-satellite data, data acquired from an unmanned orbiting spacecraft are being made available to all, inexpensively, and on an unrestricted basis. The source of information for this national and international distribution is the EROS Data Center in Sioux Falls, South Dakota.

As you review the examples of the applications of ERTS imagery in this book and the excellent collection of ERTS images in the NASA Special Publication compiled by Short, Lowman, Freden, and Finch, *Mission to Earth: Landsat Views the World,** it is hard to believe that only 100 years ago man's view of his world was generally limited to what he could see from a sailing vessel, from horseback, or afoot. Because of ERTS, anyone can now sit down at a microfilm projection console and view nearly all the land areas of the world; one can even order specific images from the EROS Data Center for more comprehensive analysis. For the first time in history the entire world is at everyone's fingertips; for many parts of the world, in particular North America (because of complete coverage afforded by several ERTS receiving stations in the United States and Canada), the changing face of our planet, whether the changes are caused by natural forces or by man's often disruptive forces, is available for analysis on an 18-day cycle.

The availability of ERTS data could not have come at a more propitious time for both the advanced and the developing countries of the world because of the pressure to manage natural resources and because of man's capacity to modify the face of the planet. To monitor dynamic phenomena (natural vegetation, crops, glaciers, snow cover), to monitor some of man's environmental impact (strip mining, reservoirs, irrigation, pollution), and to help other countries wisely develop their natural resources, the continuous acquisition of ERTS imagery has become a necessity. Four countries, Brazil, Canada, Italy, and the United States, have ERTS receiving stations in operation. Four additional ERTS receiving stations, in Canada, Chile, Iran, and Zaïre, have been designed, but construction is not yet complete. Australia, India, Japan, Norway, and Upper Volta are all seriously considering building receiving stations.

The United States has pioneered in the creation of a technology which offers us and other nations a method by which all may more wisely use their natural resources. Our small planet has limited supplies of resources which we must learn to manage and conserve for future generations. Through careful observation and planning this can be done—if tools such as ERTS and those designed for future satellites are developed and used to the maximum benefit of all mankind. ERTS–1 then truly is a new window on our planet. Our challenge now is to use this new knowledge in an effective way and to integrate such information into more traditional information systems.

We should also like to mention the foresight of Dr. William T. Pecora, Director, U. S. Geological Survey, 1965–71, and Undersecretary of the Interior, 1971–72. As first Director of the Earth Resources Observation Systems Program of the Department of the Interior (1966–72) he firmly believed that "by going to space we can learn more about the Earth." His scientific integrity and jovial enthusiasm inspired us all to work toward the success of the Earth Resources Technology Satellite (ERTS–1). Unfortunately, he died on July 19, 1972, 4 days prior to the launch of ERTS–1, and consequently never saw the realization of this long-sought goal. We think that he would have been pleased that the results contained in this book confirmed his forecast manyfold.

We wish to take this opportunity to acknowledge the response and efforts of the contributing authors. We also wish to acknowledge the efforts of Mary Ann Milosavich who coordinated the assembly of the book and typed its text; Susan Moorlag who coordinated the graphic materials; the many people of the U.S. Geological Survey who edited the text and prepared the final illustrations; and Priscilla Woll, who reviewed and proofread the manuscript as well as provided guidance in formation of the book.

Richard S. Williams, Jr.

William D. Carter

* Short, N. M., Lowman, P. D., Freden, S. C., and Finch, W. A., 1976, Mission to Earth: Landsat Views the World: NASA SP–360 (in press).

# ERTS-1, A NEW WINDOW ON OUR PLANET


Foreword, by V. E. McKelvey ---------- III

Preface, by Richard S. Williams, Jr., and William D. Carter, editors -- V

Conversion table and list of symbols and abbreviations ---------- XIX

Introduction, by John M. DeNoyer, U.S. Geological Survey ---------- 1

ERTS–1 MSS false-color composites, by Charles F. Withington, U.S. Geological Survey ---------- 3

FIGURE 1. Color composite ERTS–1 image of the upper Chesapeake Bay area -- 4
2. ERTS–1 image of the upper Chesapeake Bay area, band 4 -------- 5
3. ERTS–1 image of the upper Chesapeake Bay area, band 5 -------- 5
4. ERTS–1 image of the upper Chesapeake Bay area, band 6 -------- 5
5. ERTS–1 image of the upper Chesapeake Bay area, band 7 -------- 5
6. The electromagnetic spectrum and ERTS–1 sensor relationships --- 6

## Chapter 1. Applications to Cartography

Introduction, by Alden P. Colvocoresses, U.S. Geological Survey ---- 12

FIGURE 7. Color composite ERTS–1 image of the Denver, Colorado, area in winter ---------- 14
8. Color composite ERTS–1 image of the Denver, Colorado, area in summer ---------- 15
9. Space Oblique Mercator projection ---------- 17
10. ERTS images of southeastern Pennsylvania, showing the thin-cloud penetration capability of band 7 as compared to band 5 ------- 18
11. Comparison of maps and ERTS–1 image of Lake Balkash, U.S.S.R. -- 19
12. Thematic extraction of open water, upper Chesapeake Bay area -- 20
13. Thematic extraction of infrared-reflective vegetation, upper Chesapeake Bay area ---------- 20
14. Space imagery applied to aeronautical charting, Jebel Uweinat area, Libya, Sudan, and United Arab Republic ---------- 21
15. Comparison of nautical chart and ERTS image of Collier Bay, Australia 22

ERTS nominal scenes, by James W. Schoonmaker, Jr., and Robert B. McEwen, U.S. Geological Survey ---------- 23

FIGURE 16. Bisector format of ERTS images at 45° lat ---------- 24
17. ERTS nominal scenes of Florida ---------- 24
18. Gridded color composite ERTS–1 image of the upper Chesapeake Bay ---------- 25

Orthoimage mosaic of New Jersey, by Winston Sibert and Fitzhugh T. Clark, U.S. Geological Survey ---------- 26

FIGURE 19. Color composite ERTS–1 orthoimage mosaic of New Jersey ------- 27

Satellite image maps of the State of Arizona and of Phoenix, by Joseph T. Pilonero, U.S. Geological Survey ---------- 29

FIGURE 20. ERTS–1 image map of Arizona ---------- 30
21. ERTS–1 image map of Phoenix, Arizona ---------- 31

Digital color mosaic of parts of Wyoming and Montana, by Grover Torbert, Bureau of Land Management, and C. J. Robinove, U.S. Geological Survey ---------- 32

FIGURE 22. Computer-processed color composite ERTS–1 mosaic of parts of Wyoming and Montana ---------- 33

Geodetic control in polar regions for accurate mapping with ERTS imagery, by William R. MacDonald, U.S. Geological Survey ---- 34

FIGURE 23. Image and map of the McMurdo Sound region, Antarctica ------ 34

Antarctic cartography, by William R. MacDonald, U.S. Geological Survey ---------- 37

FIGURE 24. Topographic maps and ERTS–1 image mosaic of Drygalski Ice Tongue, Victoria Land coast area ---------- 38
25. Topographic maps and ERTS–1 image mosaic of Cape Adare, Victoria Land coast area ---------- 39
26. Sketch map and ERTS–1 image mosaic of Thwaites Iceberg Tongue, Antarctica ---------- 40
27. Map of McMurdo Sound region compared with ERTS–1 image mosaic ---------- 41
28. Australian map of the Lambert Glacier area of Antarctica compared with an ERTS–1 image mosaic ---------- 42

Cadastral boundaries on ERTS–1 images, by Grover Torbert, Bureau of Land Management, and William R. Hemphill, U.S. Geological Survey ---------- 44

FIGURE 29. Color composite ERTS–1 image of the Sheridan, Wyoming, area -- 45
30. Computer-processed combination of part of the Sheridan ERTS–1 image and cadastral survey delineation of township, range, and section boundaries ---------- 46
31. Standard U.S. Geological Survey map of the Sheridan area of Wyoming ---------- 46

References ---------- 47

## Chapter 2. Applications to Geology and Geophysics

Introduction, by William A. Fischer, U.S. Geological Survey --------- 48

Geologic analysis of the Santa Lucia Range, California, by Donald C. Ross, U.S. Geological Survey ---------- 50

FIGURE 32. Color composite ERTS–1 image of the Salinas Valley and Santa Lucia Range, California ---------- 51
33. ERTS–1 image showing interpretation of photolineaments in the northern Santa Lucia Range, California ---------- 52

An interpretation of the Jordan Rift Valley, by G. F. Brown and A. C. Huffman, U.S. Geological Survey ---------- 53

FIGURE 34. Map of the Red Sea area showing location of tectonic-plate rotation poles ---------- 54
35. Color composite ERTS–1 image mosaic of the Jordan Rift Valley- 55

Geological structure in the western Brooks Range area, by Ernest H. Lathram, U.S. Geological Survey ---------- 56

FIGURE 36. Color composite ERTS–1 image of the western Brooks Range area, Alaska ---------- 57
37. Annotated ERTS–1 image of the western Brooks Range area, Alaska, showing geologic features and place names ---------- 58

Geological evaluation of north-central Arizona, by Donald P. Elston, U.S. Geological Survey ---------- 59

FIGURE 38. Color composite ERTS–1 image of north-central Arizona ------ 60
39. Computer processed four-band color composite ERTS–1 image of north-central Arizona ---------- 61
40. Geologic map of north-central Arizona ---------- 62
41. Geologic map of north-central Arizona compiled on an ERTS–1 image base ---------- 65
42. Fault and lineament map of north-central Arizona compiled on an ERTS–1 image base ---------- 66

Glacial geology and soils in the Midwestern United States, by Roger B. Morrison, U.S. Geological Survey ---------- 67

FIGURE 43. Color composite ERTS–1 image of part of Iowa, west of Des Moines ---------- 68
44. ERTS–1 image, band 7, with interpretation of soil types --------- 70
45. Mosaic of ERTS–1 images, band 7, of west-central Illinois with interpretation of soil types ---------- 71

Enhancement of topographic features by snow cover, by Roger B. Morrison, U.S. Geological Survey ---------- 72

FIGURE 46. Color composite ERTS–1 image of western Nebraska showing snow-enhanced topographic details ---------- 73
47. Geologic terrane map compiled on ERTS–1 image, band 5 ------ 74
48. ERTS–1 image of western Nebraska in summer showing relative lack of topographic detail ---------- 75

Hydrogeology of closed basins and deserts of South America, by George E. Stoertz and William D. Carter, U.S. Geological Survey 76

FIGURE 49. Color composite ERTS–1 image of the Salar de Coipasa region of Bolivia and Chile ---------- 78
50. Geologic and hydrologic interpretation and explanations of features identified in the Salar de Coipasa region ---------- 79
51. Index map of salar revisions ---------- 80
52. Example of outlines of several salars revised by ERTS data ------- 80

Sand seas of the world, by Edwin D. McKee and Carol S. Breed, U.S. Geological Survey ---------- 81

FIGURE 53. Index map of the sand seas of Africa, Asia, Australia, and North America ---------- 82
54. Color composite ERTS–1 image mosaic of the southwest United States desert and the Gran Desierto de Sonora in Mexico ----- 83
55. Color composite ERTS–1 image showing parallel-straight or linear dunes in the Kalahari Desert, of South Africa ---------- 84
56. Color composite ERTS–1 image showing parallel-wavy or crescentic dunes (a megabarchan desert) in Saudi Arabia ---------- 85
57. Color composite ERTS–1 image showing star or radial megadunes in Algeria ---------- 86
58. Color composite ERTS–1 image showing parabolic dunes in the Rajasthan Desert of India ---------- 87
59. Color composite ERTS–1 image showing flat sheets and stringer dunes in South-West Africa ---------- 88

Detection of hydrothermal sulfide deposits, Saindak area, western Pakistan, by Robert G. Schmidt, U.S. Geological Survey ------- 89

FIGURE 60. Digitally enhanced false-color composite ERTS–1 image of the Saindak area of western Pakistan ---------- 90
61. Annotated ERTS–1 image showing location of significant geologic features of the Saindak area of Pakistan ---------- 91

Structural geology and mineral-resources inventory of the Andes Mountains, South America, by William D. Carter, U.S. Geological Survey ---------- 92

FIGURE 62. ERTS–1 image mosaic of the La Paz area, Bolivia, Peru, and Chile 94
63. Image linear map of the La Paz area ---------- 96
64. Relative confidence map of the La Paz area ---------- 97
65. Metallogenic map of the La Paz area ---------- 98
66. Seismic-hazard map of the La Paz area ---------- 98

Clues to geologic structure possibly indicating oil and gas sources, by Ernest H. Lathram, U.S. Geological Survey ---------- 99

FIGURE 67. Color composite ERTS–1 image of foothills and coastal plains near Umiat, Alaska ---------- 100
68. ERTS–1 image of the Umiat area, Alaska, showing structural features and lineation of lakes ---------- 101

Discrimination of rock types and detection of hydrothermally altered areas in south-central Nevada, by Lawrence C. Rowan and Pamela H. Wetlaufer, U.S. Geological Survey, and A. F. H. Goetz, Jet Propulsion Laboratory ---------- 102

FIGURE 69. Stretched-ratio color composite ERTS–1 image of south-central Nevada made from computer compatible tapes ---------- 103
70. Color composite ERTS–1 image of the south-central Nevada area made from computer compatible tapes ---------- 104
71. Conventional color composite ERTS–1 image of the entire south-central Nevada area ---------- 105

New method for monitoring global volcanic activity, by Peter L. Ward and Jerry P. Eaton, U.S. Geological Survey ---------- 106

FIGURE 72. Map showing instrument sites of the prototype volcano-surveillance system ---------- 107
73. Data collection platform, Mount Baker, Washington ---------- 108
74. Graph of seismic activity recorded by a data collection platform at Volcán Fuego, Guatemala ---------- 108

Dynamic environmental phenomena in southwestern Iceland, by Richard S. Williams, Jr., U.S. Geological Survey ---------- 109

FIGURE 75. Color composite ERTS–1 image mosaic of west-central and southwestern Iceland ---------- 110
76. Map of part of west-central and southwestern Iceland ---------- 112

Active faults in the Los Angeles-Ventura area of southern California, by Russell H. Campbell, U.S. Geological Survey ---------- 113

FIGURE 77. Color composite ERTS–1 image of the greater Los Angeles area of southern California especially made to enhance geologic features ---------- 114
78. Annotated ERTS–1 image of the greater Los Angeles area, of southern California showing location of major and minor faults ---------- 115

Environmental geology of the central Gulf of Alaska coast, by Austin Post, U.S. Geological Survey ---------- 117

FIGURE 79. Color composite ERTS–1 image of the central Gulf of Alaska coast ---------- 118

Debris avalanches at Mount Baker Volcano, Washington, by David Frank, U.S. Geological Survey ---------- 120

FIGURE 80. Color composite ERTS–1 image of the Mount Baker area, Washington ---------- 121
81. Enlargement of a part of the Mount Baker image, showing the area of debris avalanches ---------- 122

Structural features related to earthquakes in Managua, Nicaragua, and Cordoba, Mexico, by William D. Carter, U.S. Geological Survey, and Jack N. Rinker, U.S. Army Corps of Engineers ---------- 123

FIGURE 82. Color composite ERTS–1 image of the Managua area, Nicaragua ---------- 124
83. Map of earthquake area, Nicaragua, plotted on ERTS–1 image ---------- 125

References ---------- 126

## Chapter 3. Applications to Water Resources


Introduction, by Morris Deutsch, U.S. Geological Survey ---------- 129

Water resources in the Delaware River basin, by Richard W. Paulson, U.S. Geological Survey ---------- 132

FIGURE 84. Data collection platform sites, Delaware River basin, plotted on ERTS–1 image mosaic ---------- 133

Hydrology of the Wind River basin and adjacent areas of Wyoming, by Lynn M. Shown and J. Robert Owen, U.S. Geological Survey -- 134

FIGURE 85. Color composite ERTS–1 image of the Wind River basin and adjacent areas, Wyoming ---------- 135

Improving estimates of streamflow characteristics, by Este F. Hollyday and Edward J. Pluhowski, U.S. Geological Survey ---------- 136

FIGURE 86. Color composite ERTS–1 image of the Delmarva Peninsula area-- 137
87. Flow diagram of technique for improving estimates of streamflow characteristics ---------- 138

Monitoring water resources in Qom Playa, west-central Iran, by Daniel B. Krinsley, U.S. Geological Survey ---------- 139

FIGURE 88. Color composite ERTS–1 image of the Qom Playa area of west-central Iran on Sept. 22, 1972 ---------- 140
89. Color composite ERTS–1 image of the Qom Playa area of west-central Iran on May 14, 1973 ---------- 141
90. Comparison of the climatic data from Qom with the lake area and volume at Qom Playa, from Sept. 4, 1972, to May 14, 1973-- 142

Lake fluctuations in the Shiraz and Neriz Playas of Iran, by Daniel B. Krinsley, U.S. Geological Survey ---------- 143

FIGURE 91. Color composite ERTS–1 image of the Shiraz and Neriz Playas, Iran, on Sept. 20, 1972 ---------- 144
92. Color composite ERTS–1 image of the Shiraz and Neriz Playas, Iran, on Mar. 1, 1973 ---------- 146
93. Color composite ERTS–1 image of the Shiraz and Neriz Playas, Iran, on Aug. 28, 1973 ---------- 147
94. Diagram showing lake fluctuations at Shiraz and Neriz Playas, 1972–73 ---------- 148
95. A comparison of the climatic data from Neriz with the lake areas and volumes at Shiraz and Neriz Playas, for the period Sept. 2, 1972, to Aug. 28, 1973 ---------- 149

Ecological model in Florida, by Aaron L. Higer, A. Eugene Coker, and Edwin H. Cordes, U.S. Geological Survey ---------- 150

FIGURE 96. Color composite ERTS–1 image mosaic of the State of Florida --- 151
97. Wildlife ecological model, Shark River Slough, Florida ---------- 152
98. Data collection platform, Everglades National Park, south Florida -- 152
99. Surface-water storage model, Shark River Slough, Florida -------- 152
100. Wood storks nesting ---------- 152

Turbidity in Lake Superior, by Michael Sydor, University of Minnesota- 153

FIGURE 101. Correlation of intensity from band 5 of ERTS–1 image with turbidity ---------- 153
102. Density-sliced image using color to show turbidity ---------- 153
103. Harbor and lake image density levels identified by corresponding turbidity levels on ERTS–1 image ---------- 154
104. Computer printout of image-density levels from computer compatible tapes ---------- 154
105. Index of map of Lake Superior study area ---------- 154
106. Part of ERTS–1 image showing the Lake Superior study area ------ 155
107. Graph showing variation in MSS band signals ---------- 155

Dynamics of suspended-sediment plumes, by Edward J. Pluhowski, U.S. Geological Survey ---------- 157

FIGURE 108. Color composite ERTS–1 image of the Lake Ontario-Niagara River area, on Sept. 3, 1973 ---------- 156
109. Part of an ERTS–1 image showing sediment plumes in Lake Ontario on Apr. 12, 1973 ---------- 157
110. Part of an ERTS–1 image showing sediment plumes in Lake Ontario on Apr. 29, 1973 ---------- 157
111. Part of an ERTS–1 image made on Sept. 3, 1973, enlarged and color enhanced by Stanford University's ESIAC console, showing the Niagara River plume ---------- 158

Water-management model of the Florida Everglades, by Aaron L. Higer, Edwin H. Cordes, and A. Eugene Coker, U.S. Geological Survey ---------- 159

FIGURE 112. Color composite ERTS–1 image of the Everglades National Park area of Florida ---------- 160
113. Annotated ERTS–1 image showing water-management conservation areas in the Everglades National Park area of Florida ---------- 161
114. Determination of surface-water storage in Conservation Area No. 1 161
115. Electronically processed part of ERTS–1 image of Conservation Area No. 1 ---------- 161

Suspended sediment in Great Slave Lake, Northwest Territories, Canada, by Donald R. Wiesnet, National Oceanic and Atmospheric Administration ---------- 162

FIGURE 116. Color composite ERTS–1 image of the Great Slave Lake area, Northwest Territories, Canada ---------- 163

Discovery and significance of the Beech Grove lineament of Tennessee, by G. K. Moore and Este F. Hollyday, U.S. Geological Survey ---------- 164

FIGURE 117. Color composite ERTS–1 image of central Tennessee on Oct. 17, 1972, showing location of the Beech Grove lineament ---------- 165
118. Index map showing the location of the Beech Grove lineament ---------- 166
119. Color composite ERTS–1 image of central Tennessee on Dec. 28, 1972 ---------- 167

Western Lake Superior ice, by Michael Sydor, University of Minnesota ---------- 169

FIGURE 120. Color composite ERTS–1 image of western Lake Superior showing typical ice pack ---------- 170
121. Density-sliced ERTS–1 image using color to identify areas of intense ice packing ---------- 171
122. Graph showing albedo, western Lake Superior ---------- 171
123. Graph showing ice growth, Duluth-Superior harbor ---------- 172
124. Graph showing estimate of volume of ice cover that is highly packed, western Lake Superior ---------- 172

Measuring snow-covered area to predict reservoir inflow, by Robert M. Krimmel and Mark F. Meier, U.S. Geological Survey ---------- 173

FIGURE 125 Color composite ERTS–1 image mosaic of the Puget Sound region, Washington ---------- 174
126. Index map of Cascade Mountains drainage basins ---------- 174
127. Graph showing percentage of drainage basin area covered by snow 175

Mapping snow extent in the Sierra Nevada of California, by Donald R. Wiesnet and David F. McGinnis, National Oceanic and Atmospheric Administration ---------- 176

FIGURE 128. Composite of parts of three different ERTS–1 images (band 4) showing retreat of snowpack at three stages during the spring of 1973 ---------- 177

Surging and nonsurging glaciers in the Pamir Mountains, U.S.S.R., by Robert M. Krimmel, Austin Post, and Mark F. Meier, U.S. Geological Survey ---------- 178

FIGURE 129. Color composite ERTS–1 image of the Pamir Mountains, U.S.S.R. 179

Measuring the motion of the Lowell and Tweedsmuir surging glaciers of British Columbia, Canada, by Austin Post, Mark F. Meier, and Lawrence R. Mayo, U.S. Geological Survey ---------- 180

FIGURE 130. Color composite ERTS–1 image of the Lowell Glacier and Tweedsmuir Glacier areas of British Columbia, Canada ---------- 181
131. Annotated ERTS–1 image of the Lowell and Tweedsmuir Glaciers, British Columbia, Canada ---------- 182
132. Graph showing velocity of movement of the Tweedsmuir Glacier in 1973 ---------- 183
133. Maps showing displacement vectors and changes in medial moraines of the Lowell Glacier, 1954–73 ---------- 184

Monitoring the motion of surging glaciers in the Mount McKinley massif, Alaska, by Mark F. Meier, U.S. Geological Survey ---------- 185

FIGURE 134. Color composite ERTS–1 image of the Mount McKinley area, Alaska ---------- 186
135. Annotated enlargement of ERTS–1 image of the Mount McKinley area, Alaska ---------- 187

Vatnajökull icecap, Iceland, by Richard S. Williams, Jr., U.S. Geological Survey ---------- 188

FIGURE 136. Annotated enlargement of ERTS–1 image of the Vatnajökull area, Iceland, in the winter ---------- 189
137. Annotated color composite ERTS–1 image of the Vatnajökull area Iceland, in the summer ---------- 191
138. Annotated color composite ERTS–1 image of the Vatnajökull area, Iceland, in the fall ---------- 192
139. Sketch map of the Vatnajökull area of Iceland ---------- 193

Glaciology in Antarctica, by William R. MacDonald, U.S. Geological Survey ---------- 194

FIGURE 140. Enlargement of ERTS–1 image of Erebus Ice Tongue, Antarctica ---------- 194
141. ERTS–1 image of Ronne Ice Shelf, Antarctica ---------- 194
142. Sketch map of the Lützow-Holm Bay area of Antarctica compiled from ERTS imagery ---------- 195

Monitoring flood inundation, by Roger B. Morrison and P. Gary White, U.S. Geological Survey ---------- 196

FIGURE 143. Annotated ERTS–1 image showing confluence of the Mississippi and Ohio Rivers in preflood condition on Nov. 24, 1972 ---------- 197
144. Annotated ERTS–1 image showing confluence of the Mississippi and Ohio Rivers in flood on May 5, 1973 ---------- 199
145. Annotated ERTS–1 image showing confluence of the Mississippi and Ohio Rivers as rivers retreat to normal stage on June 10, 1973 ---------- 200
146. Annotated ERTS–1 image of the St. Louis area, Missouri, showing preflood conditions of the Missouri, Mississippi, and Illinois Rivers on Aug. 28, 1972 ---------- 201
147. ERTS–1 image showing flood swollen rivers in the St. Louis area on Mar. 31, 1973 ---------- 202
148. Preflood color composite ERTS–1 image of Gila River Valley, Arizona, on Aug. 22, 1972 ---------- 203
149. Color composite ERTS–1 image shows dramatic increase in the San Carlos Lake and soil erosion areas upstream that resulted from the flood of Oct. 21, 1972 ---------- 204
150. Preflood ERTS–1 image (band 7) of the Gila River Valley, Arizona, on Aug. 22, 1972 ---------- 205
151. Postflood ERTS–1 image (band 7) of the Gila River Valley, Arizona, on Nov. 2, 1972 ---------- 205
152. Preflood ERTS–1 image (band 5) of the Gila River Valley, Arizona, on Aug. 22, 1972 ---------- 206
153. Postflood ERTS–1 image (band 5) of the Gila River Valley, Arizona, on Nov. 2, 1972 ---------- 206
154. Preflood ERTS–1 image of southwestern Iowa on Aug. 14, 1972 ---------- 207
155. Annotated ERTS–1 image mosaic showing the West and East Nishnabotna Rivers in flood on Sept. 19, 1972 ---------- 208

Optical processing of ERTS data for determining extent of the 1973 Mississippi River flood, by Morris Deutsch, U.S. Geological Survey 209

FIGURE 156. Preflood and flood ERTS–1 image mosaics of the central Mississippi valley, 1972–73, compared with optically combined temporal color composite image mosaic to show areas of flooding 211
157. Temporal color composite of preflood October ERTS–1 image and postflood March and May ERTS–1 images of the St. Louis area 212

Monitoring cloud-seeding conditions in the San Juan Mountains of Colorado, by Archie M. Kahan, Bureau of Reclamation 214

FIGURE 158. Annotated color composite ERTS–1 image of the San Juan Mountain region, Colorado, showing location of data collection platforms 215
159. Wolf Creek Pass data collection platform 216

TABLE 1. Samples of Project Skywater DCS platform data 216

Hydrology of arid and semiarid areas, by J. Robert Owen and Lynn M. Shown, U.S. Geological Survey 217

160. Annotated color composite ERTS–1 image of the northern Colorado Plateau 218

References 220

## Chapter 4. Applications to Land-Use Mapping and Planning

Introduction, by James R. Anderson, U.S. Geological Survey 223

Land use in northeast Colorado, by Larry D. Cast, Bureau of Reclamation 225

FIGURE 161. Color composite ERTS–1 image of the South Platte River valley, Colorado 226
162. Annotated ERTS–1 image of the South Platte River valley showing irrigated lands, grasslands, and dryland farming areas 227

Thematic mapping of forested and cultivated land in Alabama, by Gary W. North, U.S. Geological Survey, and Neal G. Lineback, University of Alabama 228

FIGURE 163. Color composite ERTS–1 image mosaic of the State of Alabama 229

Monitoring change in land use over large regions, by John L. Place, U.S. Geological Survey 230

FIGURE 164. Color composite ERTS–1 image of the Phoenix area, Arizona 231
165. Land-use map of the Phoenix area, 1970, with changes detected by ERTS through April 1973 232
166. Color composite ERTS–1 image of the Phoenix area, Arizona, on Oct. 16, 1972 233

Computer-aided mapping of land use, by Richard Ellefsen, California State University, and Leonard Gaydos and James R. Wray, U.S. Geological Survey 234

FIGURE 167. Color composite ERTS–1 image of the San Francisco Bay area, California 235
168. Enlarged aerial photograph-map pair of Hayward, California 237
169. Part of a computer-classified land-use map of the San Francisco Bay region 238
170. Map, orthophotograph, two enlargements of color composite ERTS–1 images, and computer-classified land-use map of a small area near Phoenix, Arizona 239
171. Color composite ERTS–1 image of Phoenix, Arizona, on Oct. 16, 1972 240
172. Color composite ERTS–1 image of Phoenix, Arizona, on May 2, 1973 241

References 242

## Chapter 5. Applications to Agriculture, Forestry, and Rangeland Management


Introduction, by Grover Torbert, Bureau of Land Management ------- 243

Monitoring forest-fire burn areas in Alaska, by Grover Torbert, Bureau of Land Management ---------- 244

FIGURE 173. Annotated color composite ERTS–1 image of a forest fire in northern Alaska ---------- 245

Detection of short-term changes in vegetation of southern Arizona, by Raymond M. Turner, U.S. Geological Survey ---------- 246

FIGURE 174. Color composite ERTS–1 image of the Tucson area, Arizona---- 247

175. Thematic extraction of relatively dense vegetation from ERTS–1 images by ratioing (late summer, winter, and spring) -------- 248

Monitoring ephemeral livestock-forage production, by R. Gordon Bentley, Jr., Bureau of Land Management ---------- 249

FIGURE 176. Color composite ERTS–1 image of the Phoenix area, Arizona-- 250

177. Annotated color composite ERTS–1 image of the Phoenix area, Arizona, showing perennial and ephemeral vegetation and production ---------- 251

References ---------- 252


## Chapter 6. Applications to Environmental Monitoring


Introduction, by C. F. Withington, U.S. Geological Survey ---------- 253

Changes in landscape due to strip mining, by John B. Rehder, University of Tennessee ---------- 254

FIGURE 178. Changes in the landscape created by strip mining on the Cumberland Plateau, Tennessee, Apr. 18 through Oct. 15, 1972, from aerial photography and ERTS–1 imagery ---------- 255

179. Strip mines on the Cumberland Plateau from enlargement of ERTS–1 image acquired on Oct. 15, 1972 ---------- 256

180. Strip mines on the Cumberland Plateau from NASA high-altitude aerial photography acquired on Apr. 18, 1972 ---------- 257

Oil-well fire on ERTS–1 images, by C. F. Withington, U.S. Geological Survey, and Roy M. Breckenridge, Wyoming Geological Survey ---------- 258

FIGURE 181. Smoke plume from wildcat oil-well fire, Converse County, Wyoming, on ERTS–1 image, Dec. 20, 1973 ---------- 259

182. Enlargements of three ERTS–1 images showing comparison of reflectance of smoke plume ---------- 260

Air pollution from the Ohio River and Monongahela River valleys, by Fred R. Brown and Fred S. Karn, U.S. Bureau of Mines ---------- 261

FIGURE 183. Color composite ERTS–1 image of smoke plumes from power-generating plants in the Ohio River and Monongahela River valleys ---------- 262

184. Index map of the Ohio River and Monongahela River valleys ---- 263

185. Enlargement of part of image of the Beverly, Ohio, area showing smoke plumes on different MSS bands on Jan. 12, 1973 -------- 264

186. Enlarged parts of four ERTS–1 images showing steam plumes from coke ovens near Pittsburgh, Pennsylvania, November 1972 through March 1973 ---------- 265

A Lake Michigan "Whiting," by Alan E. Strong, National Oceanic and Atmospheric Administration ---------- 266

FIGURE 187. Color composite ERTS–1 image mosaic of Lake Michigan ------ 267

188. Nonconventional color composite ERTS–1 image mosaic of Lake Michigan to emphasize "whiting" phenomenon ---------- 268

189. ERTS–1 image mosaic of band 4 images of Lake Michigan ----- 269

Algal blooms in Utah Lake, by Alan E. Strong, National Oceanic and Atmospheric Administration ---- 270

FIGURE 190. Color composite ERTS–1 image of algal blooms in Utah Lake --- 271
191. Comparison of a part of ERTS–1 image, showing algal blooms in Utah Lake on bands 4, 5, 6, and 7 ---- 272

Wetland classification and mapping along the south Atlantic coast, by Virginia Carter, U.S. Geological Survey, and Richard R. Anderson and John W. McGinness, Jr., The American University ---- 273

FIGURE 192. Enlargement of part of band 7 ERTS–1 image of the Charleston area, South Carolina ---- 274
193. Wetland map of the Charleston, Lake Moultrie, and Cooper River area, South Carolina ---- 274
194. ERTS–1 image of the Charleston area, South Carolina, showing wetland vegetation on Oct. 12, 1972 ---- 275
195. ERTS–1 image of the Charleston area, South Carolina, showing wetland vegetation on Mar. 23, 1973 ---- 276

Coastal wetland mapping in the central Atlantic region, by Virginia Carter, U.S. Geological Survey, and Richard R. Anderson, The American University ---- 277

FIGURE 196. Color composite ERTS–1 image of the lower Chesapeake Bay -- 278
197. Enlargement of band 7 ERTS–1 image of the Chincoteague Bay salt-marsh complex ---- 279
198. Wetland map of the Chincoteague Bay salt-marsh complex ---- 279

Computer mapping of coastal wetlands, by Virginia Carter, U.S. Geological Survey ---- 280

FIGURE 199. Color composite ERTS–1 image of the Chincoteague Bay area of the Virginia Eastern Shore on Aug. 30, 1973 ---- 281
200. Computer-processed wetland map of the Chincoteague Bay salt-marsh complex ---- 282

Tidal effects in coastal wetlands, by Virginia Carter, U.S. Geological Survey, and Richard R. Anderson, The American University ---- 283

FIGURE 201. Color composite ERTS–1 image of the Georgia-South Carolina coast and band 7 ERTS–1 image of Port Royal Sound, South Carolina, on June 3, 1973, at high tide ---- 284
202. Color composite ERTS–1 image of the Georgia-South Carolina coast and band 7 ERTS–1 image of Port Royal Sound, on Apr. 28, 1973, at low tide ---- 285

Wetland mapping in a large tidal brackish-water marsh in Chesapeake Bay, by Virginia Carter, U.S. Geological Survey, John W. McGinness, Jr., and Richard R. Anderson, The American University 286

FIGURE 203. Color composite ERTS–1 image of the Delmarva Peninsula and band 7 ERTS–1 image of Nanticoke Marsh on Oct. 10, 1972 --- 287
204. Color composite ERTS–1 image of the Delmarva Peninsula and band 7 ERTS–1 image of Nanticoke Marsh on July 7, 1973 ---- 288
205. Wetland map of Nanticoke Marsh compiled from ERTS images --- 289

Environmental assessment of remote areas of Colombia, South America, by William D. Carter, U.S. Geological Survey ---- 290

FIGURE 206. Color composite ERTS–1 image of southeastern Colombia, South America ---- 291
207. A portion of U.S. Air Force Operational Navigation Chart (ONC L 26) of southeastern Colombia ---- 292

Man's impact upon wetlands, by Virginia Carter, U.S. Geological Survey, and Linda Alsid and Richard R. Anderson, The American University ---- 293

FIGURE 208. Color composite ERTS–1 image of the New Jersey-Delaware coastal wetlands ---- 294
209. Color composite ERTS–1 image of the Georgia coastal wetlands near Savannah ---- 295

Selection of a road alinement through the Great Kavir in Iran, by Daniel B. Krinsley, U.S. Geological Survey ---------- 296

FIGURE 210. Index map of Iran showing location of the Great Kavir ---------- 297
211. Color composite ERTS–1 image of the Great Kavir in its driest period on Sept. 20, 1972 ---------- 298
212. Color composite ERTS–1 image of the Great Kavir in its wettest period on May 12, 1973 ---------- 299

Tornado tracks, by Este F. Hollyday, U.S. Geological Survey, and James G. Cook, U.S. Army Corps of Engineers ---------- 300

FIGURE 213. Color composite ERTS–1 image of tornado tracks in the William B. Bankhead National Forest near Guin, Alabama ---------- 301

References ---------- 302

## Chapter 7. Applications to Conservation

Introduction, by Richard D. Curnow, U.S. Fish and Wildlife Service -- 303

Archaeological analysis of imagery of Chaco Canyon region, New Mexico, by Thomas R. Lyons and James I. Ebert, National Park Service, and Robert K. Hitchcock, University of New Mexico--- 304

FIGURE 214. Index map showing location of the Chaco Canyon National Monument, New Mexico ---------- 305
215. Color composite ERTS–1 image of the Chaco Canyon National Monument, New Mexico ---------- 306

Cape Cod and the Cape Cod National Seashore of Massachusetts, by Richard S. Williams, Jr., U.S. Geological Survey ---------- 307

FIGURE 216. Color composite ERTS–1 image of the Cape Cod area of Massachusetts ---------- 308
217. Part of the Boston sheet of the International Map of the World showing the same area as figure 216 ---------- 309

Land-use planning in Yellowstone National Park, Wyoming, Montana, and Idaho, by Harry W. Smedes, U.S. Geological Survey ------ 310

FIGURE 218. Color composite ERTS–1 image of the Yellowstone National Park and vicinity on Nov. 23, 1972 ---------- 311
219. Color composite ERTS–1 image of the Yellowstone National Park and vicinity on Aug. 7, 1972 ---------- 313
220. High-altitude color aerial photomosaic of the Yellowstone National Park ---------- 314
221. Computer-processed terrain map of the Yellowstone National Park made from computer compatible tapes ---------- 315

The Great Dismal Swamp of Virginia and North Carolina, by Virginia Carter, U.S. Geological Survey ---------- 316

FIGURE 222. Map of the Great Dismal Swamp study area, Virginia-North Carolina ---------- 317
223. Enlargement of part of color composite ERTS–1 image showing the Great Dismal Swamp ---------- 317
224. Color composite ERTS–1 image of northern Pamlico Sound and the Great Dismal Swamp with partial snow cover on Feb. 13, 1973 -- 319
225. Color digital display of the Great Dismal Swamp in simulated false-color infrared ---------- 320
226. Thematic extraction of Atlantic white-cedar, Great Dismal Swamp-- 320
227. Thematic extraction of surface water below deciduous trees, Great Dismal Swamp ---------- 320
228. Thematic extraction of drier deciduous areas, Great Dismal Swamp 320

Monitoring breeding habitat of migratory waterfowl, by David S. Gilmer and A. T. Klett, U.S. Fish and Wildlife Service, and Edgar A. Work, Environmental Research Institute of Michigan ------- 321

TABLE 2. Part of a computer printout for the July 7, 1973, ERTS–1 image (fig. 230) showing size-frequency distribution of surface water and location and size of water bodies ---------- 322

FIGURE 229. Index map showing coverage provided by three ERTS images in a primary waterfowl-breeding area in North Dakota --------- 323
230. Color composite ERTS–1 image showing waterfowl-habitat study area near Jamestown, North Dakota ---------- 324

References ---------- 325

## Chapter 8. Applications to Oceanography

Introduction, by William J. Campbell, U.S. Geological Survey -------- 326

Mapping surface current flow in turbid nearshore waters of the northeast Pacific, by Paul R. Carlson, U.S. Geological Survey ------- 328

FIGURE 231. Winter ERTS–1 image of turbid-water plumes along the northern California coast on Jan. 6, 1973 ---------- 329
232. Spring ERTS–1 image of turbid-water plumes along the northern California coast on Apr. 24, 1973 ---------- 329

Detection of turbidity dynamics in Tampa Bay, Florida, by A. Eugene Coker, Aaron L. Higer, and Carl R. Goodwin, U.S. Geological Survey ---------- 330

FIGURE 233. Color composite ERTS–1 RBV image of the Tampa Bay area of Florida ---------- 331
234. Oblique aerial photograph of shell-dredging operations and turbidity plume ---------- 332
235. Sketch map showing turbidity in Tampa Bay ---------- 332
236. Velocity-vector grid of turbidity in Tampa Bay ---------- 332
237. Black and white photograph of RBV bands enchanced by a color-additive viewer and sketch map of turbidity plume ---------- 333

Movement of turbid-water masses along the Texas coast, by Ralph E. Hunter, U.S. Geological Survey ---------- 334

FIGURE 238. Turbidity patterns in the Gulf of Mexico and Galveston Bay on annotated ERTS–1 image ---------- 335
239. Turbidity patterns along the Texas coast between Galveston and Pass Cavallo on annotated ERTS–1 image ---------- 336

Tracking ice floes by sequential ERTS imagery, by William J. Campbell, U.S. Geological Survey ---------- 337

FIGURE 240. Ice floes in eastern Beaufort Sea in the Arctic on ERTS–1 image of Aug. 19, 1972 ---------- 338
241. Map showing trajectories of two ice floes ---------- 339

Ice lead and polynya dynamics, by William J. Campbell, U.S. Geological Survey ---------- 340

FIGURE 242. ERTS–1 image of the ice cover in the central Beaufort Sea on Apr. 5, 1973 ---------- 341
243. ERTS–1 image of the ice cover in the central Beaufort Sea on Apr. 6, 1973 ---------- 342

Seasonal metamorphosis of sea ice, by William J. Campbell, U.S. Geological Survey ---------- 343

FIGURE 244. ERTS–1 image mosaic of large ice floes in the eastern Beaufort Sea on June 16, 1973, before onset of the summer melt -------- 344
245. ERTS–1 image mosaic of large ice floes in the eastern Beaufort Sea 17 days later ---------- 345

Dynamics of arctic ice-shear zones, by William J. Campbell, U.S. Geological Survey ---------- 346

FIGURE 246. ERTS–1 image of northwest coast of Banks Island Northwest Territories, Canada, on Apr. 10, 1973 ---------- 347
247. ERTS–1 image of northwest coast of Banks Island, Northwest Territories, Canada, 24 hours later ---------- 348
248. ERTS–1 image of northwest coast of Banks Island, Northwest Territories, Canada, 17 days after figure 247 was imaged ---------- 349

Morphology of Beaufort Sea ice, by William J. Campbell, U.S. Geological Survey ---------- 350

FIGURE 249. ERTS–1 image mosaic of eastern Beaufort Sea on Aug. 22, 1972 -- 351
250. ERTS–1 image mosaic of western Beaufort Sea on Aug. 22, 1972-- 353
251. ERTS–1 image mosaic of eastern Beaufort Sea area on Sept. 8, 1972 354
252. Polar projection map of the North Pole from Nimbus–5 ESMR data- 355

Flooding of sea ice by the rivers of northern Alaska, by Peter W. Barnes and Erk Reimnitz, U.S. Geological Survey ---------- 356

FIGURE 253. ERTS–1 image showing an area of river flooding on sea ice near Prudhoe Bay, Alaska, on May 24, 1973 ---------- 357
254. ERTS–1 image showing an area of river flooding on sea ice near Prudhoe Bay, Alaska, on May 26, 1973 ---------- 358
255. ERTS–1 image showing an area of river flooding on sea ice near Prudhoe Bay, Alaska, on May 27, 1973 ---------- 359

Influence of sea ice on sedimentary processes off northern Alaska, by Erk Reimnitz and Peter W. Barnes, U.S. Geological Survey--- 360

FIGURE 256. Annotated color composite ERTS–1 image of the Prudhoe Bay area, Alaska, on June 14, 1973 ---------- 361

References ---------- 362

## CONVERSION TABLE

1 board foot measure=144 cubic inches.
1 centimeter=0.39 inch.
1 hectare=2.47 acres.
1 kilogram=2.2 pounds.
1 kilometer=0.62 mile.
1 liter per second=0.04 cubic foot per second.
1 meter=3.28 feet.
1 micrometer=0.00004 inch.
1 microradian=0.057 degree.
1 millimeter=0.04 inch.
1 nautical mile=1.15 statute miles.

## ABBREVIATIONS

A --------Angstrom (=nanometer).
AIDJEX ---Arctic Ice Dynamics Joint Experiment.
C --------Celsius.
cm -------centimeter.
CCT ------computer compatible tape.
$m^3$ -------cubic meter.
$m^3/s$ ------cubic meters per second.
DCP ------data collection platform.
DCS ------data collection system.
EROS -----Earth Resources Observation Systems.
ERTS -----Earth Resources Technology Satellite.
ESIAC ----electronic satellite image analysis console.
ESMR -----electronically scanning microwave radiometer.
fbm ------foot board measure.
g-cal -----gram-calorie
G.m.t. ----Greenwich mean time.
ha -------hectare.
h --------hour.
IBM ------International Business Machines.
IMW -----International Map of the World.
JTU ------Jackson turbidity units.
K --------kelvin.
kg -------kilogram.
km -------kilometer.
km/h -----kilometers per hour.
kn -------knots.
kWh ------kilowatt hour.
lat -------latitude.
l/s -------liters per second.
long -----longitude.
m --------meter.
m/s ------meters per second.
$\mu$m -------micrometer.
$\mu$rad ------microradian.
mg/l -----milligrams per liter.
mm ------millimeter.
min ------minute.
mo -------month.
MSS ------multispectral scanner.
NASA ----National Aeronautics and Space Administration.
NOAA ----National Oceanic and Atmospheric Administration.
nmi ------nautical miles.
pixel -----picture element of ERTS–1 image (unit of area measurement: 79m×56m)
PDP ------Programmable Digital Processor.
RBV ------return beam vidicon.
rms ------root mean square.
s --------second
$km^2$ ------square kilometer.
t ---------tonne ($10^3$ kg).
UTM -----Universal Transverse Mercator.
VHRR ----very high resolution radiometer.
yr -------year.

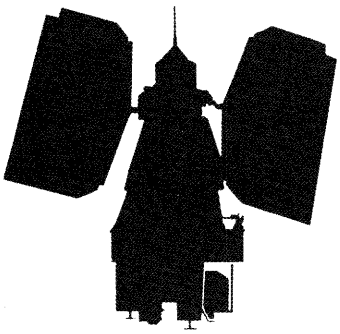

# ERTS-1, A NEW WINDOW ON OUR PLANET

Richard S. Williams, Jr., and William D. Carter, Editors

## INTRODUCTION

By John M. DeNoyer,
U.S. Geological Survey

An objective of the ERTS Program is to obtain one-time imaging of the land areas of the world; the ERTS–1 spacecraft has accomplished approximately 80 percent of this task.

The data base acquired by ERTS–1 is also a documentation of environmental conditions for the entire North American continent. This documentation will be of critical importance and will form a baseline for the recognition of environmental changes that may occur in the future. The capability to make continued comparable observations will be necessary to use effectively and wisely this baseline of information. An objective, factual data base will be essential to both developers and environmentalists as large-scale resource production is pursued.

The ERTS spacecraft is providing a data base that is used by many scientific disciplines. The fact that a common data base is useful to so many is a significant accomplishment in itself, establishing interdisciplinary communications and evolving multidisciplinary programs. The advantages of newly established channels of scientific communication may well be as important as many of the benefits to individual disciplines.

The entire North American continent has been imaged at least once during the ERTS–1 experiment; many parts of North America have been imaged several times. This repetitive coverage has provided a data base used in examining changes that occur from natural and manmade causes and has opened a new field for documenting and understanding changes that occur on the surface of the Earth. No longer is it assumed that a one-time picture accurately describes the surface phenomena. Optimum times for observing different phenomena vary seasonally. For example, the total extent of forests can be mapped during the summer. Separation of deciduous trees and evergreens can be more easily accomplished using both summer and winter imagery. The relation of vegetation to soil moisture, soil type, and underlying geology is also more apparent by seasonal observations. Topographic features are made more apparent by thin snow cover or water-saturated soil. Observing these changing conditions at any one location will require a number of years, if not decades, for data acquisition. The optimum interpretation often requires observation under different conditions (for example, low Sun angle of illumi-

nation) even though the phenomena being observed (such as topography) may be relatively static.

The ERTS spacecraft is in a near-polar orbit; it travels around the Earth every 103 min and can image selected portions of the Earth on each orbit. The satellite has capability for international data acquisition, and international interest in the initial ERTS investigations was in fact high. An even larger number of proposals for follow-up international investigations has been submitted. International training courses and workshops in the use of ERTS data have been conducted during the past few years, and plans call for a continuation of these training programs. Some nations have made major investments to be able to utilize ERTS data effectively. Canada and Brazil have constructed data-reception and data-processing facilities that are being used directly with ERTS, and other nations are actively negotiating with NASA to create similar capabilities.

Data from ERTS can be interpreted through analysis of photographic-type images or through highly sophisticated automatic information-extraction procedures. Every gradation between these two extremes of sophistication in analytical methods can be found in the data utilization program. This range of techniques opens the door for wide and extensive benefits to be obtained by a large segment of the world's population.

All data received and processed from ERTS are available to anyone throughout the world. Several data formats are available to match user's needs, but the investigator can do additional processing to meet his specific needs. The contributions included in this professional paper illustrate a number of applications of ERTS data. Several additional studies are also being conducted. Technical reports on the NASA-sponsored ERTS investigations can be obtained through the Department of Commerce, National Technical Information Service (NTIS), Springfield, Virginia 22151. Summaries of results are published on a weekly basis. Topics of interest can be identified from these summaries, and brief interim or comprehensive final reports can be obtained from NTIS. A number of scientific symposia and other meetings have been convened since the launch of ERTS–1.

The ERTS–1 spacecraft and ground processing system have been an outstanding technological success, a good example of the application of space technology to the solution of man's problems on Earth.

# ERTS-1 MSS FALSE-COLOR COMPOSITES

By Charles F. Withington,
U.S. Geological Survey

False-color or color-infrared composite pictures are made from multispectral imagery taken by NASA's ERTS–1 from an altitude of 915 km. Such a picture is the one of the upper Chesapeake Bay area (fig. 1). The scale of an 18.5- × 18.5-cm image (9- × 9-in. print) is 1:1,000,000; each image encompasses an area of 34,000 km². The four black and white ERTS MSS images (figs. 2–5) are in four different bands of the electromagnetic spectrum (fig. 6): the green band (designated band 4 on ERTS imagery) approximately 0.5–0.6 $\mu$m; the red band (band 5) approximately 0.6–0.7 $\mu$m; and 2 bands in the near-infrared range, band 6, 0.7–0.8 $\mu$m and band 7, 0.8–1.1 $\mu$m. The two infrared bands measure the reflectance of the Sun's rays off the surface of the Earth outside the range of light sensitivity of the human eye. One of the best reflecting materials is chlorophyll; generally speaking, the healthier the vegetation, the brighter the reflectance. False-color imagery is made by projecting the different bands through the proper filters and combining them. Red is assigned to the near-infrared, thus vegetation appears red; the healthier the vegetation, the redder the image. Water absorbs the Sun's rays, so clear water appears black on infrared. However, silt in water reflects the Sun's rays and appears light blue on the image. Buildings and roads of cities also appear in bluish-gray hues.

In the image of the upper Chesapeake Bay area (fig. 1), taken Oct. 11, 1972, the predominant feature is Chesapeake Bay extending from north to south near the eastern edge of the image. The Delmarva Peninsula is east of the bay. Baltimore, Md., is near the top center; Washington, D.C., is just left of the center of the image. The vigorous vegetation of urban open spaces can be easily seen, such as the Mall and Hains Point in Washington.

Urban areas stand out plainly; notice the growth patterns radiating out from the larger cities. Urban and suburban growth can be measured and monitored with subsequent ERTS images, providing valuable information for regional and transportation planners.

Notice that part of the course of the Potomac River (center part of image) is light blue. This is the silt that resulted from a storm that traveled northward up the coast on October 5–7 and dumped more than 25 mm of rain on the headwaters of this river. Tidal action has restricted the dispersion of sediment in the estuary of this river.

The bare ground (white) seen east of Chesapeake Bay are fields from which crops have been harvested. The redder tone in the far upper right is a

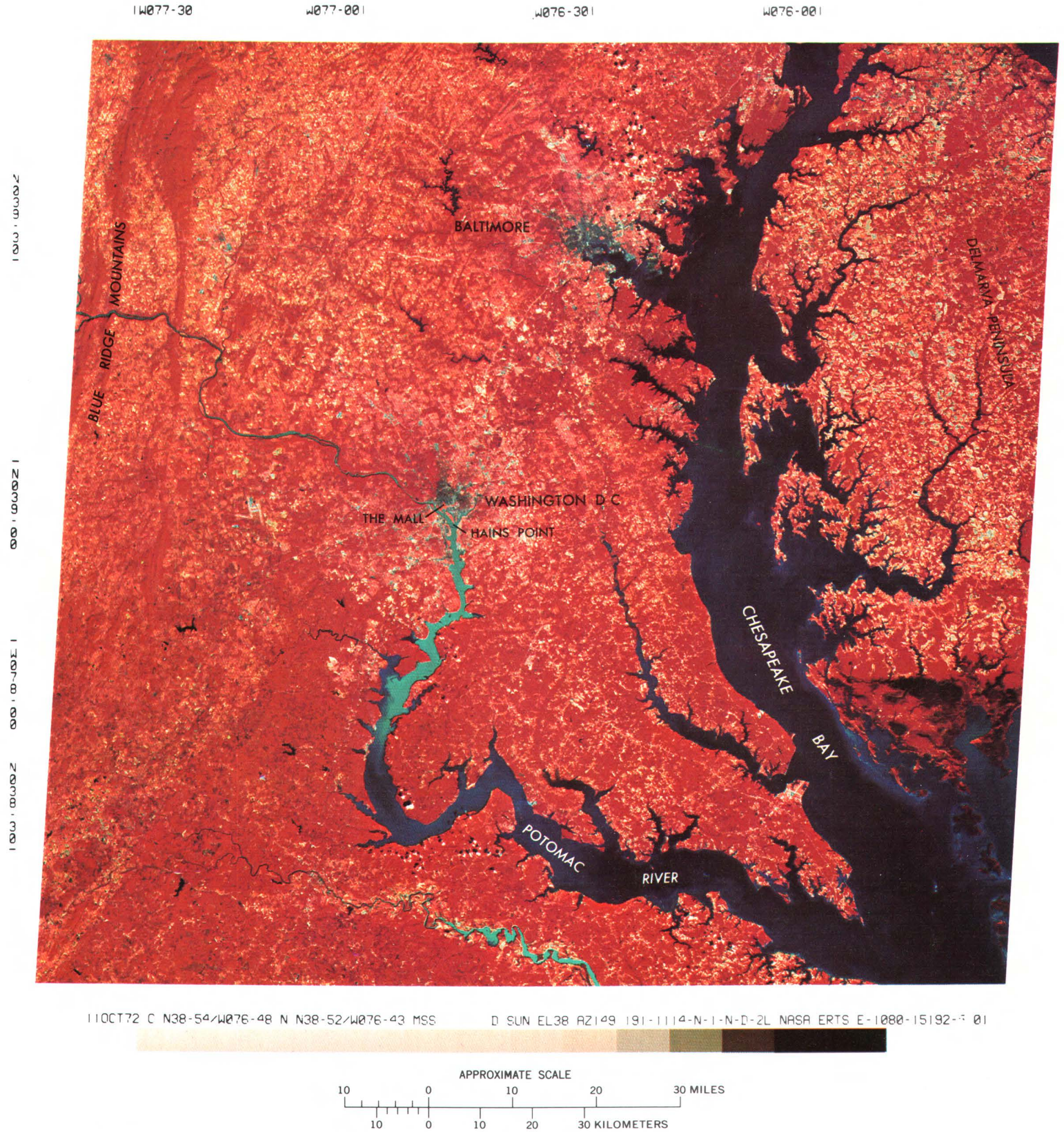


FIGURE 1.—Annotated color composite ERTS–1 image of the upper Chesapeake Bay area made by combining bands 4, 5, and 7 (1080–15192).

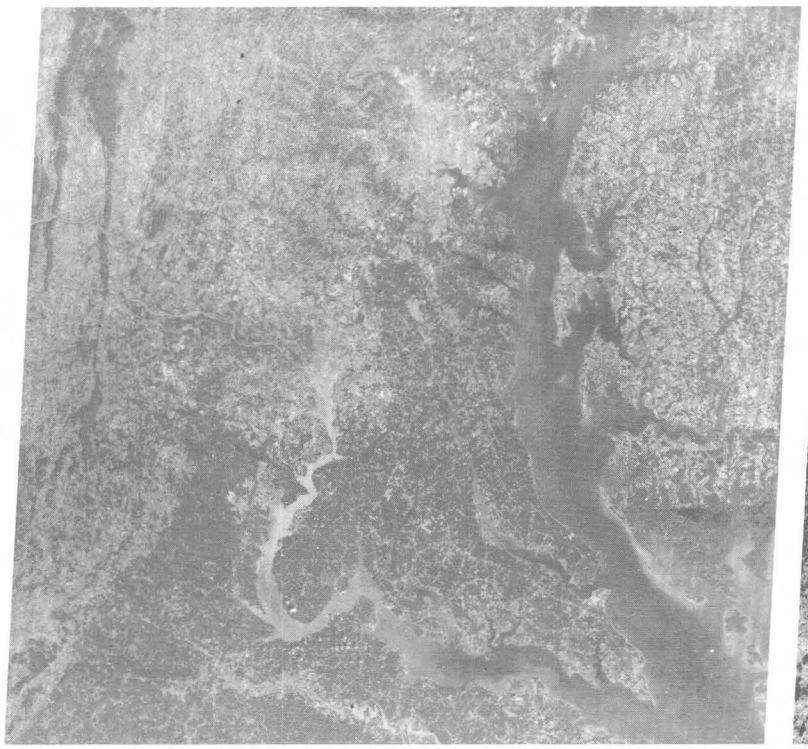

FIGURE 2.—ERTS–1 image of the upper Chesapeake Bay area, showing reflectance in the 0.5- to 0.6-$\mu$m (green) range of the spectrum (1080–15192, band 4).

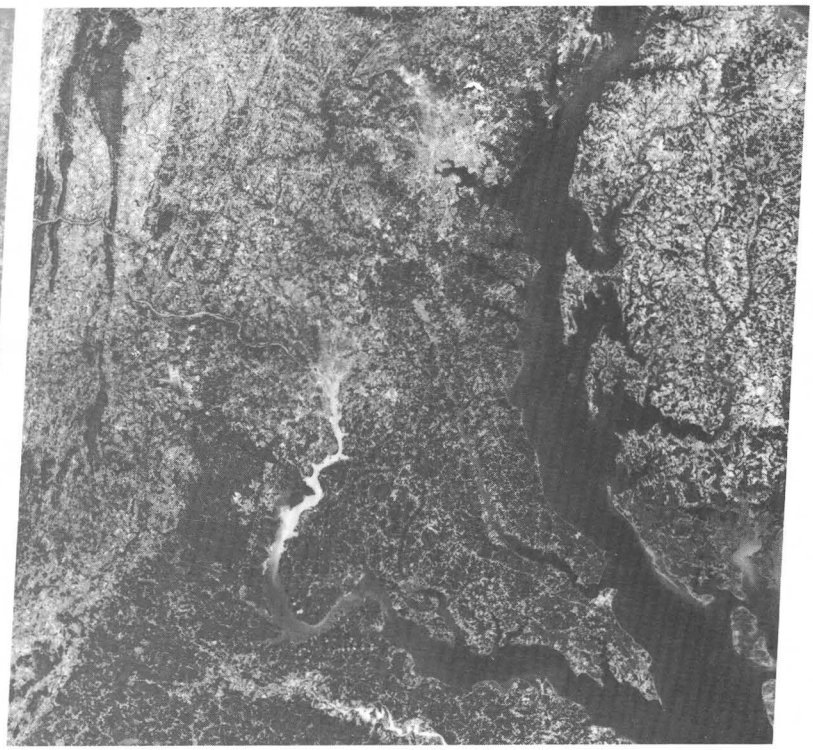

FIGURE 3.—ERTS–1 image of the upper Chesapeake Bay area, showing reflectance in the 0.6- to 0.7-$\mu$m (red) range of the spectrum (1080–15192, band 5).

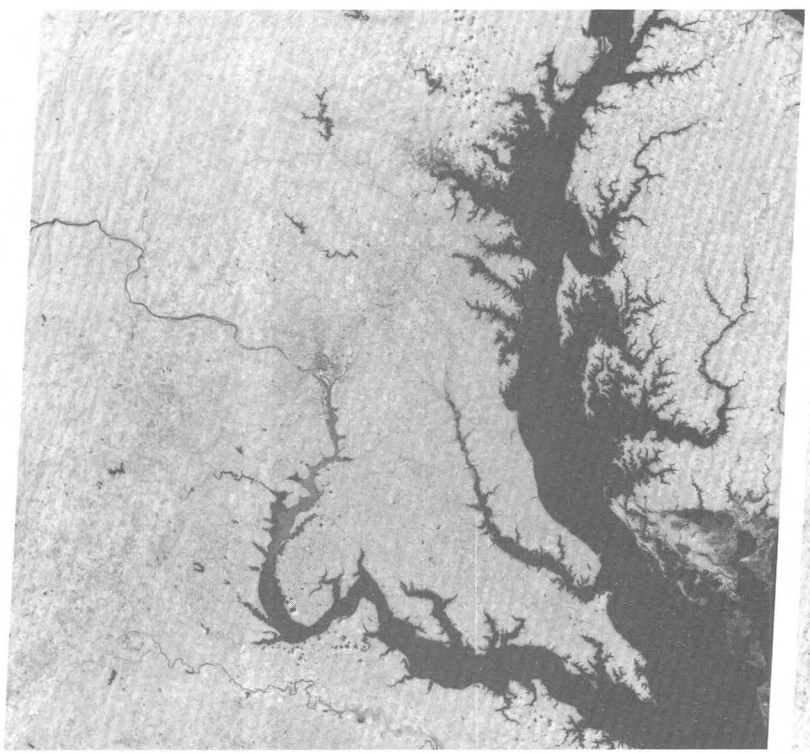

FIGURE 4.—ERTS–1 image of the upper Chesapeake Bay area, showing reflectance in the 0.7- to 0.8-$\mu$m (near-infrared) range of the spectrum (1080–15192, band 6).

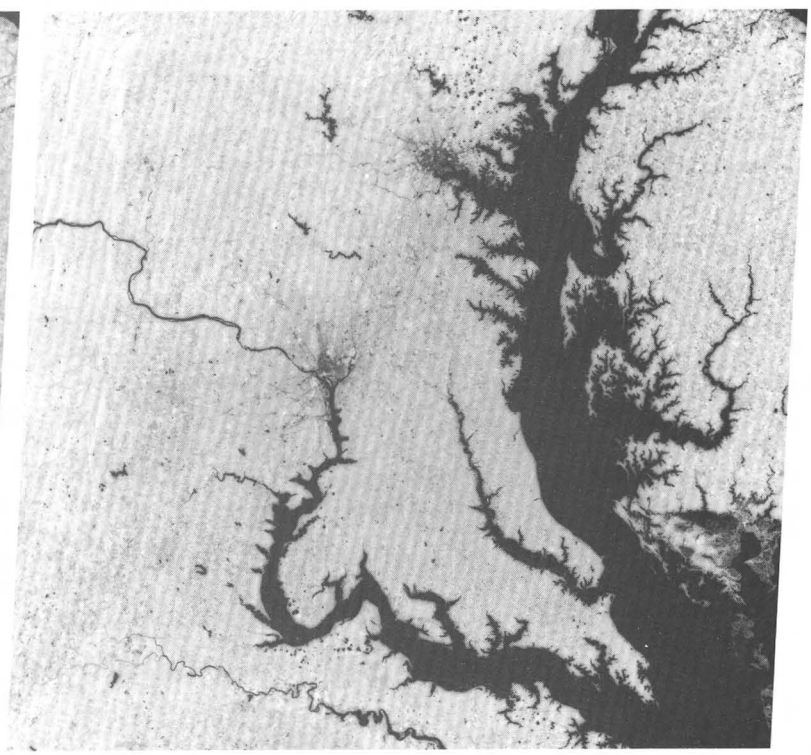

FIGURE 5.—ERTS–1 image of the upper Chesapeake Bay area, showing reflectance in the 0.8- to 1.1-$\mu$m (near-infrared) range of the spectrum (1080–15192, band 7).

APPROXIMATE SCALE

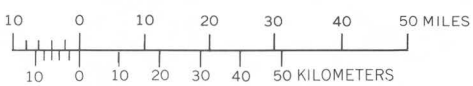

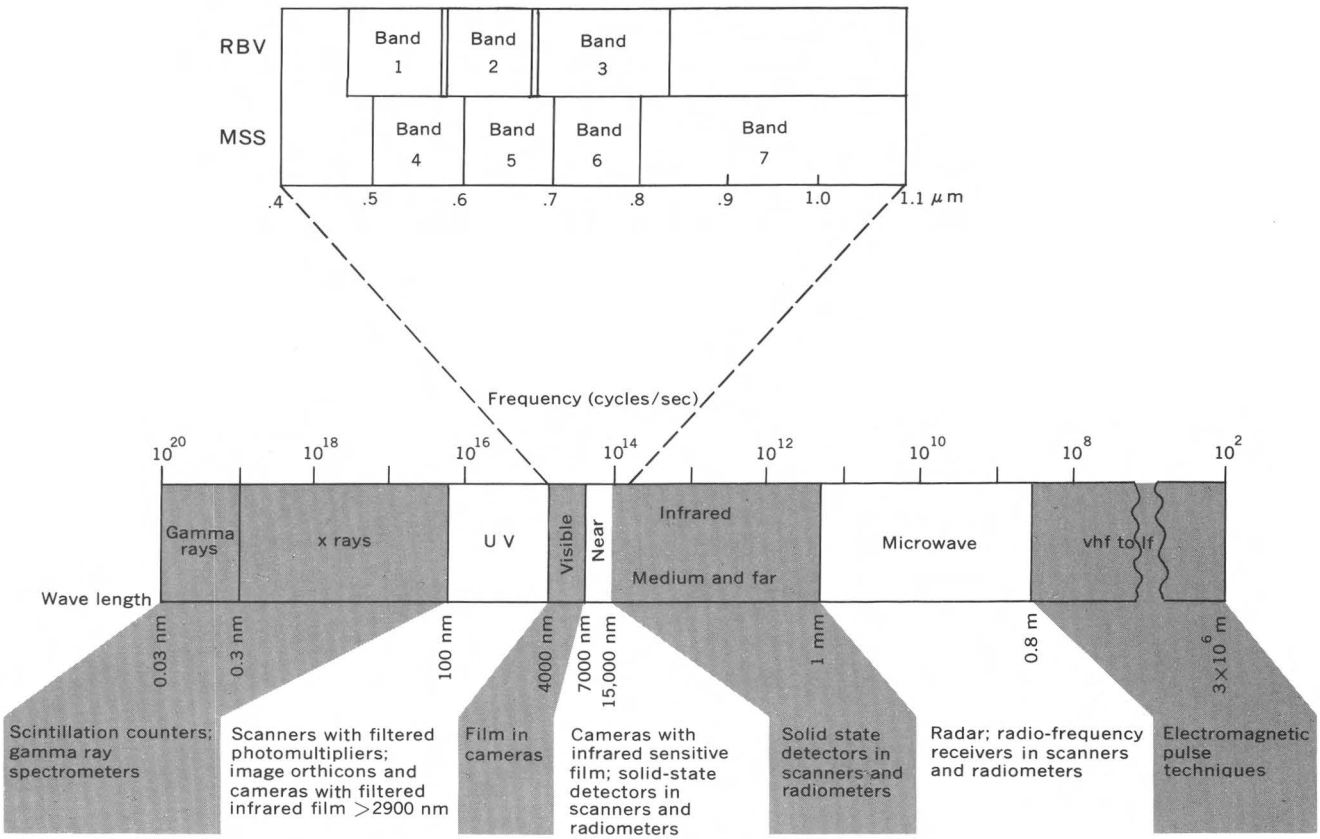


FIGURE 6.—The electromagnetic spectrum and ERTS–1 sensor relationships. (Modified from Parker, D. C., and Wolff, M. F., 1965, Remote sensing: International Science and Technology, July.)

poorly drained area where the fields are small, the land less fertile, and the forested area more extensive.

Geologic structures show up particularly well. The elongate forested areas in the upper left of the picture, for instance, are the Blue Ridge Mountains. Lineaments can be seen throughout the area, especially the northeast-trending lineaments north of Baltimore and the north-trending lineament parallel to the upper right edge of the image.

The following list is a guide to the image information at the bottom of all original ERTS images. Enlargements and specially processed ERTS images may not include such image data, however.

*Description of annotation at margins of an ERTS image*

110CT72—Day, month, and year of image exposure.

C N38–54/W076–48—Geometric extensions of spacecraft yaw attitude axis to Earth's surface:

C—Format center, latitude/longitude, degrees-minutes.

N N38–52/W076–43—Intersection with Earth's surface of a line from the satellite perpendicular to Earth ellipsoid:

N—Nadir, latitude/longitude, degrees-minutes.

MSS 457D—Sensor used (MSS—Multispectral Scanner, RBV—Return Beam Vidicon):

Band or bands, in this case a color composite of bands 4, 5, and 7.

D—Direct.

R—Recorded type of transmission.

SUN EL38 AZ149—Sun angles specified at time of MSS midpoint or RBV time of exposure to nearest degree:
- EL—Elevation.
- AZ—Azimuth.

191—Spacecraft heading, including yaw (toward image annotation).

1114—Orbit revolution number since time of launch.

N—U.S. ground recording station:
- N—Greenbelt, Md.
- A—Alaska.
- G—Goldstone, Calif.

1—Image size:
- 1—100 nmi × 100 nmi.
- 2—50 nmi × 50 nmi.
- 3—25 nmi × 25 nmi.

N—Image processing procedure:
- N—Normal.
- A—Abnormal.

D—Orbit ephemeris data:
- D—Definitive.
- P—Predicted.

2—Mode of MSS signal processing before transmission from satellite:
- 1—Linear.
- 2—Compressed.

L—Gain:
- L—Low gain.
- H—High gain.

NASA/ERTS—Agency and project identifier.

E–1080–15192—Frame identification number.
- E—Encoded project identifier.
- 1—ERTS mission (1—ERTS–A, 2—ERTS–B; after 999 days, numbers change to 5 and 6, respectively).
- 080—Day number relative to launch at time of observation.
- 15—Hour at time of observation (G.m.t.).
- 19—Minute at time of observation (G.m.t.).
- 2—Seconds at time of observation (G.m.t.) rounded off to the nearest 10 s.

4/5/7—Band number:
- RBV: 1(0.475–0.575 μm), 2(0.580–0.680 μm), 3(0.630–0.830 μm)
- MSS: 4(0.5–0.6 μm), 5(0.6–0.7 μm), 6(0.7–0.8 μm), 7(0.8–1.1 μm)
- Color composite: 4/5/7

01—Regeneration number

Tic marks and numbers around margins of the ERTS image refer to an approximate latitude and longitude (degrees and minutes) grid for the image.

Note: The original MSS or RBV ERTS image is created on photographic film from an electron beam recorder at a scale of 1:3,360,000. Negative or positive transparencies or prints (black and white or false-color) are available at this scale or at standard enlargement scales of 1:1,000,000; 1:500,000; 1:250,000 from the EROS Data Center, Sioux Falls, S. Dak. 57198. Computer compatible tapes (CCT's) of every ERTS image are also available from the EROS Data Center.

As an example of how the satellite images the surface of the Earth on successive orbits, the dates and orbit numbers for ERTS–1 from Aug. 3, 1974, to Jan. 11, 1975, over the conterminous United States and from Apr. 17, 1974, to Aug. 20, 1974, over Alaska and Hawaii are shown on the following pages.

# ERTS-1 COVERAGE C

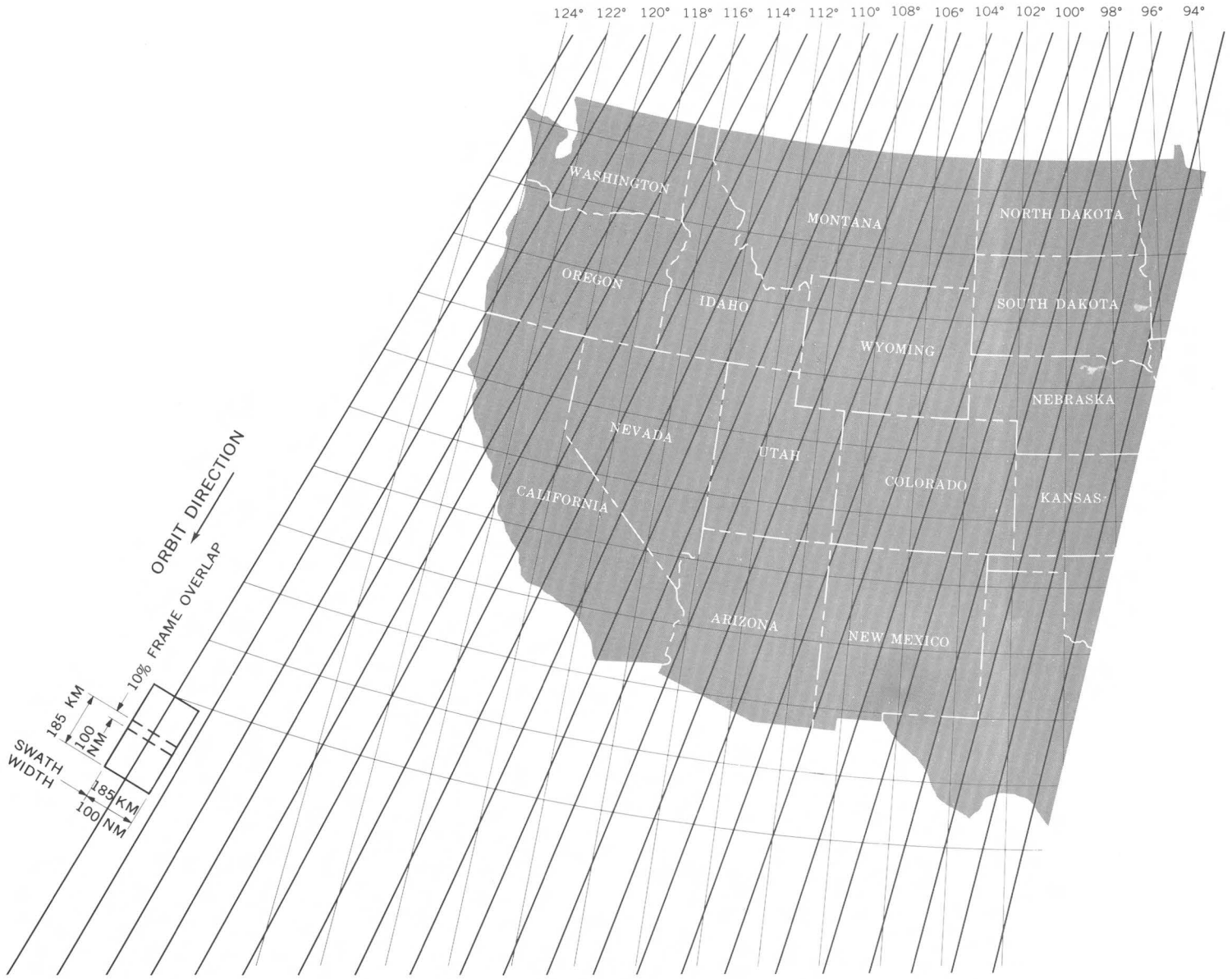


| | | | | | | | | | | | | | | | | | | | | | | |
|---|---|---|---|---|---|---|---|---|---|---|---|---|---|---|---|---|---|---|---|---|---|---|
| DATE | 8/8 | 8/7 | 8/6 | 8/5 | 8/4 | 8/3 | 8/20 | 8/19 | 8/18 | 8/17 | 8/16 | 8/15 | 8/14 | 8/13 | 8/12 | 8/11 | 8/10 | 8/9 | 8/8 | 8/7 | 8/6 | 8/5 |
| ORBIT NO. | 10403 | 10389 | 10375 | 10361 | 10347 | 10333 | 10570 | 10556 | 10542 | 10528 | 10514 | 10500 | 10486 | 10472 | 10458 | 10444 | 10430 | 10416 | 10402 | 10388 | 10374 | 10360 |
| | 8/26 | 8/25 | 8/24 | 8/23 | 8/22 | 8/21 | 9/7 | 9/6 | 9/5 | 9/4 | 9/3 | 9/2 | 9/1 | 8/31 | 8/30 | 8/29 | 8/28 | 8/27 | 8/26 | 8/25 | 8/24 | 8/23 |
| | 10654 | 10640 | 10626 | 10612 | 10598 | 10584 | 10821 | 10807 | 10793 | 10779 | 10765 | 10751 | 10737 | 10723 | 10709 | 10695 | 10681 | 10667 | 10653 | 10639 | 10625 | 10611 |
| | 9/13 | 9/12 | 9/11 | 9/10 | 9/9 | 9/8 | 9/25 | 9/24 | 9/23 | 9/22 | 9/21 | 9/20 | 9/19 | 9/18 | 9/17 | 9/16 | 9/15 | 9/14 | 9/13 | 9/12 | 9/11 | 9/10 |
| | 10905 | 10891 | 10877 | 10863 | 10849 | 10835 | 11072 | 11058 | 11044 | 11030 | 11016 | 11002 | 10988 | 10974 | 10960 | 10946 | 10932 | 10918 | 10904 | 10890 | 10876 | 10862 |
| | 9/31 | 9/30 | 9/29 | 9/28 | 9/27 | 9/26 | 10/12 | 10/11 | 10/10 | 10/9 | 10/8 | 10/7 | 10/6 | 10/5 | 10/4 | 10/3 | 10/2 | 10/1 | 9/31 | 9/30 | 9/29 | 9/28 |
| | 11156 | 11142 | 11128 | 11114 | 11100 | 11086 | 11323 | 11309 | 11295 | 11281 | 11267 | 11253 | 11239 | 11225 | 11211 | 11197 | 11183 | 11169 | 11155 | 11141 | 11127 | 11113 |
| | 10/18 | 10/17 | 10/16 | 10/15 | 10/14 | 10/13 | 10/30 | 10/29 | 10/28 | 10/27 | 10/26 | 10/25 | 10/24 | 10/23 | 10/22 | 10/21 | 10/20 | 10/19 | 10/18 | 10/17 | 10/16 | 10/15 |
| | 11407 | 11393 | 11379 | 11365 | 11351 | 11337 | 11574 | 11560 | 11546 | 11532 | 11518 | 11504 | 11490 | 11476 | 11462 | 11448 | 11434 | 11420 | 11406 | 11392 | 11378 | 11364 |
| | 11/6 | 11/5 | 11/4 | 11/3 | 11/2 | 11/1 | 11/18 | 11/17 | 11/16 | 11/15 | 11/14 | 11/13 | 11/12 | 11/11 | 11/10 | 11/9 | 11/8 | 11/7 | 11/6 | 11/5 | 11/4 | 11/3 |
| | 11658 | 11644 | 11630 | 11616 | 11602 | 11588 | 11825 | 11811 | 11797 | 11783 | 11769 | 11755 | 11741 | 11727 | 11713 | 11699 | 11685 | 11671 | 11657 | 11643 | 11629 | 11615 |
| | 11/24 | 11/23 | 11/22 | 11/21 | 11/20 | 11/19 | 12/6 | 12/5 | 12/4 | 12/3 | 12/2 | 12/1 | 11/30 | 11/29 | 11/28 | 11/27 | 11/26 | 11/25 | 11/24 | 11/23 | 11/22 | 11/21 |
| | 11909 | 11895 | 11881 | 11867 | 11853 | 11839 | 12076 | 12062 | 12048 | 12034 | 12020 | 12006 | 11992 | 11978 | 11964 | 11950 | 11936 | 11922 | 11908 | 11894 | 11880 | 11866 |
| | 12/12 | 12/11 | 12/10 | 12/9 | 12/8 | 12/7 | 12/24 | 12/23 | 12/22 | 12/21 | 12/20 | 12/19 | 12/18 | 12/17 | 12/16 | 12/15 | 12/14 | 12/13 | 12/12 | 12/11 | 12/10 | 12/9 |
| | 12160 | 12146 | 12132 | 12118 | 12104 | 12090 | 12327 | 12313 | 12299 | 12285 | 12271 | 12257 | 12243 | 12229 | 12215 | 12201 | 12187 | 12173 | 12159 | 12145 | 12131 | 12117 |
| | 12/30 | 12/29 | 12/28 | 12/27 | 12/26 | 12/25 | 1/11 | 1/10 | 1/9 | 1/8 | 1/7 | 1/6 | 1/5 | 1/4 | 1/3 | 1/2 | 1/1 | 12/31 | 12/30 | 12/29 | 12/28 | 12/27 |
| | 12411 | 12397 | 12383 | 12369 | 12355 | 12341 | 12578 | 12564 | 12550 | 12536 | 12522 | 12508 | 12894 | 12480 | 12466 | 12452 | 12438 | 12424 | 12410 | 12396 | 12382 | 12368 |

NOTE: ORBIT TRACKS REPRESENT NOMINAL LOCATIONS BASED ON DATA USERS HANDBOOK TABLES. PERIODIC ORBIT DRIFT AND ADJUSTMENTS CAUSE SHIFTS OF UP TO 37 KILOMETERS. FOR MORE LOCATIONAL ACCURACY ON A GIVEN DATE, CONTACT ERTS USER SERVICES AT THE NASA GODDARD SPACE FLIGHT CENTER, GREENBELT, MARYLAND

# HE UNITED STATES

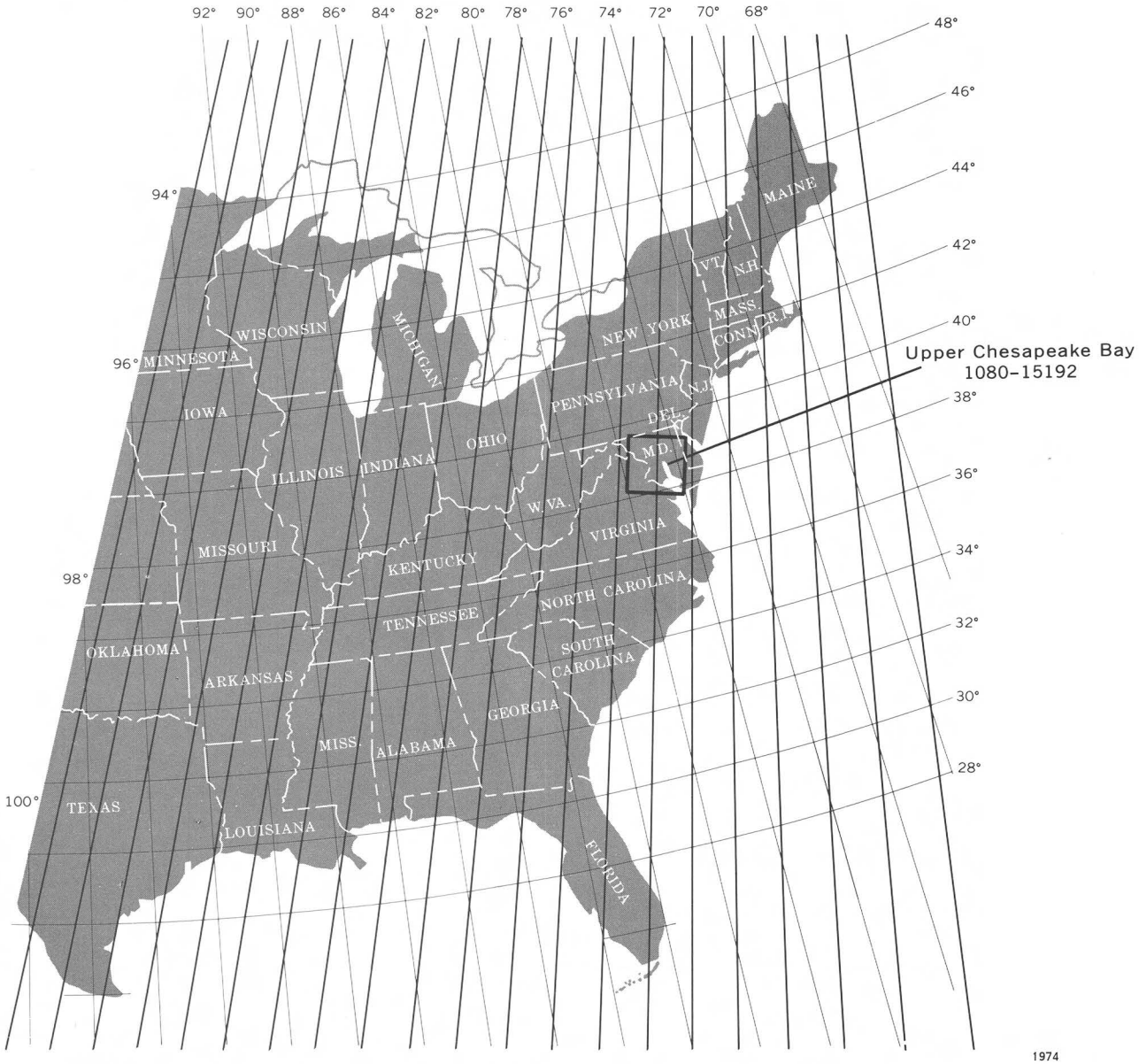


1974

| | | | | | | | | | | | | | | | | | | | | | |
|---|---|---|---|---|---|---|---|---|---|---|---|---|---|---|---|---|---|---|---|---|---|
| 8/4 | 8/3 | 8/20 | 8/19 | 8/18 | 8/17 | 8/16 | 8/15 | 8/14 | 8/13 | 8/12 | 8/11 | 8/10 | 8/9 | 8/8 | 8/7 | 8/6 | 8/5 | 8/4 | 8/3 | 8/20 | AUGUST |
| 10346 | 10332 | 10569 | 10555 | 10541 | 10527 | 10513 | 10499 | 10485 | 10471 | 10457 | 10443 | 10429 | 10415 | 10401 | 10387 | 10373 | 10359 | 10345 | 10331 | 10568 | |
| 8/22 | 8/21 | 9/7 | 9/6 | 9/5 | 9/4 | 9/3 | 9/2 | 9/1 | 8/31 | 8/30 | 8/29 | 8/28 | 8/27 | 8/26 | 8/25 | 8/24 | 8/23 | 8/22 | 8/21 | 9/7 | AUGUST/SEPTEMBER |
| 10597 | 10583 | 10820 | 10806 | 10792 | 10778 | 10764 | 10750 | 10736 | 10722 | 10708 | 10694 | 10680 | 10666 | 10652 | 10638 | 10624 | 10610 | 10596 | 10582 | 10819 | |
| 9/9 | 9/8 | 9/25 | 9/24 | 9/23 | 9/22 | 9/21 | 9/20 | 9/19 | 9/18 | 9/17 | 9/16 | 9/15 | 9/14 | 9/13 | 9/12 | 9/11 | 9/10 | 9/9 | 9/8 | 9/25 | SEPTEMBER |
| 10848 | 10834 | 11071 | 11057 | 11043 | 11029 | 11015 | 11001 | 10987 | 10973 | 10959 | 10945 | 10931 | 10917 | 10903 | 10889 | 10875 | 10861 | 10847 | 10833 | 11070 | |
| 9/27 | 9/26 | 10/12 | 10/11 | 10/10 | 10/9 | 10/8 | 10/7 | 10/6 | 10/5 | 10/4 | 10/3 | 10/2 | 10/1 | 9/31 | 9/30 | 9/29 | 10/28 | 9/27 | 9/26 | 10/12 | SEPTEMBER OCTOBER |
| 11099 | 11085 | 11322 | 11308 | 11294 | 11280 | 11266 | 11252 | 11238 | 11224 | 11210 | 11196 | 11182 | 11168 | 11154 | 11140 | 11126 | 11112 | 11098 | 11084 | 11321 | |
| 10/14 | 10/13 | 10/30 | 10/29 | 10/28 | 10/27 | 10/26 | 10/25 | 10/24 | 10/23 | 10/22 | 10/21 | 10/20 | 10/19 | 10/18 | 10/17 | 10/16 | 10/15 | 10/14 | 10/13 | 10/30 | OCTOBER |
| 11350 | 11336 | 11573 | 11559 | 11545 | 11531 | 11517 | 11503 | 11489 | 11475 | 11461 | 11447 | 11433 | 11419 | 11405 | 11391 | 11377 | 11363 | 11349 | 11335 | 11572 | |
| 11/2 | 11/1 | 11/18 | 11/17 | 11/16 | 11/15 | 11/14 | 11/13 | 11/12 | 11/11 | 11/10 | 11/9 | 11/8 | 11/7 | 11/6 | 11/5 | 11/4 | 11/3 | 11/2 | 11/1 | 11/18 | NOVEMBER |
| 11601 | 11587 | 11824 | 11810 | 11796 | 11782 | 11768 | 11754 | 11740 | 11726 | 11712 | 11698 | 11684 | 11670 | 11656 | 11642 | 11628 | 11614 | 11600 | 11586 | 11823 | |
| 11/20 | 11/19 | 12/6 | 12/5 | 12/4 | 12/3 | 12/2 | 12/1 | 11/30 | 11/29 | 11/28 | 11/27 | 11/26 | 11/25 | 11/24 | 11/23 | 11/22 | 11/21 | 11/20 | 11/19 | 12/6 | NOVEMBER/DECEMBER |
| 11852 | 11838 | 12075 | 12061 | 12047 | 12033 | 12019 | 12005 | 11991 | 11977 | 11963 | 11949 | 11935 | 11921 | 11907 | 11893 | 11879 | 11865 | 11851 | 11837 | 12074 | |
| 12/8 | 12/7 | 12/24 | 12/23 | 12/22 | 12/21 | 12/20 | 12/19 | 12/18 | 12/17 | 12/16 | 12/15 | 12/14 | 12/13 | 12/12 | 12/11 | 12/10 | 12/9 | 12/8 | 12/7 | 12/24 | DECEMBER |
| 12103 | 12089 | 12326 | 12312 | 12298 | 12284 | 12270 | 12256 | 12242 | 12228 | 12214 | 12200 | 12186 | 12172 | 12158 | 12144 | 12130 | 12116 | 12102 | 12088 | 12325 | |
| 12/26 | 12/25 | 1/11 | 1/10 | 1/9 | 1/8 | 1/7 | 1/6 | 1/5 | 1/4 | 1/3 | 1/2 | 1/1 | 12/31 | 12/30 | 12/29 | 12/28 | 12/27 | 12/26 | 12/25 | 1/11 | DECEMBER/JANUARY |
| 12854 | 12340 | 12577 | 12563 | 12549 | 12535 | 12521 | 12507 | 12493 | 12479 | 12465 | 12451 | 12437 | 12423 | 12409 | 12395 | 12381 | 12367 | 12353 | 12339 | 12576 | |

(8/74)

GENERAL ELECTRIC COMPANY,
SPACE DIVISION PO BOX 8555,
PHILADELPHIA, PENNSYLVANIA
19101

# ERTS-1 COVERAGE

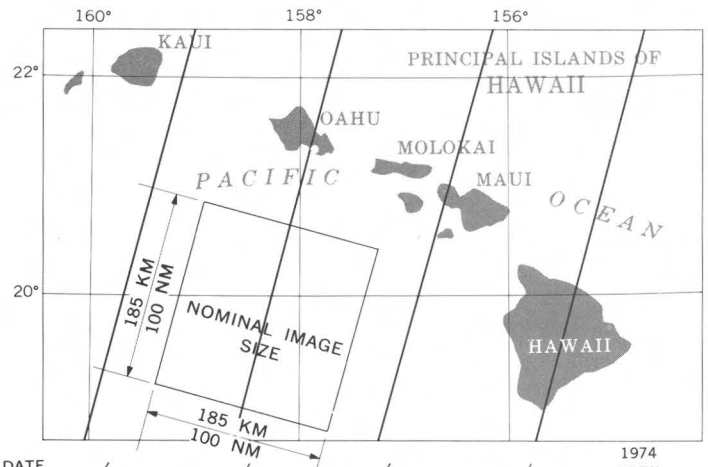


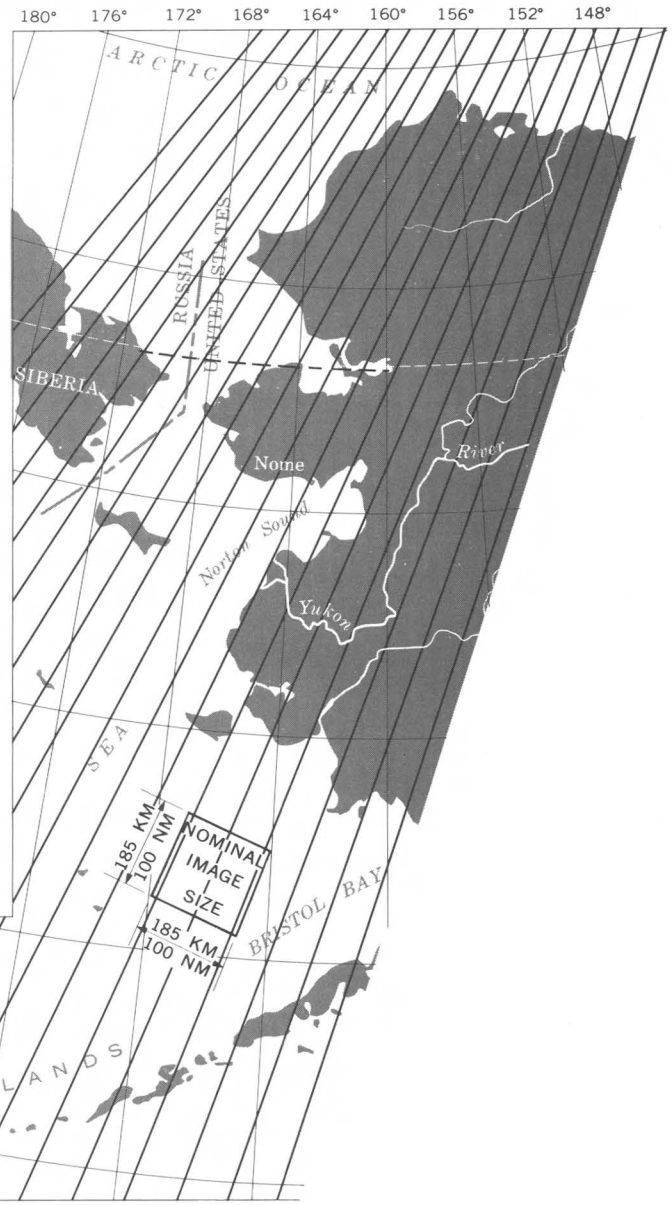


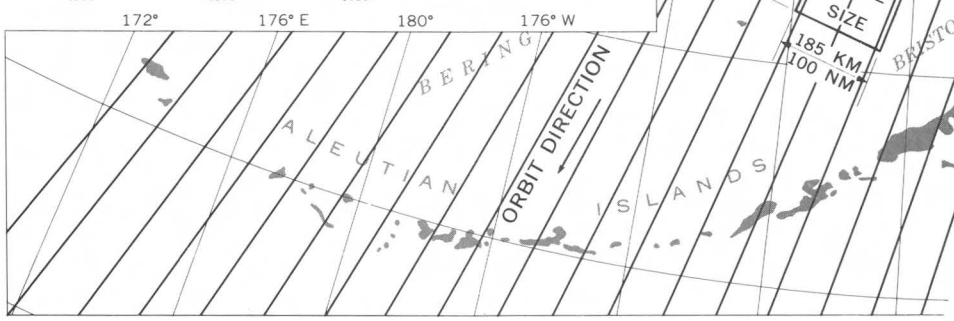


| DATE | | | | 1974 |
|---|---|---|---|---|
| ORBIT NUMBER | | | | |
| 4/22 | 4/21 | 4/20 | 4/19 | APRIL |
| 8898 | 8884 | 8870 | 8856 | |
| 5/10 | 5/9 | 5/8 | 5/7 | MAY |
| 9149 | 9135 | 9121 | 9907 | |
| 5/28 | 5/27 | 5/26 | 5/25 | MAY |
| 9400 | 9386 | 9372 | 9358 | |
| 6/15 | 6/14 | 6/13 | 6/12 | JUNE |
| 9651 | 9637 | 9623 | 9609 | |
| 7/3 | 7/2 | 7/1 | 6/30 | JUNE/JULY |
| 9902 | 9888 | 9874 | 9860 | |
| 7/21 | 7/20 | 7/19 | 7/18 | JULY |
| 10153 | 10139 | 10125 | 10111 | |
| 8/8 | 8/7 | 8/6 | 8/5 | AUGUST |
| 10404 | 10390 | 10376 | 10362 | |

| | | | | | | | | | | | | | | | | |
|---|---|---|---|---|---|---|---|---|---|---|---|---|---|---|---|---|
| 4/30 | 4/29 | 4/28 | 4/27 | 4/26 | 4/25 | 4/24 | 4/23 | 4/22 | 4/21 | 4/20 | 4/19 | 4/18 | 4/17 | 5/4 | 5/3 | 5/2 |
| 9011 | 0997 | 8983 | 8969 | 8955 | 8941 | 8927 | 8913 | 8899 | 8885 | 8871 | 8857 | 8843 | 8829 | 9066 | 9052 | 9038 |
| 5/18 | 5/17 | 5/16 | 5/15 | 5/14 | 5/13 | 5/12 | 5/11 | 5/10 | 5/9 | 5/8 | 5/7 | 5/6 | 5/5 | 5/22 | 5/21 | 5/20 |
| 9262 | 9248 | 9234 | 9220 | 9206 | 9192 | 9178 | 9164 | 9150 | 9136 | 9122 | 9108 | 9094 | 9080 | 9317 | 9303 | 9289 |
| 6/5 | 6/4 | 6/3 | 6/2 | 6/1 | 5/31 | 5/30 | 5/29 | 5/28 | 5/27 | 5/26 | 5/25 | 5/24 | 5/23 | 6/9 | 6/8 | 6/7 |
| 9513 | 9499 | 9485 | 9471 | 9457 | 9443 | 9429 | 9415 | 9401 | 9387 | 9373 | 9359 | 9345 | 9331 | 9568 | 9354 | 9540 |
| 6/23 | 6/22 | 6/21 | 6/20 | 6/19 | 6/18 | 6/17 | 6/16 | 6/15 | 6/14 | 6/13 | 6/12 | 6/11 | 6/10 | 6/27 | 6/26 | 6/25 |
| 9764 | 9750 | 9736 | 9722 | 9708 | 9694 | 9680 | 9666 | 9652 | 9638 | 9624 | 9610 | 9596 | 9582 | 9819 | 9805 | 9791 |
| 7/11 | 7/10 | 7/9 | 7/8 | 7/7 | 7/6 | 7/5 | 7/4 | 7/3 | 7/2 | 7/1 | 6/30 | 6/29 | 6/28 | 7/15 | 7/14 | 7/13 |
| 10015 | 10001 | 9987 | 9973 | 9959 | 9945 | 9931 | 9917 | 9903 | 9889 | 9875 | 9861 | 9847 | 9833 | 10070 | 10056 | 10042 |
| 7/29 | 7/28 | 7/27 | 7/26 | 7/25 | 7/24 | 7/23 | 7/22 | 7/21 | 7/20 | 7/19 | 7/18 | 7/17 | 7/16 | 8/2 | 8/1 | 7/31 |
| 10266 | 10252 | 10238 | 10224 | 10210 | 10196 | 10182 | 10168 | 10154 | 10140 | 10126 | 10112 | 10098 | 10084 | 10321 | 10307 | 10293 |
| 8/16 | 8/15 | 8/14 | 8/13 | 8/12 | 8/11 | 8/10 | 8/9 | 8/8 | 8/7 | 8/6 | 8/5 | 8/4 | 8/3 | 8/20 | 8/19 | 8/18 |
| 10517 | 10503 | 10489 | 10475 | 10461 | 10447 | 10433 | 10419 | 10405 | 10391 | 10377 | 10363 | 10349 | 10335 | 10572 | 10558 | 10544 |

NOTE: ORBIT TRACKS REPRESENT NOMINAL LOCATIONS BASED ON DATA USERS HANDBOOK TABLES. PERIODIC ORBIT DRIFT AND ADJUSTMENTS CAUSE SHIFTS OF UP TO 37 KILOMETERS. FOR MORE LOCATIONAL ACCURACY ON A GIVEN DATE, CONTACT ERTS USER SERVICES AT THE NASA GODDARD SPACE FLIGHT CENTER, GREENBELT, MARYLAND

# ASKA AND HAWAII

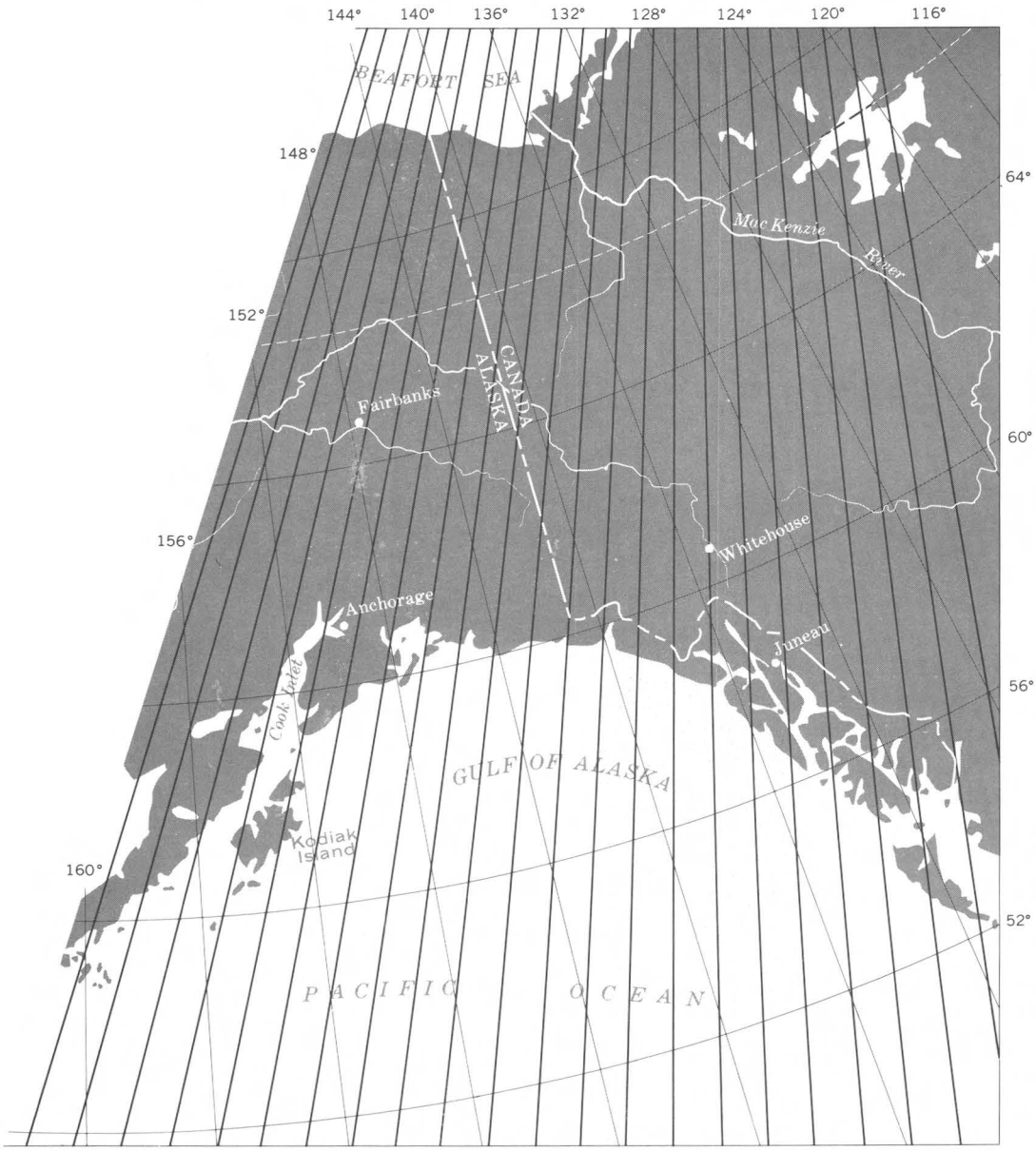


1974

| | | | | | | | | | | | | | | | | | | | | | |
|---|---|---|---|---|---|---|---|---|---|---|---|---|---|---|---|---|---|---|---|---|---|
| 5/1 | 4/30 | 4/29 | 4/28 | 4/27 | 4/26 | 4/25 | 4/24 | 4/23 | 4/22 | 4/21 | 4/20 | 4/19 | 4/18 | 4/17 | 5/4 | 5/3 | 5/2 | 5/1 | 4/30 | 4/29 | APRIL/MAY |
| 9024 | 9010 | 8996 | 8982 | 8968 | 8954 | 8940 | 8926 | 8912 | 8898 | 8884 | 8870 | 8856 | 8842 | 8828 | 9065 | 9051 | 9037 | 9023 | 9009 | 8995 | |
| 5/19 | 5/18 | 5/17 | 5/16 | 5/15 | 5/14 | 5/13 | 5/12 | 5/11 | 5/10 | 5/9 | 5/8 | 5/7 | 5/6 | 5/5 | 5/22 | 5/21 | 5/20 | 5/19 | 5/18 | 5/17 | MAY |
| 9275 | 9261 | 9247 | 9233 | 9219 | 9205 | 9191 | 9177 | 9163 | 9149 | 9135 | 9121 | 9107 | 9093 | 9079 | 9316 | 9302 | 9288 | 9274 | 9260 | 9246 | |
| 6/6 | 6/5 | 6/4 | 6/3 | 6/2 | 6/1 | 5/31 | 5/30 | 5/29 | 5/28 | 5/27 | 5/26 | 5/25 | 5/24 | 5/23 | 6/9 | 6/8 | 6/7 | 6/6 | 6/5 | 6/4 | MAY/JUNE |
| 9526 | 9512 | 9498 | 9484 | 9470 | 9456 | 9442 | 9428 | 9414 | 9400 | 9386 | 9372 | 9358 | 9344 | 9330 | 9567 | 9553 | 9539 | 9525 | 9511 | 9497 | |
| 6/24 | 6/23 | 6/22 | 6/21 | 6/20 | 6/19 | 6/18 | 6/17 | 6/16 | 6/15 | 6/14 | 6/13 | 6/12 | 6/11 | 6/10 | 6/27 | 6/26 | 6/25 | 6/24 | 6/23 | 6/22 | JUNE |
| 9777 | 9763 | 9749 | 9735 | 9721 | 9707 | 9693 | 9679 | 9665 | 9651 | 9637 | 9623 | 9609 | 9595 | 9581 | 9818 | 9804 | 9790 | 9776 | 9762 | 9748 | |
| 7/12 | 7/11 | 7/10 | 7/9 | 7/8 | 7/7 | 7/6 | 7/5 | 7/4 | 7/3 | 7/2 | 7/1 | 6/30 | 6/29 | 6/28 | 7/15 | 7/14 | 7/13 | 7/12 | 7/11 | 7/10 | JUNE/JULY |
| 10028 | 10014 | 10000 | 9986 | 9972 | 9958 | 9944 | 9930 | 9916 | 9902 | 9888 | 9874 | 9860 | 9846 | 9832 | 10069 | 10055 | 10041 | 10027 | 10013 | 9999 | |
| 7/30 | 7/29 | 7/28 | 7/27 | 7/26 | 7/25 | 7/24 | 7/23 | 7/22 | 7/21 | 7/20 | 7/19 | 7/18 | 7/17 | 7/16 | 8/2 | 8/1 | 7/31 | 7/30 | 7/29 | 7/28 | JULY/AUGUST |
| 10279 | 10265 | 10251 | 10237 | 10223 | 10209 | 10195 | 10181 | 10167 | 10153 | 10139 | 10125 | 10111 | 10097 | 10083 | 10320 | 10306 | 10292 | 10278 | 10264 | 10250 | |
| 8/17 | 8/16 | 8/15 | 8/14 | 8/13 | 8/12 | 8/11 | 8/10 | 8/9 | 8/8 | 8/7 | 8/6 | 8/5 | 8/4 | 8/3 | 8/20 | 8/19 | 8/18 | 8/17 | 8/16 | 8/15 | AUGUST |
| 10530 | 10516 | 10502 | 10488 | 10474 | 10460 | 10446 | 10432 | 10418 | 10404 | 10390 | 10376 | 10362 | 10348 | 10334 | 10571 | 10557 | 10543 | 10529 | 10515 | 10501 | |

(4/74)

GENERAL ELECTRIC COMPANY,
SPACE DIVISION PO BOX 8555,
PHILADELPHIA, PENNSYLVANIA
19101

# CHAPTER 1.

# APPLICATIONS TO CARTOGRAPHY

## INTRODUCTION

By Alden P. Colvocoresses,
U.S. Geological Survey

Cartography is defined for use in this chapter as planimetric mapping of the surface of the Earth to conform to a specified standard of map accuracy. Uncontrolled mosaics and other image renditions which are not related to precise position on the Earth's surface are excluded from this chapter.

Man's efforts to map the Earth date from prebiblical times, and prodigious efforts have been expended on the task ever since. Even so, many areas have never been adequately mapped, and to complicate matters, man and nature are rapidly changing that which we try to map. ERTS alone cannot solve all the problems because maps of a tremendous variety of scales and formats are required. Nevertheless, it can continually provide imagery of the entire globe, except for small areas around each pole, in a form that mapmakers can readily use.

When ERTS–1 was first designed, mapping was not one of the primary applications intended. The cartographers as a group were highly skeptical of a scanner such as the MSS as an image producer and therefore looked to the RBV's, which included 81 reseau marks per camera, as their only hope for suitable source data from ERTS. As the RBV's were turned off shortly after launch because of a switching malfunction, the cartographers had to make a choice—either use MSS imagery in their experiments or give up. They chose the first alternative and soon found that scanner imagery, when properly processed, has the following truly amazing cartographic characteristics (Colvocoresses, 1973a):

1. *Long life and global coverage.*—About a full year was needed to complete cloud-free imaging of the United States even though the MSS was turned on for nearly every pass. ERTS–1 promises to survive for more than 3 yr and is thus providing repetitive imaging of the United States. ERTS has been used only selectively in foreign areas because of the need to tape-record the data and play it back when in range of a ground station. If an adequate number of ground stations are installed, the system could comprehensively cover virtually all the land and shallow sea areas of the Earth, as it has so far done for the United States.

Repetitive imaging provides some unexpected bonuses for the cartographer. Seasonal mapping is a distinct possibility, and information as a function of season is significant. For example, winter snow-covered scenes often delineate topography and cultural features, such as roads and urban areas, with a clarity well beyond that of summer imagery. The two images of Denver (figs. 7 and 8) are a good example. The summer image, however, is required to map the surface water, vegetation, and also certain phases of land use. By comparison of both images, the distinction between the forests (dark in the winter scene) and the mountain grasslands (red on the summer scene but white on the winter scene) is clearly indicated. Floods are seasonal phenomena of importance to the cartographer because he should portray areas subject to inundation. The areal extent of leafy (infrared-reflective) vegetation is another important feature that can be mapped seasonally with ERTS imagery and that indicates droughts and other conditions associated with general plant vigor as well as the extent of agricultural crops.

2. *Near-real time.*—The advantage of electronic transmission in near-real time is obvious even though the capability of realizing the advantages has not been fully developed. For example, a cartographic product was produced within 2 weeks after image acquisition by ERTS, and there is no reason why the time cannot be reduced to a few days in special applications.
3. *Orthogonality.*—The field of view of the ERTS MSS extends only 5.76° from the nominal vertical. This near-orthogonality of imagery limits compilation to topographic (contour) maps but simplifies small-scale planimetric mapping and revision. Because topography changes little, maintaining up-to-date planimetry is the major mapping problem once an area has been topographically mapped. A map consisting of little more than a multispectral image precisely referenced to the figure of the Earth is probably the most effective method of portraying up-to-date planimetry. ERTS imagery is ideal for small-scale image mapping for two reasons. First, external errors such as relief displacement are so small that the image can be used directly, except in some areas of extreme relief, without going through the complex transformation provided by an analytical plotter or an orthophotoprinter. Second, the narrow field of view means that the entire scene is being imaged with a nearly constant vertical aspect and thus provides uniform spectral response from similar objects throughout the scene.
4. *Suitability for planimetric mapping.*—It is hard for a photogrammetrist to accept the proposition that an optical-mechanical scanner can generate imagery that has the geometric fidelity characteristic of a frame camera. However, the MSS is indeed generating data that, as corrected by NASA, are printed out in a form containing relative spatial errors on the order of 50- to 100-m rms, indicating a system of high internal geometric fidelity as the scanner spot size (instantaneous field of view) is 79 m. The 50-m rms error equals about 15 $\mu$m at the original MSS imagery scale of 1:3,369,000, approaching the figure expected of a calibrated mapping camera. Although the internal geometric accuracy of the MSS may not be as great as that of a good mapping camera, the accuracy it does have, when coupled with the external advantage of the continuous near-orthographic view, results in two-dimensional (planimetric) mapping of geometric precision which may well exceed that obtainable from camera systems under like conditions. Accuracy of

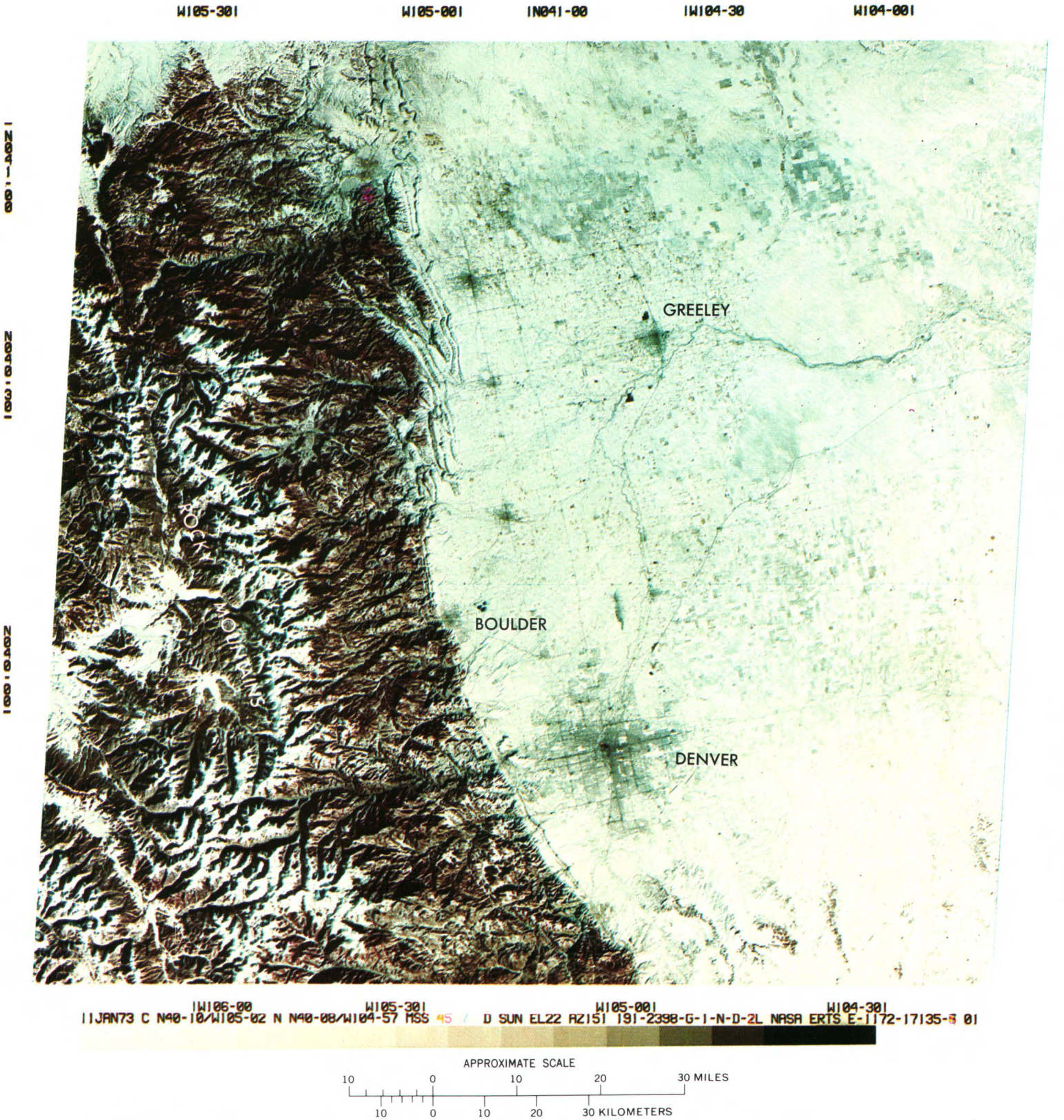


FIGURE 7.—Annotated color composite ERTS–1 image of the Denver, Colo., area in winter (1172–17135).

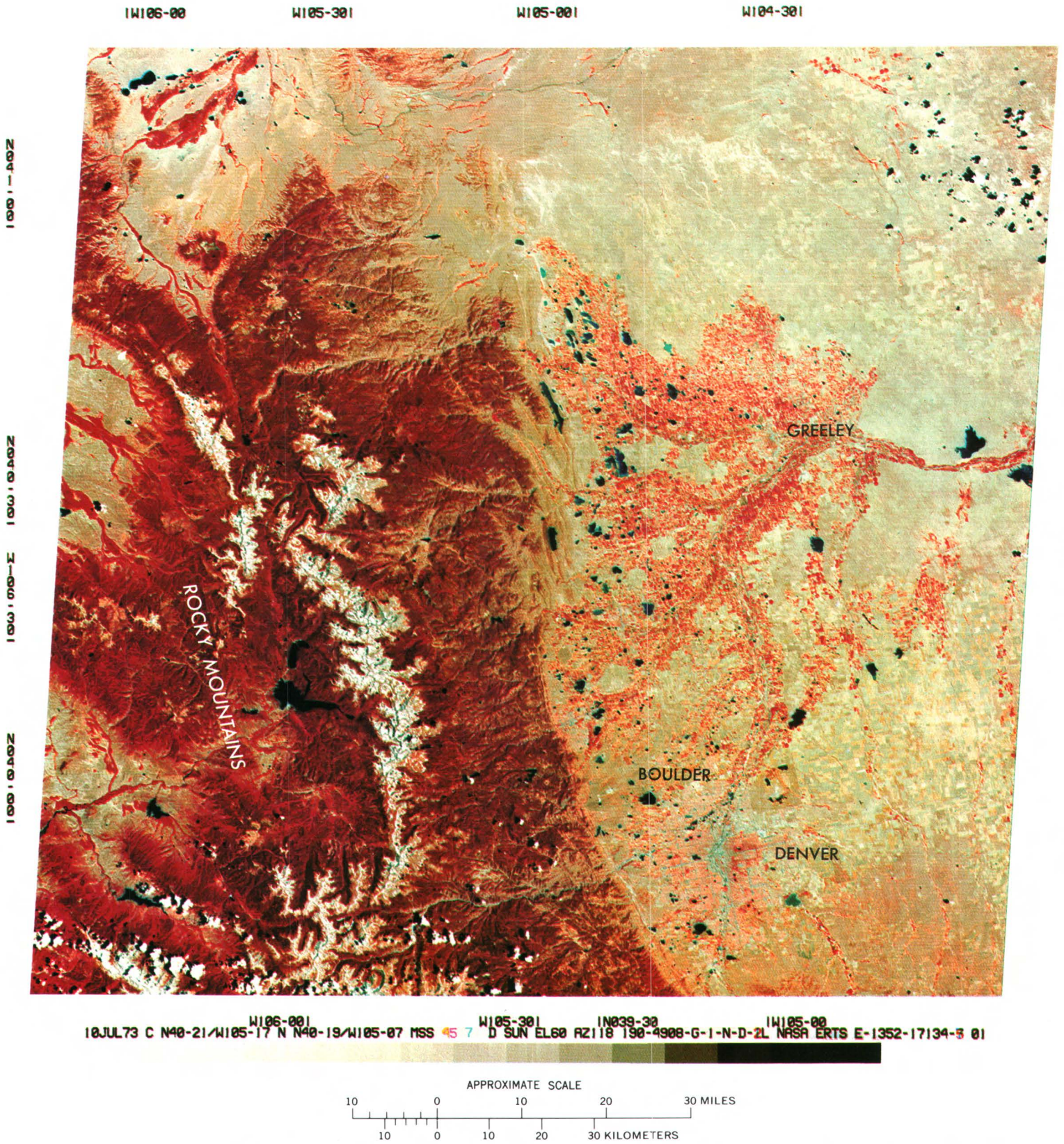


FIGURE 8.—Annotated color composite ERTS–1 image of the Denver, Colo., area in summer (1352–17134).

various MSS modes and products are indicated in the following tabulation:

| *Mode and Form* | *Error Range (rms)* |
|---|---|
| Raw, referenced to lat/long indicators | 1–8 km |
| Referenced to ground control: | |
| Best fit to UTM projection | 150–350 m |
| UTM grid fitted to single-band image | 50–100 m |
| UTM grid fitted to single-band mosaic of 2 and 4 images | 100–150 m |
| UTM grid fitted to multiband (colored) single scene (lithographed) | [1] 150 m |
| UTM grid fitted to multiband (colored) mosaic of 2 and 4 images (lithographed) | [1] 240 m |
| Precision processed to UTM projection | 125–150 m |

[1] Based on the single products so far produced.

5. *Suitability for automation.*—Frame cameras and vidicon imagers record discrete scenes on a plane. Each photograph or image frame has its own geometric characteristics (projection), and, unless extensive analytical adjustments are made, images in adjacent photographs will not form a continuous map. A scanner such as the MSS can produce a basically continuous image on a mathematically definable map projection of negligible distortion (fig. 9) (Colvocoresses, 1974a). Thus a means is established for relating image positions to the figure of the Earth continuously and, within the limitations of the corrections, rigorously. This characteristic provides the potential for development of an automated image-mapping system by either analog or digital techniques with a significant decrease in requirements for ground control and processing.

   The automation aspect is further enhanced by the fact that ERTS–1 repeats its imaging with considerable precision. Subject to visibility, the same nominal Earth scene (see article by Schoonmaker, p. 23) is covered every 18 days as long as ERTS is properly operating. Thus a worldwide map series defined by the nominal ERTS scene is established. The age-old mapping problem of fitting together source materials of different forms and epochs is thus eliminated as far as the individual scene map is concerned: an ERTS scene covers over 34,000 $km^2$ of the Earth.

6. *Radiometric fidelity.*—The ERTS signals, particularly those of the MSS, are in effect those of a focusing radiometer recording radiated energy with a range and precision well beyond the capability of any current film system. As ERTS records four wavelength bands, the images can be combined to provide a response optimized for particular scenes or sizable objects. Film cameras can record up to three bands on one film in color or color infrared, but altering the combination for a particular scene or object is complex and imprecise. The separate-band characteristic of ERTS is particularly important for mapping objects or areas that have unique spectral responses or that are imaged under unusual conditions of illumination. The charting of underwater features and the depiction of polar conditions are examples that require this high degree of radiometric fidelity and versatility. The Sun-synchronous aspect of ERTS, which means that imaging at any given latitude occurs at the same time of day, further enhances the utility of the spectral response.

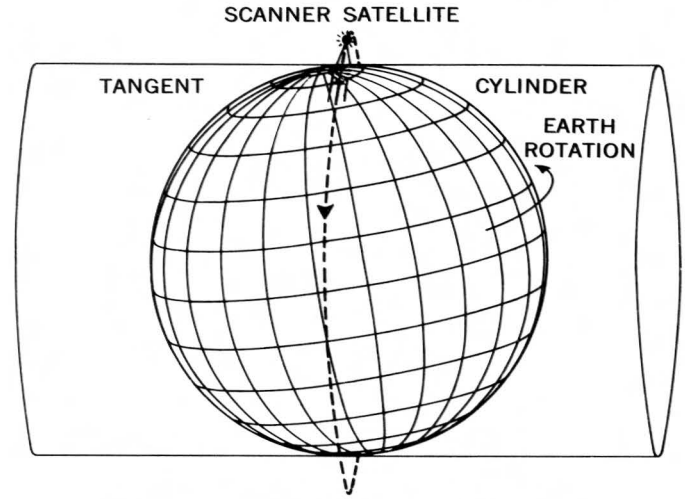


SPACE OBLIQUE MERCATOR PROJECTION

Images the earth from N 82° to S 82° every 18 days

MOTIONS INVOLVED

| | |
|---|---|
| Scanner sweep | Earth rotation |
| Satellite orbit | Orbit precession |

FIGURE 9.—Space oblique Mercator projection.

7. *Extension into the near-infrared wavelengths.*—Available aerial films can record up to a wavelength between 0.8 to 0.9 $\mu$m, which is about the same limit as for band 6. Band 7, at 0.8 to 1.1 $\mu$m, has opened a window for remote sensing which operational film systems do not have. The band is enormously powerful and has demonstrated the following unique capabilities:

   a. Effective penetration of thin clouds and contrails under certain conditions (fig. 10).

   b. Definition of the water/land interface with high precision, enabling detection and identification of circular water bodies as small as 200 m in diameter and linear water bodies of only 20- to 50-m width. Under suitable conditions, where gently sloping areas of known elevations exist, the water stage can be determined to a small fraction of a meter. This capability is particularly remarkable when one considers that the instantaneous field of view of the MSS is 79 m.

   c. Superior delineation of vegetation, largely because of the differential sensitivity of band 7 to vegetation types.

   d. Superior definition of natural features. Many scientists are selecting band 7 as the best single band for depicting the Earth's physiography.

   e. In some cases cultural features are best defined on band 7—for example, the pattern of major streets in western U.S. cities as so far recorded by ERTS.

The U.S. Geological Survey, through the EROS Program, has conducted six NASA-approved and NASA-funded ERTS cartographic experiments, as follows (Colvocoresses, 1972; Colvocoresses and McEwen, 1973):

1. Photomapping of the United States.
2. Map revision.
3. Basic thematic mapping.
4. Polar region mapping.
5. Mapping from orbital data.
6. Overall cartographic application.

Results from these six experiments are only now being realized. The most significant are:

1. Preparation of prototype image maps at scales ranging from 1:250,000 to 1:1,000,000 and in a wide variety of formats and modes.
2. Duplication and public sale of prototype image-format and State base maps in color at 1:500,000. The image-format maps meet the horizontal requirement of the National Map Accuracy Standards (Colvocoresses, 1973b).
3. Selective revision of features on small-scale line maps and the delineation of areas that require revision from other source material. Figure 11 shows the relationship of the ERTS image to small-scale line maps and indicates where revision is needed.
4. Demonstration of the thematic-extraction suitability of ERTS imagery. Figures 12 and 13 illustrate this application to open water and infrared-reflective vegetation, respectively.
5. Preparation of prototype image maps of Antarctica.
6. Demonstration of the potential application of ERTS-type imagery to aeronautical and nautical charting (figs. 14 and 15).
7. Geometric analysis of RBV and MSS imagery that indicates capability of 1:250,000-scale monochromatic image mapping at National Map Accuracy Standards under proper conditions.

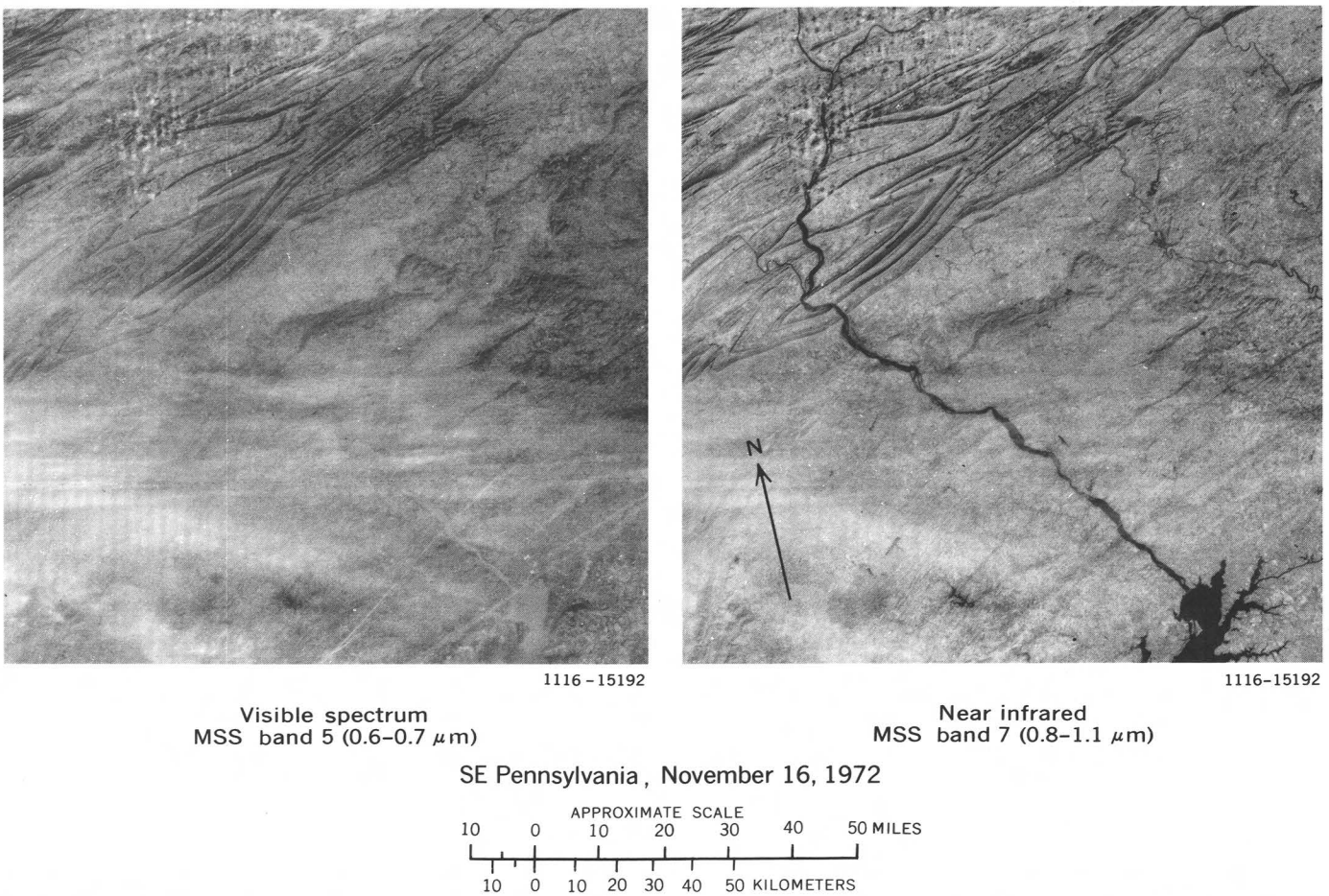


FIGURE 10.—ERTS images of southeastern Pennsylvania, showing the thin-cloud penetration capability of band 7 as compared to band 5 (1116–15192).

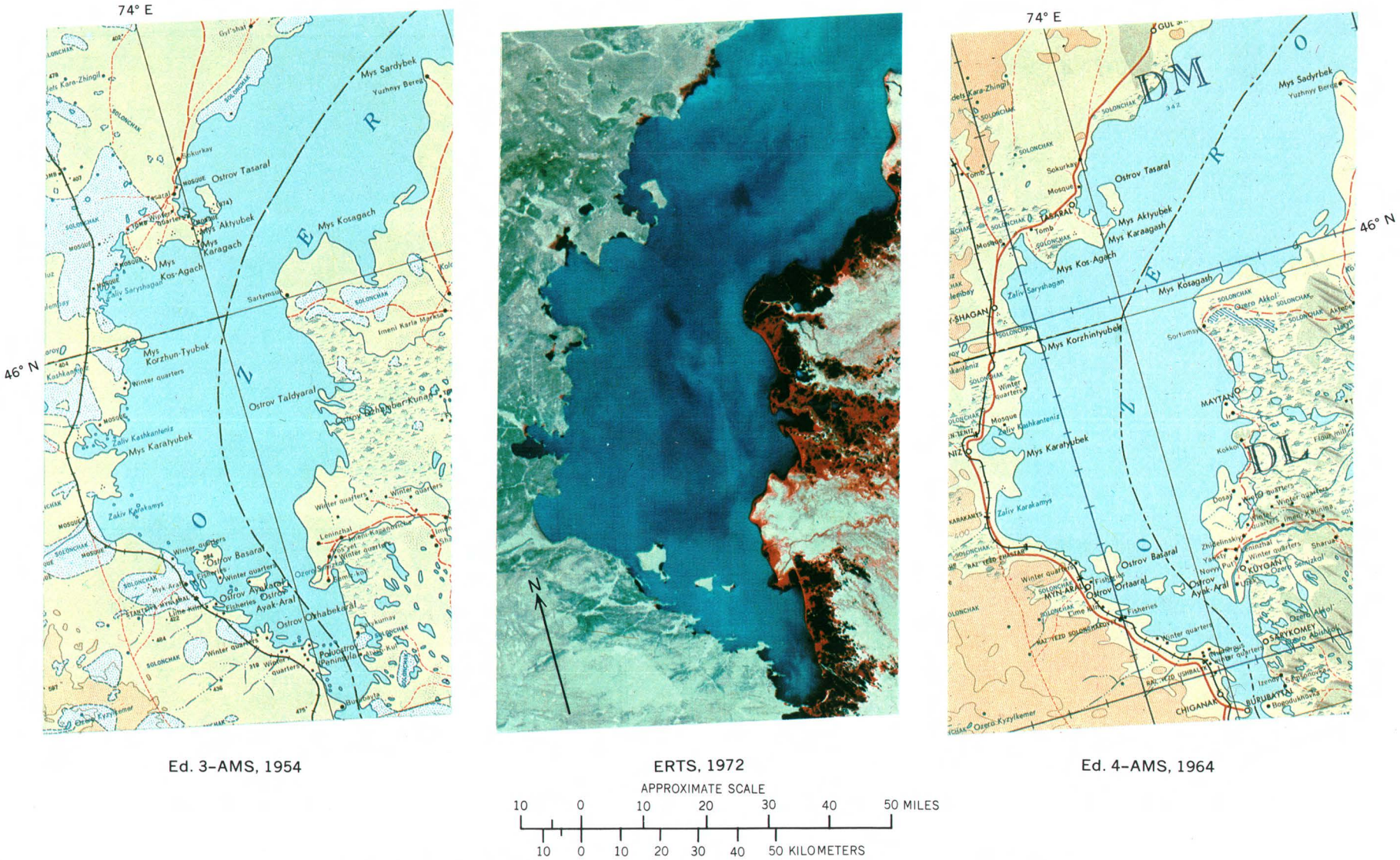


Ed. 3–AMS, 1954

ERTS, 1972

Ed. 4–AMS, 1964

FIGURE 11.—Comparison of maps and ERTS–1 image of Lake Balkash, U.S.S.R. (1049–05260).

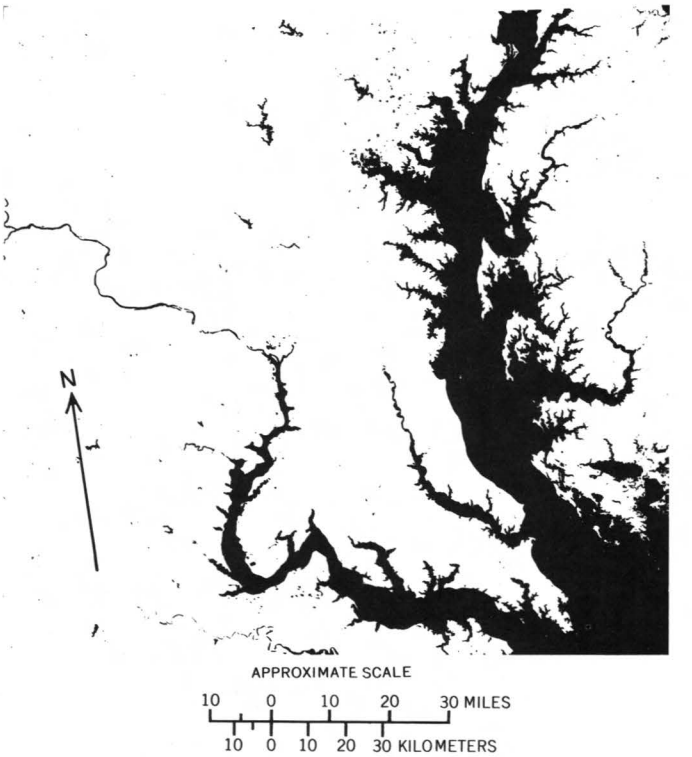


FIGURE 12.—Thematic extraction of open water, upper Chesapeake Bay area (1080–15192, band 7).

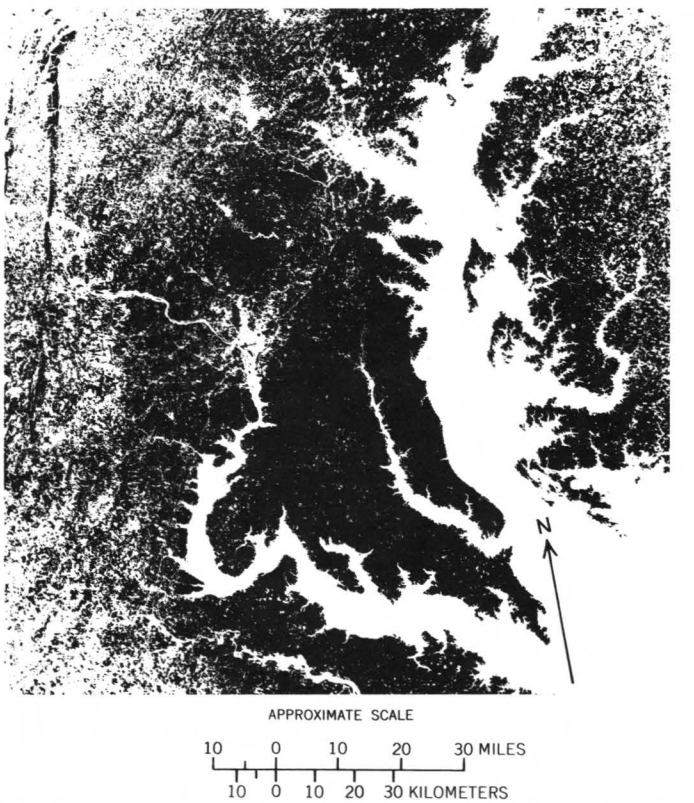


FIGURE 13.—Thematic extraction of infrared-reflective vegetation, upper Chesapeake Bay area (1080–15192, band 7).

8. Defined improvements in MSS processing, which further improve the accuracy of ERTS images.
9. Definition of a map projection and processing procedures that will permit the cartographic processing of ERTS imagery in a matter of days using automated procedures.

In summary, from the mapping viewpoint, ERTS has exceeded expectations. For the first time in history, cartographers have the source material from which image maps of small scale can be produced efficiently and accurately. Moreover, ERTS has introduced a revolutionary concept, automated mapping of the Earth (Colvocoresses, 1974b).

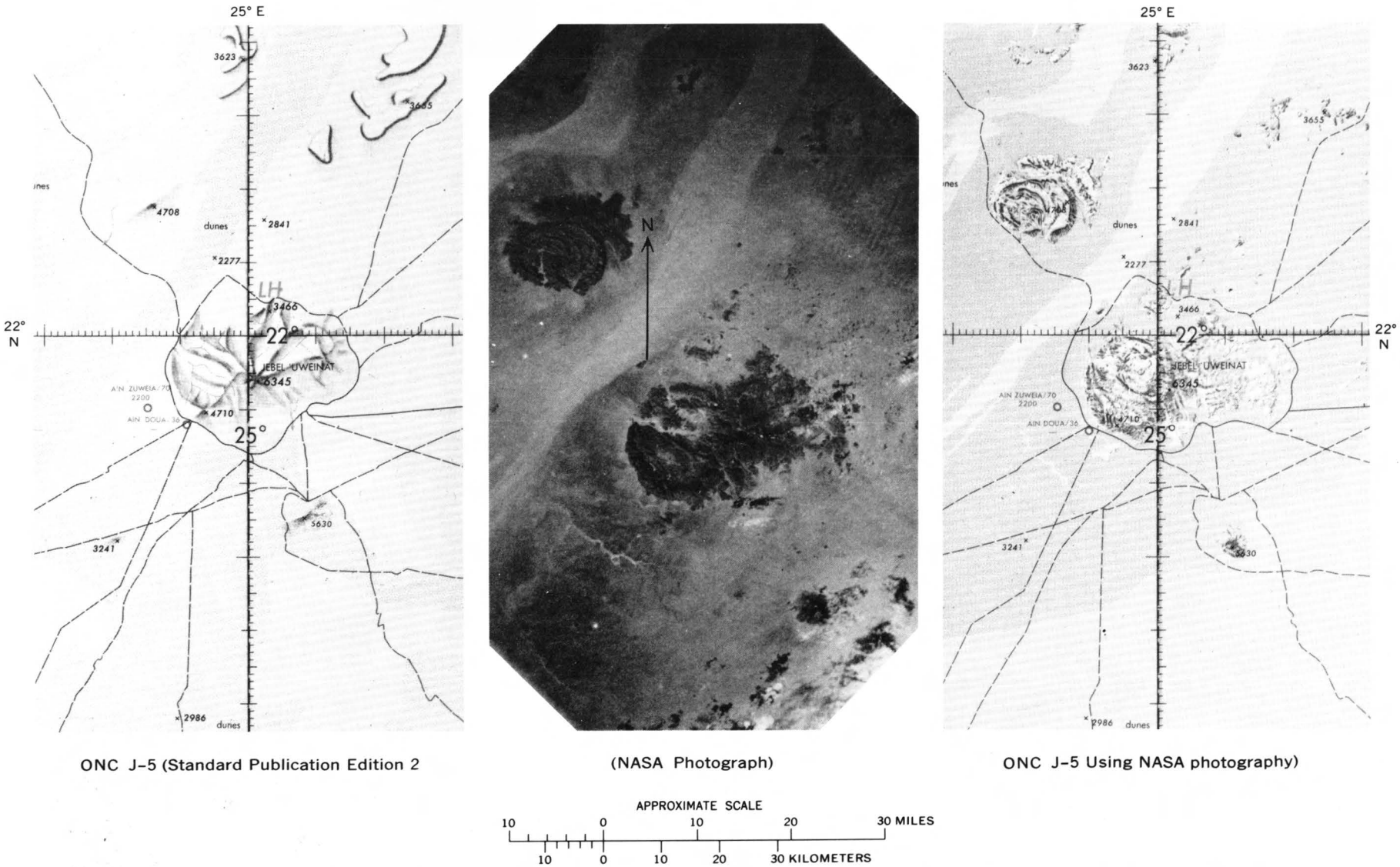


ONC J-5 (Standard Publication Edition 2

(NASA Photograph)

ONC J-5 Using NASA photography)

FIGURE 14.—Space imagery applied to aeronautical charting, Jebel 'Uweinat area, Libya, Sudan, and United Arab Republic (AS–9–23–3533) (modified from Stine, 1971).

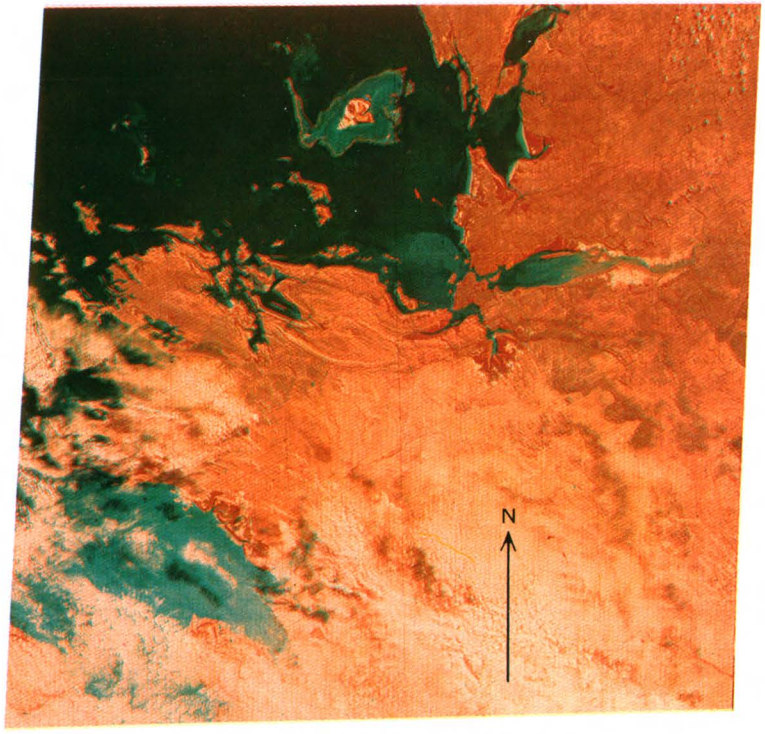


ERTS IMAGE

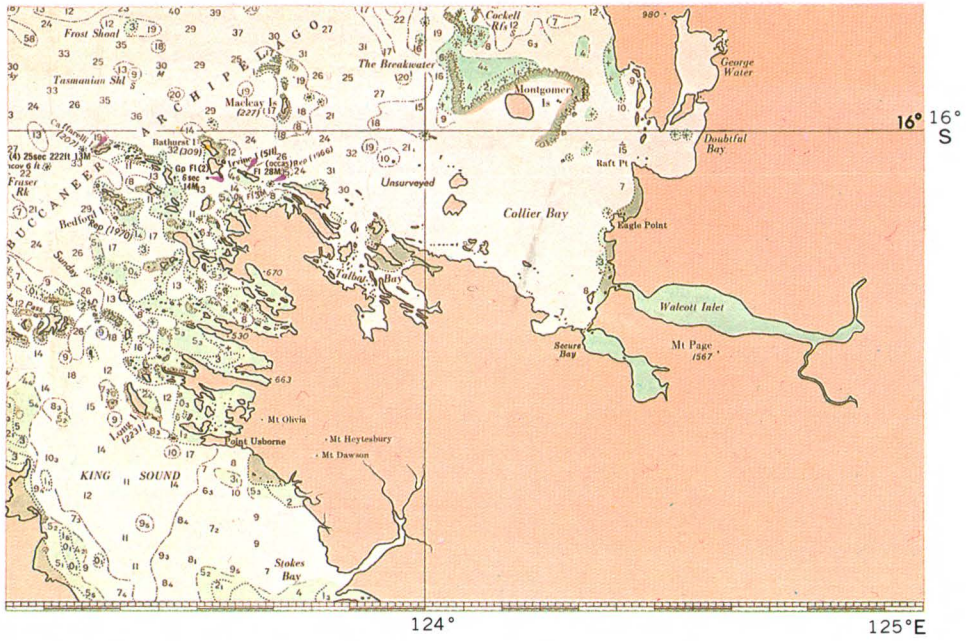


Nautical Chart
Mercator Projection

APPROXIMATE SCALE

10 0 10 20 30 40 MILES

10 0 10 20 30 40 KILOMETERS

FIGURE 15.—Comparison of nautical chart and ERTS image of Collier Bay, Australia (1020–01143).

# ERTS NOMINAL SCENES

By James W. Schoonmaker, Jr., and Robert B. McEwen,
U.S. Geological Survey

ERTS has the capacity for repetitive imaging which permits the definition of bisector- or nominal-scene formats, a unique image-indexing system for that part of the Earth imaged by the satellite. The bisector- or nominal-scene format is defined from the geodetic coordinates of the nominal center of each ERTS–1 image. Each scene is formed by lines drawn midway between the nominal centers, which are fixed as a function of ideal repeating orbits. No overlap exists between the nominal scenes, and therefore no ambiguity exists about what scene covers what area. Additionally, as long as the actual image centers are within ±13 km of nominal, each frame will image an entire bisector scene, even at the Equator where image overlap is minimal. Figure 16 shows the relationship between bisector scenes and typical ERTS–1 images.

If a ±13-km specification were enforced, the actual centers of repeated images obtained over a nominal center might vary, but the image area of 185×185 km would be sufficiently large to always cover the nominal scene with some overlap. The difference between nominal and actual centers is due to two components, orbital drift and attitude (tilt) variations of the satellite. Orbital drift is currently permitted up to 37 km (±16.5 km from nominal) before correction. The present attitude specifications are ±0.7 on the roll and pitch axes, which projects to ±11.3 km from a 925-km orbit. Thus, achieving the ±13-km tolerance will require some combined improvement in specifications of attitude and orbital drift, and such improvement is understood to be within the capabilities of the ERTS system.

The U.S. Geological Survey has programs to compute the geodetic latitude and longitude of the four corner points of all nominal scenes worldwide. The program uses the NASA nominal centers as input. This computer program also generates a unique identification code for each bisector scene based upon the geodetic coordinates of its center. Each code number is composed of 11 alphanumeric characters; 1 to 5 designate the center latitude, 6 to 11 the center longitude. The first character of each group is a letter, N or S for latitude and E or W for longitude, and the remaining characters are numerals designating degrees and minutes. For example, the upper Chesapeake Bay bisector scene, the center coordinates of which are lat 38°49′N., and long 76°49′W. would be encoded N3849W07649. The identification codes are easily readable and computer compatible; a complete listing of them for the conterminous United States has been prepared.

Several index sheets with bisector-scene corners and identification codes that overlay standard U.S. base maps have been computer-plotted. The first is a plot of the conterminous United States at a 1:5,000,000 scale on the Albers equal-area projection. A digital data file of State and national boundaries was used to plot these features simultaneously. This scale and projection were chosen because the base map is utilized for a variety of purposes, including the mapping of State and county boundaries, large-scale mapping status, and area coverage of 1:250,000 maps. A second index sheet of Florida, compatible with the "National Atlas" sheet (1:2,000,000, Albers equal area), also has been plotted. Figure 17 illustrates the nominal scenes of Florida at a reduced scale. The Appalachian area of the United States at 1:2,500,000 scale has also been plotted with state boundaries, and the Caribbean Sea area has been plotted at 1:5,000,000. It is possible to computer-plot overlays of any part of the world on any scale map projection that has been mathematically defined and digitized. The next planned step is to determine the different base maps of the world that are suitable for such portrayal.

Nominal ERTS–1 scenes and identification codes have been used for indexing purposes on the upper Chesapeake Bay satellite image (fig. 18). It is expected that future satellite images will also employ the nominal-scene format and identification code. This simple computer-compatible system has potential as an indexing tool for the enormous quantities of data and images produced from ERTS–1.

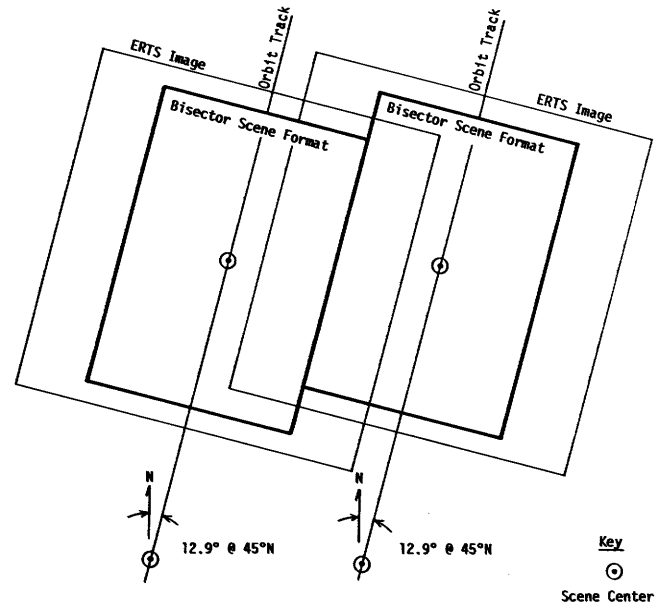


FIGURE 16 (right).—Bisector format of ERTS images at 45° lat.

FIGURE 17 (below).—ERTS nominal scenes of Florida.

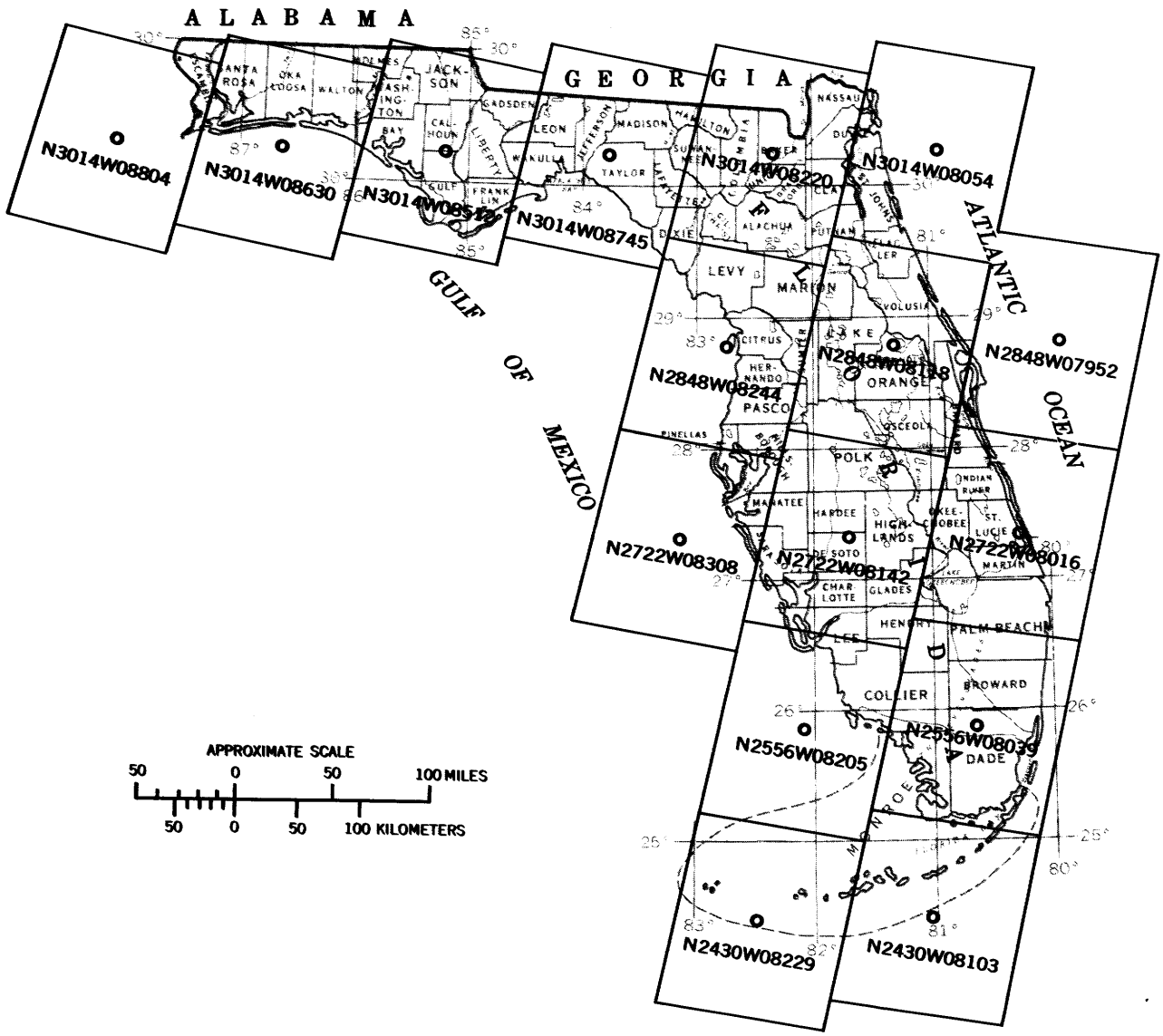

UNITED STATES
DEPARTMENT OF THE INTERIOR
GEOLOGICAL SURVEY

# UPPER CHESAPEAKE BAY

NASA ERTS-1 SATELLITE GRIDDED IMAGE

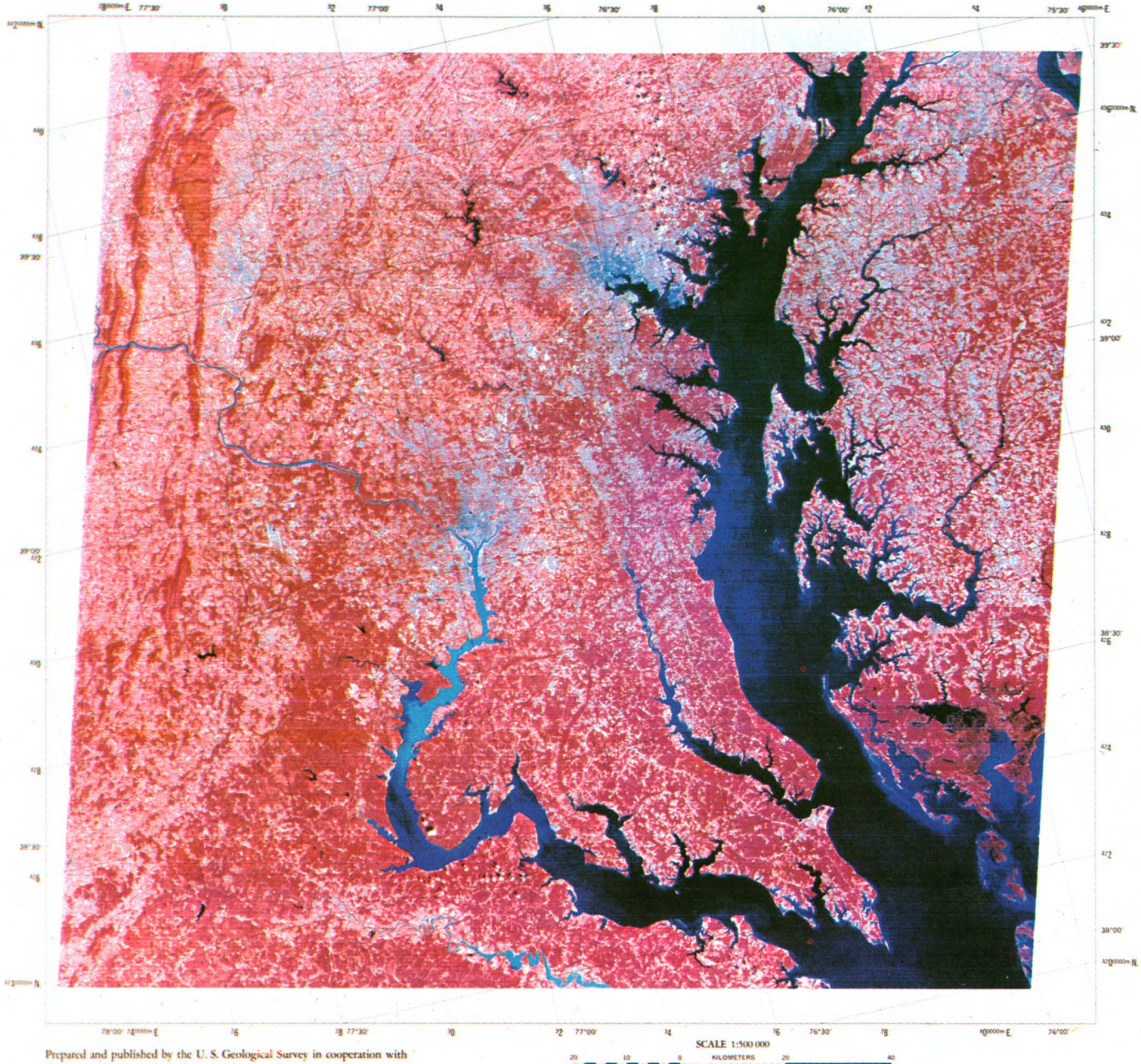

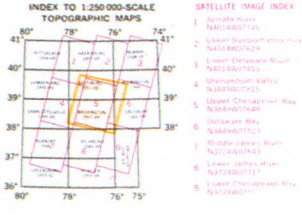


Imagery recorded with Multispectral Scanner (MSS) on NASA ERTS-1 satellite, orbit 1114, 11:19 a.m. e.d.t., Oct. 11, 1972
NASA image E 1080-15192. Orbital altitude 900 km (560 mi)
Area 33 000 km² (13 000 mi²)

Recorded simultaneously in discrete spectral bands and printed in selected colors, as follows:
Band 4—0.5 to 0.6 micrometer
Band 5—0.6 to 0.7 micrometer
Band 6—0.7 to 0.8 micrometer (infrared)
Band 7—0.8 to 1.1 micrometers (infrared)

Repetitive imagery obtained by ERTS sensors will show different conditions of snow cover, vegetation, hydrography, and urban areas

Imagery controlled to photoidentified ground positions
The root-mean-square error in position of well-defined features in relation to the grid is estimated to be 150 meters

20 000-meter Universal Transverse Mercator grid, zone 18
1927 North American datum

Prepared and published by the U. S. Geological Survey in cooperation with the National Aeronautics and Space Administration

Information on cost and availability of ERTS-1 imagery may be obtained from U. S. Geological Survey, EROS Data Center, Sioux Falls, South Dakota 57198

SCALE 1:500 000
KILOMETERS 20 10 0 20 40
METERS 20 000 10 000 0 20 000 40 000
MILES 20 10 0 20

FOR SALE BY U. S. GEOLOGICAL SURVEY, RESTON, VIRGINIA 22092. PRICE $1.25

UTM GRID AND 1972 MAGNETIC NORTH DECLINATION AT CENTER OF IMAGE

UPPER CHESAPEAKE BAY
SATELLITE GRIDDED IMAGE
APPROXIMATE CENTER OF IMAGE

1972

FIGURE 18.—Gridded color composite ERTS-1 image of the upper Chesapeake Bay (1080-15192).

# ORTHOIMAGE MOSAIC OF NEW JERSEY

By Winston Sibert and Fitzhugh T. Clark,
U.S. Geological Survey

One of the more striking products of the ERTS system is the false-color image produced by printing the various bands in different colors. This printing is facilitated by the inherent registry between the different bands. A natural expansion of this capability has been the production of color mosaics of areas of substantial size. Such a mosaic (fig. 96, p. 151) was prepared by the classic method of producing paper prints and joining them on a base board with the best possible fit, the difference being in this case that the prints were in color. The individual sensors for each of the four spectral bands of the ERTS MSS are accurately alined so that the four black and white images, one for each band, will all register accurately. Each band is produced by a digital-to-analog conversion of the basic data, which is then recorded on film by an electron beam recorder. The satellite orbital altitude combined with the narrow field of view eliminates the need for rectification. Moreover, measurements have shown that the bulk-processed ERTS imagery has excellent geometric fidelity.

The satellite image mosaic of New Jersey (fig. 19) exceeds the National Map Accuracy Standards for planimetric maps at a scale of 1:5,000,000. The unique process used in making this mosaic is the combination of a common lithographic technique of double printing one or more halftone images on a single sheet of film, giving tone matching, and the image-matching and ground-control techniques of classical mosaicing. The New Jersey mosaic is made of parts of three ERTS images and has two join lines.

Because the density range of film is greater than that of paper, every copying operation results in resolution degradation. Therefore, film mosaics of each spectral band were used to prepare the lithographic plates. This minimized the loss of spatial detail and maximized the information in the final printed product.

Four plates were used: a black plate containing the grid and all border information and the three color plates—one for band 4 printed in yellow, one for band 5 printed in magenta, and one for band 7 printed in cyan.

Band 5 was selected as the master plate because of the greater ease of identification and measurement of the ground control points of known locations which ensures geometric accuracy. All 12 frames (three images of four bands each) were enlarged to final scale of 1:500,000, as positives, with careful attention given to obtaining a uniform tone match. A contact negative was made of the center image, and the north and south images were processed to

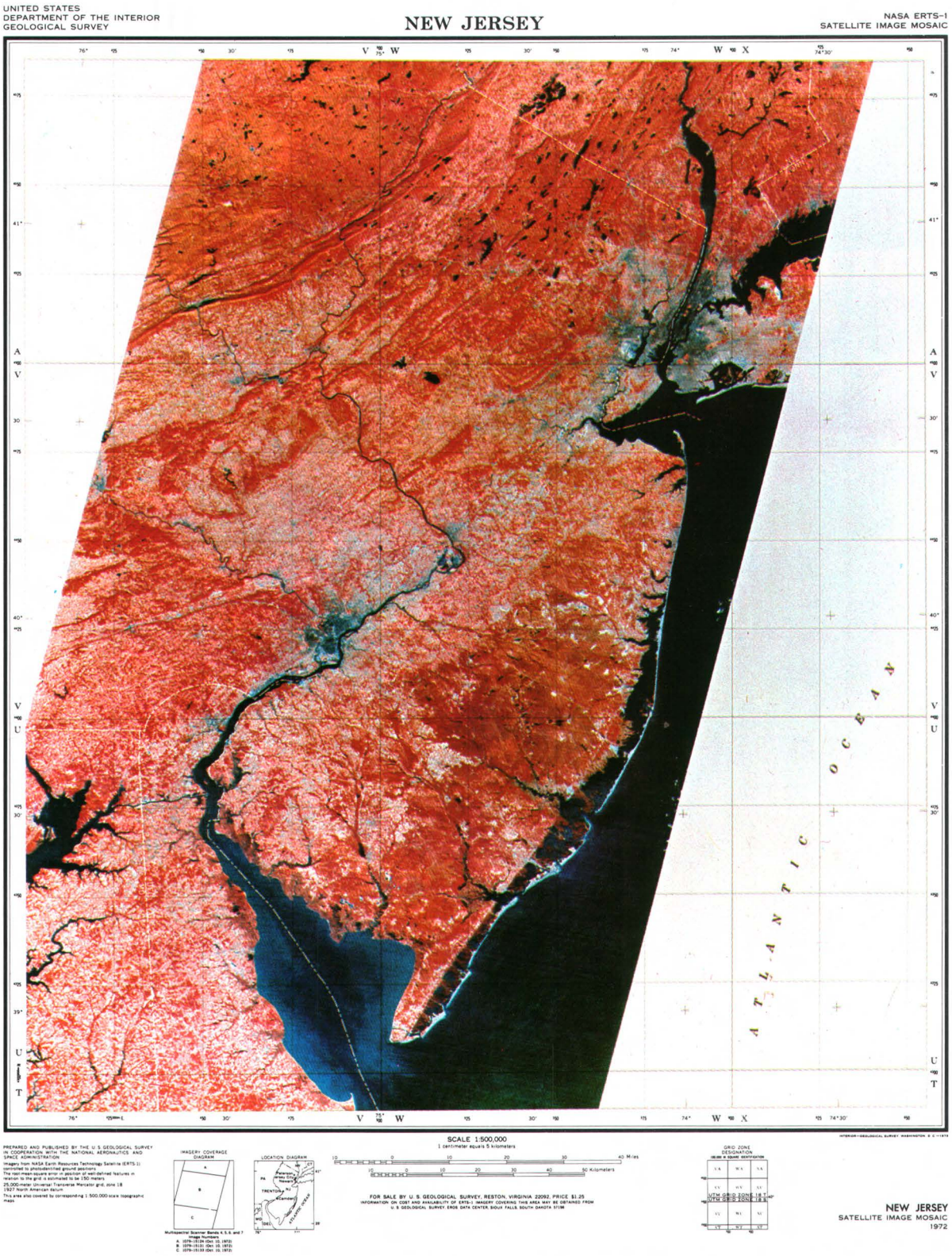


FIGURE 19.—Color composite ERTS–1 orthoimage mosaic of New Jersey (part of 1079–15124, 1079–15131, and part of 1079–15133).

maintain the same tone in the 10 percent overlap parts of the images, allowing a very accurate spatial junction between images. This use of a positive-negative combination permits accurate registration, because a perfectly registered pair appears as an even gray tone on a light table and misregistrations of 0.01 mm are readily apparent.

The three images registered by this process were secured to a Mylar base sheet and were pin registered. Pin registration consists of punching holes through the multiple sheets so that when a pin is inserted into the holes the sheets are forced into the correct relative positions. This process insures that, in the creation of photomosaics and in all subsequent printing operations, true image relationships are preserved.

Two photographic masks were prepared and pin registered to the master base sheet. One mask outlined the area of the center image to be printed and obscured the north and south images. The other mask covered the center image and permitted the exposure of the north and south images. The dimensions of the windows in the masks were accurately controlled to permit slight double printing at the join lines between images, thus obscuring the join lines.

The master negatives were secured to their respective masks while both the negatives and masks were pin registered to the base sheet. The two assemblies (center image and mask and north and south images and mask) were then sequentially printed on a single piece of film using pin registration. This process yielded a master mosaic of band 5 of the entire State.

The images for bands 4 and 7 were image registered to this master mosaic, pin registered to the photomasks, and then were double printed on single sheets of film, giving three mosaics, one for each band, with the entire State in perfect registry. These master transparencies were halftoned and lithographed by normal techniques.

Identifiable control points of known position were measured on the band 5 master transparency, and a UTM grid was computed to yield a best fit to the identified ground control points. This grid was incorporated in the black printing plate and was overprinted on the color images in the normal lithographic four-color sequence, thereby ensuring accurate tone information and dimensional control. The result of this hybrid process is a color lithographic mosaic that exceeds the National Map Accuracy Standards when referenced to the grid.

This was the first time that this process was applied to ERTS imagery. A mosaic of the State of Florida has recently been prepared using this technique and contains parts of at least 17 ERTS images.

# SATELLITE IMAGE MAPS OF THE STATE OF ARIZONA AND OF PHOENIX

By Joseph T. Pilonero,
U.S. Geological Survey

The Arizona satellite image map (fig. 20) is a Lambert conformal conic projection at 1:1,000,000 scale. It is the first black and white State map of ERTS imagery precisely related to the figure of the Earth (the geoid) and is presently for public sale at scales of 1:1,000,000 and 1:500,000.

The entire map comprises the 24 ERTS images that are diagramed and listed at the bottom of the sheet. The imagery is from band 6, wholly in the near-infrared. The original photographic source product for the map consisted of third-generation film positives, 18.5×18.5 cm at 1:1,000,000.

Photographic processing of individual scenes entailed making intermediate contact negatives from the film positives on a LogEtronic printer, then making × 2 enlarged prints at 1:500,000 on stable paper. The scale was established by reference to the recently compiled 1:500,000-scale Arizona State base (line) map.

In mosaicing, individual prints were trimmed inside the borders, and the join edges were feathered to insure smooth, nearly imperceptible joins. The joins were made mostly along streams and dry washes.

A wax adhesive was used for mounting the prints to the mosaic board, and a stable copy of the Arizona State base map was used to maintain positional accuracy. Compliance with the horizontal requirement of the National Map Accuracy Standards, as determined from fitting a UTM grid, has been achieved for the 1:1,000,000 mosaic but not for the 1:500,000 mosaic.

The Phoenix satellite image map (fig. 21) is a photoimage map produced from ERTS–1 imagery. The map scale of 1:250,000 is at present the largest scale at which the current photographic imagery from ERTS-type satellites is aesthetically acceptable.

The map is a mosaic of five images from band 6 enlarged to 1:1,000,000 and furnished as third-generation film positives. A LogEtronic printer was used to make intermediate contact negatives, and stable-paper prints enlarged to 1:250,000 were used for the actual mosaicing. In this specific case the map meets the horizontal requirement of the National Map Accuracy Standards, as determined from the UTM grid.

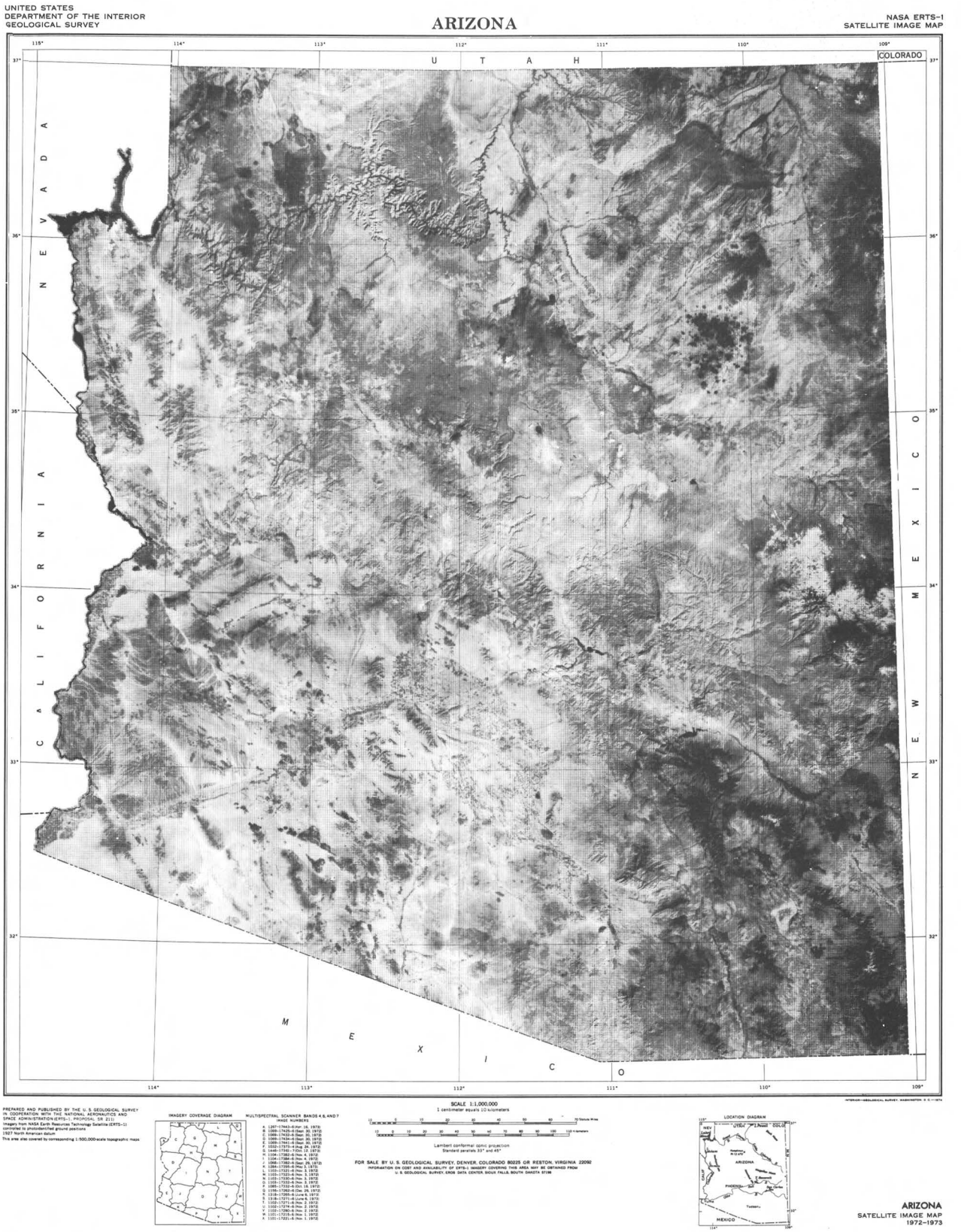


FIGURE 20.—ERTS–1 image map of Arizona.

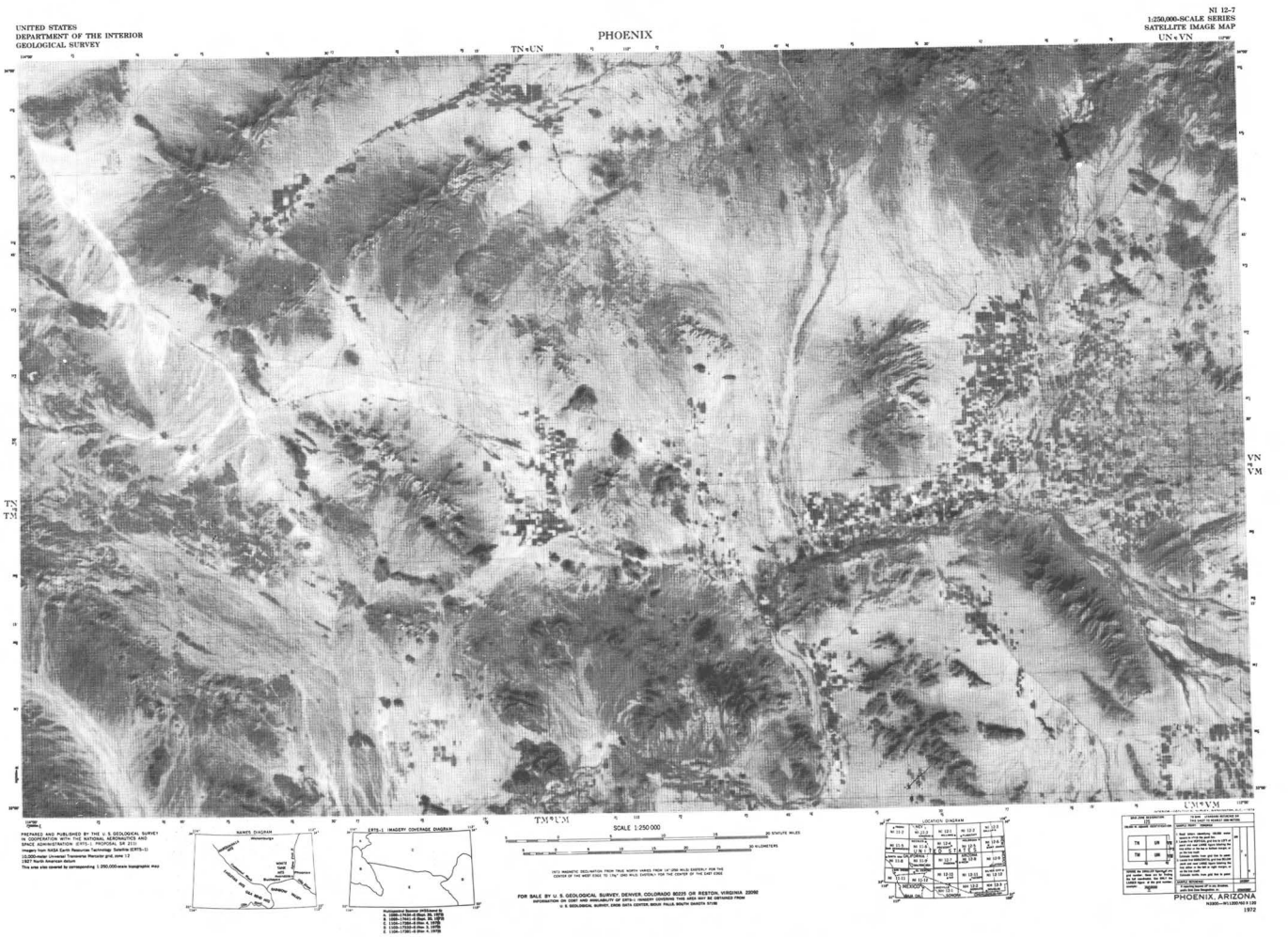


FIGURE 21.—ERTS–1 image map of Phoenix, Ariz.

# DIGITAL COLOR MOSAIC OF PARTS OF WYOMING AND MONTANA

By Grover Torbert, Bureau of Land Management,
and C. J. Robinove, U.S. Geological Survey

A digital precision processed mosaic (fig. 22) of eight ERTS images, taken on July 30 and 31, 1973, was produced by IBM for the Bureau of Land Management. The mosaic depicts parts of eastern Wyoming and eastern Montana where some coal strip mines now exist and where extensive coal stripping is expected in the future. The area includes part of the northern Great Plains in Montana and the Fort Peck Reservoir along the Missouri River. To the south is the Yellowstone River, and to the south of that river is the Powder River Basin where a large reserve of mineable coal exists. The Bighorn Basin of Wyoming, bounded by the Bighorn Mountains to the east, is well portrayed in the mosaic; areas of extremely high reflectance are desert, and the irrigated crop land along the river valleys shows in dark contrast. At the southern end of the mosaic is the Wind River Basin, including the Riverton irrigation project.

Digital processing provides corrected images having a geometric accuracy of approximately one pixel, and, by controlling the images with geodetic control points, the resulting images can be made to meet the National Map Accuracy Standards. Ralph Bernstein (1974) of IBM, who produced the mosaic, states that the computer can combine the input images without picture-element overlap or space, geometric corrections can be applied to correct the images so that the fit in the overlapped regions is nearly perfect, and nonlinear intensity corrections can be made to the image to provide radiometric matching between images. The original mosaic, as supplied by IBM, is at a scale of 1:1,000,000 and contains the UTM grid.

Processing and mosaicing of ERTS images in this form provide a highly usable base map for terrain and water studies, greatly aid in the multispectral classification of terrain features, and also aid in detecting such temporal changes in the terrain as those produced by strip mining and by strip-mine rehabilitation.

FIGURE 22.—Annotated computer-processed color composite ERTS–1 mosaic of parts of Wyoming and Montana (1372–17225, 1372–17231, 1372–17234, 1372–17240, 1373–17283, 1373–17290, 1373–17292, and 1373–17295). ▶

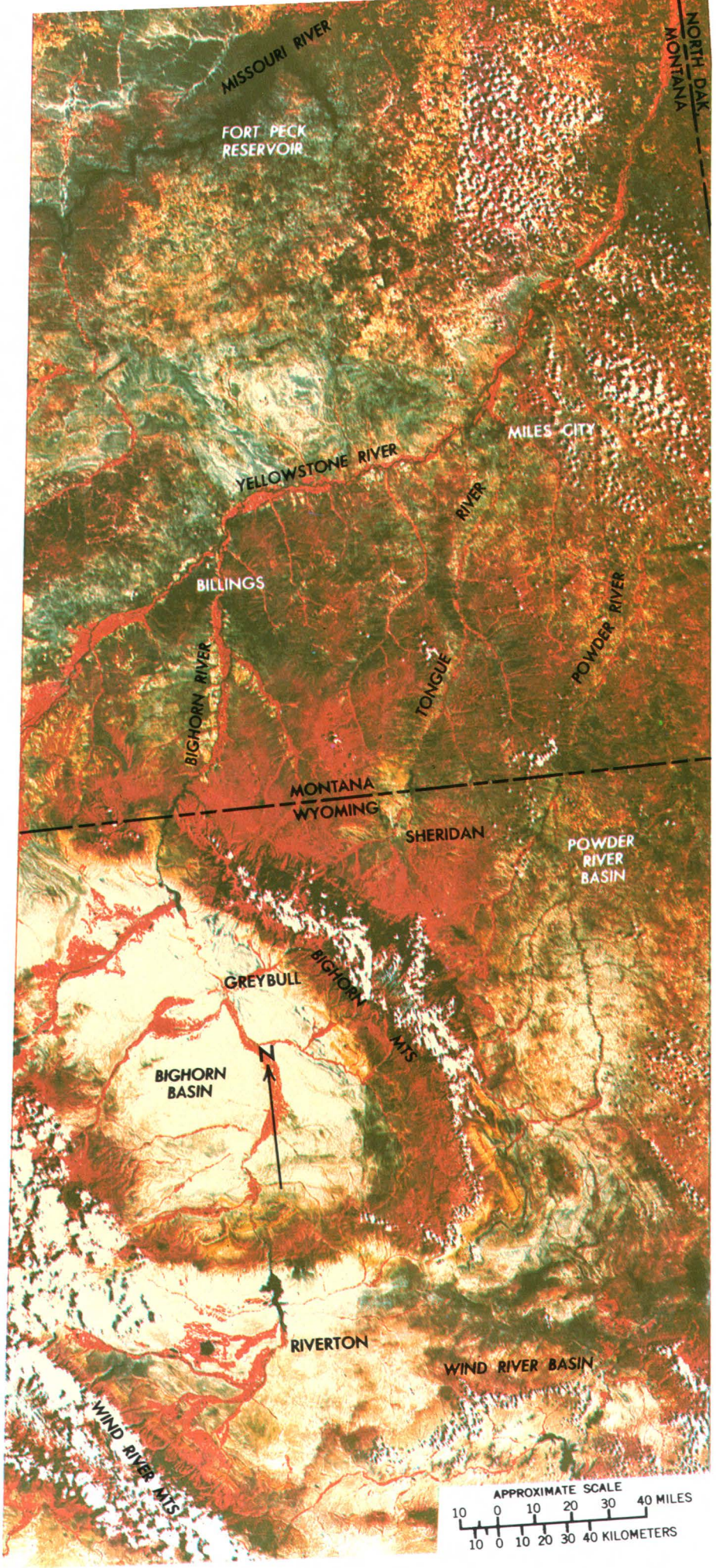
MISSOURI RIVER
FORT PECK RESERVOIR
NORTH DAK
MONTANA
MILES CITY
YELLOWSTONE RIVER
RIVER
BILLINGS
POWDER RIVER
TONGUE
BIGHORN RIVER
MONTANA
WYOMING
SHERIDAN
POWDER RIVER BASIN
GREYBULL
BIGHORN MTS
N
BIGHORN BASIN
RIVERTON
WIND RIVER BASIN
WIND RIVER MTS
APPROXIMATE SCALE
10 0 10 20 30 40 MILES
10 0 10 20 30 40 KILOMETERS

# GEODETIC CONTROL IN POLAR REGIONS FOR ACCURATE MAPPING WITH ERTS IMAGERY

By William R. MacDonald, U.S. Geological Survey

FIGURE 23.—McMurdo Sound region, Antarctica. Image at right shows locations of geodetic control stations used to construct the fitted grid for the satellite image at the left (1174–19433, band 7).

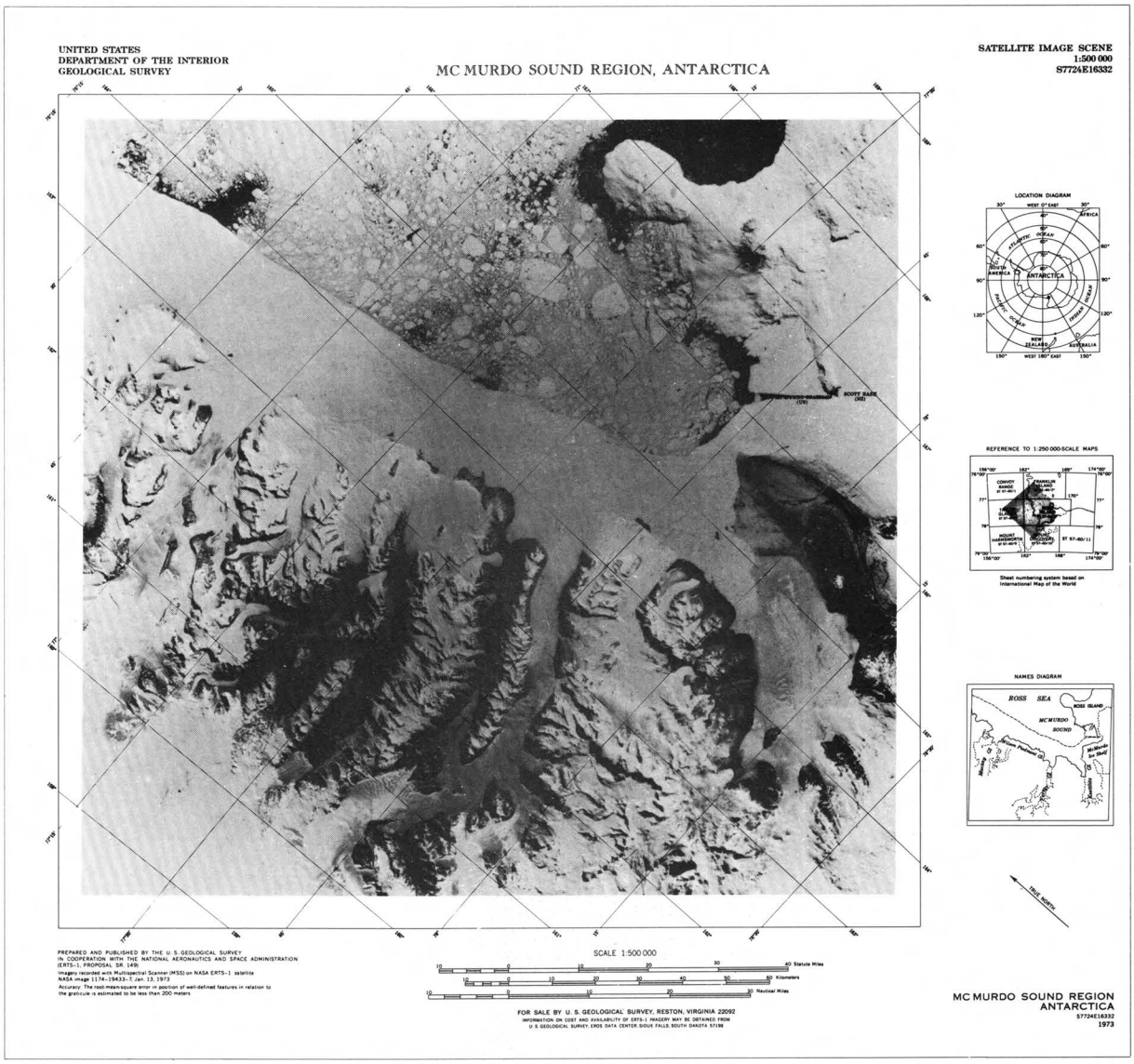

Because geodetic control in the polar regions is very limited and extremely expensive and difficult to establish, it was necessary to find an economical means of acquiring the amount of control needed to maintain the integrity of ERTS cartographic products.

In Antarctica the U.S. Geological Survey investigated the practicality of using recently developed Doppler positioning and navigation systems for establishing the much-needed control. The mode tested was the single-point positioning method, which consists of a receiver tracking a satellite pass and computing the position from the Doppler shift and the satellite ephemeris. The experiments proved that Doppler-equipped polar-orbiting satellites can be used as surveying tools and that mapping control can be obtained under Antarctic field conditions.

As a result of the Doppler positioning experiments, it is now possible to make maximum cartographic use of ERTS imagery in polar regions by deploying specially equipped teams of topographic engineers to establish ERTS ground control.

Positions obtained during the Doppler positioning experiments were used along with existing control to fit a grid to a single image (fig. 23) of the McMurdo Sound region, Antarctica.

FIGURE 23.—Continued.

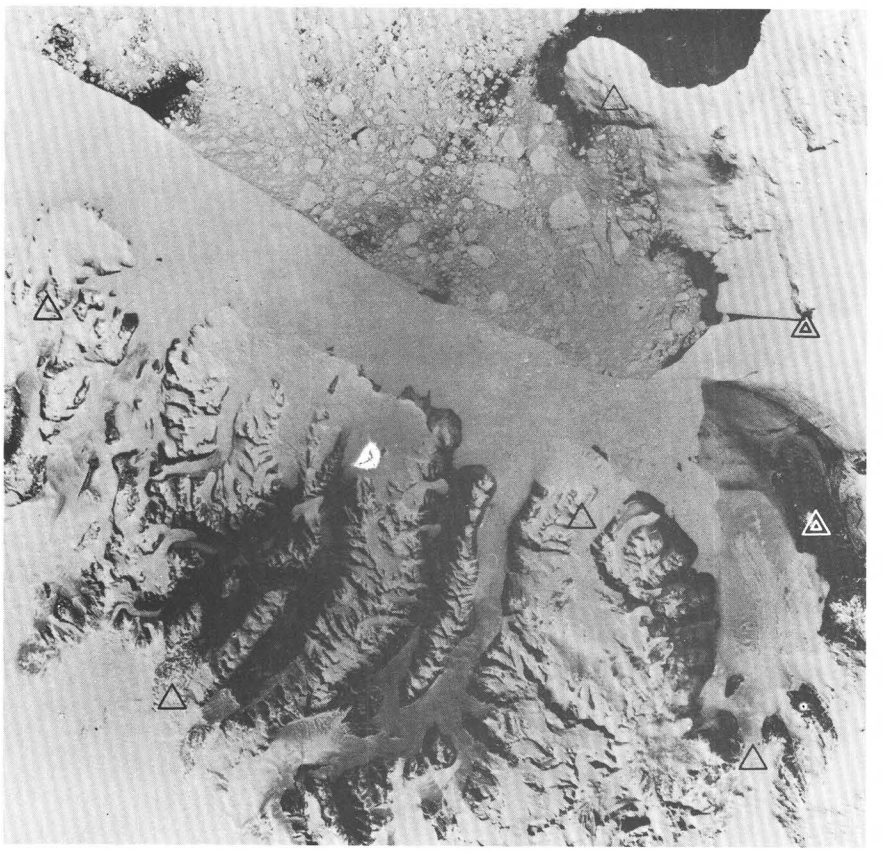

EXPLANATION

△ Geodetic control (Standard surveying methods)

⊿ Geodetic control (Derived from Doppler satellite data)

The technique of converting an ERTS image into a cartographic product by following the grid rather than the image rectification appears to be the most practical and cost-effective way of relating polar ERTS-image data to the Earth's surface. Normally the procedure is to modify the photoimage through tilt analysis and rectification to fit a grid. When applying these procedures to ERTS imagery, however, geometry is improved, but too much detail (resolution) is lost during the photographic processes. Four steps are required to fit a grid to an ERTS image:

1. Identification of discrete image points for which coordinates are known.
2. Accurate measurement of the $x$ and $y$ values of these control points on the image scene.
3. Determination of the transformation parameters to relate one system to the other, and computation of the intersection of the grid lines in an image coordinate system, warping the grid to fit the image.
4. Plotting the grid on an overlay keyed to the image.

The accuracy of image identification of the control points is the primary element that determines the accuracy of the grid fit. In the mid-latitudes, where large-scale accurate maps are available, good results can be obtained by using images of timber corners, fence lines, centers of bridges over streams, pipe and powerline crossings, and so on, as control points. In these areas, in most cases, the grid can be fitted to the image so that the image product meets the National Map Accuracy Standards at scales of 1:500,000 and smaller. In the poorly mapped polar regions, especially in Antarctica for which good maps and where control are scarce, there is less certainty in the selection of points used in the gridding process. Therefore, the resulting grid fit may not meet the National Map Accuracy Standards, which require that 90 percent of all well-defined planimetric detail fall within 0.5 mm of correct map position at 1:500,000 scale.

The grid fit to the McMurdo Sound image (fig. 23) using 13 triangulation points gave rms error of 183 m, or only about 10 m over accuracy standards. However, if discrete points had been preselected on the imagery and if the ground positions for these points had been established by the Doppler field techniques previously described, it is reasonable to believe that the National Map Accuracy Standards could be met at 1:500,000 scale and smaller.

# ANTARCTIC CARTOGRAPHY

By William R. MacDonald,
U.S. Geological Survey

For the preparation of maps in support of the U.S. Antarctic Research Program, the United States has obtained aerial photography over an area of about 3,250,000 km². This effort has taken many years and has cost many millions of dollars. ERTS–1 now provides the capability of producing a single image covering an area of about 34,000 km² (185 by 185 km). About 100 ERTS images would cover the same area now covered by more than 100,000 aerial photographs.

An important current objective is the compilation of 1:1,000,000 image mosaics of the coastal areas of western Antarctica and, eventually, of all the coastal areas of Antarctica. These image mosaic products will enable the U.S. Geological Survey to build a historical record which, when compared against existing maps and sequential ERTS coverage, will show changes in size, shape, and position of such features as ice shelves, glaciers, and ice tongues.

Further investigations have proved that ERTS imagery can be used effectively for planimetric revision of small-scale maps, and this technique is being applied to six 1:250,000 topographic maps of the area of the Victoria Land strip mosaic. The coastline shown on the images was carefully compared with existing maps, and several major changes in coastal features were discovered. The comparison showed that the new satellite imagery can greatly facilitate accurate planimetric revision of the existing maps (figs. 24, 25).

Figure 26 illustrates the application of ERTS imagery for evaluating and revising published maps. The bottom part is a composite of two 1:500,000 sketch maps compiled from conventional aerial photographs taken during the austral summer of 1965–66. The top part is a mosaic of parts of seven MSS images. The area shown is about 117,000 km². The two triangles represent geodetic positions used to fit the imagery mosaic to the map base. A single ERTS image covers the same area as 1,320 photographs at a scale of 1:40,000. When comparing the two parts of figure 26, note the change in the configuration of the coast, as indicated by numbers 1, 3, and 4, and in the position of Burke Island, number 2. Also note the change in size and position of the Thwaites Iceberg Tongue, number 5. Its area has increased from 44,200 km² (map) to 71,500 km² (image), and the position has shifted about 8 km.

Because of the logistical requirements and the extremely high cost of taking photographs with conventional aircraft at altitudes high enough for efficient 1:1,000,000 mapping, efforts before the launching of ERTS–1 were directed primarily toward mapping the coastal and mountain areas at 1:250,000. ERTS imagery does, however, meet the need for 1:1,000,000 planimetric mapping. To cover an IMW map area, cartographers will only have to assemble 15 to 20 ERTS images rather than 12,000 conventional photo-

graphs. Production cost will decrease as production rate increases. The user will have at his disposal a visual representation of vast areas that have never been mapped. Moreover, he will not have to wait years before the image maps are available as he would for conventional planimetric or topographic maps.

Comparisons of image mosaics with the USGS-compiled McMurdo Sound region, IMW sheet ST 57–60 (fig. 27), and with the Australian-compiled IMW sheet, SS 40–42 (fig. 28), clearly demonstrate the application. Revisions and additions indicated for the two IMW sheets are readily apparent. The most obvious addition is the large block of previously unmapped geographical features revealed by the ERTS imagery. Noteworthy revisions include correcting the positions of the Ross Ice Shelf front (about 6.4 km north) and Franklin Island (7.2 km south). The position of Franklin Island has been in

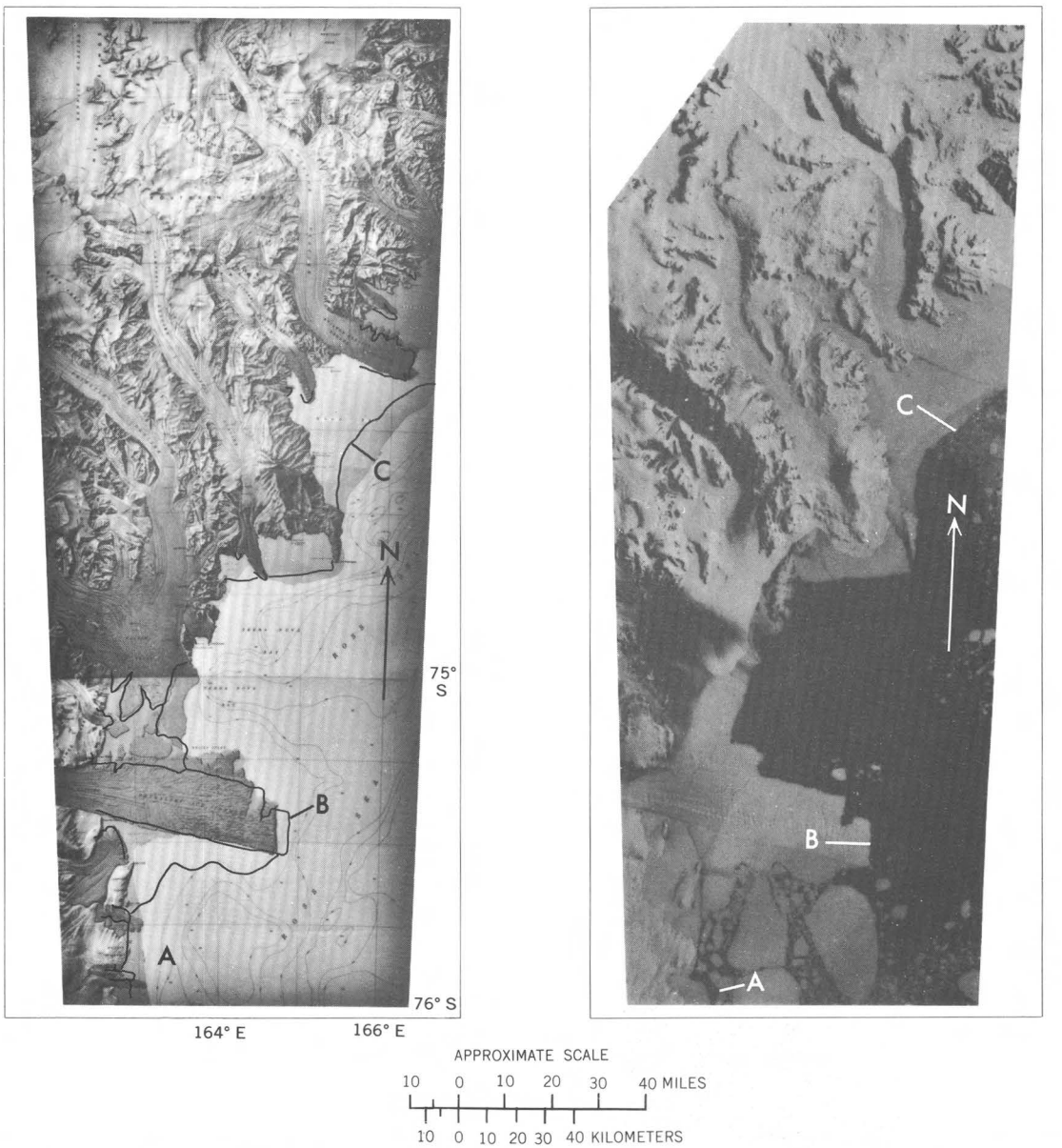


FIGURE 24.—Drygalski Ice Tongue, Victoria Land coast area of Antarctica. At left is a mosaic of three 1:250,000 U.S. Geological Survey topographic maps compiled from source data, 1955–64. Annotated revisions are based on the ERTS–1 image mosaic shown at right. Significant changes are: A, Harbord Glacier; B, Drygalski Ice Tongue; and C, fast ice (1128–20290, 1128–20293, 1163–20224, 1163–20230, and 1177–20001; all band 7).

contention for many years and has been continually reported to be wrong by ships.

ERTS imagery promises to be highly cost effective and of great scientific benefit to research on Antarctica, the most remote region on Earth. As a cartographic tool, ERTS offers the most practical means available to obtain cloud-free imagery of the millions of square kilometers of the continent still unmapped and to monitor coastal glaciological features (Southard and MacDonald, 1973).

In summary, these experiments underway with ERTS–1 imagery of Antarctica have already demonstrated the feasibility of (1) planimetric revision of available small-scale maps, (2) detection of gross changes in the northern limits of the three largest ice shelves in the world, (3) monitoring coastal glaciers, and (4) exposing hitherto unknown geographic features.

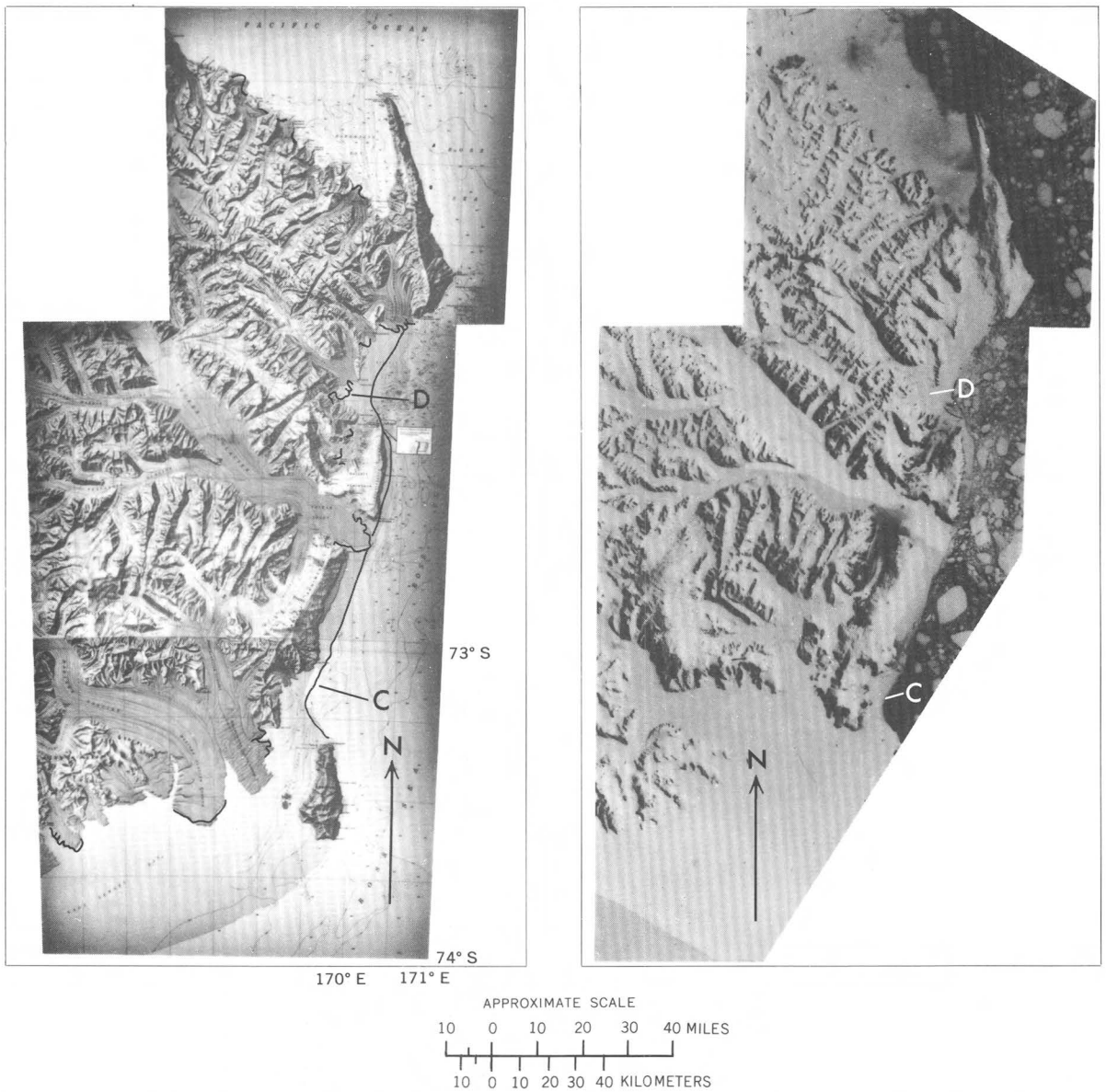


FIGURE 25.—Cape Adare, Victoria Land coast area of Antarctica. At left is a mosaic of three 1:250,000 U.S. Geological Survey topographic maps from source data, 1961–64. Annotated revisions are based on the ERTS–1 image mosaic shown at right. Significant changes are: C, boundary of fast ice and bay ice has changed, and D, shape of Honeycomb and Ironside Glaciers has changed, and their tongues have advanced about 3.2 km (1128–20275, 1128–20281, and 1128–20284; all band 7).

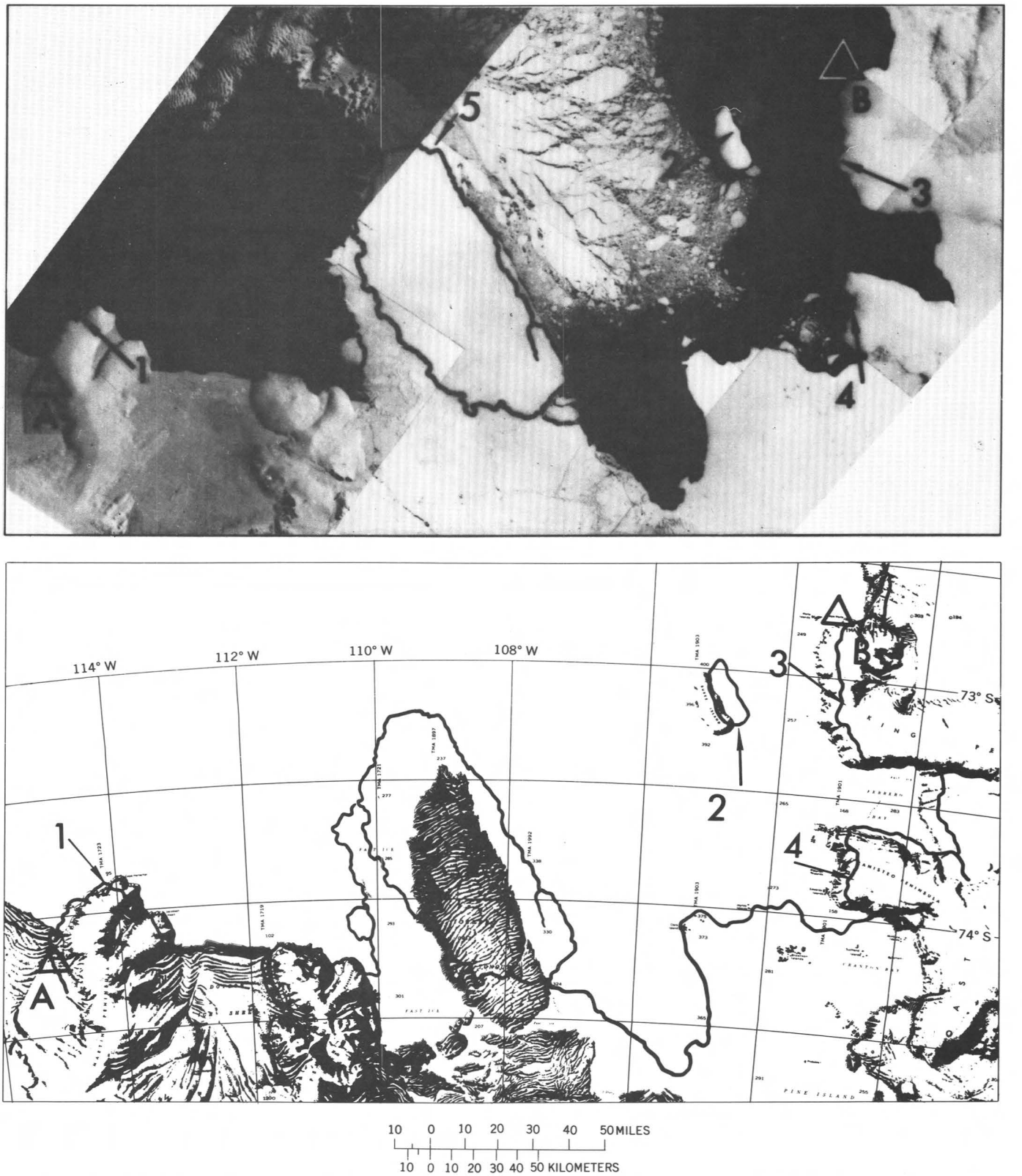


FIGURE 26.—Thwaites Iceberg Tongue, Amundsen Sea area of Antarctica. Comparison of the annotated mosaic of ERTS–1 image mosaic (top) and the corresponding sketch map (below) shows significant changes of the coastline and position changes of map features made by using ERTS imagery. Geodetic control points are shown at A and B (1137–14265, 1137–14271, 1157–14374, 1157–14380, 1157–14383, 1160–14551, and 1160–14554; all band 7).

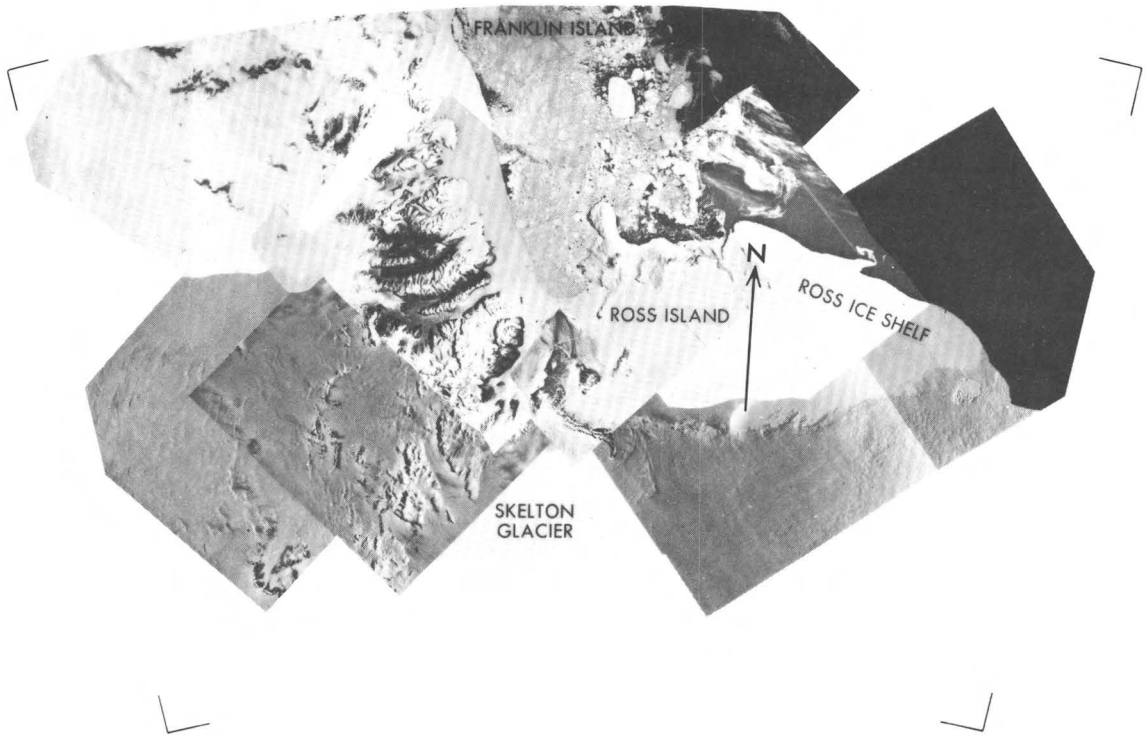


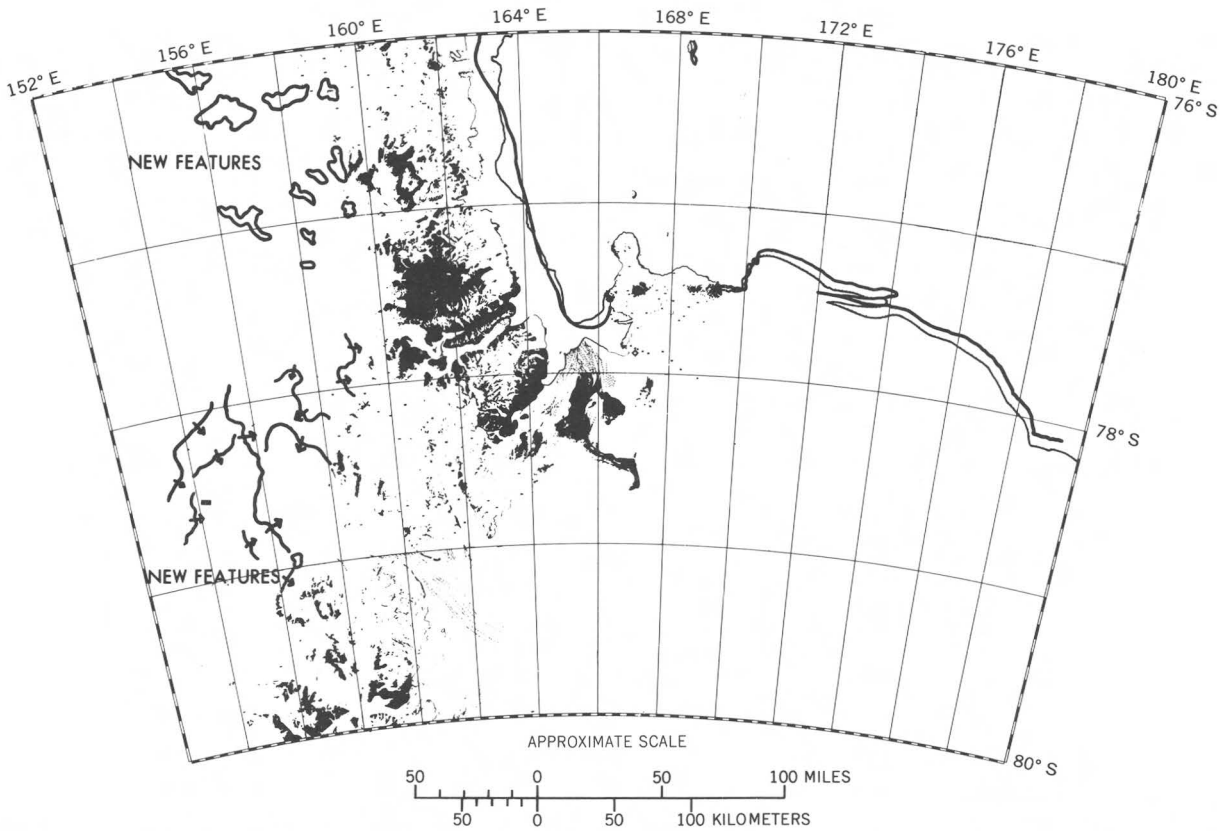


FIGURE 27.—McMurdo Sound region of Antarctica, 1:1,000,000 map (IMW Series, ST 57–60) compared with annotated ERTS–1 image mosaic. With the aid of the mosaic, newly discovered mountains, other land features, and coastline corrections will be added to a new U.S. Geological Survey 1:1,000,000-scale manuscript map before it is published (1128–20290, 1128–20293, 1143–20124, 1151–19151, 1154–19322, 1163–20230, 1165–18520, 1165–18523, 1174–19431, 1174–19433, 1177–20001, 1191–19383, and 1194–19555; all band 7).

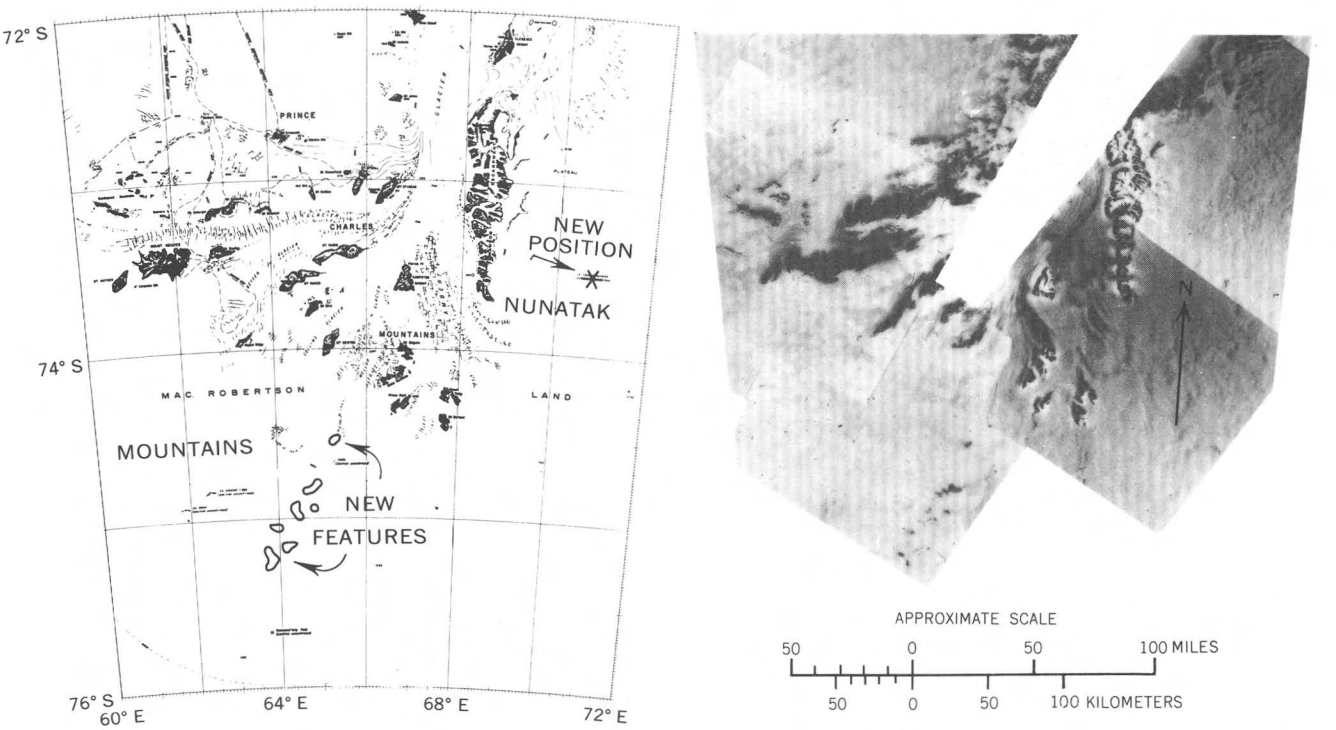


FIGURE 28.—Australian 1:1,000,000 map (IMW Series, SS 40–42) of the Lambert Glacier area of Antarctica compared with an annotated ERTS–1 image mosaic. With the aid of the mosaic, existing source maps can be analyzed and evaluated. The imagery reveals previously unknown mountains and other significant land features that can be added to a revision of this map (1145–03101, 1148–03261, 1148–03263, 1148–03270, 1168–03374, 1168–03381, 1196–02521, 1196–02523, and 1196–02530; all band 7).

If we are to have a better understanding of the way the polar regions affect man, particularly in assessing the potential resources of Antarctica, there is an immediate need to know what's there and where. Space technology offers a new method for producing small-scale imagery products of remote regions that is substantially cheaper and quicker than production by conventional means. The reasons for this are:

*Advantages of ERTS synoptic coverage:*

1. Current, complete, and repetitive imaging.
2. First-look imagery of unmapped areas.
3. Weather conditions not dominant.
4. Fewer exposures and greater areal coverage per image.
5. Reduced compilation cost for small-scale products (for example, 1:1,000,000).
6. Single scene and synoptic views.

*Special uses and benefits:*

1. Source for medium- and small-scale orthoimage products.
2. Source for medium- and small-scale planimetric-map revision.
3. Source for orthoimage mosaics.
4. Time-lapse sequence of images for thematic mapping: coastal change detection, sea-ice studies, ice-movement studies, and so forth.
5. Planning document.
6. Visual navigational aids (near-real time).

# CADASTRAL BOUNDARIES ON ERTS IMAGES

By Grover Torbert, Bureau of Land Management,
and William R. Hemphill, U.S. Geological Survey

The ERTS–1 CCT's permit combining a part of the image of the Sheridan area of Wyoming (fig. 29) with a cadastral-survey delineation of township, range, and section boundaries. The combination of image and cadastral map (fig. 30) shows 939 $km^2$ of Sheridan and Big Horn Counties in Wyoming and Montana, respectively. Standard U.S. Geological Survey quadrangle maps of the area are shown in figure 31 for comparison.

The cadastral data, together with four selected ground control points recognized in the ERTS image, were digitized from written descriptions and existing maps and combined with the ERTS–1 CCT in a PDP 11/45 computer. The combination of image and cadastral delineation was printed with a Calcomp plotter Model 728 flatbed. The gray scale of each pixel is represented by varying the amount of ink distributed to each dot. Cadastral boundaries, roads, and streams are represented by plotting one-third the normal pixel area.

The Tongue River flows eastward and northward in the central and northeastern parts of the image map, respectively. The foothills of the Bighorn Mountains can be seen in the southwest corner. Dark-toned circular patterns in the west-central part are radial irrigation systems.

This image map was produced by Computer Research Corp., Arvada, Colo., for the Bureau of Land Management to use for recording changes in land ownership and land use on a pictorial base. Such a base can be used to relate land ownership to seasonal change in grassland areas as a guide to the release or withdrawal of grazing leases on public lands administered by the bureau. The image map will also facilitate interaction with a computer-implemented land-information system that is being designed. The bureau is especially interested in this area because of the marked increase in coal strip mining that has occurred since 1972.

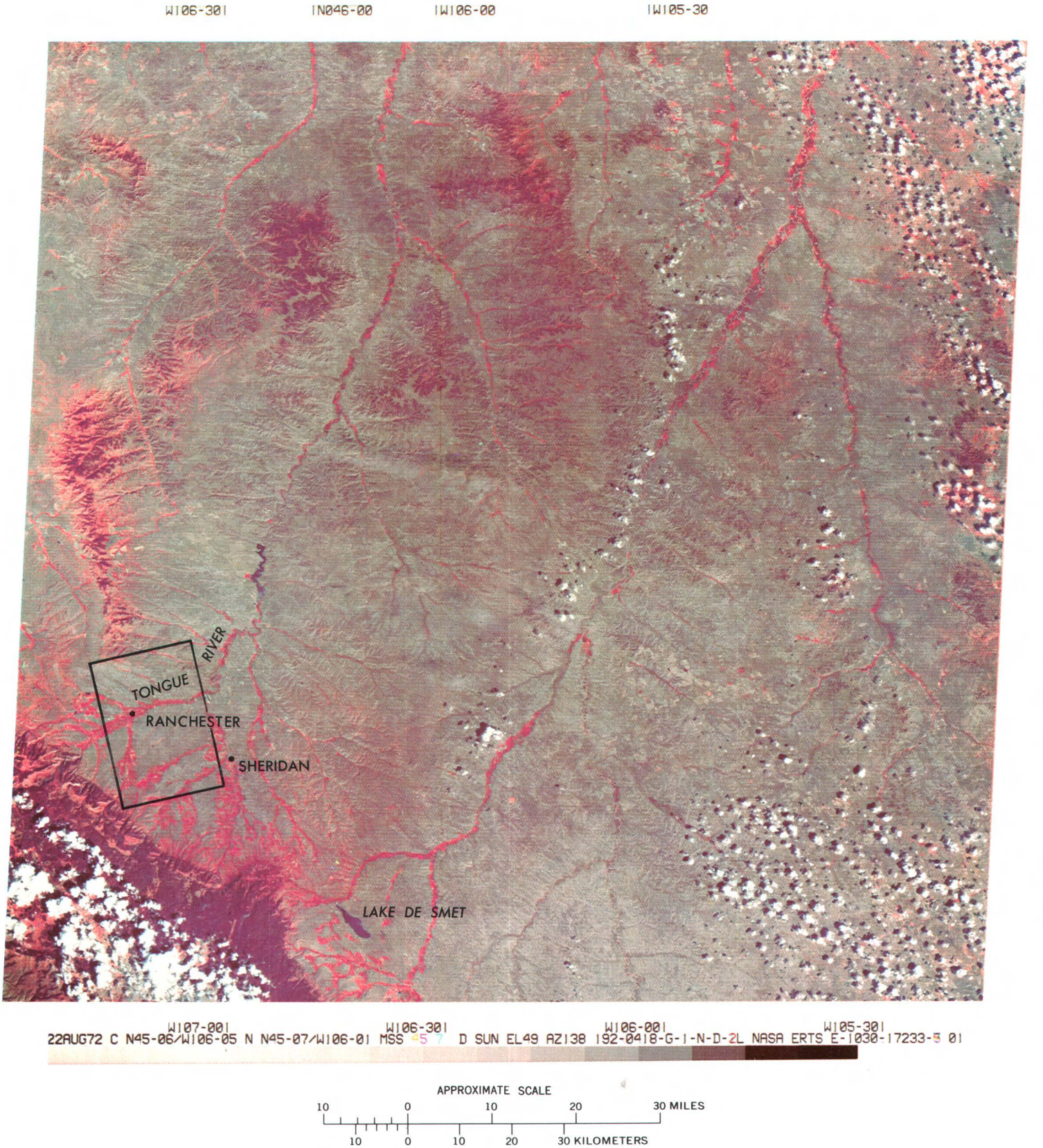


FIGURE 29.—Annotated color composite ERTS–1 image of the Sheridan area of Wyoming (1030–17233).

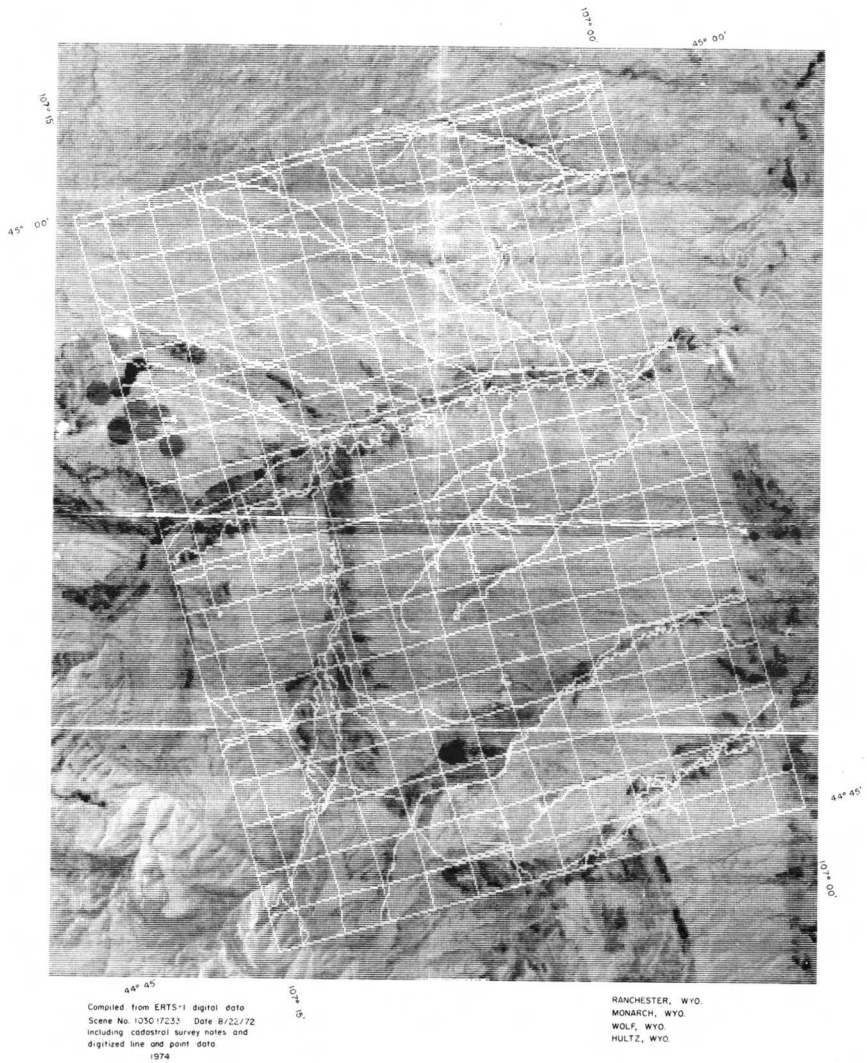


FIGURE 30.—Computer-processed combination of part of the Sheridan ERTS–1 image and the cadastral survey delineation of township, range, and section boundaries (part of 1030–17233, band 4).

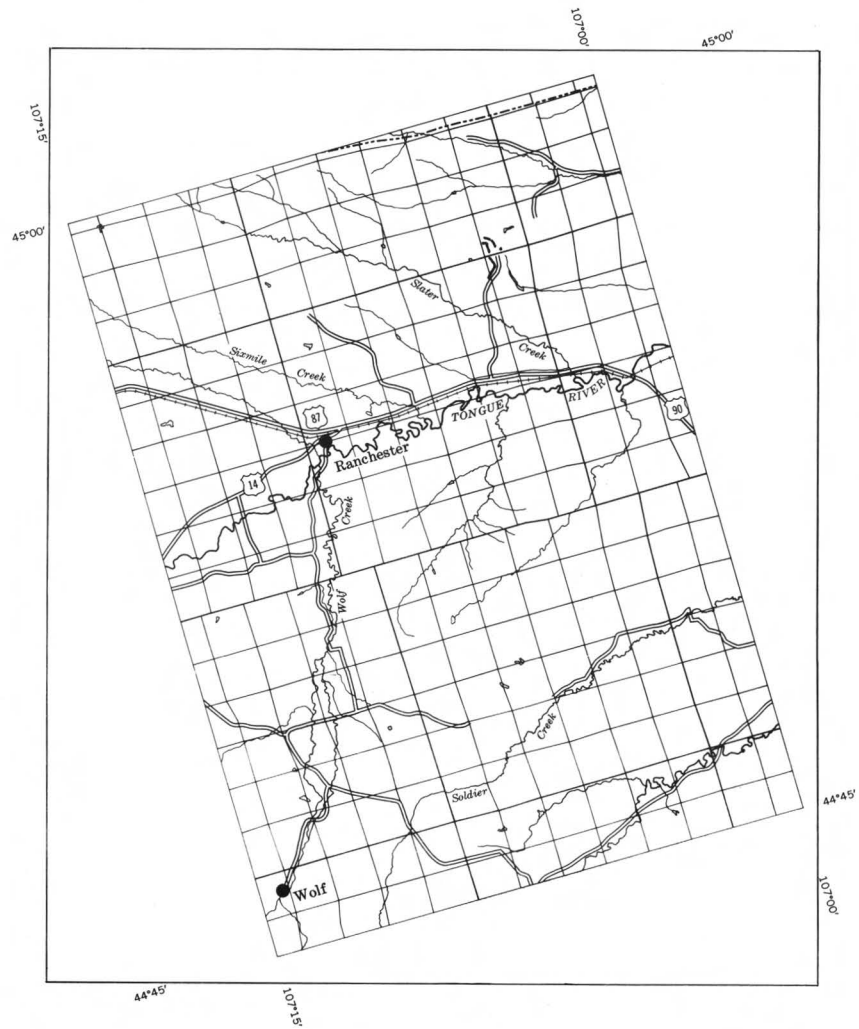


APPROXIMATE SCALE

10,000 0 10,000 20,000 30,000 40,000 FEET

2000 0 2000 4000 6000 8000 METERS

FIGURE 31.—Standard U.S. Geological Survey map of the Sheridan area of Wyoming from published 7½-min quadrangle maps: Ranchester, Monarch, Wolf, and Hultz Draw.

## REFERENCES

Bernstein, Ralph, 1974, Digital image correction and information extraction [abs.]: Internat. Symposium on Remote Sensing of Environment, 9th, Ann Arbor, Mich., 1974, Proc., v. 2, p. 851–852.

Colvocoresses, A. P., 1972, Cartographic applications of ERTS imagery: NASA Goddard Space Flight Center, Earth Resources Technology Satellite Symposium, Sept. 1972, Proc., p. 88–94.

———1973a, Unique characteristics of ERTS: NASA Goddard Space Flight Center, Symposium on Significant Results Obtained from the Earth Resources Technology Satellite–1, 2d, New Carrollton, Md., Mar. 1973, Proc., v. 1, sec. B, p. 1523–1525.

———1973b, The ERTS image format as the basis for a map series: Am. Soc. Photogrammetry, Symposium on Management and Utilization of Remote Sensing Data, Sioux Falls, S. Dak., 1973, Proc., p. 142–143.

———1974a, Space Oblique Mercator: Photogramm. Eng., v. 40, no. 8, p. 921–926.

———1974b, Towards an operational ERTS—Requirements for implementing cartographic applications of an operational ERTS-type satellite: NASA Goddard Space Flight Center, Symposium on the Earth Resources Technology Satellite–1, 3d, Washington, D.C., Dec. 1973, Proc., v. 1, sec. A, p. 539–546.

Colvocoresses, A. P., and McEwen, R. B., 1973, Progress in cartography, EROS Program: NASA Goddard Space Flight Center, Symposium on Significant Results Obtained from the Earth Resources Technology Satellite–1, 2d, New Carrollton, Md., Mar. 1973, Proc., v. 1, sec. B, p. 887–898.

Southard, R. P., and MacDonald, W. R., 1973, The cartographic and scientific application of ERTS–1 imagery in polar regions [abs.]: COSPAR Plenary Mtg., 17th, Konstanz, Germany, 1973, Program Abs., p. 70.

Stein, G. E., 1971, Portrayal of earth features with NASA photography, *in* American Congress on Surveying and Mapping, Papers from the 1971 ASP–ACSM Fall Convention * * *: Washington, D.C., Am. Cong. Surveying and Mapping, p. 308–314. [Sample chart areas, NASA photos, and revised samples are available under separate cover from: Aeronautical Chart and Information Center, Cartography Division, 2d and Arsenal Sts., St. Louis, Mo. 63118.]

# CHAPTER 2.

# APPLICATIONS TO GEOLOGY AND GEOPHYSICS

## INTRODUCTION

By William A. Fischer,

U.S. Geological Survey

Geologic knowledge is essential for determining the optimum use of our land. This knowledge provides an understanding of geologic hazards—such as landslides, earthquakes, volcanic eruptions, and land subsidence—as well as the engineering properties of soils and rocks. In addition, such knowledge aids in pinpointing potential sources of minerals and fuels. ERTS has permitted geologists to rapidly expand their geologic knowledge by revealing features that were never before recognized and that are worthy of investigative priority. Furthermore, ERTS has provided geologists and other scientists throughout the world with a common set of data, so that communication in the profession is vastly improved and progress toward geologic understanding is accelerated.

This chapter is one of the largest in this book and reflects geologists' long history of using aerial photography and their seemingly inherent desire to always view the study area from the "highest hill." The broad involvement of geologists and their willingness to contribute to this work are testimony to the geologic values inherent in the ERTS data.

Papers in this chapter primarily deal with the use of imagery, but the use of the ERTS data collection system to collect information from ground sensors located in remote areas is also described. Collectively, the papers present a cross section of preliminary results gleaned from satellite data.

Although ERTS was designed for a variety of scientific purposes, a series of geologic hypotheses that were advanced played a major role in determining the final design criteria. These hypotheses were:

1. That large features (including glacial features, faults and other lineaments, and volcanic features) are present on the surface of the Earth that, because of their size and subtle expression, had gone unrecognized in conventional ground and aerial surveys but that can be seen on images having sufficient areal coverage and spectral uniformity.
2. That color or multispectral images properly recorded and processed to preserve color uniformity would be useful in mapping distributions of rock types and alteration products.
3. That some environmental features are only intermittently visible depending on angle of illuminatiton and on snow, water, or vegetation distributions.

4. That some geologic processes, such as sedimentation and glacial motion, could be better understood if viewed in a "time-lapse" mode.

The need to test these hypotheses was a significant factor in the decisions that led to adoption of the repetitive, time-uniform, multispectral character and narrow-angle field of view of the ERTS system.

All the papers in this chapter support one or more of these hypotheses. Most present results that have relatively short-term economic significance in that they provide information that will add to the efficiency of exploration for minerals, fuels, and ground water. Some, such as Brown and Huffman's study of the Jordan Rift Valley (p. 53), have immediate scientific impact but are of longer range economic significance. Most papers in the section deal with the mapping of large previously unknown geologic structures—principally lineaments and faults—that may constitute geologic hazards or that may control localization of mineral deposits, suspected folds that may be oil bearing, and glacial features that may be sources of large quantities of ground water.

Morrison's paper (p. 72) on the enhanced visibility of snow-covered terrain features provides good examples of geologic features that are only intermittently visible. Further documentation of the advantages of the multispectral approach to viewing the Earth is given by Schmidt, who discusses the detection of hydrothermal sulfide deposits in the Saindak area of western Pakistan (p. 89) and by Stoertz and Carter (p. 76) in citing the conclusion of Dr. Brockmann of Bolivia that color adds 40 to 50 percent more to the geologic information that can be interpreted from a given ERTS image. Full use of the multispectral qualities of ERTS, however, requires that the interpretations be made using the digital magnetic tapes (CCT's) of the data instead of the analog images. These tapes preserve the spectral qualities of the data to a larger extent than do photographs and permit the various bands to be compared or ratioed, as in the case of the study by Rowan, Wetlaufer, and Goetz (p. 102).

The articles dealing with foreign areas indicate the tremendous amount of geologic information that is being derived from the relatively straightforward use of ERTS data to improve the world cartographic base maps; Stoertz and Carter (p. 76) point out that of 150 salars (salt-encrusted-basins) in parts of Chile, Bolivia, Argentina, and Peru, 20 were unmapped before ERTS.

The new classification system for the desert sand seas developed by McKee and Breed (p. 81) is illustrative of the value of uniform global coverage; the long-range value of their work for improving geologic communication and education will be great.

The deployment of seismic-event counters and other sensors on 15 volcanoes, the successful relay of measurements via the ERTS satellite, and the receipt of "telltale" warning signals from Volcan Fuego in Guatemala 5 days before eruption clearly demonstrate the technological and economic feasibility of building a global volcano-surveillance system (see Ward and Eaton, p. 106).

I believe that the reports in this chapter demonstrate that geologists, having tested ERTS as a new working tool, have not found it wanting.

# GEOLOGIC ANALYSIS OF THE SANTA LUCIA RANGE, CALIFORNIA

By Donald C. Ross,

U.S. Geological Survey

Geologic interpretation of the granitic and metamorphic basement of the Santa Lucia Range is hindered by structural complexity, dense vegetation cover, and a lack of distinctive mappable units. Evidence for faulting is common and widespread, but the distinction of through-going zones that may distinguish major movement from local minor faults is difficult to make.

A northwest-trending group of lineaments is visible on 1:1,000,000 ERTS imagery of the area (figs. 32 and 33). Most of the better displayed lineaments are unusually straight segments of stream courses that combine to form relatively continuous linear features tens of kilometers long. Many of these straight stream courses have been interpreted and mapped as faults by earlier workers.

Interpretation of orbital imagery (fig. 33) takes into account most of the previously mapped fault segments and suggests an overall simpler and more continuous pattern of faulting than earlier published interpretations of this basement block (Jennings and Strand, 1958). The interpretation points to an anastamosing fault system that cuts completely through the Santa Lucia Range basement block. Other evidence suggests that the easternmost faults of this system do not noticeably disturb the basement (displacements are on the order of a few thousand feet), whereas the westernmost "solid-line" fault juxtaposes some very different rocks and may reflect a major basement offset. The relatively continuous nearly 50-km lineament at A, which may reflect this fault, certainly supports the hypothesis that this is a major basement break.

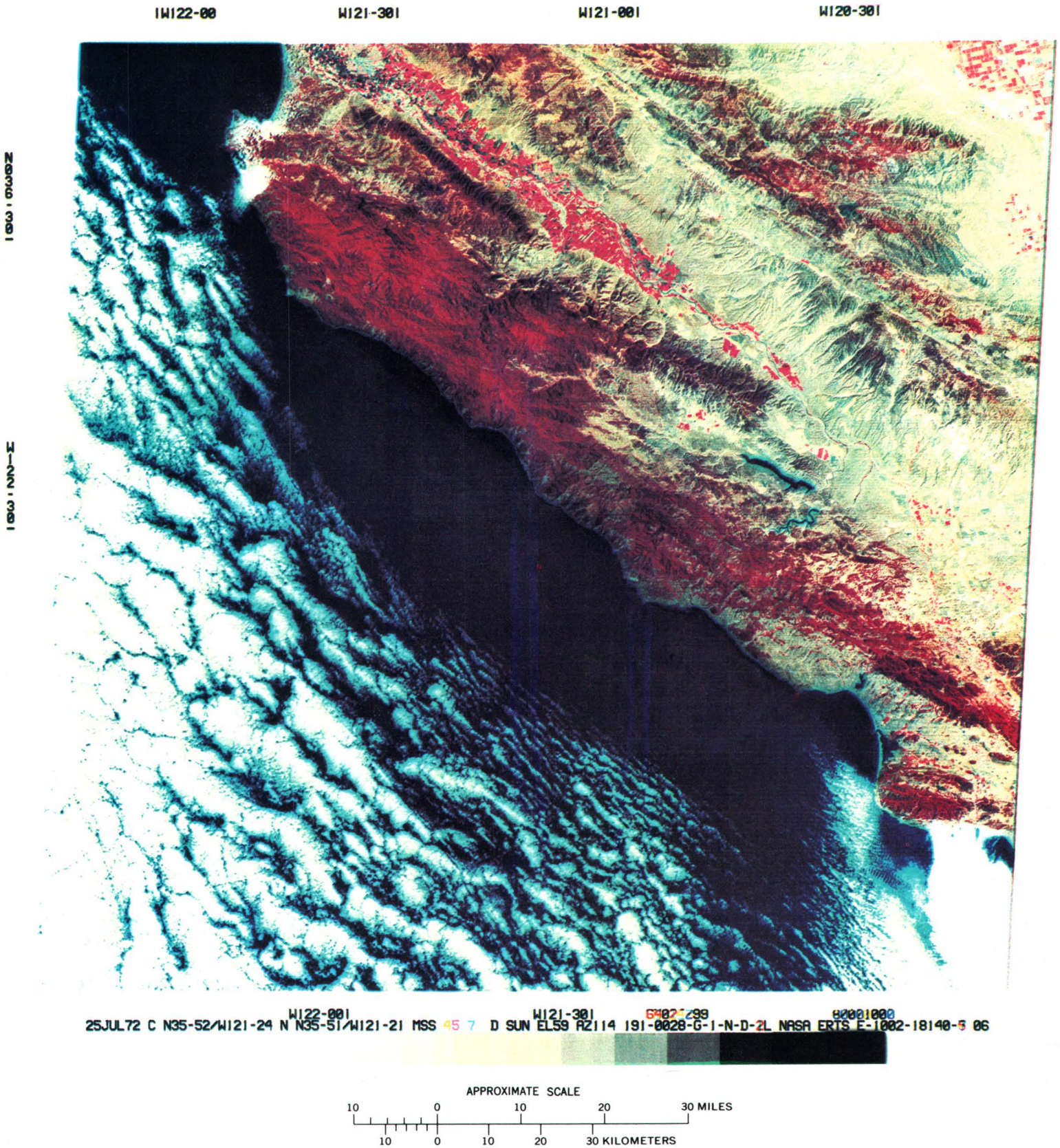


FIGURE 32.—Color composite ERTS–1 image of the Salinas Valley and the Santa Lucia Range, Calif. (1002–18140).

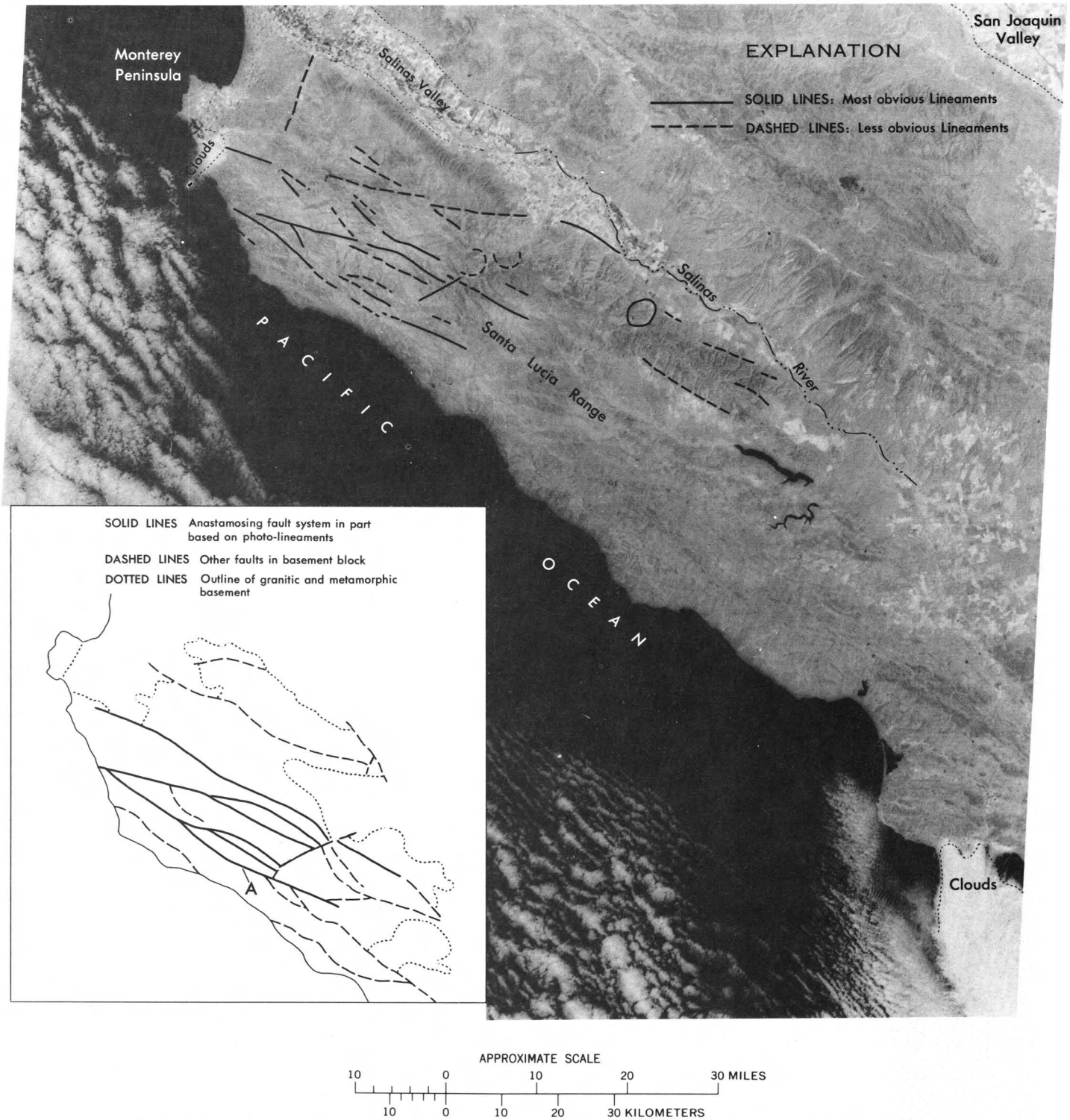


FIGURE 33.—ERTS–1 image showing interpretation of photolineaments in the northern Santa Lucia Range, Calif. (1002–18140). Letter A indicates continuous 50-km lineament.

# AN INTERPRETATION OF THE JORDAN RIFT VALLEY

By G. F. Brown and A. C. Huffman,

U.S. Geological Survey

Among the more discernible features on ERTS imagery are the large linear features associated with faulting along rift valleys. Of these the opening of the Red Sea and the Gulf of Aden have received widespread attention (Girdler, 1962; Le Pichon and Heirtzler, 1968; and McKenzie and others, 1970). Following Euler's fixed-axis theorem for the nature of plate movement (that is, that relative movement of any segment of the globe with regard to another segment requires rotation around a pole through the center of a sphere), the openings of the Red Sea and the Gulf of Aden (fig. 34, R and A, respectively) require at least two poles. Also, as seems likely, Gulf spreading began earlier along transform faults with meridional shearing along the Red Sea rift. Using azimuths to transform faults and fault-plane solutions from first-motion studies, Girdler (1972) has postulated the location of two poles of rotation. For the Gulf of Aden (Arabian-Somalian plates) he favors McKenzie's position of lat 26°30′N.; long 21°30′E., and for the Red Sea (Arabian-Nubian plates) he favors a location at lat 31°30′N.; long 23°00′E. (fig. 34).

The Jordan Rift Valley is a striking example of the large linear features, and, if Girdler's pole locations and two periods of rapid separative movement are accepted, we would expect to see a difference in bearing of the Jordan rift north of its junction with the Red Sea. Examination of the latest geologic maps of the Levant does show a bearing of about N. 10° E. for the earlier opening, swinging to a meridional trend toward Lebanon from the pole of lat 26°30′N.; long 21°30′E., where a fault zone appears to swing into the Mediterranean Sea between Beirut and Tyre; an examination of a mosaic of ERTS images (fig. 35) confirms this bearing. Indeed, the European geologic map (von Gaertner and Walther, 1971) shows the northeast-trending Carmel fault (Freund, 1970, fig. 1) extending into the Mediterranean Sea at Haifa, some kilometers farther south, which fits a rotation around the southernmost pole even better. As would be expected, the older fault zone is more obscure, even though the lineament is well-defined on the ERTS imagery. Inspection of this feature along the Beirut-Tyre road in southern Lebanon reveals extensive disturbance that approaches a crushed-zone appearance. North of Beirut, the younger, more pronounced faults trend north-northeast, in keeping with a pole location farther north than the location of the Gulf of Aden pole. Earlier

locations by McKenzie and others (1970) at lat 36°30′N.; long 18°00′E., west of Greece in the Mediterranean Sea, fit the bearing of the faults north of Beirut as well as the transverse fault between Masirah Island and Oman in the southeastern shore of the Arabian Peninsula. Thus, in this example, ERTS imagery tends to clarify and confirm one interpretation for the history of the Red Sea and the Gulf of Aden.

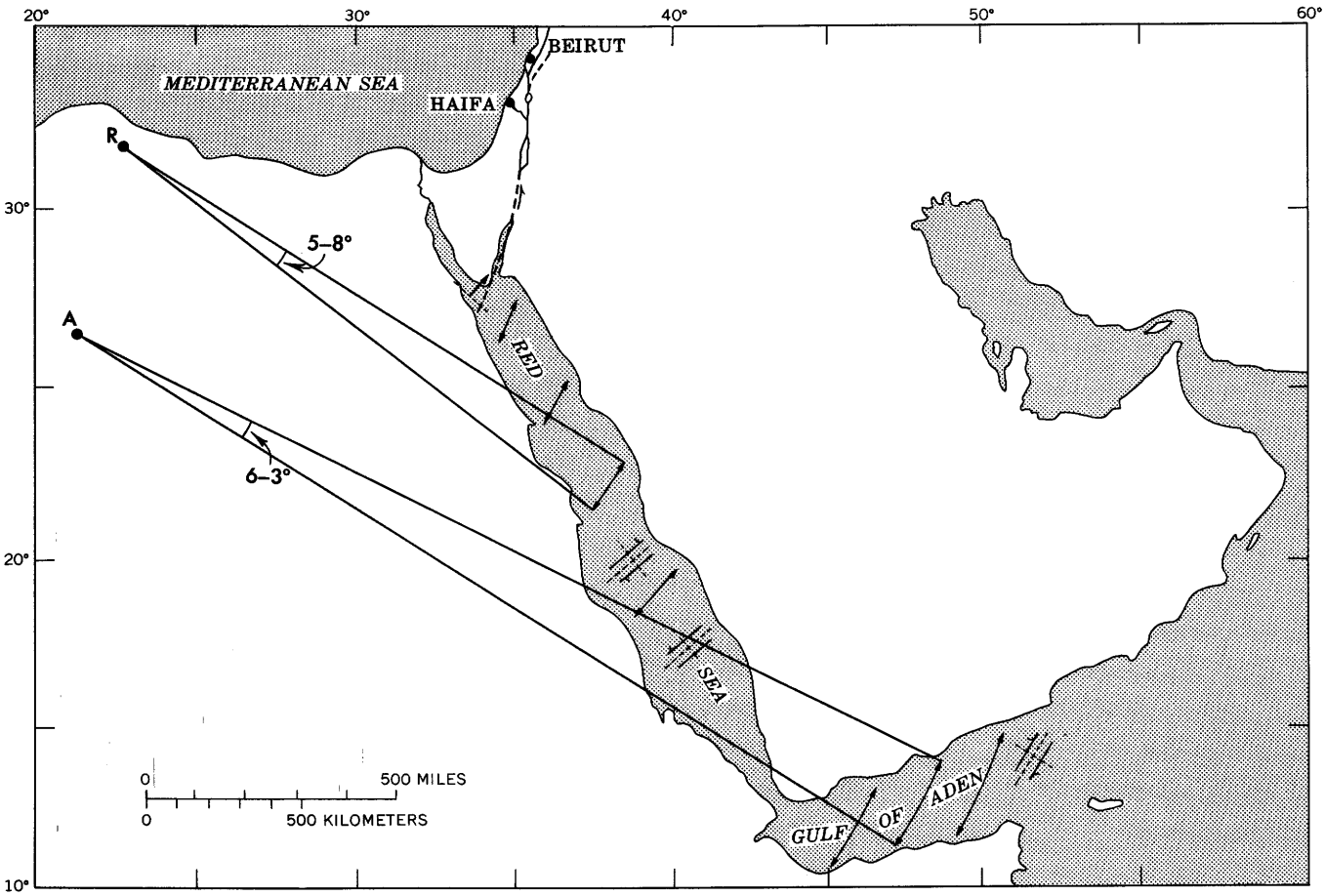


Figure 34.—Map of the Red Sea area showing location of tectonic-plate rotation poles.

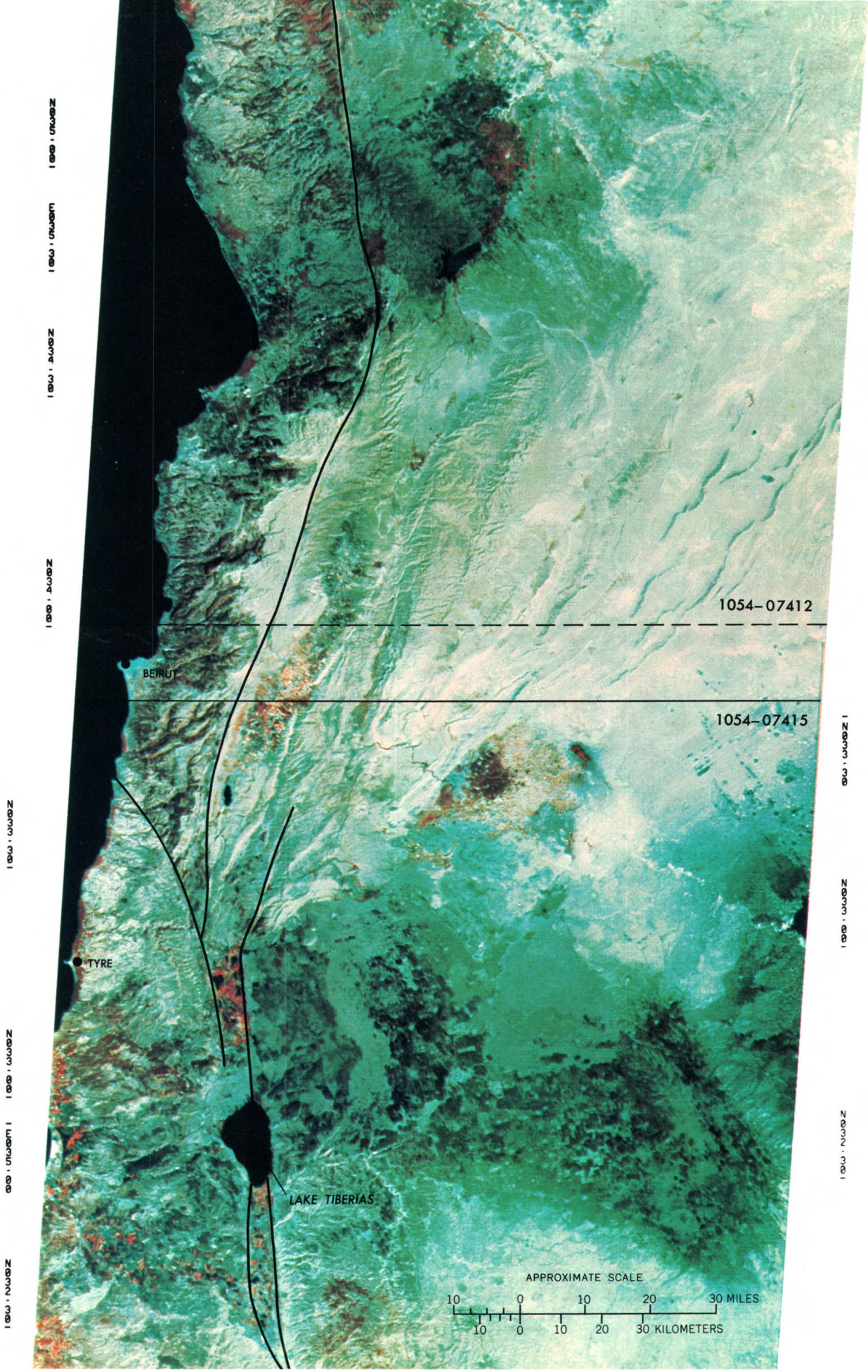


E035-30 E036-001 E036-301 E037-001
15SEP72 C N34-29/E036-33 N N34-28/E036-37 MSS 4 R SUN EL49 AZ135 190-0747-G-1- D-2L NASA ERTS E-1054-07412 01

15SEP72 C N33-03/E036-07 N N33-02/E036-10 MSS 4 R SUN EL50 AZ134 190-0747-G-1- D-2L NASA ERTS E-1054-07415 01

FIGURE 35.—Annotated color composite ERTS–1 image mosaic of the Jordan Rift Valley (1054–07412 and 1054–07415).

# GEOLOGICAL STRUCTURE IN THE WESTERN BROOKS RANGE AREA

By Ernest H. Lathram,

U.S. Geological Survey

Despite several seasons of exploration by private companies and by the U.S. Geological Survey, the ubiquitous tundra cover and the paucity of outcrops along the shallow streams and rivers in the lowland area of the Ipewik and Kukpuk Rivers have prevented recognition of the distribution of structural elements. Examination of conventional aerial photographs has revealed little additional data. This ERTS image (fig. 36), however, displays a startlingly clear and detailed representation of the area (Lathram, 1973). The image shows clearly the complexity of structure in the lowland and the pronounced difference between the structural pattern in this area and that in the areas of strata of comparable age (to the north and east) and of older strata in the mountains (to the south and east) (fig. 37). The change to greater structural complexity in the lowlands may be due to oroclinal bending around an axis trending northwest through the lowlands (Tailleur and Brosgé, 1970) or, more probably, due to the superimposition of a younger belt of east-directed thrust faults in the western part of the area upon an older belt of north-directed thrust faults in the Brooks Range (Grantz and others, 1970). Recognition of the structural complexity and determination of its cause are critically important in determining the potential for petroleum accumulations at depth in the area (Lathram and others, 1973).

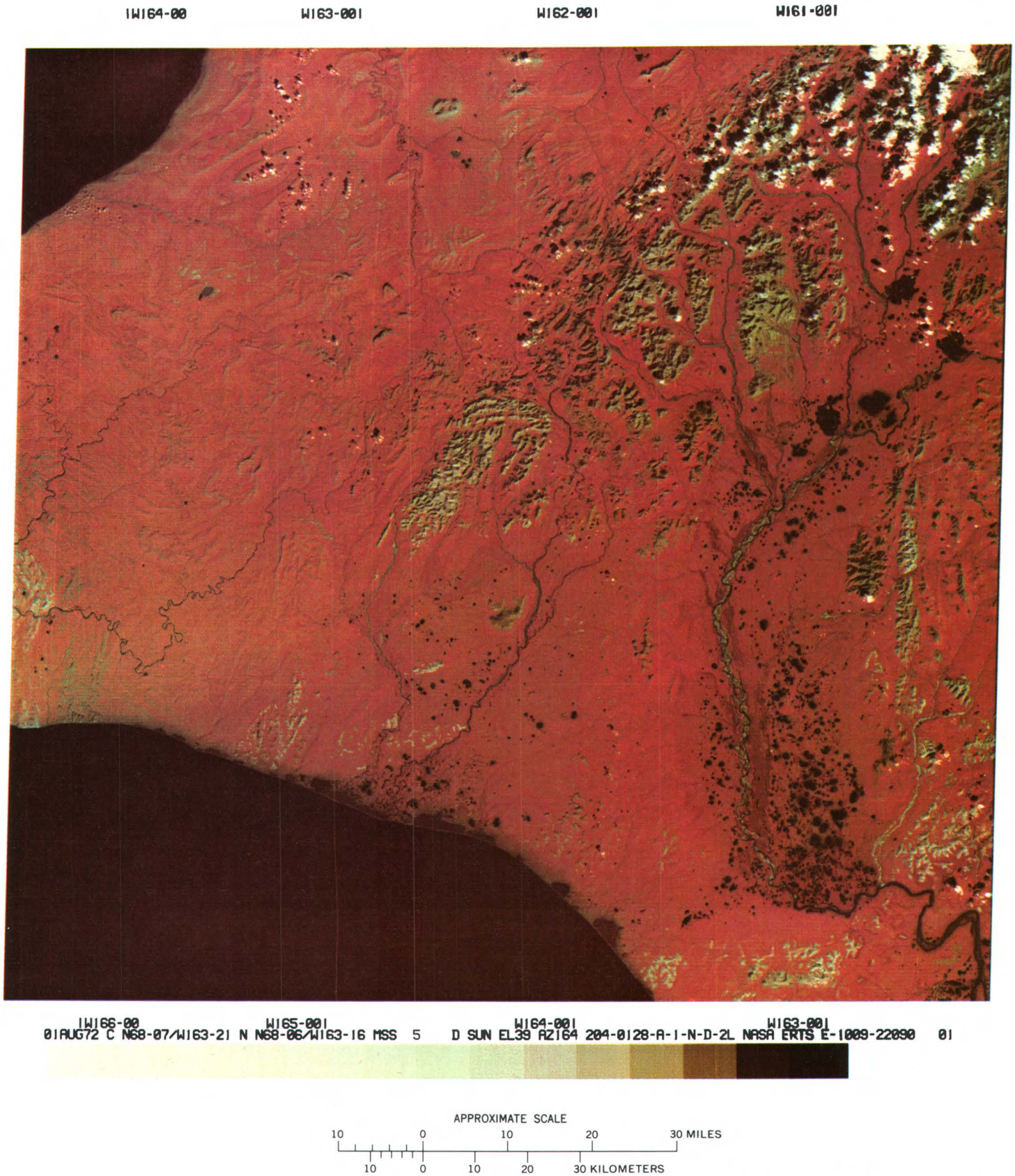


FIGURE 36.—Color composite ERTS–1 image of the western Brooks Range area of Alaska (1009–22090).

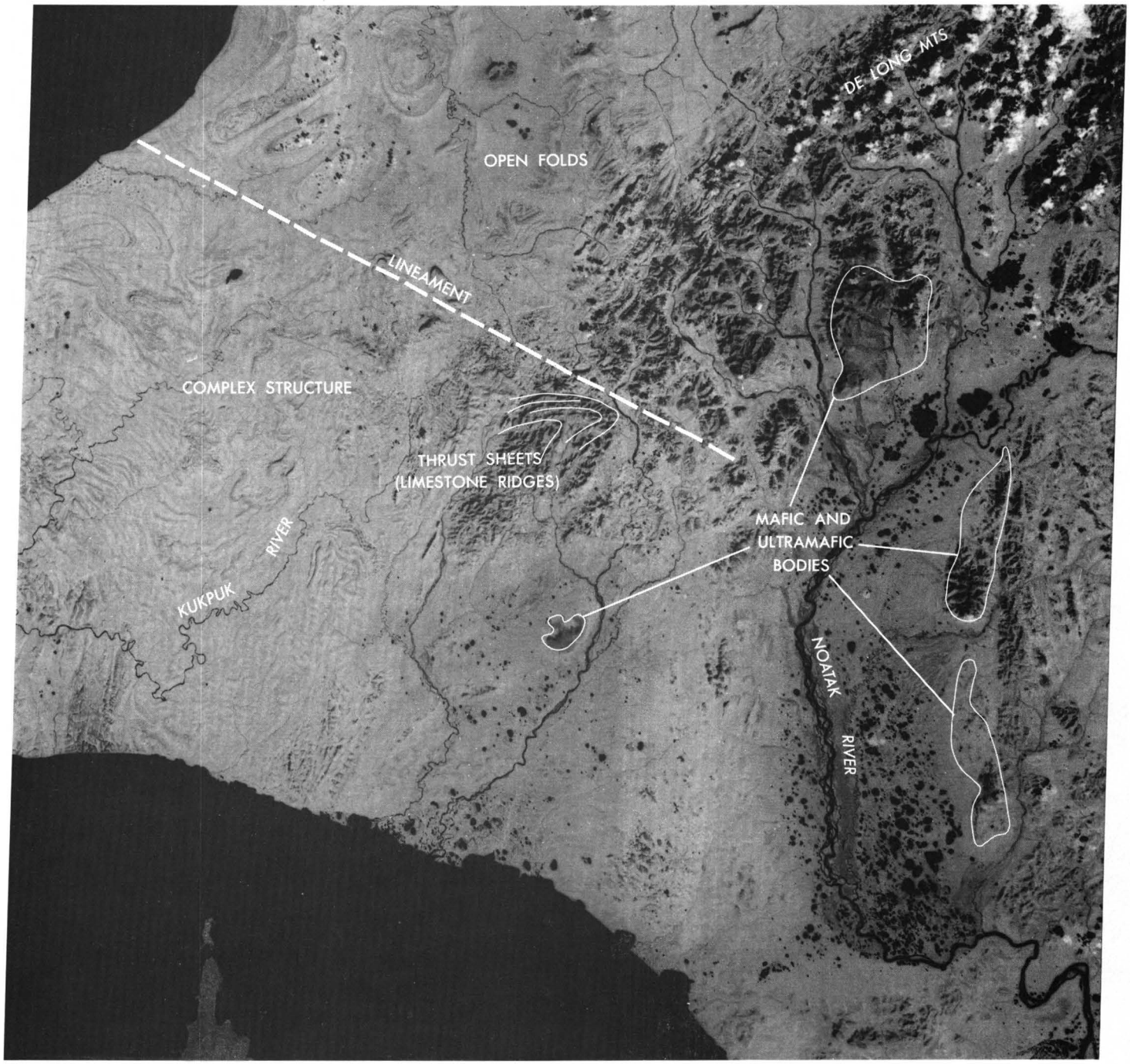


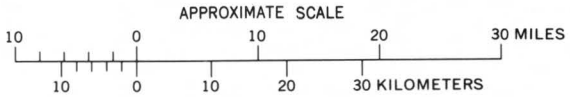


FIGURE 37.—Annotated ERTS–1 image of the western Brooks Range area of Alaska, showing geologic features and place names (1009–22090, band 7).

# GEOLOGICAL EVALUATION OF NORTH-CENTRAL ARIZONA

By Donald P. Elston,

U.S. Geological Survey

High-quality ERTS–1 images of north-central Arizona, computer processed by the Jet Propulsion Laboratory, Pasadena, Calif., to enhance detail and enlarged to approximately 1:200,000, were analyzed monoscopically and stereoscopically for their geologic information (Goetz and others, 1973). Figure 38 is a standard ERTS MSS color composite image, and figure 39 is a computer-enhanced nonconventional color composite image of north-central Arizona. The ERTS project test site in north-central Arizona includes areas that have been mapped in detail at 1:48,000 and 1:62,500. A large part of the area, however, has only been mapped in reconnaissance at 1:375,000 for the geologic map of Arizona that was published at 1:500,000 (Wilson and others, 1969). A north-central part of the Arizona geologic map is shown in figure 40.

Use of the ERTS images, principally bands 6 and 7, improves the distribution of several of the geologic units shown on the State geologic map; units shown in figure 41 and the accompanying explanation were discriminated using both the images and detailed geologic maps. The product is a regional geologic map referenced to a near-orthographic image base. Geologic detail, of course, is less than that of large-scale standard geologic quadrangle maps, but it is greater in areas that only have been mapped in reconnaissance. It is especially useful to plot geology on an orthographic image base because relations of geologic units to physiographic, vegetational, and structural characteristics of the terrain can be evaluated from a single display. Transfer of the planimetric geology to a topographic base allows complementary analysis using standard techniques.

Basalt of late Tertiary age crops out in much of the area, and for the most part it was readily discriminated on the ERTS images. Within an area mapped as basalt on the State geologic map, a light-colored area that proved to be highly tuffaceous was recognized and mapped. Quaternary and Tertiary sediments also were recognized and mapped on the ERTS images, and details of their distribution were better than on the State geologic map. Fine details of the stratigraphy in gray to white Paleozoic rocks (sandstone and limestone) could not be resolved, however, although the red sandstone of the Supai Formation of Permian and Pennsylvanian age was identified on false-color images. All Paleozoic rocks therefore were mapped as one unit; thus, at least for Paleozoic rocks, the State geologic map is far superior. In contrast, more Pre-

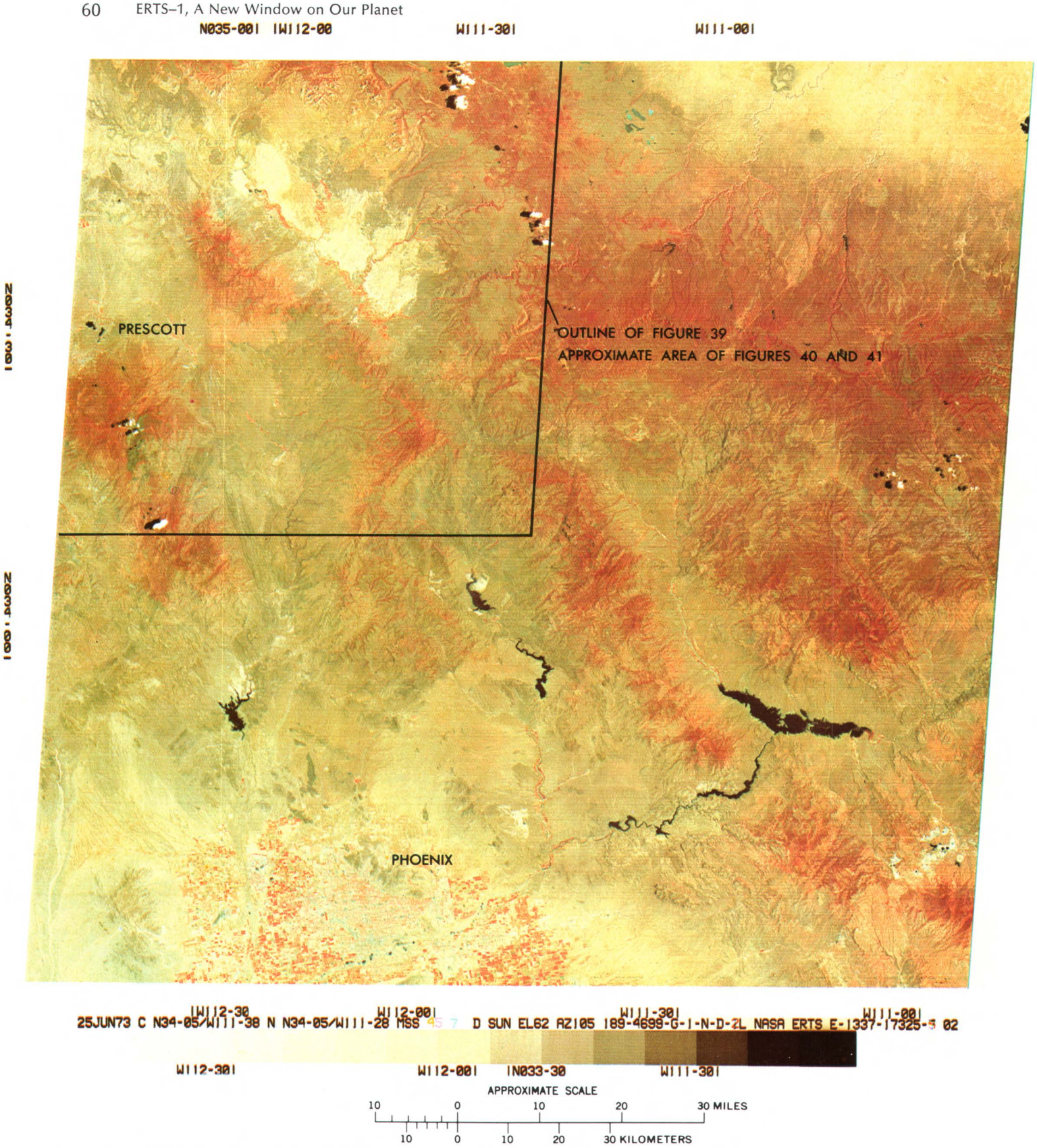


FIGURE 38.—Annotated color composite ERTS–1 image of north-central Arizona (1337–17325).

FIGURE 39.—Computer-processed four-band color composite ERTS–1 image of north-central Arizona. This image has undergone a nonlinear (gaussian) computer contrast stretch at the Jet Propulsion Laboratory, Pasadena, Calif. Color units and tone boundaries correlate with stratigraphic and vegetation units. Bronze, mountain and plateau vegetation (mainly Ponderosa pine); yellowish orange, vegetation along stream courses (mainly cottonwood and sycamore trees); greenish tan in north-central part of scene, red beds (red brown) of Supai Formation of Pennsylvanian and Permian age; greenish blue, basaltic flows of late Tertiary (Miocene and Pliocene) age; creamy white, lake beds (siltstone and marl) of late Tertiary Verde Formation (enlargement of part of 1337–17325, fig. 38). ▶

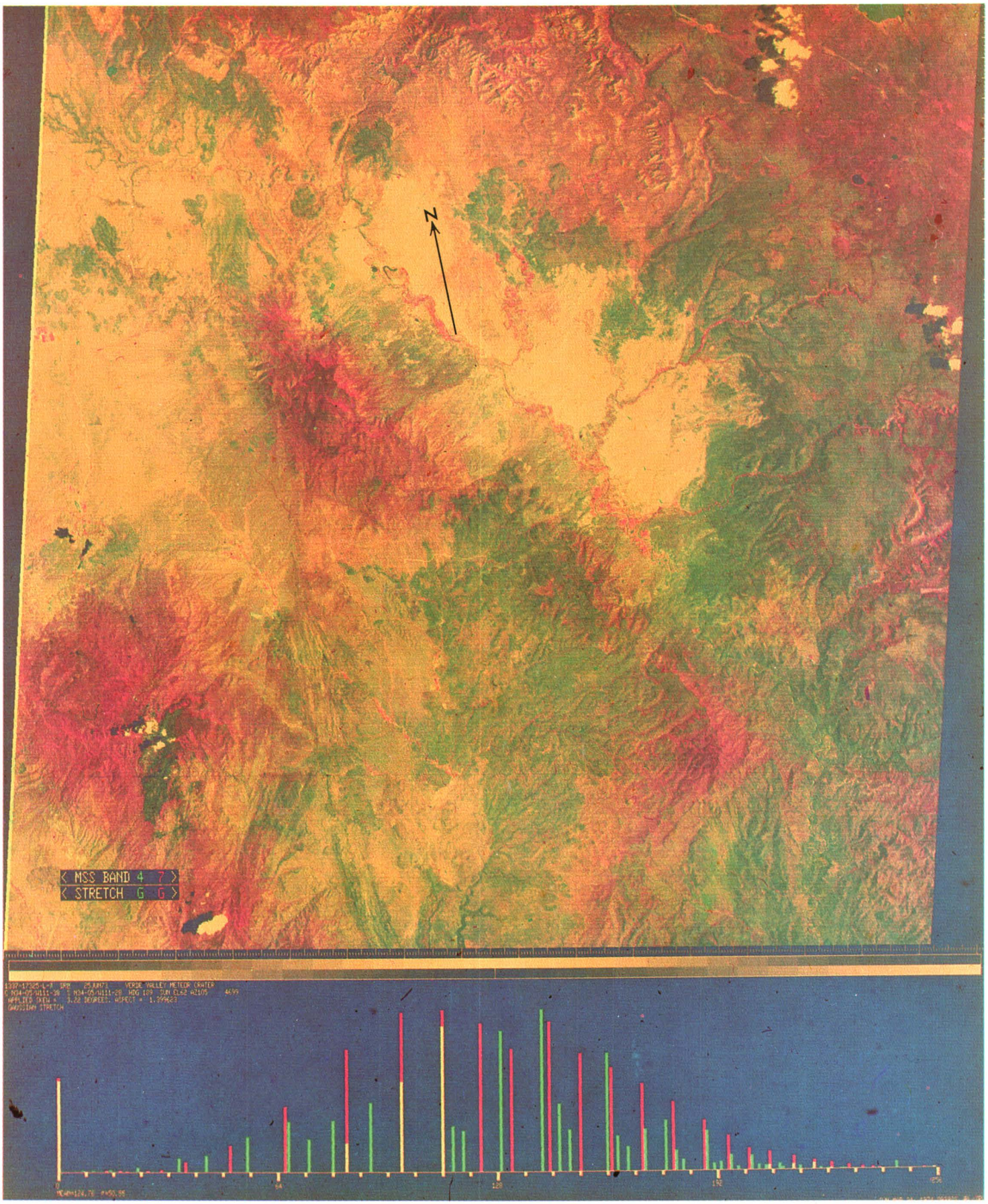


APPROXIMATE SCALE

10 0 10 MILES

10 0 10 KILOMETERS

FIGURE 40.—Geologic map of north-central Arizona (from Wilson and others, 1969).

cambrian units could be identified in the ERTS images than are shown on the State geologic map, apparently because of the structural grain and, locally, color; for the older rocks, therefore, the ERTS photogeologic map is an improvement over the State map. ERTS images at approximately 1:200,000 combined with conventional photogeologic and field geologic techniques can thus lead to more efficient reconnaissance geologic mapping and improved reconnaissance maps.

The most striking geologic advantage of the ERTS images is their synoptic view of fracture and lineament patterns that occur in basement rocks and in surficial deposits that mask the bedrock and basement. Faults and lineaments in north-central Arizona are shown in figure 41. The faults are from published maps. The traces of some faults were less clear than the traces of nearby linear features. Faults are shown as heavy lines on figure 41 merely to differentiate them from the lineaments.

The north-central Arizona site lies within the Colorado Plateau province, and only comparatively simple high-angle normal or gravity faults displace the Tertiary and Paleozoic rocks. Thus, where Precambrian rocks are exposed, the structure that is seen is principally of Precambrian age. The dominant Precambrian lineament systems trend north, northeast, and east, with north- and northeast-trending systems strongly developed. Northwest-trending faults and lineaments, which mainly reflect much later structural adjustments that occurred during the Tertiary, are mostly subdued compared to the other systems.

A comparison of the geologic and lineament maps shows that the Precambrian structural grain clearly has been imparted to the overlying Phanerozoic rocks and that the Precambrian lineament systems apparently have been sites of renewed structural adjustments. The north-trending Oak Creek fault in the northeast (fig. 42) can be seen at the surface to displace only Paleozoic and Tertiary rocks. It very likely reflects a north-trending fracture system in the basement, one that appears en echelon to the Precambrian Shylock fault zone in the south-central part of the map area. Northeast-trending lineament systems also occur in Tertiary and Paleozoic rocks on the Colorado Plateau. Near Williams, Ariz. (near lat 35°15′N.; long 112°12′W.), eruptive centers of the upper Tertiary San Francisco volcanic field are localized along some of these lineaments. The northeast-trending lineaments presumably reflect an underlying northeast-trending Precambrian fracture system along which renewed structural adjustments occurred; they are similar in trend to the Chaparral and Spud faults and associated northeast-trending lineaments in Precambrian terrane in the southern part of the map area.

A myriad of fractures and lineaments occur in well-exposed Paleozoic strata in the Sedona area, west of the Oak Creek fault. Northwest-trending fractures in the Sedona area were believed to be dominant until mapping with ERTS images revealed the existence of strongly developed east- and northeast-trending lineaments, the existence of which appears to have been responsible for the development of an erosional embayment in the margin of the Colorado Plateau here. Fracture systems and lineaments in the Sedona area are currently being mapped in detail using NASA high-altitude-aircraft photographs, supplemented by field mapping, to provide data for a comparative evaluation of similar data from images obtained from still higher altitudes and orbit (Skylab and ERTS). Lineaments that have been plotted from ERTS images, and those to be plotted from Skylab images, will be compared to the detailed geologic map.

The geologic work in the Sedona area has the practical objective of defining areas structurally favorable for the localization of ground-water resources in an area having a burgeoning population. Anticipated targets for future exploration for ground water are places where ancient concealed karst (limestone cavern) ground in the Redwall Limestone of Mississippian age is intersected by through-going fracture systems at structurally favorable elevations.

## EXPLANATION FOR FIGURES 41 AND 42

### SEDIMENTARY ROCKS

*Quaternary*

Qg — Gravel and alluvium

*Tertiary*

$Ts_2$ — Sandstone and lake beds

$Ts_1$ — Sandstone

*Paleozoic*

P€u — Sandstone and limestone, undivided

*Precambrian*

p€ms — Quartzite

### METAMORPHIC ROCKS

p€msv | p€s — Metasedimentary and metavolcanic rocks and schist

### VOLCANIC ROCKS

Tvb | Tvt — Tvb, basalt; Tvt, tuff

### IGNEOUS ROCKS

p€qd | p€g — Quartz diorite and granite

p€r — Rhyolite

p€gb — Gabbro

Contact

*Dashed where approximately located; short dashed where indefinite*

### FAULT AND LINEAMENT MAP

Fault

*From published geologic maps. Bar and ball on downthrown side. Dashed where approximately located; dotted where concealed*

Lineament

*Long traces reflect strongly developed trends, some of which are inferred to be faults. Intermediate and short dashed lines reflect degree of traceability of individual lineaments; dots reflect an alinement of one or more vague linear features*

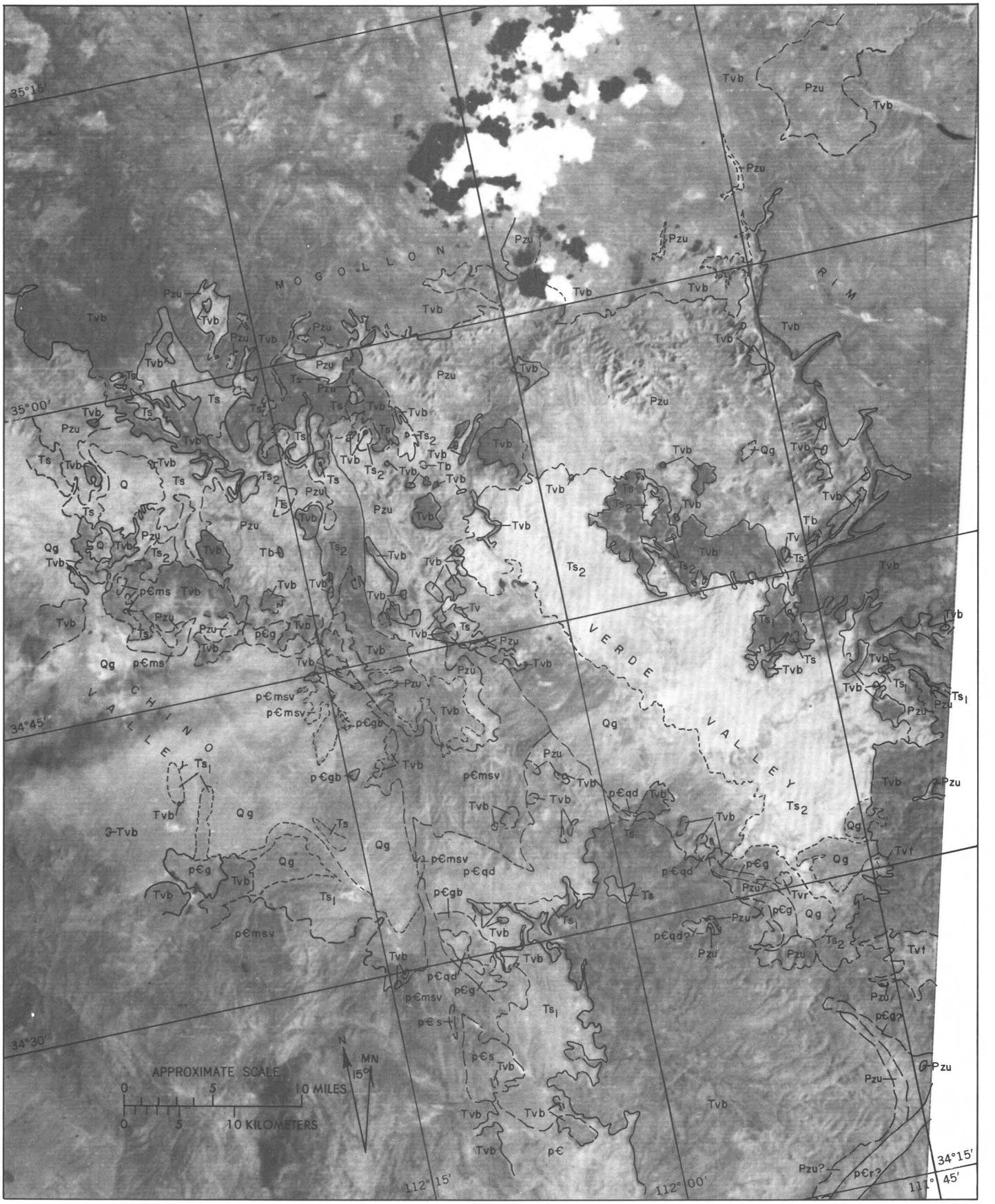


FIGURE 41.—Geologic map of north-central Arizona compiled on an ERTS–1 image base (part of 1337–17325, band 6). Data are from published and unpublished sources.

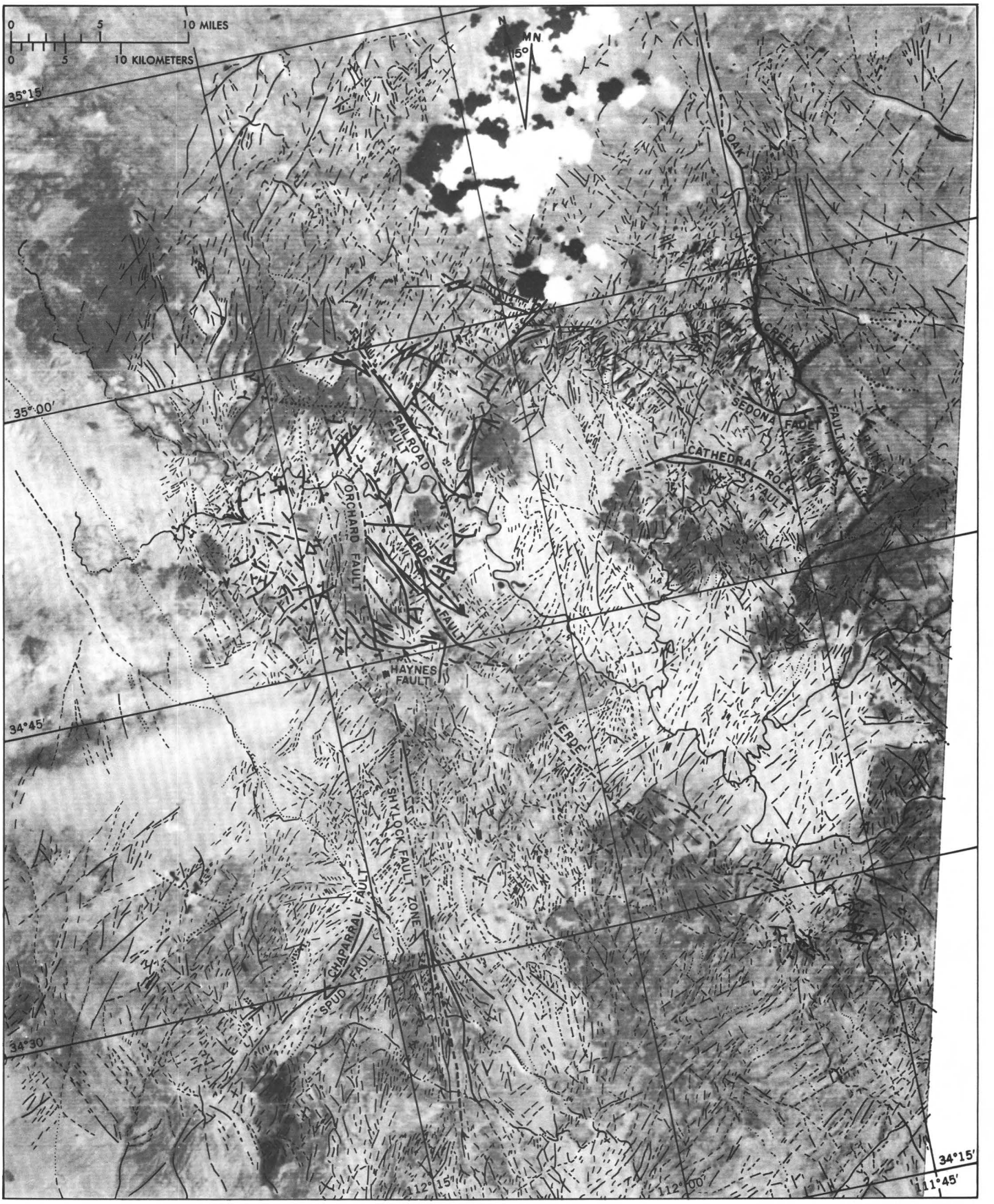


FIGURE 42.—Fault and lineament map of north-central Arizona compiled on an ERTS–1 image base (part of 1337–17325, band 6). Faults from published information; lineaments interpreted from ERTS images. Explanation is on page 64.

# GLACIAL GEOLOGY AND SOILS IN THE MIDWESTERN UNITED STATES

By Roger B. Morrison,

U.S. Geological Survey

Interpretation of geology and soils from ERTS images is especially difficult in the glaciated Midwestern United States because of low relief, lush vegetative cover during the growing season, and frequently clouds, haze, and smog. A few images, however, taken under just the right conditions yield, by means of subtle variations in tone, a remarkable amount of information on macroscale geologic and physiographic features that have little topographic expression (Morrison and Hallberg, 1973).

The best time of year for getting images showing the differences between surficial deposits and soils in the Midwest, caused mainly by variations in soil moisture, is middle to late spring after the croplands have been newly plowed and while soil moisture still is high and while the cropland, pasture, and woodland areas still are relatively bare of foliage (fig. 43).

Figure 44, the eastern half of figure 43, shows a large part of Iowa west of Des Moines that is nearly all cultivated, mainly in grains. Gallery forests along streams are the chief natural vegetation. The image was taken on May 10, 1973, when the fields were either newly plowed or in young crops and when soil moisture remained relatively high; thus the darker tones registered in band 7 represent relatively moist soils, and the lighter tones, drier soils. Subtle variations in tone register the types of glacial and other surficial deposits and landforms on which the soils have developed. Drainage patterns provide considerable information on the relative ages and types of glacial deposits and on the trends of both young and ancient end moraines. Combined with data from geologic, soil, and topographic maps, this image reveals useful information about surficial deposits and soils.

Two principal units are obvious: (1) a relatively dark toned plain, the Wisconsinan till plain, in the northern half of the scene, and (2) a lighter toned, more dissected plain, the Kansan till plain, in the southern half of the scene. Clayey Wisconsinan till was deposited by a late-glacial ice lobe that reached as far as Des Moines about 14,000 yr ago, after the last period of active loess deposition had ended; consequently, its soils are moderately poorly drained and appear dark toned in this image. The narrow light-toned irregular ribbons that traverse the Wisconsinan till plain in the image are well-drained sandy-gravelly glacial outwash and alluvium along stream valleys. An inner dark zone along some larger streams in the image represents poorly drained bottomland soils.

The Kansan till plain has a mostly lighter tone in the image because widespread loess deposition has resulted in better-drained soils. Here the streams are more deeply incised and more numerous than in the Wisconsinan till plain,

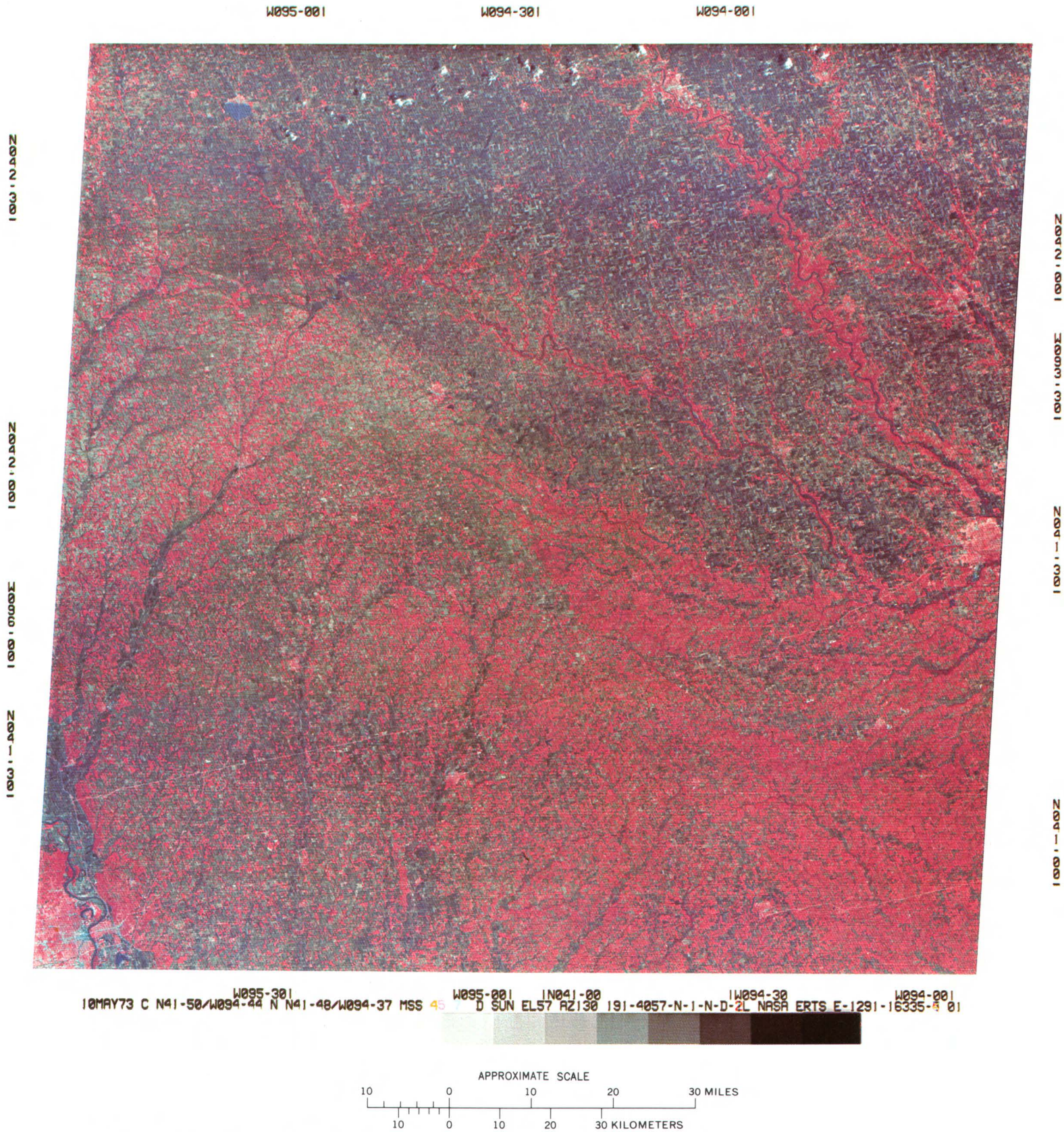


FIGURE 43.—Color composite ERTS–1 image of part of Iowa west of Des Moines (1291–16335).

and the main ones have cut deeply into bedrock. From stream alignments, two divisions of this area can be distinguished: a zone (2a1, 2a2) of arcuate drainage immediately south of and parallel to the Bemis moraine and, farther south, a zone (2b) characterized by more deeply incised streams that radiate outward normal to the zone of arcuate drainage and the Bemis moraine. In the northern zone, the interstream divides commonly are tabular; they are widest in unit 2a2. About five principal divides can be identified. The parallelism of the streams to the Bemis moraine suggests that their alinement, before their entrenchment into bedrock, may have been controlled by a series of middle Pleistocene end moraines and/or ice-marginal streams. The till beneath the present tabular divides may represent relics of these ancient moraines that were previously unrecognized. Supporting this hypothesis is the fact that the stream valleys cut across the boundaries of formations having considerable differences in rock type and resistance to erosion and are also transverse to a buried preglacial valley.

In the southernmost zone (unit 2b), the streams run transverse to those to the north and show little or no control by former moraines. Because the drainage network is denser and the streams are more deeply incised than in the northern zone, probably a longer time has elapsed since this area was glaciated.

Figure 45 is another example of the usefulness of spring ERTS infrared imagery for mapping and analysis of glacial landforms, deposits, and soils in the Midwest. This region, in west-central Illinois, is almost entirely cultivated, and the natural vegetation generally is confined to the steeper slopes and stream borders. The variations in tone are caused mainly by differences in permeability and moisture content of the soils, which in turn are related to the surficial deposits on which the soils have developed.

On the mosaic, the Wisconsinan till plain is mainly dark toned (moist soils), and the Illinoian till plain is dominantly light toned (dry soils). On the Wisconsinan till plain, various end moraines are easy to distinguish from glaciolacustrine plains and ground moraine. On the Illinoian till plain, end moraines generally cannot be distinguished from ground moraines because here all the moraines are older and have been considerably modified by weathering, erosion, and loessial cover. An exception is the Buffalo Hart moraine (unit 2a), of late Illinoian age, that is intermediate in age and tone between the main Illinoian till plain (unit 2b) and the Wisconsinan units; this moraine also has light-toned mottles caused by hills of well-drained sand and gravel (kames) large enough to be detected on the image.

Images also facilitate mapping soil associations for both agronomic and engineering applications. Comparison of ERTS-interpreted maps, such as figure 45, with soil association maps of Illinois shows that the boundaries between certain soil associations stand out much more clearly on the ERTS images than on conventional aerial photographs and permit rapid yet highly accurate soil mapping over large regions. A striking example is the ribbon-like areas of well-drained soils the light tones of which contrast conspicuously with the prevailing dark tones of the Wisconsinan till plain. Although limited in areal extent, these soils are very important; they commonly overlie sandy-gravelly outwash deposits, locally of commercial quality, that are shallow aquifers and significant in places for domestic and municipal water supplies. They tend, however, to be droughty, of moderate to low agricultural productivity, and undesirable sites for sanitary landfills unless the fill is sealed off from the aquifer.

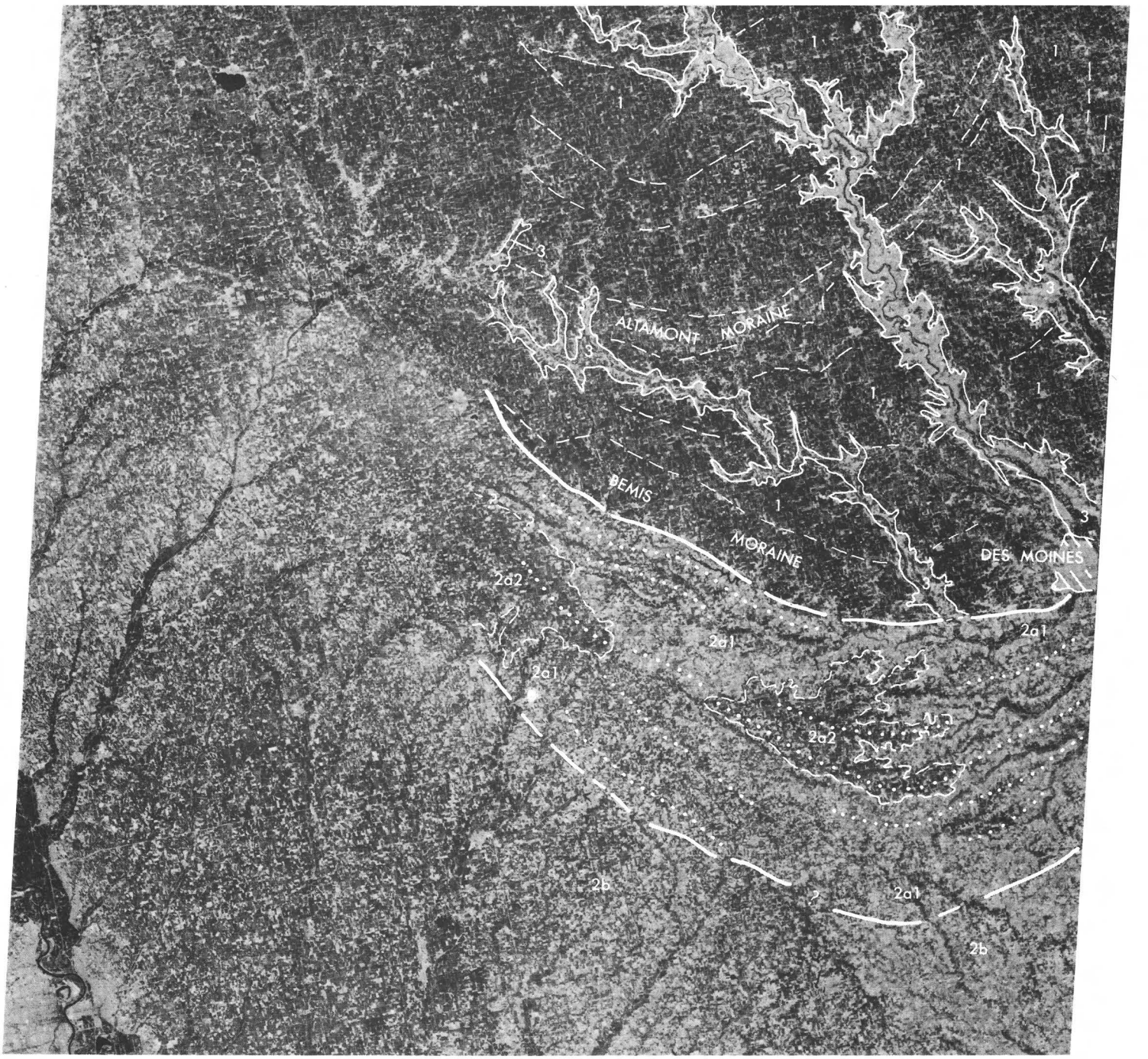


APPROXIMATE SCALE

10 0 10 20 30 MILES

10 0 10 20 30 KILOMETERS

FIGURE 44.—Annotated ERTS–1 image 1291–16335, band 7 (fig. 43), with interpretation of soil types.

FIGURE 45 (next page).—Mosaic of ERTS–1 images 1322–16051 and 1322–16054, band 7, west-central Illinois with interpretation ▶ of soil types.

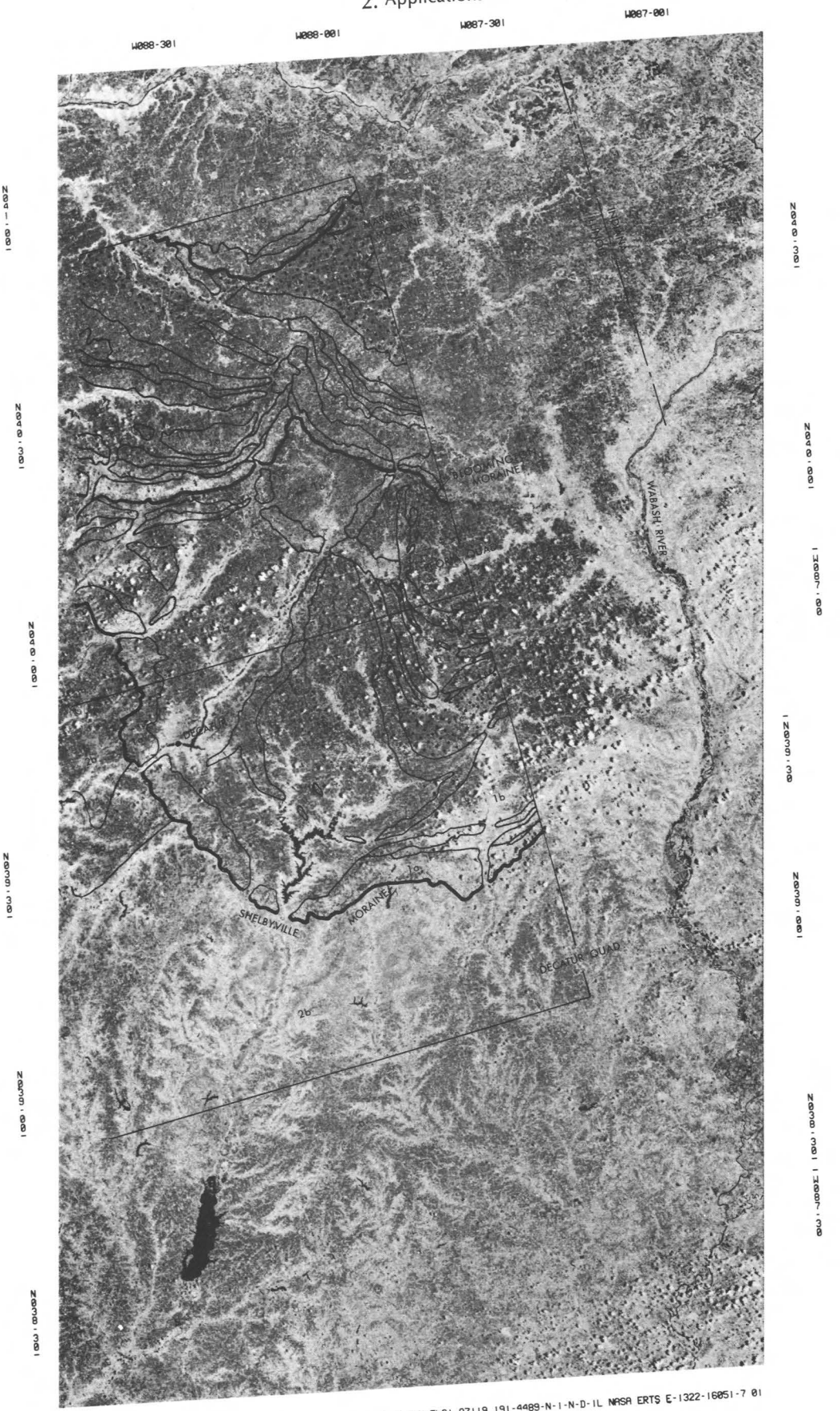


10JUN73 C N40-26/W088-03 N N40-25/W087-54 MSS 7 D SUN EL61 AZ119 191-4489-N-1-N-D-IL NASA ERTS E-1322-16051-7 01

10JUN73 C N39-01/W088-33 N N38-59/W088-24 MSS 7 D SUN EL62 AZ117 190-4489-N-1-N-D-IL NASA ERTS E-1322-16054-7 01

APPROXIMATE SCALE

10 0 10 20 30 MILES

10 0 10 20 30 KILOMETERS

# ENHANCEMENT OF TOPOGRAPHIC FEATURES BY SNOW COVER

By Roger B. Morrison,

U.S. Geological Survey

Winter ERTS images of snow-covered areas are the most favorable for showing topographic detail, particularly in regions of low to moderate relief. A continuous snow cover masks out the distracting tone differences caused by variations in soils, rocks, and vegetative cover. Also, the low Sun-elevation angle, which is characteristic of winter images, results in shadowing and emphasis of even minor topographic features.

Although the snow cover masks all spectral information about soils, rocks, and most types of vegetation, some deductions about soils and rock materials can be made from the landform and land-use characteristics. For example, one knows that sand dunes are composed of eolian sand and that valley bottom lands are underlain by young alluvial soils.

A good example of the enhancement of an image of a snow-covered region of low to moderate relief is shown in figure 46. This image of western Nebraska is representative of the semiarid central Great Plains. The maximum local relief is about 400 m. The bedrock units are nearly flat lying weakly consolidated silt, sand, clay, and some gravel and shale, capped in places by resistant limestone and carbonate-cemented sandstone that produce plateaulike uplands. The bedrock is commonly covered by a veneer of unconsolidated eolian sand and alluvium, but it is well exposed in various escarpments, bluffs, and dissected areas. This image was taken on Jan. 28, 1973, after widespread snowstorms and when the Sun-elevation angle was 24°. Note the fine details of gully patterns in the various escarpments and the dune morphology in the Sand Hills. Images of this area without snow cover show much less topographic detail.

Using this winter image alone, without information from images taken at other seasons and without any field data, three kinds of terrain can be identified: (1) dune fields (part of the Sand Hills of Nebraska), (2) valley bottom lands (flood plains and low terraces along several rivers), and (3) bedrock escarpments and surfaces of several types, some having thin veneers of surficial deposits (fig. 47). The dune fields can be divided into three subunits on the basis of dune morphology, degree of blowout development and (or) dune stabilization, and the abundance and pattern of croplands. The valley bottom lands are evident from their topographic position, land uses, and lack of relief. Four classes of bedrock surfaces can be distinguished from their topographic position, local relief, including depth and closeness of stream dissection, and field abundance and field patterns.

Figure 48 illustrates the relatively poor topographic detail discernible in summer images. This band 5 image, taken Aug. 19, 1972, covers part of the same area shown in figure 46.

In areas of high relief or of coniferous forest, snow cover provides less enhancement of topographic detail. Much detail is lost in the shadowed parts of mountains and canyons and on slopes that are more or less perpendicular to the Sun's rays. The dark foliage of dense coniferous forests obscures the ground, snow-covered or not, the year around. Deciduous forests are less of an impediment because the leafless trees in winter do not entirely obscure the snow-covered ground.

*Description of geologic terrane-map symbols used in figure 47 (p. 74)*

**1a** ---------High transverse sand dunes, closely spaced, with subparallel alinement; probably many active dunes; many interdune lakes and ponds. (Clearly inferred from dune forms.)

**1b** ----------Transverse and upsiloidal/longitudinal dunes with numerous blowouts; irregular alinement; probably many active dunes; interdune lakes and ponds more numerous than in **1a**. (Clearly inferred from topographic form.)

**1c** ----------Poorly developed and/or eroded low dunes and cover sands; mostly stabilized; few interdune lakes and ponds; moderately thick to thin veneer of unconsolidated sand over bedrock. (Inferred from subdued dune morphology and variable field density.)

**2** ----------Valley bottomlands. Flood plains and low terraces along main streams. (Inferred from topographic position.)

**3a** ----------Low-lying erosion surfaces commonly between units **2** and **3b**, sloping gently toward main streams; low dissection and local relief; probably widespread thin veneer of unconsolidated alluvium and local eolian sand and/or loess. (Deduced from topographic position, local relief, and field patterns.)

**3b** ----------Escarpments, bluffs, and hills without significant surficial deposits; highly dissected, commonly grading into "badlands." (Inferred from topographic detail.)

**3c** ----------Upland plains with few streams and shallow dissection; low relief; probably extensively veneered by loamy soils. (Deduced from topographic detail and generally dense field pattern.)

**3d** ----------Upland plains underlain by resistant caprock; few streams, shallow dissection, and low relief; probably patchy veneer of sand or loamy soil. (Inferred from topographic detail and less dense field patterns than in **3c**.)

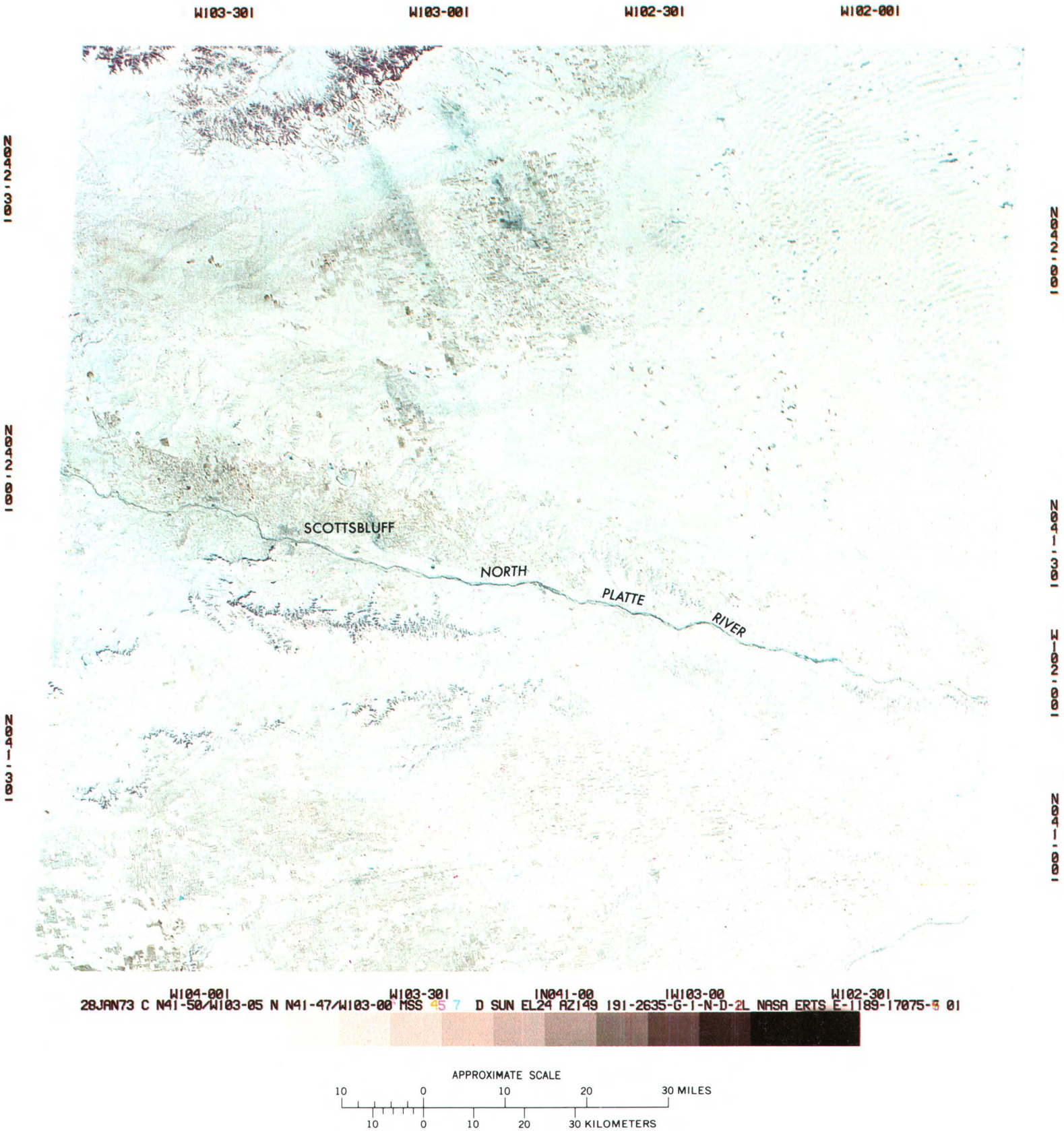


FIGURE 46.—Color composite ERTS–1 image of western Nebraska showing snow-enhanced topographic details (1189–17075).

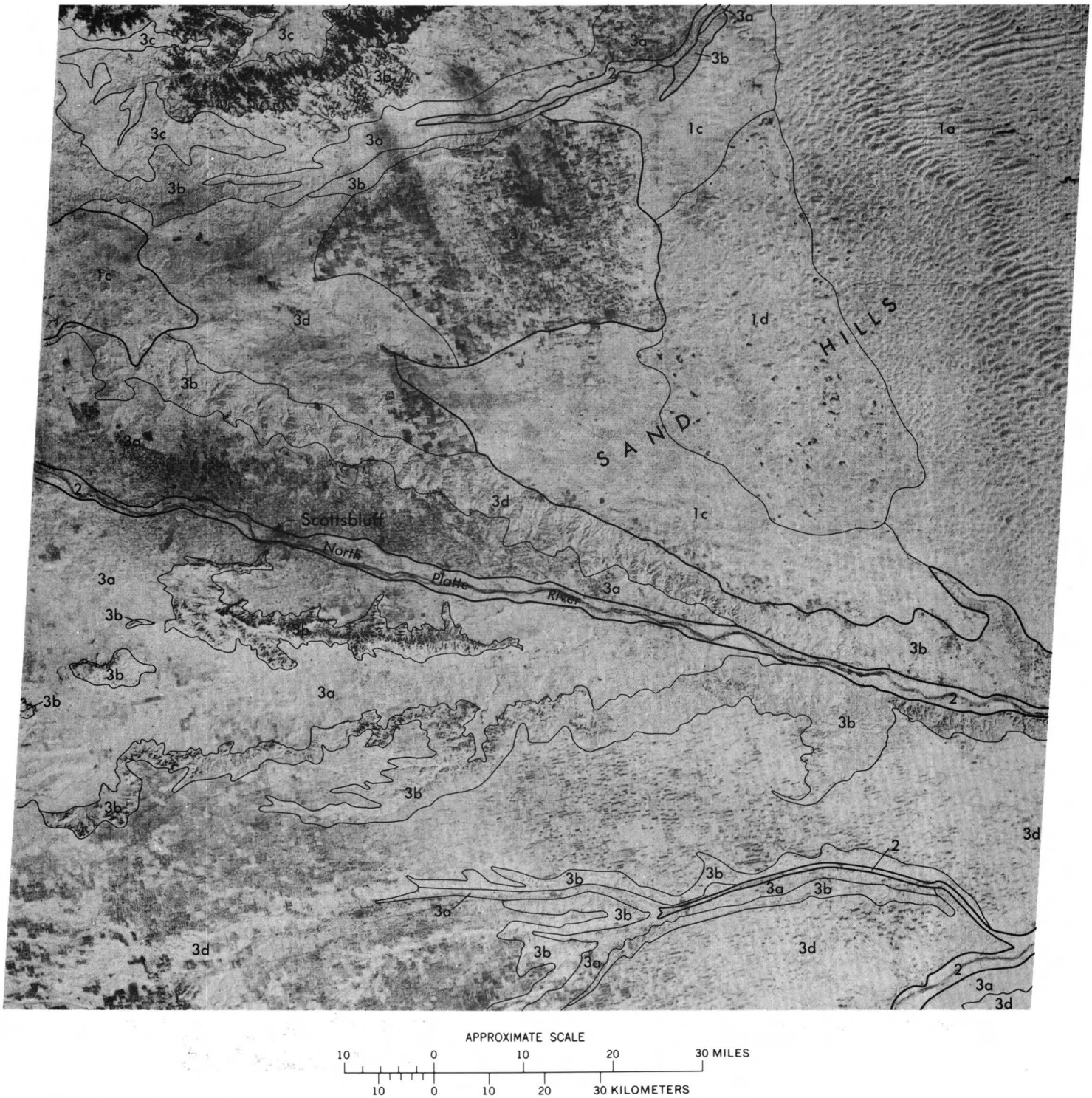


APPROXIMATE SCALE

10 0 10 20 30 MILES

10 0 10 20 30 KILOMETERS

FIGURE 47.—Geologic terrane map compiled on ERTS–1 image 1189–17075 (fig. 46). Explanation of symbols is on page 72.

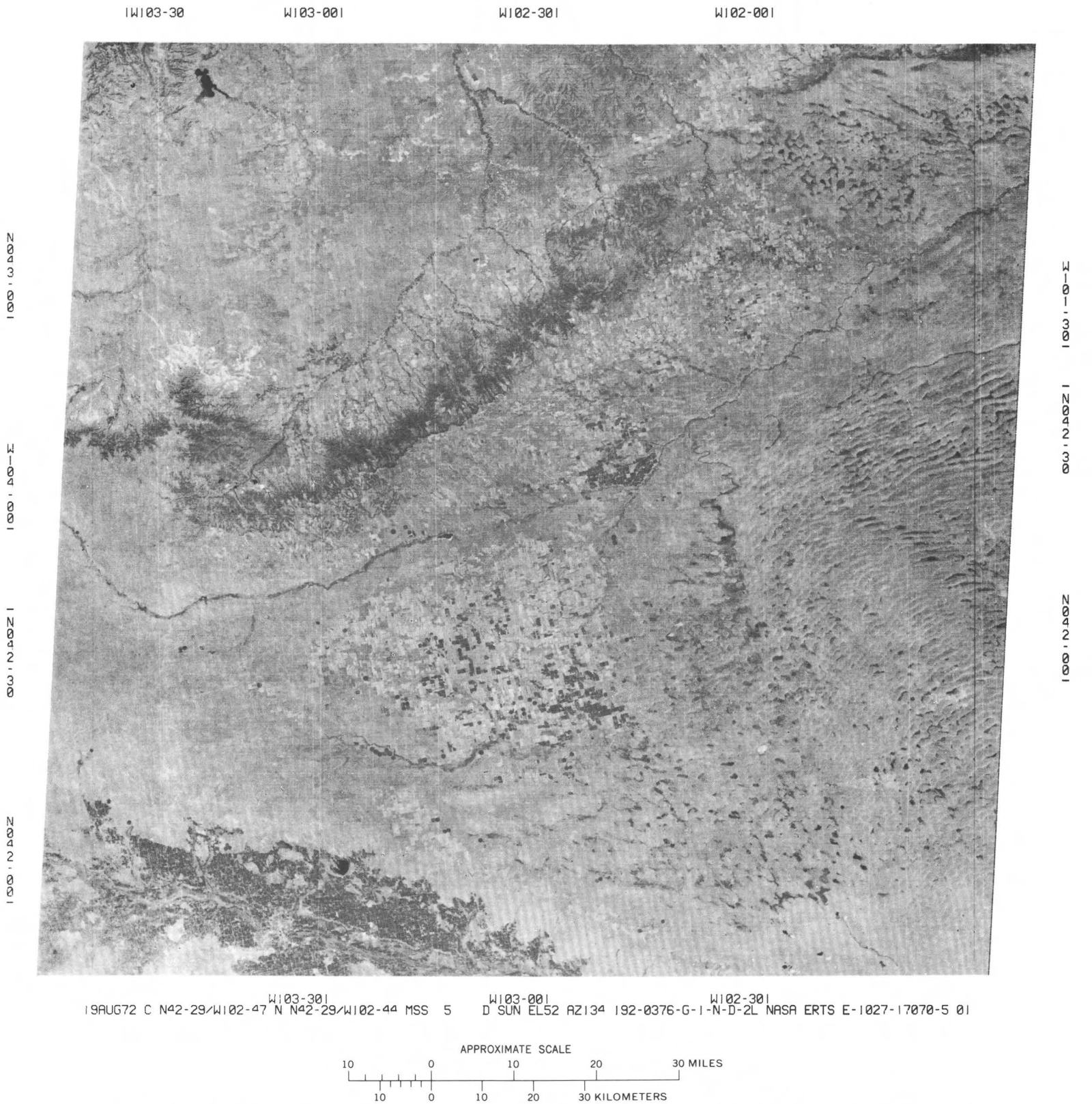


FIGURE 48.—ERTS–1 image of western Nebraska in summer showing relative lack of topographic detail (1027–17070, band 5).

# HYDROGEOLOGY OF CLOSED BASINS AND DESERTS OF SOUTH AMERICA

By George E. Stoertz and William D. Carter,

U.S. Geological Survey

ERTS images, obtained from July 30 to Oct. 30, 1972, of the central Andes, Atacama Desert, and Altiplano have been analyzed for hydrologic and geologic data. The study area includes southwest Bolivia, northwest Argentina, southeast Peru, and northern Chile, extending from lat 16°30′ S. to 27°30′ S. and from long 66°30′ W. to 70°30′ W. Synoptic seasonal conditions revealed by ERTS for the first time, and delineated in this study, include midwinter and early spring snowpack on the main range of the Andes from lat 21°00′ S. to 25°20′ S. and seasonal floodwaters on the floors of closed drainage basins throughout the study area. Permanent features mapped at 1:1,000,000 from ERTS imagery include salars (salt-encrusted playas), drainage basins, volcanic craters, calderas, conjectural faults, major structural trends, and the approximate extent of the ancient Lake Minchin.

Experience has shown that color composite images provide 40 to 50 percent more environmental information than black and white images of the same scene. This was the conclusion of Dr. Carlos Brockmann and his associates of the Geological Survey of Bolivia (Geobol) after they made detailed studies of the stratigraphy, structural geology, hydrology and drainage basins, relative permeability, and geomorphology in the area.

The ERTS–1 false-color composite image shown in figure 49, taken on Aug. 2, 1972, is the first prepared for this region of the Andes, and it dramatically displays the rugged terrain. Being largely composed of exposed bedrock and soil, the terrain pictured is dominantly pale green. The Salar de Coipasa is in the right; the distribution of water (black to pale blue) and salt (white) is obvious. Part of the Salar de Uyuni is in the lower right corner. The Altiplano comprises the plains area to the north and is studded on the west by many volcanic cones. Some are lightly dusted with ephemeral snow, whereas others appear to have well-established snowcaps. Faint patches of vegetation appear as small spots of pinkish orange, and most are natural vegetation near springs, but some patches may be farm plots and grazing areas frequented by indigenous Indians and llamas. Linear features near the crest of the Western Cordillera (lower left) are part of the major copper belt—for which the Andes are famous—extending from Chile in the south into Peru to the north.

Maps compiled largely from ERTS images and completed in manuscript form (Stoertz and Carter, 1973) (figs. 50, 51, 52) show the following:

1. Of 150 salars, 86 were found to be in agreement with existing published and unpublished maps, 32 were modified by the ERTS data, 20 were revealed solely by ERTS, 7 were not identified on ERTS images but were retained from other sources and were unverified, and 5 were in small deflation basins (figs. 51, 52).
2. Of 184 closed drainage basins, 58 were classed as largely reliable and verified by ERTS, 69 were largely reliable but unverified, 10 were fairly reliable and modified by the ERTS data, and 47 were still unreliable or doubtful.
3. Of an experimental evaluation of part of a published geologic map (1:1,000,000) covering 9,300 km², 40 percent appeared to be essentially in agreement with boundaries visible on ERTS images, 35 percent appeared subject to improve-

ment by boundary adjustments, and 25 percent was estimated to be subject to significant revision with the aid of ERTS imagery.

4. Of 681 volcanoes or craters, including 9 active volcanoes, the position of 1 was corrected from ERTS data.
5. Of 15 calderas, 5 were mapped solely from ERTS images.
6. 2,160 km of previously mapped faults were recognized on ERTS images, plus 225 km were mapped solely from ERTS data, the latter consisting of conjectural extensions of known faults and realinements of mapped faults.
7. Major structural trends associated with the prominent bend in the Andean fold system, chiefly in Bolivia and Argentina, were identified.
8. Of 9,840 km² of early spring (October 30) snowpack on the main range of the Andes, 6,215 km² was in interior drainage basins of Chile, 1,295 in Bolivia, 1,035 in Argentina, and 1,295 in the external drainage basin of the Río Loa.
9. Of 88 lakes or seasonal floodwaters in midwinter and early spring (August-October), 29 were similar to lakes on existing maps, 23 were modified by ERTS, and 36 were mapped solely from ERTS.

A special study of the relation between seasonal floodwaters in the high Andes and drainage-basin characteristics revealed that, where more than 0.3 percent of a drainage basin was covered by water during August-October, the basin generally was found to meet the following criteria: (1) mean elevation of 4,050 m or higher, (2) mean elevation of drainage divides, 4,350 m or higher, and (3) snowpack covering more than 10 percent of the basin on October 30. Of 36 drainage basins for which October snow-cover data were available from ERTS data, 16 basins met all three criteria. These 16 basins included every one of the 13 extensive lakes or floodwaters seen on ERTS images at that season and in the special study area, extensive being defined as exceeding 0.3 percent of basin area. These conclusions will assist in future water-resources appraisal and prediction.

No single source of data previously has permitted identification of all these features, and observation of synoptic snow cover and surface water was not possible before ERTS. The satellite thus provides an invaluable source and type of data for Earth resources surveys and development in this large and relatively undeveloped area.

## EXPLANATION FOR FIGURE 50

*International boundary*

*Settlement of Sabaya, approximate (not visible on ERTS image)*

*Inactive volcanoes verified approximately correct as previously mapped (only principal volcanoes are shown)*

*Inactive volcano moved eastward about 3.2 kilometers from position previously mapped*

*Active volcanoes, the northern one shown 3.2 kilometers east of position previously mapped*

*Portion of caldera verified correct as previously mapped (near left edge)*

*Portion of caldera modified from ERTS imagery (near left edge)*

*Caldera mapped solely from ERTS imagery (near left edge)*

*Principal faults visible on ERTS image, shown approximately as previously mapped (6 faults trending NW and NE)*

*Faults inferred or modified from ERTS imagery (3 faults trending northwest)*

*Major lineaments in the Andean fold belt (limited to northeast corner)*

*Zone of lead-zinc and copper mineralization (from published sources)*

*Zone of silver mineralization (from published sources)*

*Surface flooding in Lago de Coipasa, August 2, 1972 (elevation approximately 3680 meters)*

*Deep water*

*Shallow water*

*Very shallow water and surface moisture*

*Lakes approximately as previously mapped (4 are shown)*

*Lakes or seasonal floodwaters significantly different from, or not delineated on, available maps (17 are shown)*

*Salar margins verified approximately correct as previously mapped*

*Salar margins modified from ERTS imagery*

*Rivers verified approximately correct as previously mapped*

*River modified from ERTS imagery (southwest corner)*

*Strand line of ancient Lake Minchin, approximately as delineated on previous maps*

*Probable strand line of Lake Minchin, as inferred from ERTS imagery*

Notes: Coordinates shown in margin are as shown on ERTS image but are not in agreement with coordinates on published maps
Image ID No.: NASA ERTS E-1010-14035-4/5/7

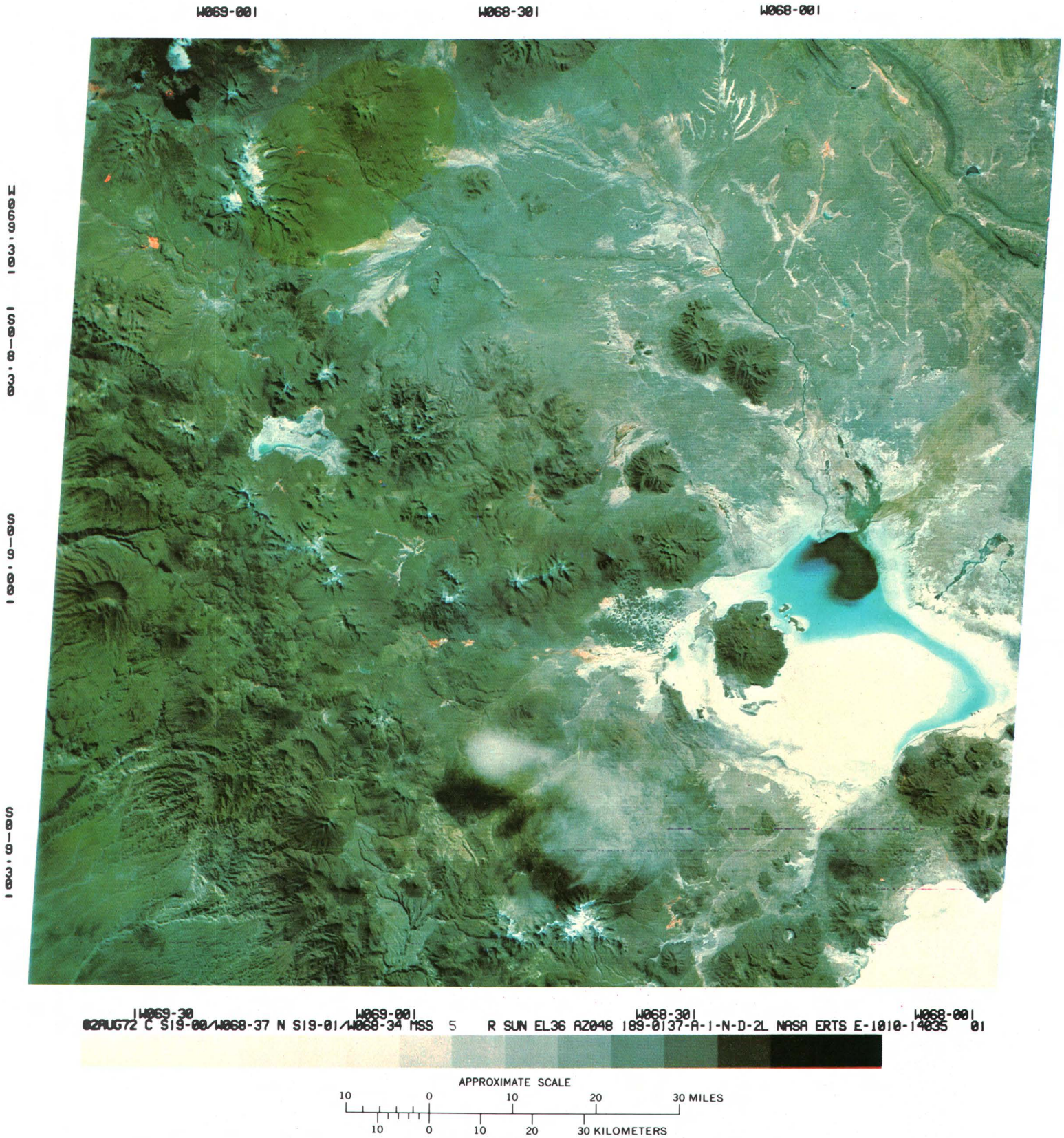


FIGURE 49.—Color composite ERTS–1 image of the Salar de Coipasa region of Bolivia and Chile (1010–14035).

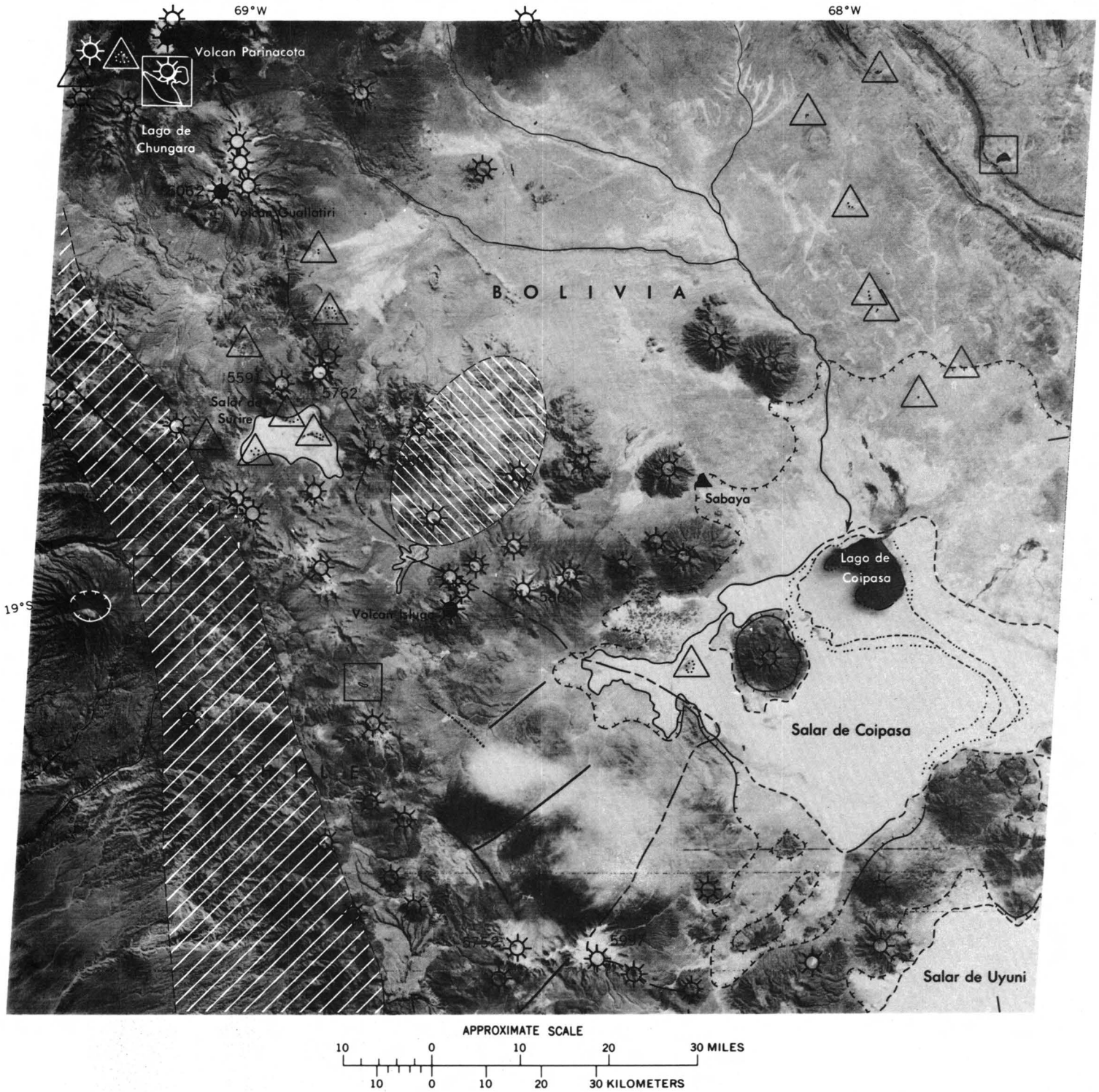


FIGURE 50.—Geologic and hydrologic interpretation and explanation of features identified in the Salar de Coipasa region as derived from ERTS–1 image 1010–14035, band 5 (fig. 49). Explanation is on page 77.

FIGURE 51.—Index map of salar revisions with area of figure 52 outlined. From sheet 14 of "The World," 1:5,000,000, published by the Defense Mapping Topographic Command, 1973, series 1106, edition 4; original map compiled and drawn by the American Geographical Society.

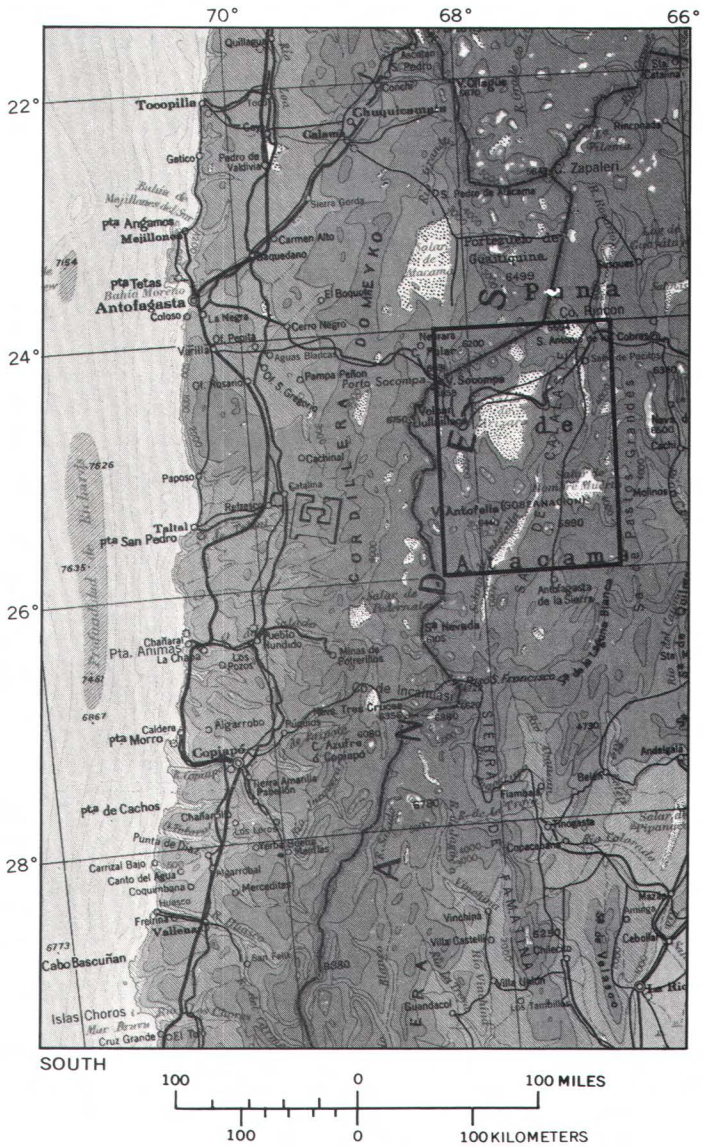


Original map compiled and drawn by the American Geographical Society of New York, Broadway at 156 St., N. Y.
Copyright by the American Geographical Society of New York.

Prepared and published by the Defense Mapping Agency Topographic Center, Washington, D. C.

FIGURE 52.—Example of outlines of several salars revised by ERTS data.

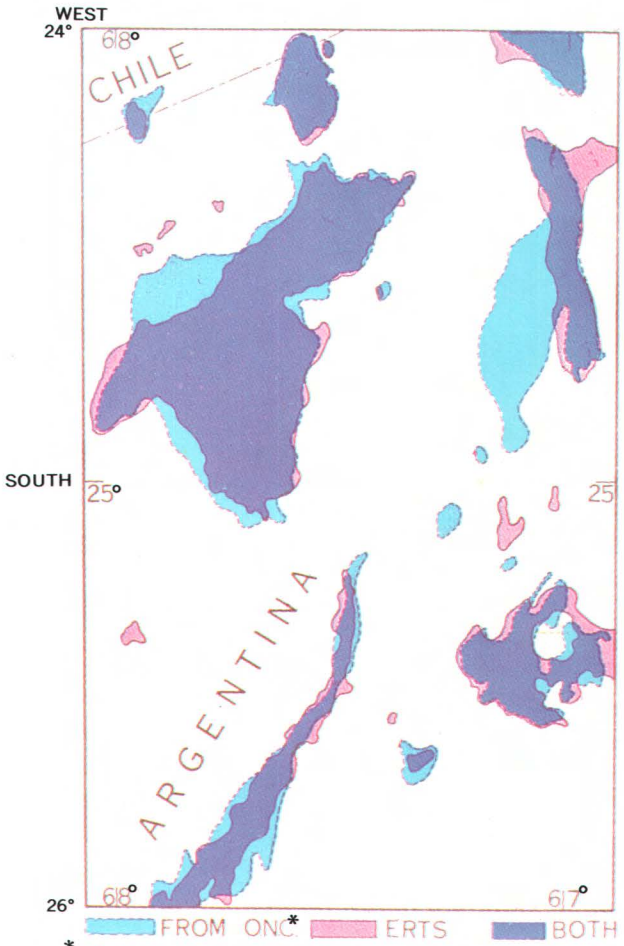


*U.S. Air Force Operational Navigational Charts

# SAND SEAS OF THE WORLD

By Edwin D. McKee and Carol S. Breed,
U.S. Geological Survey

This investigation is a global study of desert sand seas and illustrates the use and value of ERTS imagery for this purpose (McKee and Breed, 1974). The study consists of the identification, description, and measurement of characteristic forms and structures within the world's principal sand bodies. This work will facilitate the determination of world distribution of the various dune types and their classification. In addition, the basic forms of sand deposits, analyzed together with data derived from field observations, make it possible to determine the processes responsible for each dune type.

The advantages of employing ERTS images in this study are readily apparent. Because all images have the same scale, direct comparisons of widely separated areas are possible. Further, the relations of the sand areas to their surrounding features are easy to recognize, and major lineations or other patterns in the sand areas are clearly defined. Finally, mosaics made from combinations of images make excellent map bases on which to superimpose many kinds of data.

For purposes of this study, 15 desert or semidesert areas, all of them in the Eastern Hemisphere, were initially selected (fig. 53). Subsequently some of these study areas were combined and others were reduced in size in order to eliminate nonsandy areas and to consolidate mosaics for greater efficiency in handling data. A few relatively small areas located in the Western Hemisphere (fig. 53, inset) were later included in the study primarily because they were easily accessible. These small areas were chosen because they can be checked readily by aerial photography, and, for most of them, field notes are available for interpreting the origin of the morphology.

The methods used in this investigation have gradually evolved from experience in employing the various types of ERTS imagery as they have become available. Initially, only small black and white negatives were received, and they were scarcely adequate for careful analysis. With the availability of relatively large prints and their enhancement by photoprocessing methods, both through printing techniques and differences in paper, considerable improvement was made. Being able to compare prints from the green, red, and near-infrared bands was another major advance, for it facilitated the recognition of water, vegetation, and other associated features bordering sand bodies. Finally, when false-color images became available (fig. 54), the discernment of sand through its characteristic yellow color placed the study of sand bodies through the interpretation of ERTS images on a high level of accuracy.

A principal aim of this study is to develop an objective classification system of the major types of eolian sand deposits (McKee and others, 1973). Although a final proposal is as yet far from ready, a preliminary classification, based on dune forms seen on the ERTS imagery thus far examined, recognizes the following five basic types: (1) parallel straight or linear, (2) parallel wavy or crescentic, (3) star or radial, (4) parabolic or U-shaped, and (5) sheets or stringers.

Parallel-straight or linear dune complexes are defined as sand bodies in which the length is much greater than the width, slip faces or steep avalanche surfaces occur on both sides, and the ratio of dune area to interdune area is roughly 1:1. Examples of such linear complexes are conspicuous on ERTS images of the Simpson Desert of Australia, the Kalahari Desert of South Africa (fig. 55), the Empty Quarter of Saudi Arabia, and the Sahara of North Africa. Variants of the linear form are the feather type in Saudi Arabia

and the wide-intradune type in the Sahara.

Parallel-wavy or crescentic dune complexes consist of nearly parallel rows of cuspate segments, as represented in the Kara Kum Desert of the U.S.S.R. and in the Nebraska Sand Hills of the Western United States. Variants of the simple basic type are referred to as the fish-scale type of the Great Eastern Erg of Algeria, the giant-crescent or megabarchan type of Saudi Arabia (fig. 56), the bulbous, warty type of the Gobi Desert in China, and the chevron or basket-weave type of the Takla Makan Desert in China.

Star or radial megadunes commonly attain great height and include a few to many arms that project out from a central cone in various directions. The basic type, resembling a giant pinwheel, is scattered at random in parts of the Great Eastern Erg of Algeria. In other parts of Algeria (fig. 57) and in the Gran Desierto de Sonora in Mexico (fig. 54), chains of star dunes are characteristic, whereas in the Empty Quarter of Saudi Arabia there are star dunes of graduated sizes, from small to very large.

Parabolic dunes that typically develop U-shapes with arms drawn out on the sides are common in areas where vegetation or moisture, or both, tend to anchor the arms while the center is blown out and its sand moves forward. Good examples of these dunes are in the Rajasthan Desert of India (fig. 58) and at White Sands, N. Mex.

In some sand seas, definite geomorphic forms fail to develop, and the sand accumulates in flat sheets, as near Lima, Peru. Elsewhere it may form stringers extending downwind without appreciable relief, for example, as in South-West Africa (fig. 59).

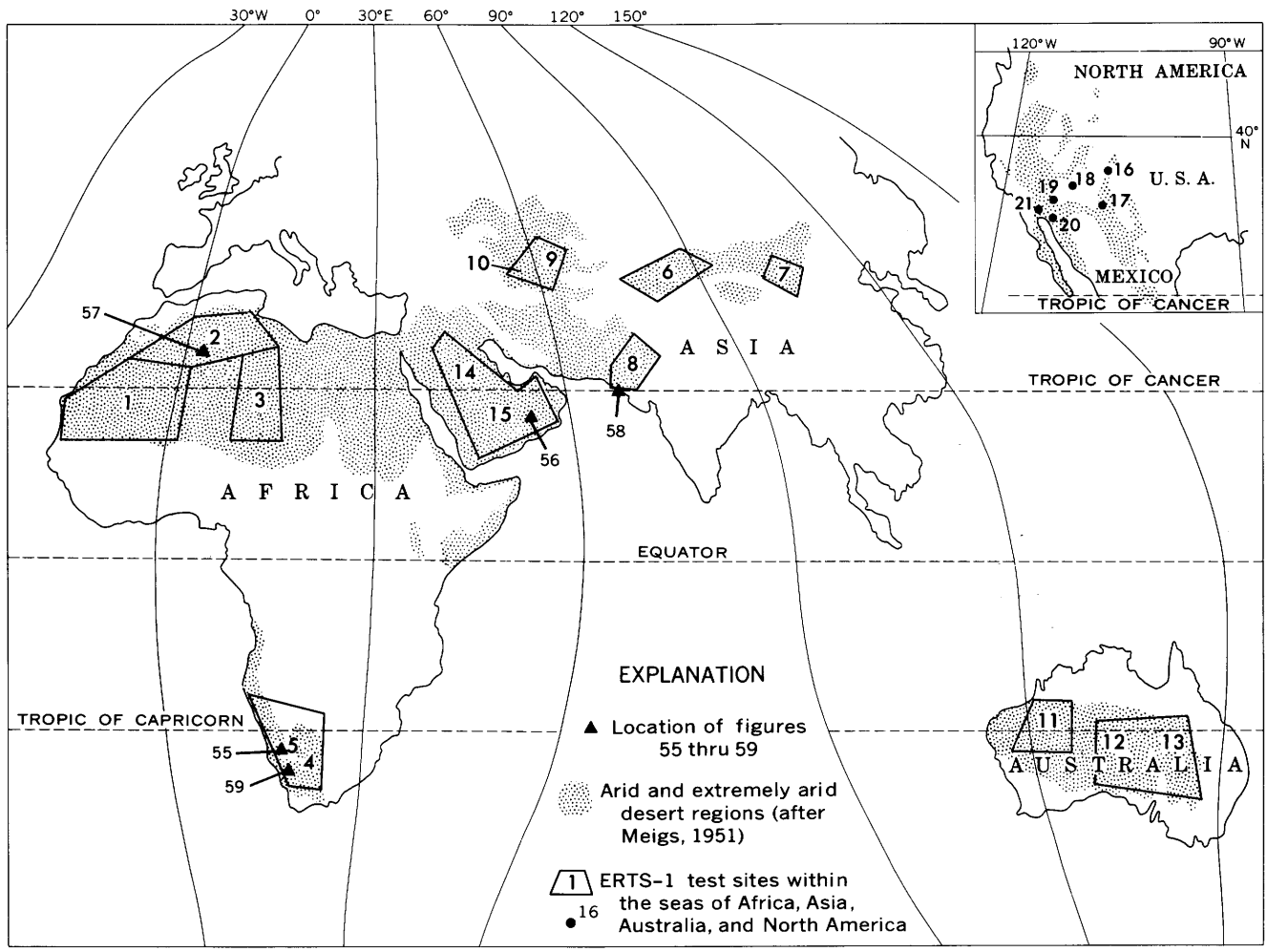


FIGURE 53.—Index map of the sand seas of Africa, Asia, Australia, and North America.

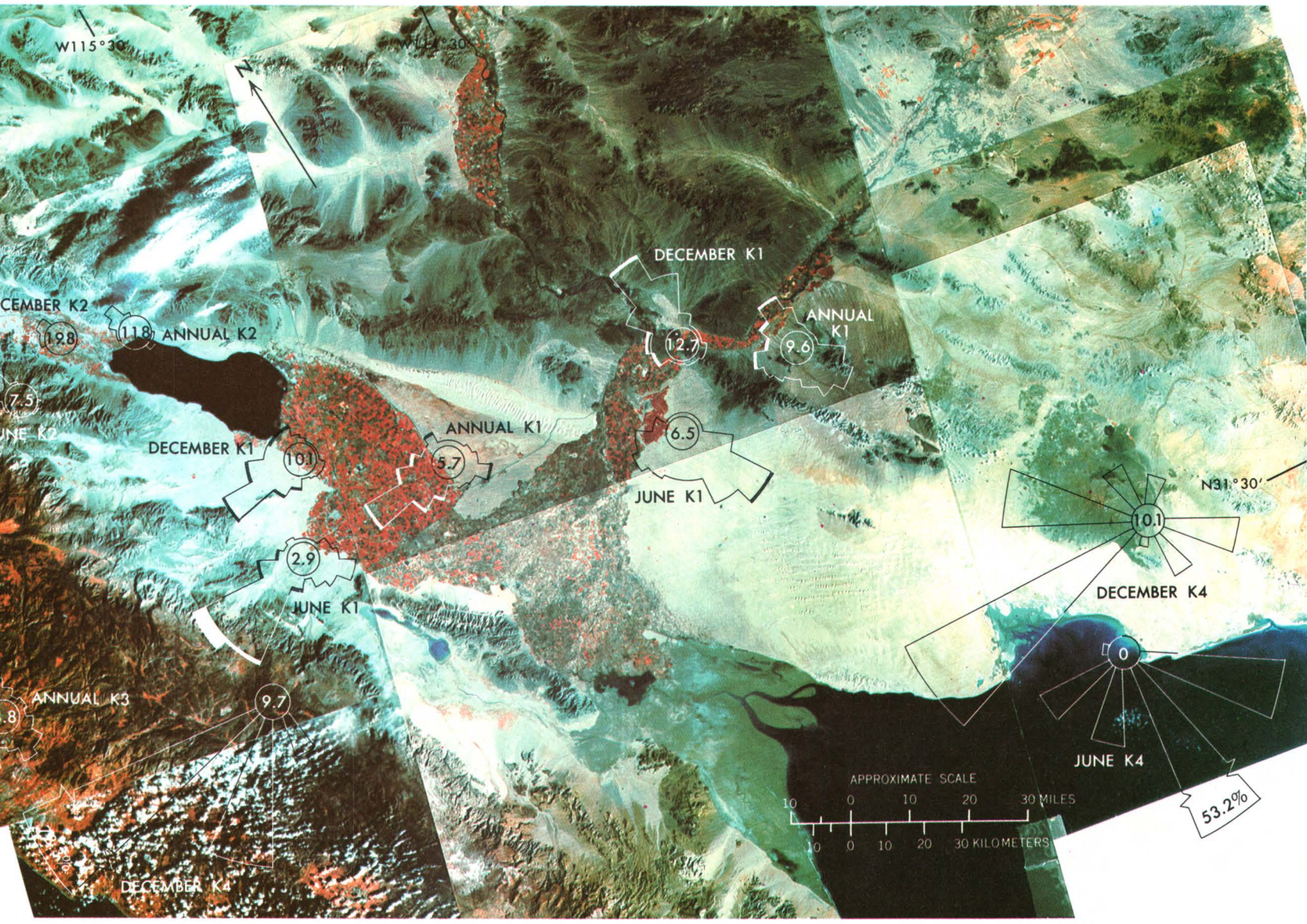


KEYS TO SAND-MOVING WINDS

Wind rose arms point upwind
Length proportional to occurrence of given speed
Group from given direction as percentage of all observations
5.5 mm arm length equals 10% occurrence

| | | | |
|---|---|---|---|
| K1 | Winds 17–21 kn | | Winds >21 kn |
| K2 | Winds 11–21 kn | | Winds >21 kn |
| K3 | Winds 4–21 kn | | Winds >21 kn |
| K4 | Percent occurrence by direction only-no speed data | | |

GENERALIZED WIND ROSE

High energy winds
Moderate energy winds
12.5 Percentage calm
JULY Period of observations
MORNING Time of observations (if available)
K1 Key number

FIGURE 54.—Color composite ERTS–1 image mosaic of the southwest United States desert and the Gran Desierto de Sonora in Mexico. ERTS–1 images 1178–17495, 1160–17503, 1178–17504, 1159–17445, 1159–17451, 1176–17385, 1176–17391, and 1230–17400.

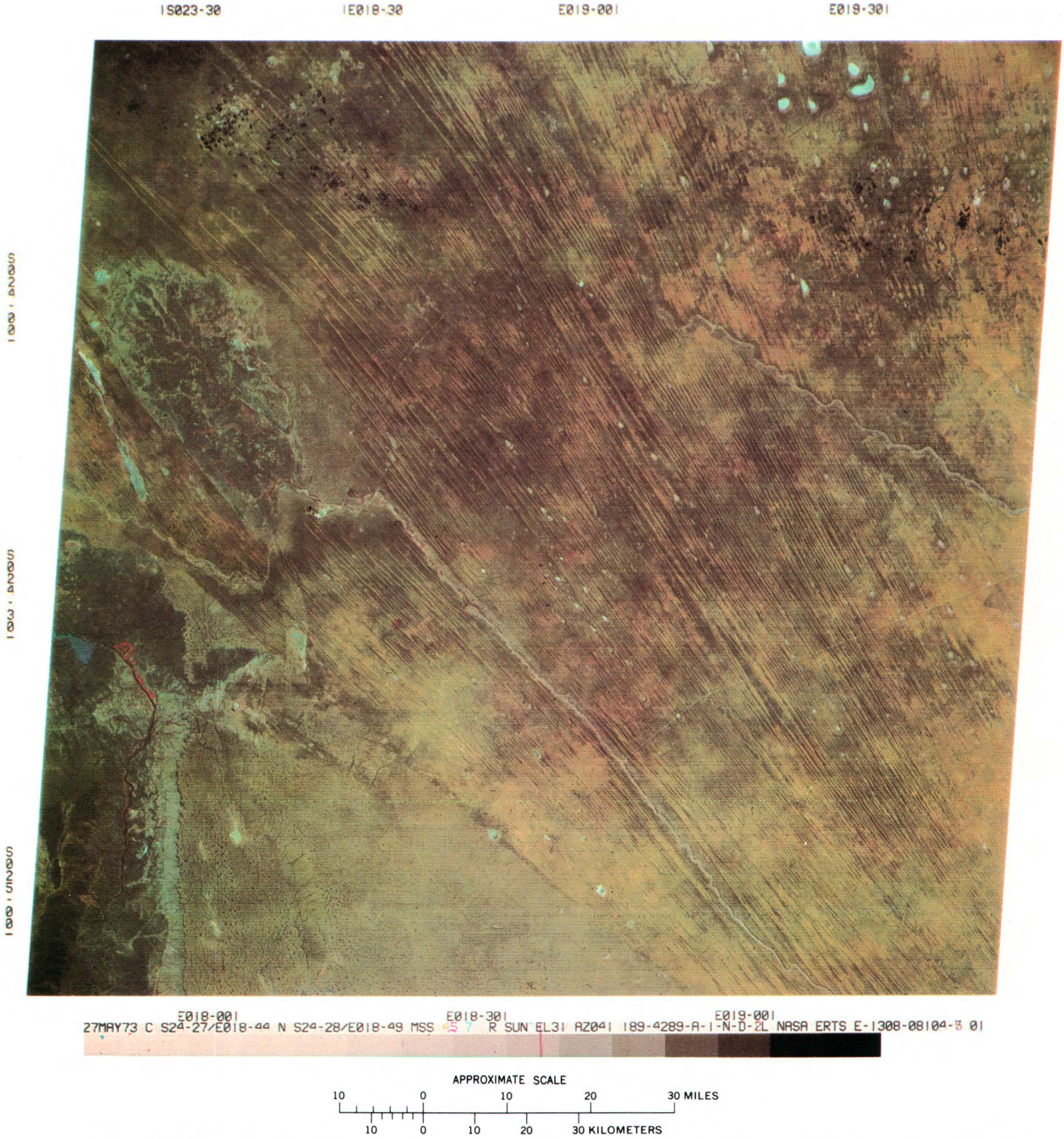


FIGURE 55.—Color composite ERTS–1 image showing parallel-straight or linear dunes in the Kalahari Desert of South Africa (1308–08104).

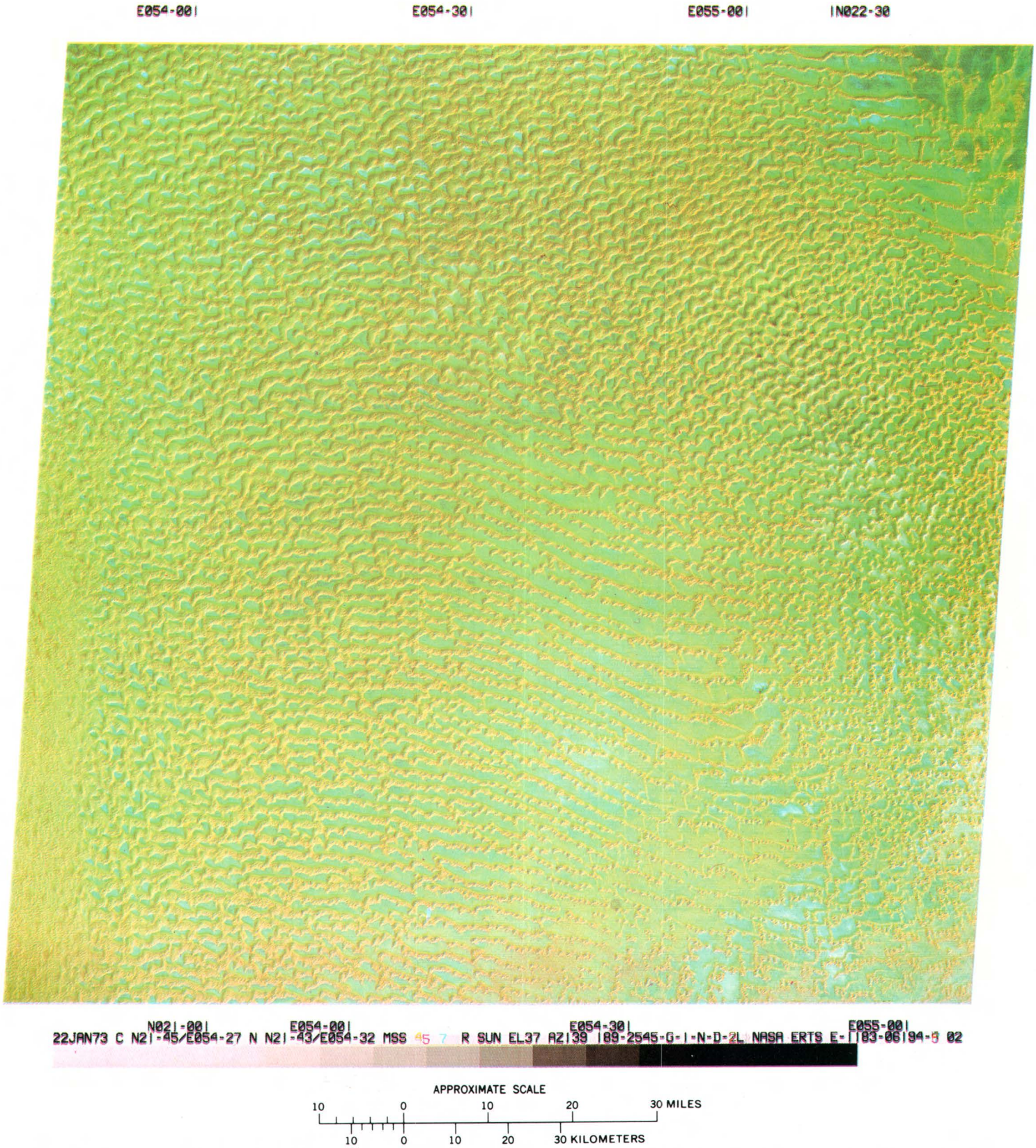


FIGURE 56.—Color composite ERTS–1 image showing parallel-wavy or crescentic dunes (a megabarchan desert) in Saudi Arabia (1183–06194).

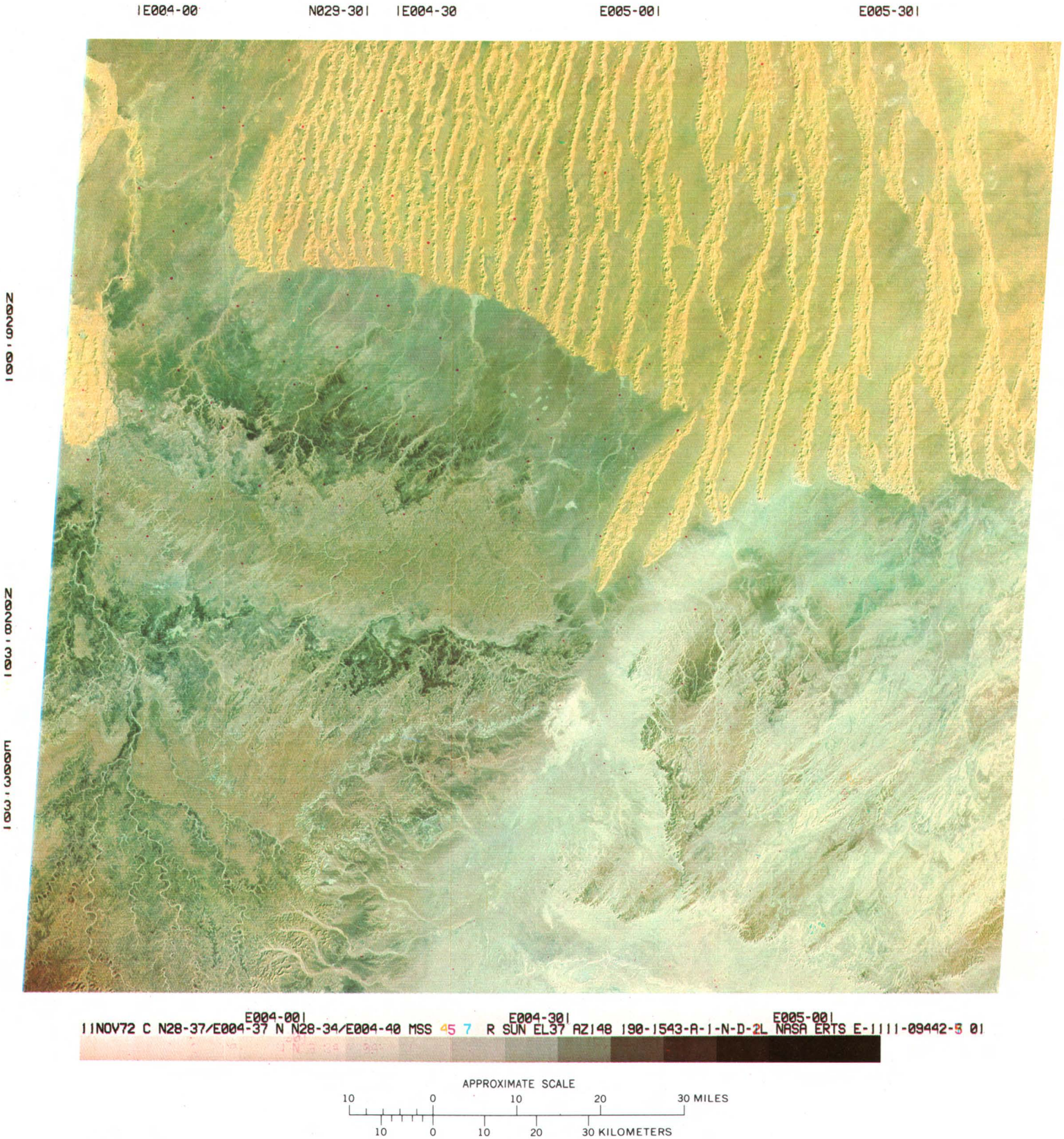


FIGURE 57.—Color composite ERTS–1 image showing star or radial megadunes in Algeria (1111–09442).

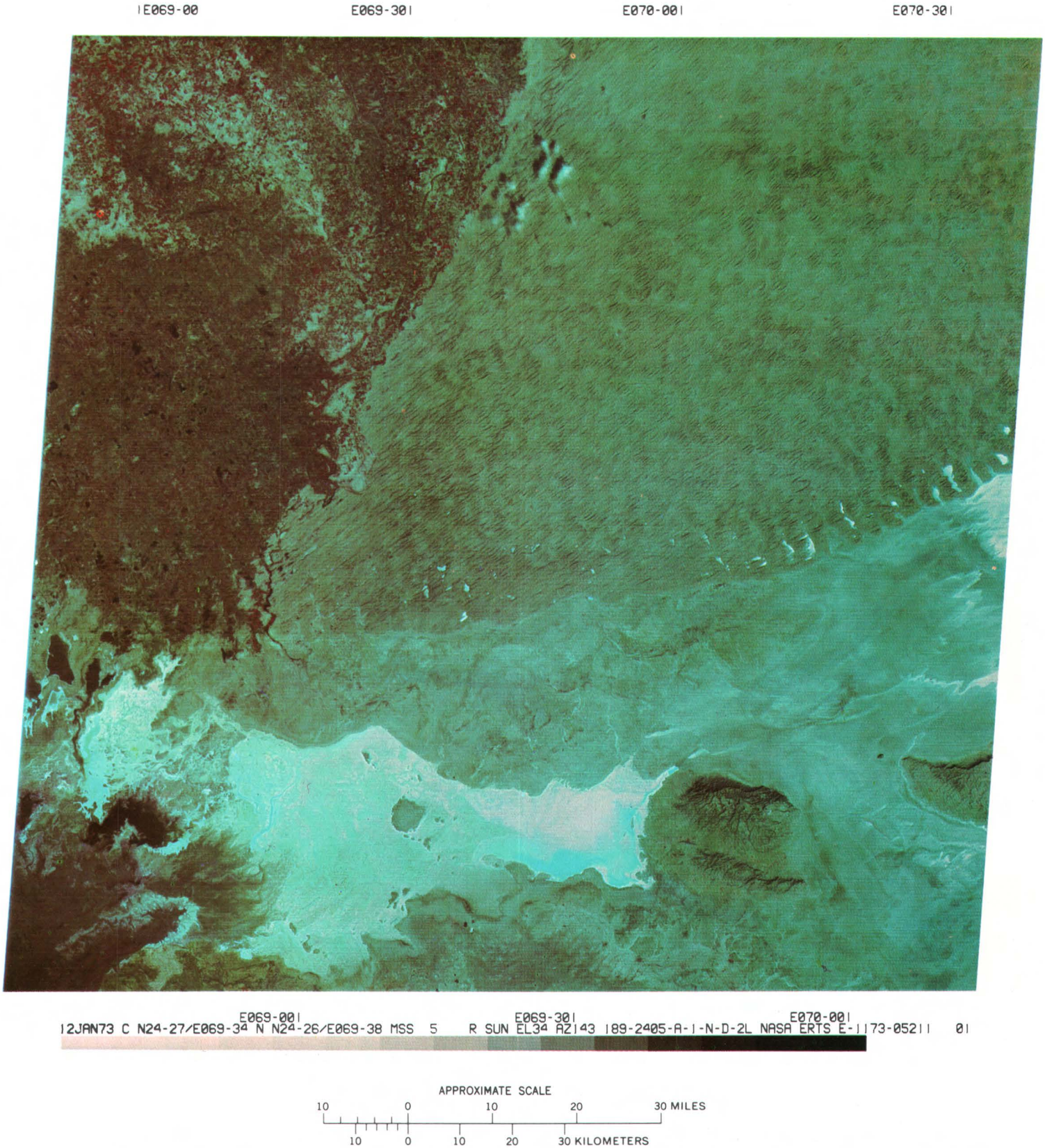


FIGURE 58.—Color composite ERTS–1 image showing parabolic dunes in the Rajasthan Desert of India (1173–05211).

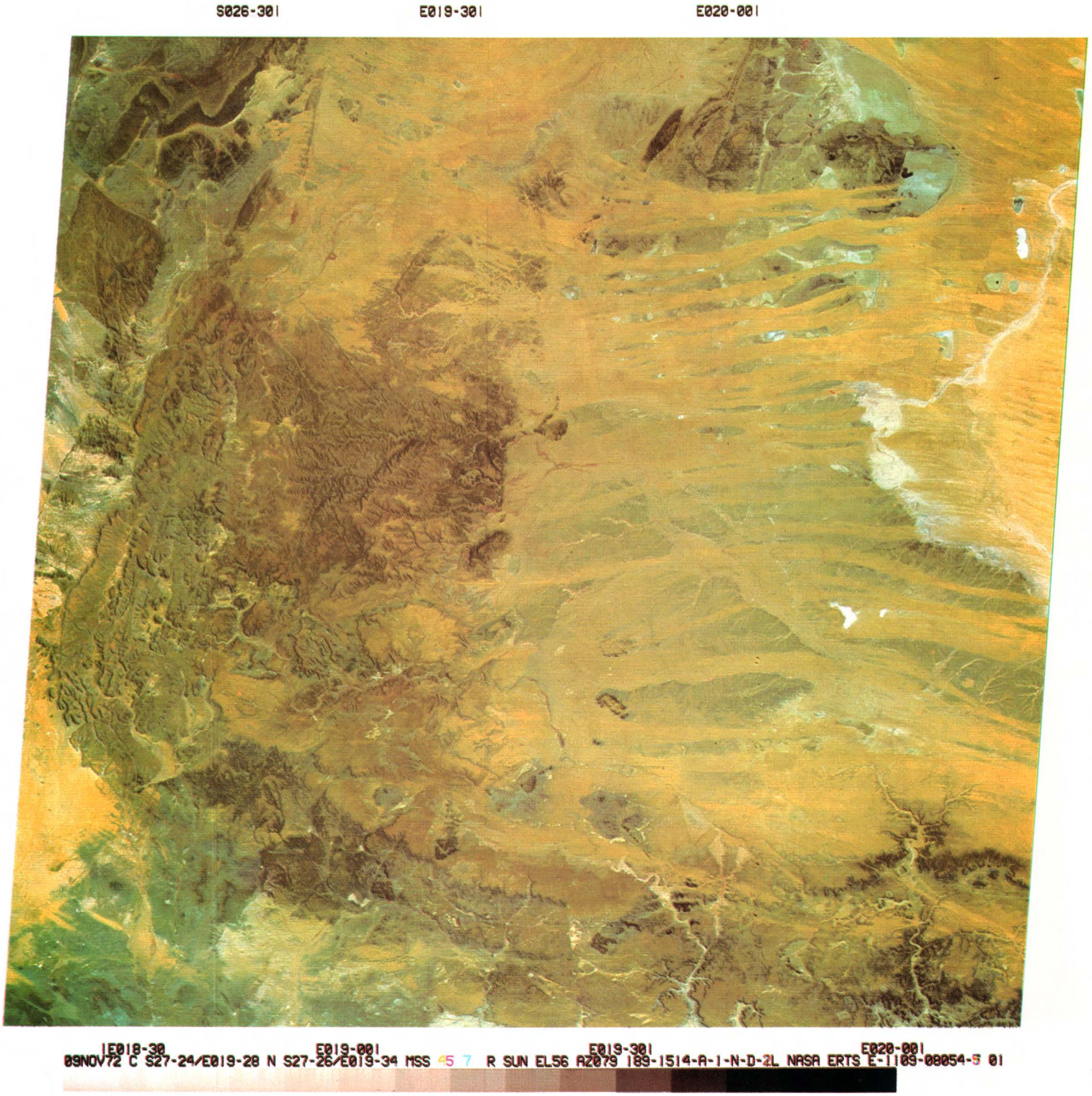


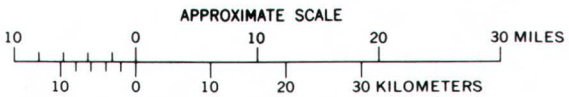


FIGURE 59.—Color composite ERTS–1 image showing flat sheets and stringer dunes in South-West Africa (1109–08054).

# DETECTION OF HYDROTHERMAL SULFIDE DEPOSITS, SAINDAK AREA, WESTERN PAKISTAN

By Robert G. Schmidt,

U.S. Geological Survey

The digitally enhanced false-color composite of an ERTS–1 image dated Nov. 25, 1972, (fig. 60) shows the known porphyry copper deposit at Saindak, in western Pakistan, and several sites chosen for further prospecting on the basis of information from this image and known geologic data (Ahmed and others, 1972; Schmidt, 1973).

Porphyry copper deposits are large bodies of weakly mineralized rock generally containing minerals associated with hydrothermal alteration. Zones containing different alteration minerals tend to be concentric outward from a core and commonly include large volumes of pyrite-bearing rock. Under optimum conditions, the topographic forms and surface-coloration anomalies of light-toned anomalies related to the weathering of these deposits are so large and distinctive that they can be recognized on ERTS–1 images.

At Saindak a group of small copper-bearing porphyritic quartz diorite stocks surrounded by zones of hydrothermal-alteration minerals cut northward across the entire folded lower Tertiary stratigraphic section. The stocks have undergone intense sericitic alteration and contain copper sulfides. The stocks are enclosed in a pyrite-rich envelope that is in turn surrounded by a hard dark-appearing zone of propylitic alteration. The sulfide-rich zone, including the porphyry stocks, has been eroded out to form a valley that appears light toned on the image (fig. 61, A). The zone of propylitic alteration forms a symmetrical rim of hills more rugged than the surrounding region and appears darker in tone (B). Together these features are several kilometers across and form a visible target on the image that is much larger than the actual exposed area of mineralized rock. Both the central valley and dark rim are displaced left laterally by a major east-trending fault (C).

The region around the Saindak deposit is a geologically favorable area for deposits of the porphyry copper type, and it was studied for evidence of other deposits by using composite images and photogeologic maps and field mineral-reconnaissance data. Three sites on this image, not formerly regarded as potential prospects for large sulfide deposits, were identified (D, E, and F), and one former prospect (G) was reevaluated. These four sites are recommended for field examination. All are areas of known intrusive stocks. At site D, a small rugged area near the intrusive may be due to propylitic alteration. Dark-appearing hilly areas surround central cores having a light tone and low topographic form at sites E, F, and G, and skarn-type hematite or magnetite bodies have been reported from the vicinity of E, F, and G. Unfortunately, because windblown sand is abundant in the central cores of these three sites, the image does not show absolutely that the bedrock there has a light tone, although the combinations of colors and bands were chosen in this and other composites to enhance the difference.

Evaluation of the techniques used here will be possible after field checks have been made of the sites suggested, but positive identification of any porphyry-type deposit must be followed by extensive evaluation before it can be known whether the deposit is exploitable.

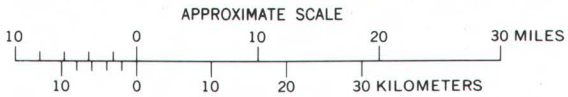


FIGURE 60.—Digitally enhanced false-color composite ERTS–1 image of the Saindak area of western Pakistan, prepared by IBM Corp., Gaithersburg, Md., using band 4 (blue light), band 5 (green light), and band 7 (red light) (1125–05545).

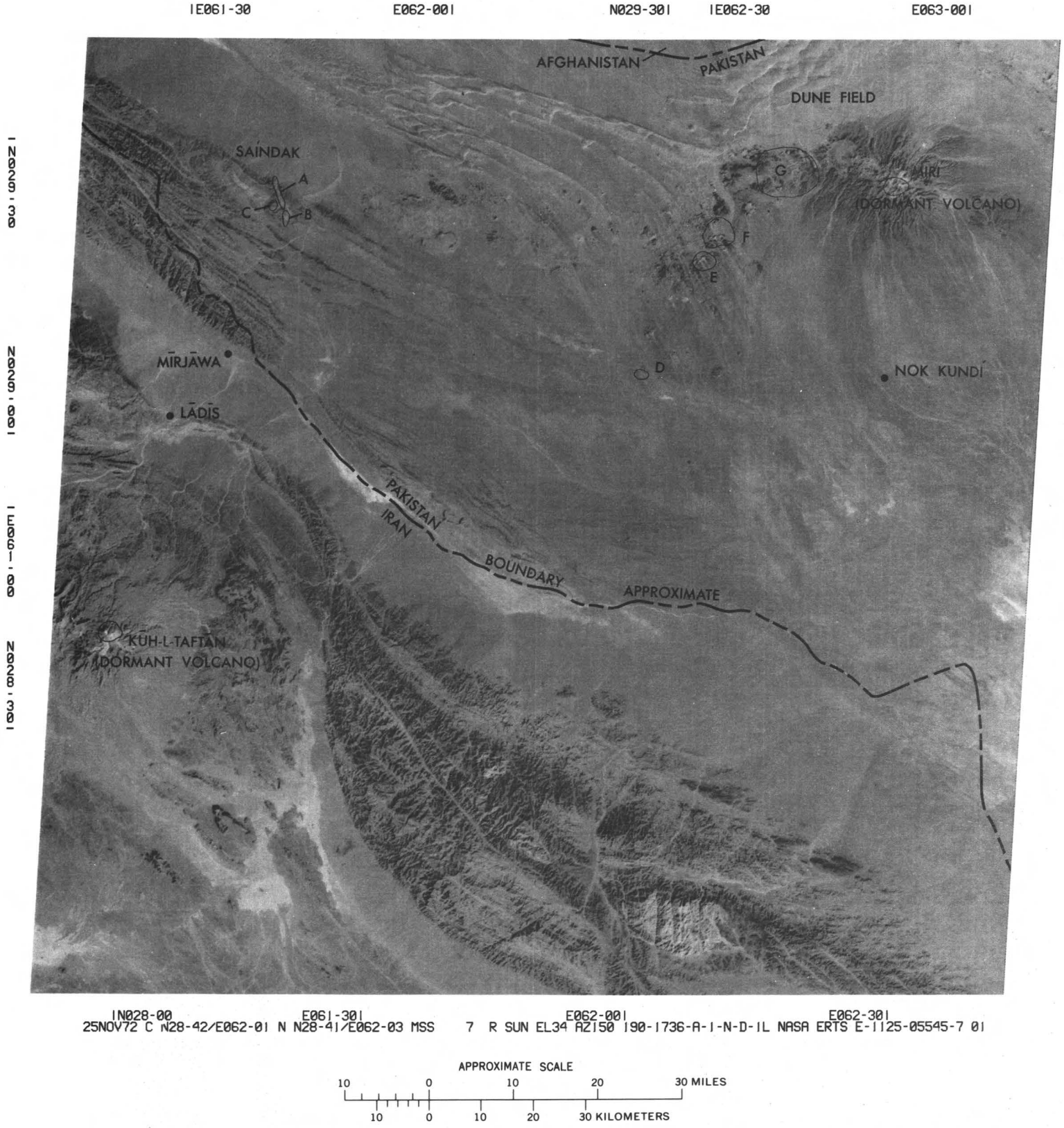


FIGURE 61.—Annotated ERTS–1 image showing location of significant geologic features of the Saindak area of Pakistan (1125–05545, band 7).

# STRUCTURAL GEOLOGY AND MINERAL-RESOURCES INVENTORY OF THE ANDES MOUNTAINS, SOUTH AMERICA

By William D. Carter,

U.S. Geological Survey

The evaluation of the use of ERTS–1 images as a tool for improving knowledge of the structural geology and mineral resources of the Andes is a cooperative project with geologists of South American resource agencies. The program is based on the idea that exchange of interpretive results between scientists will raise the level of confidence in interpretation and improve the use of these new data acquired by remote sensing. The objective is to establish models and procedures that will ultimately lead to mapping of the entire Andean chain—and eventually the South American continent—on a common base and with standard procedures. Hopefully this work will provide new information for the "Tectonic and Metallogenic Maps of South America" and will define new areas for mineral exploration.

Of 12 areas proposed for study under this experiment, the first area for which an ERTS image collection was most complete was that of the La Paz region. A mosaic of 22 images covering an area of 275,000 km$^2$ between lat 16° and 20° S. and long 66° and 72° W. was compiled at a scale of 1:1,000,000 by the U.S. Geological Survey (fig. 62). Band 6 images of reflectance in the near-infrared region (0.7–0.8 $\mu$m) were selected for the mosaic. Copies were then sent to cooperating investigators in Bolivia, Chile, and Peru for evaluation and interpretation.

Four map overlays of the La Paz orthoimage mosaic have thus far been prepared that provide a preliminary understanding of the region. The first was an image linear map (fig. 63) in which all natural linear features, generally greater than 10 km in length, have been identified. Those lineations, believed to be mostly fractures and faults, are indicated by long dashed lines; lineations related to bedding planes of strata are indicated by short dashed lines. Volcanic cones, craters, and calderas are also depicted to place them in the regional tectonic framework. The completed interpretation was then compared to existing published maps and to the interpretive products made by other cooperating investigators. This comparison resulted in a "relative confidence map" (fig. 64) on which linear features noted on published maps

were indicated in red and those noted on ERTS imagery by two or more interpreters in green. Coincidence of the preliminary plotting of linear features from ERTS imagery to the other sources was high.

A metallogenic map was made by combining published information from Peru, Bolivia, and Chile at a common scale of 1:1,000,000. From this and the image linear map, a revised metallogenic map for the area was drafted (fig. 65). This product is now being evaluated by the cooperating investigators.

A fourth map of related interest is a seismic-hazard map (fig. 66) that shows the location of epicenters of earthquakes occurring between 1963 and 1973 and having a Richter magnitude of 5 or greater. These data were acquired from the World Wide Seismic Net, and the epicenters are believed to be accurate within 25 to 50 km. Although the relationships between linear features shown on the image linear map and the areas of high seismic hazard are not necessarily direct, one may infer that some of the surficial structures indicated on the image linear map are connected to deep-seated seismically active structures. The relationship of volcanic activity to the movement of ore-forming fluids remains an interesting geological problem.

Whereas much remains to be done in this program, the following conclusions can be stated:

1. ERTS–1 images, because of their synoptic view of large areas, consistent Sun angle, and internal geometry, are ideal for mapping geologic structures in large remote areas of the world.
2. The flexibility provided by several multispectral bands produces useable data for both arid plains and humid jungles as well as intermediate regions. Bands 6 and 7, providing near-infrared reflectance information, are considered the best for most geologic information because water bodies and soil moisture are depicted so clearly and the effects of vegetative cover are reduced.
3. Color composite images, although the number available of South America still is very low, have been found to increase geologic interpretability by 40 percent (Brockmann, 1974). This fact provides strong support for constructing future mosaics in color.

NASA (ERTS–1)

LA PAZ

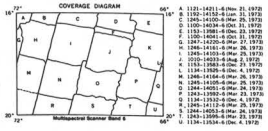


A. 1121–14211–6 (Nov. 21, 1972)
B. 1192–14152–6 (Jan. 31, 1973)
C. 1245–14100–6 (Mar. 25, 1973)
D. 1100–14034–6 (Oct. 31, 1972)
E. 1153–13981–6 (Dec. 23, 1972)
F. 1100–14041–6 (Oct. 31, 1972)
G. 1247–14220–6 (Mar. 27, 1973)
H. 1246–14161–6 (Mar. 26, 1973)
I. 1245–14103–6 (Mar. 25, 1973)
J. 1010–14033–6 (Aug. 2, 1972)
K. 1153–13983–6 (Dec. 23, 1972)
L. 1134–13929–6 (Dec. 4, 1972)
M. 1246–14164–6 (Mar. 26, 1973)
N. 1245–14105–6 (Mar. 25, 1973)
O. 1244–14051–6 (Mar. 24, 1973)
P. 1243–13992–6 (Mar. 23, 1973)
Q. 1134–13932–6 (Dec. 4, 1972)
R. 1245–14112–6 (Mar. 25, 1973)
S. 1244–14053–6 (Mar. 24, 1973)
T. 1243–13996–6 (Mar. 23, 1973)
U. 1134–13934–6 (Dec. 4, 1972)

# LA PAZ

SCALE 1:1 000 000

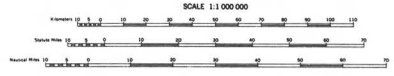


Ticks outside the margin indicate the 100,000-meter grid lines of the Universal Transverse Mercator grid, zone 19, International Spheroid. The imagery was not controlled or positioned with reference to the grid

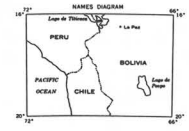


ERTS EXPERIMENT NO. 189
NATIONAL AERONAUTICS AND SPACE ADMINISTRATION

INTERIOR–U. S. GEOLOGICAL SURVEY, RESTON, VIRGINIA

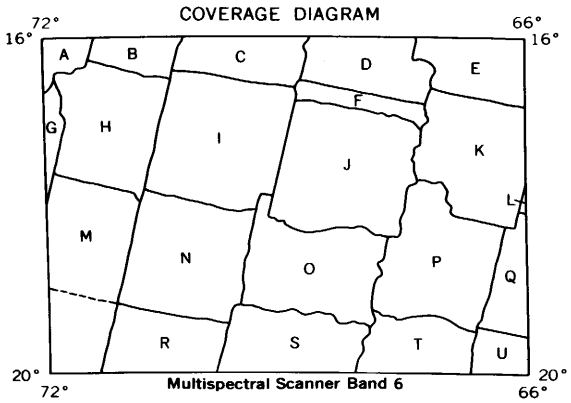


A. 1121-14211-6 (Nov. 21, 1972)
B. 1192-14152-6 (Jan. 31, 1973)
C. 1245-14100-6 (Mar. 25, 1973)
D. 1100-14034-6 (Oct. 31, 1972)
E. 1153-13581-6 (Dec. 23, 1972)
F. 1100-14041-6 (Oct. 31, 1972)
G. 1247-14220-6 (Mar. 27, 1973)
H. 1246-14161-6 (Mar. 26, 1973)
I. 1245-14103-6 (Mar. 25, 1973)
J. 1010-14033-6 (Aug. 2, 1972)
K. 1153-13583-6 (Dec. 23, 1972)
L. 1134-13525-6 (Dec. 4, 1972)
M. 1246-14164-6 (Mar. 26, 1973)
N. 1245-14105-6 (Mar. 25, 1973)
O. 1244-14051-6 (Mar. 24, 1973)
P. 1243-13592-6 (Mar. 23, 1973)
Q. 1134-13532-6 (Dec. 4, 1972)
R. 1245-14112-6 (Mar. 25, 1973)
S. 1244-14053-6 (Mar. 24, 1973)
T. 1243-13595-6 (Mar. 23, 1973)
U. 1134-13534-6 (Dec. 4, 1972)

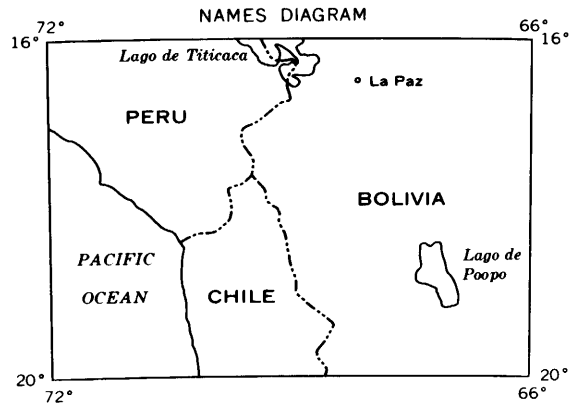


FIGURE 62.—ERTS-1 image mosaic of the La Paz area of Bolivia, Peru, and Chile.

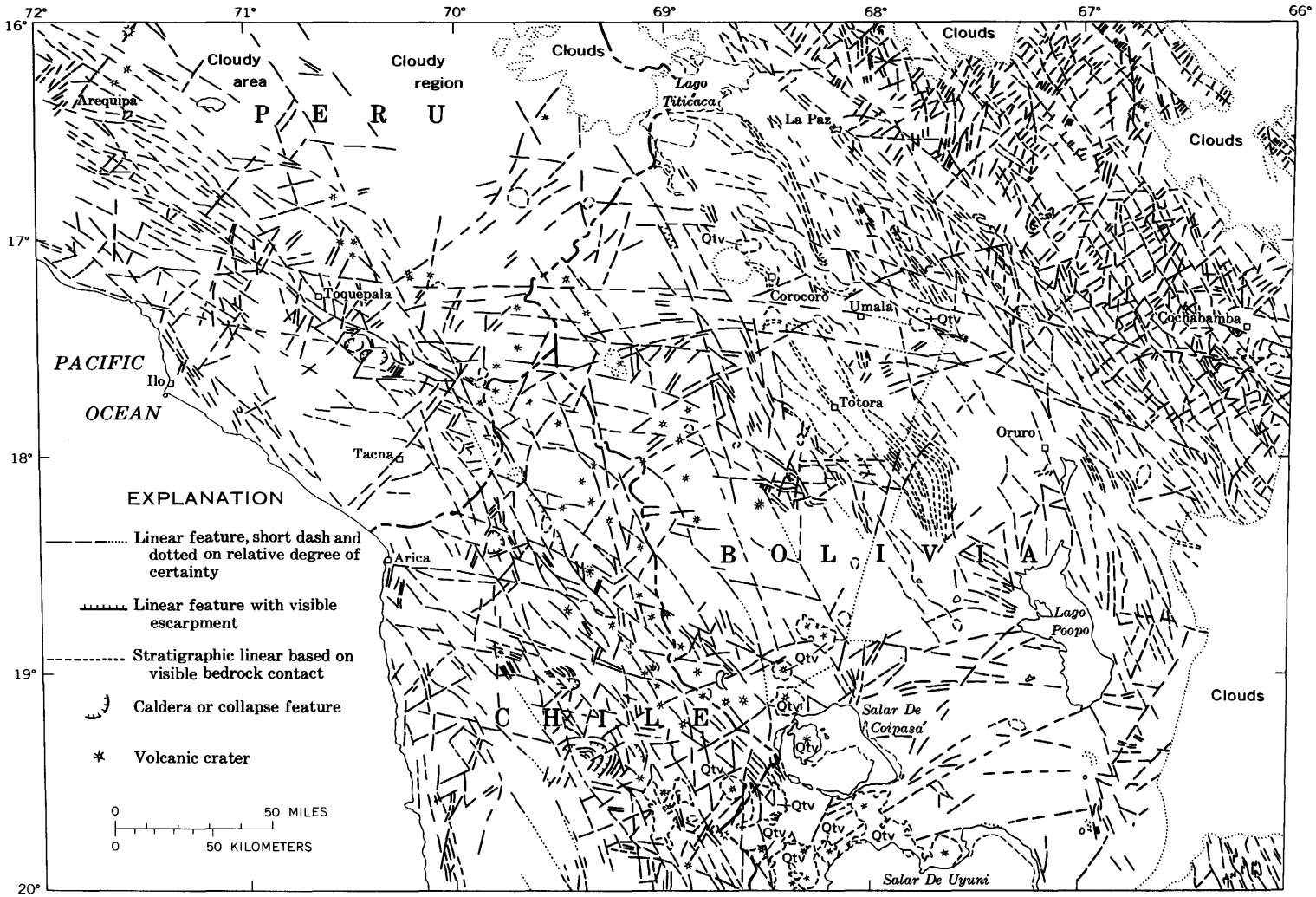


FIGURE 63.—Image linear map of the La Paz area.

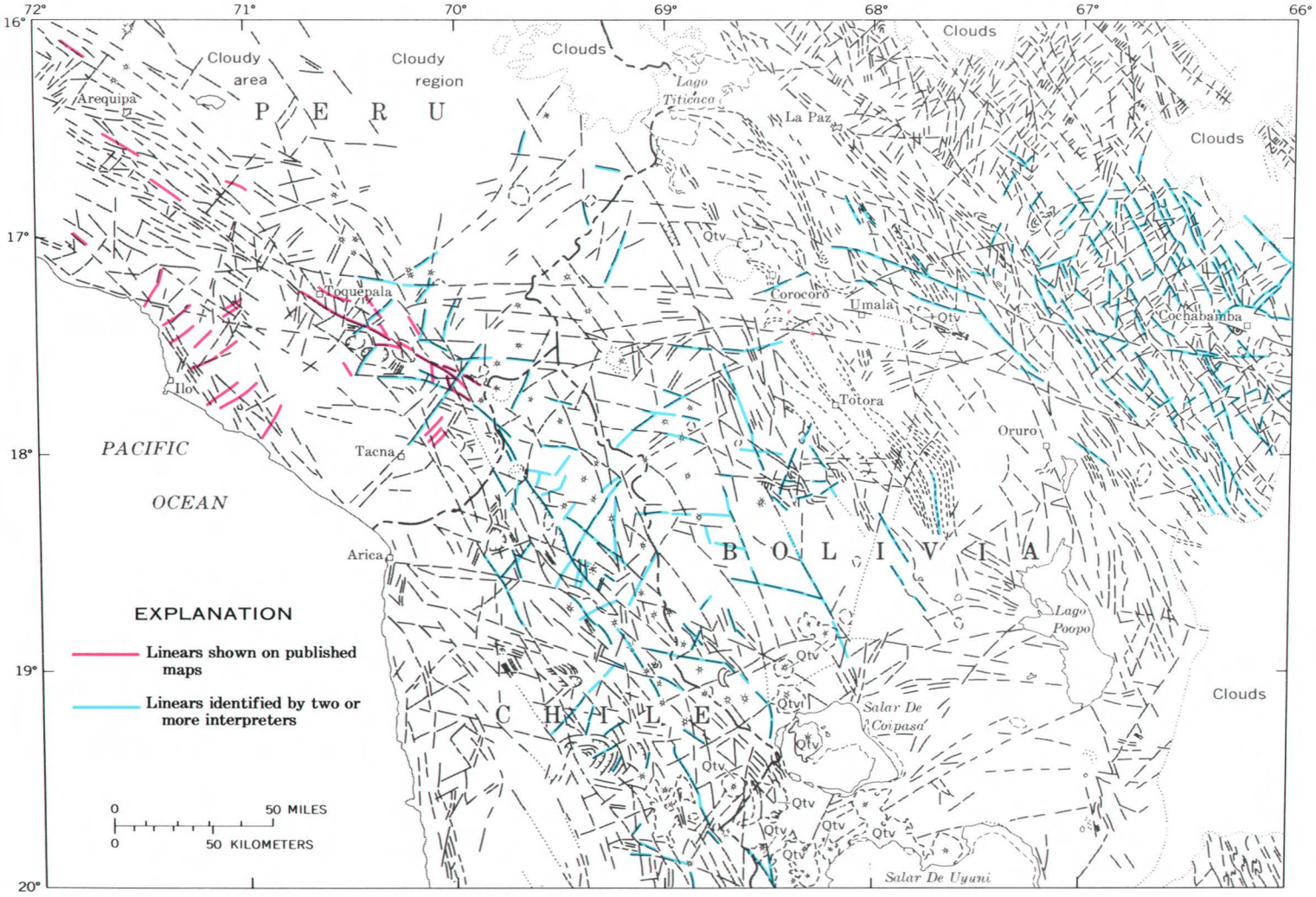


FIGURE 64.—Relative confidence map of the La Paz area.

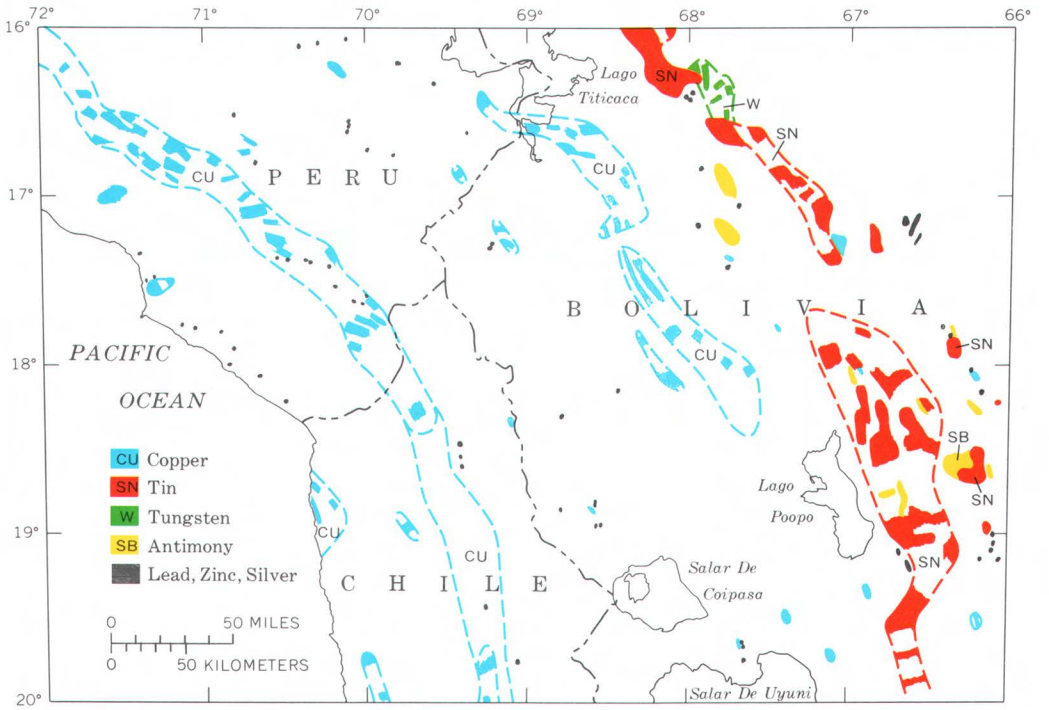


FIGURE 65.—Metallogenic map of the La Paz area.

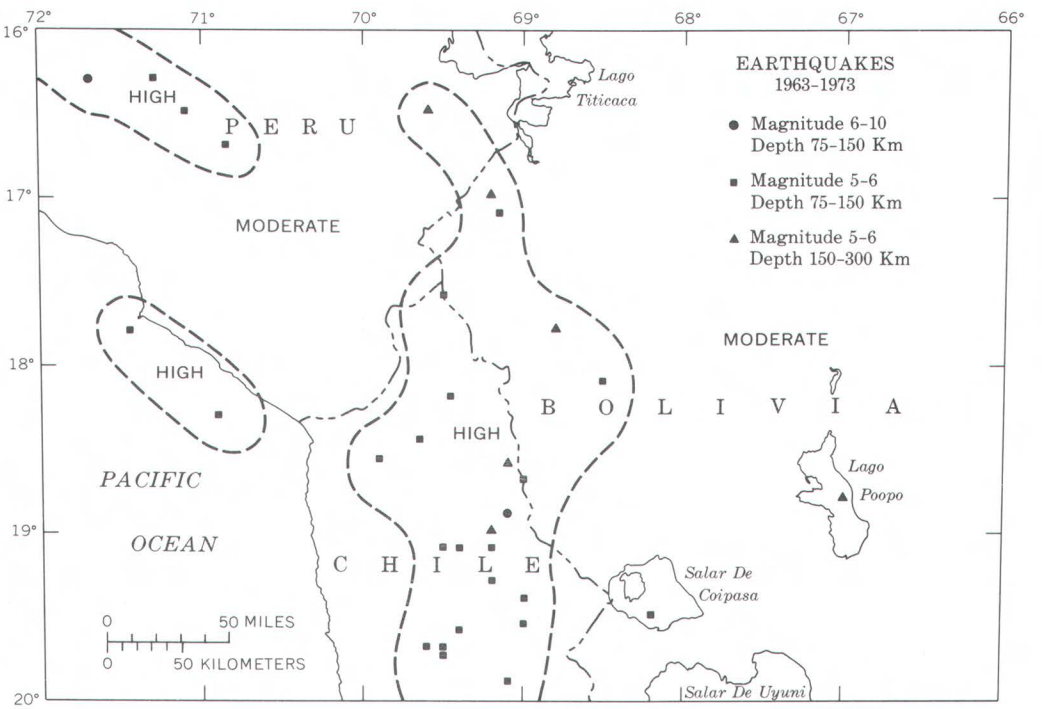


FIGURE 66.—Seismic-hazard map of the La Paz area.

# CLUES TO GEOLOGIC STRUCTURE POSSIBLY INDICATING OIL AND GAS SOURCES

By Ernest H. Lathram,

U.S. Geological Survey

An ERTS image of northern Alaska (fig. 67) taken only 4 days after the launch of the satellite shows a part of the foothills and coastal plains near Umiat, Alaska. Umiat was the major staging area for the Navy Department's exploration of Petroleum Reserve No. 4 in 1945–52 and is the site of a medium-sized oilfield discovered during that work. The image represents the near-infrared light reflected from Earth at the time of the overflight, and, because water absorbs infrared light, lakes and streams appear black in sharp contrast to land areas. The clear view of the distribution of lakes in the coastal plain over this large area provided information on the geologic structure not heretofore recognized (Fischer and Lathram, 1973).

Lakes in the coastal plain are known to be predominantly elongate, their long axes parallel and trending about N. 9° W. In figure 68, an additional strong east-trending regional lineation, not previously recognized on aerial photographs or in field study, is seen in linear interlake areas, alinement of some lakes, and elongation of some others. The trend of this lineation is parallel to the trend of deflections in contours of the magnetic and gravity fields in the area and is parallel to westerly deflections in the northwest ends of northwest-trending folds mapped to the south. In addition, the alinement of many small lakes forms a large and small ellipse superimposed on the regional lineation. Sparse seismic profiles show both periodic reversals in dip and a regional arching in shallow strata beneath the lineated area. These data suggest that concealed structures may exist in this area that may have concentrations of gas in shallow strata and of oil in deeper strata at or near basement.

Study of additional ERTS images shows that the observed lineation is prominent in the coastal plain from the Ikpikpuk River east to the Canning River and that this lineation may be useful as a guide to petroleum exploration throughout this area. The lineated area includes the sites of Prudhoe Bay and other recently discovered oilfields.

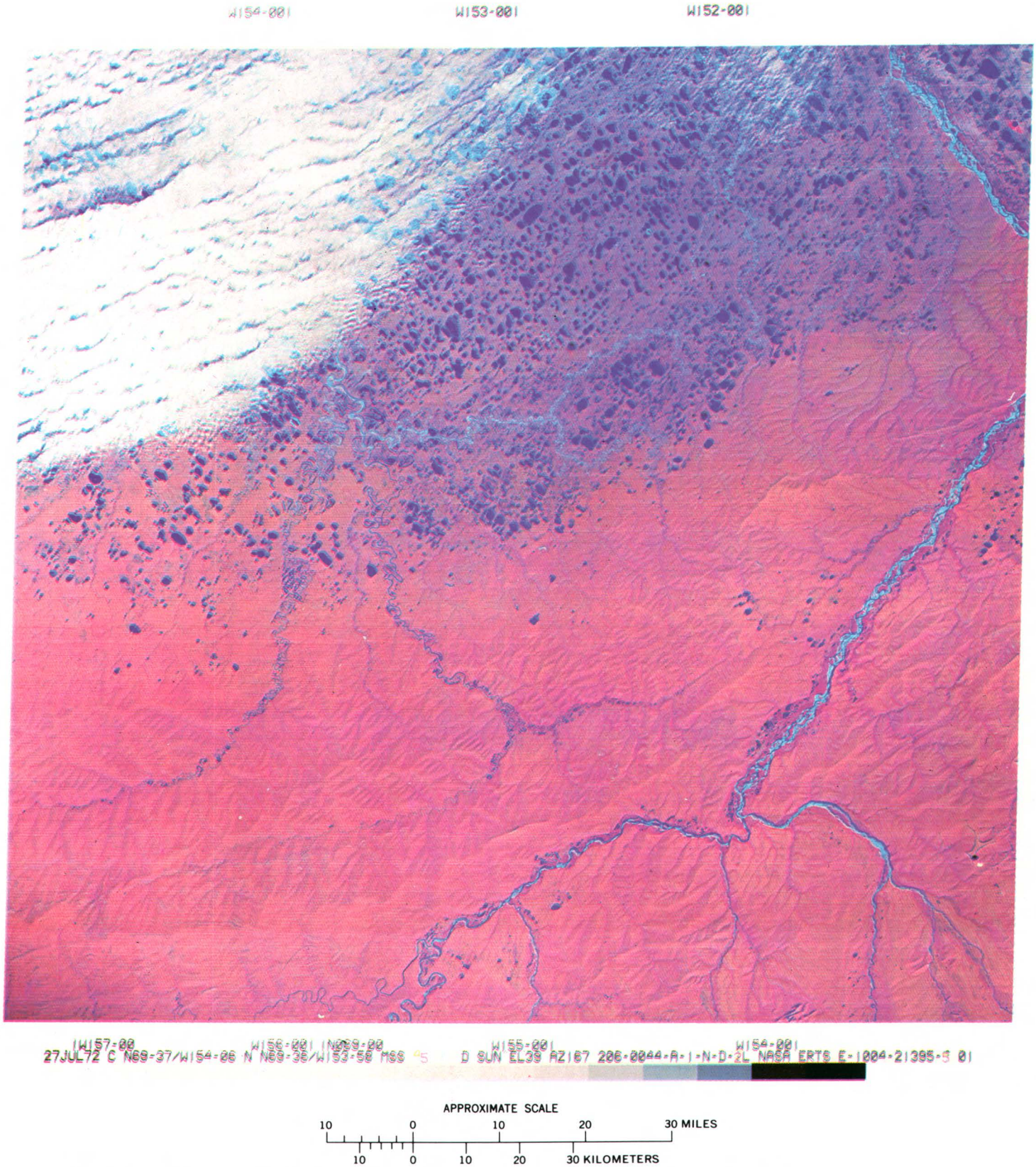


FIGURE 67.—Color composite ERTS–1 image of the foothills and coastal plains near Umiat, Alaska (1004–21395).

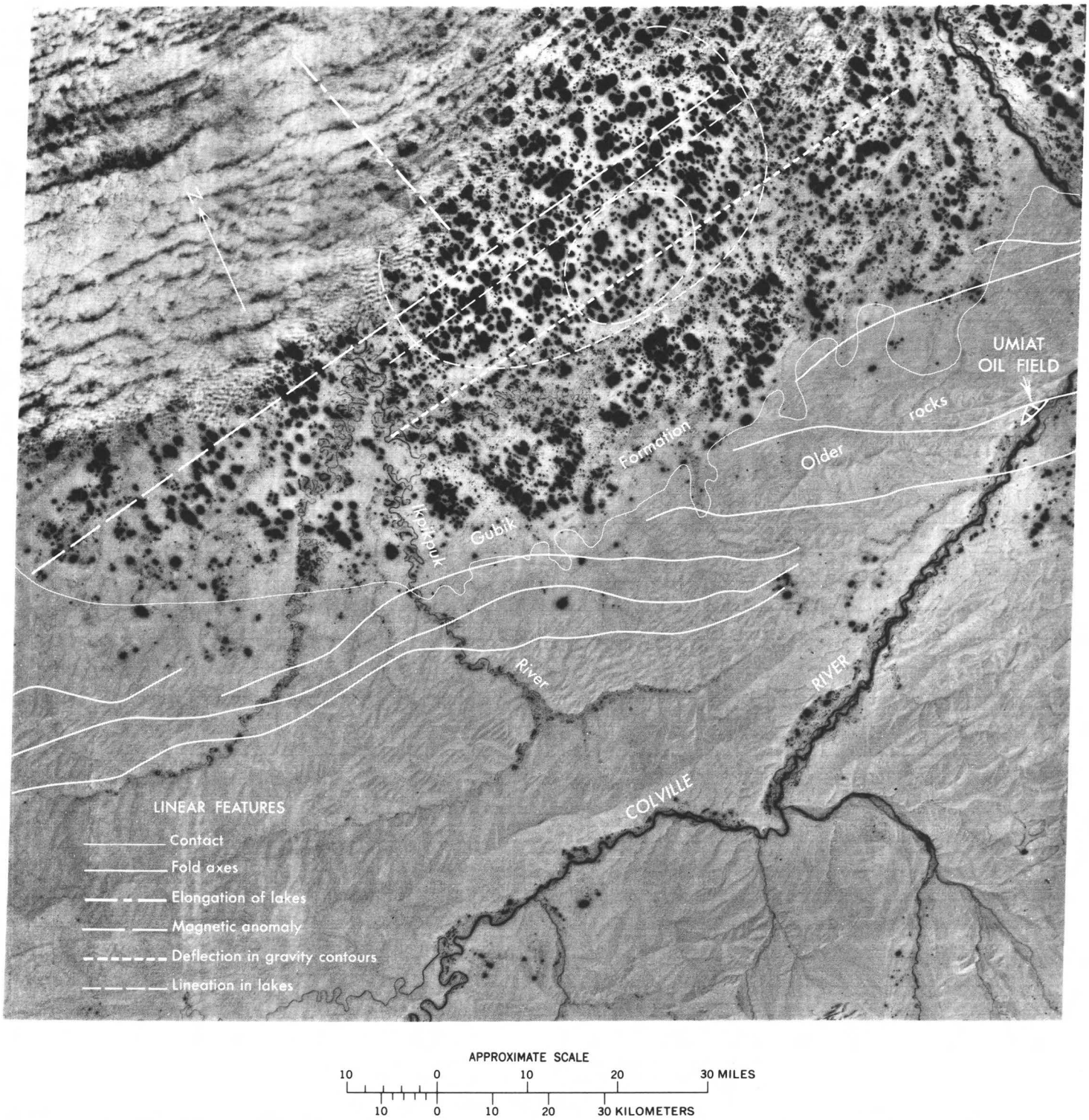


FIGURE 68.—ERTS–1 image of the Umiat area of Alaska showing structural features and lineation of lakes (1004–21395, band 7).

# DISCRIMINATION OF ROCK TYPES AND DETECTION OF HYDROTHERMALLY ALTERED AREAS IN SOUTH-CENTRAL NEVADA

By Lawrence C. Rowan and Pamela H. Wetlaufer, U.S. Geological Survey,

and A. F. H. Goetz, Jet Propulsion Laboratory

A combination of digital computer processing and color compositing of ERTS MSS images has been used to detect and map hydrothermally altered areas and to discriminate most major rock types in south-central Nevada (Rowan and others, 1974). The technique is based on enhancement of subtle visible and near-infrared reflectivity differences associated with variations in bulk composition. MSS spectral bands are ratioed, pixel by pixel, by a computer and are subsequently contrast stretched to enhance the spectral differences. These stretched-ratio values are used to produce a new black and white image that shows the subtle spectral reflectivity differences and concurrently minimizes radiance variations due to albedo and topography. Additional enhancement is achieved by preparing color composites of two or more stretched-ratio images. Color variations seen in these stretched-ratio color composites represent spectral reflectance differences (fig. 69).

The choice of MSS bands for ratioing depends on the spectral reflectance properties of the surface materials to be discriminated. For south-central Nevada, the most effective stretched-ratio color composite for discriminating between altered and unaltered areas and between the regional rock units was prepared using the following color and stretched-ratio image combination: blue for MSS 4/5; yellow for MSS 5/6; and magenta for MSS 6/7. In this composite (fig. 69), mafic rocks, mainly basalt and andesite (A), are white, whereas felsic extrusive and intrusive rocks are pink (B). The felsic rocks are especially notable because they have a large intrinsic albedo range, which commonly prevents their discrimination from mafic rocks in other types of images and photographs.

Vegetation in the composite is orange, the darker hues representing denser vegetation. Although rock type is generally masked by the denser vegetation, some discrimination is possible among the flows and tuffs on Pahute Mesa (C) where the vegetation cover is less dense (light orange). Playas and the two mining dumps on the western border of the Goldfield mining district (D) are blue. Clouds (pink-brown) and cloud shadows (white) can be identified with the aid of the standard color composite image in figure 70.

Altered areas on figure 69 are represented by green (D) to dark-green (E) and brown (F) to red-brown (G) patterns in the color-ratio composite. Except for two areas (H and I), the green areas represent hydrothermally altered, commonly limonitic rock. The dark-green, brown, and red-brown patterns are less prevalent. Dark-green areas are limonitic and limonite-free altered rocks. Areas that are brown in the color-ratio composite have been studied in less detail, but they appear to be predominantly light-colored hydrothermally altered volcanic rocks. The red-brown pattern represents limonite-free, silica-rich, light-colored volcanic rocks that have conspicuous alteration in two areas and questionable alteration in two other areas.

Altered outcrops mapped from the stretched-ratio color composite show a pronounced coincidence with known mining areas. In the Goldfield mining district (fig. 69, D), the most productive district in the study area, the degree of agreement between the green patterns and the previously mapped alteration zone is very striking. These altered areas are not apparent on the individual MSS images, color-infrared composite (fig. 71), or on color photographs obtained from Skylab. Therefore, the technique used in this study appears to have important applications in mineral-resources exploration and regional geologic mapping. Future research should focus on refinement of this technique, especially on defining more clearly the relationships between visible and near-infrared spectral reflectivity and mineralogical composition and on testing the technique in a variety of geologic settings and environmental conditions.

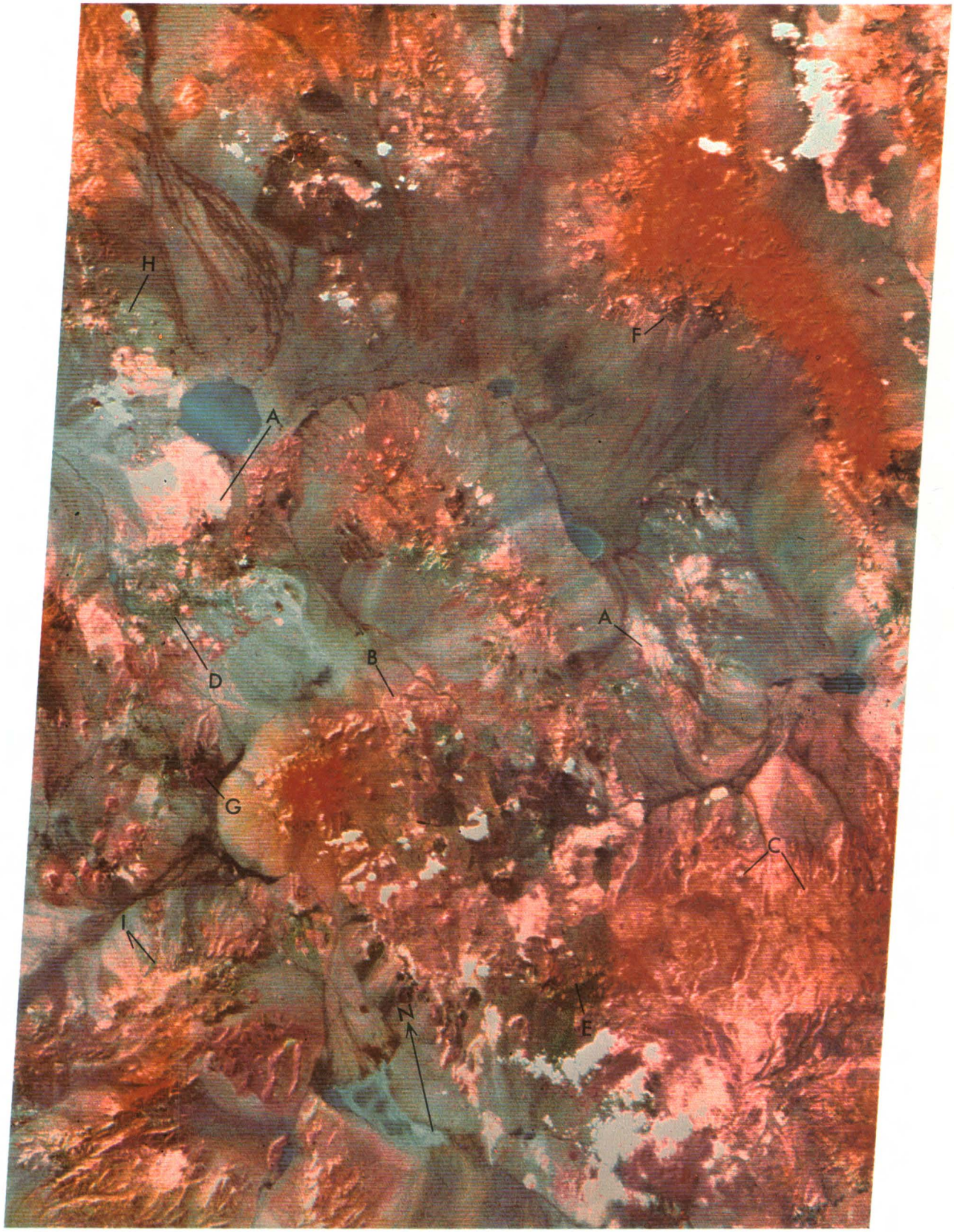


APPROXIMATE SCALE

5 0 5 10 15 MILES

5 0 5 10 15 KILOMETERS

FIGURE 69.—Stretched-ratio color composite ERTS–1 image of south-central Nevada made from computer compatible tapes (part of 1072–18001).

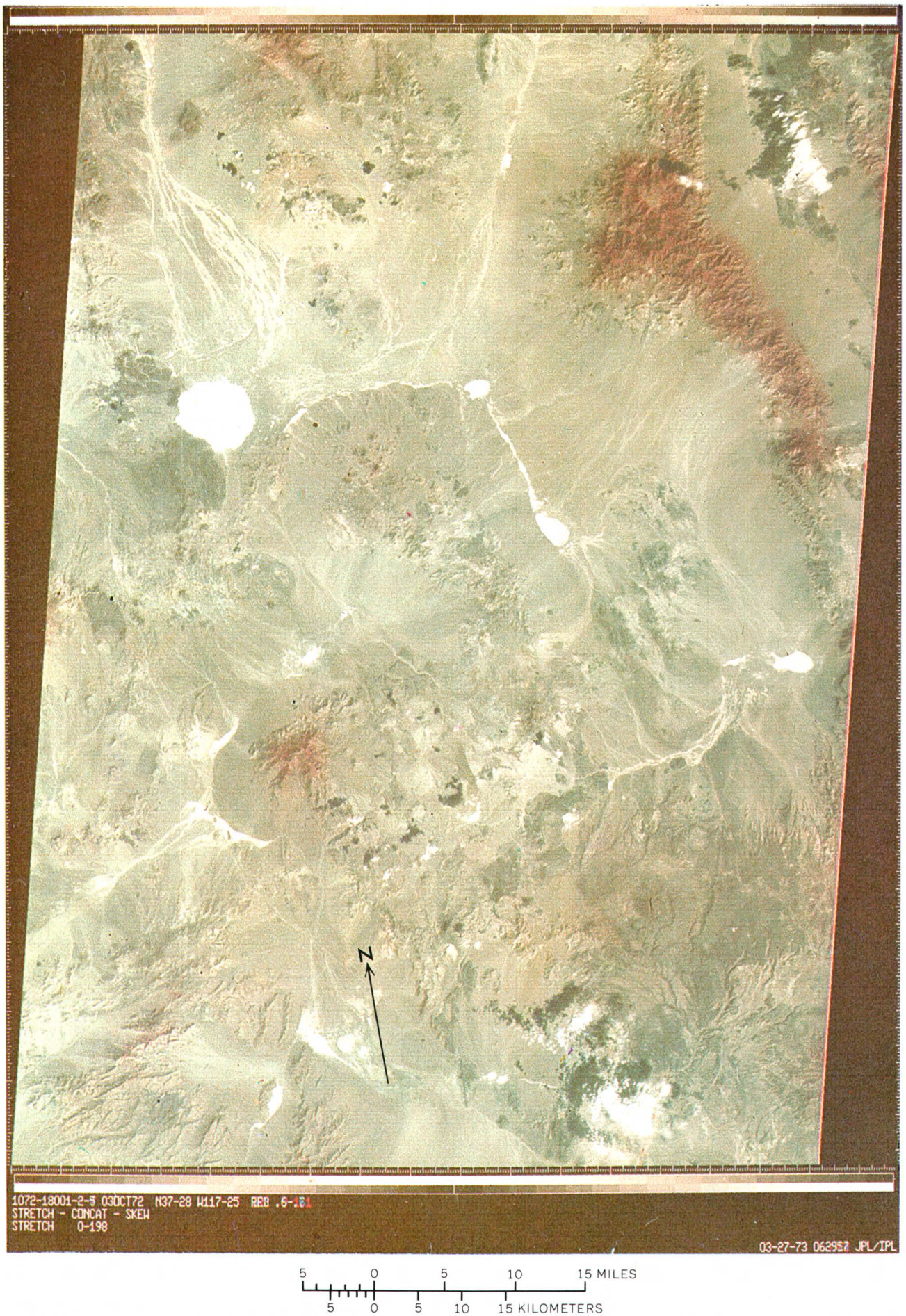


FIGURE 70.—Color composite ERTS–1 image of the south-central Nevada area made from computer compatible tapes (part of 1072–18001).

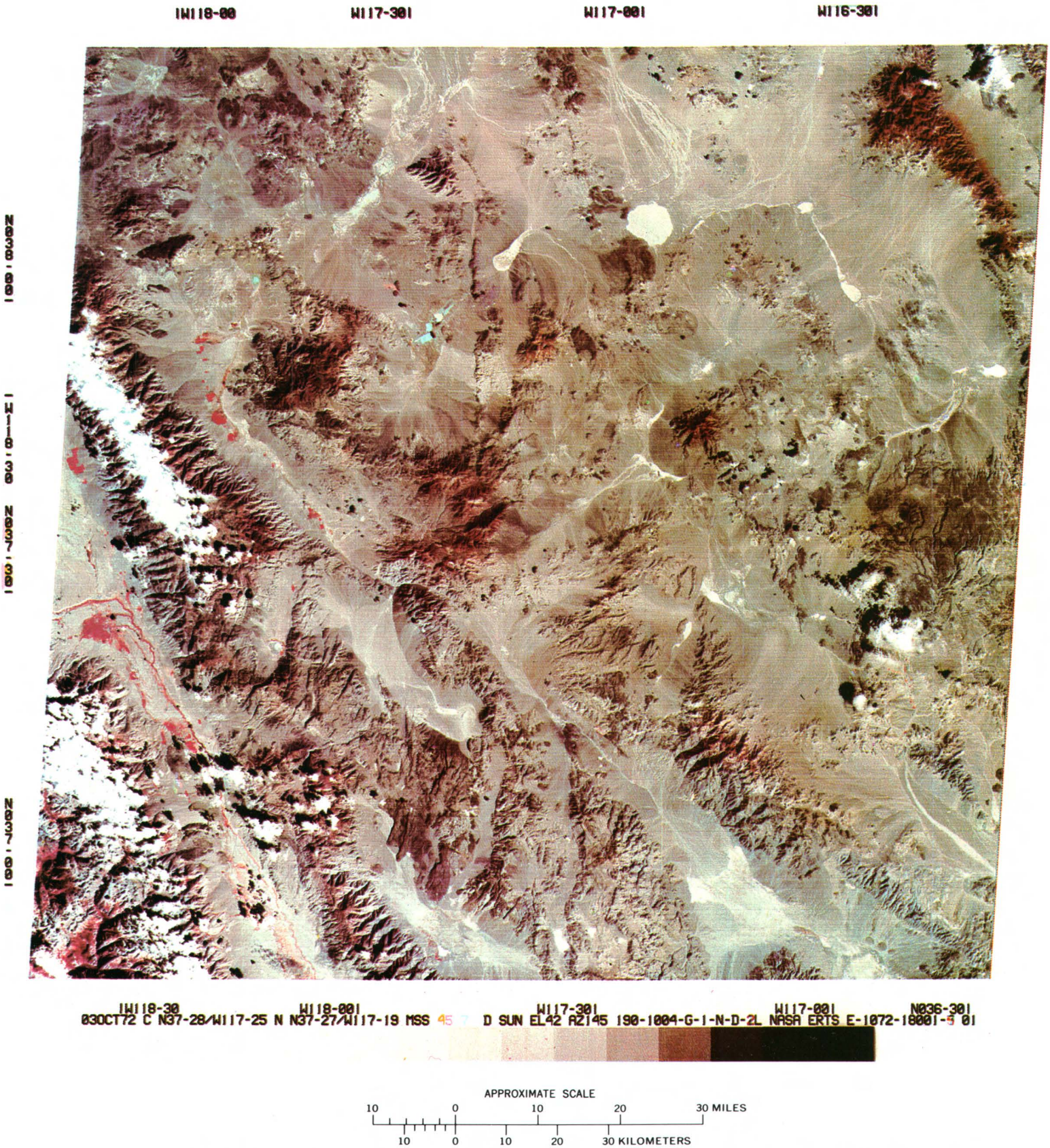


FIGURE 71.—Conventional color composite ERTS–1 image of the entire south-central Nevada area (1072–18001).

# NEW METHOD FOR MONITORING GLOBAL VOLCANIC ACTIVITY

By Peter L. Ward and Jerry P. Eaton,

U.S. Geological Survey

The ERTS data collection system (DCS) makes it feasible for the first time to monitor the level of activity at widely separated volcanoes and to relay these data rapidly to one central office for analysis (Ward and others, 1974). This capability opens a new era in volcanology, and the hundreds of normally quiescent but potentially dangerous volcanoes near populated regions around the world can now be economically and reliably monitored daily to warn when any one volcano is becoming active again. Before ERTS was launched, only a few volcanoes in the world were monitored continuously because of the high cost of building and staffing volcano observatories. Yet it is known from data collected in this century that while visible signs of pending eruptions may occur only minutes to days in advance, invisible but measurable signs may be detected days, weeks, months, and even years before a major eruption. Although the prediction of specific eruptions is still an evasive goal, early warning of a reawakening of a quiescent volcano is now a distinct possibility.

A prototype global volcano-surveillance system was established as part of the ERTS program. In cooperation with local scientists, instruments have been installed on 15 volcanoes in Alaska, Hawaii, Washington, California, Iceland, Guatemala, El Salvador, and Nicaragua at the sites shown in figure 72 (Ward and others, 1974). Data from these low-powered instruments in each of these many remote locations are being relayed 6 to 10 times daily through the satellite to the ground tracking stations at Goldstone, Calif., and Goddard Space Flight Center, Greenbelt, Md. The data are processed at Goddard and then relayed within 90 min by teletype to the National Center for Earthquake Research in Menlo Park, Calif.

The sensors include 19 seismic-event counters, which count four different sizes of earthquakes, and six biaxial borehole tiltmeters, which measure ground tilt with a resolution of 1 $\mu$rad. Only seismic and tilt data are collected because these have been shown in the past to indicate most reliably the level of volcano activity at many different volcanoes. Furthermore these parameters can be measured relatively easily with new instrumentation. A fourth-generation seismic-event counter was especially developed for this project. This instrument compresses seismic data gathered at the rate of about 2 million digital bits per 12 h to the 64 bits that can be economically relayed through a satellite. This compression is not easy, and some data are lost. For the pur-

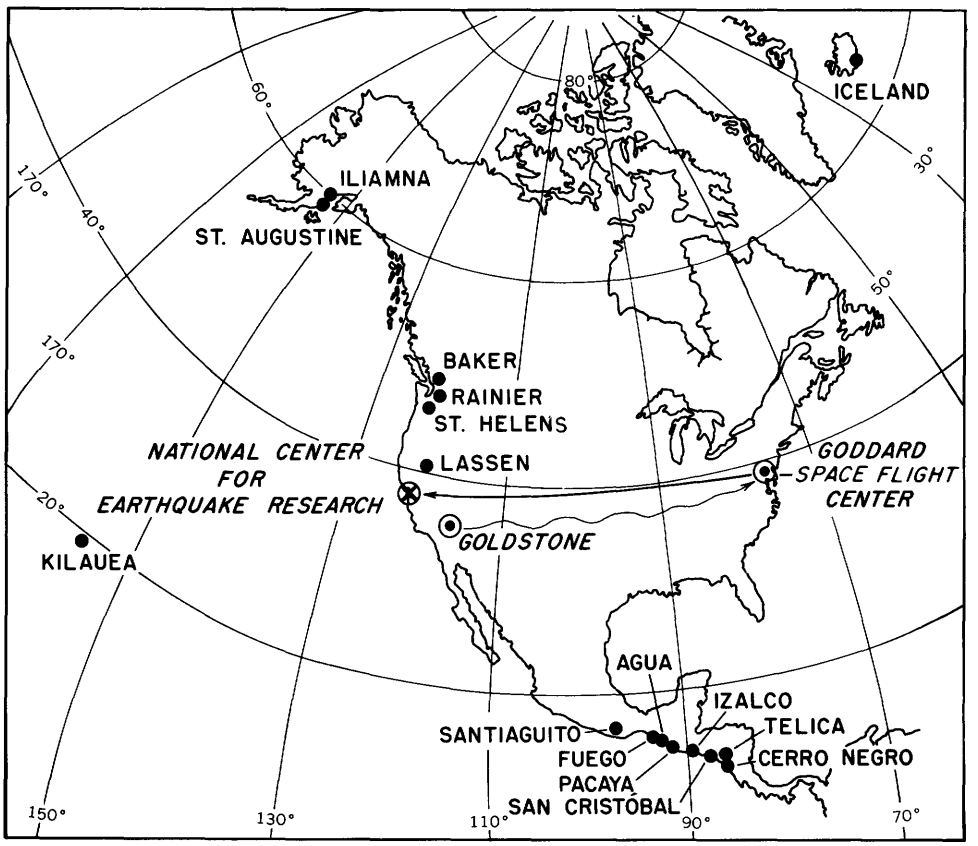


FIGURE 72.—Map showing instrument sites of the prototype volcano-surveillance system.

poses of this project, however, the main data desired are simply the number of events of different sizes. These numbers typically change by orders of magnitude before eruptions. The criteria adopted for detecting events are (1) that 10 peaks of the full-wave rectified seismic signal must be above a given threshold in 1.2 s and (2) that there must have been no peak above this threshold in the previous 15 s. The second criterion effectively inhibits the counter during periods of high ground noise caused by wind, harmonic tremor, people, and so on. The time that a channel is inhibited is counted separately and indicates the relative level of ground noise. The number of earthquakes greater than four different amplitudes and the noise counts for each channel are relayed through the satellite. A typical installation is shown in figure 73. A tiltmeter is also used in this project. The bottom of the pipe, which is about 5 cm in diameter, contains a precise electrically monitored bubble level that has been adapted for this use from a defense application. The pipe is placed in a 1.3- to 3-m hole in rock or, more typically, sandy soil or ash. The output of the electronic equipment shown connects directly to the satellite transmitter.

Data received through the satellite show that the instruments work as anticipated. Three tiltmeters in Hawaii recorded a 10- to 30-$\mu$rad subsidence of the summit Kilauea Volcano during an eruption of May 5, 1973. Volcán Fuego in Guatemala inflated by about 25 $\mu$rad during the 6 mo following an eruption in February 1973.

Events of two different sizes counted on Volcán Fuego, which erupted beginning on Feb. 22, 1973, show an increase in activity during the eruption (fig. 74). The counter was installed in early February. There was a significant increase in activity about 5 days before this small eruption began. The seismic

activity was high during the eruption and returned to a low level after the eruption was over. A different counter 30 km from Fuego showed no change in seismic activity during the whole period. This fact implies that the seismic activity was indeed at Fuego.

The prototype global volcano-surveillance system developed as part of the ERTS program clearly demonstrates the technological and economic feasibility of building a global surveillance system, but many details in the design of highly reliable instruments still need to be worked out. The primary effort in the future will be the collection and analysis of data from these different volcanoes to establish clearly the scientific feasibility of this novel and potentially revolutionary approach to surveillance of hazardous volcanoes.

FIGURE 73.—Data collection platform, Mount Baker, Wash. The diameter of the Plexiglas-covered antenna is 1.2 m.

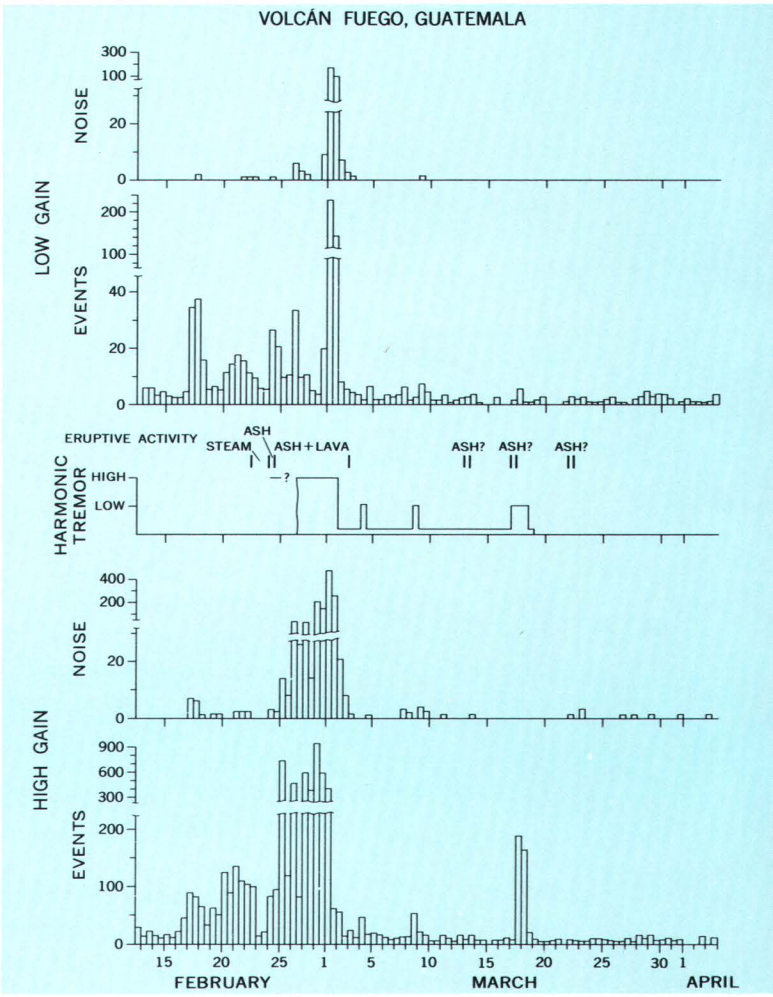


FIGURE 74.—Graph of seismic activity recorded by a data collection platform at Volcán Fuego, Guatemala.

# DYNAMIC ENVIRONMENTAL PHENOMENA IN SOUTHWESTERN ICELAND

By Richard S. Williams, Jr.,

U.S. Geological Survey

The ERTS image mosaic in figure 75 shows a part of west-central and southwestern Iceland, an island republic with a relatively small but rapidly growing population of 213,070 (Dec. 1, 1973) in an area of 103,000 km², or a population density of about 2 persons per km². Iceland, because of its cool climate, low population density, and paucity of natural resources, has early recognized the potential value of ERTS imagery and the ERTS data collection system to provide at low cost and in near real time certain types of dynamic environmental data, such as variable snow cover, changes in the area of glaciers, and seasonal changes in grasslands. Because Icelanders depend on the surrounding seas for fish and crustaceans and on the limited area of arable land for agricultural products, their economic well-being is greatly determined by their natural environment. Understanding and recognizing changes in, and redirecting human and capital resources in response to, the often capricious nature of the natural environment of Iceland have important economic and social implications (Williams and others, 1973a and 1973b).

ERTS imagery of Iceland provides the basis for the study of several different geological and geophysical phenomena that relate in an important way to the natural resources of Iceland (Williams, 1972).

Within the area shown by the late summer color composite ERTS–1 image mosaic live the majority of the inhabitants of Iceland. More than half the population lives in and around the capital city of Reykjavík at **1**. The rich grasslands and cultivated areas (túns) in the lower Thjórsá valley near the coast at **2** and the diminution of vegetation towards the less hospitable interior can be clearly seen. Besides the cultivated and grassland areas, the variations in hues of red permit the mapping of reclaimed land, dwarf forests, and lichen-covered basalts. Barren lands are distinctive by their dark-gray tones and the absence of red colors that indicate a lack of vegetation.

Iceland sits astride the Mid-Atlantic Ridge and is one of the most active areas of volcanism in the world. Within the last 12 yr Iceland has had four volcanic eruptions: Askja in 1961, Surtesy in 1963–67, Hekla in 1970, and Heimaey in 1973. The effects of three of these volcanic eruptions are visible on figure 75. Surtesy at **3** is the small (2.5-km²) volcanic island off the south coast. Heimaey at **4**, an island to the northeast in the same archipelago, was the scene of an extremely damaging volcanic eruption in early 1973. Nearly half the fishing port of Vestmannaeyjar was destroyed or damaged (Williams

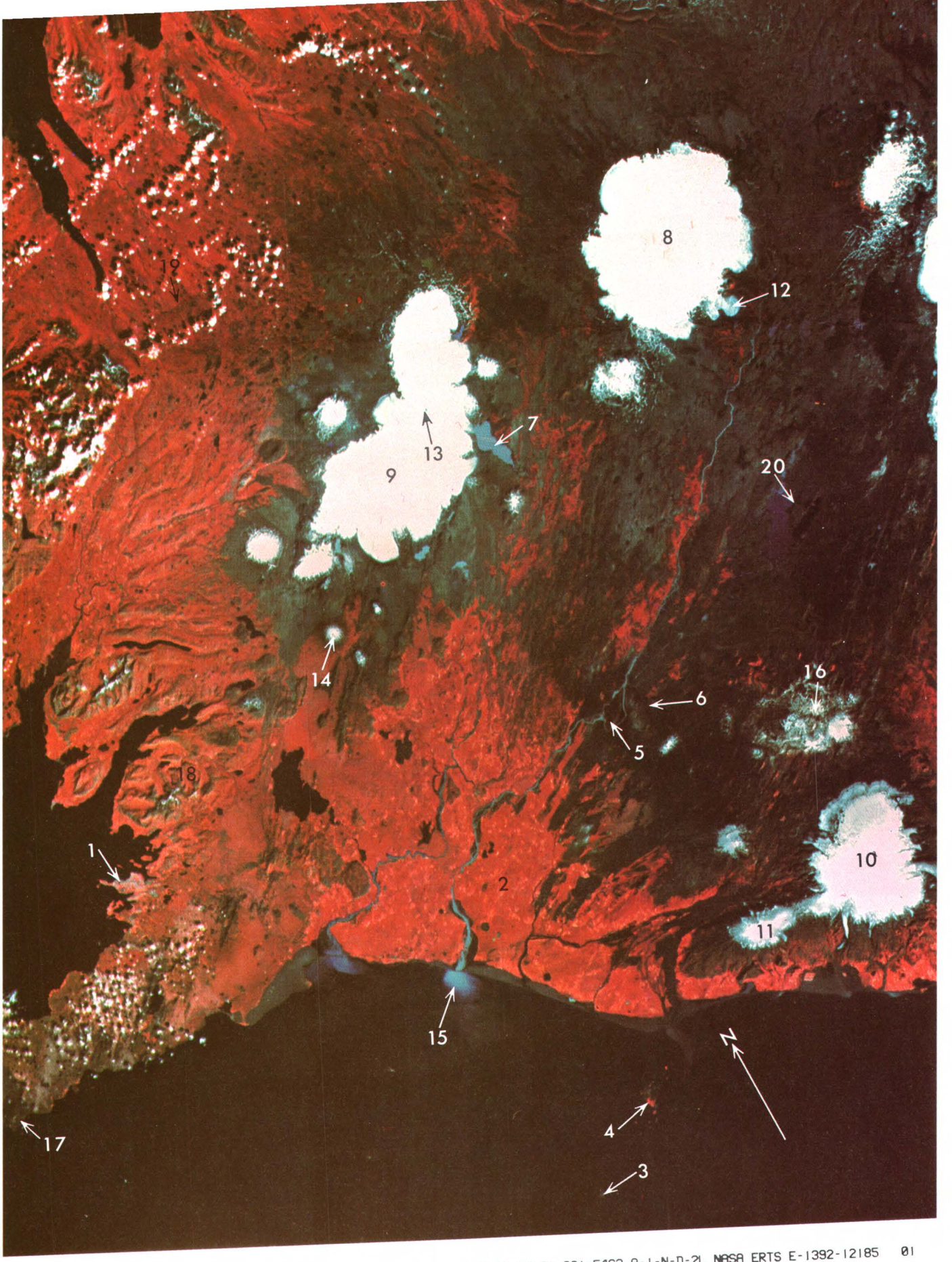


19AUG73 C N65-25/W019-10 N N65-22/W019-00 MSS 5 R SUN EL36 AZ161 201-5463-A-1-N-D-2L NASA ERTS E-1392-12185 01

19AUG73 C N64-04/W020-32 N N64-01/W020-21 MSS 7 R SUN EL37 AZ159 200-5463-A-1-N-D-1L NASA ERTS E-1392-12191 01

APPROXIMATE SCALE

10 0 10 20 30 MILES

10 0 10 20 30 KILOMETERS

FIGURE 75.—Annotated color composite ERTS-1 image mosaic of west-central and southwestern Iceland (1392–12185 and 1392–12191).

and Moore, 1973). The new land area on the east side of Heimaey can be seen. The ash-fall pattern at 5 and new lava flows at 6 from the 1970 volcanic eruption from the famous Hekla Volcano are evident. The 1970 ash fall, containing high concentrations of fluorides, contaminated grasslands that were grazed by sheep. At least 7,000 head were lost in the area because of fluoride poisoning.

Several glaciological features are also prominent. The glacier-margin lake, Hvítárvatn 7, is distinctive with its powder-blue color characteristic of turbidity caused by glacial sediment. The snowline can be delineated on the Hofsjökull 8, Langjökull 9, Mýrdalsjökull 10, and Eyjafjallajökull 11 icecaps. Note the absence of vegetation at 12 from an area where one of the outlet glaciers of Hofsjökull has receded. A prominent nunatak at 13 can be seen in the center of Langjökull. The snow-capped shield volcano, Skjaldbreidur, can be seen at 14 and tectonic fissures that extend to the southwest. Sediment plumes from the mouths of rivers laden with glacial rock flour are prominent, particularly the one at the mouth of Thjórsá 15.

The circular caldera form, light-colored rhyolitic rocks, and lighter colored altered-ground areas of Iceland's largest geothermal area, Torfajökull at 16, contrast sharply with the surrounding darker basaltic rocks or glacial deposits derived from such rocks. The altered ground of the Reykjanes geothermal area is just barely discernible at 17. A circular pattern of a possible Tertiary central volcano is visible at 18. At 19 a faint line represents a difference in grass conditions resulting from the installation of a fence to control the grazing of sheep in this district. Finally, an engineering project has reversed the flow of water from the solitary outlet of the V-shaped lake, Thórisvatn at 20. This reversal has resulted in sediment-laden water from a glacial river entering the western arm of the lake, and the gradational plume can be clearly delineated. The comprehensive environmental information from this ERTS mosaic contrasts markedly with the line map of the same area (fig. 76). Although such line maps are revised at intervals, there is no way that conventional maps can keep up with or depict such seasonal changes in the grasslands, variations in size of sediment plumes, changes in glaciological phenomena, and other environmental variables.

Because of the wide variety of geological and geophysical phenomena that can be observed in Iceland, and because of the clear and direct historical impact of the dynamic natural environment on the country's natural resources, Iceland has been particularly well suited as an area for experimental studies to establish the operational feasibility of using Earth resources satellite sensors and other systems to meet resource inventory and management needs on a timely and cost-effective basis. Iceland shares with the United States, and with most other countries of the world, a need for accurate and timely information on the status of its natural resources in order to make wise decisions about the best use of such resources. ERTS–1 provides a first-time capability for the acquisition of many types of environmental information, particularly for data on dynamic environmental phenomena (Williams and others, 1974).

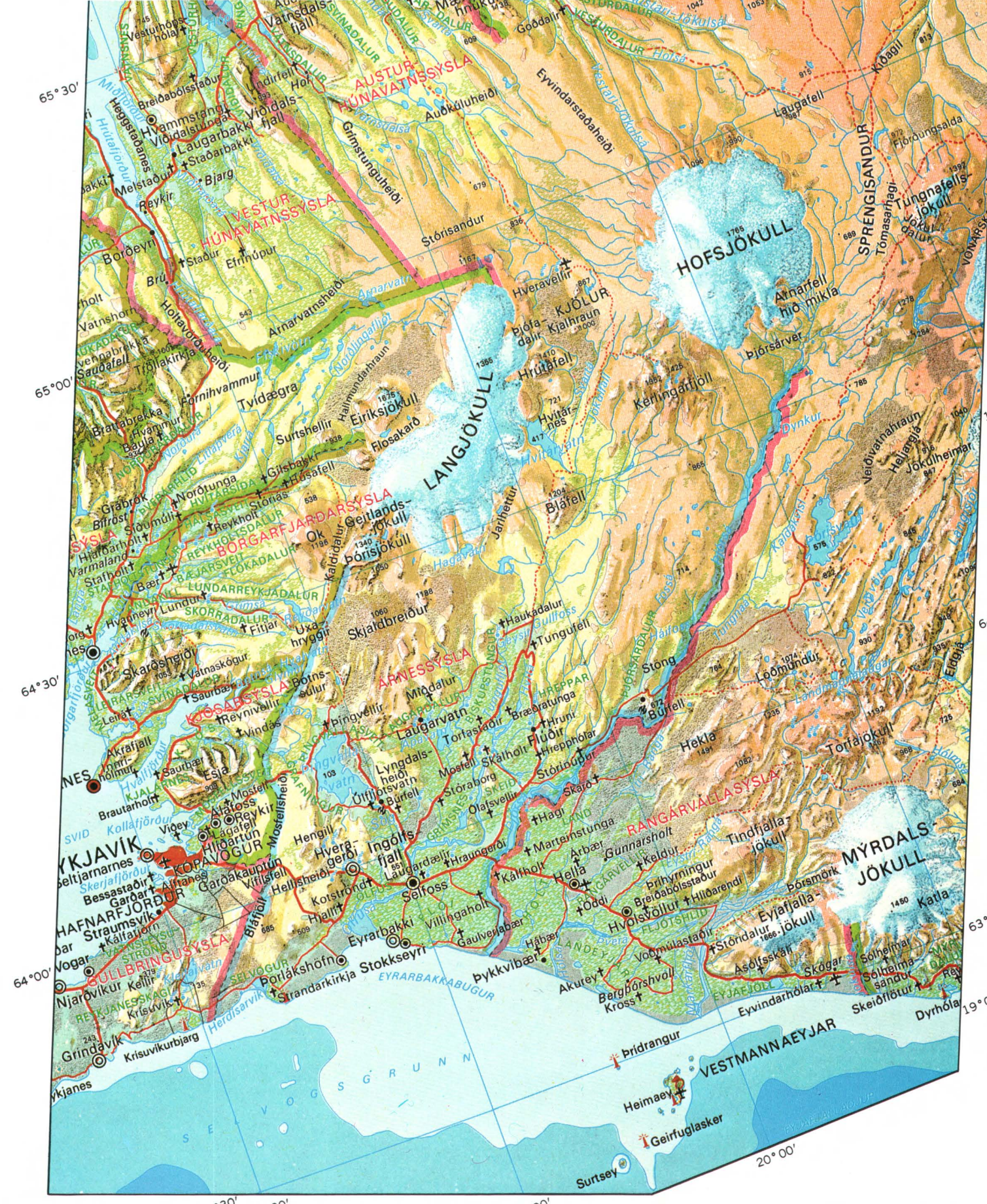
HOFSJÖKULL
LANGJÖKULL
VESTUR-HÚNAVATNSSÝSLA
AUSTUR-HÚNAVATNSSÝSLA
BORGARFJARÐARSÝSLA
KJÓSARSÝSLA
ÁRNESSÝSLA
RANGÁRVALLASÝSLA
GULLBRINGUSÝSLA
SPRENGISANDUR
MÝRDALSJÖKULL
VESTMANNAEYJAR
Reykjavík
KÓPAVOGUR
HAFNARFJÖRÐUR
Selfoss
Hella
Hvolsvöllur
Stykkishólmur
Borðeyri
Blönduós
Sauðárkrókur
Akureyri
Egilsstaðir
Höfn
Grindavík
Keflavík
Njarðvík
Vogar
Stóri-Dímon
Surtsey
Heimaey
Geirfuglasker
Þrídrangur
EYRARBAKKABUGUR
SELVOGSGRUNN
65°30′
65°00′
64°30′
64°00′
63°30′
22°00′
21°00′
20°00′
19°00′
18°00′
gróður
akvegur
ógreiðfær leið
sýslumörk
jökull
laug eða hver
sandur
hraun
ár og vötn
yfir 800
500 – 800
200 – 500
0 – 200
0 – 100
100 – 200
undir 200
APPROXIMATE SCALE
10
0
10
20
30 MILES

# ACTIVE FAULTS IN THE LOS ANGELES-VENTURA AREA OF SOUTHERN CALIFORNIA

By Russell H. Campbell,

U.S. Geological Survey

Figure 77 is a color composite ERTS–1 image especially made to enhance geologic features by combining bands 4, 6, and 7. The annotated map overlay combined with band 5 (fig. 78) shows the system of active faults that traverse the greater Los Angeles area. This single image shows all the area from Ventura to Santa Ana and from east of Lancaster to Grapevine at the southern tip of the San Joaquin Valley.

Most of the faults shown have been active historically or in the last 30,000 to 40,000 yr. Many features that mark the traces of these faults are eminently visible in the image, which offers a striking synoptic view of their relations to each other and to landmarks familiar to all inhabitants of the region.

In addition to known faults, the annotations indicate the locations of the epicenters of historic earthquakes that are known (or inferred) to have had magnitudes on the Richter scale of 6.0 or greater. This compilation shows that historic earthquakes and fault movements in the region are not limited to the San Andreas Fault and its clearly defined branches. Instead, the area clearly has been affected by Earth strains that have been relieved by movement along several faults.

The epicenters of earthquakes shown in figure 78 (solid circles) are labeled according to the year in which the earthquake occurred and include:

| *Year* | *Fault* | *Earthquake* | *Magnitude* | *Remarks* |
|---|---|---|---|---|
| 1852 | Big Pine | | | Ground breakage reported. |
| 1857 | San Andreas | Fort Tejon | [1]8.0 | Possibly 10 m of surface offset. |
| 1893 | San Gabriel | Pico Canyon | [1]6.0 | |
| 1916 | | Tejon Pass | [1]6.0 | |
| 1933 | Newport-Inglenook zone of folds and faults. | Long Beach | 6.3 | |
| 1952 | White Wolf | Kern County | 7.7 | About 1 m of surface offset. |
| 1971 | San Fernando | San Fernando | 6.6 | Maximum offset about 2 m. |
| 1973 | Frontal fault system of the Transverse Ranges. | Point Mugu | 6.0 | |

[1] Estimated.

◄ FIGURE 76.—Map of part of west-central and southwestern Iceland (part of 1:1,000,000 map of Iceland, Icelandic Surveying Department, 1971).

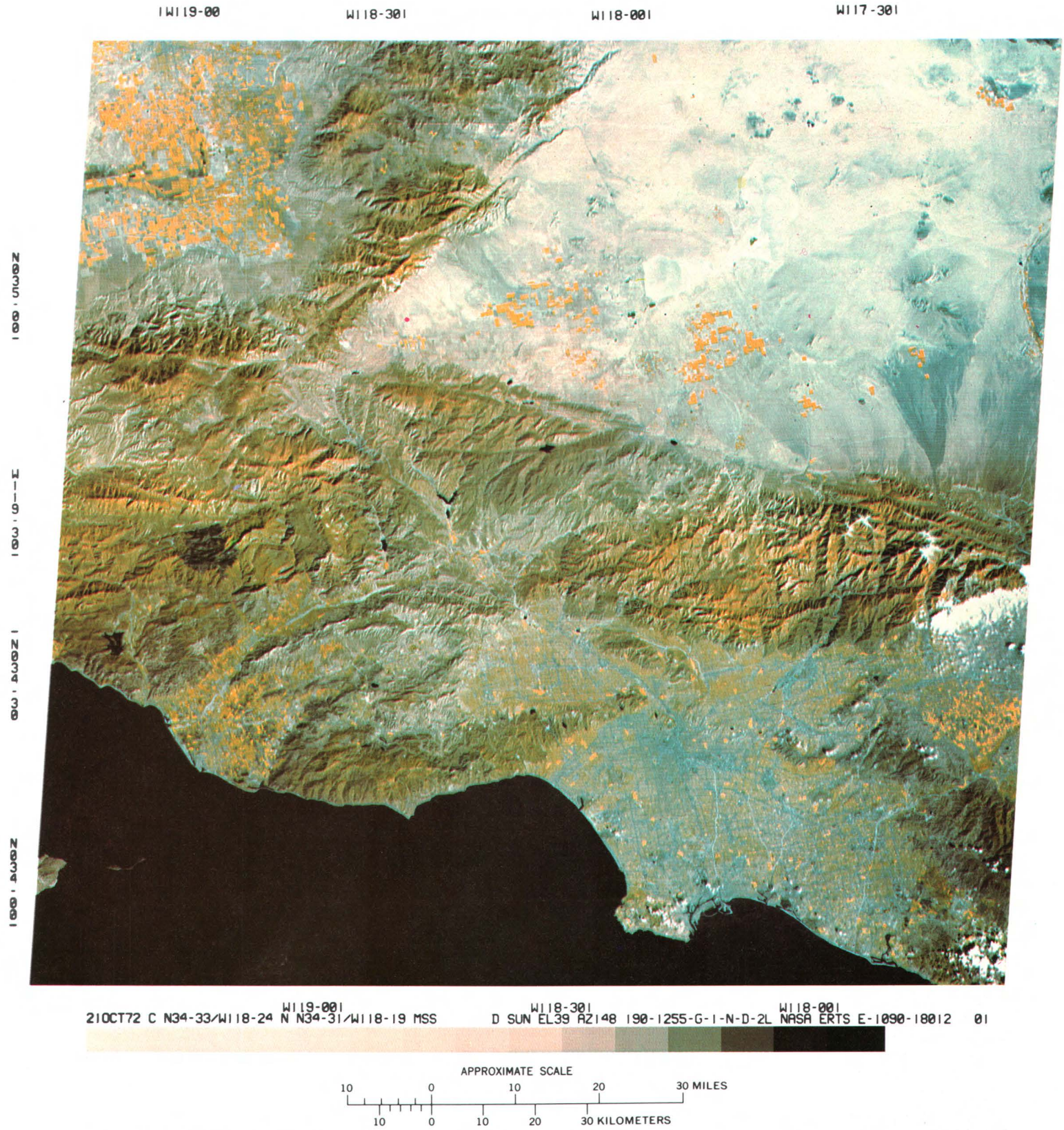


FIGURE 77.—Color composite ERTS–1 image of the greater Los Angeles area of southern California especially made to enhance geologic features (1090–18012, bands 4, 6, and 7).

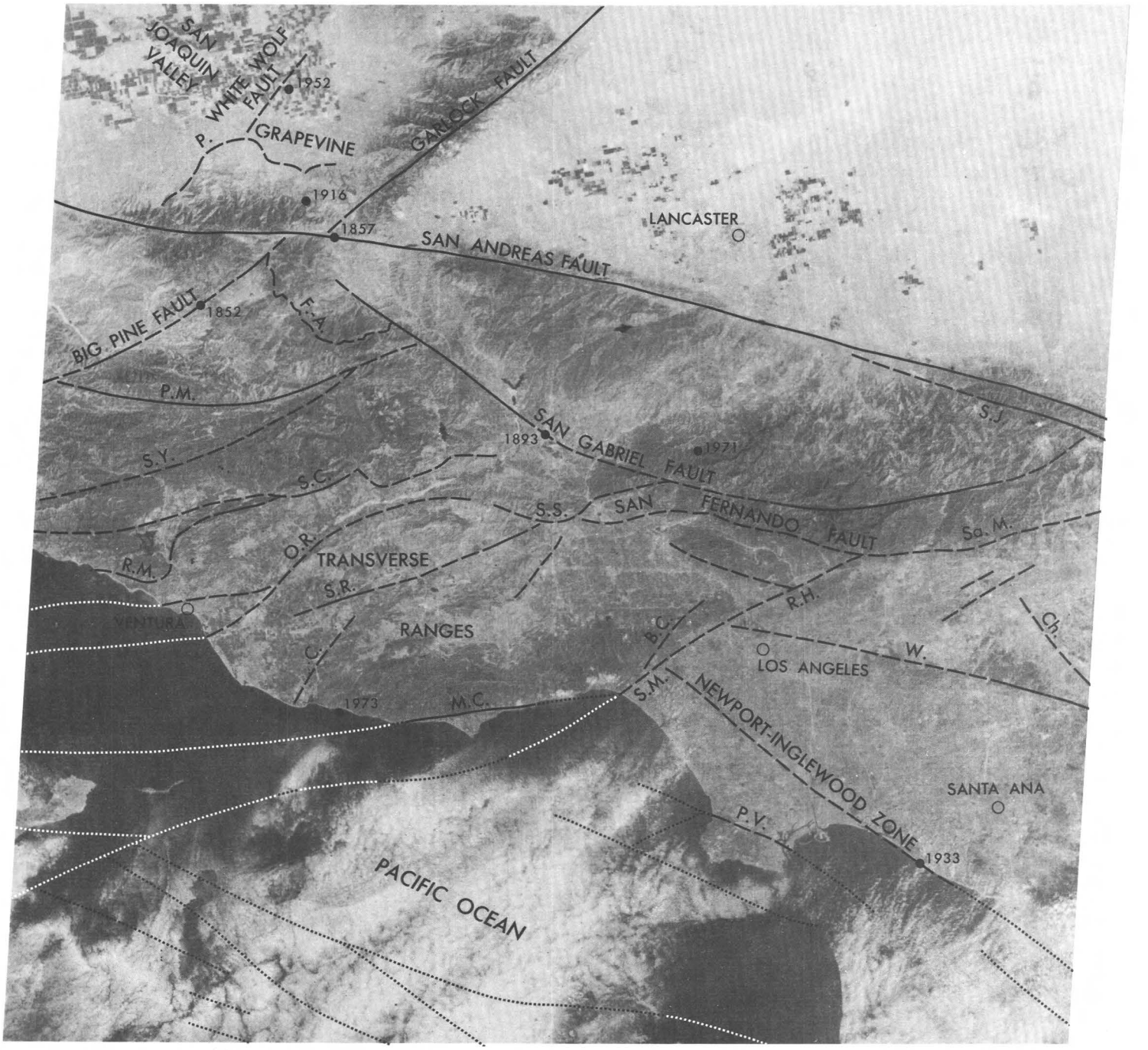


APPROXIMATE SCALE

10 0 10 20 30 MILES

10 0 10 20 30 KILOMETERS

FIGURE 78.—Annotated ERTS–1 image of the greater Los Angeles area of southern California showing location of major and minor faults (1018–18010, band 5). Symbols are explained in the text.

Faults are shown in figure 78 as solid lines where easily visible on the image, dashed where recognized with some difficulty, and dotted where concealed by the ocean. They are listed below along with the symbol used to identify them on the image.

| *Fault* | *Symbol* | *Remarks* |
|---|---|---|
| Benedict Canyon | B.C. | |
| Big Pine | ---- | |
| Callequas | C. | |
| Chino | CH. | |
| Frazier Mountain-Alamo Mountain | F.-A. | Thrust faults. |
| Garlock | ---- | |
| Newport-Inglewood | ---- | Zone of faults and folds. |
| Oak Ridge | O.R. | Thrust fault. |
| Palos Verdes Hills | P.V. | |
| Pine Mountain | P.M. | |
| Pleito | P. | |
| Red Mountain | R.M. | |
| San Andreas | ---- | |
| San Cayetano | S.C. | Thrust fault. |
| San Fernando | ---- | Do. |
| San Gabriel | ---- | |
| San Jacinto | S.J. | Historically the most active of the northwest-trending right-lateral faults south of the Transverse Ranges. |
| Santa Rosa | S.R. | |
| Santa Susana | S.S. | Thrust fault. |
| Santa Ynez | S.Y. | |
| Whittier | W. | |
| White Wolf | ---- | |

The following faults, also shown in figure 78, are segments of the south frontal fault system of the Transverse Ranges province:

| *Fault* | *Symbol* |
|---|---|
| Malibu Coast | M.C. |
| Raymond Hill | R.H. |
| Santa Monica | S.M. |
| Sierra Madre | Sa.M. |

# ENVIRONMENTAL GEOLOGY OF THE CENTRAL GULF OF ALASKA COAST

By Austin Post,

U.S. Geological Survey

In the ERTS image shown in figure 79, the Copper River valley cuts through the rugged Chugach Mountains on the left, the Bering Glacier dominates the right side, and Cape St. Elias juts into the Pacific Ocean on the south end of Kayak Island. The village of Yakataga is near the right margin of the image, and the town of Cordova is just off the image to the left.

When this image was taken on Oct. 24, 1973, cold air from interior Alaska was sweeping down the Copper River valley, picking up dust from sandbars, and blowing it more than 40 km out over the ocean. Large glaciers that flow from lateral valleys and terminate in the Copper River valley are hidden under the dust pall.

The Copper River valley is one of the few available low-level routes to the interior of Alaska from the coast. More than 60 yr ago, the river became famous during the construction of the Copper River and Northwestern Railroad to provide access to the rich Kennicott Mining District. The railroad, extremely expensive to construct and maintain, crossed the Copper River three times, one of these on a $1,000,000 steel bridge located where the Childs Glacier on the west side of the river and the Miles Glacier on the east side terminated directly into the river. Just to the north, the tracks had to be laid on the stagnant, marginal ice of Allen Glacier, which also reached the river's edge, forming Baird Canyon.

The railroad was abandoned in 1938 after the most accessible ore was exhausted. Using the same route and many of the same bridges, engineers were constructing a new highway until the 1964 Alaska earthquake abruptly halted progress by destroying most of the new bridges and severely damaging two of the largest old steel railway bridges. Construction of the highway has now resumed with replacement of bridges in the Copper River delta area.

This part of the Alaskan Coast is seismically very active and has been raised repeatedly in recent centuries. Evidence of this can be seen from (1) raised sandbars which now form islands off the mouth of the Copper River. This area was raised approximately 2 m by the 1964 Alaska earthquake: (2) parallel timbered ridges visible along the coast on the right side of this view represent former beaches. Raised beaches south and east of the Bering Glacier disappear under the glacier margin and indicate that the Bering Glacier fronted on the ocean in the not too distant past.

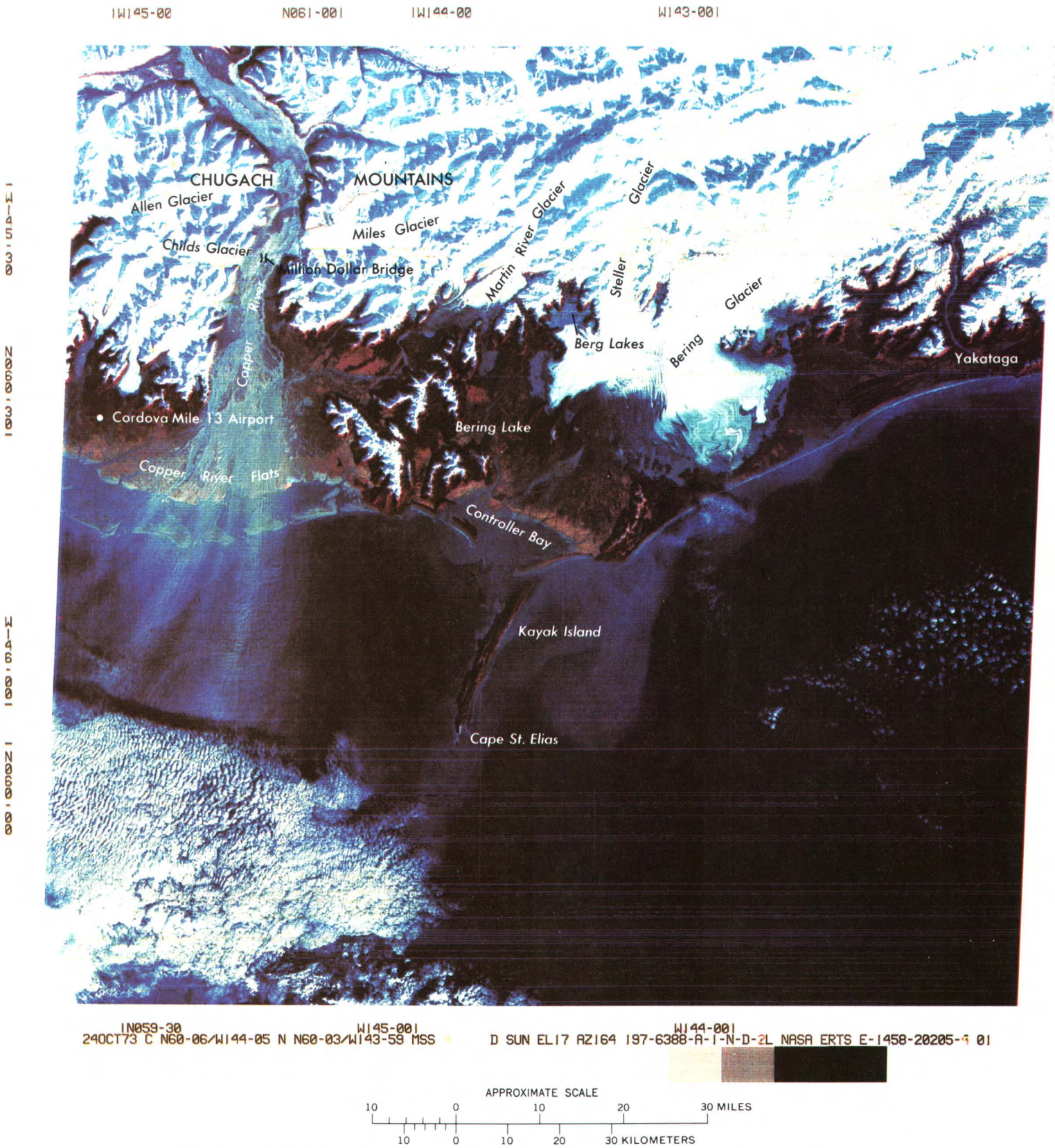


FIGURE 79.—Annotated color composite ERTS–1 image of the central Gulf of Alaska coast (1458–20205).

Extensive outwash fans constructed by streams from the Bering Glacier and by the Copper River are also changing the landscape; for instance, former beaches are being covered by the outwash east of the Bering Glacier, and the debris from the Copper River is rapidly changing the outline of the coast. Intertidal zones appear as darker areas along the coast and are particularly visible in shallow areas such as Controller Bay (center).

The Bering Glacier is the largest in mainland North America. It heads in a broad ice-filled valley, the lower part of which appears in the top right part of this image. The ice flows down a valley about 10 km wide to the coastal plain, where it spreads out in a semicircular lobe nearly 60 km wide. Down the center of this lobe is an extensive band of medial moraines that are made up of debris swept by the ice from the high mountains. Folded structures in these moraines are faintly visible in this image; in fact, the broad central band of debris is composed of a vast aggregation of parallel ridges that represent about five main medial moraines folded 20 times or more. These structures and the accordianlike folds in the eastern margin of the lobe are caused by periodic surges of this vast glacier that apparently occur about every 20 yr.

Lakes appear dark on the image, and several can be seen. In the upper center, large three-pronged Berg Lakes is dammed by an arm of Bering Glacier. Many lakes formed by glacier ice dams are notorious for sudden release when the ice dams fail, which most often occurs where subglacial channels develop and rapidly enlarge by melting as the water flows through them. Even large lakes can thus be drained in a few hours or, at the most, days. Berg Lakes has not drained for many years, but it potentially could devastate the Bering River valley should the ice dam fail. At the present time, the ice dam is considered to be unstable, and flooding could occur at any time.

ERTS images are particularly useful for determining the extent of snow cover. Figure 79 shows the snow cover as of Oct. 24, 1973. The elevation of the snowline can be determined by comparing the image with contour maps. Some idea of the snow depth can also be derived from the completeness of cover on rough surfaces such as glacier moraines. For instance, the snowline is clearly visible on Bering Glacier, covering about half of the terminal lobe. From the amount of rock visible in the large central medial moraine it is evident that the snow cover at the time of this image is very thin, probably not more than a few centimeters, at these lower altitudes.

The surface of the snow in the immense ice-filled valleys has shadings in ERTS images that are not apparent from the ground or even on most aerial photography. These shadings evidently represent subtle changes in slope that in turn probably are related to bedrock topography, deeply buried under the slowly flowing ice.

In summary, the synoptic images and repetitive coverage provided by the ERTS system enable geologists, for the first time, to monitor dynamic hydrological, geological, and meteorological phenomena that affect man and his environment.

# DEBRIS AVALANCHES AT MOUNT BAKER VOLCANO, WASHINGTON

By David Frank,

U.S. Geological Survey

The latest in a series of debris avalanches down Boulder Glacier on Mount Baker, Wash., is shown in ERTS images (figs. 80, 81) taken Sept. 16, 1973. The avalanche occurred sometime during Aug. 20–21, 1973. Mount Baker is a quiescent stratovolcano composed largely of andesitic lava flows and breccias (Coombs, 1939). Every 2 to 4 yr during recent decades, snow, ice, and hydrothermally altered rock have avalanched from the Sherman Crater rim, south of the mountain summit. The avalanches have flowed 2.0 to 2.6 km eastward, a distance just short of the Boulder Glacier terminus.

A major factor in the avalanche occurrence is geothermal emission and subsequent water saturation of the ground beneath the normally heavy snowpack (Frank and others, 1975). Within 50 m of the avalanche source is a zone of very active fumaroles, warm ground and thermal springs that currently are causing extensive hydrothermal alteration of rock to clay-rich soil. Avalanches will likely continue to occur as long as the current level of heat emission is maintained. There is at this time no evidence to indicate that fumarole activity is declining; it has been known to exist since the time of the last eruptions which probably occurred in the mid-1800's (Davidson, 1885). Temperatures in fumaroles on Mount Baker are currently being monitored using an ERTS DCP.

The ERTS image strikingly shows the significance of recurrent mass movement from the volcano. Melt water from Boulder Glacier flows down Boulder Creek (dashed line) and into two large hydroelectric reservoirs—Baker Lake and Lake Shannon. From there the water continues on to the heavily farmed Skagit River valley and finally to more highly populated areas bordering Puget Sound. Although those avalanches that have been observed have not passed the glacier terminus, it is not unlikely that, as hydrothermal alteration continues, increasing amounts of rock will be contained in future avalanches. Larger avalanches, along with the possible combination of glacier outburst floods, could probably reach the lower Boulder valley. This dangerous potential is of particular importance because of the possible impact on the reservoirs of the lower valley. An indication of the extent of past mass movement in Boulder valley is the large lobate alluvial fan that protrudes into Baker Lake. In addition to normal stream deposits, this fan contains a sequence of postglacial lahars (debris flows or mudflows) from Mount Baker (J. Hyde, U.S. Geological Survey, written commun., 1974). The most recent lahar lies on the surface and likely occurred within the past few hundred years. The cause of the recent lahars from Mount Baker is not presently known, but it is significant that such activity apparently has been common in the recent past.

FIGURE 80.—Annotated color composite ERTS–1 image of the Mount Baker area of Washington (1420–18303).

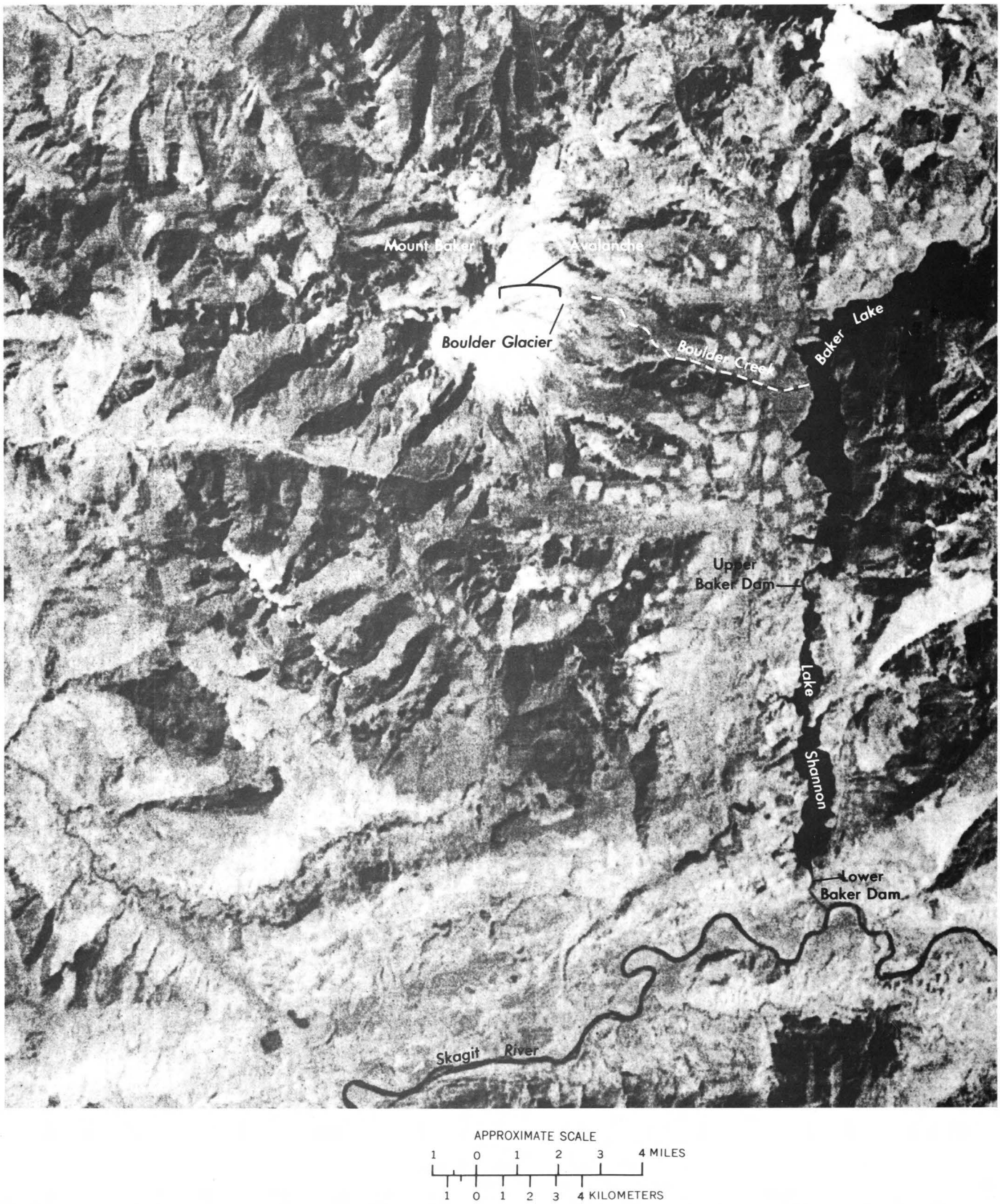


FIGURE 81.—Annotated enlargement of part of the Mount Baker image showing the area of debris avalanches (part of 1420–18303, band 5).

# STRUCTURAL FEATURES RELATED TO EARTHQUAKES IN MANAGUA, NICARAGUA, AND CORDOBA, MEXICO

By William D. Carter, U.S. Geological Survey,

and Jack N. Rinker, U.S. Army Corps of Engineers

Two major earthquakes have occurred in the Western Hemisphere during the life of ERTS–1. The first was the Managua, Nicaragua, earthquake of Dec. 23, 1972, which had a magnitude of 5.6 on the Richter scale. More than an estimated 11,000 persons died, and most of the Nicaraguan capital was devastated; property damage was estimated to be more than $0.5 billion (Brown and others, 1973). The second earthquake, having a magnitude of 7.0 on the Richter scale, occurred on Aug. 28, 1973, about 240 km southeast of Mexico City. Although deaths (500 persons) and property damage were less severe than at Managua, buildings collapsed and numerous fires caused by short circuits occurred in six Mexican cities—Ciudad Serdan, Orizaba, Córdoba, Puebla, Tehuacán, and Mexico City (Lomnitz, 1973).

Quick action by the ERTS–1 control and command center at the NASA Goddard Space Flight Center made it possible for ERTS to collect data over Managua on Dec. 24, 1972, the day after the earthquake. Figures 82 and 83 show the area of western Nicaragua. The Gulf of Fonseca and Honduras are in the upper left. Lake Managua is in the lower right corner, and Managua is under clouds southeast of the Chiltepe Peninsula that is marked by two crater lakes. Volcanic cones, many of which are often active, can be seen in the Cordillera Los Marrabios. Most are in a rather straight, narrow band 15 to 30 km from the coast. Band 7 images were most useful in studying the linear features and show the structural relationship of the Managua area to the surrounding region. The synoptic images give an insight on the directional trends of fractures and faults in the region that might be found during detailed studies of the geology of the city area (Carter and Eaton, 1973). The images also indicate that the volcanoes east of Managua were not actively emitting clouds of steam, ash, lava, or other products. The earthquake area was overflown by a NASA aircraft within 10 days after the event, and excellent detailed aerial photography was provided for study and fieldwork by Nicaraguan and U.S. Geological Survey geologists. These studies indicated that the movement during the earthquake took place along fracture systems trending N. 25° to 45° E.

During September 1973, ERTS–1 data were collected on five different days over the area of the Mexican earthquake of late August. Of eight images

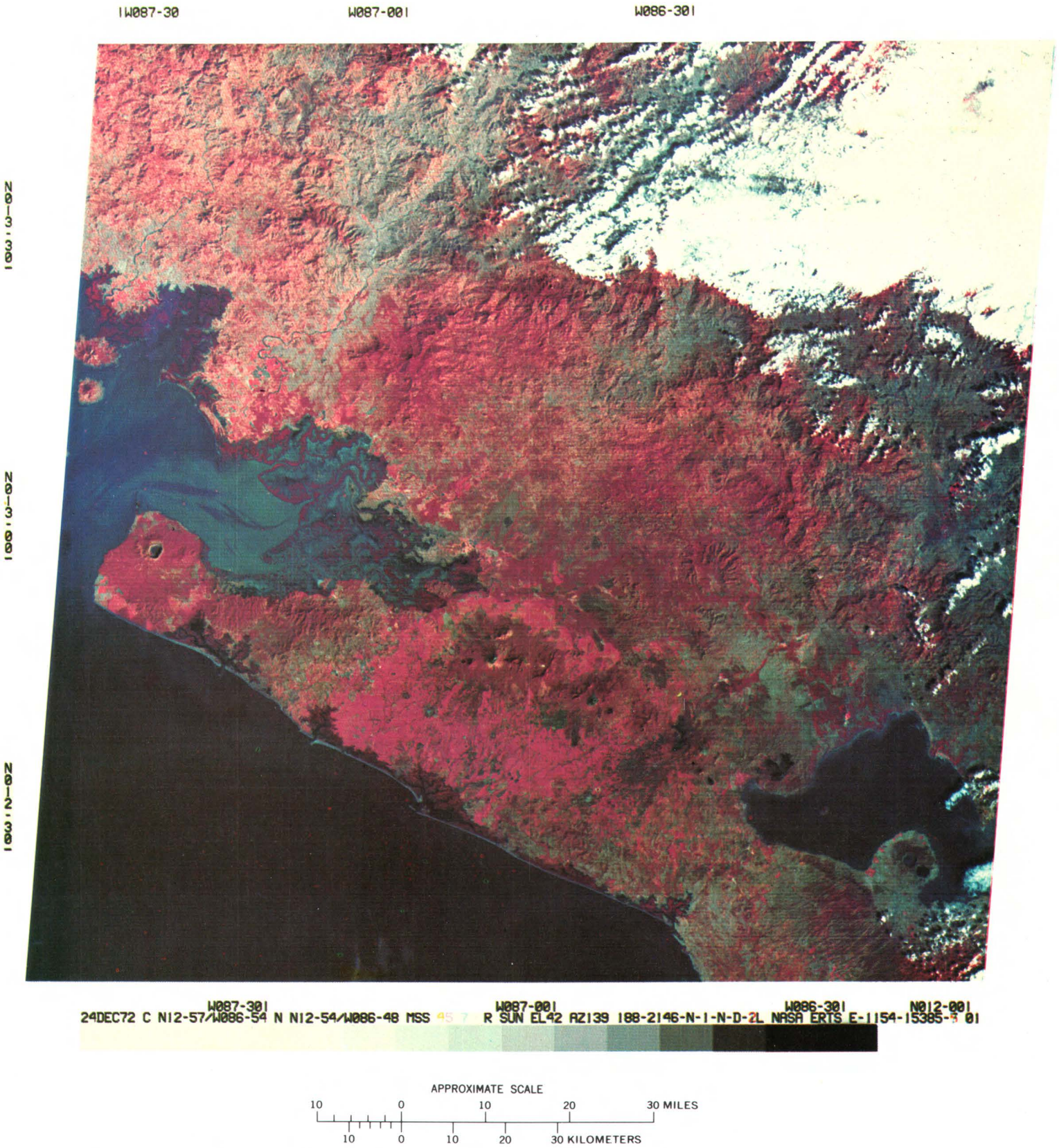


FIGURE 82.—Color composite ERTS–1 image of the Managua area of Nicaragua (1154–15385).

collected, five had 50 percent or more cloud cover and were therefore only marginally useful for analysis. Three, however, had 25 percent or less cloud cover and were useful in defining regional structural features that could contribute to seismic activity. Unfortunately, the areas most affected by the 1973 earthquake were in the cloudy regions.

Interpretation of the images indicates that a strong set of northwest-trending linear features extends from Presa Miguel Alemán through Córdoba and also in the Tehuacán Valley to the west, along which earthquake activity could take place. Lomnitz (1973) stated that the focus of the event was located at a depth of 84 km under the western edge of the Veracruz coastal plain, a location that coincides with the Córdoba lineament.

In both cases cited, it was possible to define the regional structural pattern and to determine areas where detailed ground studies might be fruitful. It was not, however, possible to define small areas where physical damage had occurred.

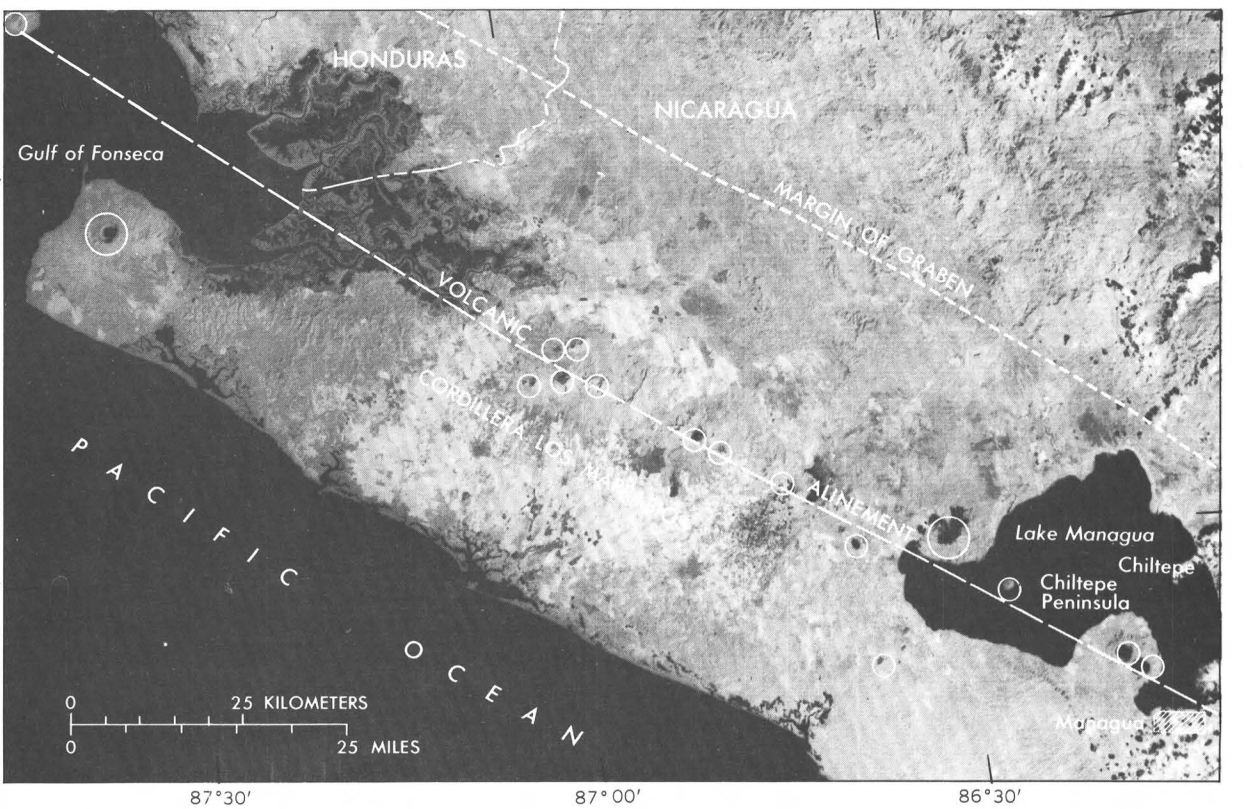


FIGURE 83.—Map of the earthquake area in Nicaragua plotted on part of ERTS–1 image 1154–15385, band 7.

## REFERENCES


Ahmed, Waheeduddin, Khan, S. N., and Schmidt, R. G., 1972, Geology and copper mineralization of the Saindak quadrangle, Chagai District, West Pakistan: U.S. Geol. Survey Prof. Paper 716A, p. A1–A21.

Brockmann, Carlos, 1974, Earth Resources Technology Satellite Data Collection Project, ERTS–BOLIVIA: NASA Goddard Space Flight Center, Symposium on the Earth Resources Technology Satellite–1, 3d, Washington, D.C., Dec. 1973, Proc., v. 1, sec. A, p. 559–577.

Brown, R. D. Jr., Ward, P. L., and Plafker, George, 1973, Geologic and seismologic aspects of the Managua, Nicaragua, earthquakes of December 23, 1972: U.S. Geol. Survey Prof. Paper 838, 34 p.

Carter, W. D., and Eaton, G. P., 1973, ERTS–1 image contributes to understanding of geologic structures related to Managua earthquake, 1972: NASA Goddard Space Flight Center, Symposium on Significant Results Obtained from the Earth Resources Technology Satellite–1, 2d, New Carrollton, Md., Mar. 1973, Proc., v. 1, sec. A, p. 459–471.

Coombs, H. A., 1939, Mt. Baker, a cascade volcano: Geol. Soc. America Bull., v. 50, p. 1,493–1,510.

Davidson, George, 1885, Recent volcanic activity in the United States; eruption of Mount Baker: Science, v. 6, no. 138, p. 362.

Fischer, W. A., and Lathram, E. H., 1973, Concealed structures in Arctic Alaska identified on ERTS–1 imagery: Oil and Gas Jour., v. 71, p. 97–102.

Frank, David, Post, Austin, and Friedman, J. D., 1975, Recurrent geothermally induced debris avalanches on Boulder Glacier, Mount Baker, Washington: U.S. Geol. Survey Jour. Research, v. 3, no. 1, p. 77–87.

Freund, R., 1970, The geometry of faulting in the Galilee: Israel Jour. Earth Sci., v. 19, p. 117–140.

Girdler, R. W., 1962, Initiation of continental drift: Nature, v. 194, no. 4828, p. 521–524.

———1972, African poles of rotation: comments on Earth sciences: Geophysics, v. 2, no. 5, p. 131–138.

Goetz, A. F. H., Billingsley, F. C., Elston, Donald, Lucchitta, Ivo, and Shoemaker, E. M., 1973, Preliminary geologic investigations in the Colorado Plateau using enhanced ERTS images: NASA Goddard Space Flight Center, Symposium on Significant Results Obtained from the Earth Resources Technology Satellite–1, 2d, New Carrollton, Md., Mar. 1973, Proc., v. 1, sec. A, p. 403–411.

Grantz, Arthur, Hanna, W. F., Holmes, M. L., and Creager, J. S., 1970, Reconnaissance geology of Chukchi Sea as determined by acoustic and magnetic profiling [abs.]: Am. Assoc. Petroleum Geologists Bull., v. 54, no. 12, p. 2,483.

Jennings, C. W., and Strand, R. G., 1958, Geologic map of California, Santa Cruz sheet: California Div. Mines and Geology.

Lathram, E. H., 1973, Geologic application of ERTS imagery in Alaska [abs.]: NASA Goddard Space Flight Center, ERTS Symposium, 3d, Washington, D.C., Dec. 1973, Abs., p. 39.

Lathram, E. H., Tailleur, I. L., Patton, W. W., Jr., and Fischer, W. A., 1973, Preliminary geologic application of ERTS–1 imagery in Alaska: NASA Goddard Space Flight Center, Symposium on Significant Results Obtained from the Earth Resources Technology Satellite–1, 2d, New Carrollton, Md., Mar. 1973, Proc., v. 1, sec. A, p. 257–261.

Le Pichon, Xavier, and Heirtzler, J. R., 1968, Magnetic anomalies in the Indian Ocean and sea-floor spreading: Jour. Geophys. Research, v. 73, no. 6, p. 2101–2117.

Lomnitz, Cinna, 1973, The Puebla-Veracruz, Mexico, earthquake of August 28, 1973: U.S. Geol. Survey Earthquake Inf. Bull., v. 5, no. 6, p. 19–22.

McKee, E. D., Breed, C. S., and Harris, L. F., 1973, A study of morphology, provenance, and movement of desert sand seas in Africa, Asia, and Australia: NASA Goddard Space Flight Center, Symposium on Significant Results Obtained from the Earth Resources Technology Satellite–1, 2d, New Carrollton, Md., Mar. 1973, Proc., v. 1, sec. A, p. 291–303.

McKee, E. D., and Breed, C. S., 1974, An investigation of major sand seas in desert areas throughout the world: NASA Goddard Space Flight Center, Symposium on the Earth Resources Technology Satellite–1, 3d, Washington, D.C., Dec. 1973, Proc., v. 1, sec. A, p. 665–679.

McKenzie, D. P., Davies, D., and Molnar, Peter, 1970, Plate tectonics of the Red Sea and East Africa: Nature, v. 226, p. 243–248.

Morrison, R. B., and Hallberg, G. R., 1973, Mapping Quaternary landforms and deposits in the Midwest and Great Plains by means of ERTS–1 multispectral imagery: NASA Goddard Space Flight Center, Symposium on Significant Results Obtained from the Earth Resources Technology Satellite–1, 2d, New Carrollton, Md., Mar. 1973, Proc., v. 1, sec. A, p. 353–361.

Rowan, L. C., Wetlaufer, P. H., Goetz, A. F. H., Billingsley, F. C., and Stewart, J. H., 1974, Discrimination of rock types and detection of hydrothermally altered areas in south-central Nevada: U.S. Geol. Survey Prof. Paper 883, 35 p.

Schmidt, R. G., 1973, Use of ERTS–1 images in the search for porphyry copper deposits in Pakistan—Baluchistan: NASA Goddard Space Flight Center, Symposium on Significant Results Obtained from the Earth Resources Technology Satellite–1, 2d, New Carrollton, Md., Mar. 1973, Proc., v. 1, sec. A, p. 387–294.

Stoertz, G. E., and Carter, W. D., 1973, Hydrogeology of closed basins and deserts of South America, ERTS–1 interpretations: NASA Goddard Space Flight Center, Symposium on Significant Results Obtained from the Earth Resources Technology Satellite–1, 2d, New Carrollton, Md., Mar. 1973, Proc., v. 1, sec. A, p. 695–705.

Tailleur, I. L., and Brosgé, W. P., 1970, Tectonic history of northern Alaska, *in* Adkison, W. L., and Brosgé, M. M., eds., Proceedings of geological seminar on the North Slope of Alaska: Los Angeles, Pacific Sec., Am. Assoc. Petroleum Geologists, p. E1–E19.

von Gaertner, H.-R., and Walther, H. W., coordinators, 1971, Internat. geologic map of Europe: Hannover, Germany, Bundesanstalt für Bodenforschung and UNESCO, Internat. Geol. Cong., Comm. for the Internat. Geol. Map of the World, scale 1:5,000,000, 2 sheets.

Ward, P. L., Eaton, J. P., Endo, E. T., Harlow, D. H., Marquez, Daniel, and Allen, Rex, 1973, Establishment, test and evaluation of a prototype volcano surveillance system: NASA Goddard Space Flight Center, Symposium on Significant Results Obtained from the Earth Resources Technology Satellite–1, 2d, New Carrollton, Md., Mar. 1973, Proc., v. 1, sec. A, p. 305–315.

Ward, P. L., Endo, E. T., Harlow, D. H., Allen, Rex, and Eaton, J. P., 1974, A new method for monitoring global volcanic activity: NASA Goddard Space Flight Center, Symposium on the Earth Resources Technology Satellite–1, 3d, Washington, D.C., Dec. 1973, Proc., v. 1, sec. A, p. 681–689.

Williams, R. S., Jr., 1972, Satellite geological and geophysical remote sensing of Iceland [abs.]: Internat. Symposium on Remote Sensing of Environment, 8th, Ann Arbor, Mich., 1972, Proc., p. 1,465–1,466.

Williams, R. S., Jr., and Moore, J. G., 1973, Iceland chills a lava flow: Geotimes, v. 18, no. 8, p. 14–17.

Williams, R. S., Jr.; Bödvarsson, Ágúst; Fridriksson, Sturla; Pálmason, Gudmundur; Rist, Sigurjón; Sigtryggsson, Hlynur; Thorarinsson, Sigurdur; and Thorsteinsson, Ingvi, 1973, Satellite geological and geophysical remote sensing of Iceland—preliminary results from analysis of MSS imagery: NASA Goddard Space Flight Center, Symposium on Significant Results Obtained from the Earth Resources Technology Satellite–1, 2d, New Carrollton, Md., Mar. 1973, Proc., v. 1, sec. A, p. 317–327.

Williams, R. S., Jr., Bödvarsson, Ágúst; Fridriksson, Sturla; Pálmason, Gudmundur; Rist, Sigurjón; Sigtryggsson, Hlynur; Saemundsson, Kristján; Thorarinsson, Sigurdur; and Thorsteinson, Ingvi, 1973b, Iceland—preliminary results of geologic, hydrologic, oceanographic, and agricultural studies with ERTS–1 imagery: Am. Soc. Photogrammetry, Symposium on Management and Utilization of Remote Sensing Data, Sioux Falls, S. Dak., 1973, Proc., p. 17–35.

Williams, R. S., Jr.; Bödvarsson, Ágúst; Fridriksson, Sturla; Pálmason, Gudmundur; Rist, Sigurjón; Sigtryggsson, Hlynur; Saemundsson, Kristján; Thorarinsson, Sigurdur; and Thorsteinsson, Ingvi, 1974, Environmental studies of Iceland with ERTS–1 imagery: Internat. Symposium on Remote Sensing of Environment, 9th, Ann Arbor, Mich., 1974, Proc., v. 1, p. 31–81.

Wilson, E. D., Moore, R. T., and Cooper, J. R., 1969, Geologic map of Arizona: Tucson, Arizona, Arizona Bur. Mines.

# CHAPTER 3.

# APPLICATIONS TO WATER RESOURCES

## INTRODUCTION

By Morris Deutsch,
U.S. Geological Survey

Since its launch late in July 1972, a wealth of hydrologic information has been derived from ERTS-1. Before describing specific data obtained by ERTS and some of the significant observations and applications made, it will be useful to examine the role of ERTS in determining hydrological conditions over any area, observing changes in storage or conditions, and providing quantitative inputs for hydrological models.

Hydrology is a science of dynamic phenomena. It is concerned with the flux of water from the atmosphere to the Earth's surface; overland storage and runoff; infiltration, subsurface storage, movement, and eventual discharge; and return to the atmosphere by means of evaporation and transpiration. Hydrology is concerned also with water quality and changes in quality occasioned by its contact with the environment and man's effect on it. A major goal of remote sensing in hydrology, therefore, is to observe and measure dynamic conditions of water quantity and quality.

Water interacts with the Earth's atmosphere, soil, vegetation, physiography, and geology, and it profoundly affects the works of man. Hence, remote-sensing techniques can be used also to assess hydrologic conditions by indirect analysis of water along with other environmental parameters. The work of Higer, Coker, and Cordes in development of an ecological model in Florida (p. 150) represents an important milestone in using satellite data for environmental monitoring. The investigators have devised a means of predicting success or failure of wood stork rookeries as one of the indices of hydrologic conditions in the Everglades National Park. Parameters upon which the predictions are based are water-level measurements that can be relayed by the ERTS data collection system, the spatial distribution of water that can be measured on ERTS images, and the population density of small aquatic animals per unit area collected in quantitative traps.

The very fact that the quantity and, generally, the quality of water in a given area are constantly changing requires that repetitive data be collected to monitor changes. Although ERTS cannot continuously measure the discharge of streams or their quality, its 18-day repeat cycle is ideal for determining changing hydrological conditions caused by climate, seasonal effects, or man's activities. The design of a water-management model for the Everglades, employing quantitative inputs for areas of water surface from band 7 and water-stage data relayed by ERTS from surface recorders has stimulated use of satellite data for operational water management for Florida.

In the Pacific Northwest and other areas throughout the world, efficient regulation of reservoirs fed by melting snow is vital for generation of hydroelectric power, irrigation withdrawals, domestic water supply, waste assimilation, and maintenance of fisheries. By studying successive ERTS images and related ground data, Krimmel and Meier (p. 173), have determined the rate of change of snow-covered areas and estimated amounts of water stored as snow. ERTS data have thus provided a basis for improving predictions about the subsequent availability of water from snowmelt.

The ERTS data-collection-system experiment by Paulson (p. 132) for the Delaware River basin is being used as the framework for an operational system. Hydrologic data relayed by the satellite and images are being provided to the Delaware River Basin Commission as a basis for improved water management. Timely satellite data can assist agencies in water-management decisions concerning reservoir releases, water-plant intake for quality control, and municipal and sewage effluent release. Future satellite data-collection systems will enable the U.S. Geological Survey to more efficiently operate the national hydrologic data network, which includes about 15,000 instrumented stations where streamflow, water level, water quality, and related water data are collected.

Before the launch of ERTS, the hydrologic scien-

tists did not expect that existing flood-applications capability would be greatly expanded by the ERTS data. Since its launch, however, ERTS has provided data, as described herein, permitting observations and analyses regarding floods far beyond those anticipated. A large synoptic view of flooding along the entire Mississippi River valley below St. Louis was provided on only 16 images collected on two dates in 1973 during a total period of about 7 min. By color combining preflood coverage with flood coverage, a color-coded display was produced in which flooded area was automatically separated from areas normally covered by water. The unique water-detection capability of band 7 has made it possible for the first time to delineate areas from which flood waters have receded inasmuch as the flood waters leave a spectral signature on the surface. This capability is tremendously significant since it is not necessary to photograph or image the flood in progress. Imaging a flood in progress, of course, is of limited value because river valley reaches downstream from the peak have not yet experienced maximum inundation.

Water in streams less than a few meters to tens of meters wide, or lakes less than a few hectares in areal extent, cannot be detected by ERTS. The presence of water in the soil or in vegetation along the stream valley, however, is readily detectable. Indeed, a highly significant fact, vividly portrayed by ERTS color composite images of much of the United States and Canada, is the immense amount of water transpired to the atmosphere by vegetation. The vast extent of the vegetation is indicated by the almost totally red composite summer images covering large areas of the United States. On standard color composite images (bands 4, 5, and 7), vegetation is red, and the denser vegetation is depicted by deeper tones of red. The hydrologist thus has at hand a powerful tool for determining the percentage of the water budget involved in transpiration and the duration of the period of transpiration for the predominant classes of vegetation. Turner (p. 246) has shown, for example, changes in the patterns of dense plant growth. This type of information will be useful in determining a variety of hydrobiological conditions, including range readiness for grazing by livestock.

An estimated 90 percent of the freshwater resources of the Earth consists of ground water stored in regional aquifers. Data from ERTS contain much information about the distribution of ground water and the extent of its utilization (Deutsch, 1974).

Precise delineation of geologic formations—especially the upper or shallow units that, in most areas, form the best aquifers—is a requisite for hydrogeologic investigations. ERTS images of areas underlain by glacial, alluvial, eolian, and other unconsolidated sediments often provide an excellent basis for delineation of shallow aquifers. Indurated sedimentary rocks, especially limestone and sandstone formations, comprise important and extensive aquifers in many regions of the world. In some instances, ERTS data can be used directly to determine their boundaries, recharge areas, and discharge areas, including the location of springs. The imagery is potentially useful in depicting the detailed surface structures of crystalline rocks in igneous and metamorphic terranes, where ground water commonly is stored in openings along joints and fractures.

Most applications of remotely sensed data deal with surface phenomena inasmuch as it is the surface that is being imaged by ERTS and other satellites or aircraft. The hydrogeologist, however, commonly infers subsurface hydrological conditions from such surface indicators as areal geological features and structures, as described by Moore and Hollyday (p. 164). Soils and soil-moisture anomalies, vegetative types and distribution, discontinuous ice cover on streams, differential snowmelt, and springs that are detected by ERTS may also be indicative of ground water. Accordingly, it is believed that remotely sensed data, and particularly the synoptic, worldwide, and repetitive data collected by ERTS–1, can be effectively used as a tool for the exploration of ground water and for the monitoring and management of ground-water resources in selected instances.

Evidence of irrigation from nonsurface sources on ERTS data also indicates the presence and distribution of ground water, and the repetitive data can provide a basis for estimating ground-water use.

Much has been written about the applications of ERTS for water quality, and indeed ERTS has made important contributions to that field. ERTS data can be used to reveal regional or local distribution of anomalies in water quality due to difference in turbidity attributable to varying concentrations of sediment or other particulate matter in the water.

The chemical and physical quality of the water can be analyzed in the laboratory from samples collected on the ground. In the Delaware River basin and elsewhere in the United States, water-quality parameters are measured and recorded continuously at numerous points by automated monitors, and the data are relayed via the ERTS data collection system. The data provided by ERTS are then used to extrapolate areally the point-quality data. Thus the sources, movement, and fate of pollutants, suspended sediments, or waters from different sources are determined. Significant ex-

amples of the use of ERTS data for water-quality applications have been described by Stortz and Sydor (1974), who mapped turbidity currents in Lake Superior, and by Lind, Henson, and Pelton (1973), who used turbidity as an indicator of water pollution and its source and fate in Lake Champlain. The latter study is especially significant because the data were used in litigation that the State of Vermont initiated against the alleged pollutors.

ERTS data has greatly improved scientists' knowledge of glaciers because of the synoptic and repetitive data from generally inaccessible terrain. Krimmel, Post, and Meier (p. 178) in their study of surging and nonsurging glaciers in the Pamir Mountains of the U.S.S.R. suggest a practical and valuable application for the ERTS data: glacier-surge warnings. Glaciologists now have a means of locating and mapping hazardous glacial conditions and providing warnings as to when glacier surges and surge-related floods can be expected.

In their ERTS study of the dynamics of the Lowell and Tweedsmuir Glaciers in Canada, Post, Meier, and Mayo (p. 180) have shown how river flow may become blocked and form lakes or become impeded and disrupt navigation. The ERTS imagery can be used to produce maps and quantitative displacement data for large surging glaciers far more quickly and efficiently than by use of aerial photographic techniques or ground surveys.

While an understanding of dynamic glacial processes is of great scientific interest, Meier, in his study of the glaciers in the Mount McKinley massif (p. 185), points out an important practical value of these ERTS-aided studies: Glaciers are one of the few sources of unexploited water supply, and an improved understanding of glacial processes, along with current information on their condition, can aid in their eventual development for water supply.

Williams points out that ERTS permits a glacier to be studied as a total system (p. 188) because ERTS imagery provides regional views of glaciers and icecaps from a time-lapse viewpoint. Vatnajökull icecap, the largest icecap in Iceland, has been imaged several times, and each time new knowledge of the dynamics of this icecap has been gained. A surge in one outlet glacier, rapid motion of another outlet glacier, and changes in glacier margin lakes have been observed in ERTS images in less than a year's time.

MacDonald's work with ERTS images of Antarctica, an extremely remote and inhospitable area, has been profound (p. 194). The regional synoptic view of ERTS imagery and the repetitive coverage have already contributed substantial new scientific knowledge about Antarctica, particularly on the dynamics of the coastal glaciers and ice shelves.

Morrison and White, in their analysis of ERTS data covering the 1973 Mississippi River floods (p. 196), related tone differences in the images to standing-water areas, wet areas, and well-drained soils. They found ERTS data to be of value in determining the effects of physiographic and manmade levees on the distribution of flood waters. They observed also that ERTS need not obtain data at the time of the flood crest to determine inundated areas because of the fact that floods have their effects on the surface reflectance conditions that are detectable for a week or more after the peak has passed on down the valley. Repetitive ERTS imagery, they conclude, can be used to assess the adequacy of existing flood-control systems, such as reservoirs, levees, and channelization.

Experimentation with the data collection system on ERTS by Kahan (p. 214) has shown its potential value for monitoring cloud-seeding conditions. Under Project Skywater, the Bureau of Reclamation weather-modification research program, seven data collection platforms have been installed in areas of severe environmental conditions and have proven to be very reliable and cost effective. Temperature, humidity, insolation, ice riming, wind direction, wind speed, snow-water content, and streamflow data are transmitted via ERTS and the Goddard Space Flight Center to Skywater's environmental computer network for translation into measured units.

Shown and Owen have employed ERTS data for mapping surficial geology, topography type and quality of vegetation, and land use that influence runoff and sediment yield (p. 134). In arid and semiarid regions, the combined use of ERTS imagery and reconnaissance methods can be a useful tool for estimating streamflow and sediment discharge where data are scarce or inadequate. ERTS imagery can be used effectively to aid in the interpretation of the hydrologic characteristics of large drainage basins.

The U.S. Army Corps of Engineers is using ERTS imagery in an operational program for inspection of surface-water bodies with an area of 4 ha (40,000 $m^2$) or larger (Jarman, 1973; Graybeal and others, 1973, 1974). In August 1972 the House of Representatives passed a bill (H.R. 15951) that required the Corps of Engineers to make a national inventory of all dams that impound 60,000 $m^3$ of water or that have a height of 2 m or more; repetitive coverage provided by ERTS will permit updating of this inventory at frequent intervals.

# WATER RESOURCES IN THE DELAWARE RIVER BASIN

By Richard W. Paulson,

U.S. Geological Survey

The data collection system (DCS) aboard ERTS–1 is being evaluated as a potential operational system for collecting hydrologic data from unattended field instrumentation (Paulson, 1974). The evaluation, which is being conducted by NASA, the EROS Program of the U.S. Department of the Interior, the U.S. Geological Survey, and several cooperating water-resources agencies, indicates that it is technically feasible to use Earth-orbiting satellites as vehicles for collecting data from field instruments and that there is potential application for operational satellite data-relay systems. The ERTS experiment described here is a simulation of an operational satellite data-relay and data-processing system.

The ERTS DCS is a communications system that consists of three elements: (1) a small low-power battery-operated radio transmitter attached to a stream gage or a level, temperature, or quality meter; (2) a relay transponder aboard ERTS; and (3) ground-receiver sites. The polar-orbiting ERTS makes 14 orbits of the Earth daily and can relay data from a DCP to a ground-receiver site whenever both are visible from ERTS. This occurs during a brief period of each of the several daily orbits. The DCP transmits a brief data message of 0.04 s duration once every 90 or 180 s. The number of mutually visible periods is primarily a function of geographical position and local terrain interference. Two ground-receiver sites, one at the Goddard Space Flight Center in Greenbelt, Md., and one at Goldstone, Calif., provide good coverage for the conterminous 48 States. They allow data from DCP's in these States to be relayed on 3 to 7 daily orbits during periods lasting as long as 12 to 14 min.

The mosaic of ERTS imagery (fig. 84) shows parts of Delaware, Maryland, New York, Pennsylvania, and Connecticut, all of New Jersey, and most of the Delaware River basin. DCP's have been installed in the basin on 20 water-resources instruments operated by the U.S. Geological Survey in cooperation with the Delaware River Basin Commission, the City of Philadelphia Water Department, and other local, State, and Federal agencies. The instruments are 12 water-quality monitors, 5 stream gages, and 3 ground-water observation wells, and their locations are shown in figure 84; data from them are relayed by ERTS several times daily and are provided in real time to the U.S. Geological Survey's office in Harrisburg, Pa. These data are computer processed daily using remote terminal access to the Survey's computer center in Reston, Va., and are made available to water-resources agencies in the basin. This experiment has verified that it is technically feasible to use the ERTS DCS as an operational tool for collecting data from remotely located water-resources field instruments (Paulson, 1973a,b).

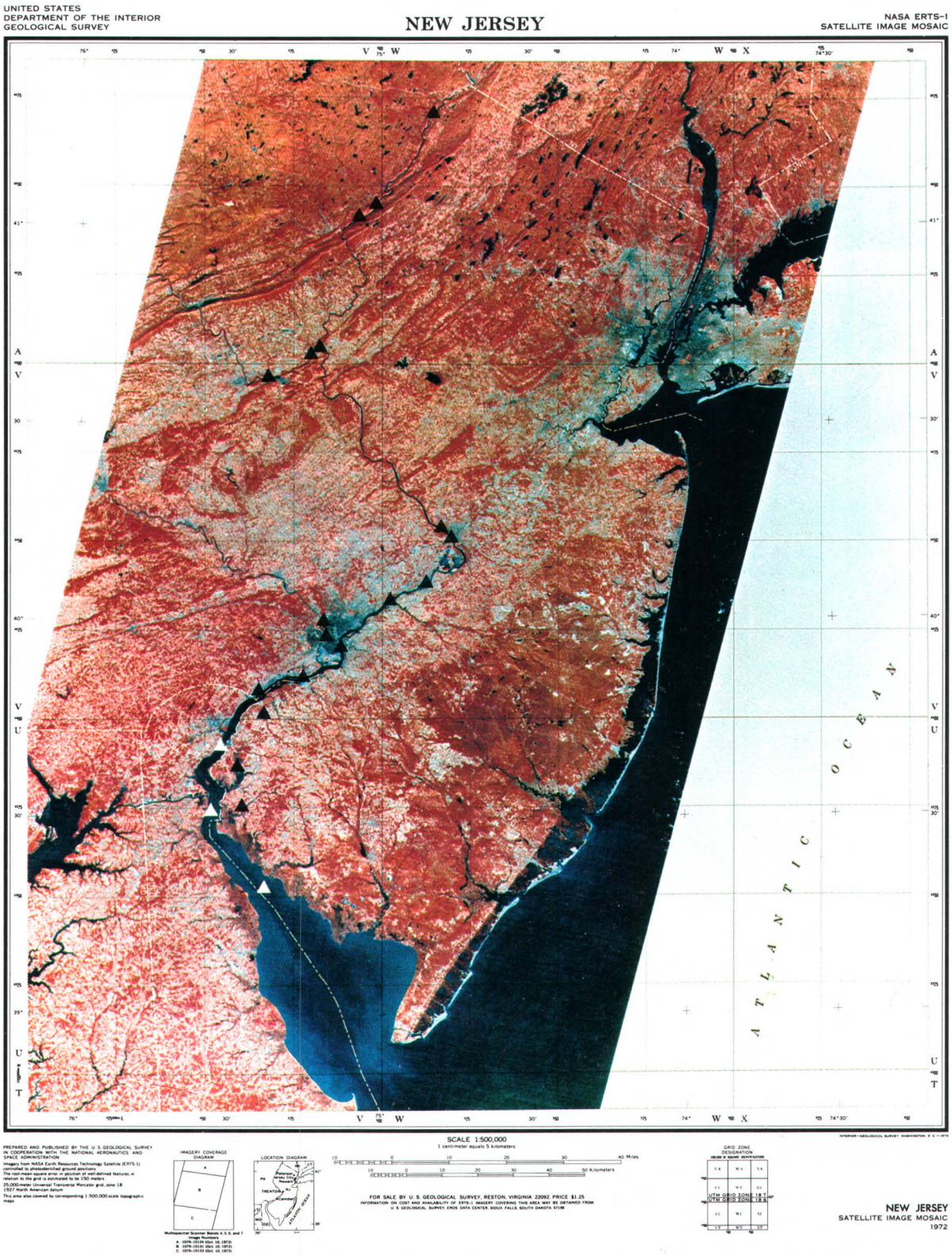


FIGURE 84.—Annotated color composite ERTS–1 mosaic showing data collection platform sites (▲) in the Delaware River basin.

# HYDROLOGY OF THE WIND RIVER BASIN AND ADJACENT AREAS OF WYOMING

By Lynn M. Shown and J. Robert Owen,

U.S. Geological Survey

Figure 85, a color composite ERTS–1 image, shows the Wind River basin and parts of adjacent basins in central Wyoming. A variety of hydrologic conditions resulting from differences in climate, geology, relief, and land use are apparent on the image.

Boysen Reservoir is the focal point of the drainage network of the Wind River basin, which is a deep structural depression. Most of the major perennial streams occur in the west half of the basin. The streams are marked along their entire courses by red, which is characteristic in color composite images of vigorously growing vegetation. Streamflow is sustained by 30 to 65 cm or more of annual precipitation in the mountains as opposed to 18 to 30 cm in the mostly ephemeral lower parts of the basin. In the eastern half of the basin, only certain reaches of the streams are perennial. In these reaches, shallow ground water is fed to the streams from permeable upland areas that are underlain by impermeable clayey siltstone (Whitcomb and Lowry, 1968). The reach of Poison Creek through the Sand Hills is the best example of this; the wider red bands of phraetophytes there indicate ground-water discharge along the streams. The identification of such conditions on a synoptic image of an area or region enables a hydrologist, with the aid of topographic maps, to prepare a generalized map of the water-table configuration that is helpful in the exploration for small supplies of ground water in the interstream areas (F. N. Visher, oral commun., 1974).

The wide sandy-bottomed ephemeral stream channels in the east half of the basin are quite evident because of their light color. This type of channel indicates sandy or gravelly alluvium that absorbs appreciable amounts of the sporadic flood flows and thus diminishes streamflow and sediment discharge in the downstream direction.

Variations in surface runoff and sediment yield in arid and semiarid regions usually correlate with variations in drainage density (Hadley and Schumm, 1961) or topographic texture, which can be quantified readily with small-scale satellite imagery for areas greater than 250 km$^2$. In the Sand Hills area, the highly permeable sandy soils absorb much of the scant 18 to 20 cm of annual precipitation, resulting in very little overland flow and, consequently, a low drainage density. This condition contrasts with the high drainage density just north of the Beaver Rim and on the flanks of the Owl Creek and Bighorn Mountains, which indicates relatively high surface runoff (Peterson, 1962).

The whitish areas south of Badwater Creek, around Boysen Reservoir, and north and west of the Wind River are steep, rugged, highly dissected and sparsely vegetated hills composed of light-colored claystones, siltstones, and sandstones (Keefer, 1965). Runoff and sediment yields from these areas are high, but, because the rocks are very fine textured and because channel vegetation is sparse, the extremely high drainage density of these areas is not apparent on the image.

Color composite satellite images can aid greatly in an analysis of the water resources of river basins or other large areas. Because water appears black in these images, rivers, lakes, reservoirs, and large ponds, greater than 150 to 300 m across, depending on contrast, can be inventoried quickly, and their areas can be estimated so that the amount of water evaporated from them can be computed. Estimates of evapotranspiration by general vegetation types can be obtained by multiplying the area of each type by an average water-use factor for that type. Forests appear on the image as extremely dark brown areas with reddish highlights in the Wind River, Absaroka, and Green Mountains. The brilliant red areas in the Wind River and Absaroka Mountains are meadows. The patchwork red and yellow areas adjacent to the Wind and Bighorn Rivers are irrigated crops, and the smooth red areas along streams such as the Sweetwater River and upper Badwater Creek are irrigated meadows. Nearly all the remaining area is rangeland, which appears variable in color. These color variations are due to different rock types that have been mapped by Love and others (1955) and also to different types and densities of vegetation. The image colors are light where the rocks and soils are eroded and vegetal cover is sparse, and the colors are dark where the rocks and soils are resistant and the cover of vegetation is relatively dense, such as in the Owl Creek Mountains.

ERTS imagery thus provides an excellent tool for improving the understanding of hydrologic processes within regional hydrologic systems. Areas for which hydrologic knowledge is deficient and areas where land-use changes may affect the water resources can readily be inventoried using such ERTS imagery.

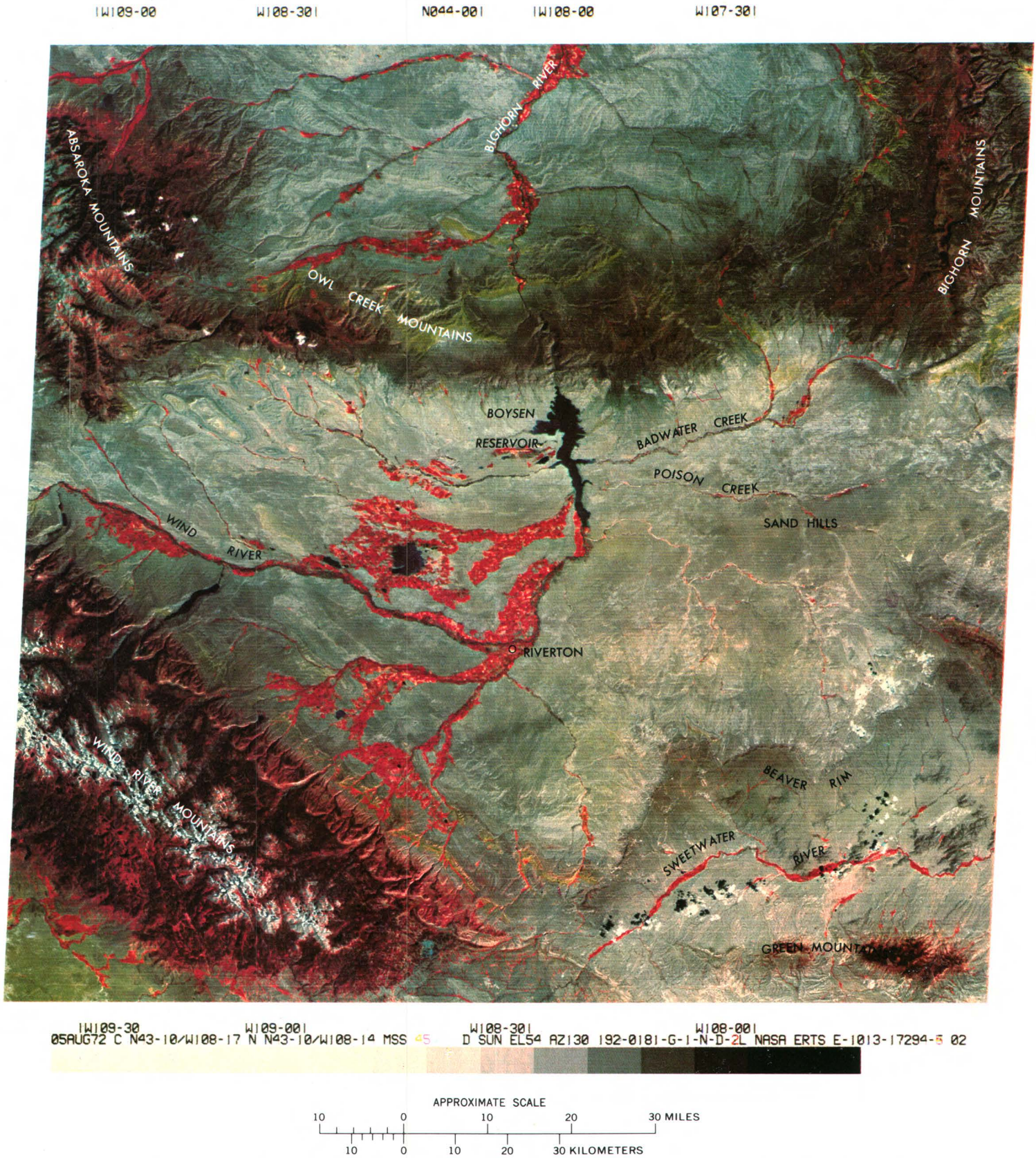


FIGURE 85.—Annotated color composite ERTS–1 image of the Wind River basin and adjacent areas of Wyoming (1013–17294).

# IMPROVING ESTIMATES OF STREAMFLOW CHARACTERISTICS

By Este F. Hollyday and Edward J. Pluhowski,

U.S. Geological Survey

Land-use data obtained from an ERTS image (fig. 86) was used to improve estimates of mean monthly streamflow for July in the Delmarva Peninsula.

Information on average streamflow and streamflow variability is needed for the utilization, management, and conservation of our water resources. Historical data on mean daily streamflow, floods, and droughts are used routinely in designing such structures as electricity-generating plants, reservoirs, bridges, and water-supply and sewage-treatment plants. The statistical measures used to characterize streamflow are determined from continuous flow records extending over 10 yr or more. Frequently, flow records are not available for a particular point on a stream. The flow characteristics at that point, however, may be estimated if regional relationships exist between the streamflow characteristics and the physiographic and climatic characteristics of nearby gaged basins. Assuming that regional relationships may be expressed by usable equations developed from records of gaged basins, it is then possible to characterize streamflow at the ungaged sites by measuring each equation parameter in the basin above the point of interest.

As part of a national program of the U.S. Geological Survey, equations were formulated using multiple regression techniques. These equations relate as many as 40 streamflow characteristics to selected basin characteristics. Gaging stations with at least a 10-yr record of unregulated flow were used in the regression analyses. Within selected error limits, these equations may be used to estimate streamflow characteristics at ungaged sites for about 50 regions in the Nation.

The ERTS image (fig. 86) contains information on the distribution of forests (brown-red), fields (white, pink, and gray), urban areas (blue-gray), and water (blue-black). A measure of the relative area of a drainage basin covered by each of these four land-use categories constitutes a basin characteristic that may be used in estimating streamflow. For example, forest areas can be separated from the other categories by visual interpretation. Automated techniques employing film-density discrimination were used to improve upon the accuracy and uniformity of this separation. The resulting extraction of forest areas (fig. 87) can be measured basin-by-basin using automated techniques and can be checked by a manual point count. The percentage of forest cover so measured can be added to the data on basin characteristics used in the streamflow regression analyses.

In the equation given in figure 87, the land-use category Uf (forest) was one of four basin characteristics selected by multiple regression analysis as being statistically significant in defining mean monthly streamflow for July. The other three significant basin characteristics include $A$ (drainage-basin area), $Si$ (soil infiltration capacity), and $I_{24,2}$ (24-h, 2-yr-recurrence rainfall intensity). Other factors in the equation include the regression constant, $a$, and regression coefficients, $b_1$, $b_2$, $b_3$, and $b_4$. Addition of Uf in the regression analysis resulted in a 20 percent improvement upon previous estimates of mean monthly streamflow for July.

In a previous related study, urban, agriculture, forest, and water areas determined from ERTS analogous aerial photography were added to the basin characteristics for 39 basins in the Piedmont and Coastal Plain provinces of Maryland and Delaware. Addition of these characteristics reduced the standard error of estimate of equations for 12 out of 40 streamflow charac-

FIGURE 86.—Annotated color composite ERTS–1 image of the Delmarva Peninsula area (1079–15133).

teristics. The standard error of estimate of seven of the equations were reduced more than 10 percent. These results are significant in that a reduced standard error of estimate indicates less variance about the curve of relation, thereby improving predictive capability of the equation.

Significant improvement (standard error reduced by more than 10 percent) upon estimates of mean monthly streamflow was computed for June, July, September, and November. Other significantly improved streamflow characteristics included the 7-day, 2-yr-recurrence low flows, 3-day, 2-yr-recurrence flood volumes, and estimates of the 50 percentile of flow-duration curves.

As a result of using remotely sensed data, estimates of some characteristics of streamflow at ungaged sites have been significantly improved. These improvements will support better utilization, management, and conservation of our water resources.

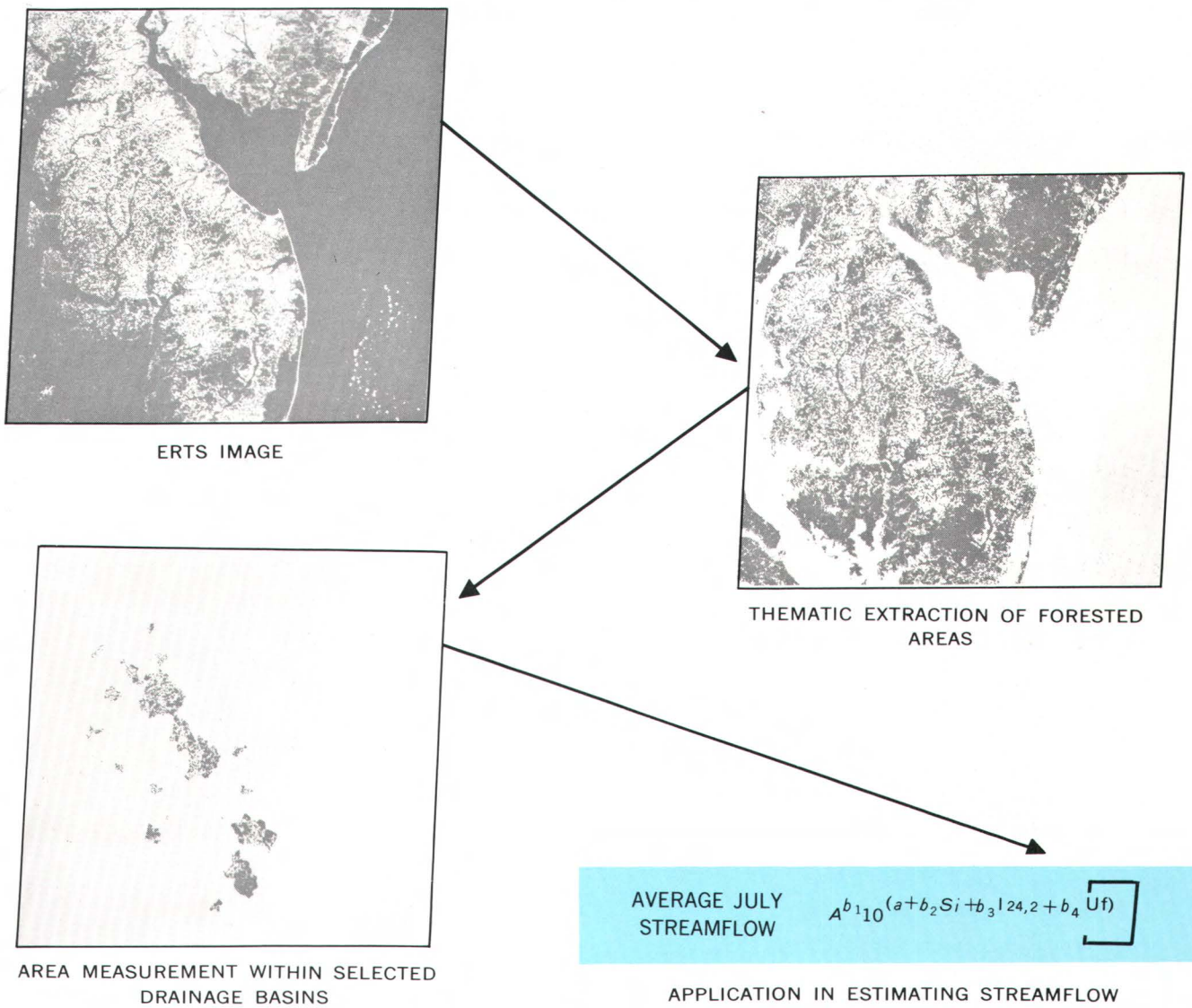


FIGURE 87.—Flow diagram of technique for improving estimates of streamflow characteristics derived from multiple regression equations by using forest data extracted from ERTS–1 image 1079–15133 (fig. 86).

# MONITORING WATER RESOURCES IN QOM PLAYA, WEST-CENTRAL IRAN

By Daniel B. Krinsley,

U.S. Geological Survey

Playas are almost flat landforms that occupy the lowest parts of desert basins. Composed of relatively homogeneous materials and characterized by a general lack of relief or of vegetation, their microrelief changes with fluctuations in the level of ground water. Playas are common features of arid landscapes, and consequently they have widespread global distribution.

Although playas occupy only 6 percent of the land area of Iran, most of the population lives adjacent to them because of the availability of flat land and moderate supplies of ground water at relatively shallow depths. The playas have not been fully utilized because of the lack of adequate knowledge concerning the seasonal changes in their surface- and ground-water hydrologies and in the physical properties of their sediments. Most playa investigations have been conducted during the summer when the surficial sediments are dry and have sufficiently high bearing strengths to support men and vehicles, but this practice has limited the understanding of these dynamic landforms.

Sixty playas within the interior of Iran have been studied since 1965 (Krinsley, 1968, 1969, 1970, 1972a,b). These range in area from 25 to 52,825 km$^2$ (Great Kavir); 33 playas are smaller than 300 km$^2$, and, except for the Great Kavir, the largest playa is 4,685 km$^2$. Visits were made to 22 playas; 20 were observed from low-flying aircraft; and 18 were viewed solely from aerial photographs and from ERTS–1 images.

The repetitive coverage of ERTS–1 is ideally suited to provide seasonal images of the Iranian playas from which changes in the areal extent and morphology of the surficial materials can be recorded along with contemporaneous or previous field studies of actual surficial conditions. Data derived from the analyses of ERTS–1 images can provide a rational basis for planning the economic utilization (salt or water extraction and agriculture) and engineering development (roads and airfields) of these geomorphic features.

Qom Playa, in west-central Iran, is a good example. The playa is the sump for a drainage basin of 86,812 km$^2$ and lies adjacent to the city of Qom and its extensive surrounding farmlands and oil resources.

During the period of this study, from Sept. 4, 1972, to May 14, 1973, Qom Playa was driest from mid-September to late-September (fig. 88). The playa was almost completely saturated by mid-May (fig. 89). The period of greatest lake fluctuation occurred in mid-December when the lake area almost tripled and the lake volume increased more than five times (fig. 90). At or near its 1973 maximum extent, the lake is conservatively estimated to have contained approximately $400 \times 10^6$ m$^3$ of water. Most of this enormous resource is annually lost to evaporation.

Diversion, storage, and utilization of this water is facilitated by the geographic location of the source and the settlement patterns around the playa. The lake's three principal streams form a composite alluvial plain that borders the western margin of the playa (fig. 89). The city of Qom and its hinterland receive their water from the streams, wells, and qanats (underground channels used to convey water) on this huge alluvial plain. There is almost no settlement along the northern, eastern, or southern margins of the playa. Small earthen dams on the plain and larger dams upstream could store the water during the period of maximum discharge (fig. 90) in April and May and extend its use during the summer dry period. There would be little or no negative economic effect of the lowered water table east of the alluvial plain. In fact, the depressed water table of the playa would result in a firm hard crust throughout the year that would facilitate transportation and exploration for salts of economic value. The juxtaposition of the agricultural and oil resources of the Qom area, possible salts of economic value in the playa, and a significantly increased supply of water are natural possibilities for economic development that should be more thoroughly investigated and considered.

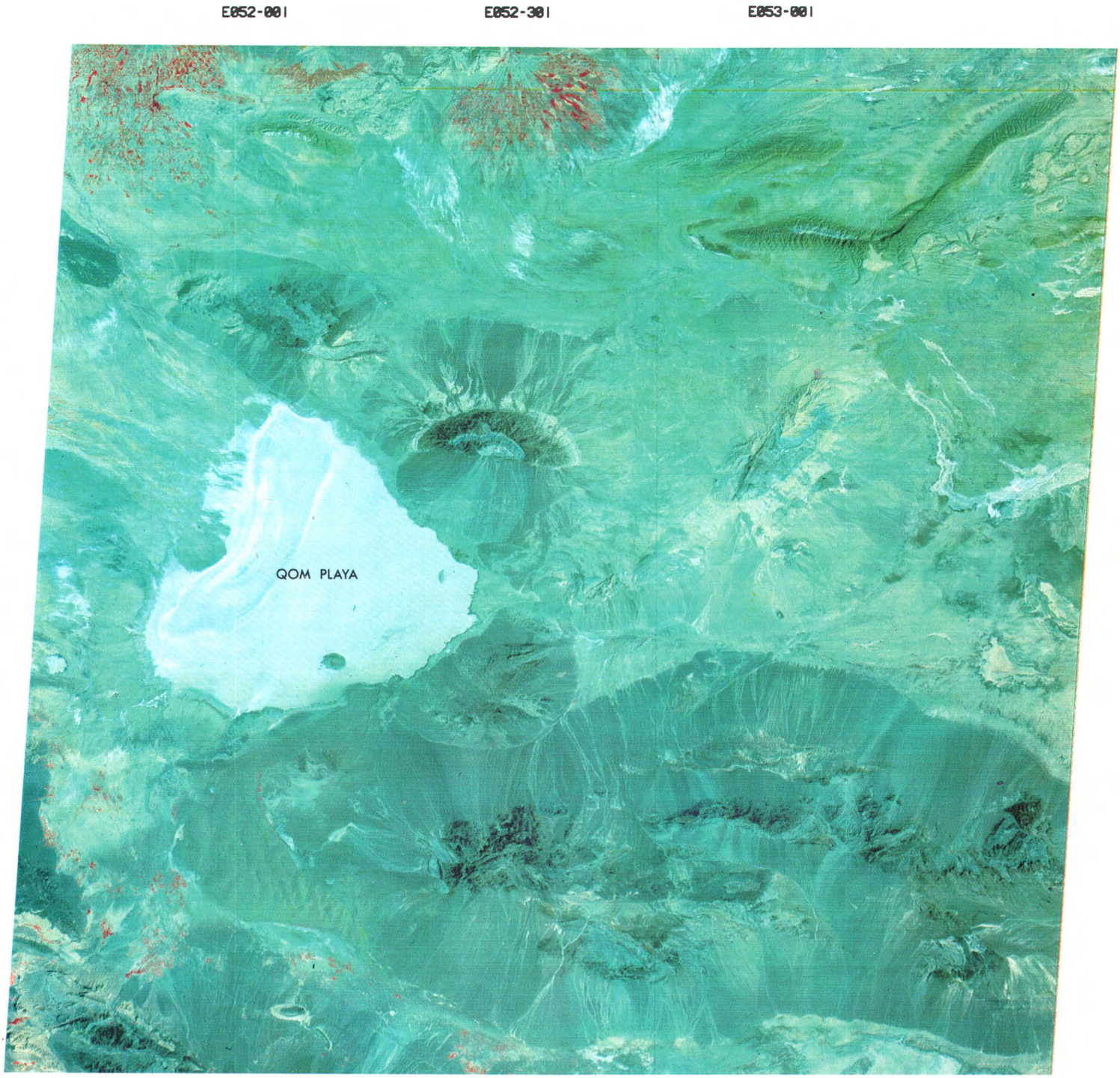


APPROXIMATE SCALE

10 0 10 20 30 MILES

10 0 10 20 30 KILOMETERS

FIGURE 88.—Color composite ERTS–1 image of the Qom Playa area of west-central Iran, Sept. 22, 1972 (1061–06381).

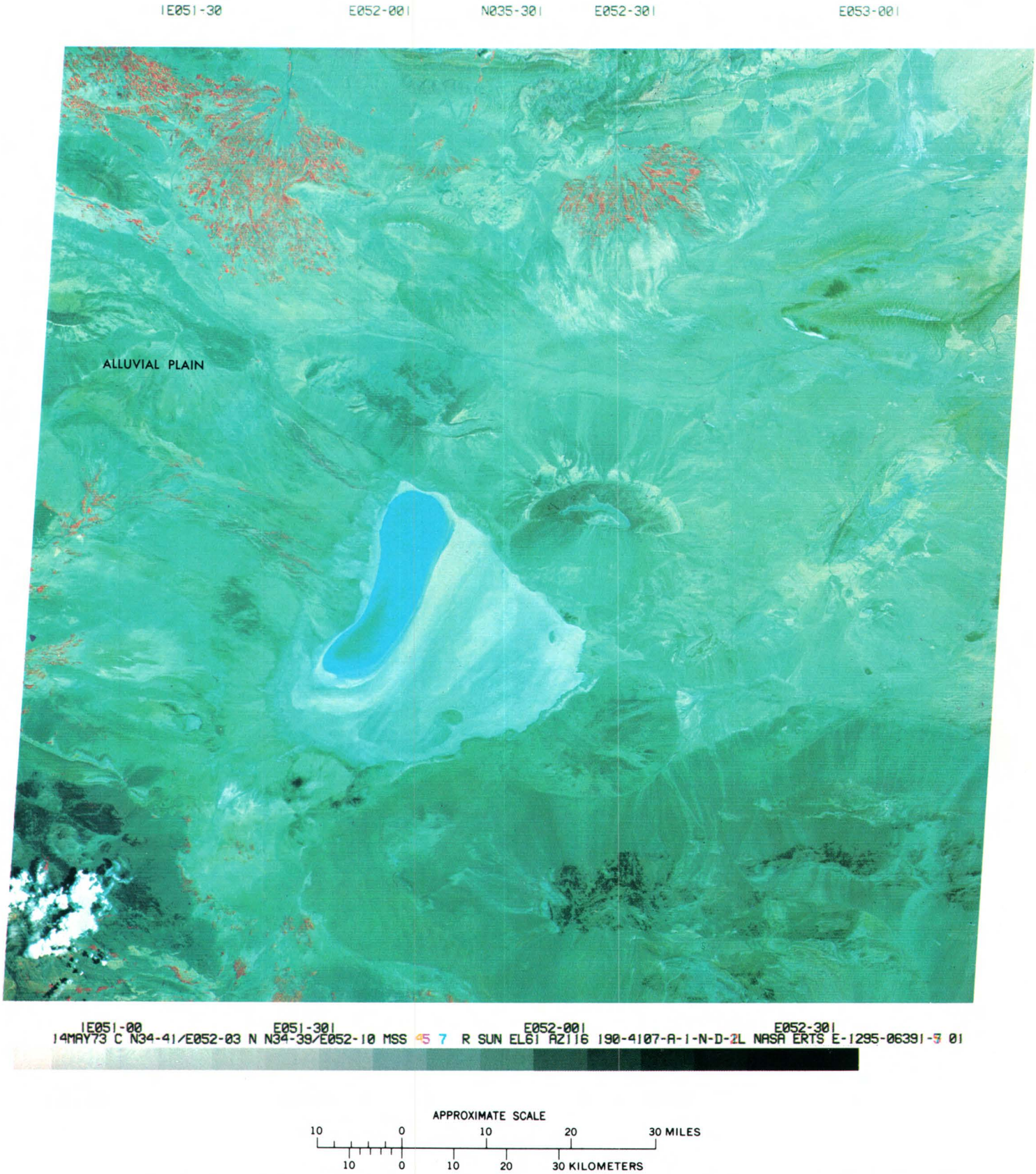


FIGURE 89.—Color composite ERTS–1 image of the Qom Playa area of west-central Iran on May 14, 1973 (1295–06391).

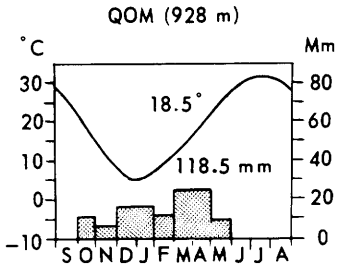


Mean monthly temperature and precipitation; mean annual temperature, total annual precipitation, and altitude of the station at Qom.

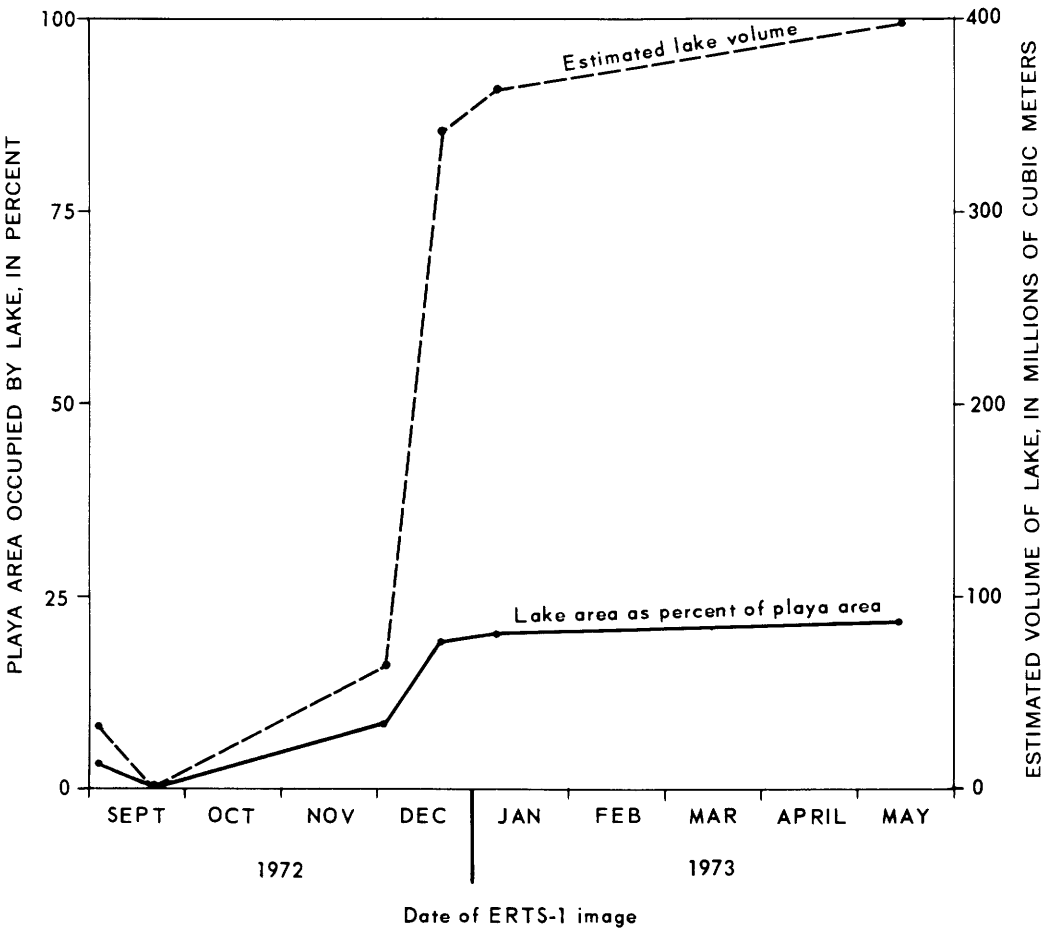


FIGURE 90.—Comparison of the climatic data from Qom with the lake area at Qom Playa, as a percentage of the playa area, and the estimated lake volume from Sept. 4, 1972, to May 14, 1973.

# LAKE FLUCTUATIONS IN THE SHIRAZ AND NERIZ PLAYAS OF IRAN

By Daniel B. Krinsley,

U.S. Geological Survey

Shiraz Playa and Neriz Playa occupy separate but adjacent basins within the Zagros Mountains watershed of southwest Iran. Pleistocene beaches that are similar in number and in relative vertical position and similar basin/playa ratios indicate that the two playas have had similar hydrologic responses to essentially the same climatic factors of precipitation, temperature, and evaporation.

The intermittent lake at Shiraz Playa (to left of image), although quite shallow, fills the center of the valley bottom during the spring runoff period. In April 1967, near its maximum seasonal extent, the greatest measured depth of the lake was 50 cm (Huber, 1967). Ground observations by Bobek (1963) at Neriz Playa in June 1963 and by Krinsley in October 1965 and August 1967 (Krinsley, 1970) and in September 1972 suggest that the maximum depth of the playa lake may have been 2 m within recent time.

Three color composites of ERTS–1 images of Shiraz and Neriz Playas (figs. 91, 92, 93) were prepared from the ERTS–1 positives of seven images from Sept. 2, 1972, through Aug. 28, 1973. Data obtained by measuring the areas of the playas and of the lakes in each scene were used in the construction of figure 94.

Lake Shiraz covered 66 percent of the playa area on Sept. 20, 1972 (figs. 91, 94), and had an estimated average depth and volume of 0.1 m and $16\times10^6$ $m^3$, respectively (fig. 95). The lake at Neriz encompassed 21 percent of the playa area and had an estimated average depth and volume of 0.4 m and $68\times10^6$ $m^3$, respectively. Except for a deep pool near the west shore of Lake Shiraz, water depths were uniformly distributed. The deepest water in the lake at Neriz was in the western part of the playa (fig. 94); the long narrow central area of the lake had very shallow water. This period at the end of the long hot summer, during which rain is generally absent (fig. 95) and evaporation rates are highest, has the lowest ground-water levels and lake areas of the year.

Lake Shiraz occupied 94 percent of its playa area on Mar. 1, 1973 (fig. 92, 94), and had an estimated average depth and volume of 0.4 m and $94\times10^6$ $m^3$, respectively (fig. 95). The lake at Neriz expanded to 99 percent of its playa area and had an estimated average depth and volume of 1.0 m and $794\times10^6$ $m^3$, respectively. It seems reasonable to assume that some of the precipitation

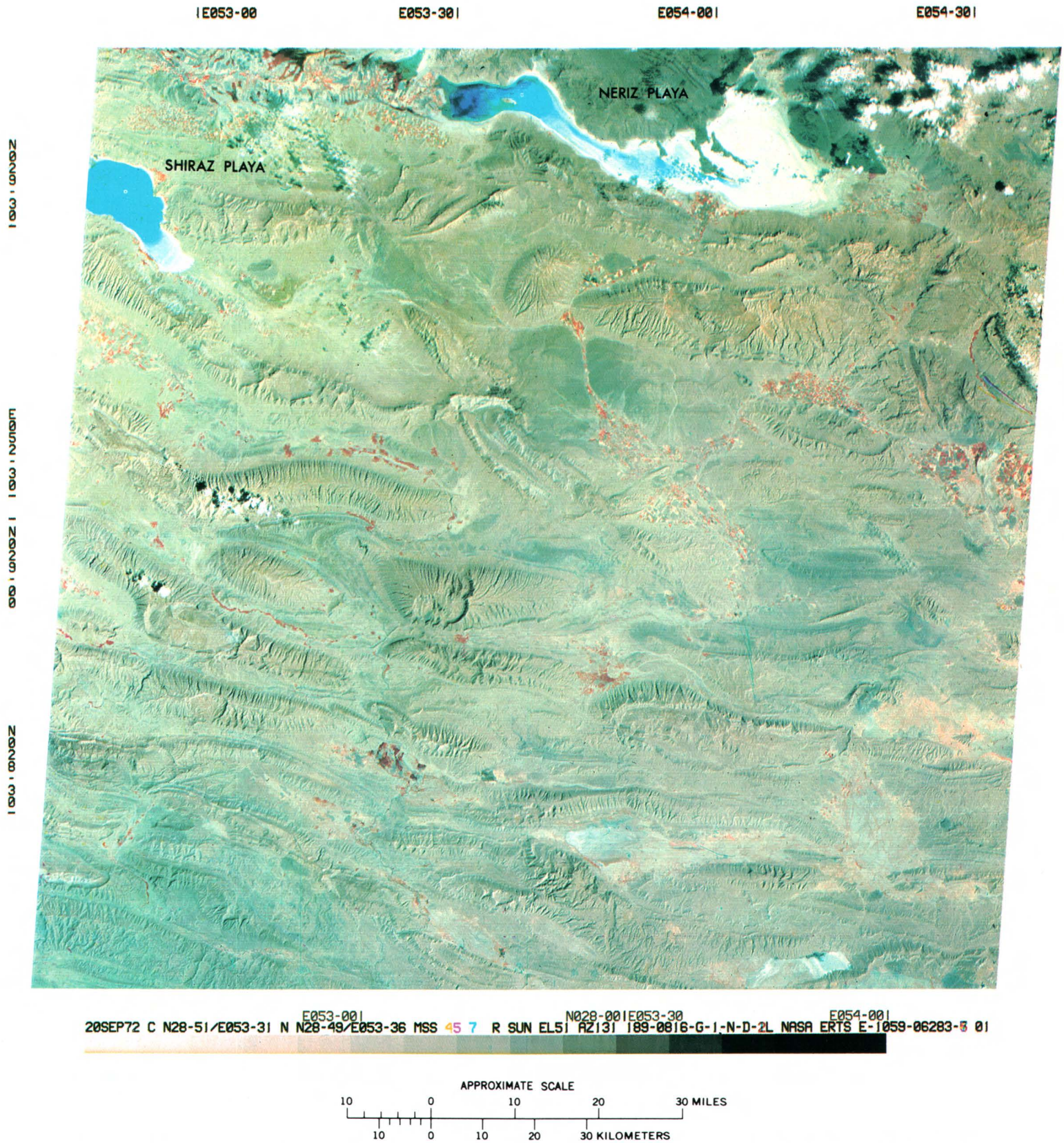


FIGURE 91.—Annotated color composite ERTS–1 image of the Shiraz and Neriz Playas of Iran on Sept. 20, 1972 (1059–06283).

falling at the highest altitudes of the narrower Shiraz basin would remain as snow, while most of the precipitation falling in the lower, broader valley of the Neriz basin would be rain that quickly moved toward the playa. These considerations combined with the period of the annual precipitation maximum (fig. 95) and evaporation minimum could explain why the lake at Neriz appeared to reach its 1973 maximum extent ahead of Lake Shiraz (figs. 94, 95).

Lake Shiraz had contracted to 1 percent of its playa area by Aug. 28, 1973 (figs. 93, 94) and had an estimated average depth and volume of 0.3 m and $0.9 \times 10^6$ $m^3$, respectively (fig. 95). The lake at Neriz contracted to 5 percent of its playa area and had an estimated average depth and volume of 0.5 and $19 \times 10^6$ $m^3$, respectively. The sequential images of these playas provided by the repetitive coverage of ERTS–1 make it possible to observe and measure efficiently and accurately the extreme variation of these lakes within a single year. Note that almost 1 full year after Sept. 2, 1972 (fig. 94), Lake Shiraz had almost disappeared and the lake at Neriz was reduced to one small lake and two separate ponds. This extreme variation is due primarily to the marginal climatic equilibrium of these lakes, the delicate balance between precipitation and evaporation. The current lack of complete synchroneity between the lakes in the periods of minimum and maximum lake fluctuation is accentuated by man's intervention in the hydrologic cycle of these lakes by his increased diversions of water through dams and pumped wells.

From February through May 1973, there were at least $600 \times 10^6$ $m^3$ of water available in the lake at Neriz (fig. 95); this figure obviously may vary annually with the climate and with the magnitude of the drainage diversions. This region is important agriculturally, and more recently it has become the site for industrial development, including a large oil refinery. Consequently there is need for the large amount of water that is lost to evaporation each year, evaporation that is facilitated in a large body of very shallow water. Larger, deeper reservoirs are required to store the water during the long dry summer. Consideration should also be given to the ecological and local economic effects of further water withdrawals from the lake. The larger villages along the southern shore of the lake have qanats (underground channels for transporting water) for fresh water but use pumped wells to augment irrigation. If the lake disappears, there will be local climatic effects of increased aridity and changes in the plant and animal communities. These hydrologic and biologic changes may be undesirable and irreversible and should be considered before any additional water is removed.

Although the salt crust at Neriz Playa is thin, there may be buried crusts that are thicker as well as brines that have salts of economic value. The general accessibility of the playa and its deposits argue for a systematic investigation of its resource potential.

Lake Shiraz had a relatively negligible water supply from February through May 1973 ($50 \times 10^6$ $m^3$ of water). Some of this could no doubt be diverted for agricultural or industrial use, but the withdrawal would seriously affect the discharge from the several pumped wells in the vicinity. The amount of water is marginal and may not justify any significant expenditures of money for diversions and storage. Salt from the west shore area is currently used for human consumption, and this use could be expanded.

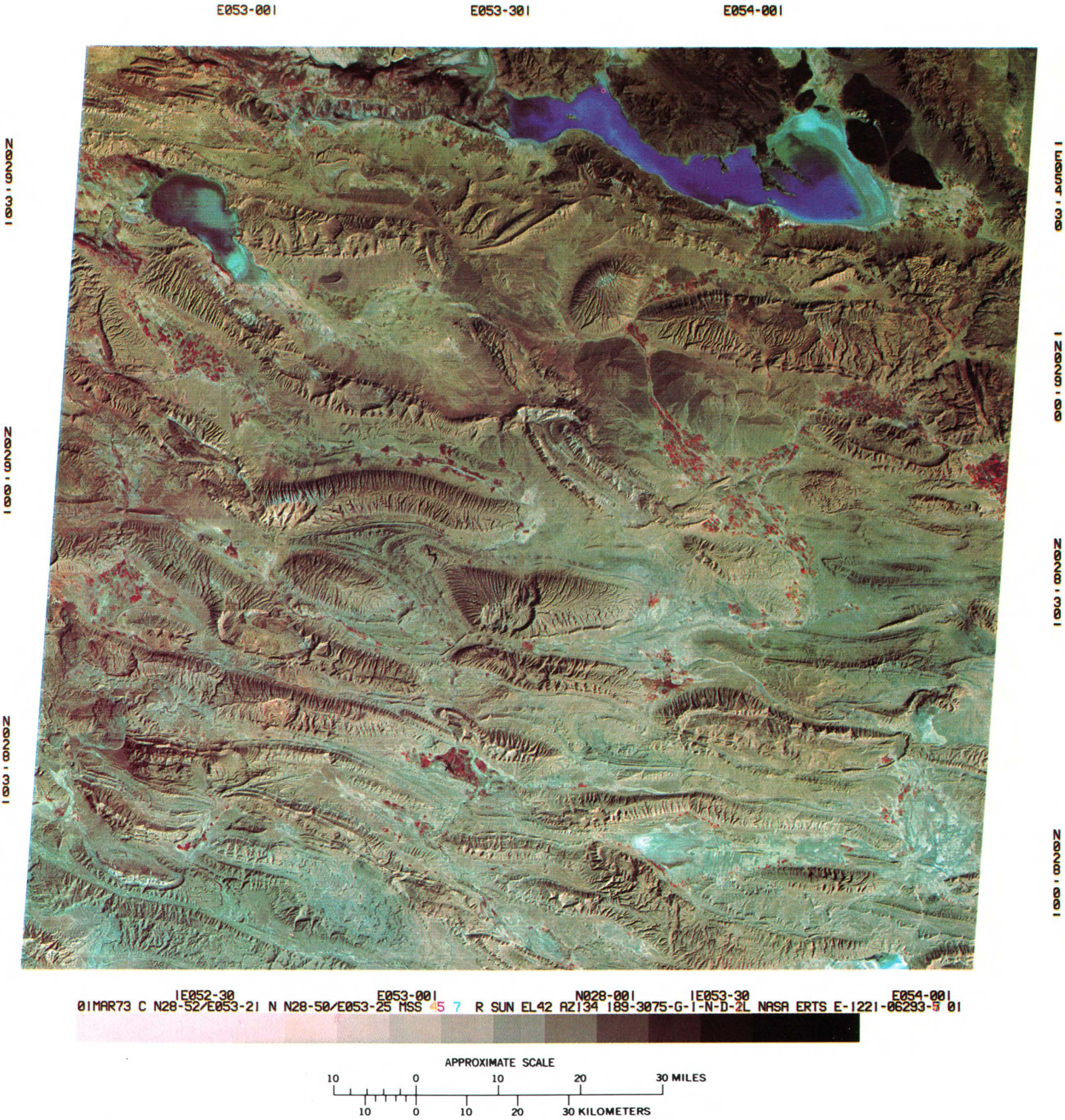


FIGURE 92.—Color composite ERTS–1 image of the Shiraz and Neriz Playas of Iran on Mar. 1, 1973 (1221–06293).

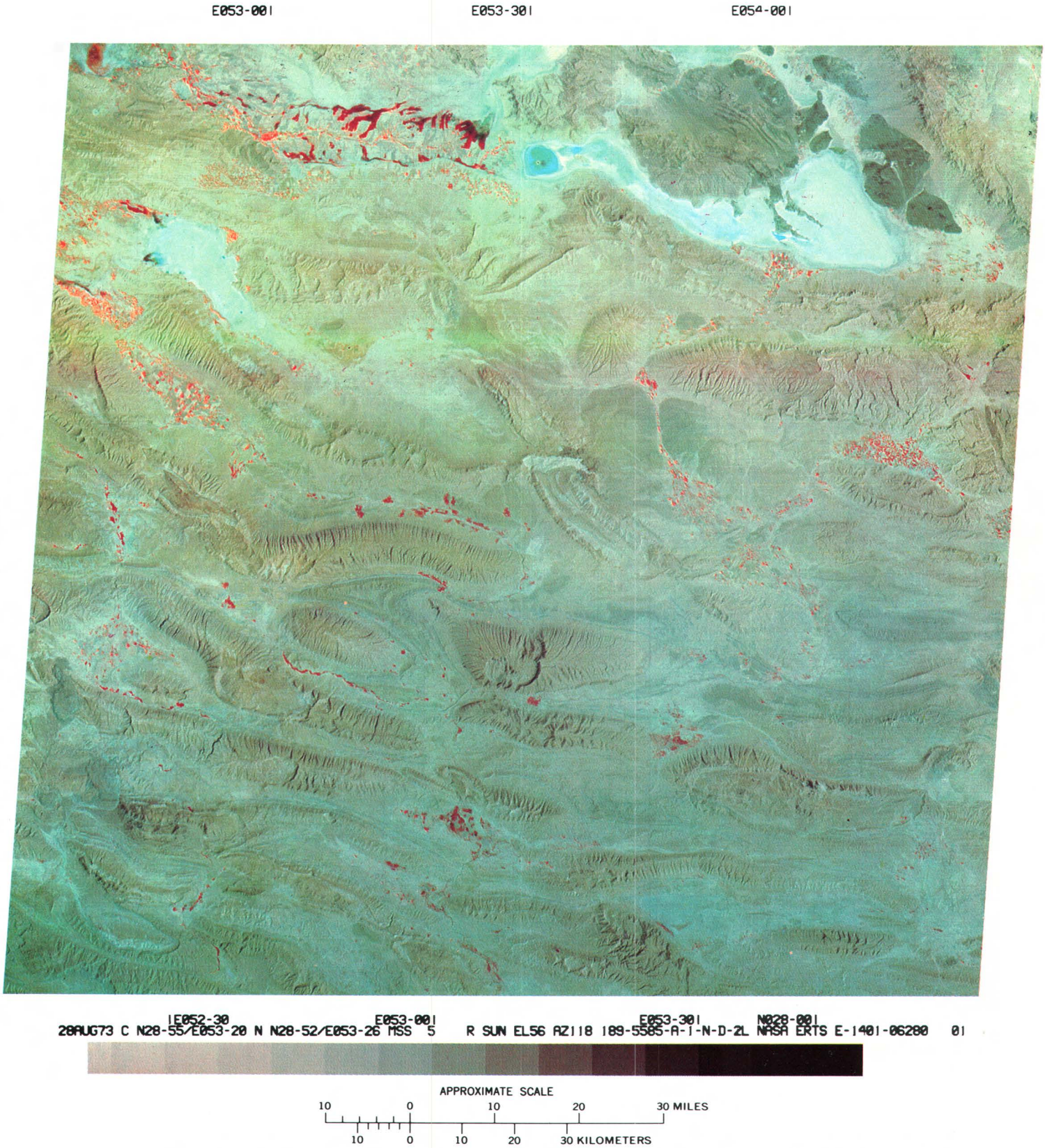


FIGURE 93.—Color composite ERTS–1 image of the Shiraz and Neriz Playas of Iran on Aug. 28, 1973 (1401–06280).

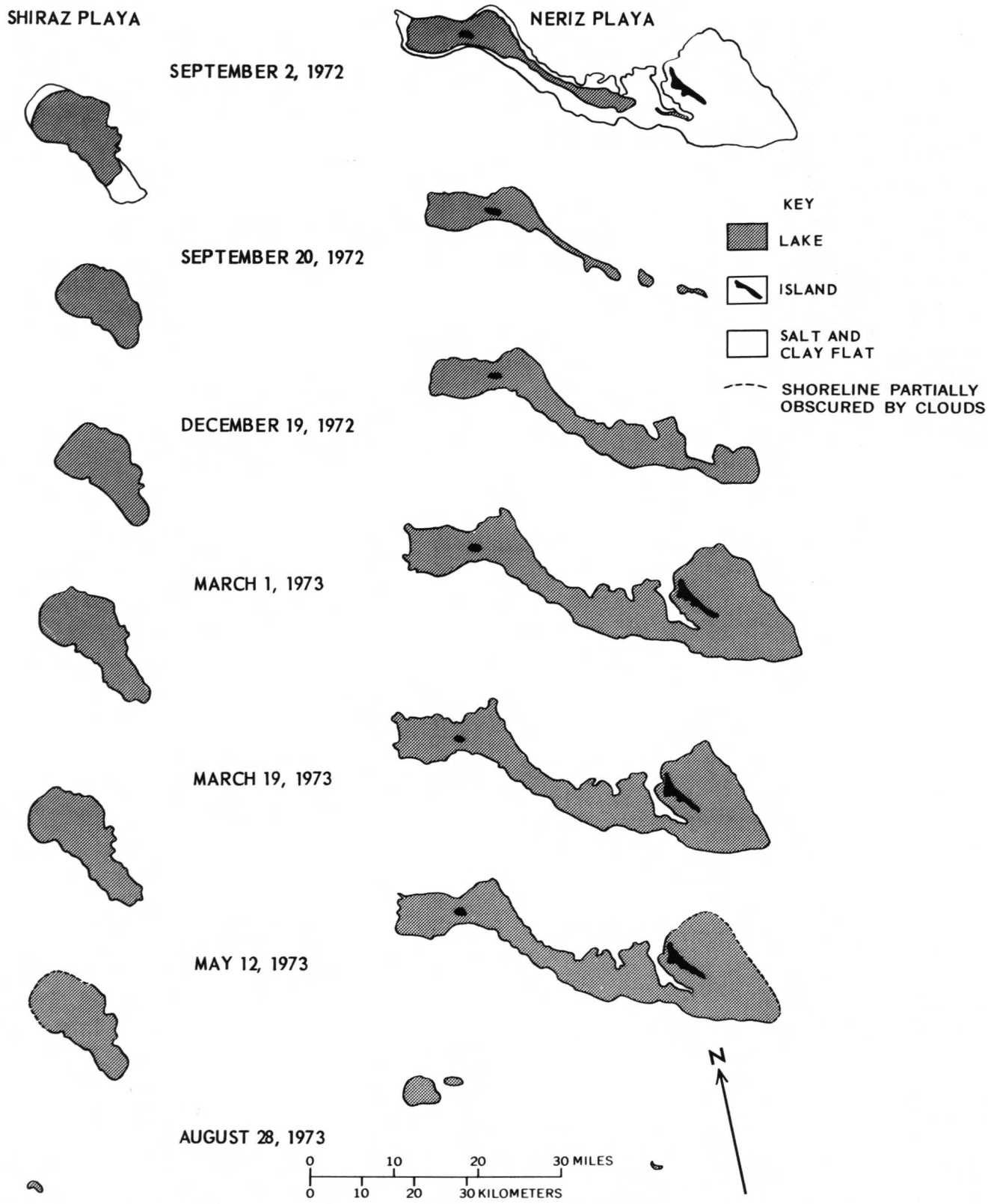


FIGURE 94.—Diagram showing lake fluctuations at Shiraz and Neriz Playas, 1972–73.

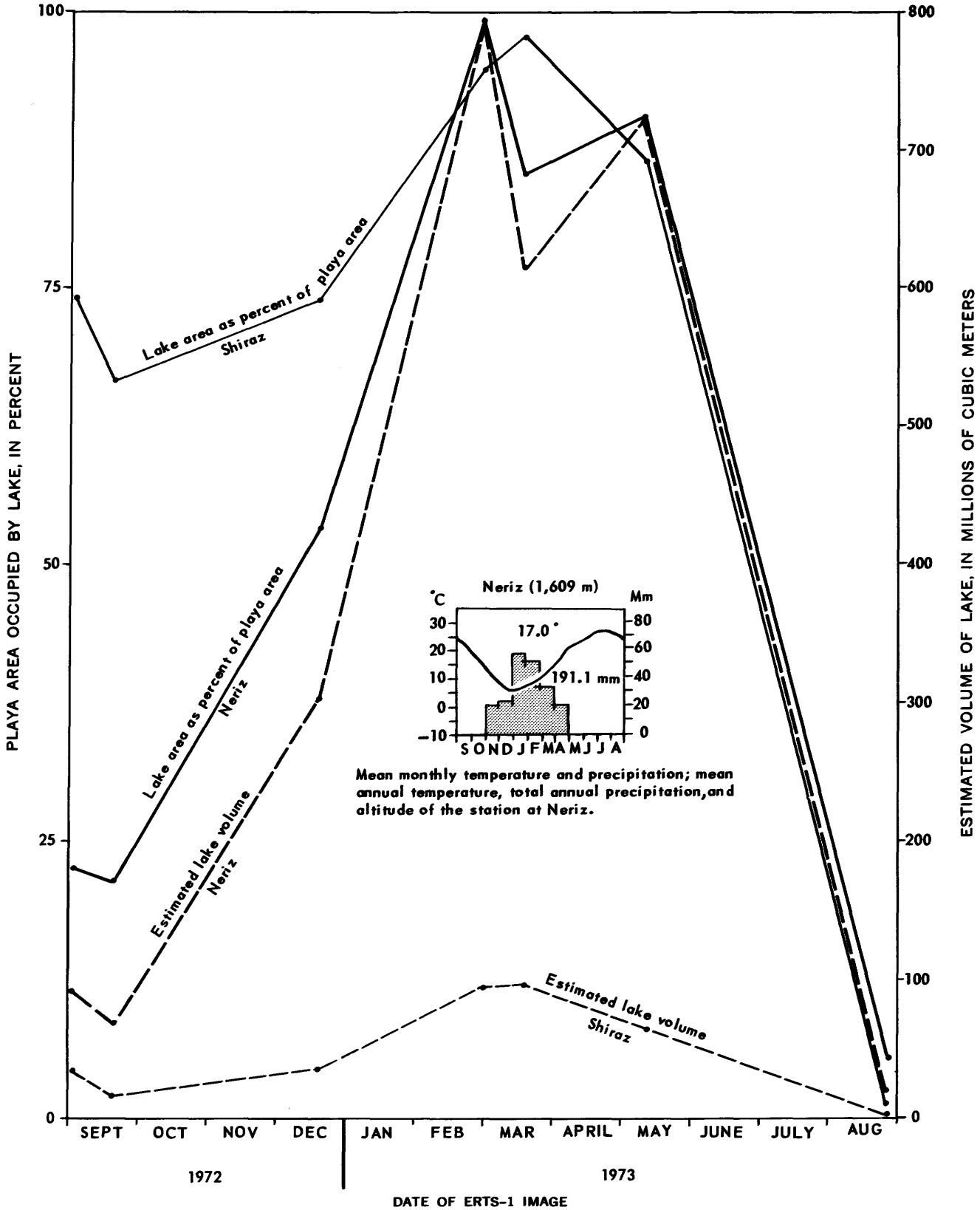


FIGURE 95.—A comparison of the climatic data from Neriz with the lake areas at Shiraz and Neriz Playas, 1972–73, as a percentage of the playa areas and the estimated lake volume from Sept. 2, 1972, to Aug. 28, 1973.

# ECOLOGICAL MODEL IN FLORIDA

By Aaron L. Higer, A. Eugene Coker, and Edwin H. Cordes,

U.S. Geological Survey

Thousands of years of seasonally fluctuating water supply, punctuated periodically by drought or unseasonally heavy rain, have resulted in a natural balance of plant and animal communities in south Florida. Water fluctuations, together with fires and hurricanes, contributed to the shaping of the ecological communities, that is, the tree islands (composed of woody vegetation) and grassland communities (wet prairies and sawgrass marshes). This natural ecological balance, however, is now influenced by a modified water regime, altered by water control within the Kissimmee-Okeechobee-Everglades watershed for flood control, crop irrigation, and coastal urban use (fig. 96). The Central and Southern Florida Flood Control District manages this watershed that contains more than 22,500 km of canals and levees.

An effect of water deficiencies in Everglades National Park is the failure of wood storks to form rookeries. Wood storks nest in winter at the inner edge of the mangrove belt in the Everglades National Park in south Dade and north Monroe Counties. According to John Ogden, an ornithologist of the National Park Service (written commun., 1973), the wood storks were successful in forming rookeries in 1959, 1960, and 1961 but failed for 5 successive years (1962–66), when low rainfall in south Florida resulted in prolonged drought in the park.

The success or failure of wood stork rookeries is a significant index of hydrologic conditions in the park. Wood stork studies in Everglades National Park by the National Park Service suggested a working hypothesis for establishing the water conditions of Shark River Slough, the largest freshwater course in the park, needed for successful formation of these rookeries. An annual prediction of success or failure of the rookeries at the inner edge of the mangrove belt could be made in November, which marks the beginning of the dry season and precedes the height of rookery formation by approximately 2 mo. The prediction can be based on recorded water-level measurements together with a synoptic view of the spatial distribution of surface water, both available from ERTS data, and on the density of small aquatic animals collected in quantitative traps.

The ecological model is designed to relate the wildlife in the Shark River Slough to the availability of food and water (fig. 97) (Higer and others, 1973). In an on-going study with the National Park Service, more than 50,000 aquatic animals have been captured and tagged. The species numbers and hydrologic data are entered into a digital computer program that provides statistical summaries of species distributions and water depths at point locations in the slough. Time-variant synoptic displays using ERTS imagery taken concurrently with stage and rainfall data presently being collected from DCS (figs. 98, 99) may provide the following information to develop an ecological model (Higer and others, 1974):

1. Knowledge of the quantity of water stored in the slough.
2. Knowledge of the spatial distribution of water in the slough as it relates to available food for the bird rookeries (fig. 100).
3. Quantitative hydrologic data that allow management to know where and when to increase water into the slough from the upstream water storage areas.
4. Ability to predict the number of aquatic animals in the slough and the success or failure of the rookeries, based on conditions of the hydrologic regime.

FIGURE 96.—Color composite ERTS–1 image mosaic of the State of Florida prepared by the General Electric Co., Beltsville, Md., in cooperation with the U.S. Geological Survey, Water Resources Division, Miami, Fla., the Central and Southern Florida Flood Control District, and NASA.

Sufficient water must be maintained in the Shark River Slough of the Everglades National Park to preserve the aquatic community and the several bird and mammal species that feed primarily on fish. The amount and time of water releases to the park are a resource-management decision based on very limited information on the water storage that may be available to the north of the park. Small-scale thematic maps of water levels provide an accurate evaluation of water distribution. A gradual reduction of water levels before the birds start nesting would result in the concentration of fish in the Shark River Slough that may ensure adequate food for successful hatches of several rare and endangered bird species.

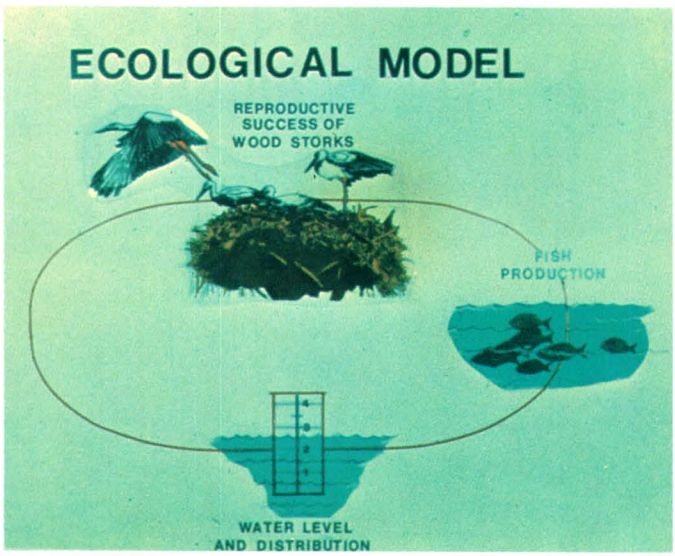


FIGURE 97.—Wildlife ecological model of the Shark River Slough, Fla.

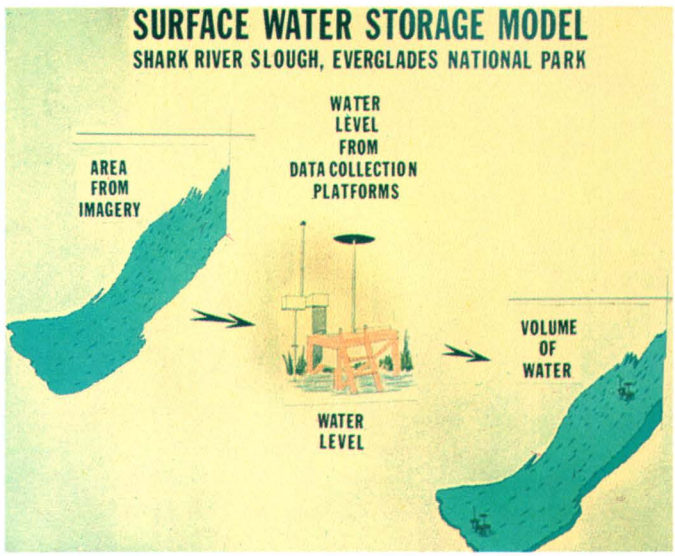


FIGURE 99.—Surface-water storage model of the Shark River Slough, Fla.

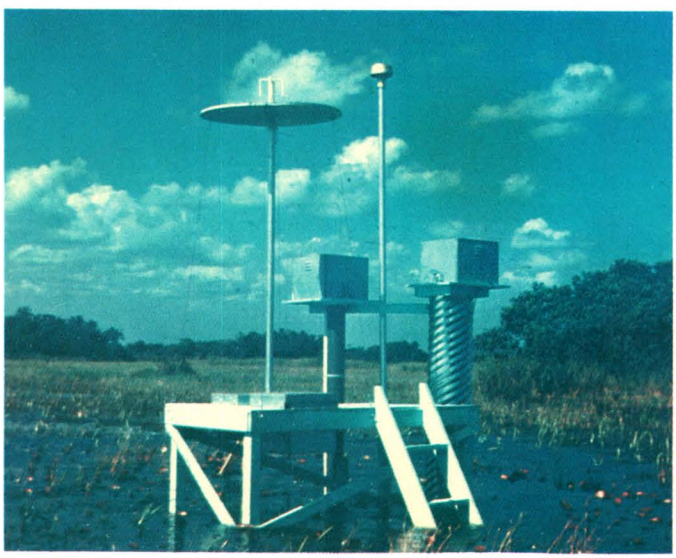

FIGURE 98.—Data collection platform in the Everglades National Park in south Florida used in the ecological model study.

FIGURE 100.—Wood storks nesting in the Everglades National Park, south Florida.

# TURBIDITY IN LAKE SUPERIOR

By Michael Sydor,
University of Minnesota

ERTS imagery of the area near Duluth, Minn., shows prominent turbidity plumes in the western arm of Lake Superior (Stortz and Sydor, 1974). The correlation of image intensity with field observational data (fig. 101) can be used to produce a water-quality map showing the concentration of suspended solids on the lake (Bennett and Sydor, 1974; Scherz and others, 1974). This is done either by use of optical density slicing of 70-mm bulk transparencies (fig. 102) and identifying each image-density range with the corresponding range of suspended solids (fig. 103) or by using CCT's in a like manner (fig. 104).

Two major sources of turbidity exist in the area (fig. 105), the polluted effluent of the St. Louis and Nemadji Rivers and the erosion of red-clay deposits along the southern shore. The measurement of turbidities on the lake and the problem of effluent tracing have important practical applications in the selection of the locations for new water intakes, in the design of filtration plants for the existing water intakes, and in studies of environmental impact on the lake due to extensive harbor dredging. The interpretation of ERTS data is based on the spectral reflectance variation of particulate matter with the various bodies of water. Notice for instance that the harbor area of the St. Louis River appears deceptively clean on the band 5 image (fig. 106), largely because of the high light-absorbing characteristics of the St. Louis River water. This fact is helpful in tracing the St. Louis effluent. The variation in the MSS signal is shown in figure 107 for bands 4, 5, and 6 for the harbor effluent, and the south shore plume indicates that the turbidity plumes on the lake could be traced to their source of origin using the ERTS CCT data.

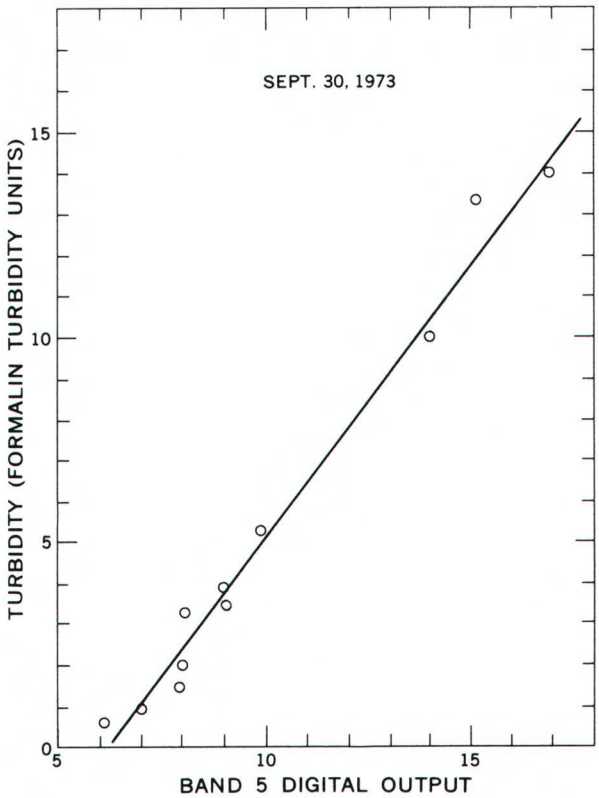


FIGURE 101.—Correlation of intensity from band 5 of ERTS–1 image 1434–16244 with turbidity.

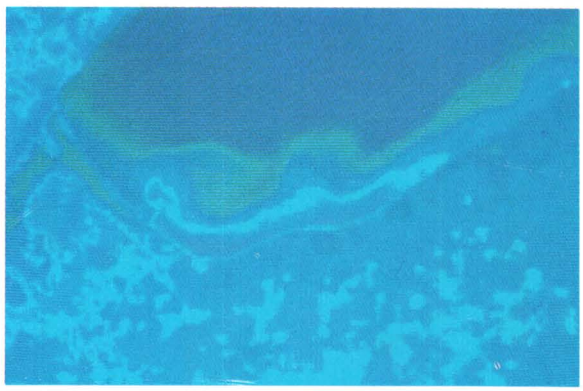

FIGURE 102.—Density-sliced image using color to show turbidity.

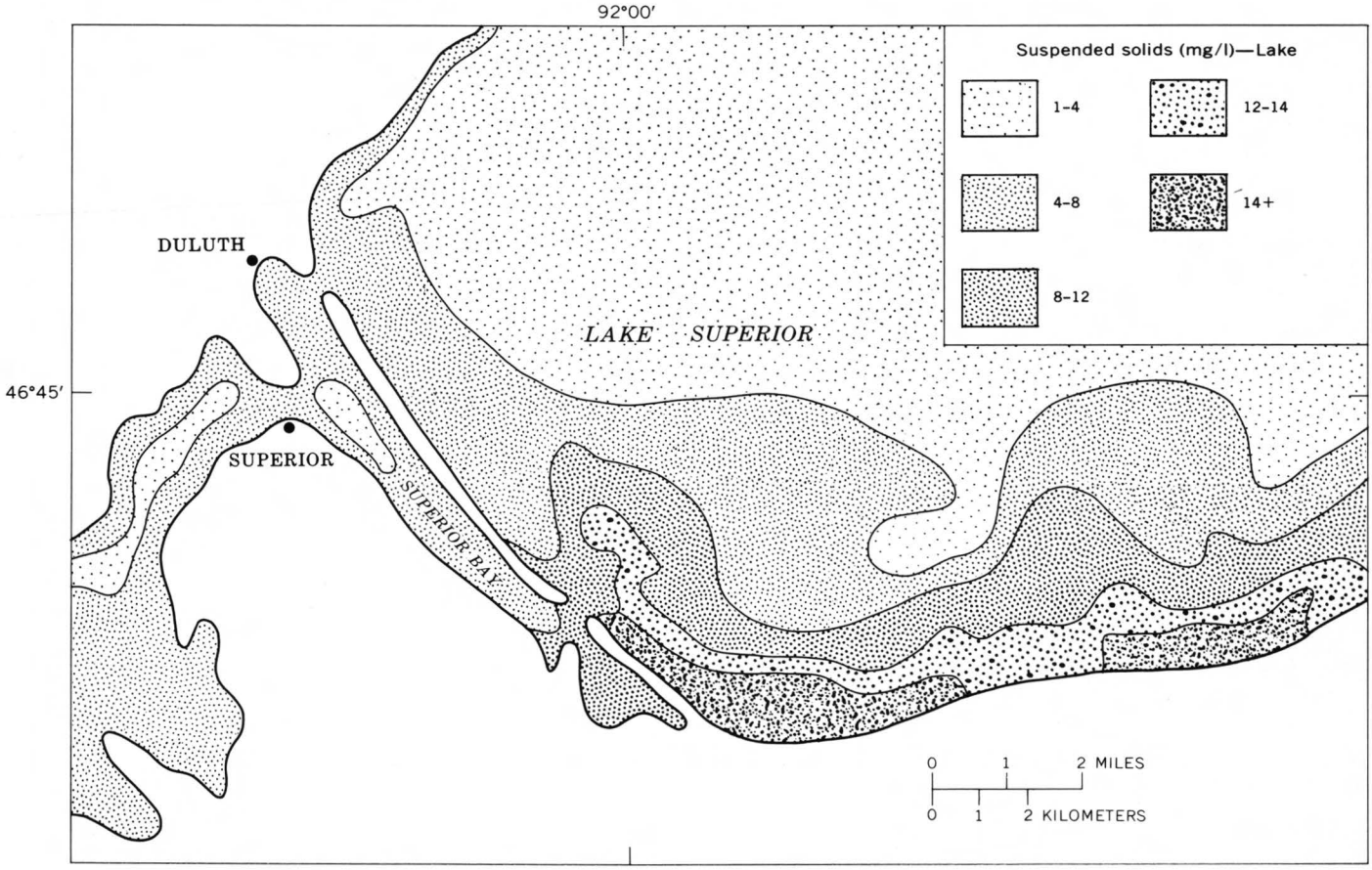


FIGURE 103.—Harbor and lake image-density levels identified by corresponding turbidity levels on ERTS–1 image 1434–16244, band 5, Sept. 30, 1973.

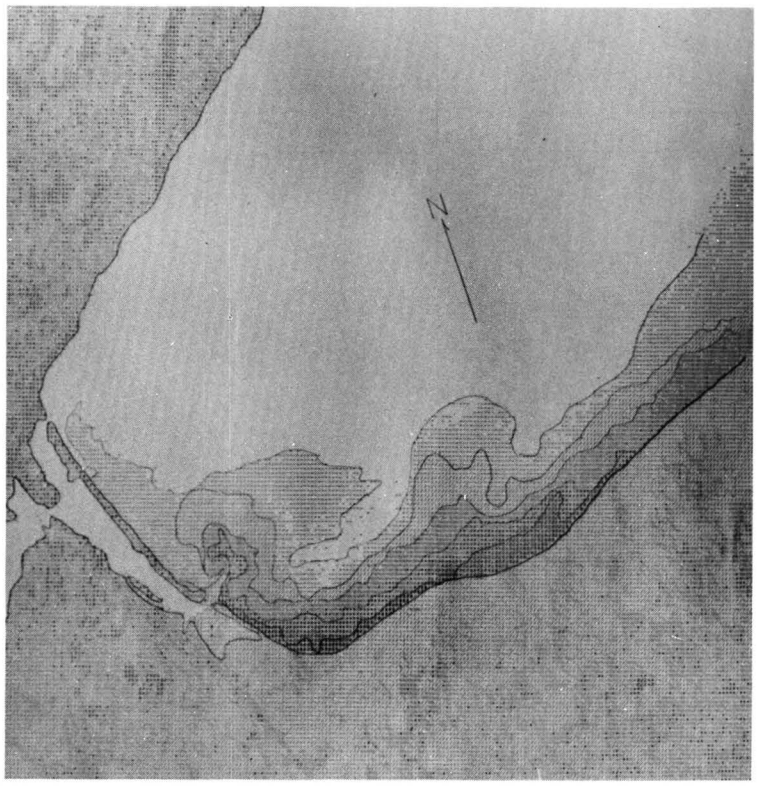


FIGURE 104.—Computer printout of image-density levels from computer compatible tapes of ERTS–1 image, 1434–16244.

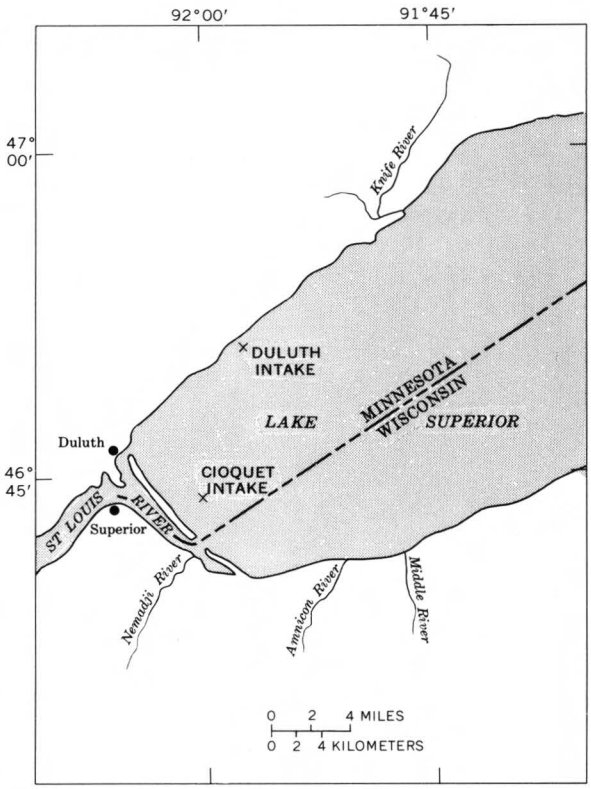


FIGURE 105.—Index map of the Lake Superior study area.

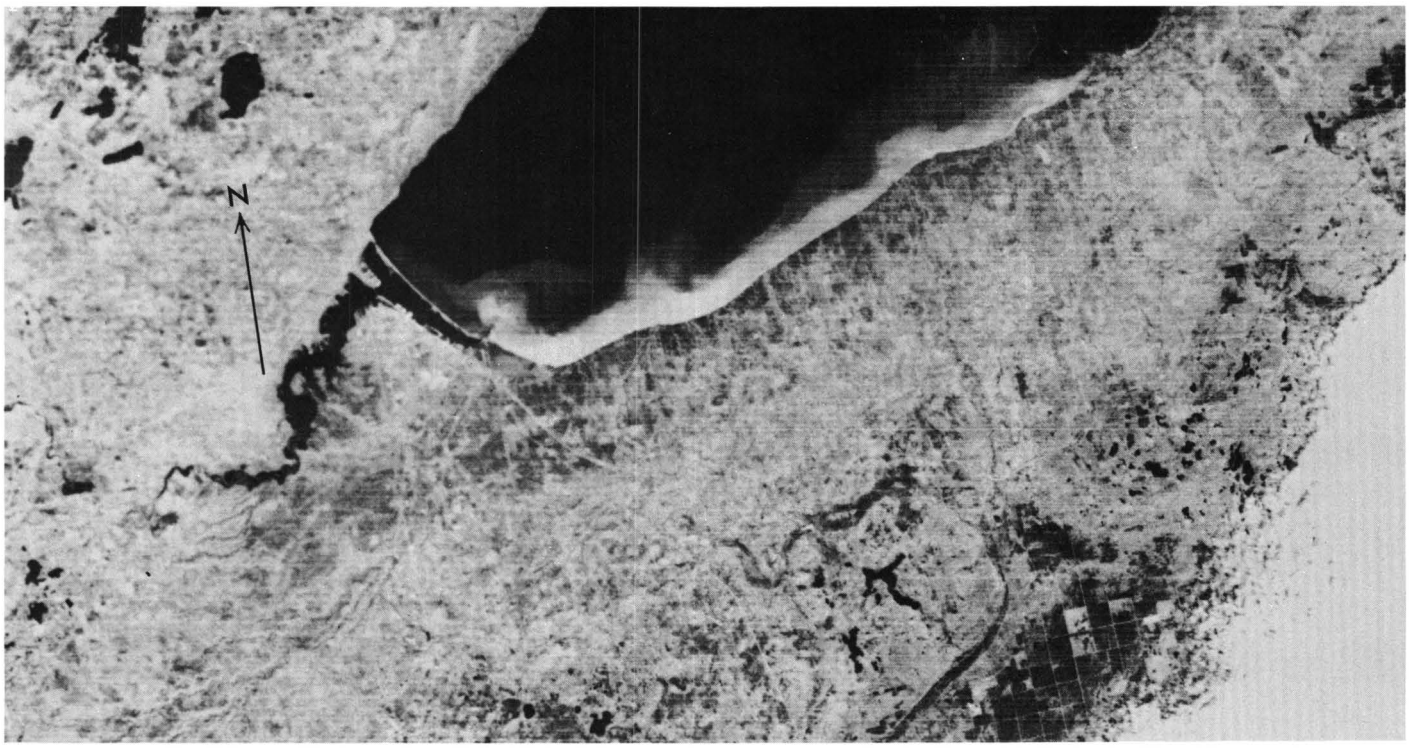


30SEP73 C N46-02/W091-32 N N46-00/W091-24 MSS 5 D SUN EL37 AZ151 192-6051-N-1-N-D-2L NASA ERTS E-1434-16244-5 01

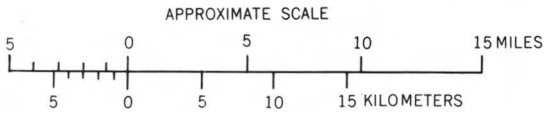


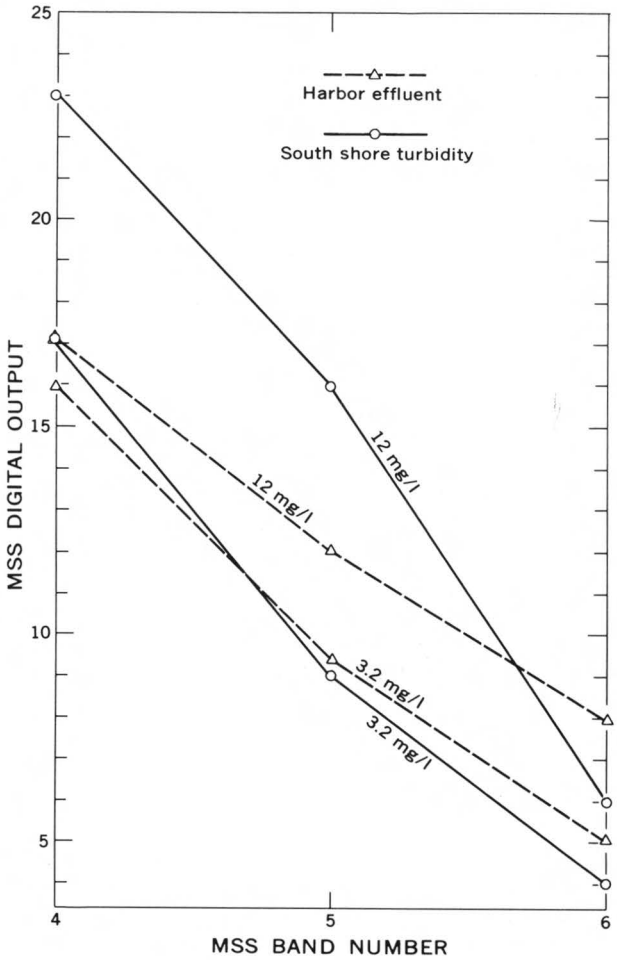


FIGURE 106 (above).—Part of ERTS–1 image 1434–16244, band 5, showing the Lake Superior study area.

FIGURE 107 (left).—Graph showing variation in MSS band signals.

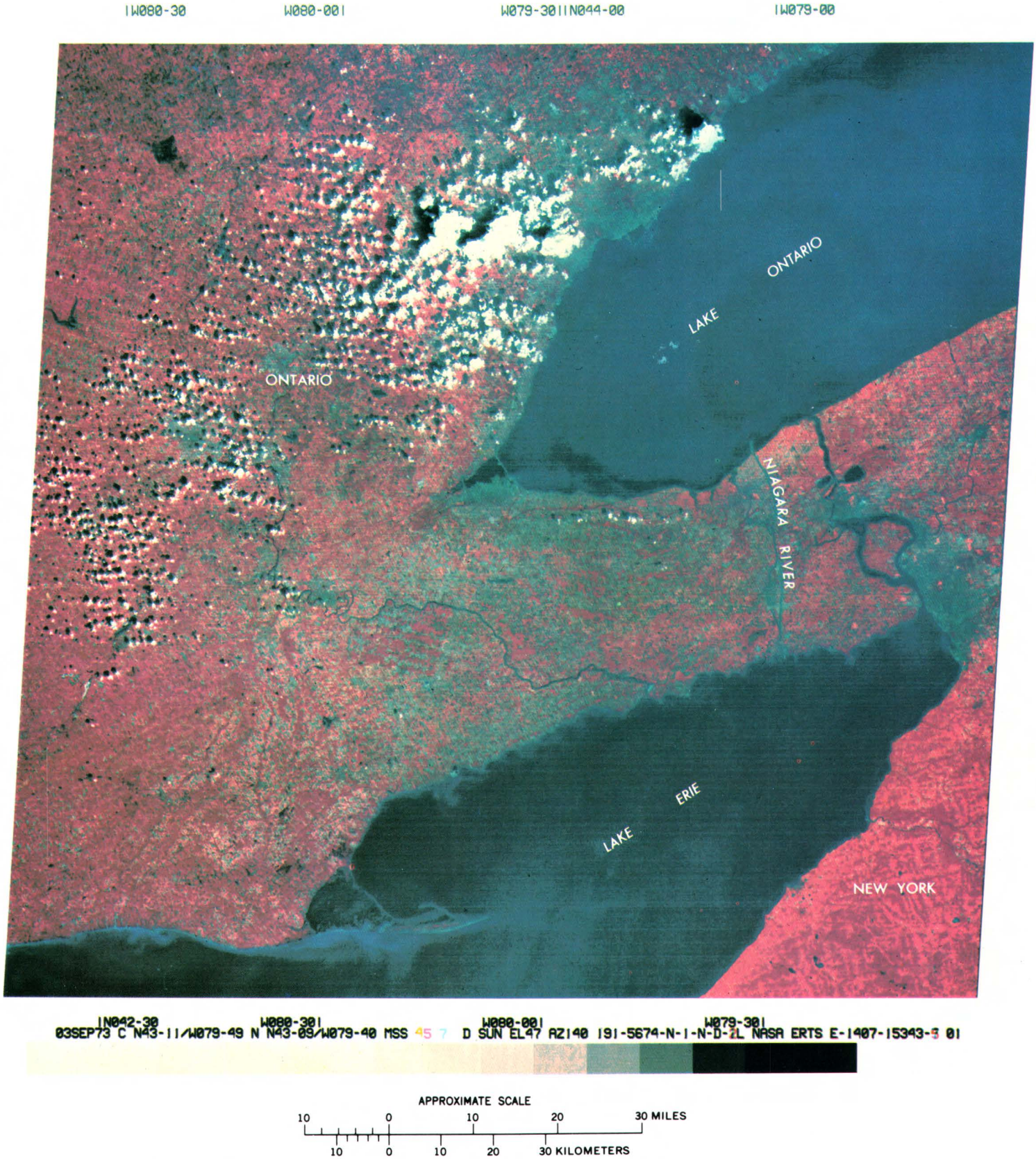


FIGURE 108.—Annotated color composite ERTS–1 image of the Lake Ontario-Niagara River area on Sept. 3, 1973 (1407–15343).

# DYNAMICS OF SUSPENDED-SEDIMENT PLUMES

By Edward J. Pluhowski,
U.S. Geological Survey

On the south shore of Lake Ontario, large turbidity features are frequently visible on ERTS imagery (Pluhowski, 1973). About 91 percent of the inflow to Lake Ontario enters the lake along its southern shoreline, 86 percent from the Niagara River alone. Thus the principal sediment and nutrient load enters Lake Ontario from the south (fig. 108).

The movement and fate of suspended material entering the lake can be determined by scrutinizing the large turbidity features generated at the mouths of the following watercourses: Welland Canal, Niagara River, Genesee River, and Oswego River. Turbidity plumes are also created by a favorable juxtaposition of wind, waves, and shoreline orientation in combination with high lake levels and exposed coastal headlands. Shoreline erosion generated by this unique combination of factors will result in extensive nearshore turbidity plumes along coastal reaches of the lake.

Examples of heavy beach erosion and highly turbid longshore currents are illustrated in the imagery shown in figures 109 and 110 obtained Apr. 12 and 29, 1973, respectively. Turbidity readings of 400 JTU and 420 JTU were obtained on Apr. 12, 1973, in the narrow band of milky white nearshore waters between the Welland Canal and Niagara River. These were by far the highest turbidity readings obtained in this study to date. Extensive beach erosion is shown in the imagery for April 12 and 29 in all shoreline areas except those immediately east of the Niagara River mouth. On both occasions an eastward-trending wave train pounded the southern shore of the lake. However, the northwest orientation of the Niagara River jet in Lake Ontario acted as a barrier to the ambient wave train, effectively shielding part of the New York State shoreline from erosive wave action.

Three distinct turbidity zones were depicted off the New York State shoreline on Apr. 29, 1973 (fig. 110). These consisted of a narrow but highly turbid littoral zone, an intermediate zone of much lower turbidity,

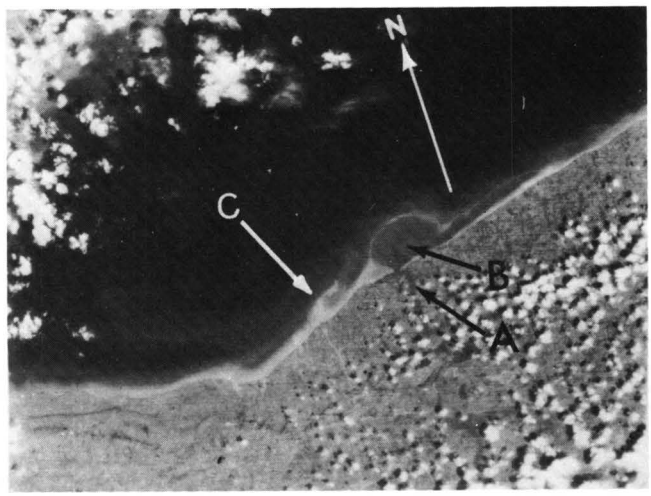


12APR73 C N43-14/W079-53 N N43-12/W079-45 MSS 5
D SUN EL48 AZ139 191-3666-N-1-N-D-2L
NASA ERTS E-1263-15361-5 01

FIGURE 109.—Part of an ERTS–1 image showing sediment plumes in Lake Ontario on Apr. 12, 1973 (1263–15361, band 5). A, Niagara River; B, Niagara River plume; and C, Welland Canal plume.

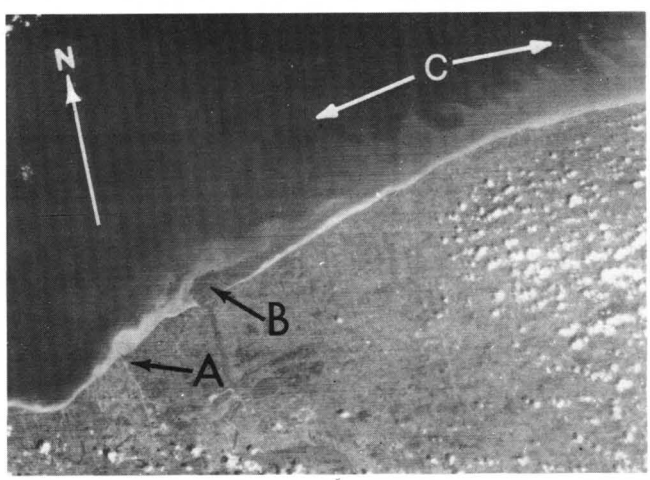


29APR73 C N43-21/W078-28 N N43-19/W078-16 MSS 5
D SUN EL54 AZ135 191-3903-N-1-N-D-2L
NASA ERTS E-1280-15302-5 01

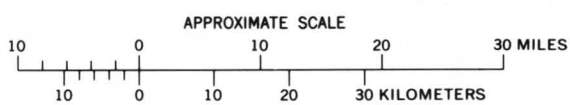


FIGURE 110.—Part of an ERTS–1 image showing sediment plumes in Lake Ontario on Apr. 29, 1973 (1280–15302, band 5). A, Welland Canal; B, Niagara River plume; and C, offshore zone of turbulent mixing.

and a relatively clear-water (dark) offshore zone. Of special interest is the zone of turbulent mixing between the intermediate and offshore clear-water zones as shown by the band of wavelike turbidity features in figure 110. The dynamic mechanism triggering these "turbidity waves" is unknown, but the amplitude and trend of the waves suggest the existence of a large westward-moving offshore current rather than an apparent eastward-moving longshore current.

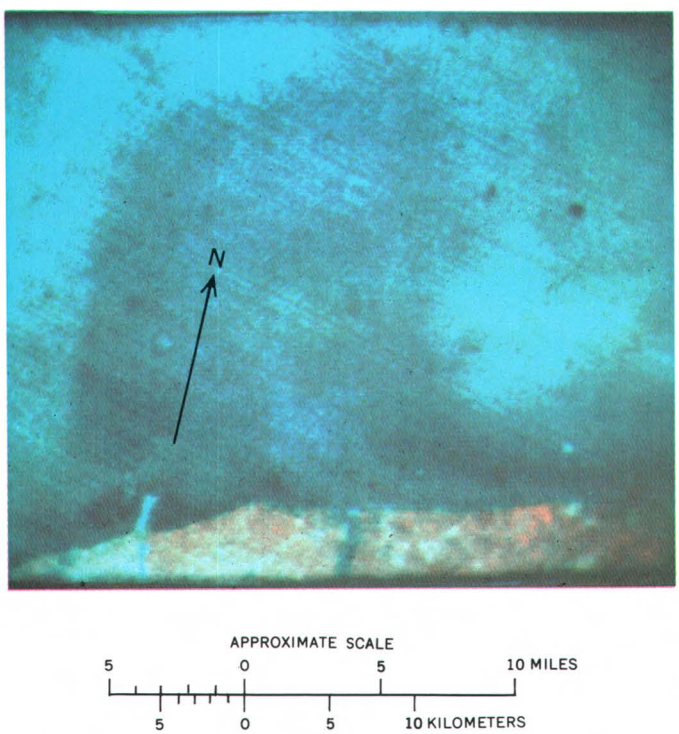


FIGURE 111.—Part of an ERTS–1 image, made on Sept. 3, 1973, and enlarged and color enhanced by Stanford University's ESIAC, showing the Niagara River plume (1407–15343).

Many factors affect the size and shape of large turbidity features such as the Niagara River or Genesee River plumes, the most important in large quiescent water bodies such as Lake Ontario being wind speed and direction, volume of runoff, and differences between the levels of turbidity of the discharging watercourse and the receiving water body. By way of illustration, on Apr. 29, 1973 (fig. 110), under the influence of brisk west-northwest winds, a strong eastward-moving longshore current was generated. The shearing effect of this current on the northward-moving Niagara River plume is shown in the image. The plume extended only 3.2 km offshore, but it was identifiable for a distance of at least 13 km downwind along the New York shoreline. The total surface area of the plume on Apr. 29, 1973, was 34 km$^2$.

Gentle offshore winds on Sept. 3, 1973, on the other hand, greatly expanded the size of the Niagara River plume. The southerly winds on that day reinforced the northward-flowing plume. The offshore winds pushed the leading edge of the Niagara plume about 30 km into the lake. As shown in figure 111, a large clear-water (dark) plume developed and covered 514 km$^2$ of lake surface.

# WATER-MANAGEMENT MODEL OF THE FLORIDA EVERGLADES

By Aaron L. Higer, Edwin H. Cordes, and A. Eugene Coker,
U.S. Geological Survey

The water supply for southeast Florida, which has a population of 2.5 million, depends upon the retention of water in four major impoundment areas in the Everglades water basin (figs. 112, 113): (1) Lake Okeechobee, (2) Conservation Area No. 1, (3) Conservation Area No. 2, and (4) Conservation Area No. 3. Shark River Slough, an important source of water for the Everglades National Park, at the downstream end of these interconnected water bodies, also depends upon overland flow from adjoining Conservation Area No. 3. An accurate accounting of the amount of water in surface storage is difficult because land-surface profiles are not available. The shallow water depths of 0.3 to 1.0 m, the flat terrain, the abundant vegetation, and the vast area of 3,600 km$^2$ of the Everglades preclude the feasibility of determining accurate volumes by conventional methods. In the conservation areas and the Shark River Slough, the water does not pond in the usual manner but slowly flows over the gently sloping land surface.

Several water-budget studies for the conservation areas are underway by the U.S. Army Corps of Engineers and the Central and Southern Florida Flood Control District. Elements that need more accurate definition in the existing water-budget studies are rainfall, evapotranspiration, seepage losses, and surface storage.

The ERTS water-management model uses the DCS to provide quantitative in-situ data on the elevation of the water surface and MSS data to provide information on the areal extent of the water surface (Higer and others, 1973). Knowing the relation between the surface-water area and surface elevation for the range of water levels, the storage can then be calculated (figs. 114, 115). In addition, knowing the change in storage and the surface inflow and outflow (input and output) from the system, it is possible to calculate evapotranspiration and seepage (Higer and others, 1974).

At present the DCS data are transmitted from the Everglades stations to the satellite and relayed via two ground tracking stations to the Goddard Space Flight Center, Greenbelt, Md. The data are then transmitted by teletype to the Miami office of the U.S. Geological Survey. The perforated teletype tape is then processed daily through a minicomputer to convert the data to engineering units and place it into the format requested by the Corps of Engineers. The data are then transmitted to the Corps of Engineers, Jacksonville, Fla., by telecopier. The time required for the transmission of the data from the Everglades via the satellite, the NASA tracking stations, and the U.S. Geological Survey to the Corps of Engineers is less than 2 h.

The importance of the space-relayed data can be shown by a comparison of the accuracy and frequency of those data received through the Miami teletype with data from the existing remote radio-transmission systems in southern Florida. The great line-of-sight distances involved in the radio-transmission systems often provide "rare" and garbled data messages. The frequent meteorologic disturbances in southern Florida prevent the transmission of the accurate synoptic information on rainfall and water stage that is essential for managing the water for optimum conservation. ERTS–1 provides the U.S. Geological Survey with five transmissions per day of these parameters and warns when any DCP recorder becomes faulty, so that it can be repaired within 24 h. This enhances the opportunity for a constant flow of information and makes it possible for the Corps of Engineers to make daily decisions to optimize its water-control policy to conserve a greater proportion of the seasonally deficient water resource.

FIGURE 112.—Color composite ERTS–1 image of the Everglades National Park area of Florida (1242–15240).

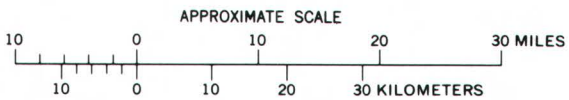


FIGURE 113.—Annotated ERTS–1 image showing water-management conservation areas in the Everglades National Park area of Florida (1242–15240, band 6).

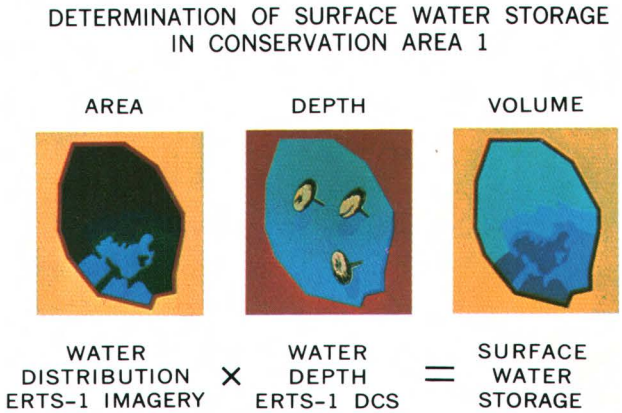


FIGURE 114.—Determination of surface-water storage in Conservation Area No. 1. Schematic diagram of the use of space-relayed data to calculate surface-water storage. ERTS data from three successive passes on Feb. 14, Mar. 4, and Mar. 22, 1973, of Conservation Area No. 1 are used to demonstrate the feasibility of determining surface-water storage.

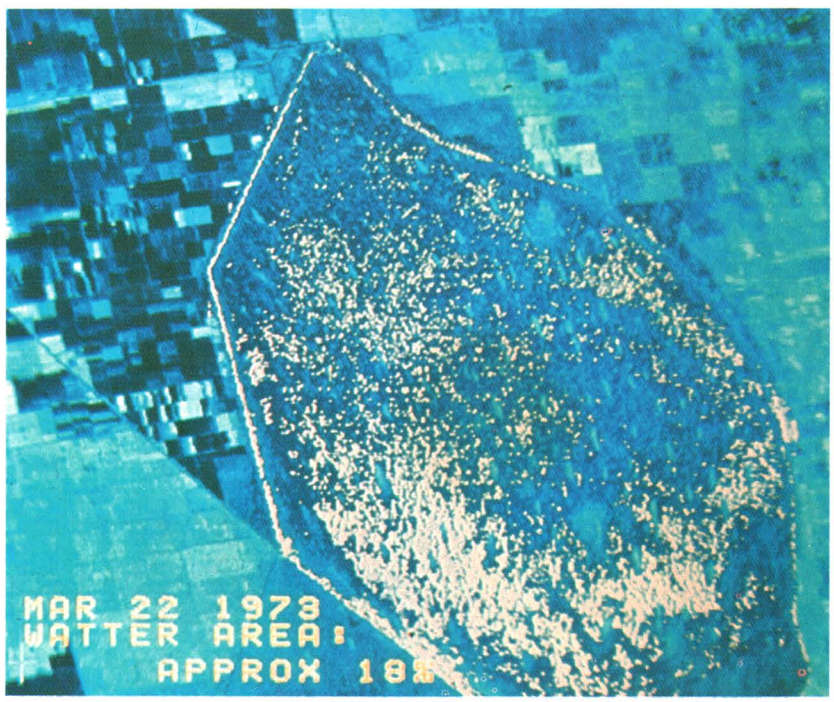


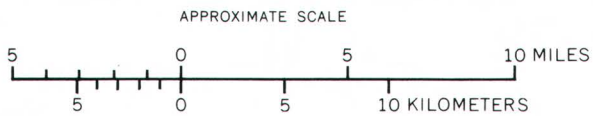


FIGURE 115.—Electronically processed part of ERTS–1 image 1242–15240 of Conservation Area No. 1. Each dot represents 4 ha of surface water.

# SUSPENDED SEDIMENT IN GREAT SLAVE LAKE, NORTHWEST TERRITORIES, CANADA

By Donald R. Wiesnet,

National Oceanic and Atmospheric Administration

Great Slave Lake, during the short summer season of the Northwest Territories, is relatively unspoiled and unpolluted, but naturally occurring silt and other suspended sediment do surge into the lake from the nearby rivers. The unfrozen season is short in this arctic area, and runoff occurs only in the summer months during the snowmelt season. In the ERTS–1 image in figure 116, sediment-laden Slave River is shown discharging turbid water into Great Slave Lake.

The delta at the mouth of the river is evident, as are the distributaries. The highest concentration of suspended sediment (lightest tone) is coming from the Old Steamboat Channel, the southernmost channel visible. Note the deep blue of the Gaudet Bay and other smaller bays northeast of the delta and compare it with the lake waters adjacent to the bays. Note also the small oxbow lake east of the delta and the intermediate blue color at that point.

Winds at 10 kn were prevalent over the lake as ERTS–1 passed over. These winds distributed the sediment in a pattern extending northeast along the shoreline, thus reflecting a northeast longshore current. The sharp westerly prong of sediment just off the northernmost channel, Resdelta Channel, occurs at a point where a sandbar is charted. The effects of a moderate southwesterly wind on the water clarity of the lake are clearly demonstrated by this image. The west half of the lake is extremely clear and free of turbid water.

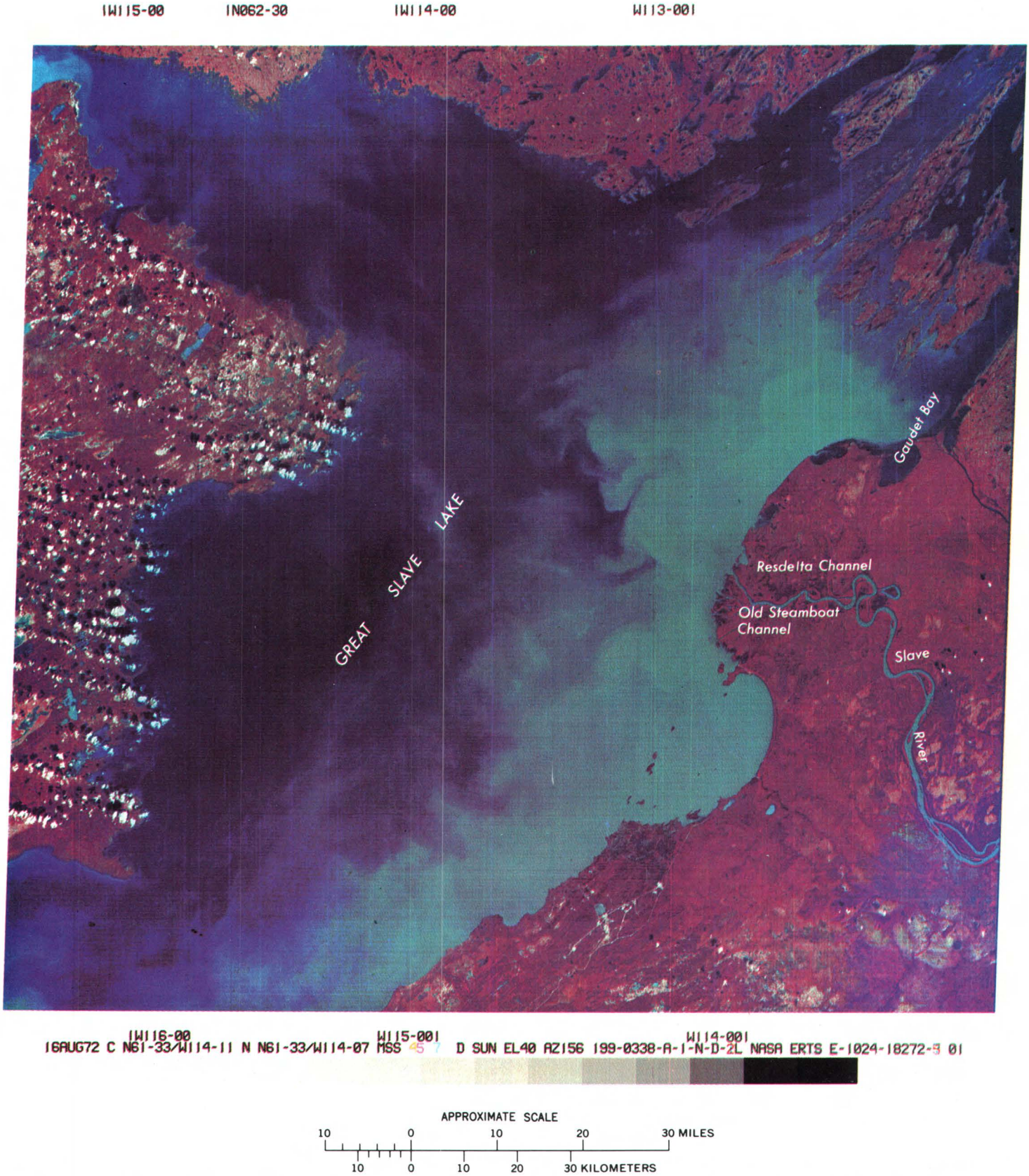


FIGURE 116.—Annotated color composite ERTS–1 image of the Great Slave Lake area of the Northwest Territories, Canada (1024–18272).

# DISCOVERY AND SIGNIFICANCE OF THE BEECH GROVE LINEAMENT OF TENNESSEE

By G. K. Moore and Este F. Hollyday,

U.S. Geological Survey

Examination of a color composite ERTS image of central Tennessee revealed a major lineament that may have considerable geologic, hydrologic, and economic importance. It was named for the community of Beech Grove (Hollyday and others, 1973), where the lineament crosses Interstate Highway 24 (open arrow, fig. 117). It extends from Lincoln to Smith Counties, Tenn. (fig. 118), a distance of about 165 km. Along most of its length, the lineament is less than 2 km wide, but in a few localities, closely spaced, parallel lineations suggest a fracture zone about 6.5 km wide.

Along the lineament, hills are steep and covered by forests. Most culture is in the relatively flat stream valleys. The contrast between agricultural land and forest land is fairly sharp on October ERTS imagery, and thus there is good contrast between the valleys and the uplands. Also, the angle of solar illumination is relatively low in October compared to the spring and summer months, so that topography is somewhat enhanced by shadowing on the image (fig. 117).

The terrain has more of a three-dimensional appearance (because of lower Sun angle) in the Dec. 28 image (fig. 119), but there is somewhat less contrast between forest land and agricultural land because all deciduous vegetation is dormant. The net effect is that the Beech Grove lineament can also be seen easily on the December image.

The Beech Grove lineament is formed mainly by the alignment of nine separate stream valleys. The combination of land-use differences and topographic enhancement by shadowing allows the lineament to be seen easily, despite the fact that it is not continuous. The trace of the lineament is obscured by woods in the upland areas, but its linearity and continuity are well expressed by the valleys.

The Beech Grove lineament is not obvious on maps or on either low- or high-altitude aerial photographs. Furthermore, it was not recognized as having regional extent during detailed geologic mapping on the ground. The lineament can be seen and traced on Skylab photographs, but its continuity and possible significance are not as obvious as on ERTS imagery; the synoptic view of ERTS imagery was necessary for detection of this lineament.

Central Tennessee is underlain by nearly flat-lying, dense, interbedded limestones and impure limy sediments of Ordovician to Mississippian age. The Chattanooga Shale separates these systems and is an important marker bed.

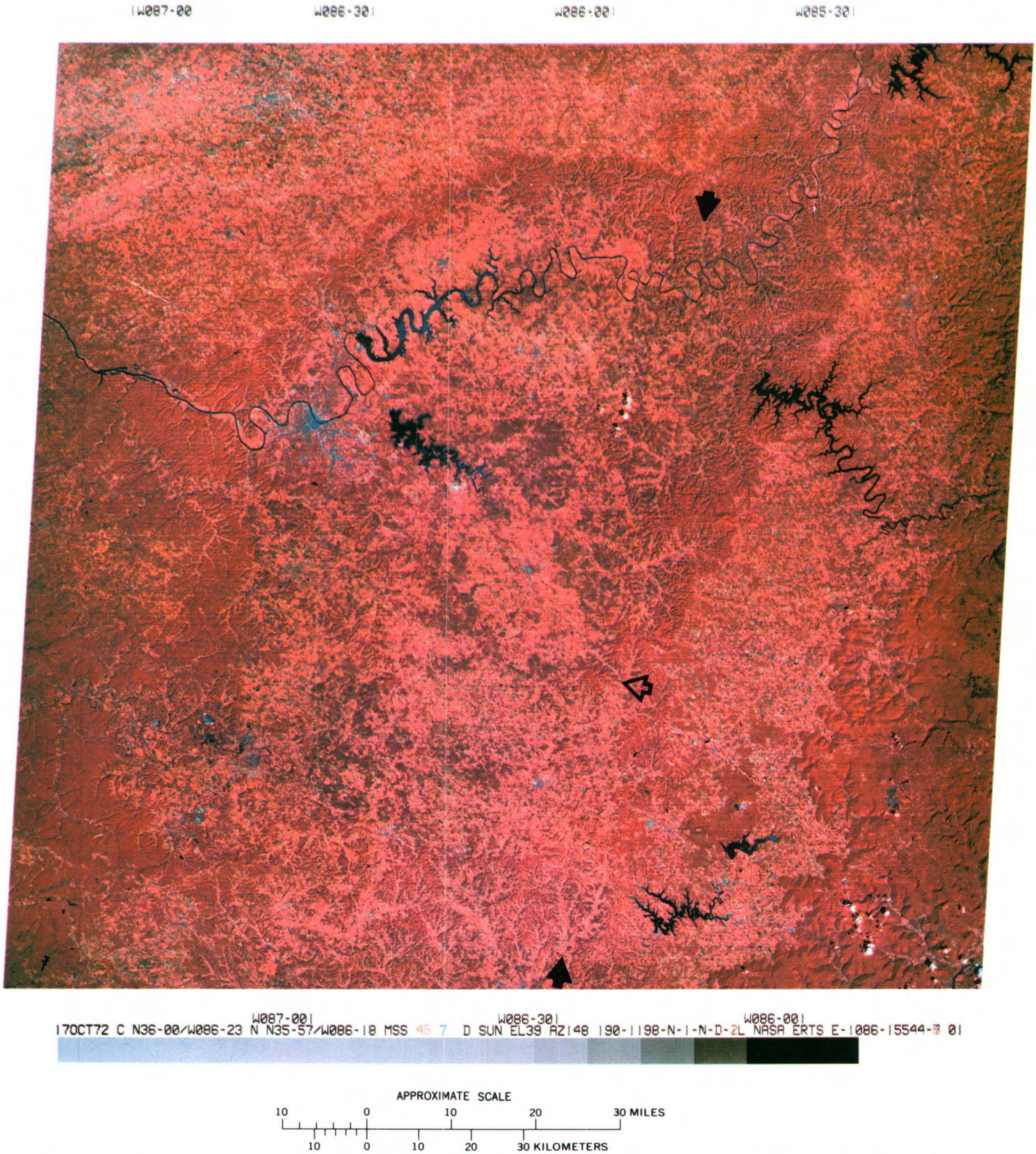


FIGURE 117.—Annotated color composite ERTS–1 image of central Tennessee on Oct. 17, 1972, showing location of the Beech Grove lineament (1086–15544). The two black arrows indicate the lineament, and the arrow below center marks the community of Beech Grove where the lineament crosses Interstate Highway I–24.

Along part of its length, the Beech Grove lineament may consist of a group of parallel normal faults. This is not conclusive, however, and outcrops to the north and south of Beech Grove show no evidence of displacement. Jewell (1947) stated that a few faults are known but that the throw generally is small. Thus most of the lineament may best be characterized as a group of closely spaced, parallel fractures. Small movements may have occurred along these fractures, but they only broke or brecciated the nearby rocks with no significant displacement, and there is no evidence of movement since Paleozoic time.

Four small zinc-bearing veins at the surface in Rutherford and Cannon Counties are located within 6.4 km of each other, but all four veins are within 3.2 km of the axis of the lineament. All these deposits are associated with broken and brecciated rocks (Jewell, 1947). In the veins the most common mineral of economic value is sphalerite.

The new Elmwood mine of the New Jersey Zinc Co. in Smith County is 3.2 km east of the axis of the lineament and 48 km north of these four veins. The zinc ore at this location occurs in brecciated Knox Dolomite of Early Ordovician and Late Cambrian age. The entire lineament is a prospect for concentrations of sphalerite.

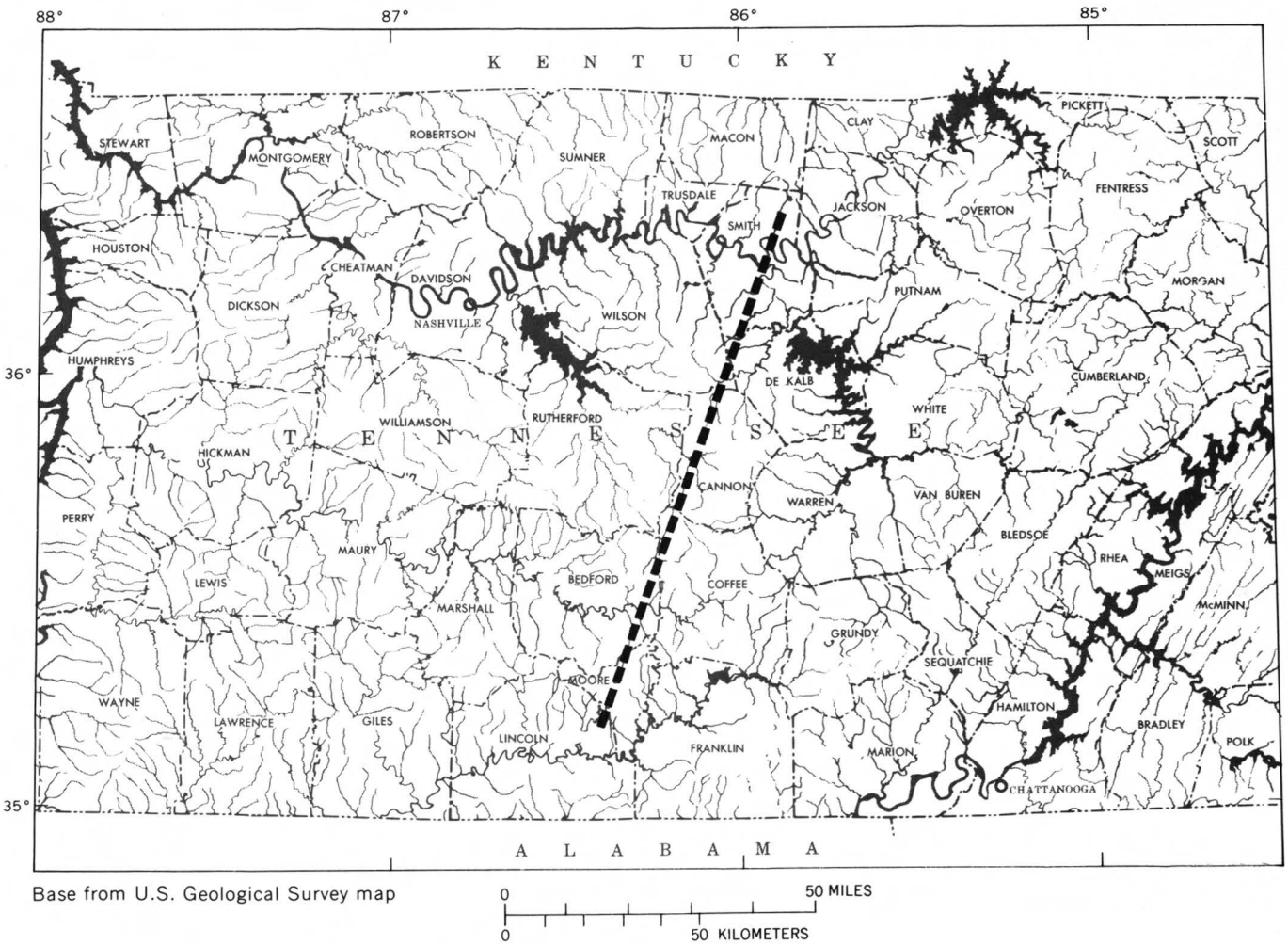


Base from U.S. Geological Survey map

0 50 MILES

0 50 KILOMETERS

FIGURE 118.—Index map showing the location of the Beech Grove lineament.

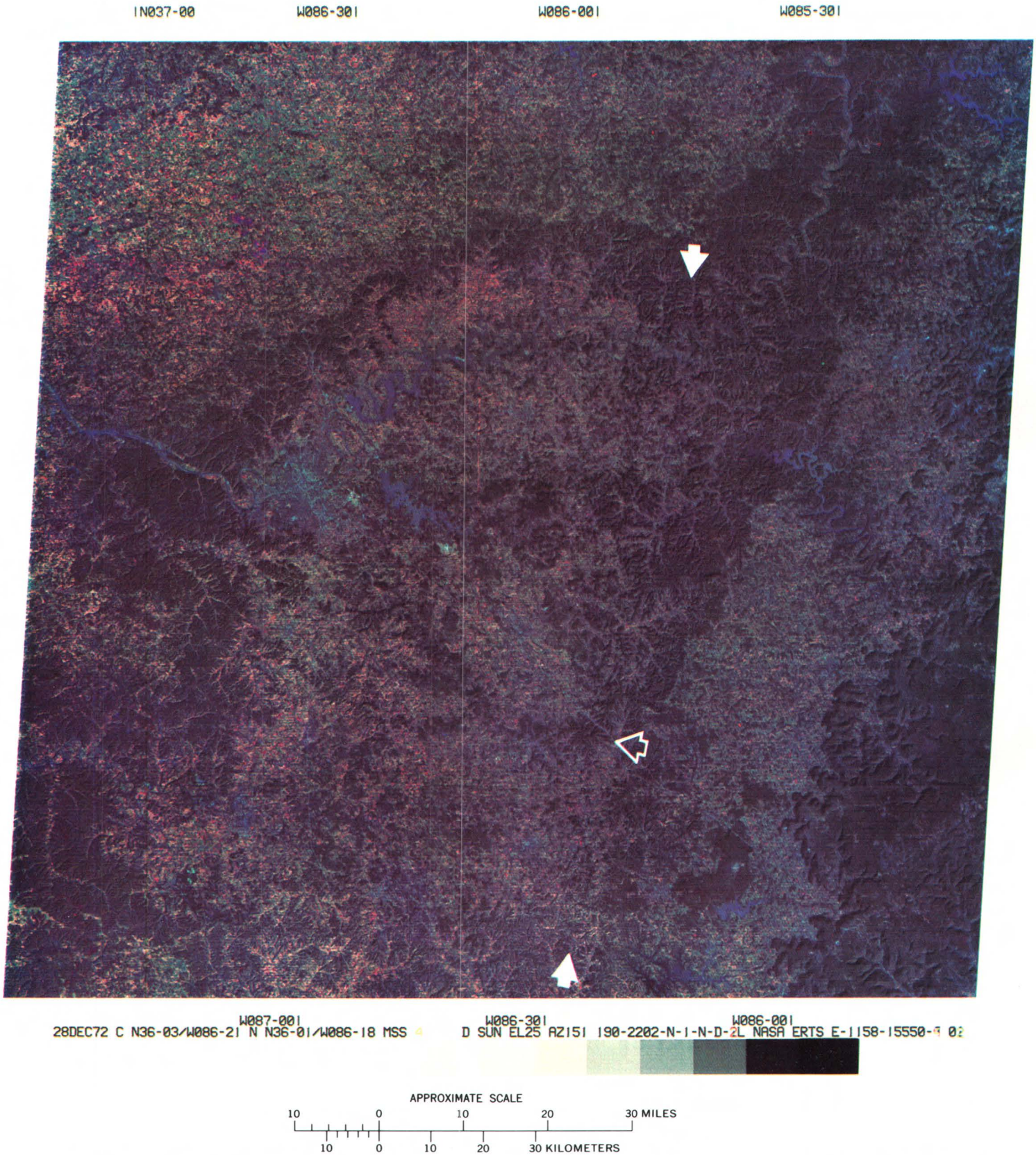


FIGURE 119.—Color composite ERTS–1 image of central Tennessee on Dec. 28, 1972 (1158–15550). The Beech Grove lineament can also be seen easily on this image and is indicated by the arrows.

R. H. Hershey, Tennessee State Geologist, has stated that the Elmwood mine of the New Jersey Zinc Co. is at the intersection of the Beech Grove lineament and one of three minor transverse lineaments; other minor lineaments also have intersections in Cannon County and Moore County. The latter two sites were termed "under-explored for the potential they have" (Nashville Banner, 1973). The three minor lineaments were interpreted from the October ERTS image (fig. 119).

Several companies have expressed an interest in these prospects; one company has begun active exploration (Robert Manning, oral commun., 1974), but results are not available.

The hydrologic significance of the Beech Grove lineament is difficult to determine because streamflows, well yields, and spring flows all have large variations in dense fractured limestone terranes. For example, most of the streams that follow the lineament have either uncommonly large or small flows of water at any particular time, but so do many other streams that are remote from the lineament. Also, the yields of wells within 3 km of the lineament range from less than 0.06 l/s to more than 6.3 l/s; a similar range in well yield also may be found in almost all other areas of similar size in central Tennessee.

Many caves, sinkholes, and springs occur near the lineament, but these features commonly are abundant in valleys at the base of steep slopes, the same topographic position as most of the lineament.

Both test drilling of wells and closely spaced measurement of streamflow along the streams will be needed to fully evaluate the hydrology of the Beech Grove lineament. The broken and brecciated rock along the lineament should serve both as a storage reservoir and as an avenue of movement for ground water.

In some cases, ground water may move along the lineament from one stream basin to another, beneath drainage divides. Movement is always from a small stream at a relatively high altitude to a larger stream at a lower altitude.

Streams that follow the lineament may lose water to the ground in upstream reaches and gain water in downstream reaches. These streams would be expected to have either uncommonly large or small flows at any point, depending on the relationship of stream-channel altitude to water-table altitude.

# WESTERN LAKE SUPERIOR ICE

By Michael Sydor,

University of Minnesota

Winter shipping on the Great Lakes is an ever-increasing possibility, particularly with the advent of the supercarriers on the Great Lakes. Duluth-Superior is a major port. Because of economy of shipping by water, considerable expenditure has been incurred by the Federal Government and private interests in attempts to extend the shipping season into the winter months. Navigation on the open lake is not often a problem, though better ice forecasting is essential. The problem generally arises in the locks, the harbors, and from severe ice packing that blocks the entries to locks and harbors. More frequent coverage by ERTS-type spacecraft would greatly aid ice forecasting. The ERTS image for Apr. 4, 1973 (fig. 120), shows a typical icepack on the western arm of Lake Superior that completely blocks the entry to the Duluth-Superior harbor. Notice, however, that the harbor itself is entirely ice free.

Forecasting ice growth and predicting ice packing are generally based on consideration of the heat budget for the ice sheet (Maykut and Untersteiner, 1971). This in turn requires measurements of light albedo for the entire ice cover. ERTS data allow accurate measurement of albedo and also allow delineation of the severely packed ice (fig. 121). Figure 122 shows the light albedo for a harbor (bay) station and a lake station used in ice growth studies. Figure 123 shows the ice growth in the harbor.

Figure 124 shows an estimate of the fraction of the ice cover on the western arm of Lake Superior displaying highly packed characteristics. The corresponding values for the volume of the lake ice, estimated from heat-budget considerations and the ERTS data, allow a rough calculation of the average thickness of the icepack blocking the shipping lanes. The average icepack thickness at the opening of the shipping season was 60 cm, a mild year. The ice packing for the 1971–72 season was much more severe, and ice remained in the area until June 9, 1972 (Sydor, 1974).

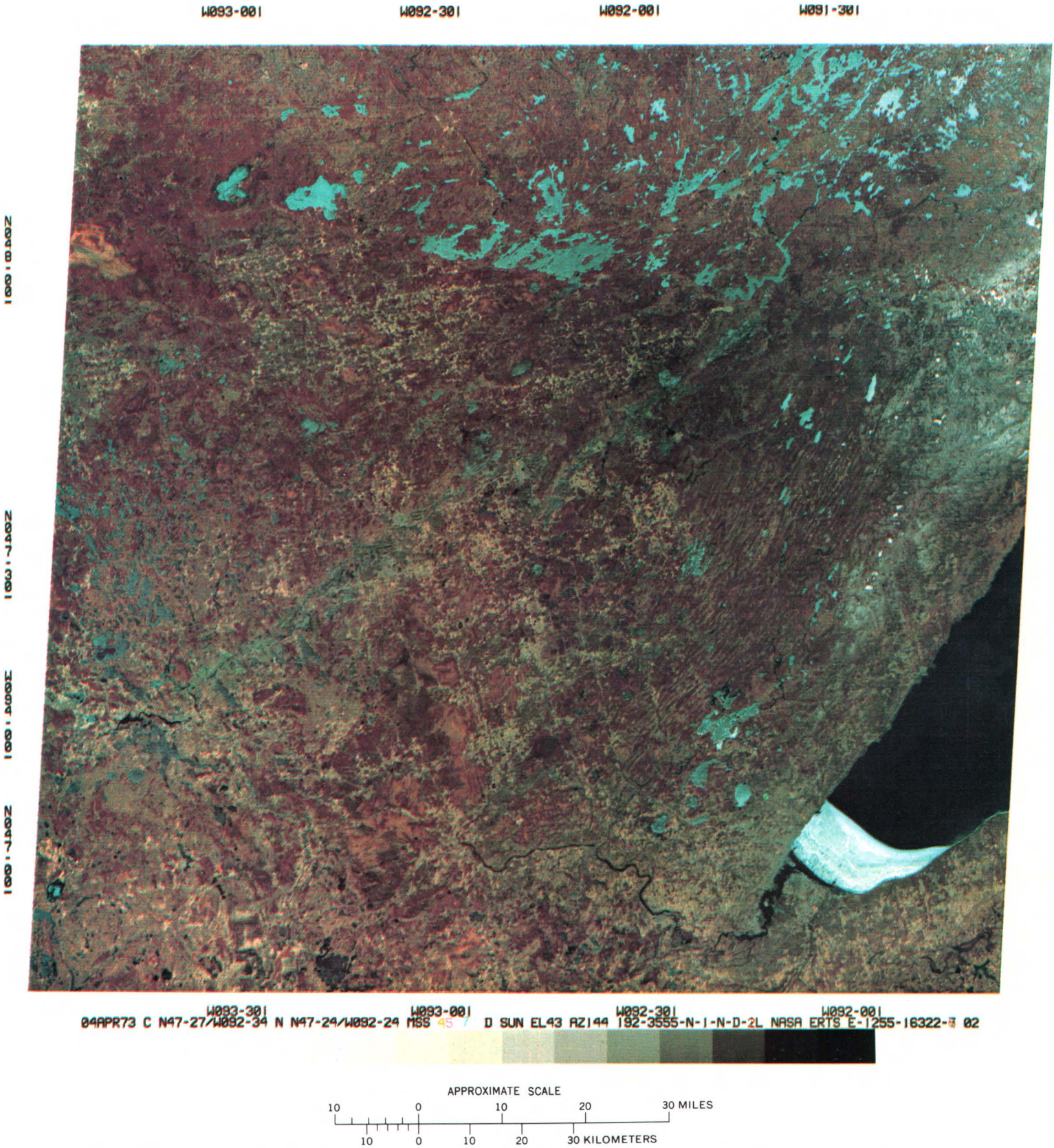


FIGURE 120.—Color composite ERTS–1 image of western Lake Superior showing a typical ice pack (1255–16322).

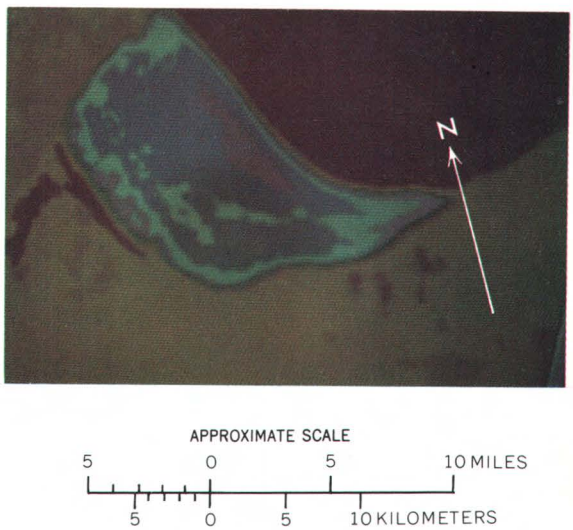


FIGURE 121.—Density-sliced ERTS–1 image of western Lake Superior derived from image 1255–16322. Color-density slicing helps differentiate areas of contrasting albedo of ice and identify areas of intense packing: rose, tightly packed; dark blue, packed; and light blue, least packed.

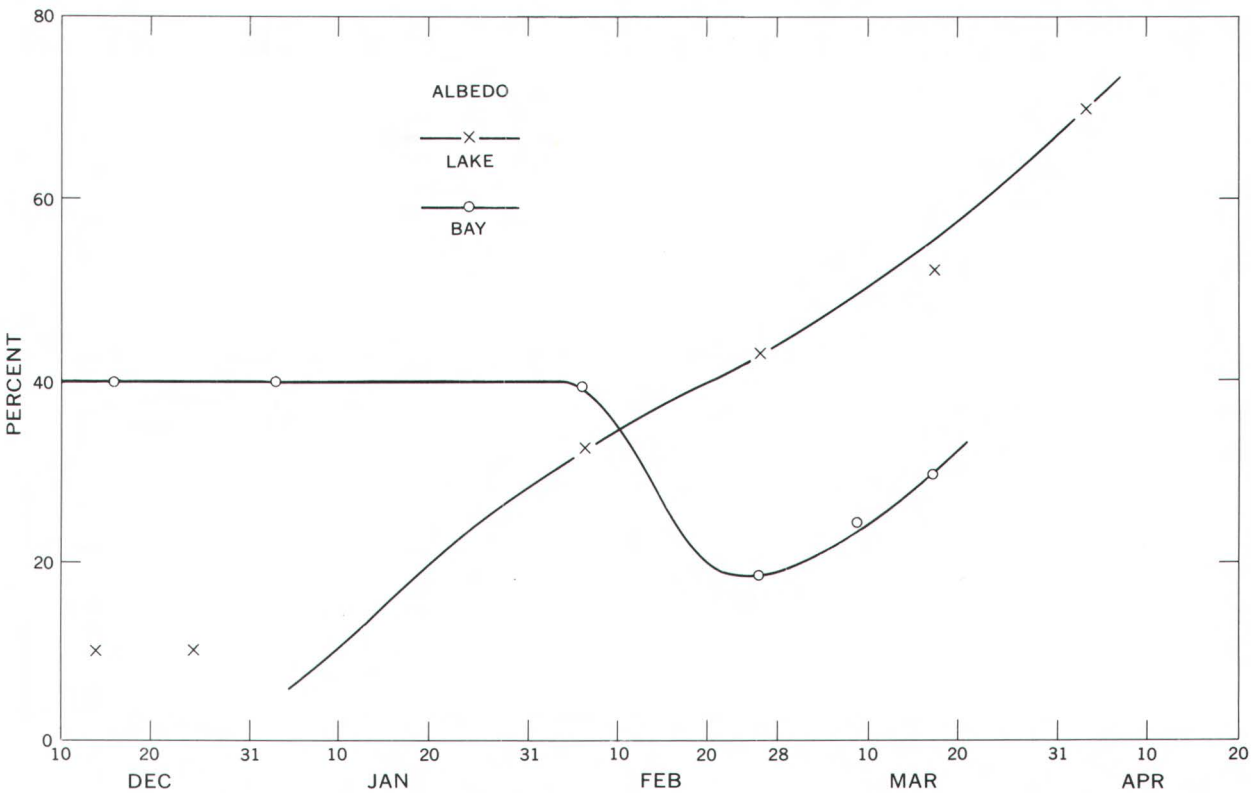


FIGURE 122.—Graph showing albedo at two stations, western Lake Superior.

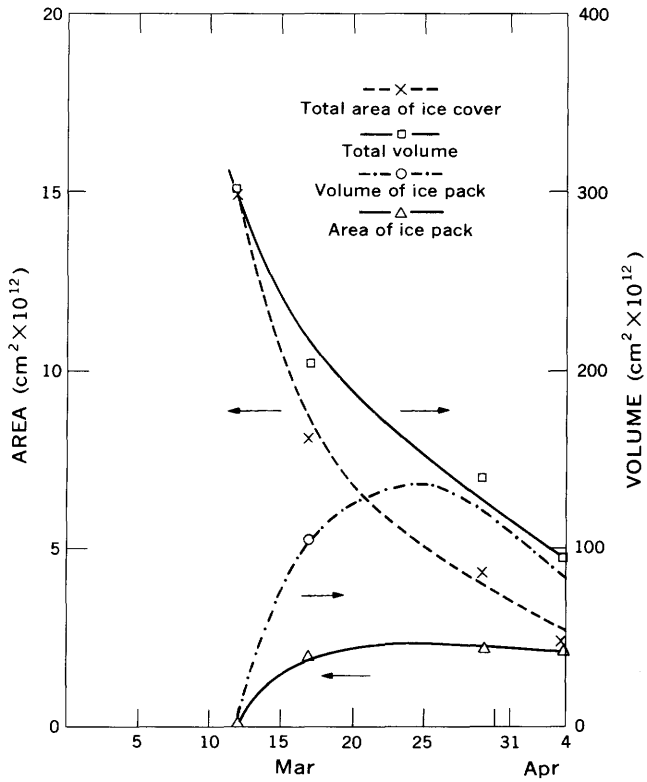


FIGURE 124.—Graph showing estimate of volume of ice cover that is highly packed, western Lake Superior.

FIGURE 123 (below).—Graph showing growth of ice in the Duluth-Superior harbor.

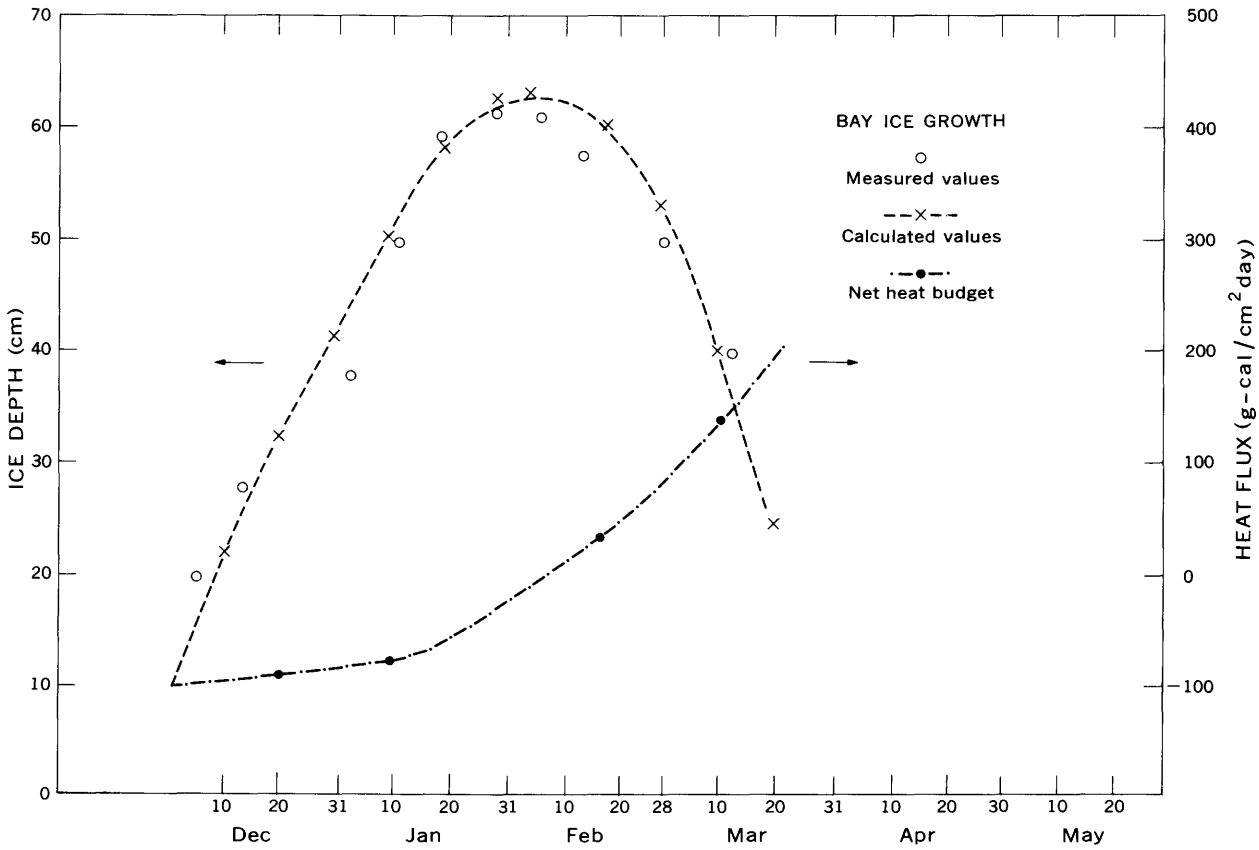

# MEASURING SNOW-COVERED AREA TO PREDICT RESERVOIR INFLOW

By Robert M. Krimmel and Mark F. Meier,

U.S. Geological Survey

About two-thirds of the population of the State of Washington live in the vicinity of Puget Sound. Approximately 80 percent of the electrical energy they consume is derived from hydroelectric power reservoirs that are fed by melting snow in the Cascade and Olympic Mountains. Regulation of this runoff is also vital for domestic water supply, dilution of wastes, and the maintenance of a healthy salmon and steelhead trout population. In order to produce the maximum amount of power and to satisfy all other demands on the water supply, it is important to be able to forecast the runoff, and this can be done by measuring the snow in temporary storage on the ground.

A mosaic of two color composite ERTS–1 images (fig. 125) shows this area from the Fraser River delta near Vancouver, British Columbia, south to the cities of Chehalis and Centralia, and from the east half of the Olympic Mountains on the left to the western part of the Cascades on the right. The cities of Everett, Seattle, and Tacoma are on the east side of Puget Sound, and Olympia is at the extreme south of this complex waterway. Major reservoirs include Ross and Diablo Lakes (upper right), Shannon and Baker Lakes (upper center), Alder Lake (lower right), Mossyrock and Mayfield Lakes (extreme lower margin), and Lake Cushman (southeast of the Olympic Mountains). Mount Rainier is the prominent snow-covered peak in the southeast part of the image.

Three spectral bands were combined to form this color composite image. Clean water appears black, silty water appears blue, snow appears white, and vegetation appears red.

Although these images were taken on July 29, 1972, note the large amount of snow still remaining in the mountains. The area of snow cover in nine important drainage basins in the Cascades (fig. 126) is being monitored from ERTS images using the Stanford Research Institute ESIAC, which uses an electronically digitized image, variable density masks, and a computer. The snow-covered areas in these basins at the time of this image are shown in the following tabulation:

| *Basin and name* | *Snow cover, Percent* |
|---|---|
| A. Thunder Creek | 44 |
| B. Cascade River | 33 |
| C. South Cascade Glacier | 85 |
| D. Stehekin River | 32 |
| E. Suiattle River | 20 |
| F. Sauk River | 39 |
| G. North Fork Skykomish River | 10 |
| H. South Fork Skykomish River | 9.1 |
| I. Snohomish River | 16 |

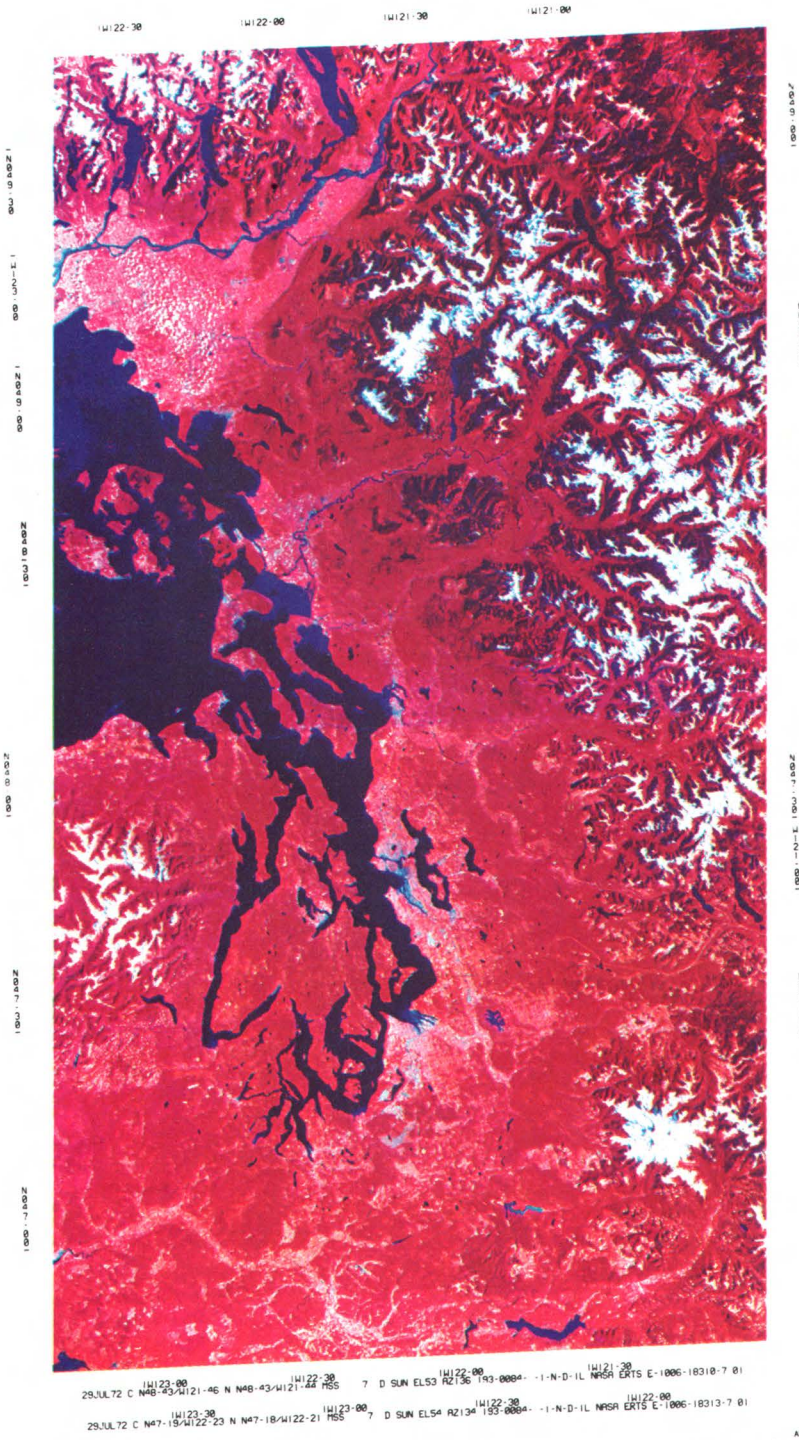


FIGURE 125.—Color composite ERTS–1 image mosaic of the Puget Sound region of Washington (1006–18310 and 1006–18313).

FIGURE 126.—Index map of Cascade Mountains drainage basins.

By carefully studying successive images and related measurements on the ground during the spring and summer seasons, hydrologists can determine the rate of change of snow-covered area and the amount of water stored as snow. The percentage of the basin covered by snow as a function of time is illustrated for four basins in figure 127. The snow-covered area during the ablation season is directly related to the volume of water stored as snow, and thus to the runoff to be expected. This allows predictions to be made on the availability of water from snowmelt for the rest of the summer. These data can be used by water managers to optimize the operation of reservoirs to balance hydroelectric-power production requirements and domestic and other water needs and to control floods. Areas where clearcutting forests is practiced—most noticeable in this image around Mount Rainier and south of the Olympics as rectangular or polygonal patches in forest lands—can appreciably alter the runoff from drainage basins and also affect the visibility of snow in the forested areas.

Evidence of the Puget lobe of the Pleistocene ice sheet can be seen on this image. The margins of the ice sheet that covered the Puget lowlands were roughly the east side of the Olympic Mountains, the west side of the Cascades, and the southern margin was roughly along the arc of lakes between the Olympics and Cascades south of Puget Sound.

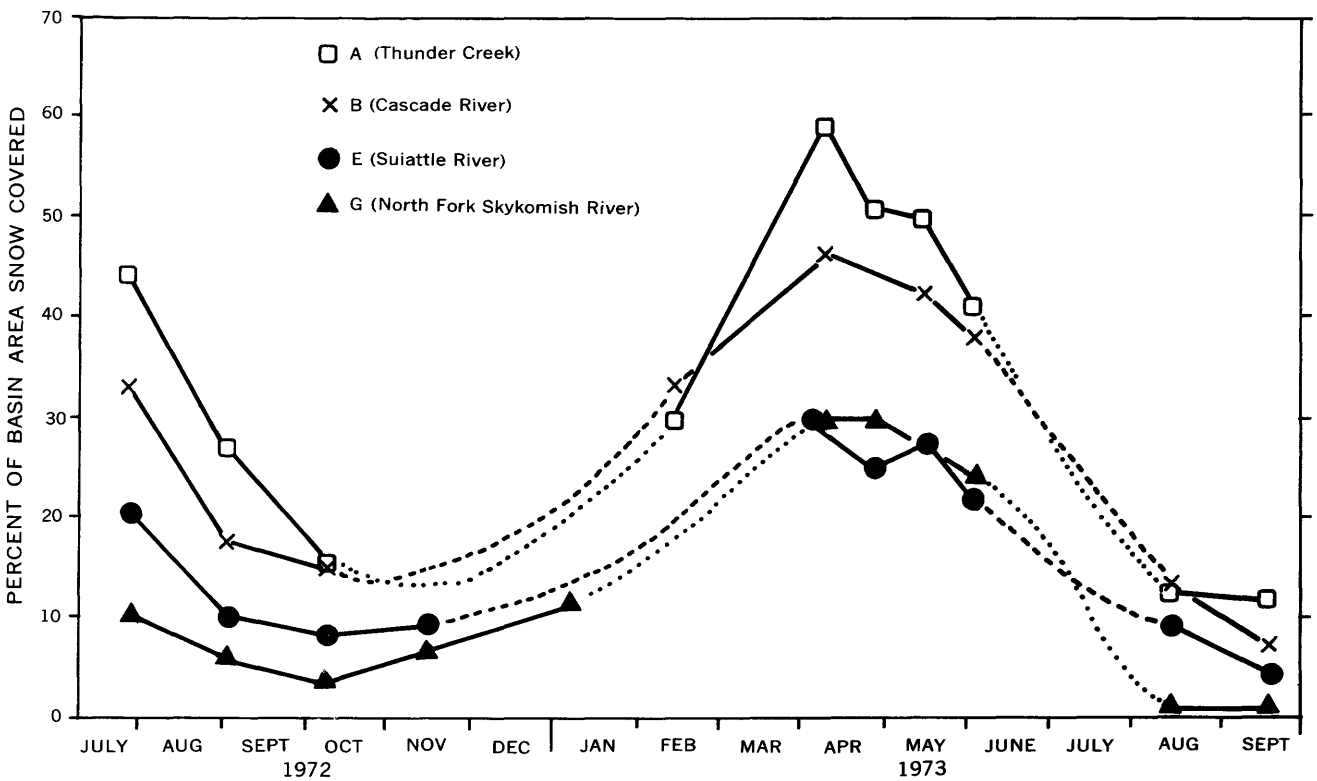


FIGURE 127.—Graph showing percentage of drainage basin area covered by snow.

# MAPPING SNOW EXTENT IN THE SIERRA NEVADA OF CALIFORNIA

By Donald R. Wiesnet and David F. McGinnis,

National Oceanic and Atmospheric Administration

The 80-m ground resolution of the MSS on board ERTS–1 provides images to measure snow extent on moderately sized (250 to 30,000 km$^2$) watersheds. Melting snowpacks in the Sierra Nevada supply much of central and southern California's water for domestic and agricultural consumption. Monitoring the extent of the snowpack via ERTS–1 is quick and less expensive than a simple altitude survey by a light plane. Figure 128, produced using a color additive viewer, is a composite of three ERTS–1 band 4 images showing the retreat of the Sierra Nevada snowpack in three stages during the spring of 1973, on Apr. 21, 1973 (1272–18122), May 9, 1973 (1290–18121), and May 27, 1973 (1308–18120).

The area shown in light green is the area of maximum extent from which the snow melted from Apr. 21 to May 9, 1973. The area shown in blue denotes the area from which snow melted during the period May 9 to May 27 (18 days). White depicts the snow cover on May 27. Some minor cloud cover appears as green in Nevada to the east of the Sierra Nevada.

ERTS–1 MSS data have been used to check snow maps prepared from the NOAA–2 satellite images, which have a lower (~900 m) resolution (Wiesnet and McGinnis, 1974).

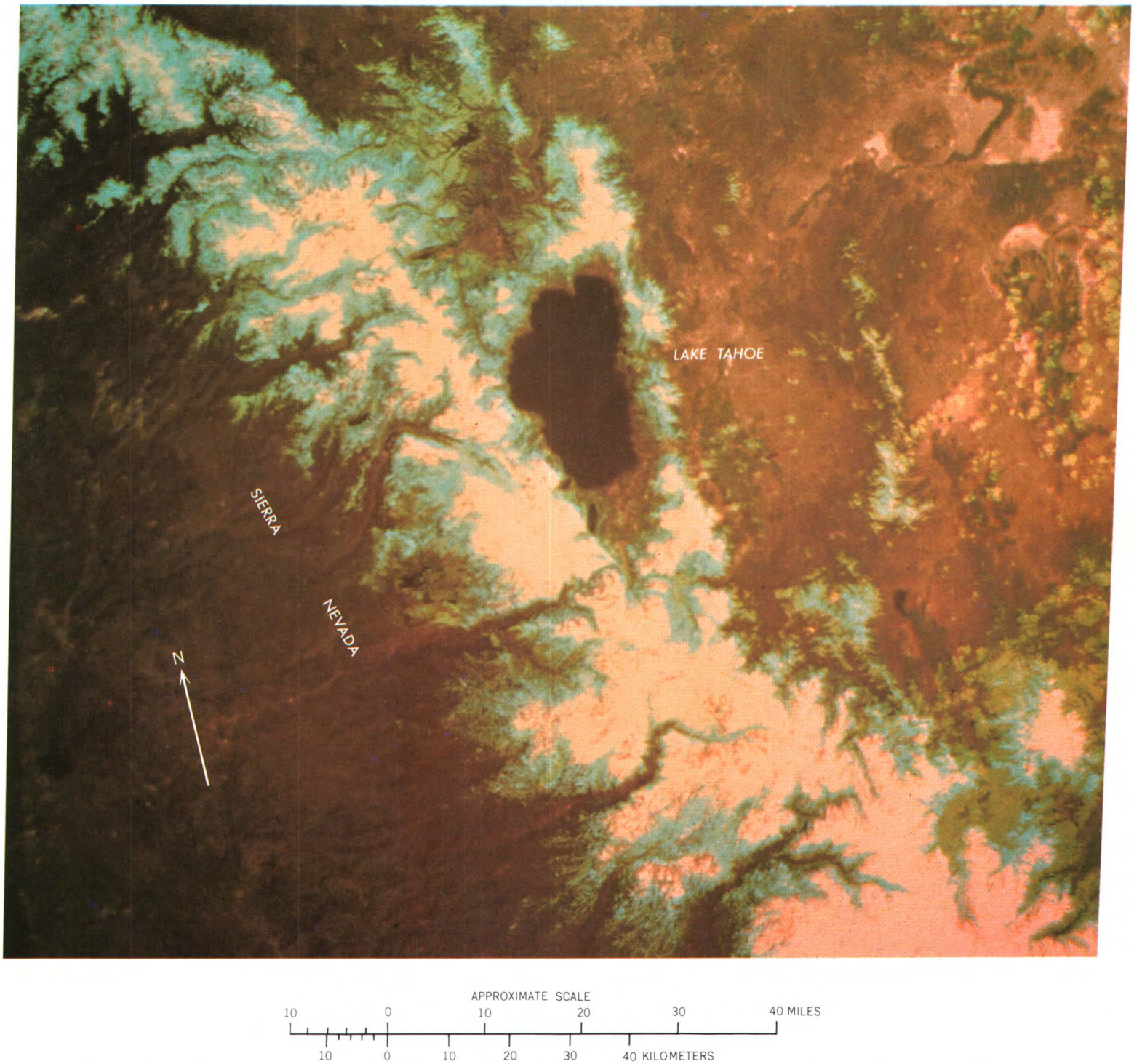


FIGURE 128.—Annotated composite of parts of three different ERTS–1 images color enhanced to show retreat of snowpack at three stages, spring 1973 (1272–18122, 1290–18121, and 1308–18120; all band 4). Light green shows greatest extent on Apr. 21, 1973; blue shows stage on May 9, 1973; off white depicts snow cover on May 27, 1973.

# SURGING AND NONSURGING GLACIERS IN THE PAMIR MOUNTAINS, U.S.S.R.

By Robert M. Krimmel, Austin Post, and Mark F. Meier,

U.S. Geological Survey

Figure 129 shows both surging and nonsurging glaciers in the Pamir Mountains in the U.S.S.R. Most mountain glaciers move a few centimeters or tens of centimeters per day and slowly adjust to changes in climate by gradual advances or retreats. Surging glaciers, on the other hand, periodically change from this slow regime to a very rapid flow, on the order of meters per hour, causing rapid advances of the terminus amounting to 1 km or more per month. Such rapid advances may cause lakes to be formed as tributary valleys are dammed by the advancing ice. Later these ice-dammed lakes may suddenly release, causing a catastrophic flood.

In this ERTS image (fig. 129), the famous Medvezhii (Bear) Glacier is shown just completing a catastrophic surge that caused widespread destruction. The glacier began to surge in April 1973 and by early June had advanced nearly 3 km. This surge created a major threat when the advancing ice dammed the Abdukagor River, forming a lake that may have been larger than 20 million $m^3$. On June 20, 1973, the lake broke through its ice dam and caused a flood in the populated Vanch River valley. Because a flood was expected to follow the damming of the river, dikes had been built, bridges had been dismantled, and other precautions had been taken, and thus no lives were lost although highways and powerlines were damaged.

The image shows the Pamir Mountains to be a vast region of deep arid valleys heading in large glaciers. As in such Western States as Washington, Montana, and Wyoming, summer ice melt from these glaciers supplies critically needed water to irrigate lands. Surges of the Medvezhii Glacier occur at intervals of 10 to 12 yr. The Medvezhii Glacier is normally confined to the tributary valley of Khirsdara and advances out to the Abdukagor Valley only during surges. This glacier has been studied intensively by glaciologist Dr. Leonid D. Dolgushin and his colleagues (Dolgushin and Osipova, 1972) of the Institute of Geography, Academy of Sciences of the U.S.S.R.

Glaciologists of the U.S. Geological Survey in Tacoma, Wash., have identified six other surging glaciers, including Fortambek and Garmo, on this ERTS image. These glaciers have the periodically looped medial moraines that are unmistakable signs of past surges. One, the Bivachnii Glacier, appears to be primed for a surge of about 2 km in the next year or so. Surging features can be seen on 16 other glaciers.

Also of interest in this image is the 77-km-long Fedchenko Glacier, the longest in the U.S.S.R. and one of the world's most studied glaciers. Its parallel medial moraines indicate that it does not surge. Some nonsurge-related ice-dammed lakes are visible at the margins of the Fedchenko Glacier and are also a potential source of floods.

As surges and related floods occur abruptly with little or no prior warning, glaciologists in countries that have surging glaciers, such as Iceland, Canada, Argentina, Chile, U.S.S.R., and the United States, are pooling information collected from intensive studies in order to locate and map hazardous situations, to provide prior warning systems when surges and surge-related floods are expected, and, hopefully, to determine the causes of these remarkable movements. Because surging glaciers usually occur in relatively inaccessible terrain, satellites such as ERTS–1 will be used more and more for the required monitoring.

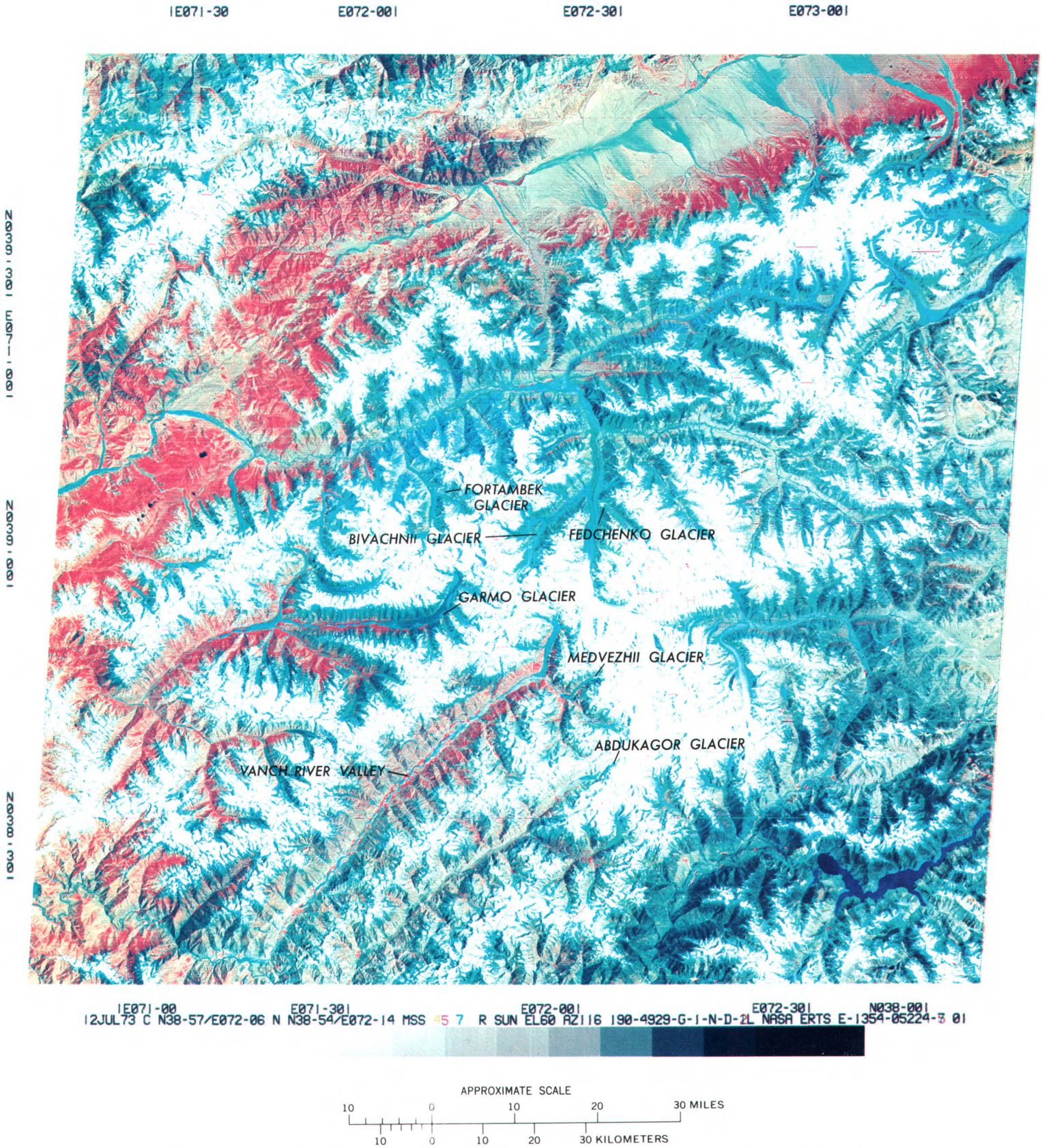


FIGURE 129.—Annotated color composite ERTS–1 image of the Pamir Mountains of the U.S.S.R. (1354–05224).

# MEASURING THE MOTION OF THE LOWELL AND TWEEDSMUIR SURGING GLACIERS OF BRITISH COLUMBIA, CANADA

By Austin Post, Mark F. Meier, and Lawrence R. Mayo,

U.S. Geological Survey

Tweedsmuir Glacier, 70 km in length and the largest glacier in British Columbia, Canada, is shown in an image taken on Sept. 13, 1973 (figs. 130, 131). At that time it was undergoing a spectacular surge (rapid advance). The glacier, situated astride the British Columbia-Yukon Territory boundary 256 km northwest of Juneau, Alaska, flows out of the St. Elias Mountains into the Alsek River valley where it spreads out in a large terminal lobe 13 km across. The lobe blocks the main river valley and forces the stream into a narrow gorge along the glacier's margin. Because this gorge is impassable to boats and is the greatest hazard on the river, it has been appropriately named Turnback Canyon.

Surges of Tweedsmuir Glacier in the past have dammed up the Alsek River at Turnback Canyon and formed lakes as much as 20 km long. The 1973 surge may again close off the river, and if this should occur, sudden, perhaps repeated, releases of water from the lake when the ice dam fails could cause hazardous flooding in downstream channels and in Dry Bay, Alaska. Thus, it is important to monitor the behavior of the glacier and to measure the changing rate of ice flow in order to predict the growth of a potential glacier-dammed lake.

Figure 132 shows changes observed or inferred on Tweedsmuir Glacier near its terminus. The ice velocity was inferred from ERTS images by measuring the changing positions of moraine loops during the intervals between Apr. 15, July 22, Sept. 13, and Nov. 7, 1973, and drawing a smooth curve through the average displacement rates. The actual advance of the terminus was measured on the ground by Dr. Gerald Holdsworth (1974) of the Canadian Department of Environment. These curves provide the data for prediction of the timing and the amount of advance of Tweedsmuir Glacier over the channel of the Alsek River.

The study of a sequence of ERTS images of the surging Tweedsmuir Glacier has revealed other interesting features. Most important of these is the existence of a "shock wave," that is, a steplike feature on the glacier that also marks the down-glacier limit of intense crevassing. (Although actual crevasses are rarely seen on ERTS images, regions of intense crevassing appear distinctly darker because of the shadows within the crevasses.) This shock wave

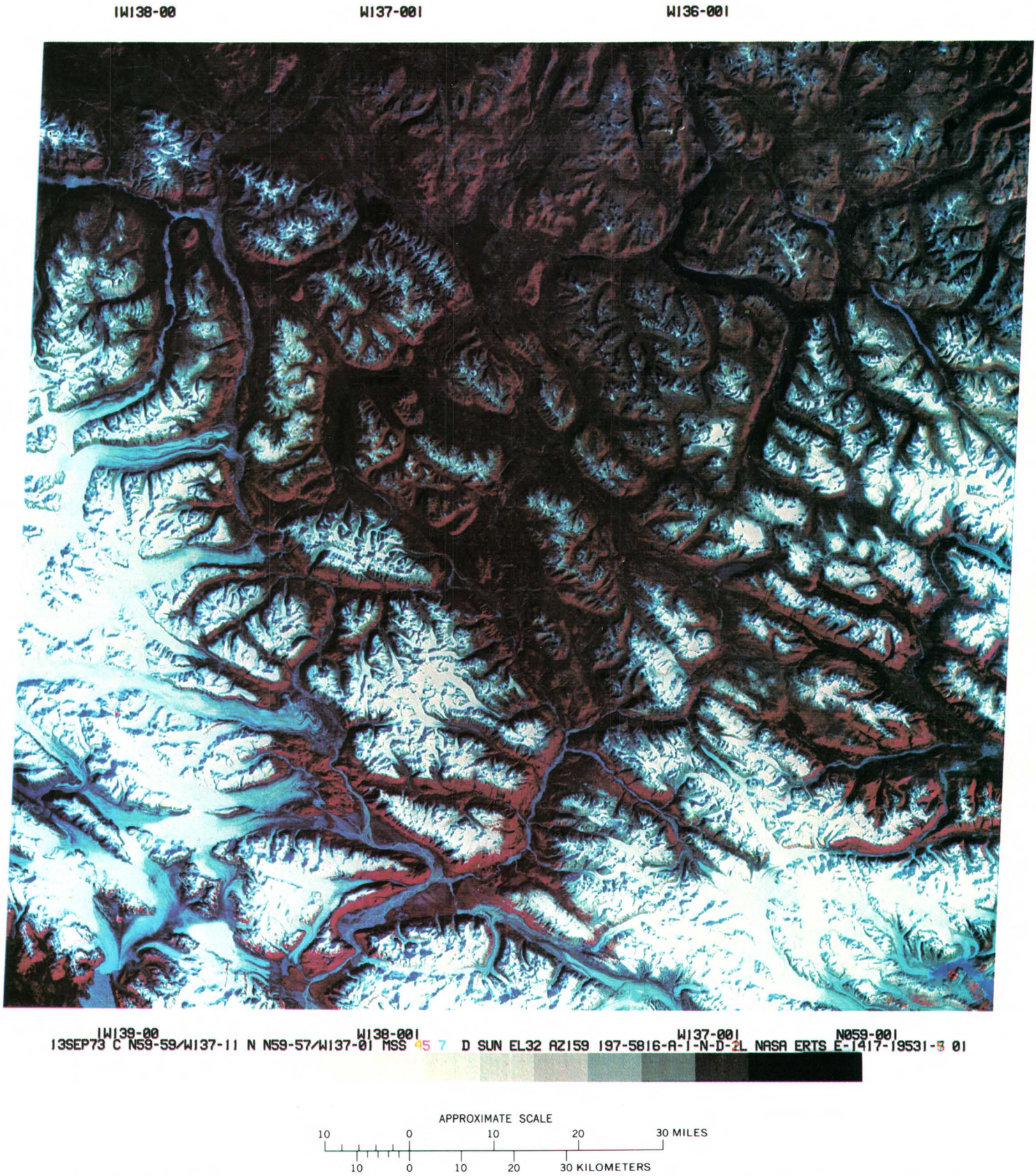


FIGURE 130.—Color composite ERTS–1 image of the Lowell Glacier and Tweedsmuir Glacier areas of British Columbia, Canada (1417–19531).

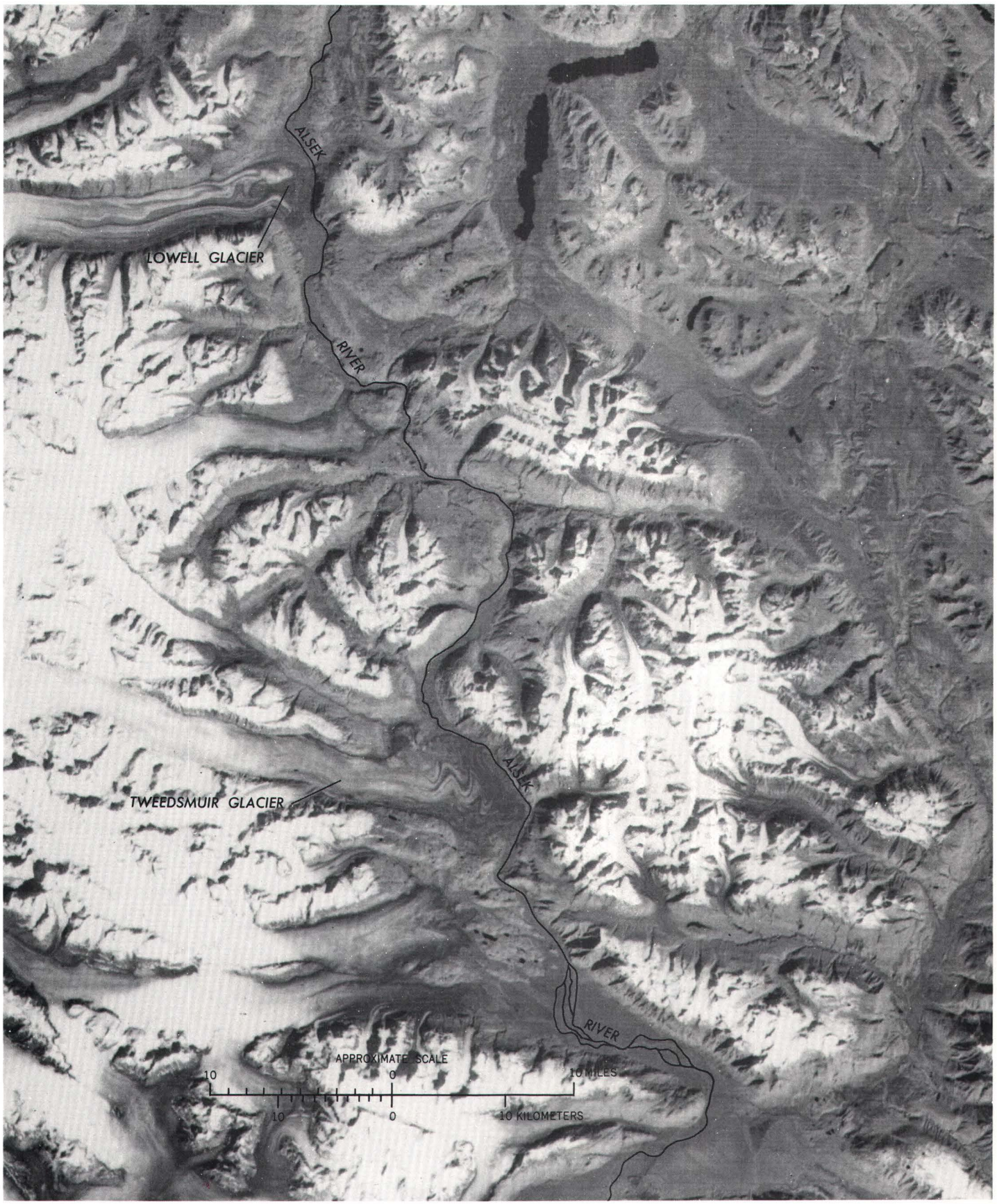


FIGURE 131.—Annotated ERTS–1 image of the Lowell and Tweedsmuir Glaciers of British Columbia, Canada (part of 1417–19531, band 4).

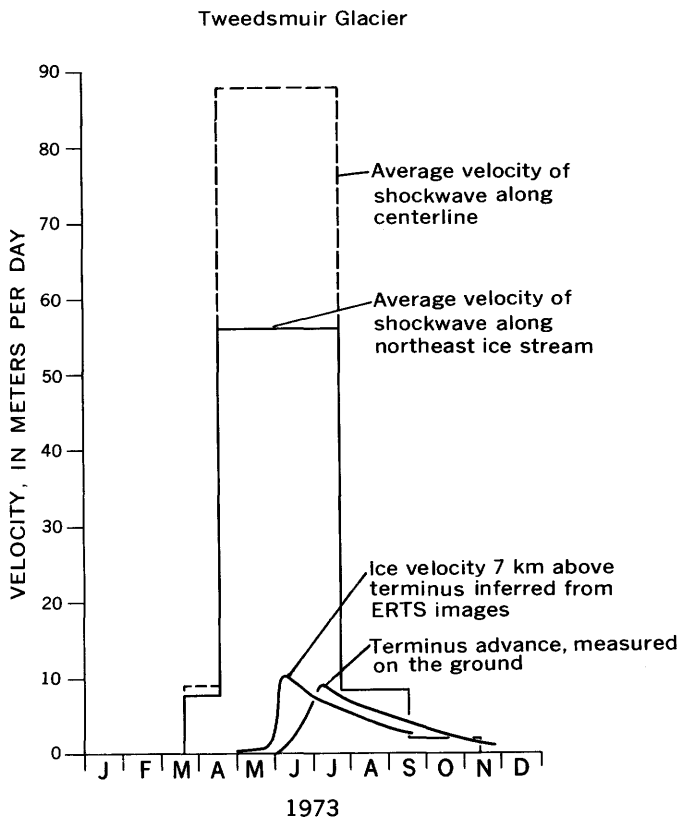


FIGURE 132.—Graph showing the velocity of movement of the Tweedsmuir Glacier in 1973.

advanced in midglacier about 8.8 km from Apr. 15 to July 22, an average rate of 88 m/day, at least an order of magnitude faster than the actual velocity of the ice. Other features that could be seen on the ERTS images include the increasing relief along the valley walls, the spreading of zones of intense crevassing, and the deformation of medial moraines.

ERTS images are thus shown to be useful records of important data for inaccessible, rarely visited areas such as the Tweedsmuir Glacier area. Furthermore, using ERTS images to produce maps and quantitative displacement data for large surging glaciers is far more quick and efficient than using conventional aerial photography or ground surveys. For instance, the Lowell Glacier, which has dammed the Alsek River in the past, surged in 1968–70. A map of the medial moraine pattern had been made before the surge, using the laborious procedure of mosaicing and rectifying many aerial photographs. A new map was made from this ERTS image, compared with the old map, and displacement vectors measured in just 1.5 h (fig. 133). This demonstrates the usefulness of ERTS imagery for the rapid mapping of large features.

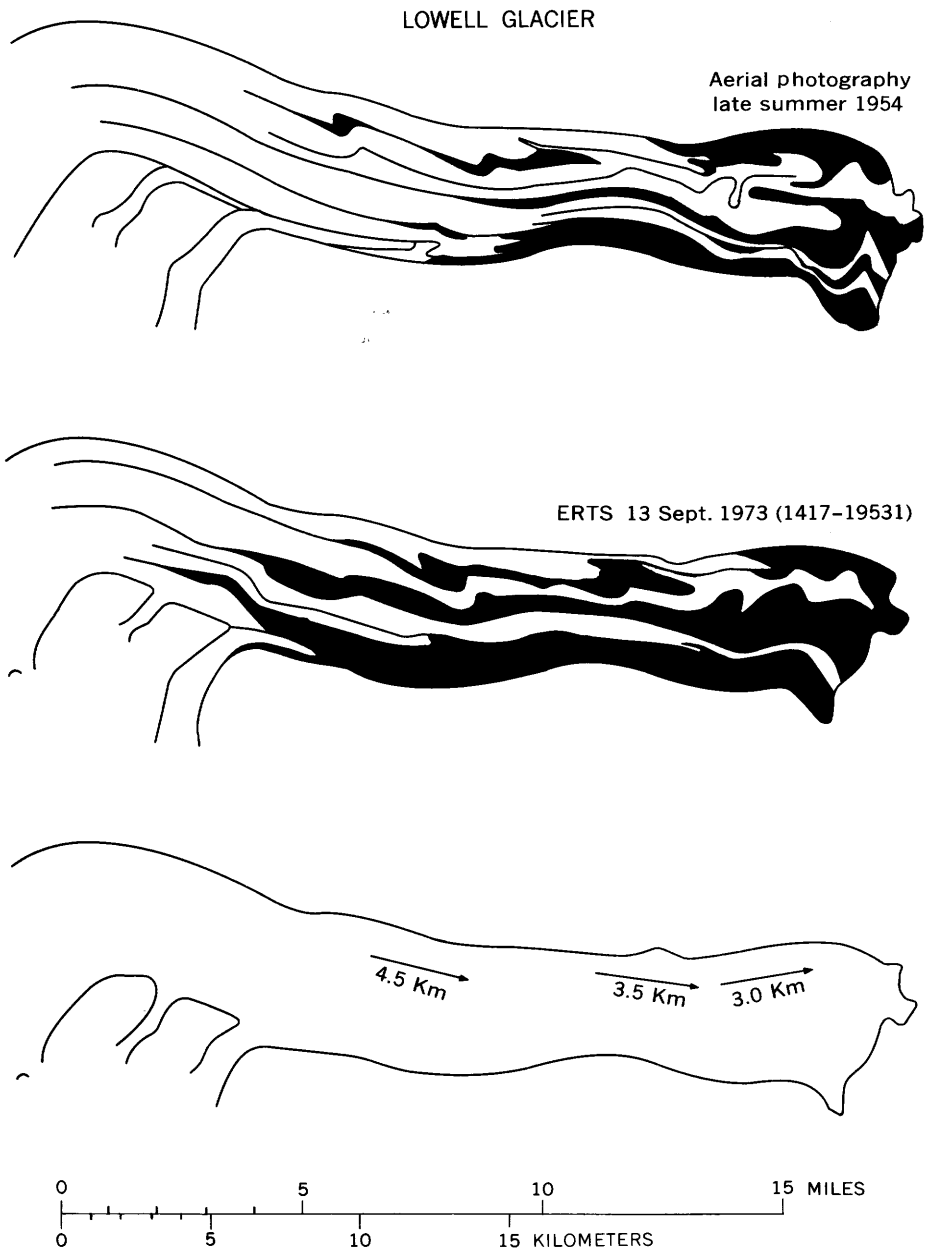


FIGURE 133.—Maps showing displacement vectors and changes in medial moraines of the Lowell Glacier, 1954–73, from late summer 1954 aerial photography and a late summer 1973 ERTS–1 image (1417–19531).

# MONITORING THE MOTION OF SURGING GLACIERS IN THE MOUNT McKINLEY MASSIF, ALASKA

By Mark F. Meier,

U.S. Geological Survey

The ERTS image in figure 134 shows both surging and nonsurging glaciers as much as 64 km in length situated around Mount McKinley in Alaska. Nonsurging glaciers, such as the Ruth and Kahiltna, flow at quite uniform rates of only a few centimeters or tens of centimeters per day, and the medial moraines—dark-colored strips of rock fragments stripped from mountains situated between tributary glaciers—are quite straight and uniform. On the other hand, such surging glaciers as the Tokositna, Lacuna, and Yentna have wiggly folded moraines that result from alternating periods of near stagnation (lasting up to 50 yr) and of extremely high flow rates (lasting 1 to 3 yr when the ice may flow faster than 1.3 m/h).

The Tokositna Glacier (fig. 135) has just completed a surge that began in 1970. The Lacuna Glacier has been in a stagnant condition for 40 or more yr, and its dirty mottled surface shows the effects of severe melting. The Yentna Glacier was first observed surging in 1972. This image shows its folded moraines displaced more than 1,800 m down valley from their positions shown on recent maps and 1970 aerial photographs. Also visible on the ERTS image is a dark line where the rapidly flowing Yentna Glacier has sheared across the stagnant ice of the Lacuna Glacier (fig. 135).

Why a glacier surges and why some glaciers surge but others do not, are questions of great scientific interest because this type of periodic sudden movement is common in many other phenomena in nature, perhaps even in the mechanism of earthquakes. Surging glaciers can advance over large areas and cause devastating floods by blocking and suddenly releasing large quantities of melt water; thus there is much practical interest in monitoring their behavior. U.S. Geological Survey scientists now are using ERTS images to keep track of many large surging glaciers in inaccessible areas.

A better understanding of glacier hydrology is becoming increasingly important because of the potential of glaciers as sources of water supply. Glaciers are one of the few sources of water supply that remain unexploited, and, with the advance of civilization into the subpolar regions, more attention should be paid to these ice masses in relation to potential water-resources development. An enormous reserve of water, about three-fourths of all the freshwater in the world, or equivalent to about 60 yr of precipitation over the entire globe, is locked in glacier ice.

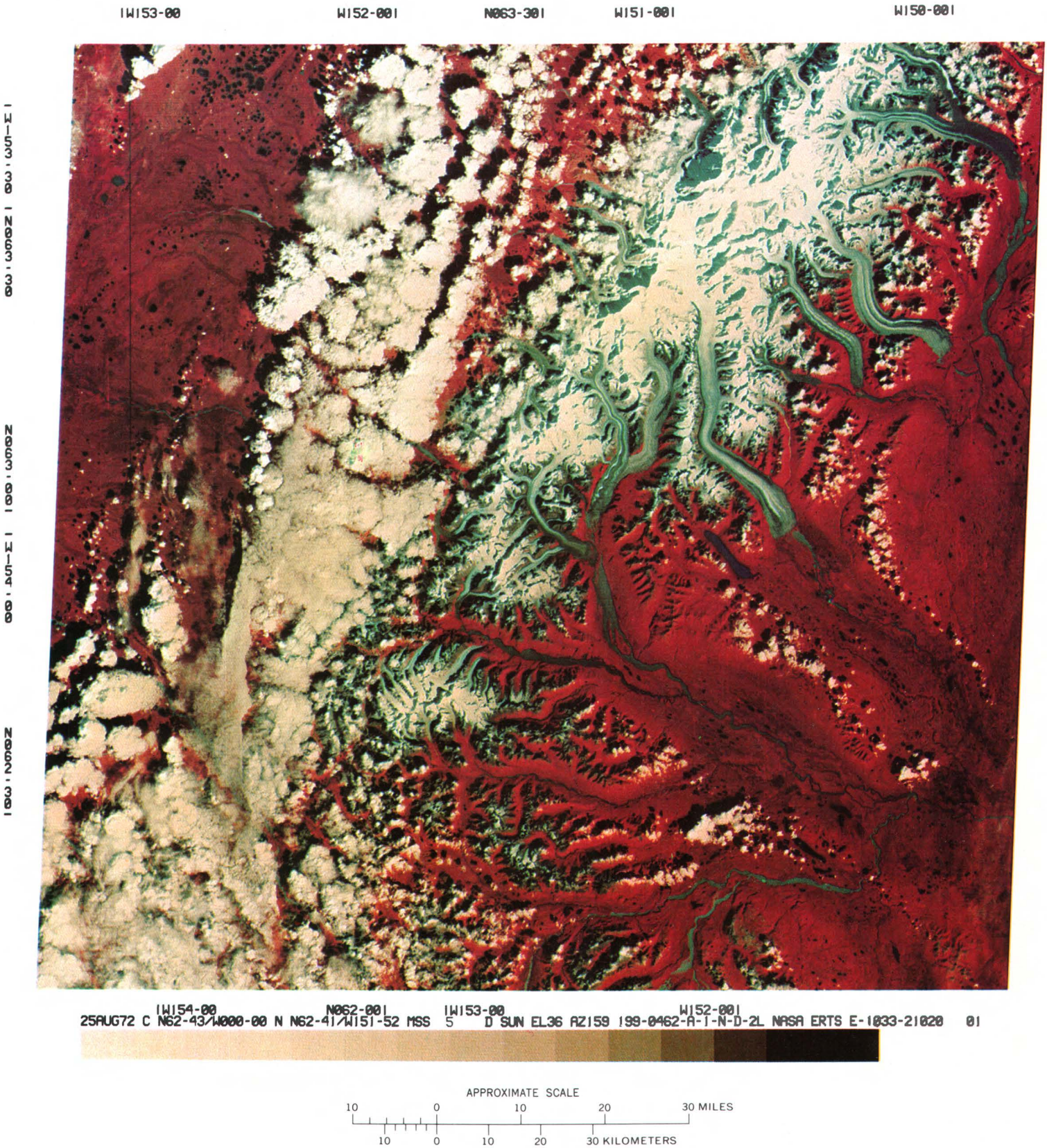


FIGURE 134.—Color composite ERTS–1 image of the Mount McKinley area of Alaska (1033–21020).

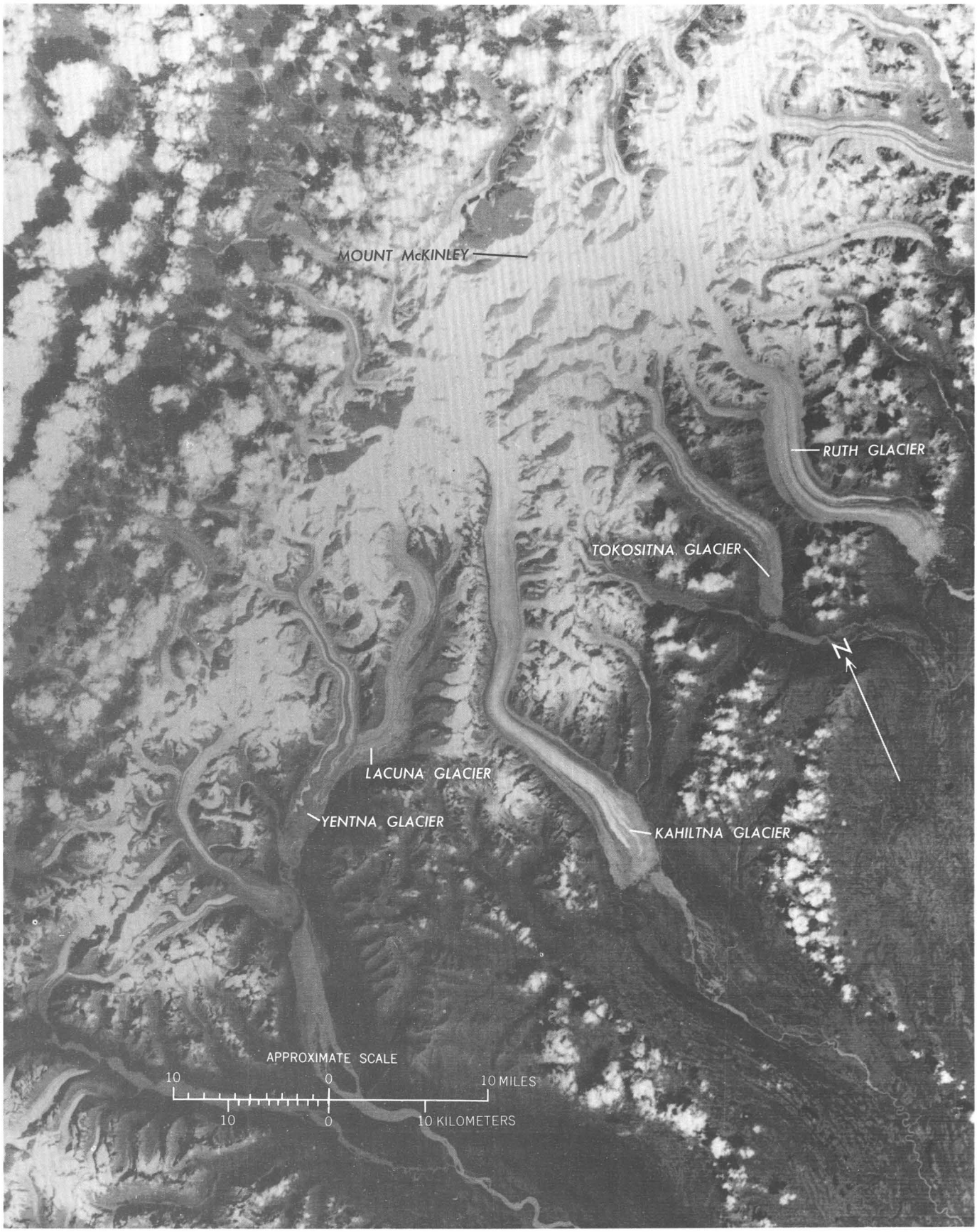


FIGURE 135.—Annotated enlargement of the ERTS–1 image of the Mount McKinley area of Alaska (part of 1033–21020, band 6).

# VATNAJÖKULL ICECAP, ICELAND

By Richard S. Williams, Jr.,

U.S. Geological Survey

There are three characteristics of ERTS MSS imagery that make it unique for mapping of environmental phenomena: (1) it can be related to the figure of the Earth; (2) it records spectral reflectivity in four broad bands of the visible and near-infrared parts of the electromagnetic spectrum on videotape rather than photographic film; and (3) most importantly, it provides systematic, routine, and repetitive coverage of an area (Williams and others, 1974). Except for areas of high population density, the availability of recent aerial photography is rather uncommon, and no aerial photography exists at all of large remote areas of the world. ERTS imagery provides a heretofore unavailable time-lapse view of many types of dynamic environmental phenomena, including seasonal variations in snow cover, vegetation, and glaciers (Williams,.1972).

Glaciers are extremely dynamic phenomena, subject to great seasonal variation, and are particularly suited for study and monitoring on ERTS imagery (Williams and others, 1975) for several reasons. Glaciers offer good contrast with surrounding terrain. Lateral, medial, and terminal moraines are usually large enough to be resolved at the 80-m maximum of ERTS sensors. The same is true of glacier-margin lakes, braided stream patterns on outwash plains, and sediment plumes of glacial rock flour in lake or marine waters. Furthermore, in images made under low-Sun-angle conditions, surface irregularities on glaciers are particularly pronounced because of enhancement of shadows on the white background.

ERTS imagery offers two unique possibilities for glaciological studies not readily available by other methods. The first is the fact that regional synoptic studies of glaciers and icecaps can be made, and an entire glacier can now be studied as a total system rather than as disparate and often temporally separated elements. The second unique aspect of ERTS, because of its 18-day cycle, is that—in addition to monitoring changes in runoff, variations in the size and location of glacier-margin lakes, and variations in the position of glacier margins—the repetitive coverage permits monitoring of surging glaciers on a year-round basis.

Figures 136, 137, and 138 are ERTS images of Vatnajökull Glacier, the largest icecap in Iceland, taken in January 1973, July 1973, and September 1973, providing a time-lapse view. Figure 139 is a sketch map of the approximate area shown by these images (Thorarinsson and others, 1974). The dynamic volcanic and glaciologic environment of Vatnajökull is strikingly shown in these images.

Figure 136 is a midwinter low-Sun-angle (7°) band 5 image of the snow-covered Vatnajökull area of Iceland that shows: 1, the elliptical shape of a

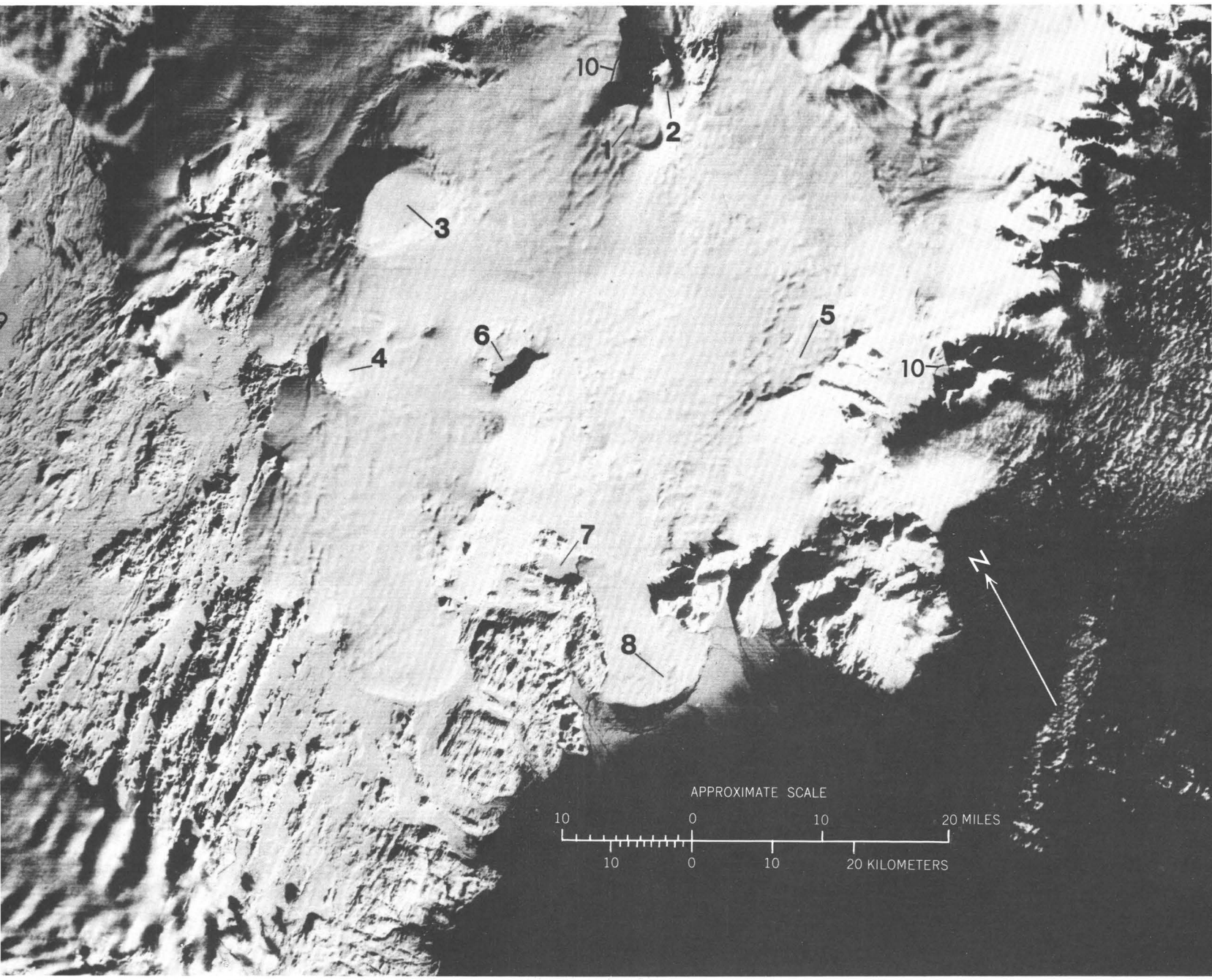


FIGURE 136.—Annotated enlargement of ERTS–1 image of the Vatnajökull area of Iceland in the winter (part of 1192–12084, band 7).

hitherto unknown subglacial caldera and 2, the elliptical shape of a partially subglacial caldera. Although dark, two subglacial craters can be seen on the western edge of this caldera; a partially subglacial geothermal area extends southwest into the icecap through the westernmost crater. Other features include: 3 and 4, elliptically shaped central volcanoes; 5, faint elliptical features and associated nunataks which may represent a partially ice-covered large central volcano; 6, a well-known subglacial caldera, source of many catastrophic jökulhlaups (glacial floods), including one in March 1972; 7, a frozen lake, another source of jökulhlaups, including one that occurred in August 1973; and 8, the partially snow-covered snout of a glacier. Around the periphery of the caldera 6 are a number of punctate features resulting from collapse after the March 1972 jökulhlaup. Several more collapse features, resulting from the August 1972 jökulhlaup, can be seen in a line between 4 and 6. Southwest of Vatnajökull are superb examples of northeast-trending grabens, crater rows, and hyaloclastite ridges. Two prominent volcano-tectonic lineaments can be seen on this image. One extends N. 45° E. for 80 km from between 1 and 2 to the southwestern edge of Vatnajökull. The second lineament extends N.35°W., just north of 7. Concentric recessional moraines in front of an outlet glacier can be seen at 9. Medial moraines are visible at 10 (Williams and Thorarinsson, 1974; Williams and others, 1973c).

Figure 137 is a midsummer color composite ERTS–1 image. The high Sun angle (42°) and high reflectivity of the snow-covered glacier limit the amount of surface detail as compared with the low Sun angle of the wintertime image (fig. 136). The icecap, however, exhibits a completely different character because summer is a time of dynamic activity around and on the glacier. Ablation is at a high rate, and runoff is at its maximum across outwash plains. Changes in glacier-margin lakes and glacier termini can be monitored systematically on ERTS images. Types and distribution of vegetation around the icecap can also be delineated (Williams and others, 1973b). Older snowpack can be seen at 1 where it has drifted. Sediment plumes can be distinguished at 2 and all along the coast. Several glacier-margin lakes are visible; note the maximum area encompassed by 3, before the August 1973 jökulhlaup. Several braided glacial rivers cross this outwash plain. Undistorted moraines can be seen at 4 and contorted moraines at 5. The retreat of the snowline can be seen on most of the glaciers, including 6 and 7 (Williams and others, 1974a).

Figure 138 is an early fall color composite ERTS–1 image. As the Sun angle drops (25°), surface detail again begins to appear, although it is not as pronounced as on the wintertime image (fig. 136). Note the reduction in sediment plumes along the coast and the decreased discharge of glacial rivers across the outwash plain. Note the retreat of the snowline as compared with figure 137. Note also the reduction in the lake area at 1 after the August 1973 jökulhlaup, as compared with figure 137 (Williams and others, 1974a).

Eyjabakkajökull began to surge in late August 1972. By the time of acquisition of the first ERTS image on Oct. 14, 1972 (Williams and others, 1973a), the glacier had apparently already moved slightly more than 1 km. The glacier was imaged again on Sept. 22, 1973 (fig. 138). According to measurements made on the two ERTS images, Eyjabakkajökull has surged an additional distance of 1.8 km. Measurements made on contorted medial moraines and volcanic ash layers at 5 on figure 137 between the two dates, Oct. 14, 1972, and Sept. 22, 1973, give an estimated 600 m of glacier motion in that part of Skeidarárjökull in a period of 11 mo.

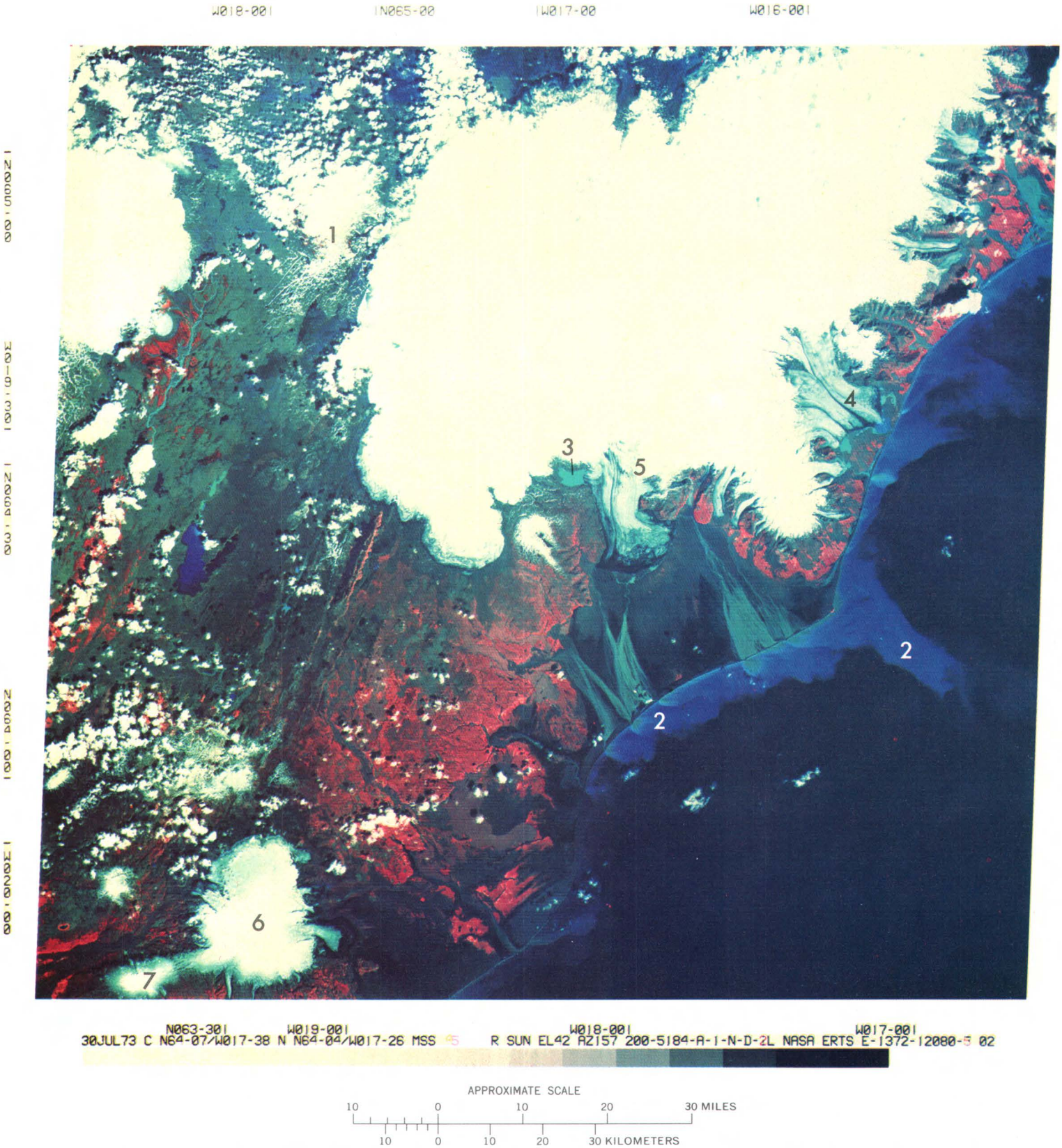


FIGURE 137.—Annotated color composite ERTS–1 image of the Vatnajökull area of Iceland in the summer (1372–12080).

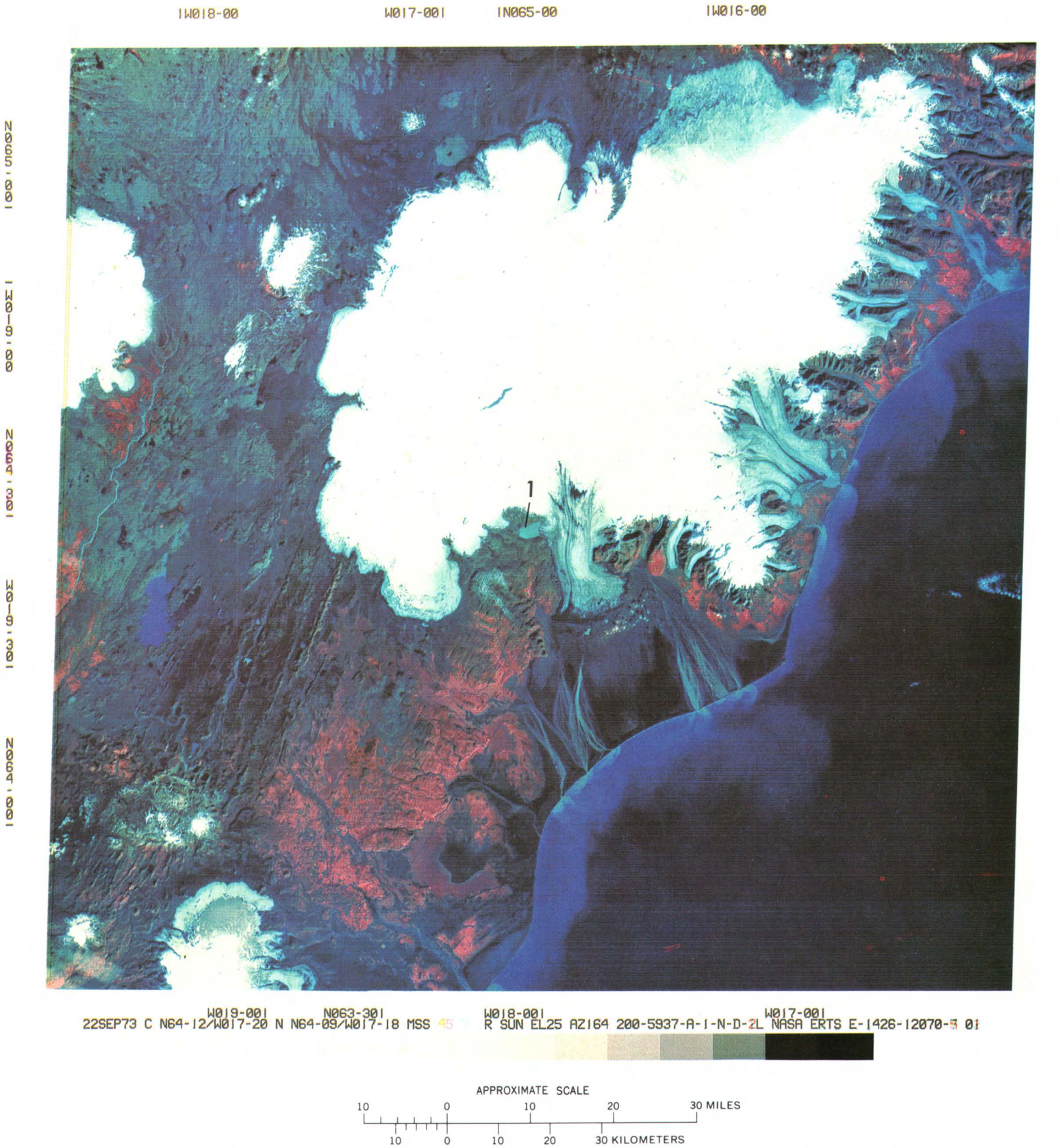


FIGURE 138.—Annotated color composite ERTS–1 image of the Vatnajökull area of Iceland in the fall (1426–12070).

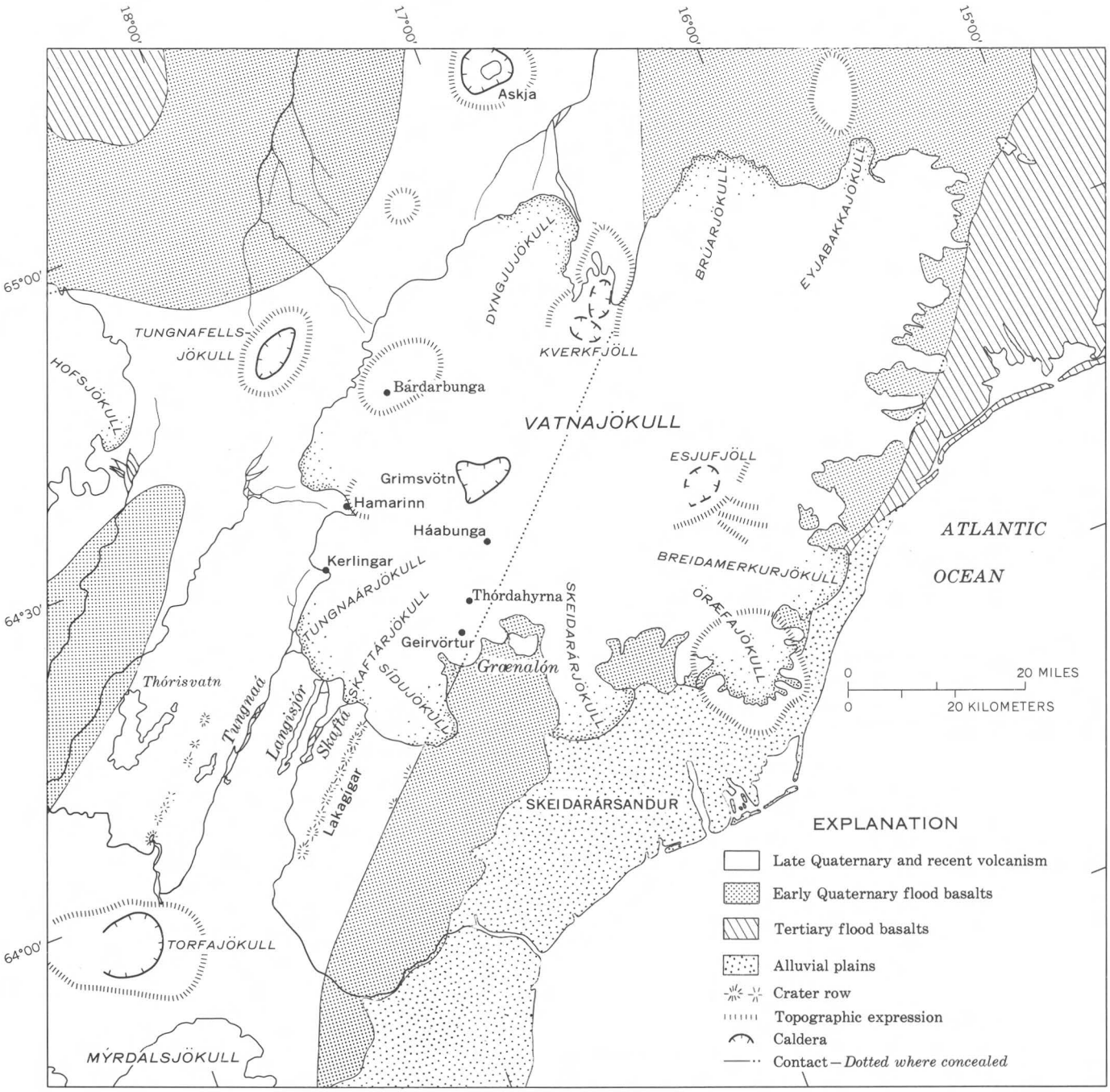


FIGURE 139.—Sketch map of the Vatnajökull area of Iceland.

# GLACIOLOGY IN ANTARCTICA

By William R. MacDonald,
U.S. Geological Survey

Comparison of an ERTS image dated Dec. 24, 1972, with the published U.S. Geological Survey 1:250,000-scale map of Ross Island disclosed a unique change in the Erebus Glacier Tongue (fig. 140). Further examination of photographs and historical maps indicated that the present position of the tongue is about the same as it was in 1910 and that the tongue had advanced about 9.6 km since 1947 and 4.8 km since 1962. A lateral shift or curving of the leading front toward the mainland seems also to have occurred since 1970. Sources are not adequate to determine whether the movement occurred gradually or rapidly. Some evidence does seem to indicate that the tongue may have gone through a surging period. Perhaps it has completed a growth cycle and will again break off as it did in 1911. If field investigations prove it to be a surging glacier, it will be the first one found in Antarctica and, therefore, of great interest to glaciologists.

Further indication that ERTS imagery is useful for detecting glaciological changes is given by figures 141 and 142. An ERTS image dated Feb. 20, 1973 (fig. 141), was compared with the published U.S. Geological Survey 1:500,000-scale sketch map of Ellsworth Land and Palmer Land and with aerial photographs and shows that the Ronne Ice Shelf has advanced about 16 km since January 1966.

Another excellent example of detecting glaciological changes on images is documented in figure 142, a planimetric sketch map compiled from ERTS images taken Jan. 21, 1974. When compared with the most recent and largest scale map available of the area, a 1:250,000-scale Japanese series chart, and other charts at scales 1:1,000,000 to 1:3,000,000 compiled by Japan, the U.S.S.R., and Norway, it is readily apparent that the Shirase Glacier (A) and Fletta Bay Glacier (B) tongues have advanced approximately 52 km and 69 km beyond the positions depicted on the maps. An important and unanswered question is whether the

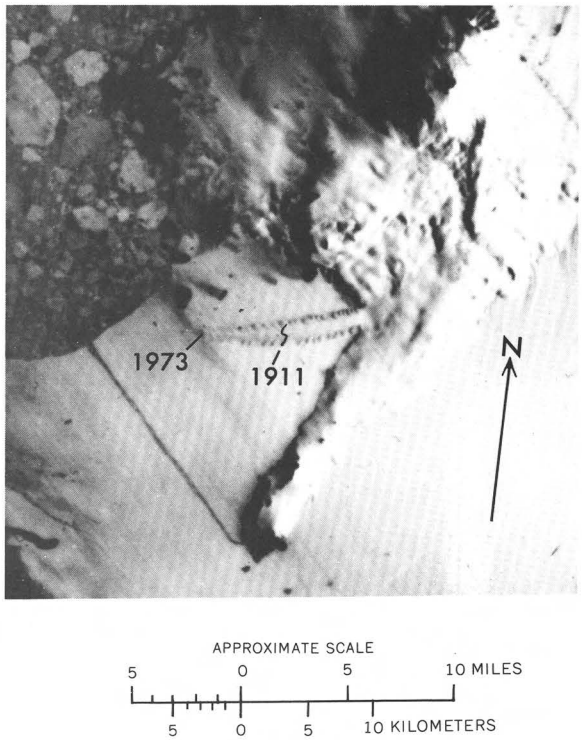


FIGURE 140.—Annotated enlargement of ERTS–1 image of the Erebus Ice Tongue of Antarctica (part of 1154–19322, band 7). Analysis of ERTS–1 images and library sources showed that the Erebus Glacier Tongue has advanced 9.6 km since 1947. Place where the tongue broke off in 1911 is indicated.

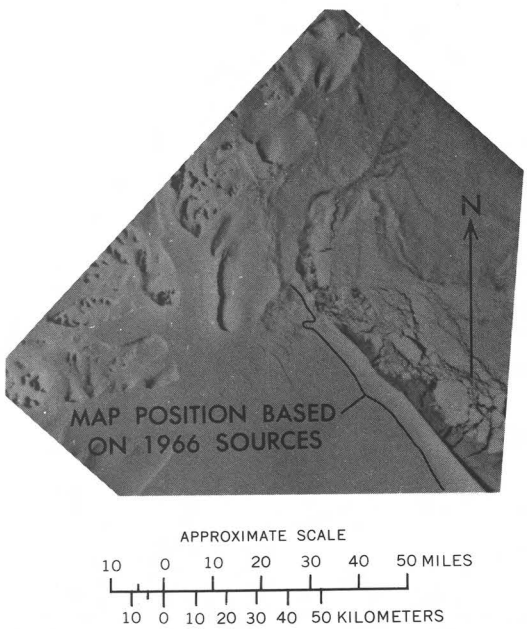


FIGURE 141.—Annotated ERTS–1 image of the Ronne Ice Shelf of Antarctica (part of 1212–11133, band 7). The edge of the shelf has advanced about 16 km since 1966.

changes have been caused by a recent glacier advance or instead reflect inadequate mapping because of limited source materials.

Of special interest is the discovery from ERTS images of new geographic features on the polar plateau northwest and southwest of Ross Island. Repetitive coverage obtained in January 1974 shows the new features in even greater detail. Cartographers expert in interpreting ice and glaciological features on photographs suggest that some of the new features have considerable height relative to the surrounding ice-and-snow terrain and that a gradient is evident, the blue ice being on the leeward side. Other characteristics indicate extensive crevassing. Detailed analysis of the newly discovered features is planned by the National Science Foundation and will start as soon as conventional low-altitude photographs are obtained. Bad weather and logistical problems prevented aerial photography during the austral summer of 1973–74.

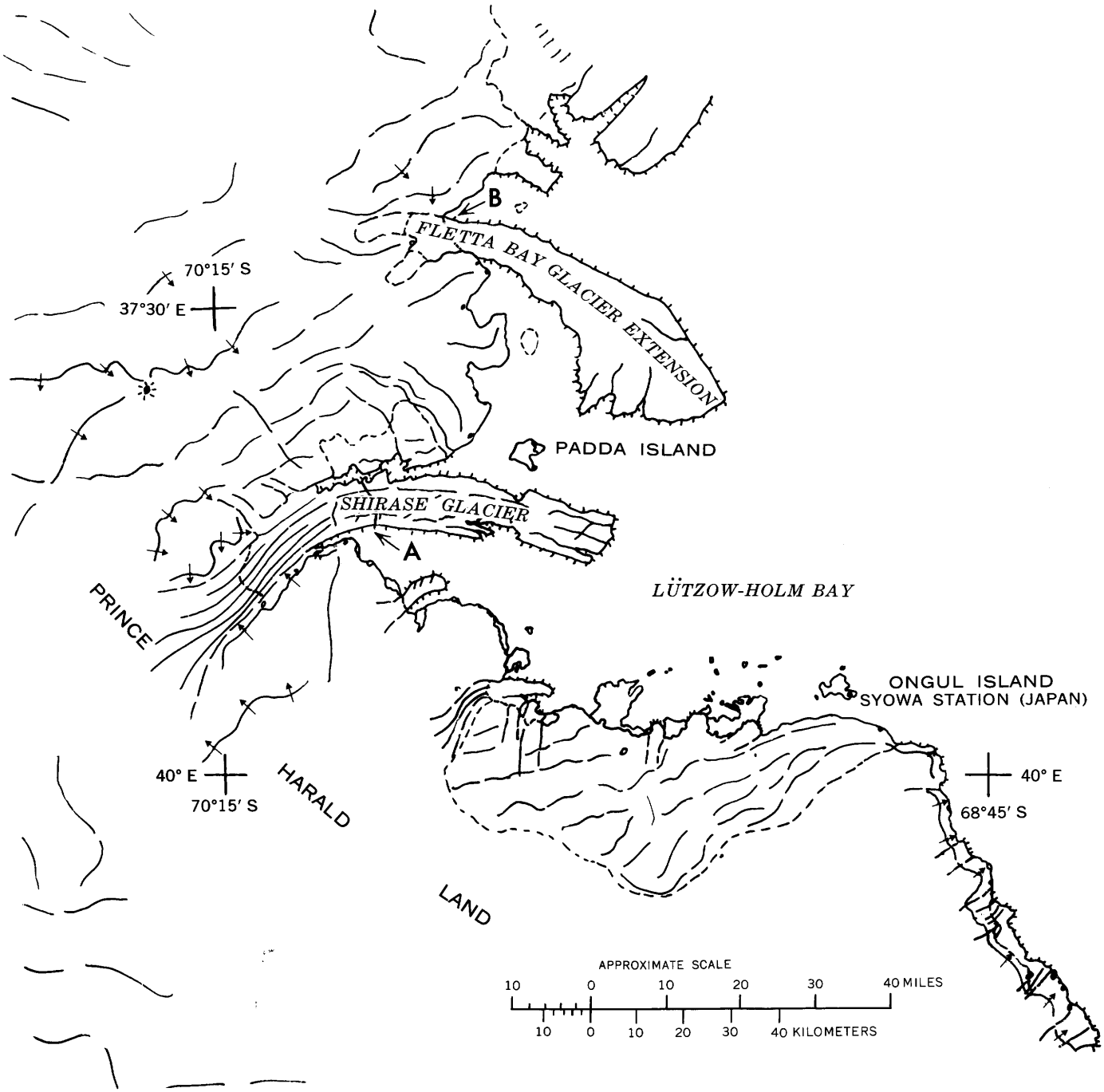


FIGURE 142.—Sketch map of the Lützow-Holm Bay area of Antarctica compiled from ERTS imagery.

# MONITORING FLOOD INUNDATION

By Roger B. Morrison and P. Gary White,
U.S. Geological Survey

ERTS infrared images from bands 6 and 7 have proven remarkably helpful for appraising and mapping rapidly the areal extent of flood inundation. The inundated areas are very sharply defined in images taken during a flood, if the water is not very muddy, and can be mapped accurately in detail because of the high contrast of the water (black) and nonflooded areas (light tones). Indeed, using computers for automatic mapping from MSS, the damage to large areas can be assessed in a fraction of the time previously required.

Figures 143, 144, and 145 eloquently document the severity of the spring 1973 floods in the Missouri-Mississippi River valleys. These, the worst Midwest floods in history, lasted 2 mo, drove 35,000 persons from their homes, and inundated more than 5.3 million ha. All these images are band 7.

The three figures show the same area of southern Illinois, southeast Missouri, and western Kentucky at the confluence of the Mississippi and Ohio Rivers. Preflood conditions on Nov. 24, 1972, are shown by figure 143. The Mississippi, Ohio, Cumberland, and Tennessee Rivers are at within-bank discharge stages. Here the flood plains are not easily distinguished because they are largely dry, but rivers and lakes are clearly evident.

Figure 144 shows conditions when the main rivers were in various stages of flood on May 5, 1973. Their flood plains are largely covered by flowing or standing water (black) and wet soils (dark tones). Light-toned areas within the flood plains are well-drained soils above the flood limit, mainly point-bar deposits. The widest and most extensively inundated flood plains are in the older, broader, ancient-valley reaches of the Mississippi (1 and 2) and Ohio (3) Rivers. Narrow flood plains and higher flood crests are in the confined reaches (4 and 5) where the rivers have had time only to incise narrow valleys. Also of interest are the effects of various artificial and natural levees. At 6 the floodwaters of the Mississippi are being dammed north of the dikes of the Headwater Diversion Channel at Cape Girardeau, Mo., creating a large slack-water area. At 7 the levees skirting the main channels control normal floods, but during large floods they keep the overbank waters from returning to the main channel and also hold back water from tributary streams; thus they deter postflood drying of the flood plain.

Figure 145 records a period of retreat of the floodwaters on June 10, 1973. The flood plain of the Ohio River is approaching normal, whereas that of the Mississippi, which drains a much larger area, is slower to dry. On the Mississippi's flood plain, much standing water remains, and the poorly drained

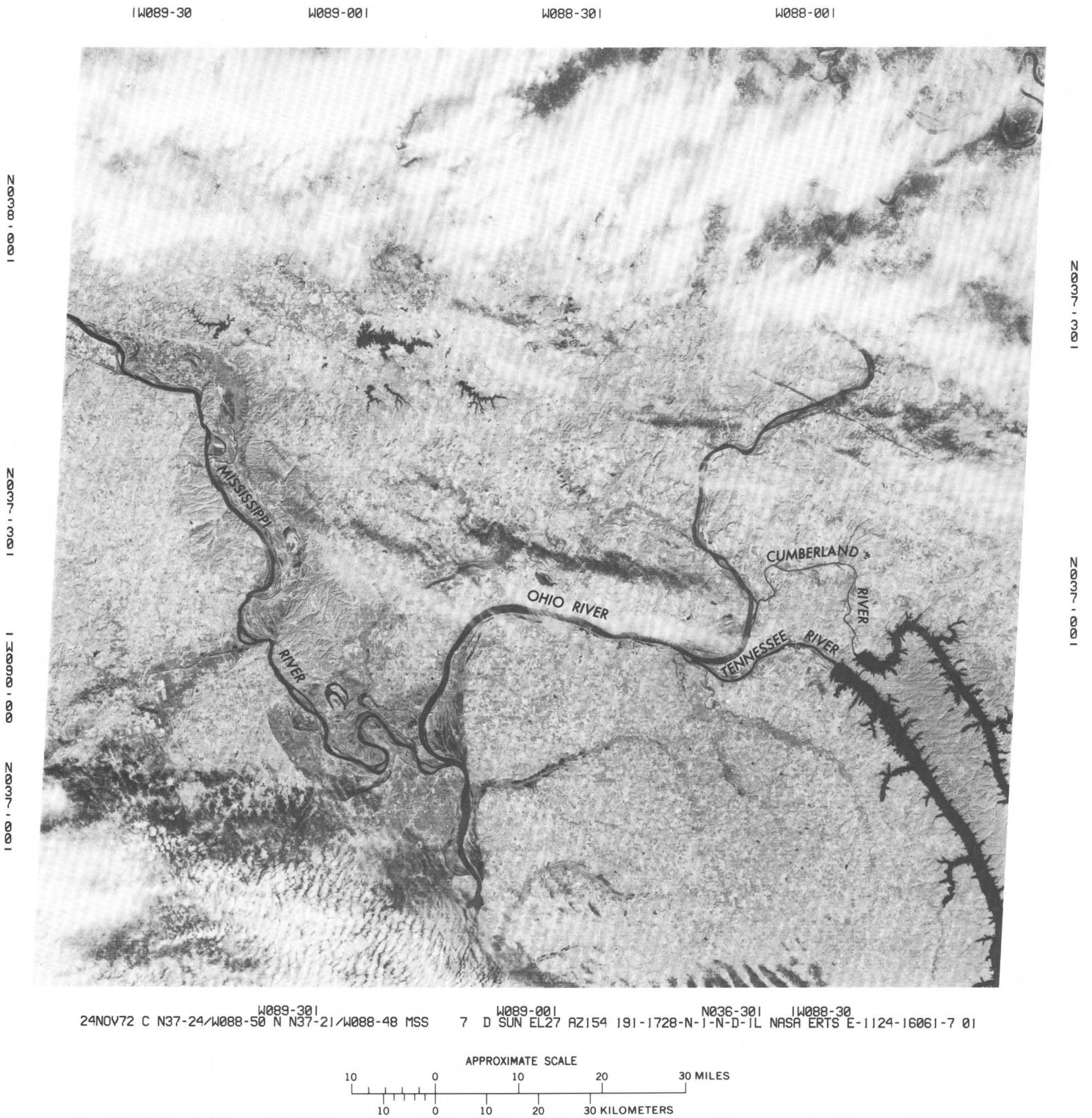


FIGURE 143.—Annotated ERTS–1 image showing the confluence of the Mississippi and Ohio Rivers in preflood condition on Nov. 24, 1972 (1124–16061, band 7).

fine alluvium of former channels still is moist although the better drained sediments, especially point-bar deposits, have dried considerably. This image also enhances various other alluvial lowlands because their still-moist soils have low infrared reflectance and appear darker than the uplands. Thus, abandoned flood plains of the Mississippi River 8 and Ohio River 9 are revealed.

Figures 146 and 147 show the St. Louis area and the junction of the Mississippi with the Missouri and Illinois Rivers. Figure 146 was taken before the flood on Aug. 28, 1972. Figure 147 shows the flood swollen rivers on Mar. 31, 1973.

Commonly it is not possible to obtain images that are contemporaneous with flood crests because of the 18-day ERTS cycle and cloud cover. Fortunately, images taken a week or more after a flood still provide faithful records of the flood inundation because areas that were flooded appear distinctly darker in the infrared bands (especially band 7) than the adjoining terrain and darker than they appeared in the preflood images. After a week or so, these areas gradually lose their relative darkness, and their boundaries become fuzzier. The slowness with which they fade suggests that the dark tones (low infrared reflectance) commonly are caused more by flood stress on the vegetation than by moist soils.

On Oct. 21, 1972, the Gila River in the vicinity of Safford, Ariz., reached a flood stage of 2,322 $m^3/s$, third highest on record, and caused about $10 million damage. Figures 148, 150, and 152 show conditions on Aug. 22, 1972, before the flood. The inner cultivated part of the Gila River valley is the prominent arcuate light-toned band. Within this band, the Gila River appears as a sinuous thin dark line. Figures 149, 151, and 153 are the first postflood images of the same area, taken 1½ weeks after the flood on Nov. 2, 1972. Note the greatly widened dark belt of reduced infrared reflectance along the Gila River. This belt corresponds with the zone that was inundated, as determined both by aerial photographs taken while the flood was in progress and by subsequent ground observations.

Many hundreds of hectares of cropland were badly eroded and/or covered by new deposits of gravel and sand. The areas of erosion and deposition show most clearly on band 5 as a light-toned strip inside the inundated belt that appears dark on the infrared bands. Thus, by comparing band 5 before- and after-flood images, a quick assessment can be made of the severely flood-ravaged land.

Figures 154 and 155 provide a comparison with results from the humid Midwest. They were taken before and after the big floods of September 1973 on the East Nishnabotna and West Nishnabotna Rivers in southwestern Iowa. Figure 154 shows preflood conditions on Aug. 14, 1972; the other image mosaic (fig. 155) from Sept. 19, 1972, shows conditions 1 week after these rivers had inundated about 35,000 ha. The areas that were flooded still appear as conspicuous dark bands because of their lowered infrared reflectance.

These examples illustrate the usefulness of the repetitive, multispectral, and synoptic ERTS imagery, not only for monitoring flood inundation and damage but also for assessing the adequacy of existing flood-control structures such as reservoirs, levees, and channelization.

APPROXIMATE SCALE

10 0 10 20 30 MILES

10 0 10 20 30 KILOMETERS

FIGURE 144.—Annotated ERTS–1 image showing the confluence of the Mississippi and Ohio Rivers in flood on May 5, 1973 (1286–16062, band 7).

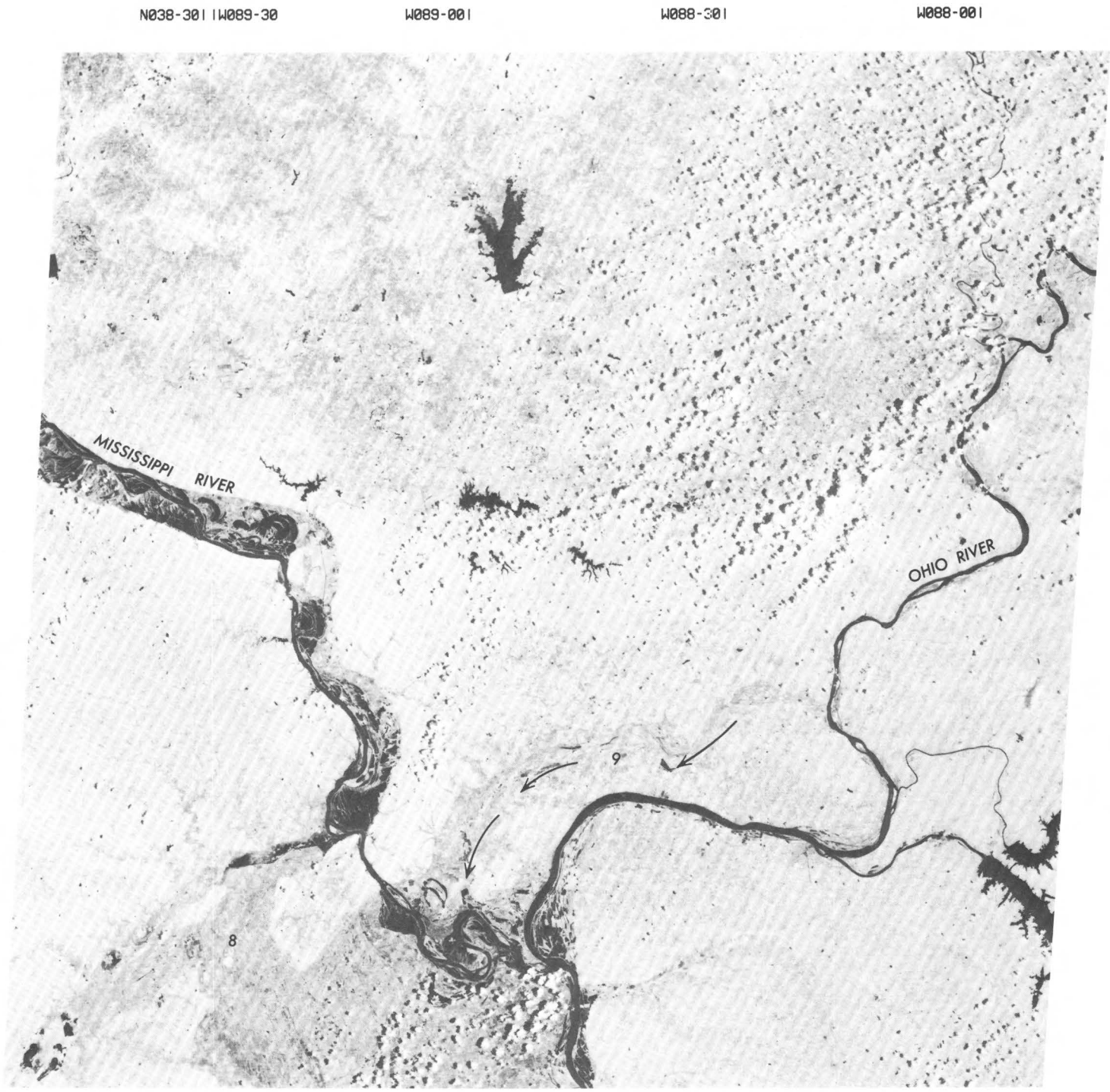


APPROXIMATE SCALE

10 0 10 20 30 MILES

10 0 10 20 30 KILOMETERS

FIGURE 145.—Annotated ERTS–1 image showing the confluence of the Mississippi and Ohio Rivers as the rivers retreat to normal stage on June 10, 1973 (1322–16060, band 7).

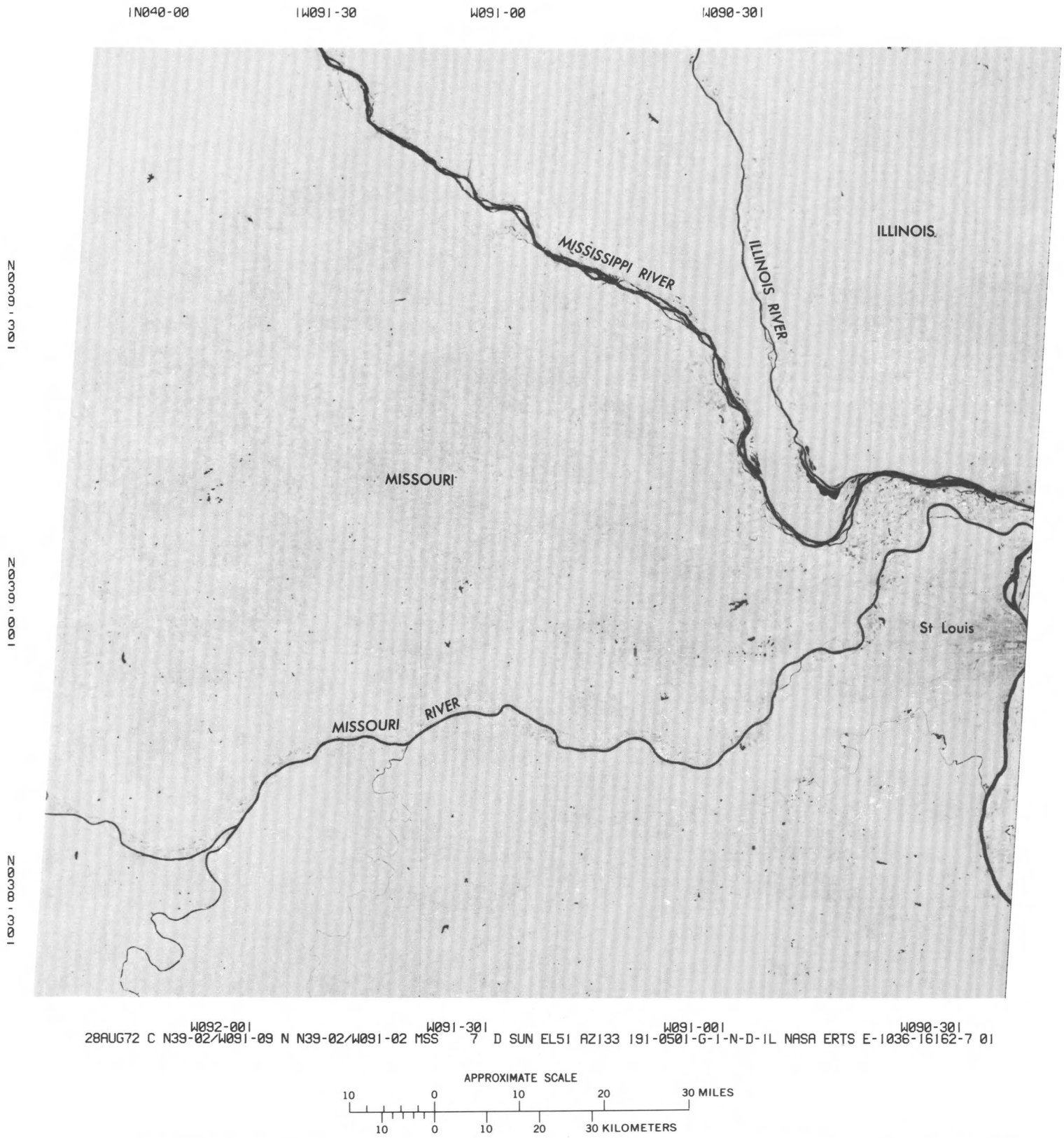


FIGURE 146.—Annotated ERTS–1 image of the St. Louis area of Missouri, showing preflood conditions of the Missouri, Mississippi, and Illinois Rivers on Aug. 28, 1972 (1036–16162, band 7).

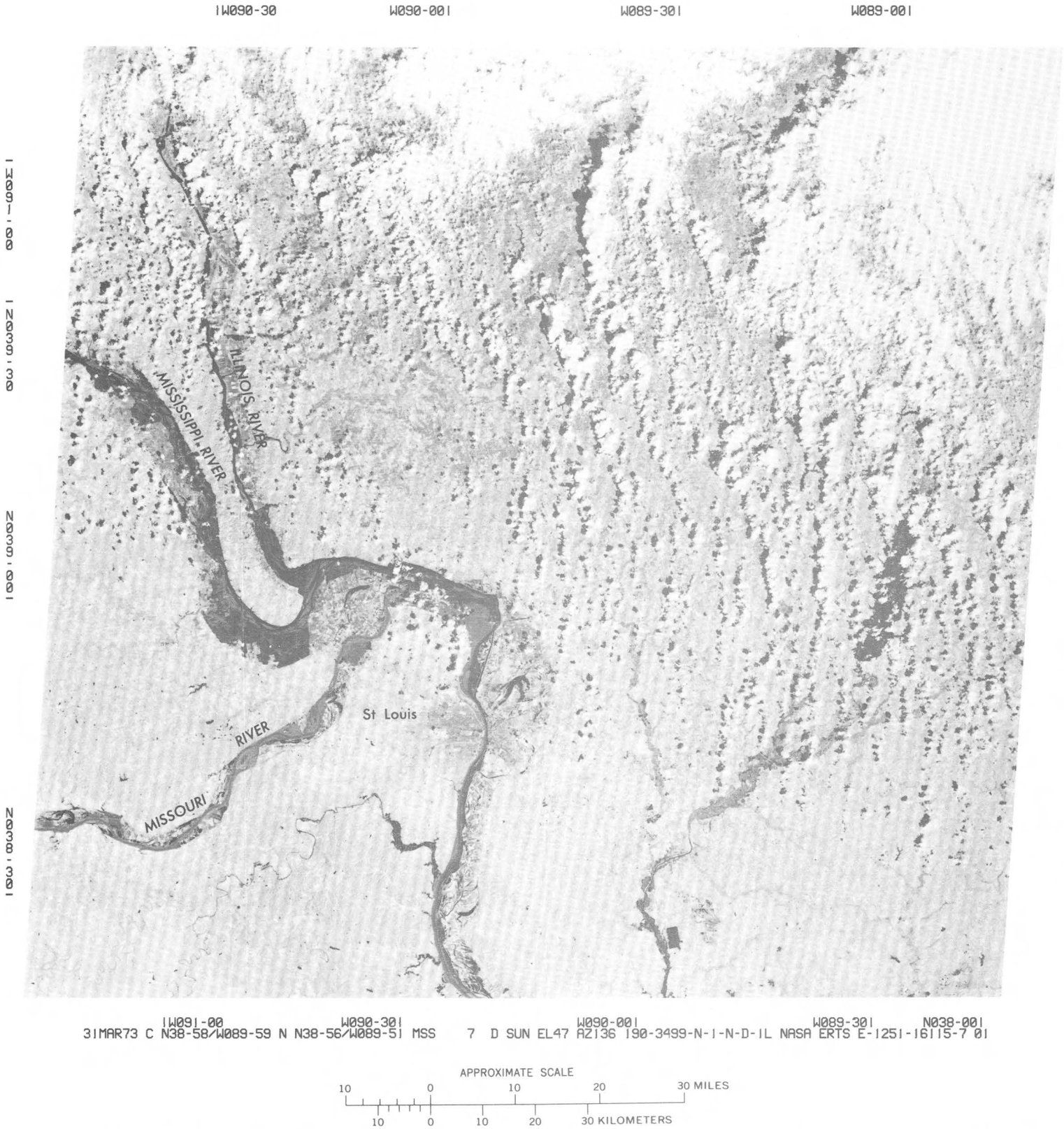


FIGURE 147.—Annotated ERTS–1 image showing flood-swollen rivers in the St. Louis area on Mar. 31, 1973 (1251–16115, band 7).

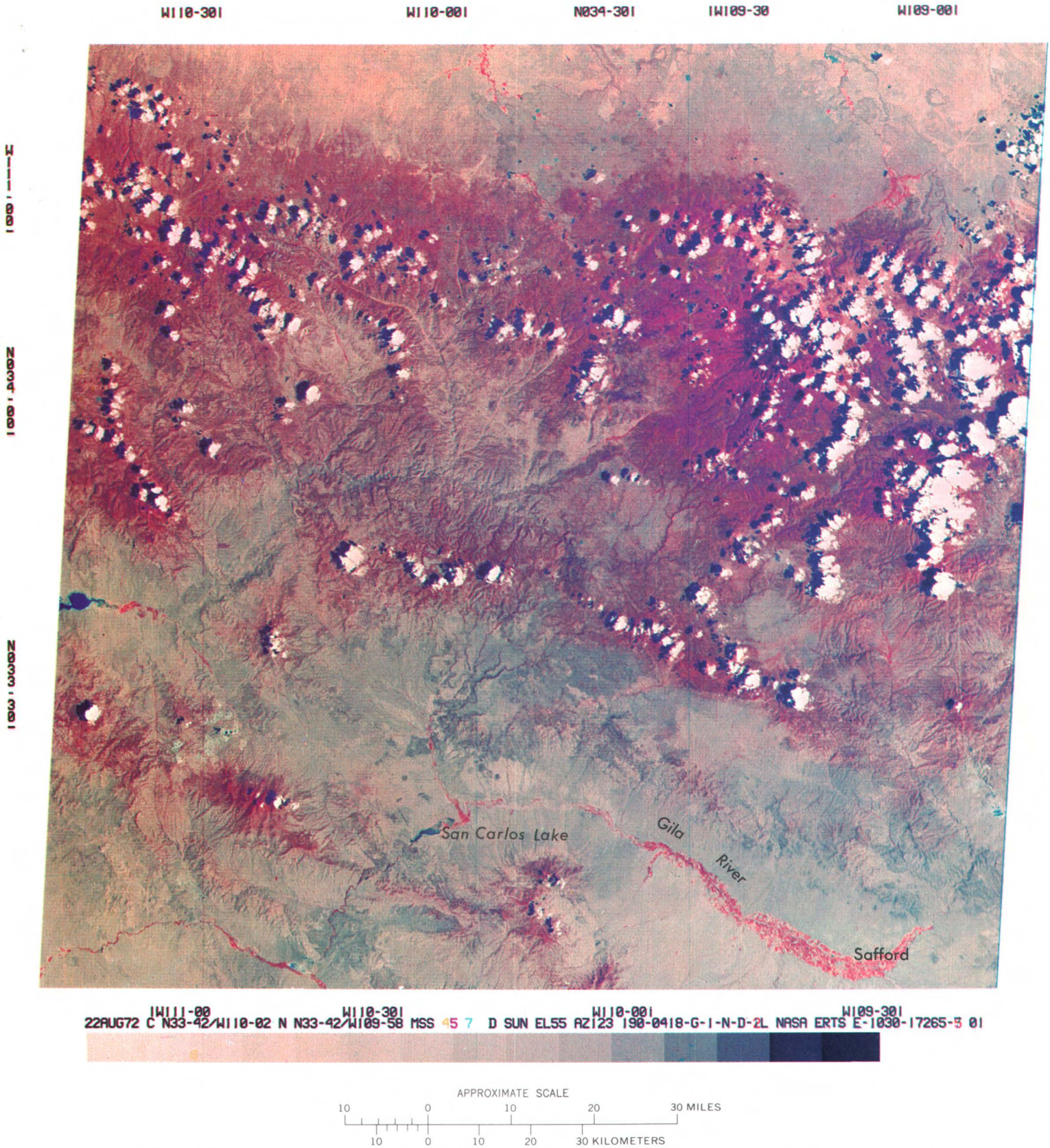


FIGURE 148.—Preflood color composite ERTS–1 image of the Gila River valley of Arizona on Aug. 22, 1972 (1030–17265).

FIGURE 149.—Color composite ERTS–1 image taken 12 days after the flood shows the dramatic increase in the San Carlos Lake and the soil erosion areas upstream that resulted from the flood of Oct. 21, 1972 (1102–17274).

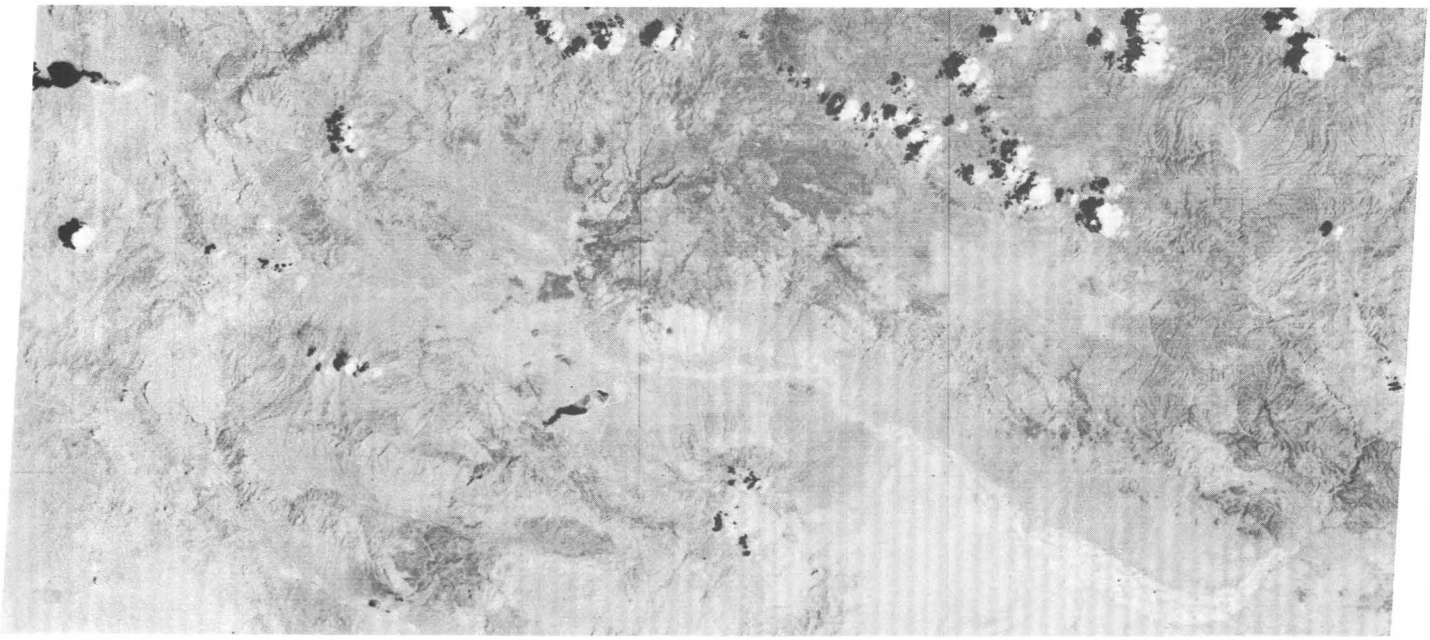


FIGURE 150.—Preflood ERTS–1 image of the Gila River valley of Arizona on Aug. 22, 1972 (part of 1030–17265, band 7).

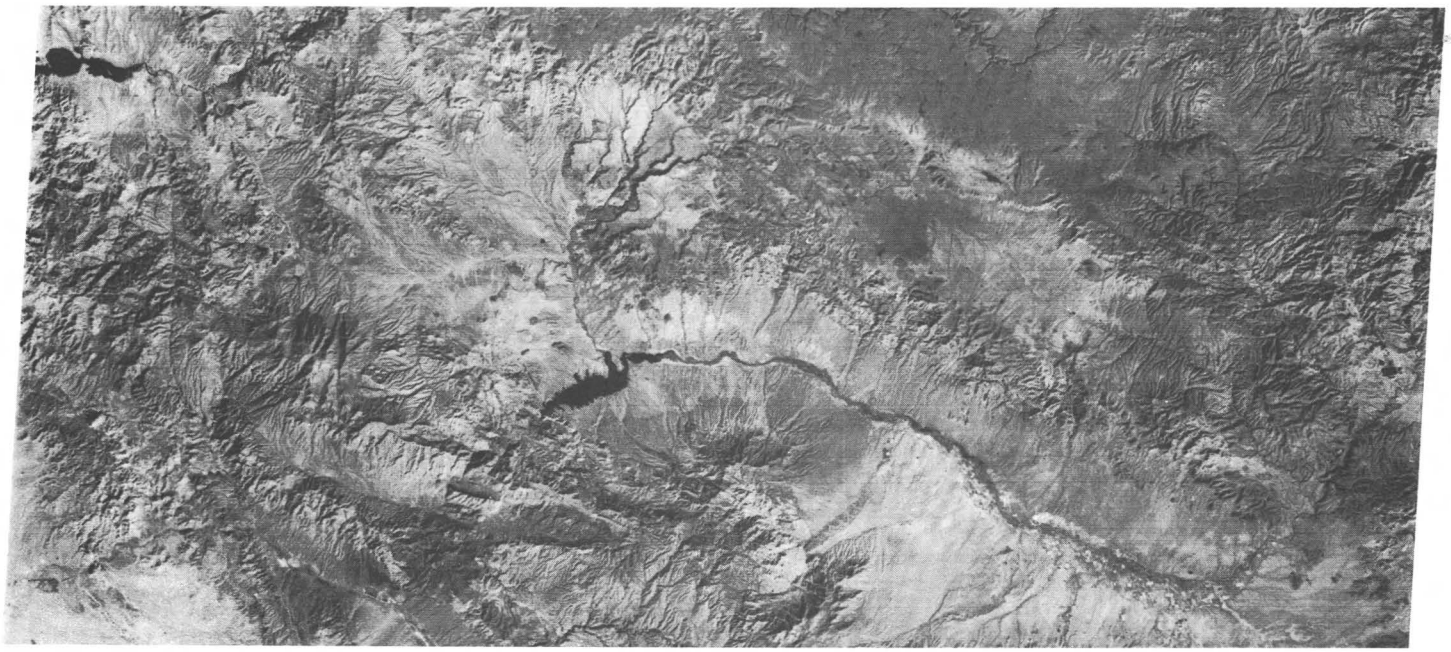


FIGURE 151.—Postflood ERTS–1 image of the Gila River valley of Arizona on Nov. 2, 1972 (part of 1102–17274, band 7).

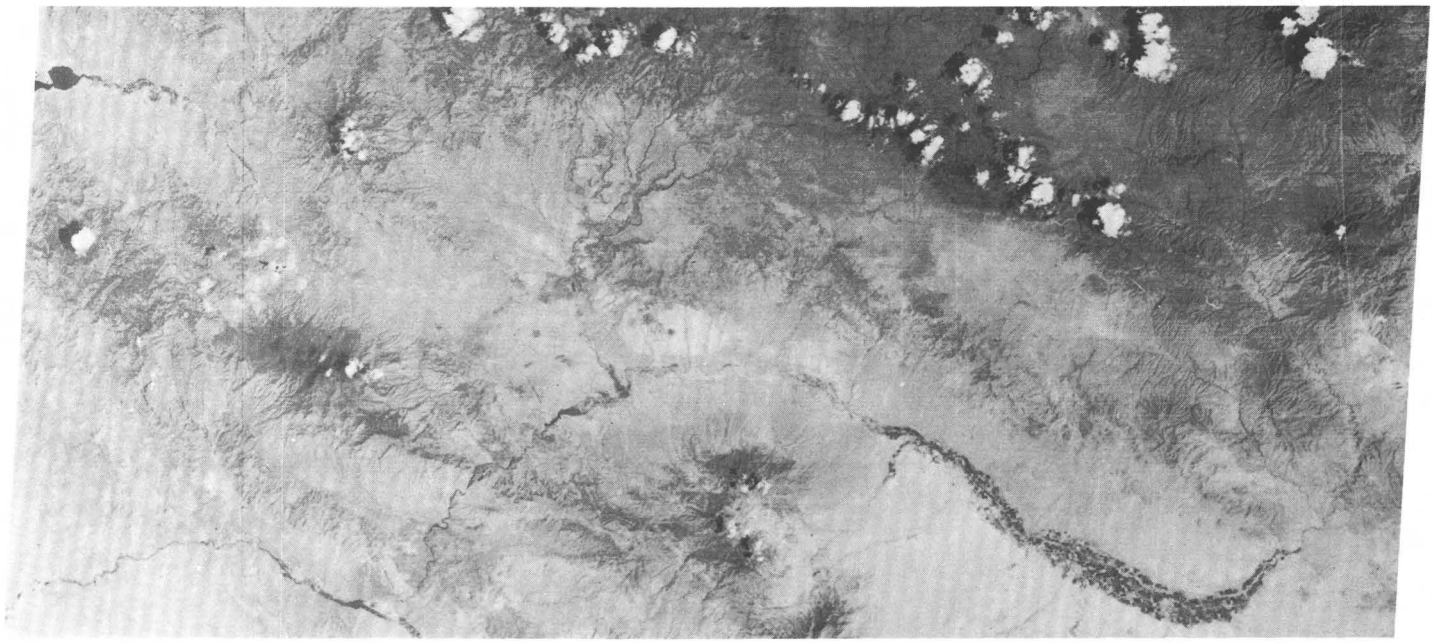


FIGURE 152.—Preflood ERTS–1 image of the Gila River valley of Arizona on Aug. 22, 1972 (part of 1030–17265, band 5).

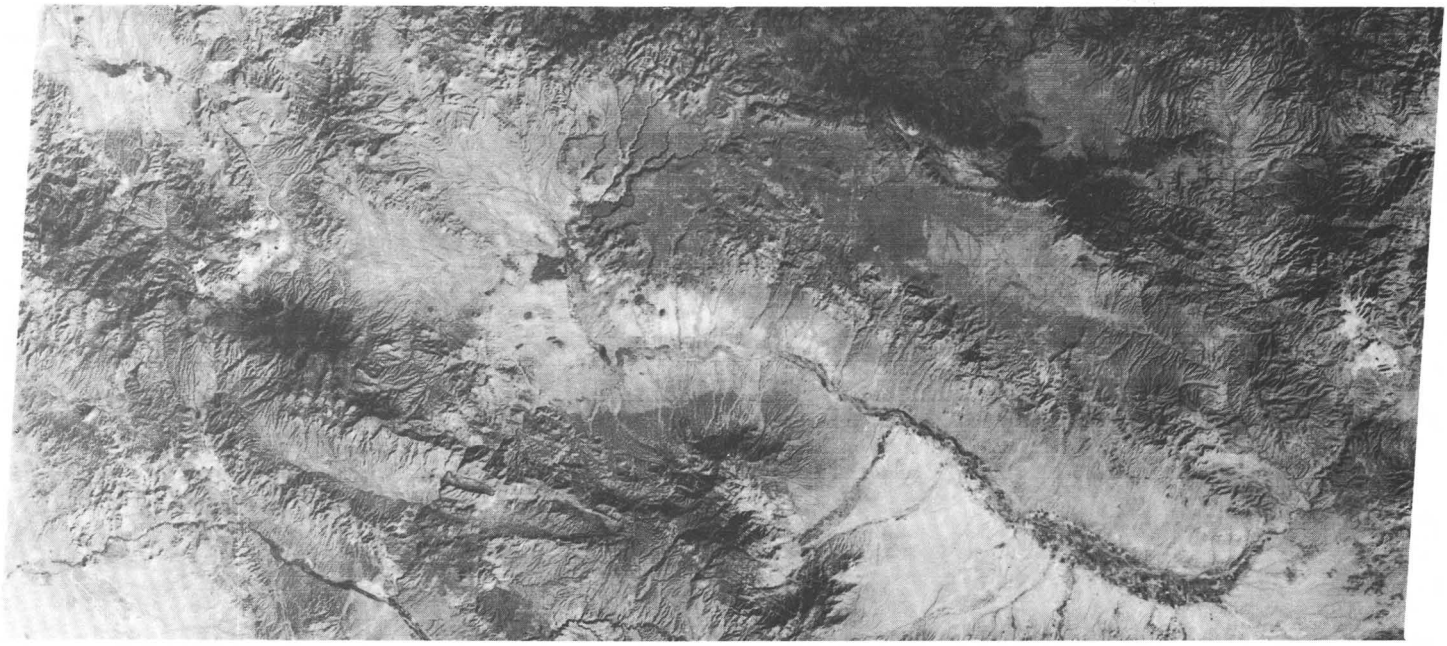


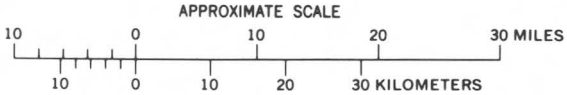


FIGURE 153.—Postflood ERTS–1 image of the Gila River valley of Arizona on Nov. 2, 1972 (part of 1102–17274, band 5).

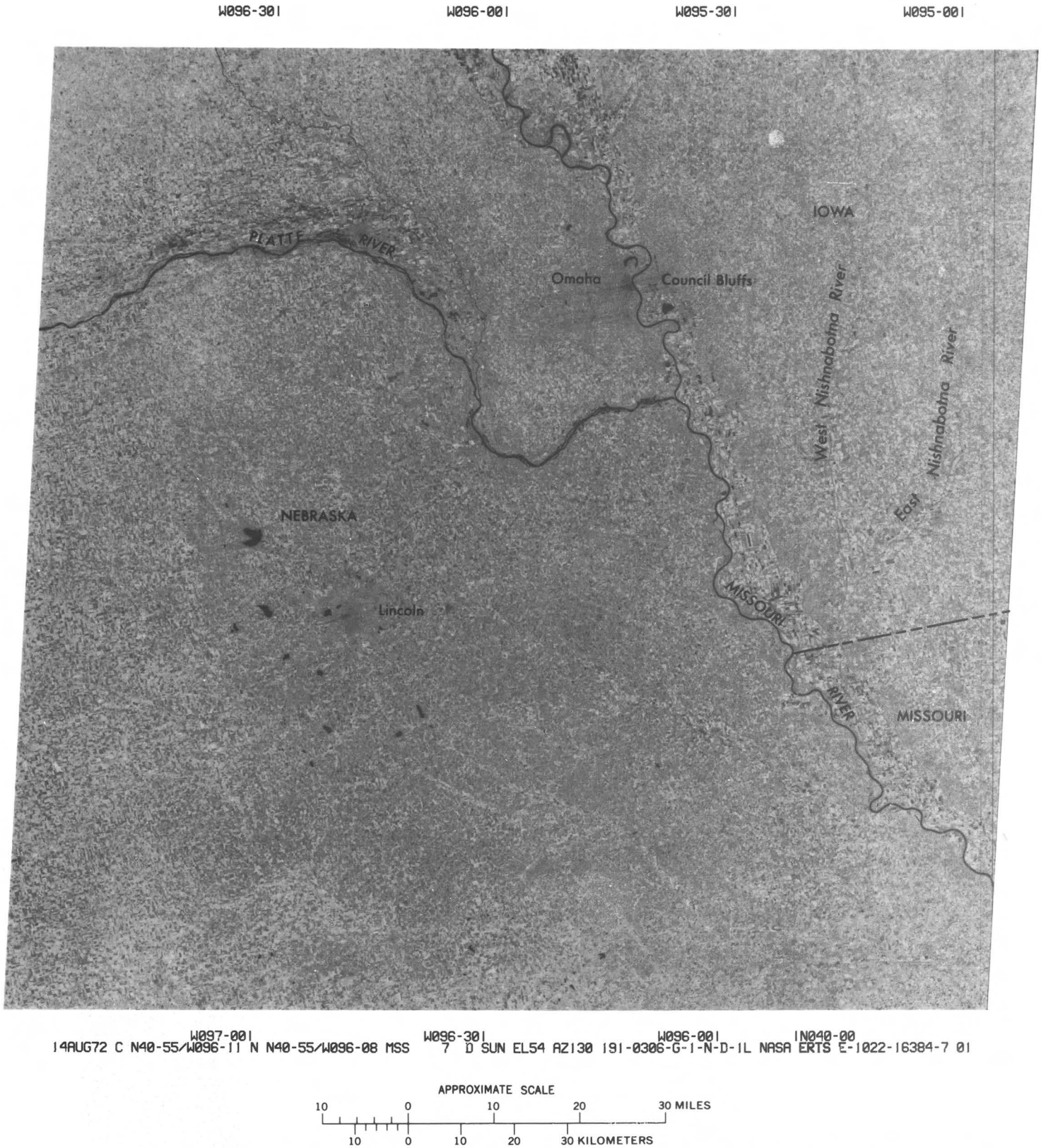


FIGURE 154.—Annotated preflood ERTS–1 image of southwestern Iowa on Aug. 14, 1972 (1022–16384, band 7).

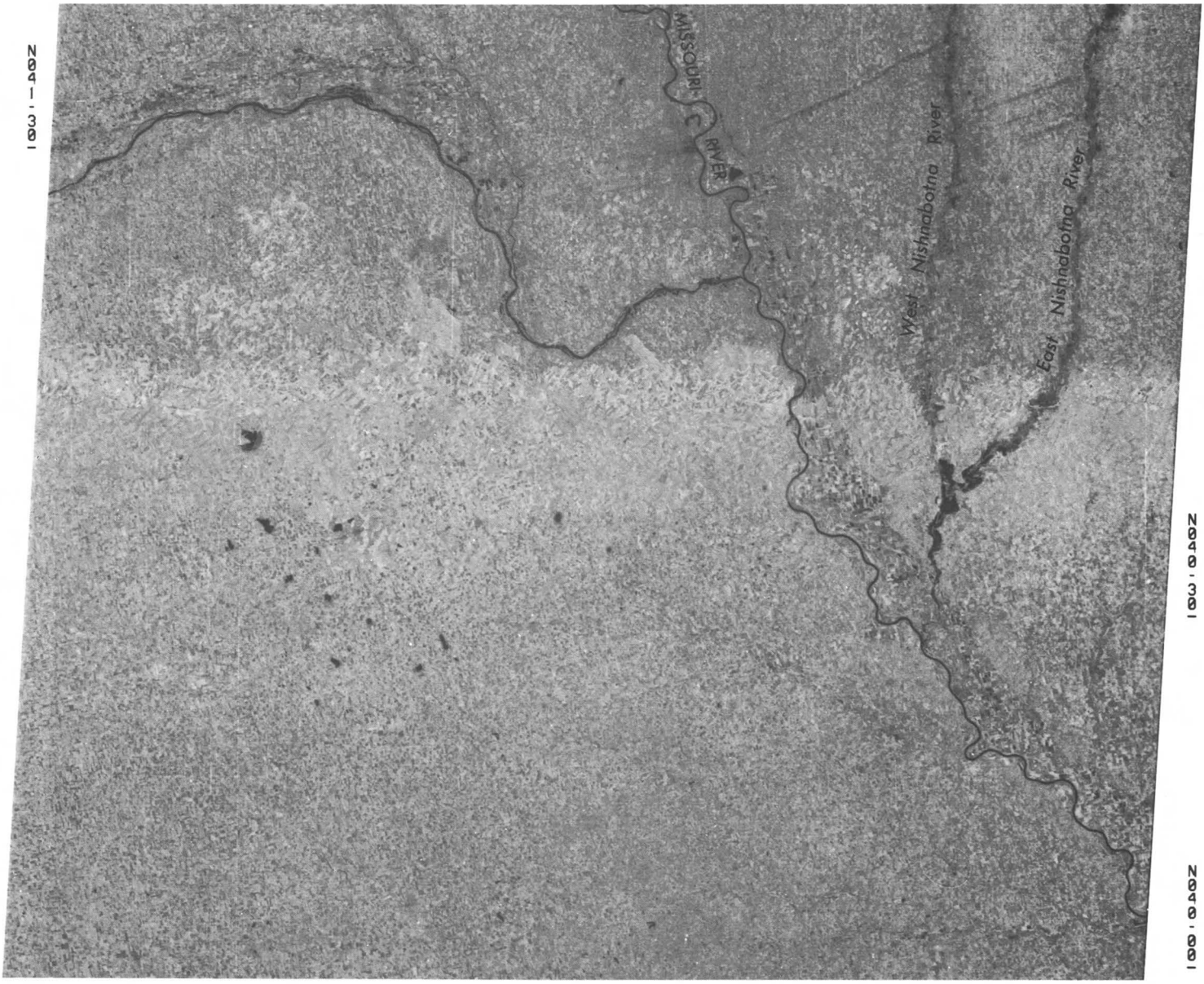


19SEP72 C N41-45/W095-55 N N41-42/W095-47 MSS 7 D SUN EL43 AZ144 191-0808-G-1-N-D-IL NASA ERTS E-1058-16383-7 01

19SEP72 C N40-19/W096-25 N N40-16/W096-18 MSS 7 D SUN EL44 AZ143 191-0808-G-1-N-D-IL NASA ERTS E-1058-16390-7 01

APPROXIMATE SCALE

10 0 10 20 30 MILES

10 0 10 20 30 KILOMETERS

FIGURE 155.—Annotated ERTS–1 image mosaic showing the West and East Nishnabotna Rivers in flood on Sept. 19, 1972 (1058–16383 and 1058–16390, band 7).

# OPTICAL PROCESSING OF ERTS DATA FOR DETERMINING EXTENT OF THE 1973 MISSISSIPPI RIVER FLOOD

By Morris Deutsch,
U.S. Geological Survey

Flood mapping by conventional methods is a time-consuming and expensive procedure. Traditionally either ground surveys or black and white panchromatic aerial photography has been used as a basic tool in flood mapping. Since the launch of ERTS–1, however, considerable interest has arisen in using ERTS data for flood applications. From some of the earliest data obtained by ERTS–1, Benson and Waltz (1973) delineated and measured an area inundated by a severe local rainstorm near Aberdeen, S. Dak. Hallberg and others (1973) mapped the Nishnabotna River flood in Iowa with ERTS data collected 1 week after the flood. They also assessed the use of color-infrared aerial photography versus traditional black and white panchromatic aerial photography for flood-mapping purposes and found the former to be highly superior. Morrison and Cooley (1973) mapped inundation limits of the Gila River flood in Arizona from ERTS imagery and obtained good agreement with maps prepared from aerial photography and ground surveys. Early in March 1973, in anticipation of flooding along the Mississippi River, the U.S. Geological Survey made a special request to NASA for data from subsequent passes of ERTS–1 over the Mississippi River valley. Basically, the objective was to map the extent of inundation as quickly as possible and with a minimum amount of conventional ground observations. It was surmised that specially processed ERTS data could provide hydrologists with a powerful new technique to supplement established methods of flood mapping, for the first time making it possible to map accurately the extent of flooding over very large areas, and to depict optically the flooded area. On March 31, ERTS–1 provided the first synoptic view of extensive flooding along two large reaches of the Mississippi River, between St. Louis, Mo., and Natchez, Miss. On May 4 and 5, ERTS–1 sensors imaged a strip of the Mississippi River reaching from midway between St. Louis and Cairo, Ill., to New Orleans and the Gulf of Mexico. The flood was at its peak within the reach between Cairo and Memphis, having peaked at Cairo on May 4 at 4.48 m above flood stage.

Figure 156, a set of mosaics prepared from band 7 images, shows the flood with the Ohio River to below its confluence with the Arkansas River. The inundation over a reach of the Mississippi River from above its confluence flood images (center) were obtained on March 31 and May 5 and were en-

larged to a scale of 1:1,000,000. In order to determine the area inundated by any flood, obviously, it is necessary to have data on the area normally covered by water. For this critical analysis, preflood data collected by ERTS–1 over the Mississippi River on Oct. 1 and 2, 1972, were used. The preflood mosaic (left) was also prepared from band 7 images. The difference in water-covered or wet surface, both in black, between October 1972 and the 1973 flood period is obvious.

The extent of flooding can be color coded by projecting a preflood image and one collected during the flood into a single composite image. Band 7 was used because there is little or no reflection of incident radiation from water in this spectral region, and thus the water appears dark in a positive print.

Display of the areas of flooding is shown on the right by a so-called "temporal composite" prepared by additive projection of the band 7 preflood images in red and the flood images in green. The composite covers the area of image overlap between the two dates. The composite shows excellent differentiation between dry soil, saturated soil, and standing water. In a properly processed positive (Deutsch and others, 1973), standing water is very dark, dry soil is relatively light, and saturated soil is intermediate in density.

When a nonflood image is projected as red, in register with a flood image projected as green, the composite color image is composed of the following elements:

1. Where there is surface water present in both images, the composite image receives little or no light and is therefore essentially black. This depicts the area normally covered by the river and other surface-water bodies.
2. Where the ground is not covered with water in both scenes, the composite image receives relatively equal amounts of red and green light and is therefore yellow. This depicts the area unaffected by flood waters.
3. Where there is surface water in the scene projected in green, and dry soil in the scene projected in red, the composite image receives only red light and is therefore a highly saturated red color. This depicts the area of flood inundation.
4. Where there is water-saturated soil in the scene projected in green, and dry soil in the scene projected in red, the composite image receives red light combined with a lesser amount of green light and results in a color on a continuum between yellow and red.

Because available ERTS–1 coverage is limited to cloud-free coverage once every 18 days, it cannot track the progress of a flood peak. Inspection of data collected by ERTS–1 on May 24, the day the Mississippi River receded to bankfull stage at St. Louis, indicates that changes in surface-reflectance characteristics caused by the flooding can be delineated, thus making it possible to map the total area flooded without the necessity of a real time, continuous system to track and image the peak flood waves. Figure 157 shows an additive temporal color composite of band 7 images showing the extent of flooding in red on March 31 against normal surface-water distribution on Oct. 2, 1972. Flood stage was at about 11.58 m on March 31, but on April 28 the flood peaked at 13.2 m, obviously inundating additional areas not flooded on March 31. Figure 157 also shows a temporal color composite of the postflood (May 24) data at St. Louis against the October images. In this composite there are areas shown in red that are not shown on the March/October temporal color composite. It is postulated that the later scene indicates changes in surface-reflectance characteristics caused by the flooding and that the area from which the flood waters receded between April 28 and May 24, including ponded flood waters, is depicted in tones of red.

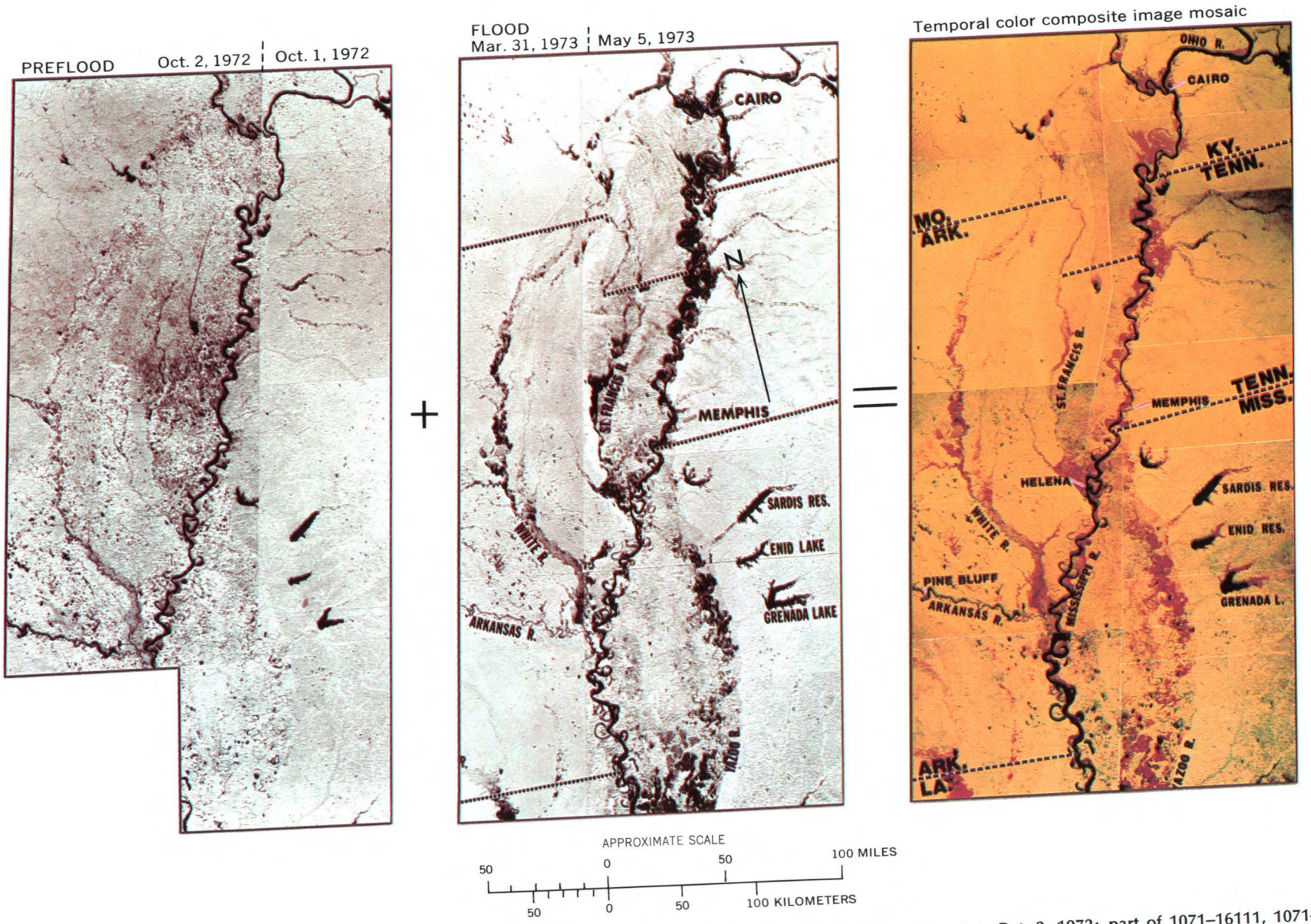


FIGURE 156.—Preflood and flood ERTS–1 image mosaics of the central Mississippi River valley, 1972–73, compared with optically combined temporal color composite image mosaic to show areas of flooding: red, flooded areas; light red, wet areas; black, normal conditions; and yellow and/or green, unflooded areas. (Oct. 1, 1972: part of 1070–16052, 1070–16055, 1070–16061, 1070–16064, band 7; Oct. 2, 1972: part of 1071–16111, 1071–16113, 1071–16120, band 7; Mar. 31, 1973: 1251–16122, 1251–16124, 1251–16131, 1251–16133, band 7; and May 5, 1973: 1286–16062, 1286–16065, 1286–16071, 1286–16074, band 7).

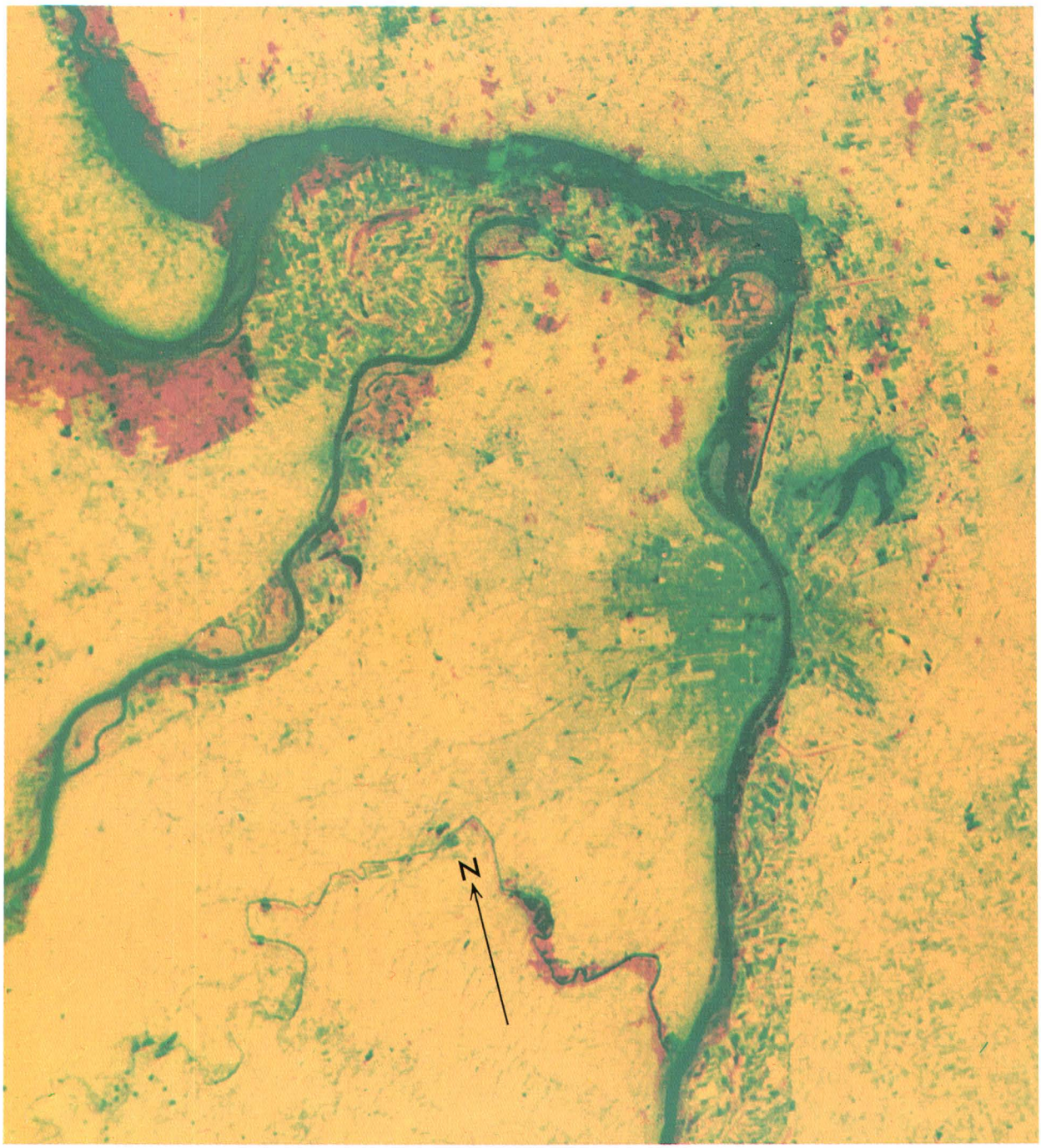


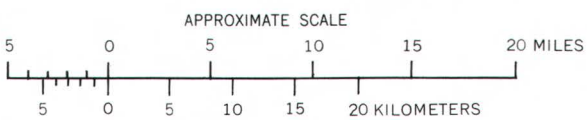


FIGURE 157.—Temporal color composite image of preflood October ERTS–1 image combined with March flood image (above) and May postflood image (opposite) of the St. Louis area (1071–16104, 1251–16115, 1305–16113, band 7).

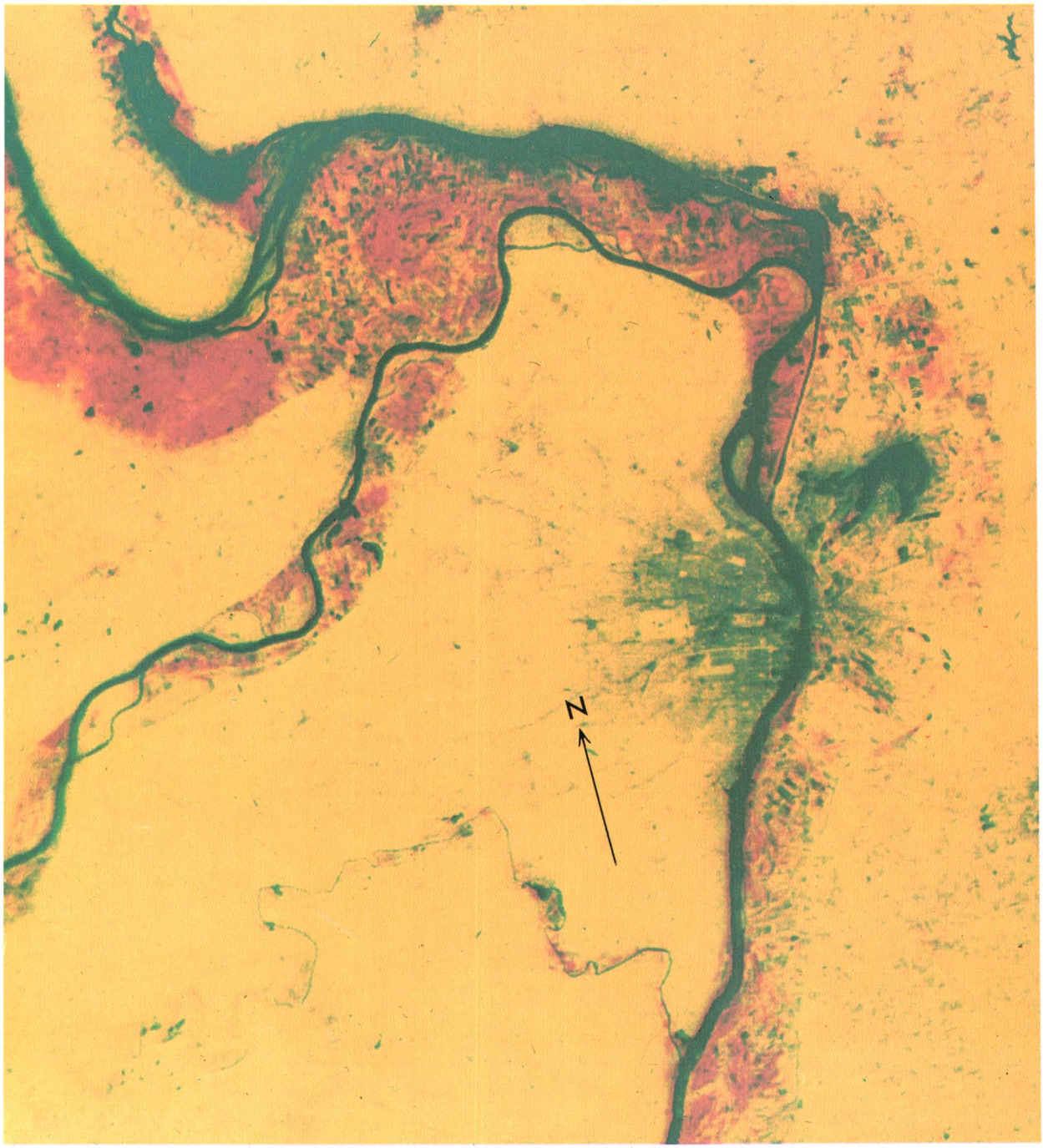


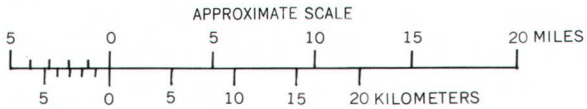


FIGURE 157.—Continued.

# MONITORING CLOUD-SEEDING CONDITIONS IN THE SAN JUAN MOUNTAINS OF COLORADO

By Archie M. Kahan,

Bureau of Reclamation

Project Skywater, the Bureau of Reclamation's weather-modification research program, has installed seven ERTS data collection platforms (DCP's) high in the rugged San Juan Mountains of southwestern Colorado (fig. 158). Here, amid wind-driven deep snow and intense cold, the platforms have proven to be extremely reliable communication tools (fig. 159).

Weather information relayed rapidly by the data collection system (DCS) is incorporated in the decisionmaking process of the Colorado River Basin Pilot Project, a part of Project Skywater and the largest winter cloud-seeding research program in the Nation.

Sensing devices linked to the platforms monitor precipitation, temperature, relative humidity, insolation, ice riming, wind direction, wind speed, snow water content, and streamflow (table 1). Data from each of the seven platforms are relayed to the satellite during each overhead orbit and then through Goddard Space Flight Center to a time-share computer in Denver where the data are translated into measured units and stored on file for access by users of Skywater's Environmental Computer Network.

The seven platforms, in remote regions accessible only by oversnow vehicles or helicopters, are being tested under severe environmental conditions to determine their operational suitability, maintenance requirements, reliability, and cost effectiveness.

The seven platform sites are in a variety of terrains, but all experience severe weather. One, near the crest of Wolf Creek Pass, is in an area that received 1,500 cm of snow during the 1972–73 winter. Winds in excess of 96 km/h are not uncommon, and temperatures plummet far below zero.

Equipment failures were anticipated in this environment, but during the first season's operation of the seven platforms, only one malfunction occurred, and it was caused by lightning.

Meteorologists have gained much data from the system, although it is still being tested. During the spring of 1973, when spring snows raised the possibility of floods in the valleys below, Project Skywater suspended the seeding project in a decision based, in part, on timely information provided by the ERTS DCS.

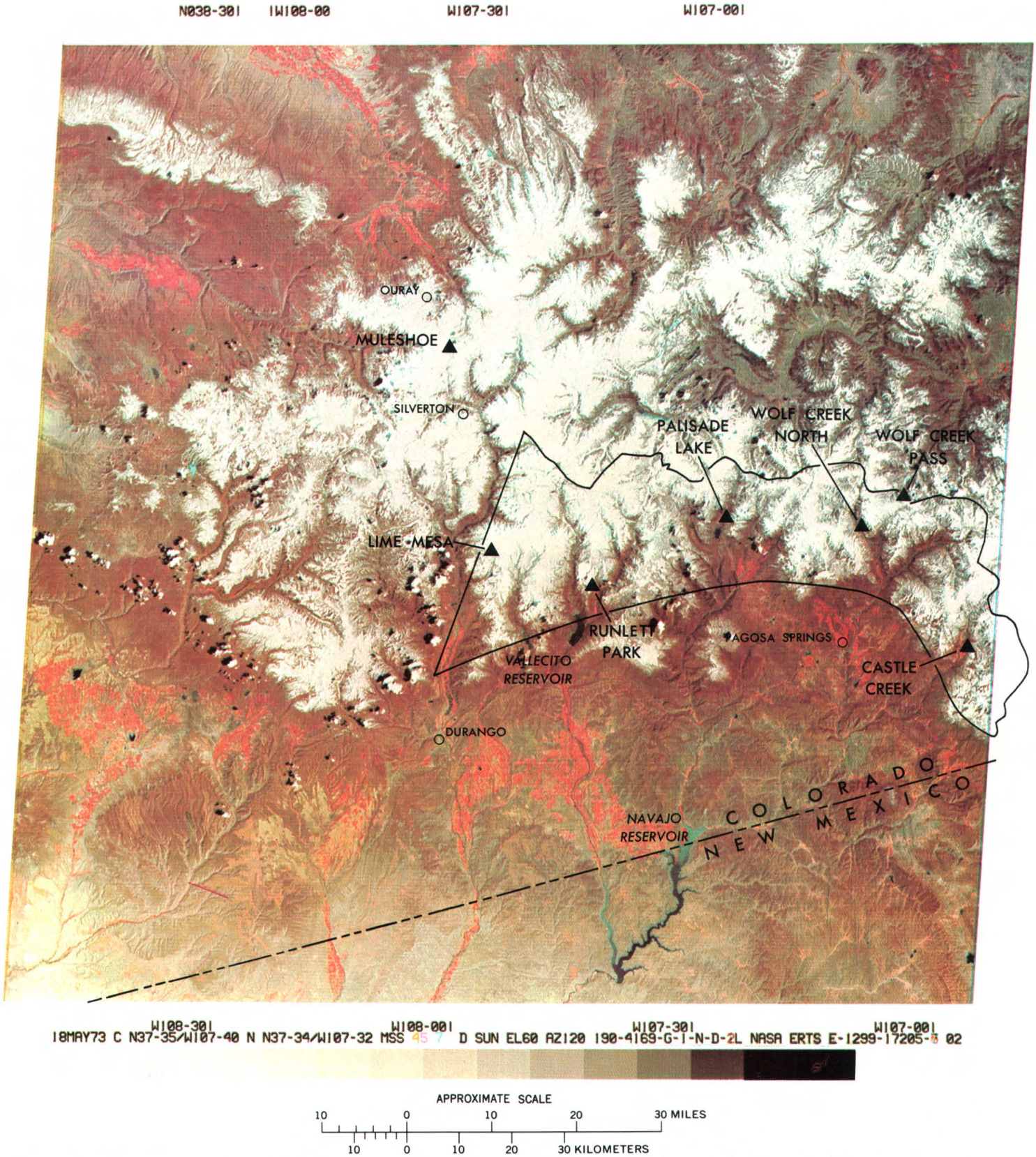


FIGURE 158.—Annotated color composite ERTS–1 image of the San Juan Mountain region of Colorado showing location of data collection platforms ▲ (1299–17205).

FIGURE 159.—Wolf Creek Pass data collection platform.

TABLE 1.—*Samples of Project Skywater DCS platform data*

| 1 | 2 | 3 | 4 | 5 | 6 | 7 | 8 | 9 | 10 | 11 | 12 | 13 |
|---|---|---|---|---|---|---|---|---|---|---|---|---|
| 100 | 6202 | | | | RUNPRK | | | | | | | |
| 110 | DATE | HHMM | SS | C | TEM | HUM | WSP | WDR | TVO | TVO | HSV | BAV |
| 120 | | | | | °C | % | MPH | DEG | BIT | BIT | V | V |
| 130 | FEB 19 74 | 0337 | 15 | 7 | −11.8 | 87. | 60.86 | 65. | 2.00 | 1.0 | 2.5 | 13.0 |
| 140 | FEB 19 74 | 0340 | 16 | 7 | −11.6 | 87. | 60.86 | 56. | 1.00 | 1.0 | 2.5 | 13.0 |
| 150 | FEB 19 74 | 0343 | 17 | 7 | −11.6 | 87. | 60.86 | 37. | 1.00 | 1.0 | 2.5 | 13.0 |
| 160 | FEB 19 74 | 0346 | 17 | 7 | −11.6 | 87. | 60.86 | 25. | 2.00 | 1.0 | 2.5 | 13.0 |
| 170 | FEB 19 74 | 0516 | 51 | 7 | −11.6 | 85. | 60.86 | 113. | 1.00 | 0.0 | 2.5 | 12.9 |
| 180 | FEB 19 74 | 0519 | 52 | 7 | −11.6 | 85. | 60.86 | 46. | 2.00 | 1.0 | 2.5 | 12.9 |
| 190 | FEB 19 74 | 0522 | 54 | 7 | −11.6 | 86. | 60.86 | 62. | 1.00 | 0.0 | 2.5 | 12.9 |
| 200 | FEB 19 74 | 0525 | 55 | 7 | −11.6 | 86. | 60.86 | 59. | 1.00 | 0.0 | 2.5 | 12.9 |
| 100 | 6212 | | | | MULESHOE | | | | | | | |
| 110 | DATE | HHMM | SS | C | TEM | HUM | WSP | WDR | RAD | ICE | HSV | BAV |
| 120 | | | | | °C | % | MPH | DEG | | | V | V |
| 160 | JAN 4 74 | 0422 | 08 | 7 | −14.5 | 13. | 12.12 | 272 | 6.74 | −2.5 | 11.9 | 12.3 |
| 170 | JAN 4 74 | 0425 | 51 | 7 | −14.3 | 13. | 24.38 | 276 | 6.74 | −2.9 | 11.9 | 12.3 |
| 180 | JAN 4 74 | 0429 | 35 | 7 | −14.3 | 13. | 10.97 | 285 | 6.74 | −2.9 | 11.9 | 12.3 |
| 190 | JAN 4 74 | 0433 | 18 | 7 | −14.7 | 13. | 13.27 | 263 | 6.74 | −2.9 | 11.9 | 12.3 |
| 200 | JAN 4 74 | 0606 | 25 | 7 | −14.1 | 13. | 21.31 | 268 | 6.74 | −2.9 | 11.9 | 12.3 |
| 210 | JAN 4 74 | 0610 | 09 | 7 | −14.3 | 13. | 12.88 | 291 | 6.74 | −2.5 | 11.9 | 12.3 |
| 220 | JAN 4 74 | 0613 | 53 | 7 | −14.5 | 13. | 10.58 | 267 | 6.74 | −2.9 | 11.9 | 12.3 |
| 230 | JAN 4 74 | 1520 | 09 | 7 | −15.7 | 13. | 18.63 | 286 | 16.32 | −2.9 | 11.9 | 12.3 |

Explanation of columns in table: 1, computer printout line number; 2, transmitter ID no. followed by date; 3, hour and minute; 4, seconds; 5, quality check; 6, temperature (°C); 7, relative humidity (percent); 8, wind speed (miles/h); 9, degrees azimuth of wind direction; 10, either null (TVO) or relative measure of sky radiation; 11, either null (TVO) or relative measure of rime ice accumulation; 12, ½ scale voltage; and 13, battery voltage. The two DCP stations listed are Runlet Park and Muleshoe.

# HYDROLOGY OF ARID AND SEMIARID AREAS

By J. Robert Owen and Lynn M. Shown,

U.S. Geological Survey

Surficial geology, topography, type and quantity of vegetation, and land use are factors that influence runoff and sediment yield. ERTS imagery is particularly useful, compared to other methods, for discerning these characteristics when the area to be surveyed is larger than about 250 km². For areas of several thousand square kilometers or more, ERTS imagery provides the most practical and rapid method of mapping these characteristics. Relationships between drainage-basin characteristics and hydrologic parameters have been developed in a variety of climatic regions (Thomas and Benson, 1970). In arid and semiarid regions, for which hydrologic data on streamflow and sediment discharge often are scarce or from widely scattered sites, the combined use of ERTS imagery and reconnaissance methods of estimating streamflow and sediment discharge can be a useful tool.

Figure 160 is a color composite ERTS–1 image that shows the canyonlands of the Colorado Plateau and the confluence of the Green and Colorado Rivers in Utah. The area of the Book Cliffs and Roan Cliffs is deeply dissected rugged topography. The dendritic drainage pattern in the vicinity of Book Cliffs indicates that the surficial geology is fairly homogeneous. The lack of reddish color in the southwest corner of the Book Cliffs indicates sparse vegetal cover, the result of low annual precipitation and shallow soils. High sediment yields and rapid runoff would be expected in that area owing to moderate to intense rainfalls on steep unprotected slopes. The reddish color in the higher Roan Cliffs area indicates more plant cover. Better protection from erosion afforded by more plant cover results in less sediment yield (J. R. Owen, unpub. data) in spite of the steep topography. Linear drainage patterns in the Roan Cliffs area indicate more geologic structural control of stream channels than in the Book Cliffs area.

An integrated channel system is another factor that determines the contribution from a source area to the water yield and sediment yield of a large drainage basin. Water and sediment from a source area generally do not leave the region when the channels are discontinuous or when flow is absorbed by dry channels and sediment is deposited during floods. For example, high sediment delivery could be expected in the area of the confluence of the Green and Colorado Rivers owing to the steep shale slopes and the well-integrated, continuous channel system. In contrast, only a few of the channels in the blue area at the base of the Book Cliffs are through-flowing to the main stream,

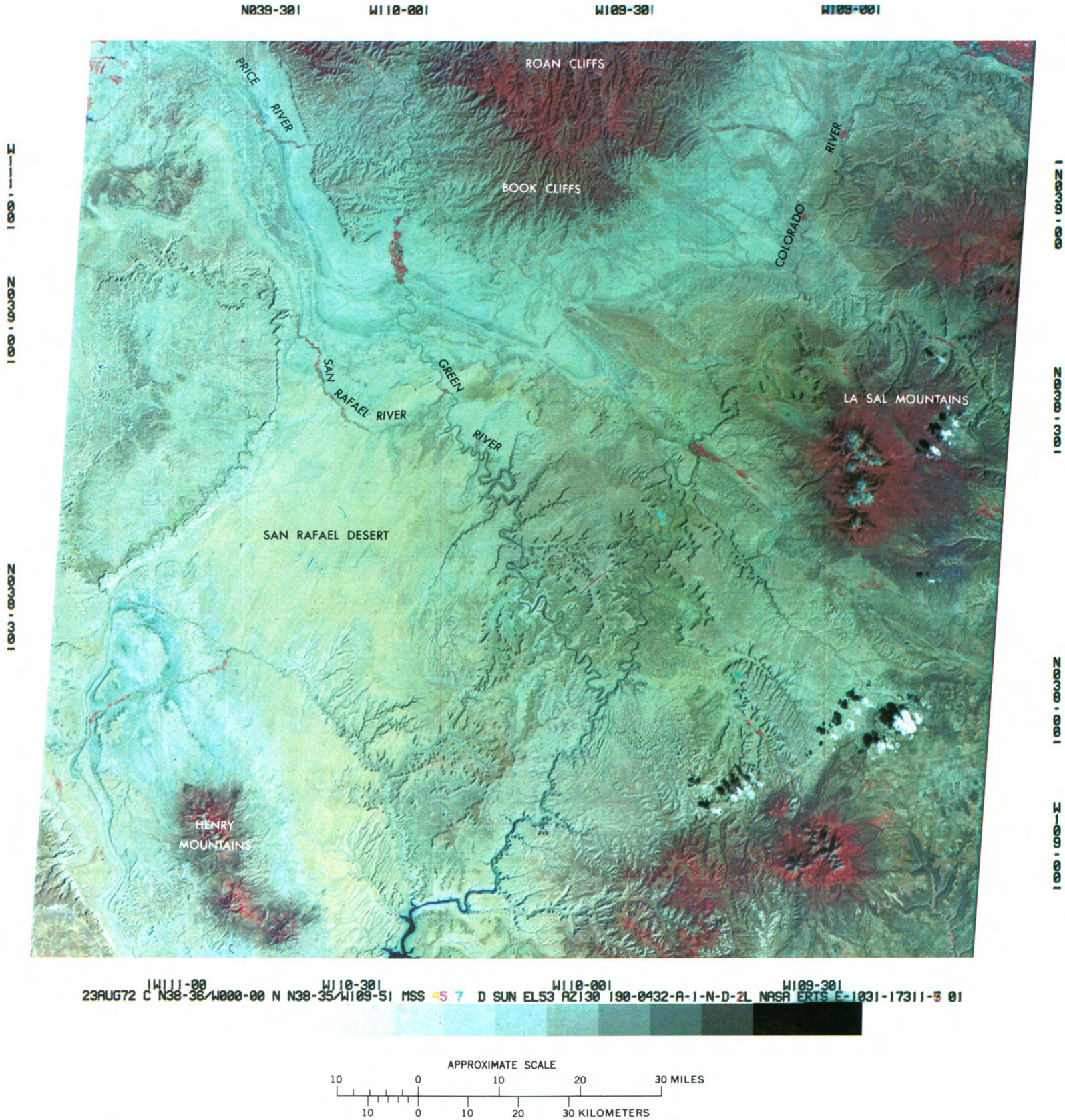


FIGURE 160.—Annotated color composite ERTS–1 image of the northern Colorado Plateau (1031–17311).

thereby tending to reduce the contribution of streamflow and sediment from this part of the drainage area.

The blue area at the base of the Book Cliffs is flat-lying marine Mancos Shale of Late and Early Cretaceous age. This area is a transport surface for streamflow originating in the Book Cliffs enroute to the Colorado, Green, and Price Rivers. The thin brownish lines are presently active channels bordered by greasewood or saltcedar. Most of the light-brown areas are pediments, and high-altitude aerial photography shows that active channels have been cut across some of them. The pediments are overlain by permeable sand and gravel, resulting in more plant cover and less water and sediment yield than is derived from the surrounding shale area. Owing to low annual rainfall, the shale area has a very sparse plant cover, as shown by the absence of red on the image. Another blue area surrounding the Henry Mountains is also underlain by Mancos Shale (Hintze and Stokes, 1964) with sparse plant cover and, therefore, may be expected to be similar to the Book Cliffs area in hydrologic response.

The orange-tan area west of the Green River is the San Rafael Desert. The longitudinal sand dunes oriented southwest to northeast are shown by the striated pattern. The sandy soil and the lack of a well-developed drainage pattern indicate that this area has a high infiltration capacity and, consequently, yields little runoff and sediment although the plant cover is sparse.

When large areas are under consideration, imagery at the scale of the synoptic ERTS imagery is a useful tool for evaluating areas for which hydrologic data are sparse. The interpretations derived from ERTS imagery relate the effects of physical features of drainage basins—such as topography, plant cover, surficial geology, and drainage patterns—to runoff and sediment yield. Reasonable limits of runoff and sediment yield for areas with similar hydrologic characteristics must be established from available streamflow records (U.S. Geological Survey, 1973), estimates of annual streamflow based on channel geometry measurements (Hedman, 1970), and sediment surveys in small stockponds (Peterson, 1962).

## REFERENCES


Bennett, P., and Sydor, Michael, 1974, Use of ERTS in measurements of water quality in Lake Superior and Duluth-Superior Harbor: Annual Remote Sensing of Earth Resources Conf., 3d, Tullahoma, Tenn., 1974, Selected Papers, p. 85–92.

Benson, L. A., and Waltz, F. A., 1973, Monitoring flood damage with satellite imagery: South Dakota State Univ. Remote Sensing Inst. Rept. 73–07, 11 p.

Bobek, H., 1963, Nature and implications of Quaternary climatic changes in Iran: UNESCO–WMO, Symposium on Changes of Climate, Rome Oct. 1961, p. 403–413.

Deutsch, Morris, 1974. Survey of remote sensing applications: Water Well Jour., v. 28, no. 7, p. 35–38.

Deutsch, Morris, Ruggles, F. H., Guss, Philip, and Yost, Edward, 1973, Mapping of the 1973 Mississippi River floods from the Earth Resources Technology Satellite: Am. Water Resources Assoc. Proc., no. 17, p. 39–55.

Dolgushin, L. D., and Osipova, G. B., 1972, Pau'satsii lednikov problema ikh prognozirovaniia na primere lednika medveshch'ego (Zapadniia Pamir): Akad. Nauk SSSR, Izv. Ser. Geog., no. 2, p. 89–98.

Graybeal, G. E., Hall, F. G., Moore, B. H., and Schlosser, E. H., 1974, ERTS–1 data in support of the National Program of Inspection of Dams: NASA Goddard Space Flight Center, Symposium on the Earth Resources Technology Satellite–1, 3d, Washington, D.C., Dec. 1973, Proc., v. 1, sec. B, p. 1023–1039.

Hadley, R. F., and Schumm, S. A., 1961, Sediment sources and drainage-basin characteristics in upper Cheyenne River Basin: U.S. Geol. Survey Water-Supply Paper 1531–B, p. 137–198.

Hallberg, G. R., Hoyer, B. E., and Rango, Albert, 1973, Application of ERTS–1 imagery to flood inundation mapping: NASA Goddard Space Flight Center, Symposium on Significant Results Obtained from the Earth Resources Technology Satellite–1, 2d, New Carrollton, Md., Mar. 1973, Proc., v. 1, sec. A, p. 745–753.

Hedman, E. R., 1970, Mean annual runoff as related to channel geometry of selected streams in California: U.S. Geol. Survey Water-Supply Paper 1999–E, 17 p.

Higer, A. L., Cordes, E. H., and Coker, A. E., 1973, Modeling subtropical water-level dynamics distribution [abs.]: NASA Goddard Space Flight Center, Symposium on Significant Results Obtained from the Earth Resources Technology Satellite–1, 2d, New Carrollton, Md., Mar. 1973, Proc., v. 1, sec. A, p. 793.

Higer, A. L., Coker, A. E., and Cordes, E. H., 1974, Water-management models in Florida from ERTS–1 data: NASA Goddard Space Flight Center, Symposium on the Earth Resources Technology Satellite–1, 3d, Washington, D.C., Dec. 1973, Proc., v. 1, sec. B, p. 1071–1088.

Hintze, L. F., and Stokes, W. L., 1964, Geologic map of southeastern Utah: Utah State Land Board, 1 sheet.

Holdsworth, Gerald, 1974, Surge of Tweedsmuir Glacier, British Columbia, Canada: Ice, no. 43, p. 23.

Hollyday, E. F., Moore, G. K., and Burchett, C. R., 1973, Preliminary assessment of a Tennessee lineament, *in* Shahrokhi, F., ed., Remote sensing of Earth resources, v. 2: Tullahoma, Tenn., Univ. of Tenn. Space Inst., p. 119–128.

Huber, H., 1967, Geological map of Maharlu Salt Lake southwest of Shiraz, Fars Province: National Iranian Oil Co. Geol. Note 157, encl. 2.

Jarman, J. W., 1973, The Earth Resources Program of the Corps of Engineers: NASA Goddard Space Flight Center, Symposium on Significant Results Obtained from the Earth Resources Technology Satellite–1, 2d, New Carrollton, Md., Mar. 1973, Proc., v. 2, p. 127–141.

Jewell, W. B., 1947, Barite, fluorite, galena, and sphalerite veins of middle Tennessee: Tenn. Div. Geology Bull. 51, 114 p.

Keefer, W. R., 1965, Stratigraphy and geologic history of the uppermost Cretaceous, Paleocene, and lower Eocene rocks in the Wind River Basin, Wyoming: U.S. Geol. Survey Prof. Paper 495–A, 77 p.

Krinsley, D. B., 1968, Geomorphology of three kavirs in northern Iran, *in* U.S. Air Force Cambridge Research Lab., Playa surface morphology: miscellaneous investigations: Cambridge Research Lab. Environmental Research Paper no. 283, U.S. Geol. Survey for U.S. Air Force, p. 105–130.

——— 1969, Caractères morpho-climatiques des kavirs d'Iran: INQUA, Congrès, 8th, Paris 1969, Résumés des Communications, p. 33.

——— 1970, A geomorphological and paleoclimatological study of the playas of Iran: U.S. Geol. Survey Interagency Rept. Military–1, 329 p.

——— 1972a, Dynamic processes in the morphogenesis of salt crusts within the Great Kavir, north-central Iran: Internat. Geol. Cong., 24th, Montreal 1972, Proc., sec. 12, p. 167–174.

——— 1972b, The paleoclimatic significance of the Iranian playas, *in* Zinderen Bakker, E. M. Van, ed., Palaeoecology of Africa: Cape Town, A. A. Balkema, v. 6, p. 114–120.

Lind, A. O., Henson, E. B., and Pelton, James, 1973, Environmental study of ERTS–1 imagery—Lake Champlain and Vermont: NASA Goddard Space Flight Center, Symposium on Significant Results Obtained from the Earth Resources Technology Satellite–1, 2d, New Carrollton, Md., Mar. 1973, Proc., v. 1, sec. A, p. 643–650.

Love, J. D., Weitz, J. L., and Hose, R. K., 1955, Geologic map of Wyoming: U.S. Geol. Survey, scale 1:500,000.

Maykut, G. A., and Untersteiner, Norbert, 1971, Some results from a time-dependent thermodynamic model of sea ice: Jour. Geophys. Research, v. 76, no. 6, p. 1550–1575.

Morrison, R. B., and Cooley, M. E., 1973, Assessment of flood damage in Arizona by means of ERTS–1 imagery: NASA Goddard Space Flight Center, Symposium on Significant Results Obtained from the Earth Resources Technology Satellite–1, 2d, New Carrollton, Md., Mar. 1973, Proc., v. 1, sec. A, p. 755–760.

Nashville Banner, 1973, Zinc exploration boom may develop in midstate: Nashville, Tenn., Nashville Banner, Mar. 29, 1973, p. 64.

Paulson, R. W., 1973a, Preliminary analysis of ERTS-relayed water-resources data in the Delaware River Basin: NASA Goddard Space Flight Center, Symposium on Significant Results Obtained from the Earth Resources Technology Satellite–1, 2d, New Carrollton, Md., Mar. 1973, Proc., v. 1, sec. A, p. 777–792.

——— 1973b, Analysis of ERTS-relayed water-resources data in the Delaware River Basin: Am. Soc. Photogrammetry, Symposium on Management and Utilization of Remote Sensing Data, Sioux Falls, S. Dak., 1973, Proc., p. 191–205.

——— 1974, An evaluation of the ERTS data collection system as a potential operational tool; NASA Goddard Space light Center, Symposium on the Earth Resources Technology Satellite–1, 3d, Washington, D.C., Dec. 1973, Proc., v. 1, sec. B, p. 1099–1111.

Peterson, H. V., 1962, Hydrology of small watersheds in western States: U.S. Geol. Survey Water-Supply Paper 1475–I, p. 217–356.

Pluhowski, E. J., 1973, Remote sensing of turbidity plumes in Lake Ontario: NASA Goddard Space Flight Center, Symposium on Significant Results Obtained from the Earth Resources Technology Satellite–1, 2d, New Carrollton, Md., Mar. 1973, Proc., v. 1, sec. A, p. 837–846.

Scherz, J. P., Sydor, Michael, and Van Domelen, J. F., 1974, Aircraft and satellite monitoring of water quality in Lake Superior near Duluth: NASA Goddard Space Flight Center, Symposium on the Earth Resources Technology Satellite–1, 3d, Washington, D.C., Dec. 1973, Proc., v. 1, sec. B, p. 1619–1636.

Stortz, Kirby, and Sydor, Michael, 1974, Remote sensing of Lake Superior: Internat. Symposium on Remote Sensing of Environment, 9th, Ann Arbor, Mich., 1974, Proc., v. 2, p. 933–937.

Sydor, Michael, 1974, Ice growth in Duluth harbor and western Lake Superior: Univ. of Tenn. Annual Remote Sensing of Earth Resources Conf., 3d, Tullahoma, Tenn., 1973, Selected Papers, p. 107–116.

Thomas, D. M., and Benson, M. A., 1970, Generalization of streamflow characteristics from drainage-basin characteristics: U.S. Geol. Survey Water-Supply Paper 1975, 55 p.

Thorarinsson, Sigurdur; Saemundsson, Kristján; and Williams, R. S., Jr., 1973 [1974], ERTS–1 image of Vatnajökull: Analysis of glaciological, structural, and volcanic features: Jökull, v. 23, p. 7–17.

U.S. Geological Survey, 1973, Surface water supply of the United States, 1966–70, pt. 9, v. 2, Colorado River basin from Green River to Compact Point: U.S. Geol. Survey Water-Supply Paper 2125, 634 p.

Whitcomb, H. A., and Lowry, M. E., 1968, Groundwater resources and geology of the Wind River basin area, central Wyoming: U.S. Geol. Surv. Hydrol. Inv. Atlas, HA–270.

Wiesnet, D. R., and McGinnis, D. F., 1974, Snow-extent mapping and lake ice studies using ERTS–1 MSS together with NOAA–2 VHRR: NASA Goddard Space Flight Center, Symposium on the Earth Resources Technology Satellite–1, 3d, Washington, D.C., Dec. 1973, Proc., v. 1, sec. B, p. 995–1009.

Williams, R. S., Jr., 1972, Satellite geological and geophysical remote sensing of Iceland [abs.]: Internat. Symposium on Remote Sensing of Environment, 8th, Ann Arbor, Mich., 1972, Proc., p. 1465–1466.

Williams, R. S., Jr.; Bödvarsson, Ágúst; Fridriksson, Sturla; Pálmason, Gudmundur; Rist, Sigurjón; Sigtryggsson, Hlynur; Thorarinsson, Sigurdur; and Thorsteinsson, Ingvi, 1973a, Satellite geological and geophysical remote sensing of Iceland—preliminary results from analysis of MSS imagery: NASA Goddard Space Flight Center, Symposium on Significant Results Obtained from the Earth Resources Technology Satellite–1, 2d, New Carrollton, Md., Mar. 1973, Proc., v. 1, sec. A, p. 317–327.

Williams, R. S., Jr.; Bödvarsson, Ágúst; Fridriksson, Sturla; Pálmason, Gudmundur; Rist, Sigurjón; Sigtryggsson, Hlynur; Saemundsson, Kristján; Thorarinsson, Sigurdur; and Thorsteinsson, Ingvi, 1973b, Iceland—preliminary results of geologic, hydrologic, oceanographic, and agricultural studies with ERTS–1 imagery: Am. Soc. Photogrammetry, Symposium on Management and Utilization of Remote Sensing Data, Sioux Falls, S. Dak., 1973, Proc., p. 17–35.

Williams, R. S., Jr.; Thorarinsson, Sigurdur; and Saemundsson, Kristján, 1973c, Vatnajökull area, Iceland—new volcanic and structural features on ERTS–1 imagery [abs.]: Geol. Soc. America, Abs. with Programs, v. 5, no. 7, p. 864–865.

Williams, R. S., Jr.; Bödvarsson, Ágúst; Fridriksson, Sturla; Pálmason, Gudmundur; Rist, Sigurjón; Sigtryggsson, Hlynur; Saemundsson, Kristján; Thorarinsson, Sigurdur; and Thorsteinsson, Ingvi, 1974, Environmental studies of Iceland with ERTS–1 imagery: Internat. Symposium on Remote Sensing of Environment, 9th, Ann Arbor, Mich., 1974, Proc., v. 1, p. 31–81.

Williams, R. S., Jr.; Bödvarsson, Ágúst; Rist, Sigurjón; Saemundsson, Kristján; and Thorarinsson, Sigurdur, 1975, Glaciological studies in Iceland with ERTS–1 imagery: Jour. Glaciology v. 15, no. 73 (in press).

Williams, R. S., Jr., and Thorarinsson, Sigurdur, 1973 [1974], ERTS–1 image of Vatnajökull area: General comments: Jökull, v. 23, p. 1–6.

# CHAPTER 4. APPLICATIONS TO LAND-USE MAPPING AND PLANNING

## INTRODUCTION

By James R. Anderson,
U.S. Geological Survey

"Of all the factors that determine the quality of our environment, the most fundamental is the use we make of our land" (Curtis, 1973). This statement is true not only in the big urban centers of our country, where such problems as air and noise pollution plague us and often go unresolved, but also in the most remote rural and relatively untouched parts of the Nation.

The growing population of this country, coupled with an increasing variety of demands being made on land resources, has brought an expanding array of pressures on the available resource base. These pressures have caused conflicts that urgently need attention. Some examples are agricultural production in conflict with real-estate development and the resulting urbanization; environmental protection versus production of energy to meet increasing demands for power; recreational development versus the use of the land for forestry, grazing, and mining; conservation of coastal areas for recreational uses in the face of needs for more port facilities and shoreline industrial sites; and preservation of wetlands for natural wildlife and fisheries habitat in the face of new demands for development of such wetlands for urban uses, agricultural production, and other uses.

One of the prime requisites for better use of land is information on existing land use and on changes in land use over time. Presently no systematic compilation of information on existing land use and its changes is made on a regional and national basis. In order to meet the need for promptness and regularity in land-use inventory and mapping, traditional approaches to the compilation and dissemination of land-use data must be revised.

We have available the remote-sensing capability to map effectively the land use of the entire United States at regional scales within a reasonable time frame compatible with the needs of people engaged in land-use planning, management, regulation, and research. Remote-sensor data from ERTS–1, from high-altitude platforms, and from other sources will provide a land-use data-collection system capable of providing a cost-effective and timely periodic updating of such data in order that the dynamics and trends in land use can be studied effectively.

Federal and State agencies need an up-to-date regional inventory of land use throughout the country on a basis that is uniform in date, scale, and definition; Anderson, Hardy, and Roach (1972) have developed a land-use classification system to meet the need for at least the more general classes (levels I and II).

The approach to land-use classification being proposed by the U.S. Geological Survey is resource oriented. In using remote-sensor data as the main data base, a "cover" approach to land-use classification must be used rather than an "activity" approach. Farming, grazing, and forestry are activities; cropland, rangeland, and forestland are cover categories.

A reasonable level of accuracy in compilations of land-use data from remote-sensor data has already been achieved. At the more generalized levels of categorization, correct interpretation of land use 85 to 90 percent of the time is considered to be an adequate level of accuracy. Often overlooked is the fact that data collected by enumeration and ground-observation techniques are generally not infallible. For example, in the Census of Agriculture taken in 1969 by the U.S. Bureau of the Census, the number of farms was low by 14 percent.

One of the possible significant advantages of ERTS–1 is the capability to identify areas where changes in land use are occurring. ERTS imagery does not generally permit a complete detailed identification of the more specialized levels of categorization (levels II and III) of land uses, but the availability of repetitive coverage on a seasonal and annual basis will enable us to become more efficient in updating land-use data. We simply cannot afford to compile entirely new land-use maps on a regular annual basis over extensive areas.

Some examples of the use of ERTS data as an aid in the inventory and mapping of land use are presented here.

North and Linebeck (p. 228) have conducted an interesting and informative experiment in extracting a single theme or land-use type, forestland, from ERTS–1 data for the entire State of Alabama within a relatively few days and within a few weeks after the ERTS overpasses were made. While such land-use data obtained from ERTS will need to be calibrated with existing definitions of land use to be most useful, the potential for inexpensive and rapid surveys of extensive land use and cover conditions, such as for forestland, tundra, and so on, offers opportunities to acquire useful information in a reasonable time frame for planning and management purposes. This is true particularly for developing nations where such information is often lacking.

The use of ERTS data by Cast (p. 225) for an area in northeastern Colorado also offers an informative example of how land use and cover conditions can in a general way be related effectively and quickly to other land characteristics such as soil type, slope, and drainage.

Place (p. 230), in using ERTS data in the Phoenix area of Arizona to monitor land-use changes, has demonstrated that land-use changes of regional significance can be monitored with reasonable ERTS–1 data. Although the detailed character of the changes actually occurring, particularly in urban areas, generally cannot be specifically identified by visual interpretation of ERTS data, it helps land planners and managers to know where land-use changes are occurring and the general extent of such changes.

Ellefsen, Gaydos, and Wray (p. 234) have been exploring the use of digital data from ERTS–1 to obtain more refined land-use data than can be obtained from the visual interpretation of ERTS–1 data. Results to date indicate that land-use mapping by the machine processing of ERTS–1 data is feasible.

# LAND USE IN NORTHEAST COLORADO

By Larry D. Cast,
Bureau of Reclamation

In the semiarid climate of the western Great Plains, man's agricultural use of the land requires supplemental moisture to ensure a harvest. The ERTS image in figure 161 readily indicates the use of the land as determined by moisture and soil. The South Platte valley—including both the present and ancestral valleys—ranges from 2.4 to 4.8 km in width and is accented on the image by the red band caused by reflectance differences between the rich irrigated crops and the dry grasses and dryland farming. Irrigation water is obtained from high-yield wells located in the valley alluvium and from river diversions. Another large block of irrigated land can be seen in the left center of the image; irrigation there is by surface water brought into the area via canals.

The areas denoted dryland farming are areas where ground water is insufficient to support an irrigation regime or where surface water is not available. The soil is suitable for dryland farming because it does have good moisture-retention properties and lends itself to a summer fallow method whereby much of the land is farmed only every other year. Areas where soil conditions are marginal for dryland farming are denoted dryland farming and grassland. In the ERTS image (fig. 162) these are areas of relatively even gray shades with numerous small light-colored rectangles. The light color is due to the characteristic reflectance from bare ground, either summer fallow or the dry stubble of harvested wheat; wheat is the primary crop of such an area.

The areas utilized strictly for a grassland (ranching) operation have a relatively even and continuous gray color. These are areas where the soil tends to be sandy and does not have sufficient moisture-retention properties to permit row-crop agriculture. Another shortcoming of this area's sandy soil is that it is susceptible to becoming active, a situation in which areas of exposed sand or blowouts can be created by wind erosion. Grassland in areas of ancient sand dunes often have areas of active sand. These appear in the image as white dots in the grassland-dune sand areas.

The larger urbanized areas, such as Denver, can be readily recognized by the gridlike pattern of highways and reflectance properties of buildings and streets.

The sandy floor of Bijou Creek stands out sharply near the center of the image. It is an intermittent stream that has a high base load of sand during periods of high runoff.

One of the more intriguing things that can be readily identified are the circular sprinkler (center pivot) irrigation systems. These systems each irrigate 50 to 60 ha and appear on the image as a small dark dot. A cluster of these systems is identified in the upper left corner of the image, but these dark dots can be seen in many parts of the image. The date of the imagery is July 27, 1973; corn, sugarbeets, and alfalfa are the principal irrigated crops, and late July finds them in their peak growth. This is also normally a dry period that emphasizes the contrast between irrigated and nonirrigated land.

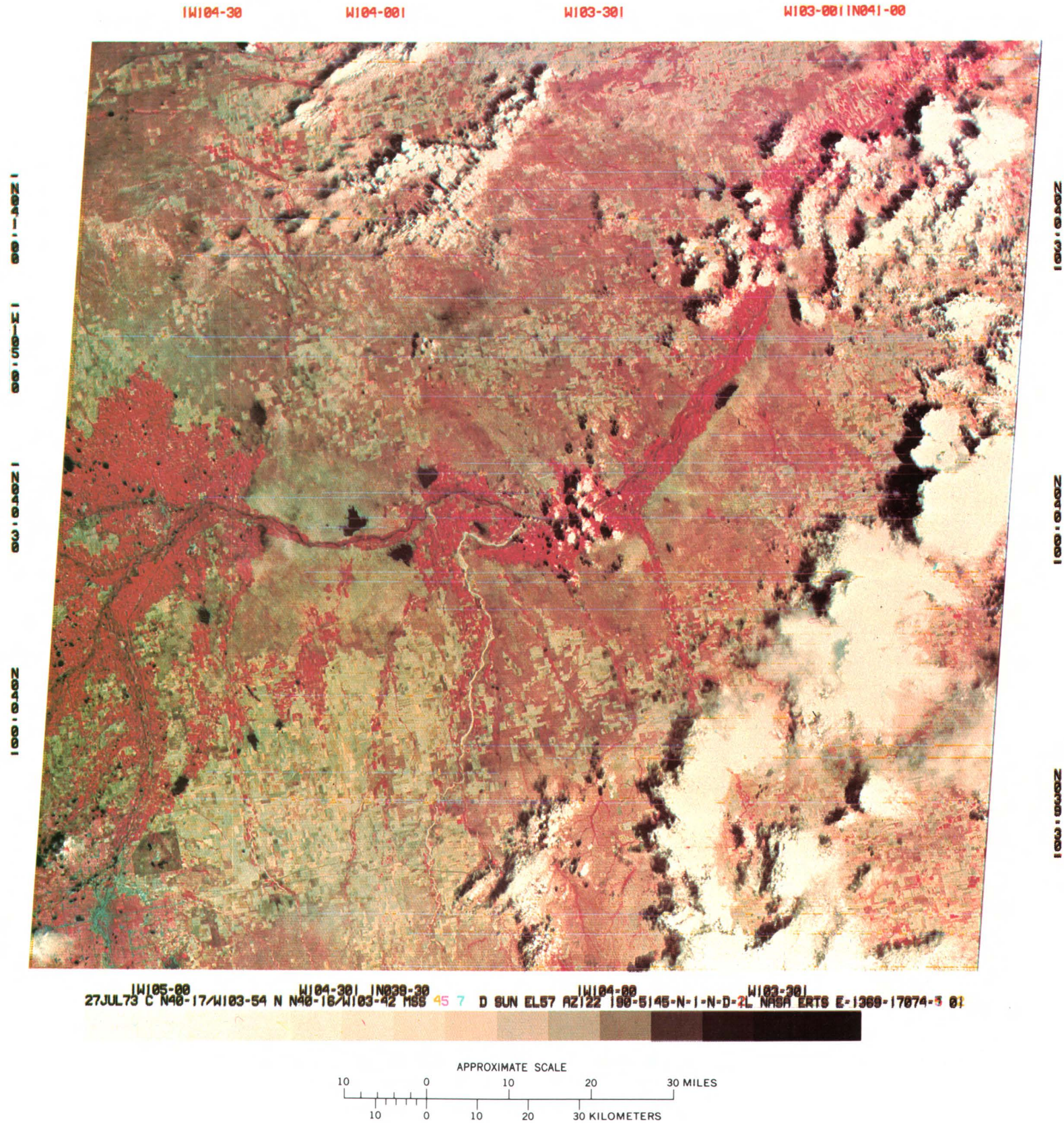


FIGURE 161.—Color composite ERTS–1 image of the South Platte River valley of Colorado (1369–17074).

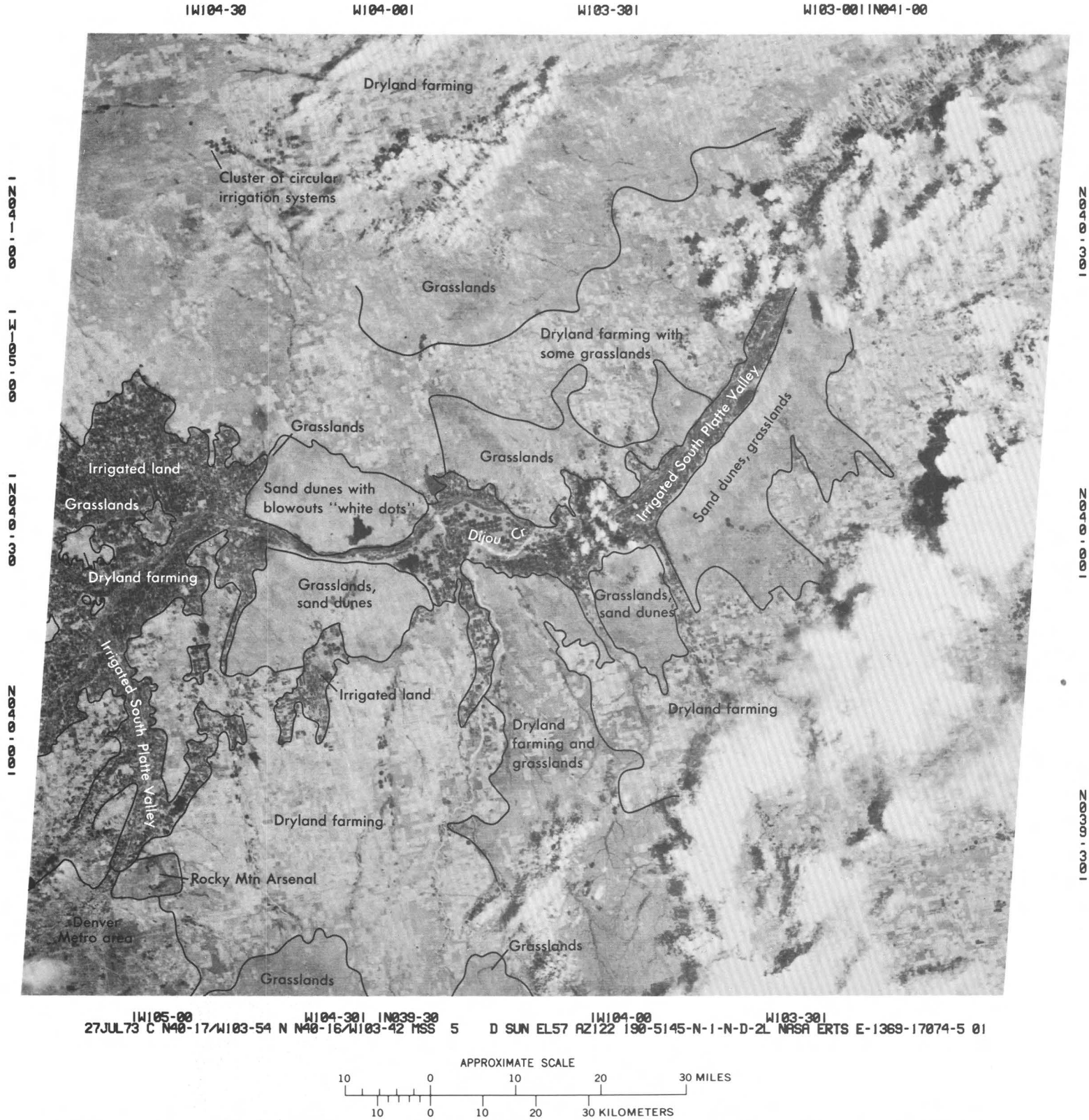


FIGURE 162.—Annotated ERTS–1 image of the South Platte River valley showing irrigated lands, grasslands, and dryland farming areas (1369–17074, band 5).

# THEMATIC MAPPING OF FORESTED AND CULTIVATED LAND IN ALABAMA

By Gary W. North, U.S. Geological Survey,
and Neal G. Lineback, University of Alabama

The ERTS–1 imagery being collected today is giving man a chance to monitor the changing face of his planet. The color composite ERTS–1 uncontrolled mosaic shown in figure 163 was made by the EROS Experiments and Evaluation Office in Bay St. Louis, Miss. The work was part of a research project being conducted by the Geological Survey of Alabama entitled, "User acceptance and implementation of ERTS–1 data in Alabama."

Eleven color composite ERTS–1 images, taken during the period from August 1972 to March 1973, were carefully mosaiced to form one large picture of the State of Alabama at an initial scale of 1:1,000,000. Major cities, such as Birmingham, located near the center of the mosaic, appear as light-blue areas. Sediment plumes, such as those in Mobile Bay in the southern part of the State, also show up as light tones, as do areas cleared for agriculture. This is best illustrated by Alabama's "Black Belt," the prominent light-tone area extending from east to west across the central part of the State, an area of intensive agricultural use because of its dark fertile soils.

To illustrate how a mosaic such as this can be used to determine land-use change, an overlay of the forested lands was prepared from interpretation of the mosaic. This so-called thematic extraction showed the cleared lands as black and the forest as white. Using an eight-color VP–8 Image Analysis System, the EROS Experiments and Evaluation Office staff determined that the forested area of Alabama encompasses 76,986 km$^2$, or 7,580,211 ha. The total area encompassed by the State of Alabama is 134,183 km$^2$, or 13,211,904 ha. which includes 1,971 km$^2$, or 194,048 ha, of water. These figures were compiled on the Image Analysis System by scanning the thematic extraction with a television camera and then displaying the black and white areas on a color television monitor as single colors. By masking off known areas on the extraction, the machine can determine the percentage of the scene that falls into each category, and these data are then converted mathematically into area figures.

The 1972 "Statistical Abstract of the United States" indicated that 9,895,000 ha of land in Alabama were in forestland as of Jan. 1, 1970. Although these figures were derived from different data using different techniques, the ERTS analysis indicates that an important new capability for inventorying forestland may be available soon. No accuracy analysis of this interpretation of ERTS data has yet been made, but studies of ERTS–1 imagery made in other places indicate that forestland can be interpreted from ERTS–1 data. Although some decline in forestland has probably occurred in recent years, the area of young forests was probably underestimated from ERTS data, but comparison of the interpretation of ERTS–1 data with other data should be possible. An assessment of this type can be made in a short perod of time for a cost of less than $100.

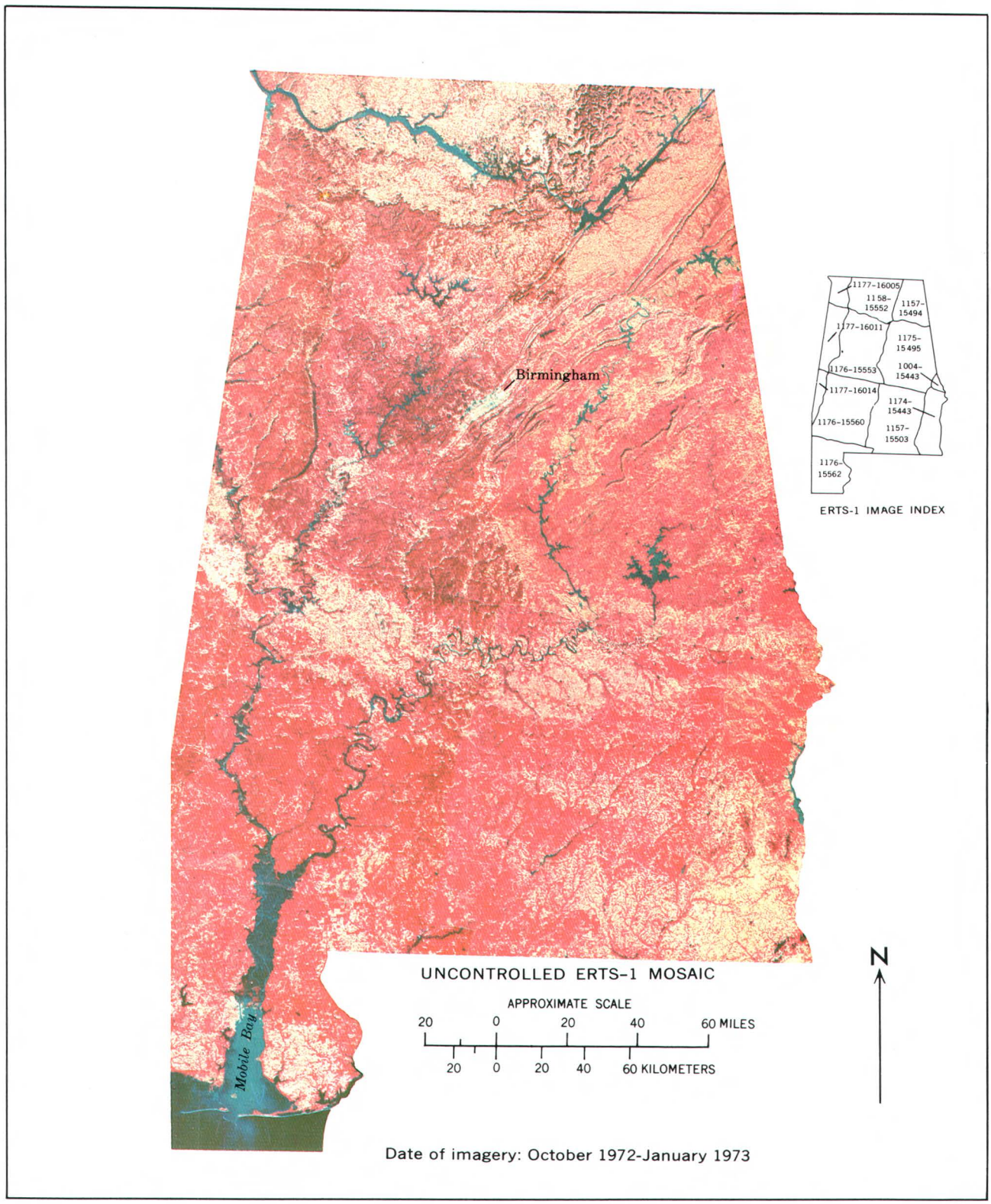


FIGURE 163.—Color composite ERTS-1 image mosaic of the State of Alabama.

# MONITORING CHANGE IN LAND USE OVER LARGE REGIONS

By John L. Place,
U.S. Geological Survey

Figure 164, a color composite image from the ERTS MSS, provides a view of Phoenix, Ariz., and its western environs as of May 2, 1973. Images of this type have been used to detect changes in land use, as illustrated by figure 165, which shows a 1970 land-use map in muted colors overlain in brighter colors by a plot of ERTS-detected residential growth. Also overlain in more intense colors on that map are new cropland plots and a replacement of cropland by a new reservoir.

In the past, it took several years to acquire and compile the data to produce a map of current land use for the Nation or even for a large multistate region. By the time such a map reached the public, parts of it were out of date. With the advent of ERTS, for the first time changes in land use nationwide can be monitored very rapidly, utilizing a new land-use classification system (Anderson and others, 1972) designed especially for work with aerial photography and satellite photography and imagery (Place, 1973).

In order to map land use nationwide, it was advisable to build upon the existing map coverage, particularly upon topographic maps which had a geometric accuracy that met the National Map Accuracy Standards. The largest scale map series presently covering the entire Nation is the 1:250,000 topographic maps (each quadrangle map covers an area of 1° of latitude and 2° of longitude), an ideal scale for use with ERTS images (Place, 1974). The test area selected for the first of such land-use maps was the Phoenix quadrangle in Arizona. As the first step in this test, a land-use map was compiled for the Phoenix quadrangle, shown in muted colors in figure 165, by interpreting high-altitude aerial photographs taken in November 1970. An ERTS experiment was conducted under NASA sponsorship to test the utility of ERTS images in updating this map. The changes detected, shown in figure 165, were used to update an existing computer data bank containing information on land use and related factors in the Phoenix quadrangle.

Of particular importance was an accuracy test performed on the ERTS findings, that is, where ERTS images were the only source of information. Aerial photographs from a NASA U–2 aircraft in November 1972 were compared with the U–2 photographs of exactly 2 yr earlier, and a new map of detected change in land use was compiled.

The clusters of urban growth detected by ERTS and by U–2 were very similar. The aircraft-detected change was more detailed and more precisely plotted as to planimetric location on the ground. However, the ERTS interpretation has two advantages over the aircraft interpretation. First, ERTS views were repeated at least monthly and allowed interpretation of changing vegetation, which aided delimitation of new cropland on the desert margin where some fields were fallow and invisible in the November aerial photo-

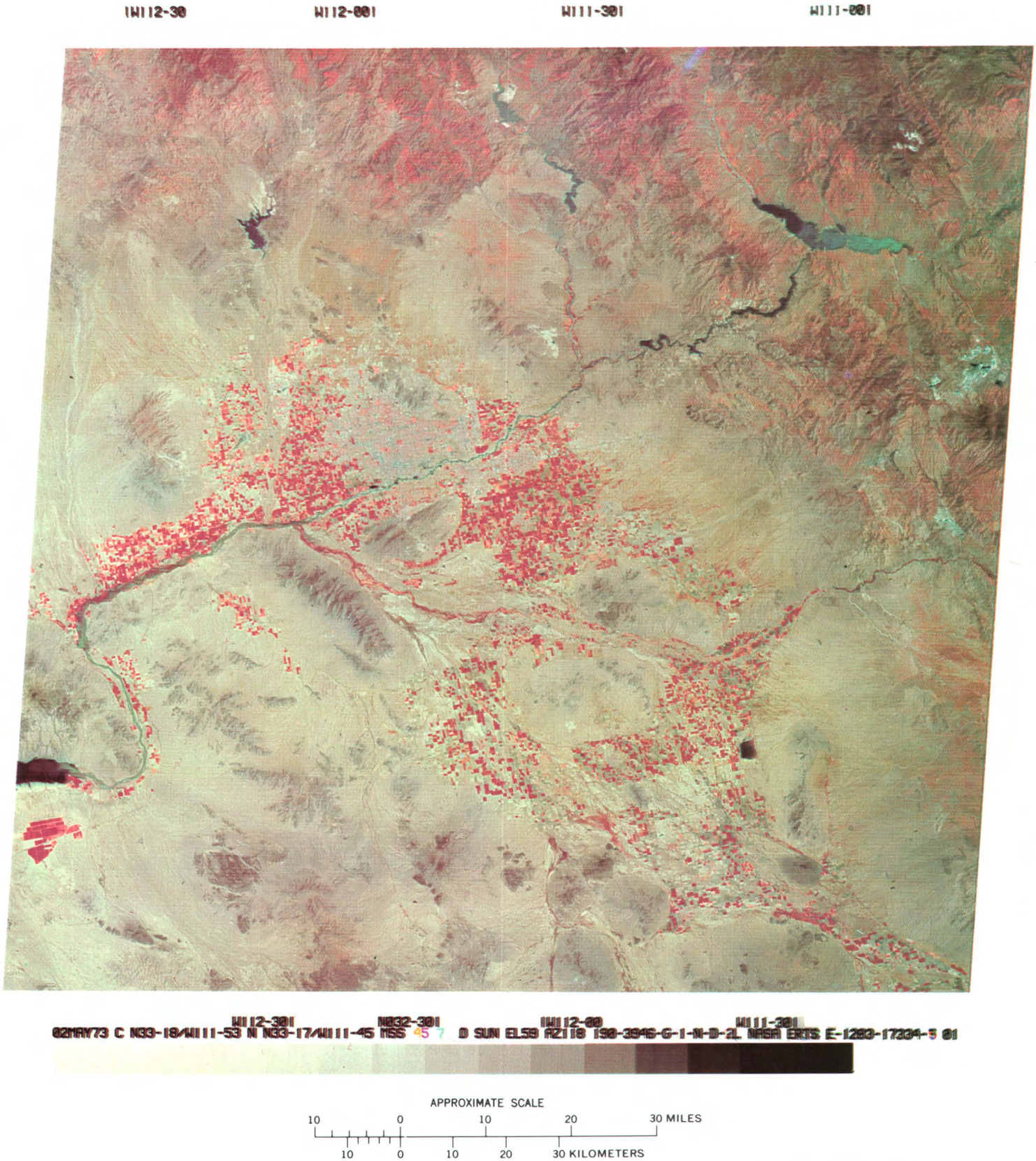


FIGURE 164.—Color composite ERTS–1 image of the Phoenix area of Arizona (1283–17334).

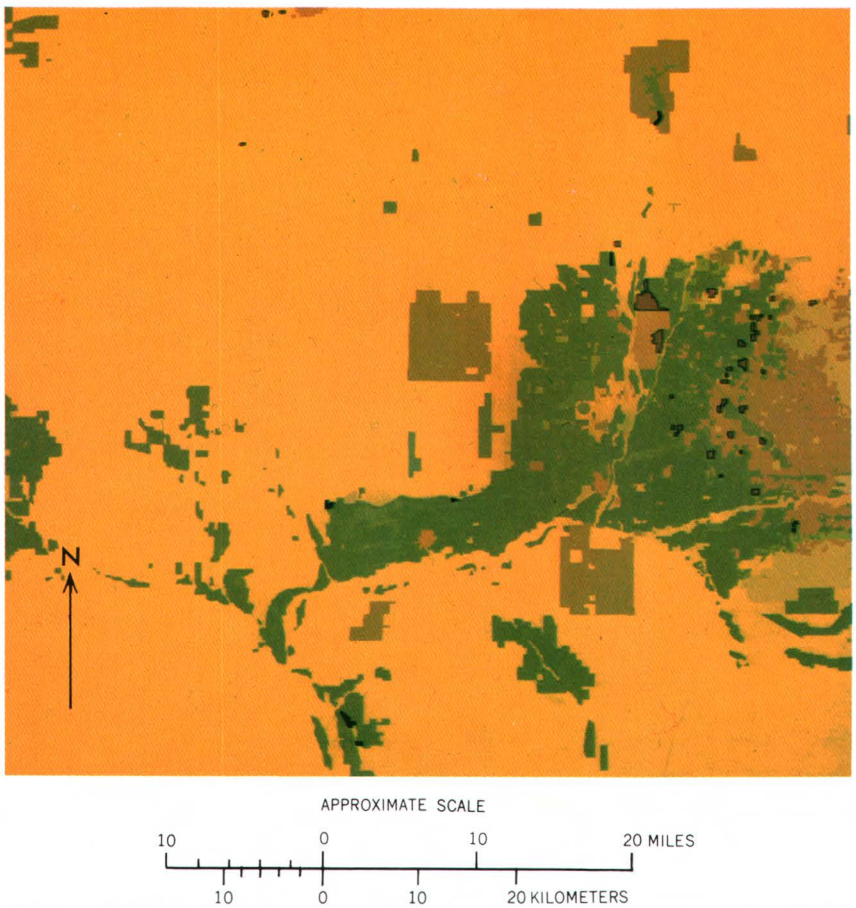


FIGURE 165.—Land-use map of the Phoenix area, 1970, with changes detected by ERTS through April 1973 shown in denser patterns: new residential in red, new cropland in black. The background colors represent land use as interpreted from high-altitude aerial photography acquired in 1970: residential in russet, cropland in green, and so on.

graphs. Second, the ERTS images cover the winter of 1972–73 and hence were more up to date than the photographs. This is a realistic example of how aerial photographs and ERTS images complement each other. In any given area of the United States, the most recent aerial photograph is likely to be several years old. Furthermore, they are taken too infrequently to allow analysis of seasonal vegetation change.

Some of the informational content of an ERTS color composite is illustrated in figure 166. Residential landscaping has a distinctive pink color, quite different from the intense red of irrigated crops or city parks. Water areas, which fluctuate seasonally, can be seen easily. Some of the wild grass that grows in the desert after heavy rains can be seen as a dark-red area in the desert north of Phoenix; monitoring wild grass is important to range managers. Commercial and industrial districts of Phoenix can be distinguished by their bluish color, that is, absence of vegetation. Airport runways and the major highways normally can be detected if the background vegetation provides an adequate silhouette.

The test has verified the utility of ERTS images for updating maps of general land use in the arid Southwestern United States and to a lesser degree in large cities such as Phoenix. At the very least, ERTS images help us to detect and focus on the areas experiencing greatest change, to which we can then apply more intensive survey techniques.

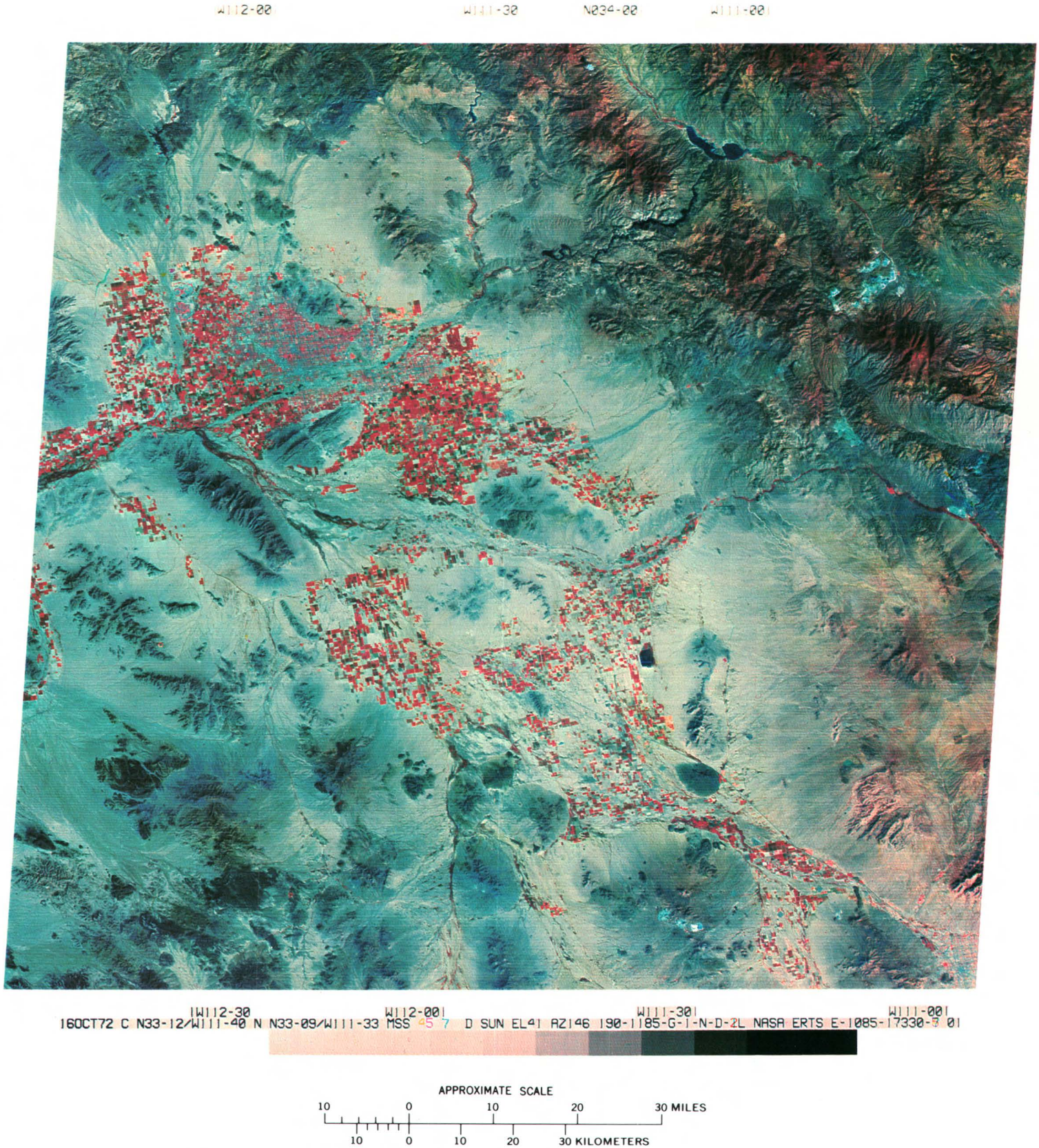


FIGURE 166.—Color composite ERTS–1 image of the Phoenix area of Arizona, on Oct. 16, 1972 (1085–17330).

# COMPUTER-AIDED MAPPING OF LAND USE

By Richard Ellefsen, California State University,
and Leonard Gaydos and James R. Wray,
U.S. Geological Survey

To date the most common remote-sensing tool used for land-use mapping has been interpretation of aerial photographs. The usual procedure is to interpret the land use from the photography and then to plot it as irregularly shaped polygons on existing topographic or planimetric maps or on photomosaics (Anderson and others, 1972). The land-use polygons may then be digitized for computer storage and handling.

This procedure is dependent on: (1) obtaining current aerial-photograph coverage, preferably with false-color infrared film of high resolution over as large an area as possible; (2) fast and objective interpretation by several interpreters; (3) reliable and inexpensive digitizing and encoding for computer storage and manipulation; and (4) aggregation of data by statistical units such as census-enumeration district, city, or county.

In practice, all these conditions can rarely be met adequately, either from conventional or nonconventional sources. Generally the requirements either go unfulfilled or are fulfilled with either a loss of speed or accuracy or at much greater cost. For many uses ERTS data in digital format can provide not only timely acquisition of land-use information but also the basis of an information system for processing it.

There are two main outputs from ERTS: computer compatible tapes (CCT's) or imagery (fig. 167). The computer has the capability of examining a large quantity of data and objectively classifying it quickly according to guidelines established by pattern-recognition algorithms and by the analyst. The unit of observation, the pixel ($79 \times 56$ m), is also the unit of area measurement.

Because the information is already digitized, there exists the basis of a geographic information system. Data concerning such factors as slope, climate, vegetation, and physical hazards can be matched with the land use to provide comprehensive information about environmental conditions. Pragmatic questions, such as how much housing occupies environmentally hazardous areas, may then be answered by manipulation of the data.

Land-use mapping procedures described here are based on a group of pattern-recognition programs collectively known as LARSYS. ERTS CCT's are preprocessed at LARS (Laboratory for Applications of Remote Sensing, Purdue University) before analysis. First, they are reformatted for interaction

FIGURE 167.—Annotated color composite ERTS–1 image of the San Francisco Bay area of California (1003–18175).

with LARSYS on an IBM 360/67 computer. Then, five linear transformations are made that correct for geometry and produce a data tape with consistent scale and data lines oriented west to east when reproduced on a line-printer.

The best results are obtained when data from two ERTS passes over the same area, but during different season, are used interactively. Over time, changes in relative spectral response occur. The agricultural and native vegetation lands change with the season and their growing cycles, whereas manmade cover changes very little. In the preprocessing, data from the second pass is matched pixel-by-pixel with data from the first in an overlaying step. The resultant tape includes eight channels of spectral data in digital form, four from each date, and is geometrically correct.

The output is a line-printer map at a scale of 1:24,000 on which each pixel is represented by an alphanumeric symbol indicative of the spectral class to which it belongs. Determination of land use then requires an interpretation of the spectral map that must be related by the analyst to known land-cover patterns on the ground. Reference is made to any other source material available, including existing maps and photographs. A few features identify readily with certain land uses, and they are used as landmarks for interpreting the rest. Gradually, patterns emerge. One by one the predominant land use for each feature is determined (fig. 168). The eventual goal is a pattern that identifies well particular land uses. Once determined, some test classifications verify the results or suggest further refinements. When they are regarded as sound, the entire area is then classified (fig. 169). The results are recorded on tape and form the basis for a variety of products.

Maps in line-printer-output form have both advantages and disadvantages. One advantage is that, as an integral part of the computational process, the line-printer output may be acquired not just once for each area analyzed but as often as desired and in as many different rearrangements of the data as the analyst might require. The similarity of all computer line-printer-output forms is another advantage and permits direct comparison of results with analysis products from other machines. Another advantage of the line-printer is the ability to aline the product, when done at full resolution of 1:24,000, with existing 7½-min quadrangle maps at the same scale. Such maps are extremely valuable to the analyst for classification and for relating the land uses to known point and line phenomena (fig. 170). Figures 171 and 172 show two seasonal views of the locale of figure 170. The cellular nature of the line-printer map also facilitates aggregation by rectangular jurisdictional units and by superimposed grid cells of varying sizes. It thus forms the basis for a geographic information system. The disadvantage of the line-printer is mostly that its product is not recognized as a traditional form of a map.

The mapping of land use from ERTS MSS data in digital form holds considerable promise. The system performs well in the diverse physical environments of California, Arizona, and Washington, D.C. (Ellefsen, 1974a and 1974b; Ellefsen and others, 1974). Todd and others (1974) report similar success in Wisconsin and Indiana. Reliable patterns are also achieved in Lubbock, Tex. (Henderson and others, 1974).

When future Earth observation satellites become operational, the scanner-computer mapping system using satellite data could serve as a continuous, silent monitor of conditions on the surface of the Earth, whereas aircraft remote-sensing equipment could be called upon for quick coverage of any particular area, as in time of environmental calamity.

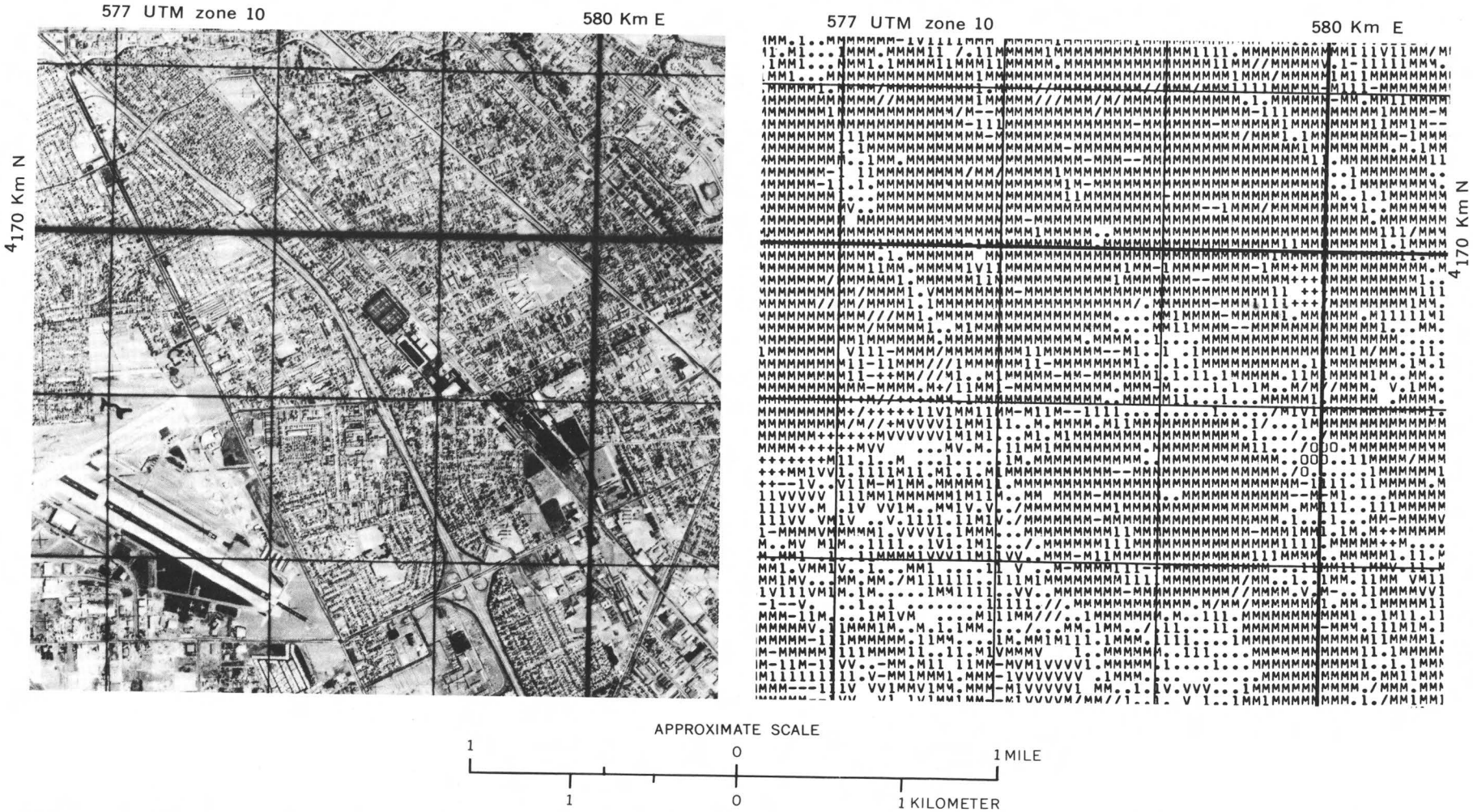


FIGURE 168.—Enlarged aerial photograph-map pair of Hayward, Calif. Photograph is part of a single high-altitude false-color infrared aerial photograph acquired at a scale of 1:50,000 on May 15, 1970, by NASA for the USGS Census Cities ERTS experiment. Map is by Purdue University LARS for the EROS program and is based on ERTS–1 scanner digital data for image 1003–18175, acquired on July 26, 1972. Scan lines have been reformatted so that they are nearly parallel to east-west UTM 1-km grid lines (Zone 10). One printout symbol represents one ERTS scanner picture element (pixel), 0.46 ha (including pixel sidelap). Urban classes: commercial-industrial, (1); mobile homes, (V); residential, (M); parking lots (·); unimproved open space, bare (—); unimproved open space, trees (/); open space, irrigated (+); water (0). Note correspondence between photo and map in mobile home area, lower left corner. Eastward expansion of mobile home park (symbol V on ERTS computer map) has been confirmed by NASA 1972 aerial photograph.

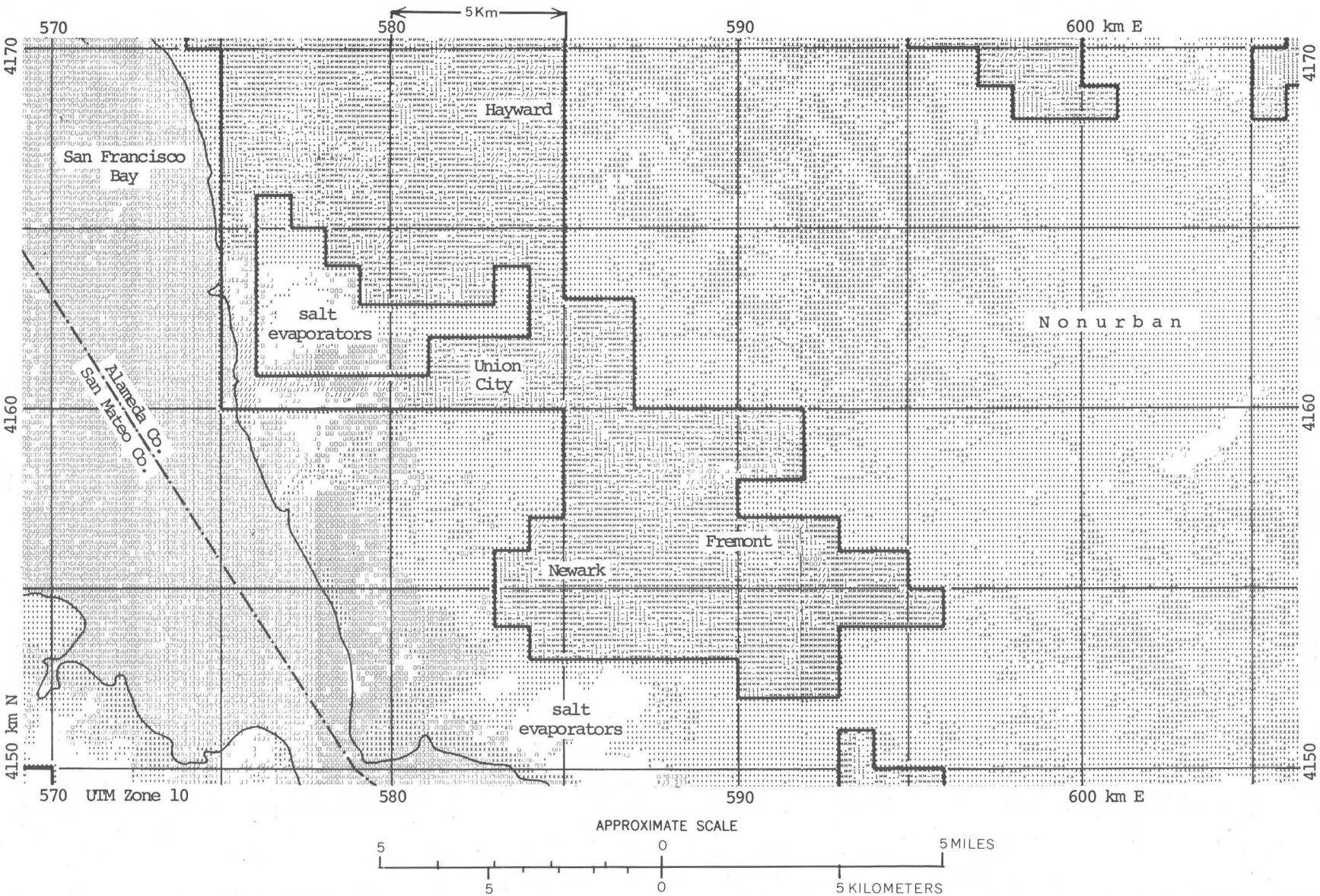


FIGURE 169.—Part of a computer-classified land-use map of the San Francisco Bay region. Map is derived from ERTS–1 scanner digital data, image 1003–18175, acquired on July 26, 1972. Classification, by Purdue University LARS, uses eight Urban classes, and three Nonurban classes. Urban area, defined by 1-km UTM grid (Zone 10), is from USGS Census Cities ERTS experiment and NASA aerial photography. The grid facilitates comparison with corresponding ERTS–1 image. The map is produced at a scale of 1:48,000 by classifying every other pixel in every other scan line. About 6,500 km² (or just under 0.1 percent of the U.S. land area) were classified on LARS IBM 360/67 in about 30 min of computer time.

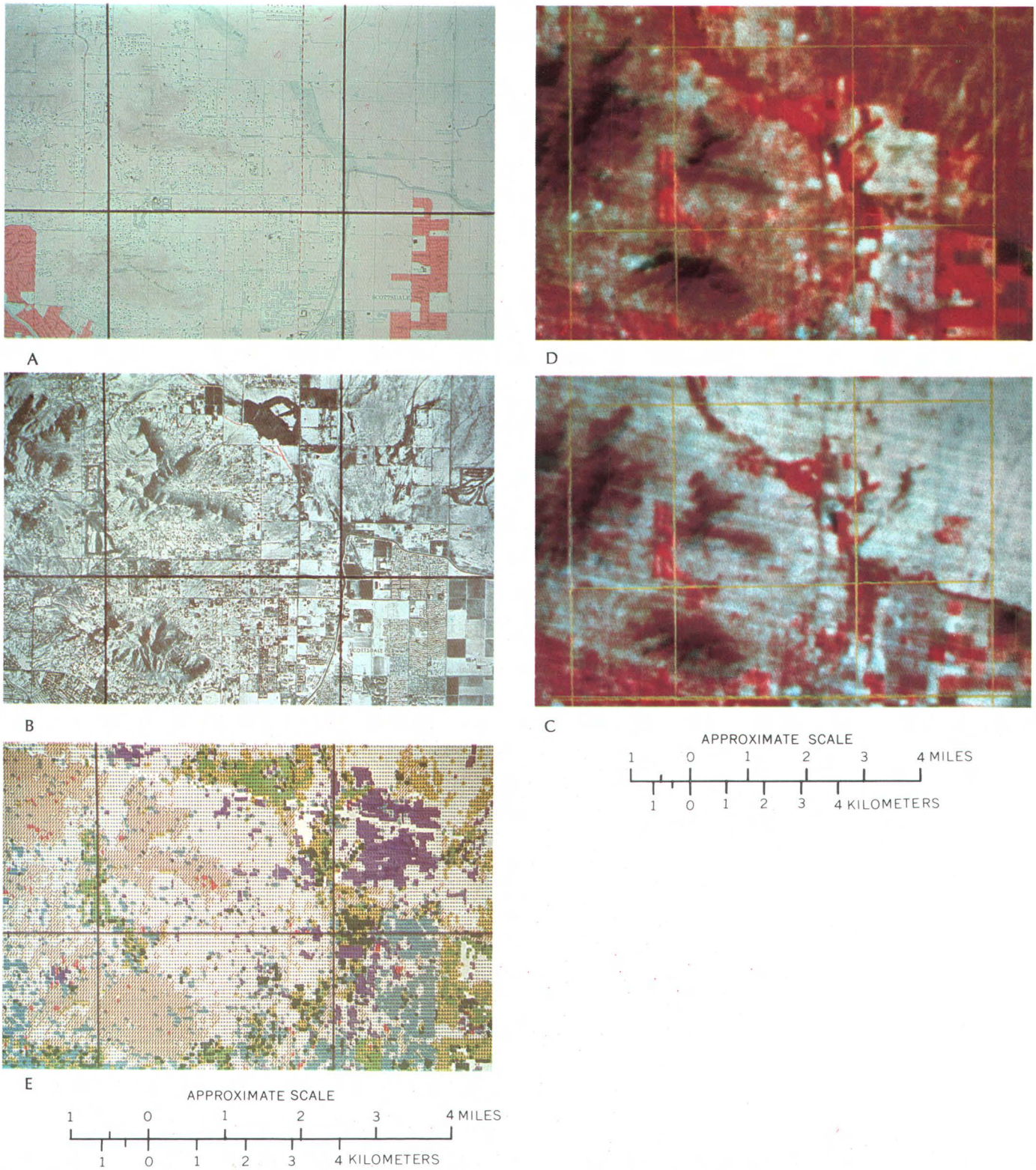


FIGURE 170.—Map (A), orthophotograph (B), two enlargements of color composite ERTS–1 images (C and D), and computer-classified land-use map (E) of a small area near Phoenix, Ariz. All these pictures represent a small part of the Phoenix area. The 7½-min quadrangle map (A) was published in 1965; the orthophoto quadrangle map (B) was produced in 1971. The same area was selected from the two ERTS–1 images from Oct. 16, 1973 (C) (1085–17330), and May 2, 1973 (D) (1283–17334), enlarged to almost the same scale. The enlargements are clear enough to identify the mountains (brown), vegetation (red), and other features as on all such ERTS images. Using the computer compatible tapes from both dates, however, a computer map (E) has been reproduced that shows distinctly, in minute detail, the land use and its changes. Colors on reduced line-printer symbols discriminate such land uses as residential (blue), commercial-industrial (orange-red), agricultural (yellow and green), newly disturbed land (purple), and highland and lowland desert vegetation (brown and tan, respectively).

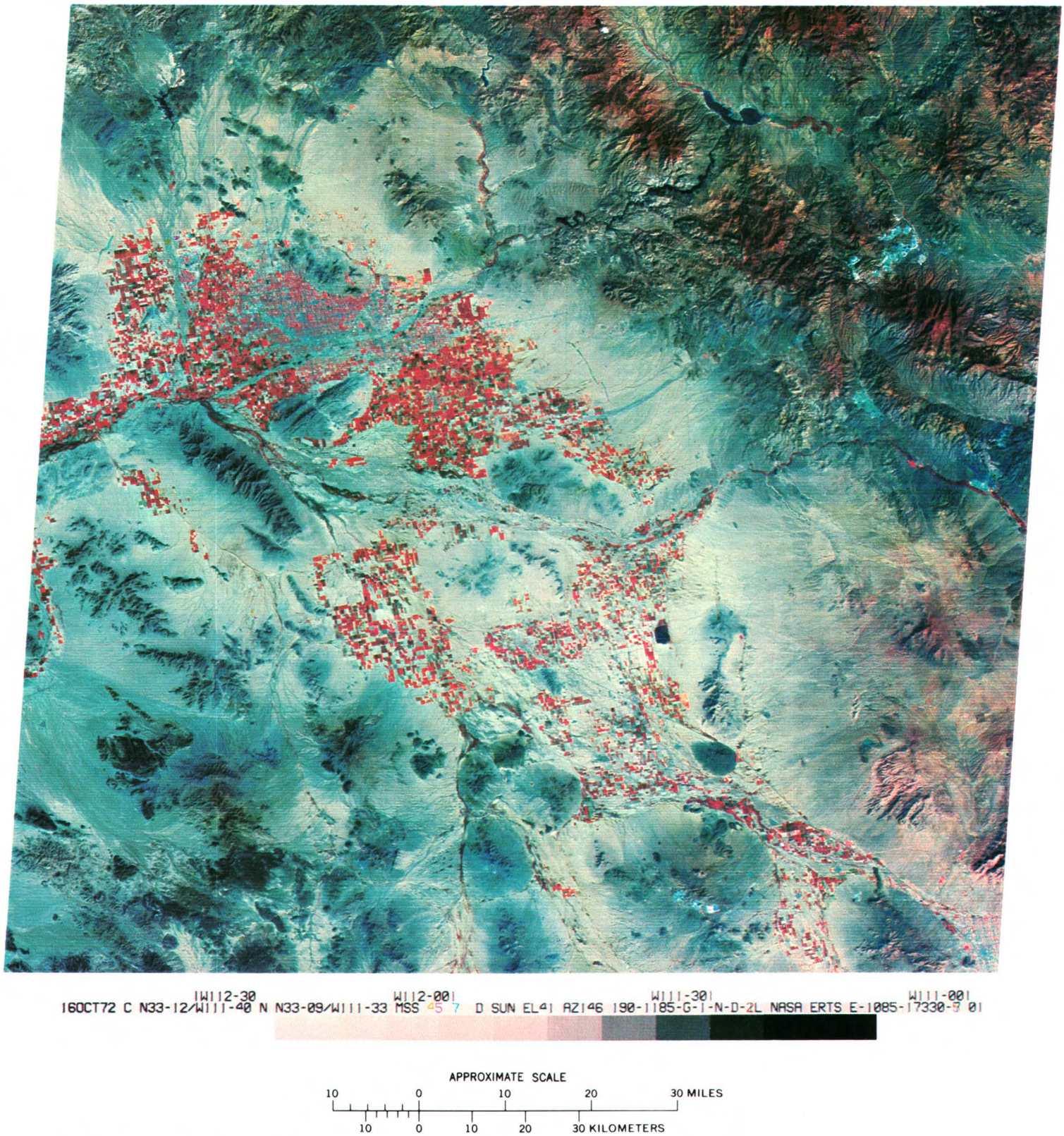


FIGURE 171.—Color composite ERTS–1 image of Phoenix, Ariz., on Oct. 16, 1972 (1085–17330).

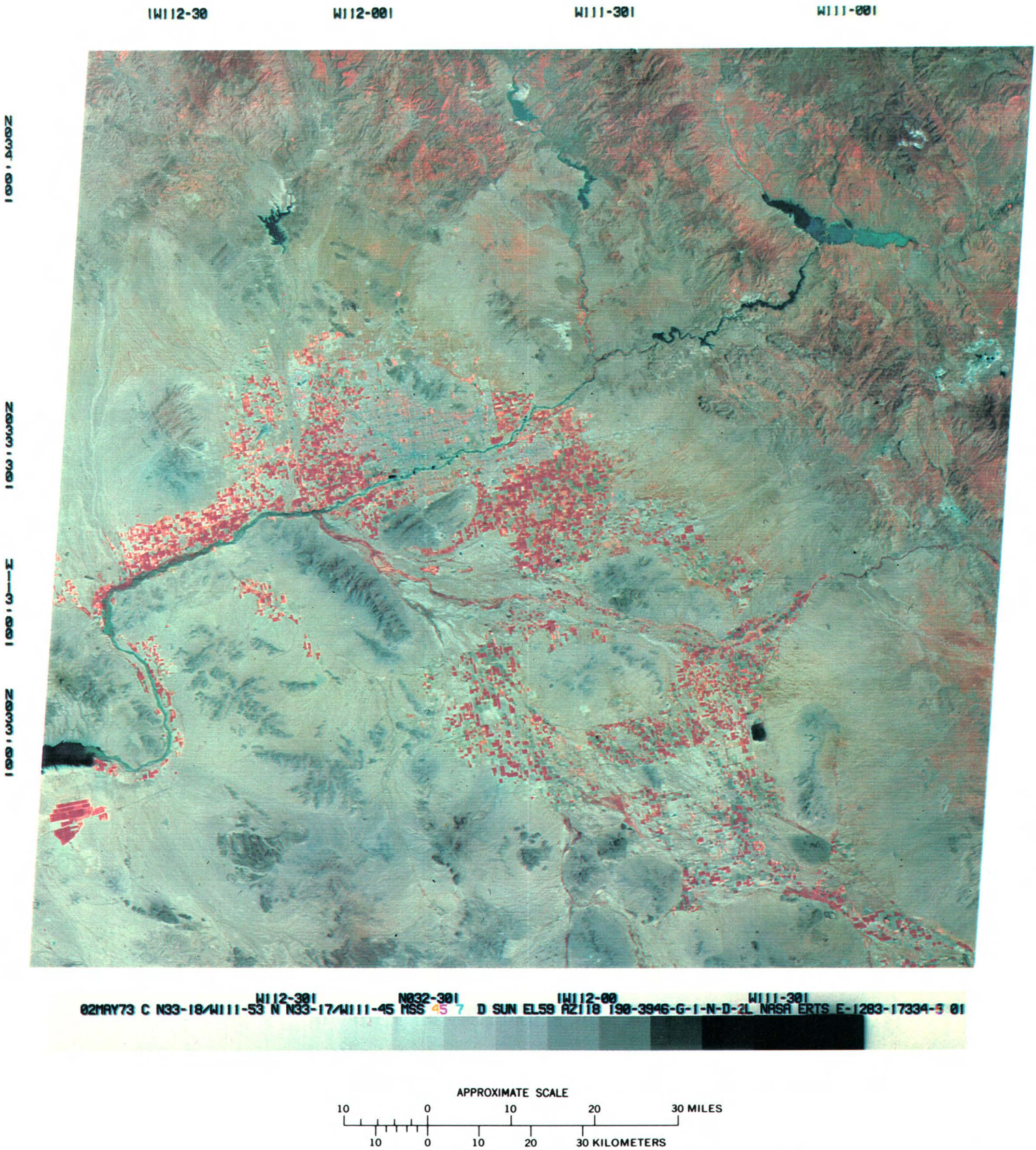


FIGURE 172.—Color composite ERTS–1 image of Phoenix, Ariz., on May 2, 1973 (1283–17334).

## REFERENCES


Anderson, J. R., Hardy, E. E., and Roach, J. T., 1972, A land-use classification system for use with remote-sensor data: U.S. Geol. Survey Circ. 671, 16 p.

Curtis, Virginia, ed., 1973, Land use and the environment, an anthology of readings: Chicago, Ill., Am. Soc. Planning Officials for Environmental Studies Div., Off. Research and Monitoring, Environmental Protection Agency, 199 p.

Ellefsen, Richard, 1974a, Automatic digital processing of ERTS–1 MSS data in an urban land-use mapping experiment: Am. Soc. Photogrammetry, Ann. Mtg., St. Louis, Mo., 1974, Proc., p. 405–416.

——— 1974b, ADP pattern recognition of urban land uses from satellite-borne multispectral scanner: Univ. of Ariz., Ann. Conf. on Remote Sensing in Arid Lands, 4th, Tucson, Ariz., 1973, Proc., p. 71–79.

Ellefsen, Richard, Gaydos, Leonard, and Wray, J. R., 1975, Computer aided mapping of land use using ERTS multispectral scanner data: Pan American Cong. on Photogrammetry, Photointerpretation, and Geodesy, 1st, Mexico City, Mexico, 1974, Proc. (in press).

Henderson, J. A., Baumgardner, M. F., and Walker, C. F., 1974, Preparing resource inventories in the southern Great Plains by machine processing of ERTS–1 multispectral data: Univ. of Ariz. Ann. Conf. on Remote Sensing in Arid Lands, 4th, Tucson, Ariz., 1973, Proc., p. 57–69.

Place, J. L., 1973, Change in land use in the Phoenix (1:250,000) quadrangle, Arizona, between 1970 and 1972—successful use of a proposed land use classification system: NASA Goddard Space Flight Center, Symposium on Significant Results Obtained from the Earth Resources Technology Satellite–1, 2d, New Carrollton, Md., Mar. 1973, Proc., v. 1, sec. B, p. 899–906.

——— 1974, Change in land use in the Phoenix (1:250,000) quadrangle, Arizona, between 1970 and 1973—ERTS as an aid in a nationwide program for mapping general land use: NASA Goddard Space Flight Center, Symposium on the Earth Resources Technology Satellite–1, 3d, Washington, D.C., Dec. 1973, Proc., v. 1, sec. A, p. 393–423.

Todd, W. J., Mausel, P. W., and Baumgardner, M. F., 1974, An analysis of metropolitan land use by machine processing of Earth Resources Technology Satellite data: Assoc. Am. Geographers, Proc., v. 6, p. 54–57.

# CHAPTER 5.
# APPLICATIONS TO AGRICULTURE, FORESTRY, AND RANGELAND MANAGEMENT

## INTRODUCTION

By Grover Torbert,
Bureau of Land Management

The agriculturist, forester, and rangeland manager all strive for efficient management of renewable natural resources: agricultural crops, timber, and forage. Improved management could provide mankind with a higher sustained yield of food and fiber. The following three articles show the capacity of remote sensing from space to contribute to the wise management of these resources.

The need of the resource manager for timely and accurate information is reflected in the complexity and volume of problems that confront him. Present-day managers, however, could resolve many of their problems through the use of remote-sensing techniques.

Vegetation conditions are generally dynamic, and a correct appraisal of conditions at any time is essential for forecasting trends. The synoptic view and the repetitive acquisition of imagery of the Earth's surface at a regular interval provide the means for measuring the vegetative characteristics on a spectral, spatial, and temporal basis. This type of coverage also provides for time-lapse observation of the Earth's surface and for monitoring ephemeral rangelands, diseased timber, food crops, and other highly dynamic natural phenomena.

The synoptic view from ERTS–1 provides the renewable-resource manager the opportunity to make comparisons between known and inaccessible areas. Geologic features that control terrane and areas suitable for cropping, forestry, and rangeland all have unique environmental characteristics. These characteristics are expressed primarily, on the surface, by the vegetation they support.

Harvesting timber, planting crops, or managing rangeland all disturb the ground surface. Through the synoptic view from a spacecraft, data necessary for the preparation and compliance of environmental impact statements are made available.

Satellite data, a major input into any natural-resource information system, provide the perspective for viewing regional problems and the repetitive coverage for forecasting seasonal change. Both are necessary when making decisions about the use of renewable natural resources and when planning major public works projects.

The following pages of this chapter provide a sampling of studies of ERTS image data to determine its usefulness in monitoring the effects of forest fires in Alaska (by Torbert), in detecting short-term changes in vegetation conditions in Arizona (by Turner), and in monitoring ephemeral livestock forage production (by Bentley). These are but a few of the applications that are being evaluated by the bureaus of the Department of the Interior.

# MONITORING FOREST-FIRE BURN AREAS IN ALASKA

By Grover Torbert,

Bureau of Land Management

Figure 173 is an ERTS image of northern Alaska that shows a forest fire (A) in progress on July 26, 1972 (Anderson, 1973). The Pah River fire was discovered on July 8, and by the time the image was scanned the fire had consumed 24,000 ha of an overstory of mixed spruce, birch, and aspen and an understory of arctic tundra and muskeg. As of September 5, when no further smoke was visible, 48,000 ha had been burned.

In the northwest part of the image is an older burn area (B), south of the Kobuk River. This lightning-caused fire, the Shaler fire, began on June 24, 1971, consumed a similar vegetation assemblage, and ultimately burned 22,300 ha.

Imagery such as this could be much more useful to firefighting management personnel, however, if it were available on a real-time basis for three things: (1) to view and evaluate the resource burned and those being threatened by large individual fires, (2) to provide a tool in decisionmaking to set priorities on control of large fires, and (3) to help provide early ordering and coordination of logistical resources for firefighting to meet priorities on large fires.

Cloudy weather during the summer months in Alaska does interfere with collection of aerial and satellite imagery, but this deficiency is partly compensated for by ERTS–1, which has greater repetition of coverage (3 days in a row of the same area at lat 65°N.). This is due to convergence of orbits in polar regions. The cloud problem could be further reduced by acquiring images twice a day by taking advantage of the light available during the summer evening hours (midnight sun) at high latitudes. Because Alaska is the site of one of the three U.S. ERTS ground receiving stations, the potential does exist for creation of a real-time quick-look image capability for use in forest-fire management. Until such an operational capability exists, however, ERTS images still retain their value for time-lapse looks at large areas and are valuable in delineating the rate of regrowth in burned areas and in assessing the general status of vegetation in such remote areas (Carter, 1973).

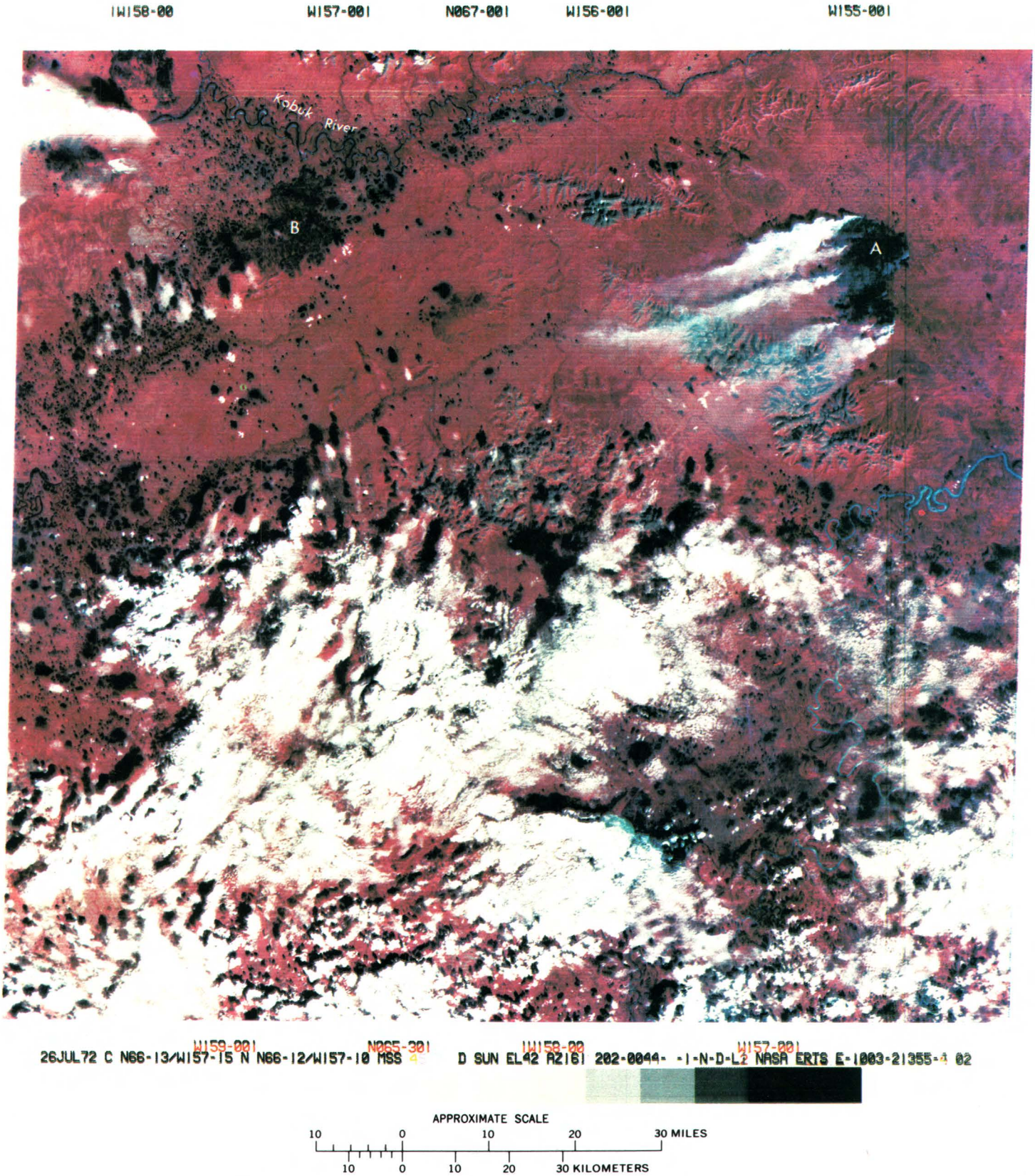


FIGURE 173.—Annotated color composite ERTS–1 image of a forest fire in northern Alaska (1003–21355).

# DETECTION OF SHORT-TERM CHANGES IN VEGETATION OF SOUTHERN ARIZONA

By Raymond M. Turner,
U.S. Geological Survey

The traditional products of pre-ERTS vegetation mapping were usually maps showing ranges of plant communities or floristic maps showing distributions of individual species. Now that ERTS is in orbit, synoptic mapping of short-term vegetation phenomena has become feasible.

Knowledge of the seasonal changes in plant cover can be used by agriculturalists to pinpoint likely areas for grazing, to anticipate locust migration areas, and to help identify crop types and woodland communities. Seasonal changes in foliation have been an elusive parameter of great importance to hydrologists studying water use within riparian and phreatic communities and to determine likely areas of subsurface water availability.

The ERTS image in figure 174 shows an area 124×169 km surrounding Tucson, Ariz. Terrain altitude within the 20,956 km² area ranges from about 610 to 2,896 m. Average annual rainfall ranges from near 254 mm to more than 762 mm.

As in most arid regions, the desert near Tucson supports an open sparse plant cover except during seasons of favorable rainfall when a dense sward of ephemeral plants may develop. These small plants reach maturity and complete their life cycles within only a few weeks. At the other extreme of plant phenologic response in the Tucson region are the conifers and oaks found at high altitudes on the isolated mountains; these plants are dominantly evergreens and should change little through the year. Riparian and phreatic vegetation occur at all altitudes.

By using ERTS images from two or more spectral bands, thematic masks can be made that show all areas within an ERTS scene where plant foliage cover is relatively dense. The technique involves a ratioing procedure whereby radiance values across paired ERTS scenes are used to generate thematic masks (Turner, 1973). In the three examples presented in figure 175, two of the four spectral bands have been combined by the ratioing procedure. A 70-mm positive transparency of band 6 is paired electronically with the identical image recorded in band 5. Thematic masks are generated by dividing band 6 radiance values by band 5 values and by electronically slicing areas that exceed some preselected ratio. In the examples given, a ratio of 1.25/1.00 was used. Use of a ratio probably largely nullifies problems arising from seasonal changes in Sun elevation and atmospheric attenuation. The technique relies on the well-known fact that leaves reflect heavily in the near-infrared range (band 6) but reflect little in the red band (band 5). Leaf reflectance in these two bands is influenced by two distinct plant systems, one involving pigment chemistry, the other, mesophyll anatomy. Both of these systems are closely related to the volume of foliage.

From top to bottom the masks show areas of relatively dense vegetation on Aug. 22, 1972, late summer (1030–17271); Dec. 26, 1972, winter (1156–17280); and Feb. 18, 1973, spring (1210–17282). The exact percentage of foliage cover identified by the 1.25/1.00 ratio use is not known, although field sampling at the time of each satellite overpass suggests a 25 percent to 50 percent foliar cover.

The three electronically sliced images show the following:

1. The highest mountains exceed the threshold ratio at all three seasons. This result is expected because these mountains all support dense stands of evergreen oaks and conifers. The color composite image (fig. 174) was taken on Jan. 13, 1973, 18 days after the imagery for the winter scene (fig. 175). Note the close relationship between the black areas on the sliced image and the red areas (dense plant growth) on the color composite.

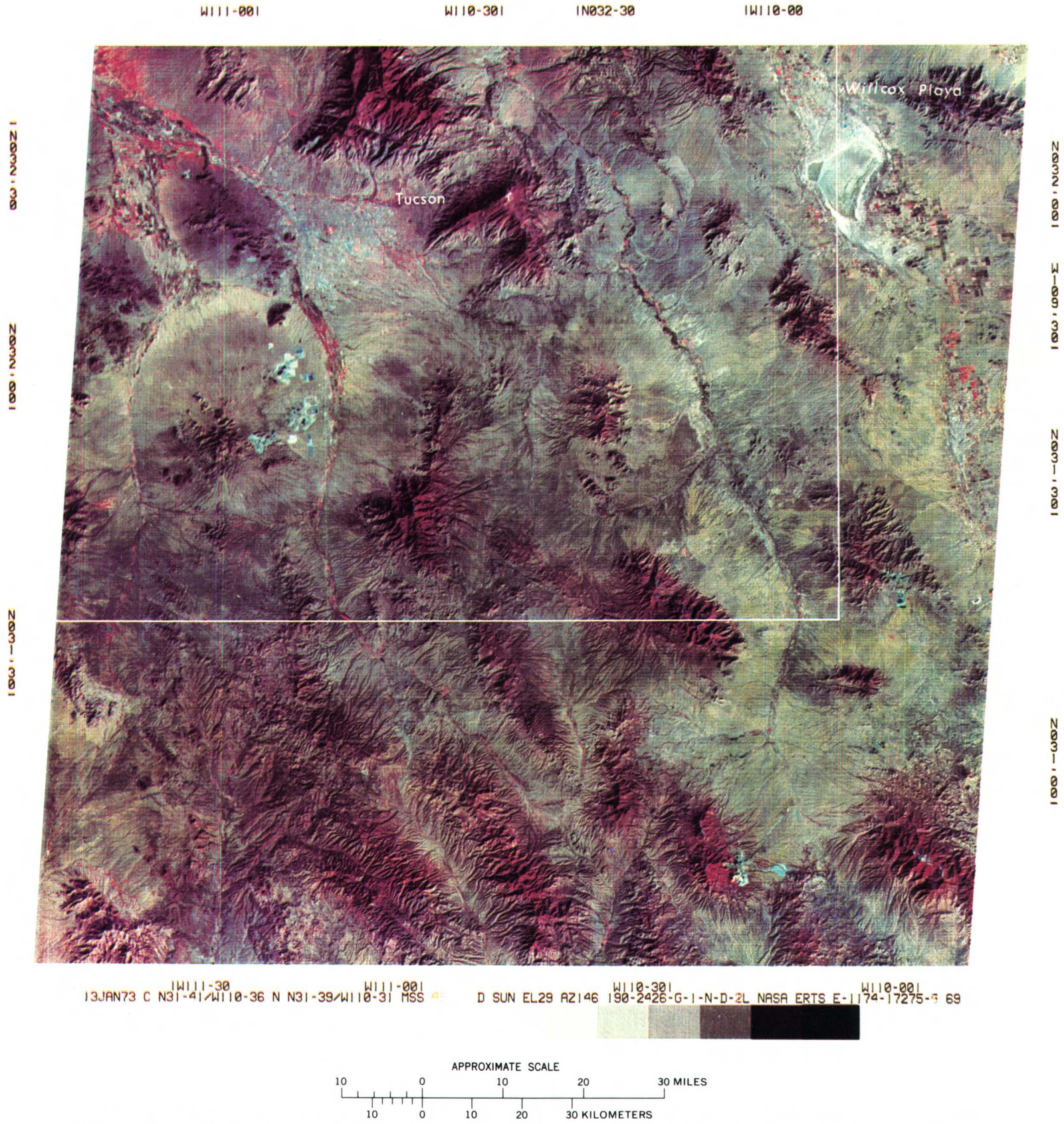


FIGURE 174.—Annotated color composite ERTS–1 image of the Tucson area of Arizona (1174–17275). Outline shows the approximate area shown in figure 175.

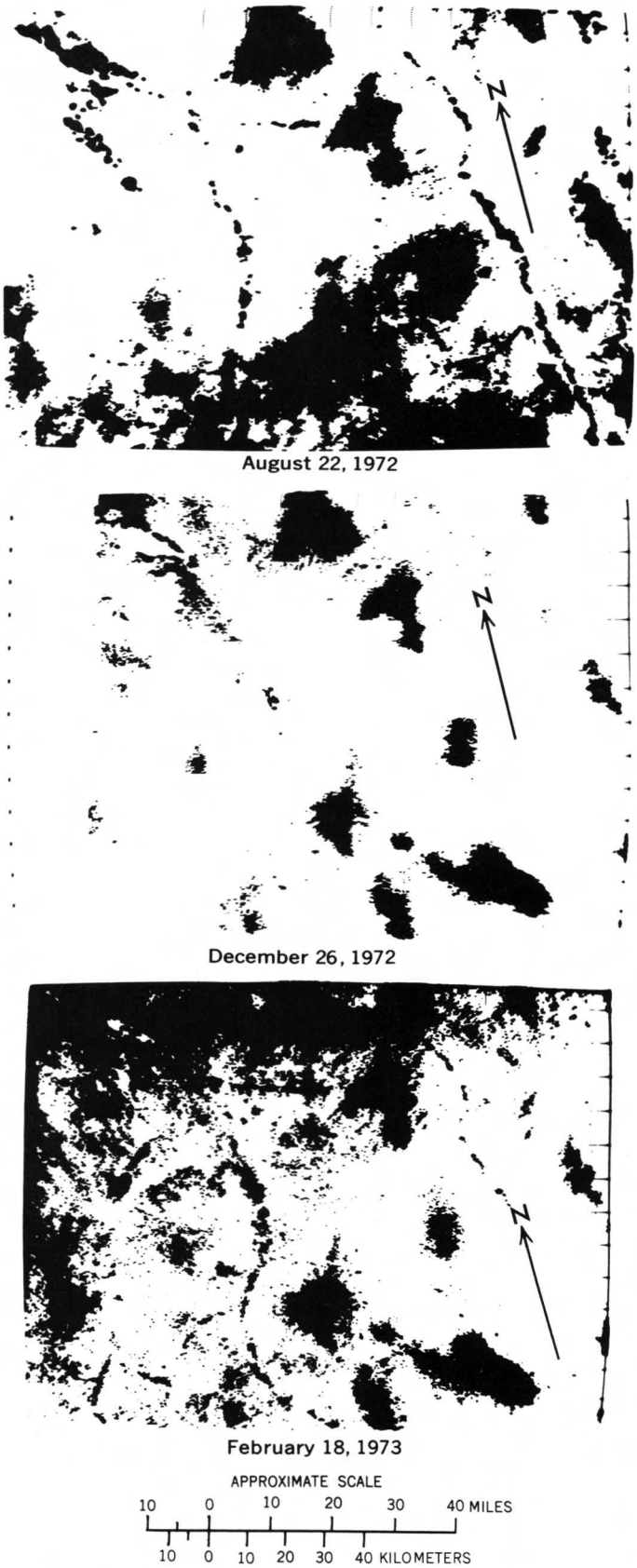


FIGURE 175.—Thematic extraction of relatively dense vegetation from ERTS–1 images by ratioing: late summer, Aug. 22, 1972; winter, Dec. 26, 1972; and spring, Feb. 18, 1973 (1030–17271, 1156–17280, and 1210–17282).

2. Foliage cover changes along the two principal streams crossing the area produce an expected pattern in the sliced images. In late summer (fig. 175), when the riparian communities and cultivated fields are in full leaf along the full length of the valleys, the valleys are clearly marked by the pattern of sliced areas. By the time of the winter view, species of the riparian communities, such as mesquite and cottonwood, are leafless, and only a few fields have active plants along these valleys. At the time of the spring view, there is heavy plant growth in cultivated areas up to an altitude of about 3,500 m in both valleys. Most riparian species were still dormant on the date of this spring image.
3. The low desert areas, seen primarily toward the upper left corner of the images, exhibit little plant growth in the late summer except for some irrigated lands and riparian communities. Many of these same desert areas exceeded the 1.25/1.00 threshold ratio on February 18, a date preceded by above average rainfall, resulting in an exceptionally heavy growth of desert ephemeral plants.
4. Vegetation at intermediate altitudes lying above the desert and below the evergreen forests (intermontane areas to the south and east within the test site) responds in a markedly different manner. There the plant communities are dominated by grasses that are active in the summer and autumn but dormant in the winter, even when moisture is plentiful. Accordingly, these intermontane areas should show response on the sliced images only during the summer, if rainfall is adequate. Not all the grassland area in the test site exceeded the threshold during the summer of 1972, however, notably along the western margin. This fact can be explained by the pattern of summer rainfall in 1972. Regional rainfall was abnormal that season, beginning in early June, roughly a month early. By the date of the August satellite image, many of the grassland areas to the south had received 200 to 225 mm of rain; on the west, grassland areas received only about a third as much rain.

From the foregoing, it appears that Earth resource satellites such as ERTS–1 can provide a sensitive synoptic evaluation of seasonal changes in the pattern of plant growth. In vast arid areas of the world, rangeland is grazed only after brief periods of unpredictable rainfall. These rangelands are extensive, poorly served by roads, and contain few meteorological stations. When ERTS-type satellites can provide imagery to potential users in only a few days' time, a large segment of the Earth's inhabitants will benefit.

# MONITORING EPHEMERAL LIVESTOCK-FORAGE PRODUCTION

By R. Gordon Bentley, Jr.,
Bureau of Land Management

The color composite ERTS–1 image in figure 176 shows an area of south-central Arizona that includes the arid desert region between Phoenix and Tucson. The desert area is similar to millions of acres of public land in the Southwestern United States administered by the Bureau of Land Management.

The desert floor accommodates a thin cover of perennial trees and shrubs throughout the year. During abnormally wet years, spaces between perennial plants may be covered with ephemeral plants, short-lived plants that complete their life cycle during the winter-spring or summer growing seasons. These plants, when growing in sufficient quantity, can provide forage for livestock, but the season when plants are green and nutritious can vary widely, from 3 weeks to several months. In order to maximize the use of forage, resource managers need a fast and reliable method of monitoring forage conditions over vast areas (Bentley, 1974).

Using the color composite ERTS–1 image, three distinct vegetative communities can be mapped (fig. 177). A photointerpretation of this type is best done visually by a person familiar with the region being mapped. The criteria used for interpreting features are differences in colors and tones, as well as textural patterns (roughness or smoothness), of the various homogeneous areas identified on the image.

Bluish areas on the image correspond to areas around the base of desert rocky mountain outcrops and on upper bajadas or outwash plains sloping away from large mountain ranges. These areas have a good mixture of desert trees and shrubs; ephemeral plants grow in the interspaces during rainy periods. These areas are designated perennial-ephemeral on the image. The different amounts of ephemerals produced (heavy, moderate, and light production) can be separated by the relative amount of red or pink blotches or streaks running through the bluish areas. Extremely rough textured areas in the center of bluish areas are rocky mountain outcrops. These areas produce a mixture of desert trees and shrubs and a small amount of ephemeral plants. Ephemeral production is light because of the shallow rocky soil. Grazing on these areas is difficult for livestock because of steep slopes and rocks.

Bright red or pink relatively smooth textured areas on the image are lower bajadas and valley floors that produce nearly pure stands of a single perennial shrub, *Larrea tridentata* (creosote- bush). These areas appear white on images made before the start of ephemeral plant growth in summer or early fall. These areas are designated ephemeral on the image. The red on creosote-bush sites reflects only ephemeral plant growth; creosote bushes cannot be seen from satellite altitudes. Heavy, moderate, and light ephemeral-forage production on creosote-bush sites corresponds to red, pink, and light pink, respectively, on the ERTS–1 image.

Brownish-red or very deep red areas on the image correspond to areas producing a relatively dense cover of perennial plants. These areas are at elevations above the desert zone and are mountainous, as shown by the rough textural pattern on the image. No desert ephemeral plants are found here. Deep-red areas correspond to dense stands of coniferous trees.

Data collected in the field at the same time the satellite passes over the area allow the resource manager to explain the various colors, tones, and textures apparent on the imagery. Measurements of the amount of ephemeral-forage production from analysis of ERTS images and field observations can therefore yield quantitative information that can be used as a basis for licensing of private livestock grazing on public ranges.

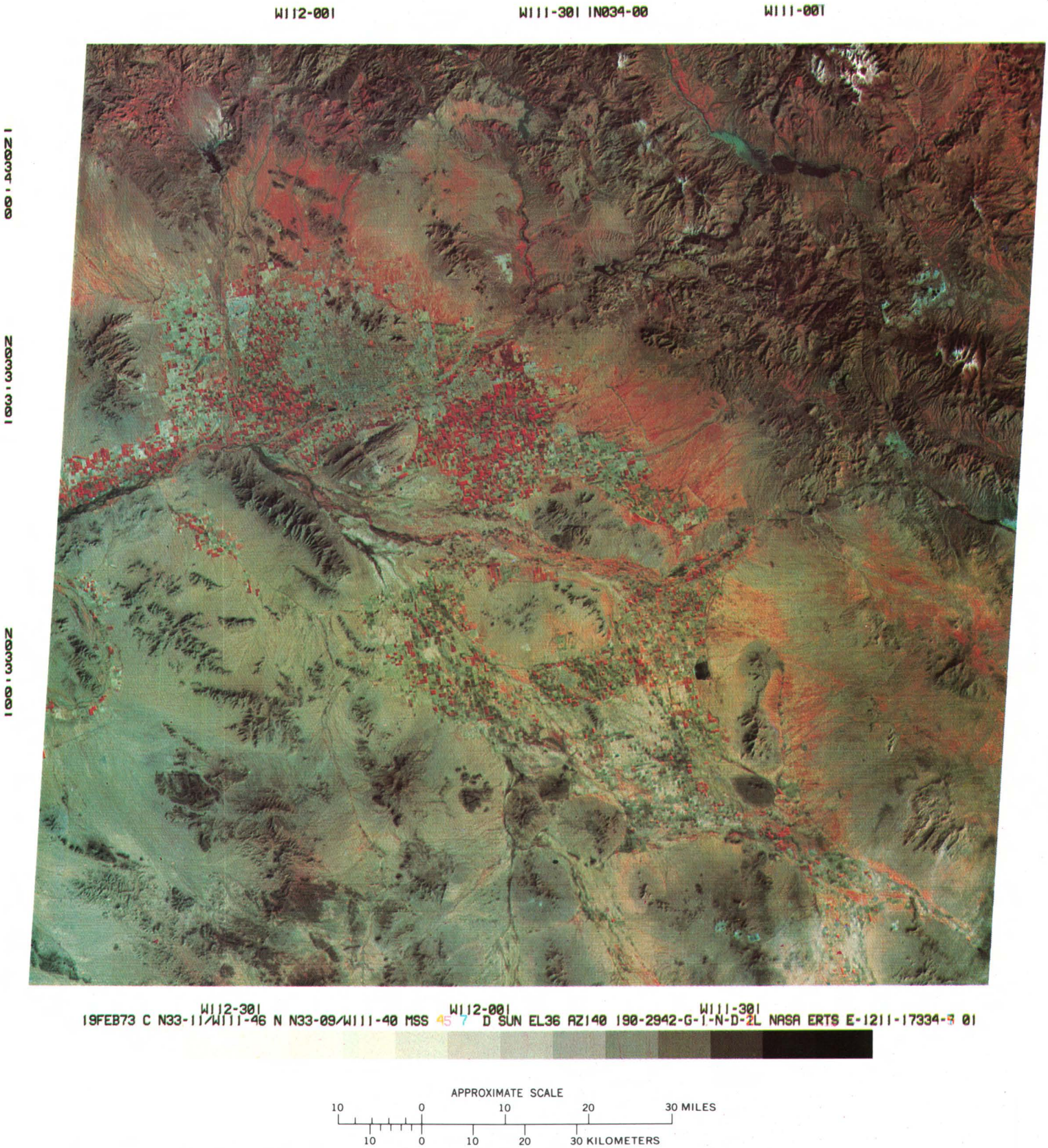


FIGURE 176.—Color composite ERTS–1 image of the Phoenix area of Arizona (1211–17334).

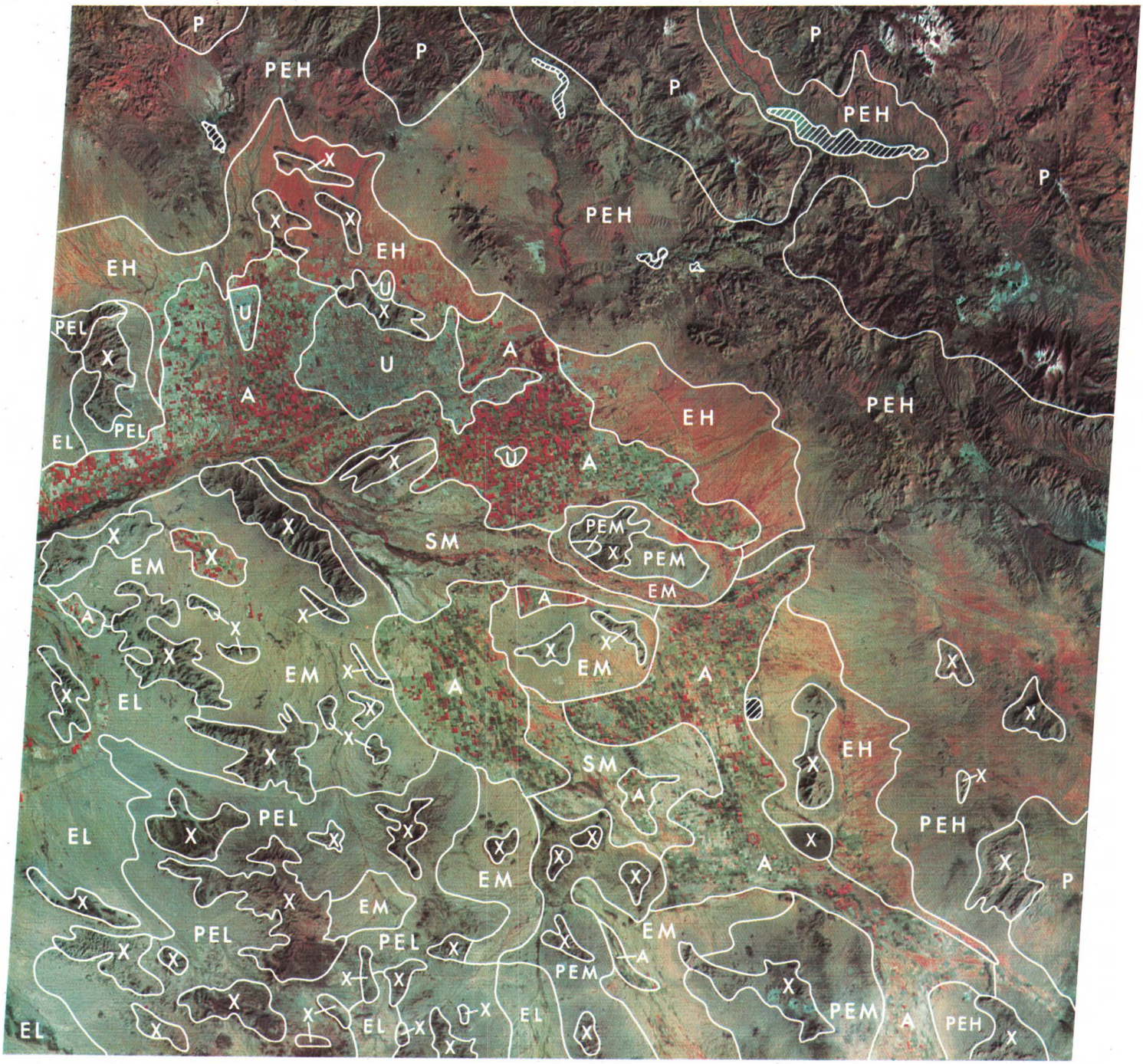


APPROXIMATE SCALE

10 0 10 20 30 MILES

10 0 10 20 30 KILOMETERS

EXPLANATION

U —Urban area
A —Agricultural land
P —Perennial plant community
PE —Perennial—ephemeral
E —Ephemeral
S —Saltbush

H —Heavy production
M —Moderate production
L —Light production
X —Rock outcrop (Light production)
Lake

FIGURE 177.—Annotated color composite ERTS–1 image of the Phoenix area of Arizona showing perennial and ephemeral vegetation and production (1211–17334).

## REFERENCES

Anderson, D. M., 1973, Delineation of permafrost boundaries and hydrologic relationships: NASA Goddard Space Flight Center, ERTS–1 Symposium, Greenbelt, Md., 1972, Proc., p. 135–138.

Bentley, R. G., Jr., 1974, Predict ephemeral and perennial range quantity and quality during normal grazing season; Type III Progress Report to NASA for Period 1 July 1972–30 June 1973: U.S. Dept. Commerce, Natl. Tech. Inf. Service, 76 p.

Carter, W. D., 1973, Geologic questions and significant results provided by early ERTS–1 data: NASA Goddard Space Flight Center, ERTS–1 Symposium, Greenbelt, Md., 1972, Proc., p. 78–87.

Turner, R. M., 1973, Use of the SRI electronic satellite image analysis console for mapping southern Arizona plant communities from ERTS–1 imagery: NASA Goddard Space Flight Center, Symposium on Significant Results Obtained from the Earth Resources Technology Satellite–1, 2d, New Carrollton, Md., Mar. 1973, Proc., v. 1, sec. A, p. 761–768.

# CHAPTER 6.
# APPLICATIONS TO ENVIRONMENTAL MONITORING

## INTRODUCTION

By C. F. Withington,
U.S. Geological Survey

The rapid increase in the Earth's population has produced an awareness of the need for proper utilization of the environment. ERTS–1 imagery is an extremely effective tool in the collection and analysis of environmental data and is especially useful in monitoring environmental change. Some of the experiments so far undertaken include monitoring strip mining, air and water pollution, coastal wetlands, environmental factors for large engineering projects, and tornado destruction.

Surface mining is one of the major disturbances of the surface of the Earth; an estimated 1.4 million ha (14,000 km$^2$) of land have been disturbed by surface mining. Approximately half this excavation can be assigned to strip mining for coal, a process that degrades the environment unless proper measures are taken to reclaim the land. Rehder's paper (p. 254) demonstrates that strip mining can easily be monitored with ERTS–1 imagery, an opportunity for which is now available in the Powder River Basin.

Determination of the sources of air pollution is important in determining the extent and distribution of pollutants. Withington and Breckenridge (p. 258) describe an image of an oil-well fire in Wyoming. Their report also discusses the control of air currents by local topography. Analysis by Brown and Karn (p. 261) of ERTS imagery of part of the Ohio and Monongahela River valleys south of Pittsburgh, Pa., shows the emissions from five coal-burning plants.

ERTS imagery has been used to determine the extent of water pollution in the Great Lakes. Strong (p. 266) describes the effects of upwelling in Lake Michigan which causes massive phytoplankton blooms, raises pH, and initiates a precipitation of calcium carbonate. A bloom of algae in Utah Lake is also described in another report by Strong (p. 270).

Coastal waters and adjacent wetlands are of utmost importance in maintenance of marine life, as the wetlands and estuaries are breeding grounds for many fish and the nutrient source for many more. It has been difficult to determine the extent of the wetlands and to monitor their use, but several experiments have shown the usefulness of ERTS–1 imagery in accomplishing this. Experiments with imagery in the vicinity of Charleston, S.C., for instance, show that wetland-dryland boundaries can be mapped, along with major vegetation associations, wetland types, and the effects of man's encroachment on wetland. Maps at scales as large as 1:250,000 have been made by Carter, Anderson, and McGinness (p. 273).

ERTS digital data provide maximum spatial and radiometric information for accurate mapping of eight different vegetation types, of dredged material, and of open water with extremely accurate results. Tapes of ERTS taken at different times allowed for mapping by Carter (p. 280) of other types of vegetation. Carter, Anderson, and McGinness (p. 286) state that ERTS–1 imagery can show the effects of varying tidal stages, which must be considered in vegetation analysis and wetland boundary determinations. Carter estimates that fieldwork in the Dismal Swamp, Virginia-North Carolina, can be cut from 3 weeks to 3 days using ERTS imagery and that reliable maps can be made from ERTS imagery alone.

A proper consideration of the environmental factors in man's efforts to develop the surface of the Earth can be made through ERTS imagery. For instance, ERTS–1 imagery has proven useful in determining the best location for a highway across the Great Kavir in Iran through observation of sequential series of ERTS images (Krinsley, p. 296). In remote areas of Colombia, South America, man's effort to conquer and tame the elements is seen in an ERTS image studied by Carter (p. 290).

Finally, the last several years have seen a high incidence of tornadoes, particularly in the central part of the United States. Considerable loss of life and property damage resulted from such storms in 1974. The paper by Hollyday and Cook (p. 300) shows how ERTS imagery can be used to delineate tornado paths and to assess environmental damage.

# CHANGES IN LANDSCAPE DUE TO STRIP MINING

By John B. Rehder,
University of Tennessee

The application of ERTS–1 imagery to the detection and monitoring of strip-mining landscape change is feasible and capable of becoming operational. The strip-mining landscapes on the Cumberland Plateau of Tennessee are excellent examples of dynamic landscape modification (Rehder, 1973a).

From ERTS–1 imagery and RB–57 high-altitude aerial photography, a map of strip-mining landscape changes on the Cumberland Plateau between April 1972 and October 1972 has been produced (fig. 178). To facilitate the determination of landscape change, the map was prepared at a scale of 1:120,000, which is the scale of the high-altitude aerial photography. The darkest tones on the map represent the landscape areas stripped as of Apr. 18, 1972, mapped from the high-altitude aerial photography. The light-gray tones represent additional stripping operations and expansion of mining as mapped from the ERTS imagery dated Oct. 15, 1972 (Rehder, 1973b).

The analysis of ERTS imagery for strip-mine detection and monitoring depends on the ability of the interpreter to identify strip mining on the imagery. Strip mines on an original band 5 black and white transparency from ERTS appear as light-toned jagged lines on a dark forested background. By negative print enhancement, the same image can be printed so that the strip mines appear as dark solid jagged lines on a light-toned background, as illustrated in figure 179.

Using the RB–57 photography as a data base and identification medium, strip mines are identified as irregular jagged lines that follow the contours of the mountains. Unlike local dirt roads, strip mines do not link geographical points. In the negative print of figure 180, the mines are enhanced in dark tones on a white forested background. Note the extent of cleared, stripped land in April 1972 indicated at the mine north of the arrow. By comparison with figure 179, one can see not only the configuration of the same strip mine, but can also detect from the October 1972 image additional dark tones immediately north of the arrow. Of considerable importance is the capability of the ERTS negative print to enhance and display strip mines in dark tones. Such enhancements aid in the detection and identification of newly cleared lands and favor the mapping of cleared, stripped, or otherwise deforested landscapes.

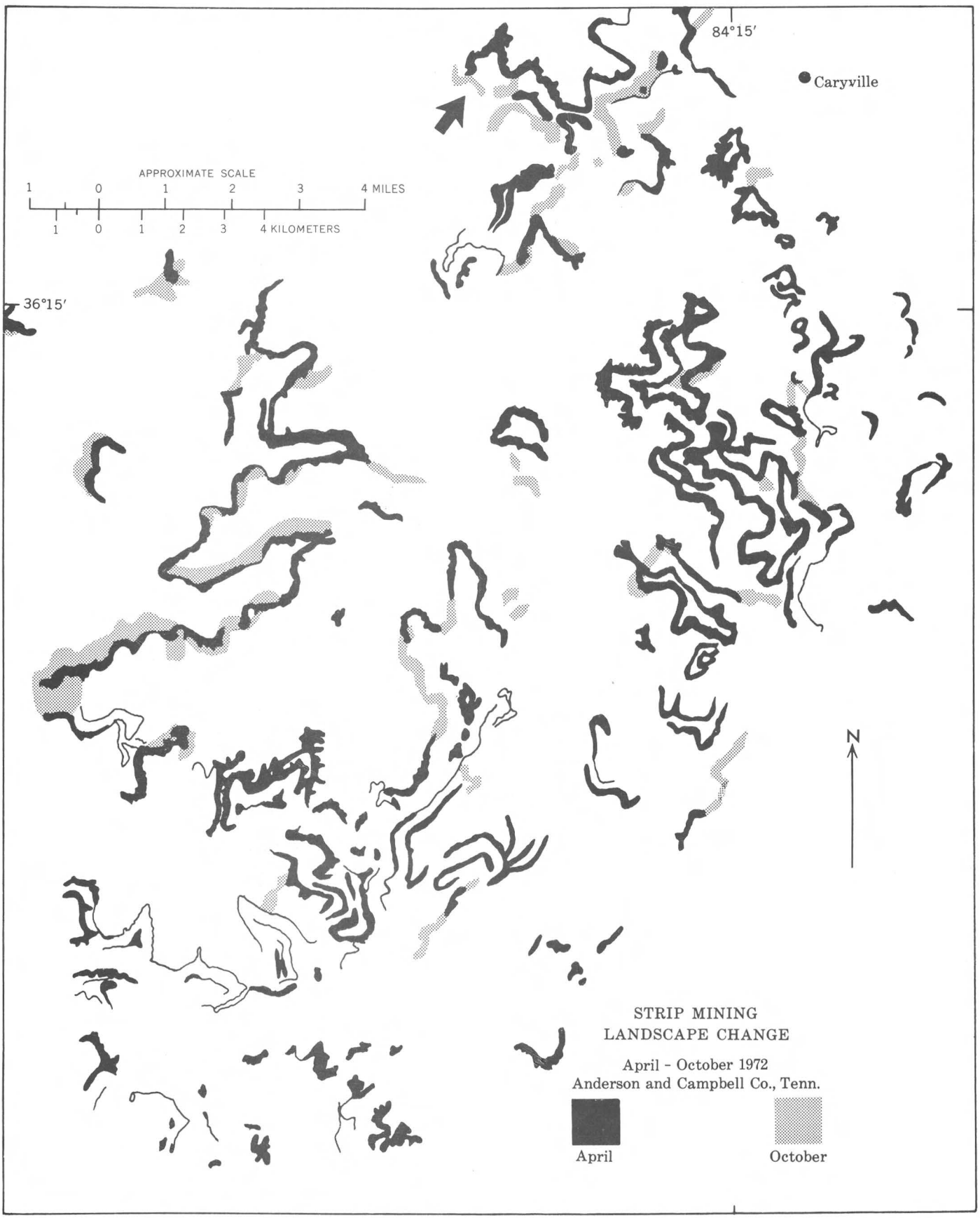


FIGURE 178.—Changes in the landscape created by strip mining on the Cumberland Plateau of Tennessee, from Apr. 18 through Oct. 15, 1972. Data sources: NASA Johnson Space Center Mission 197 aerial photographs 26–0050 and 26–0063 and ERTS–1 image 1084–15431, band 5.

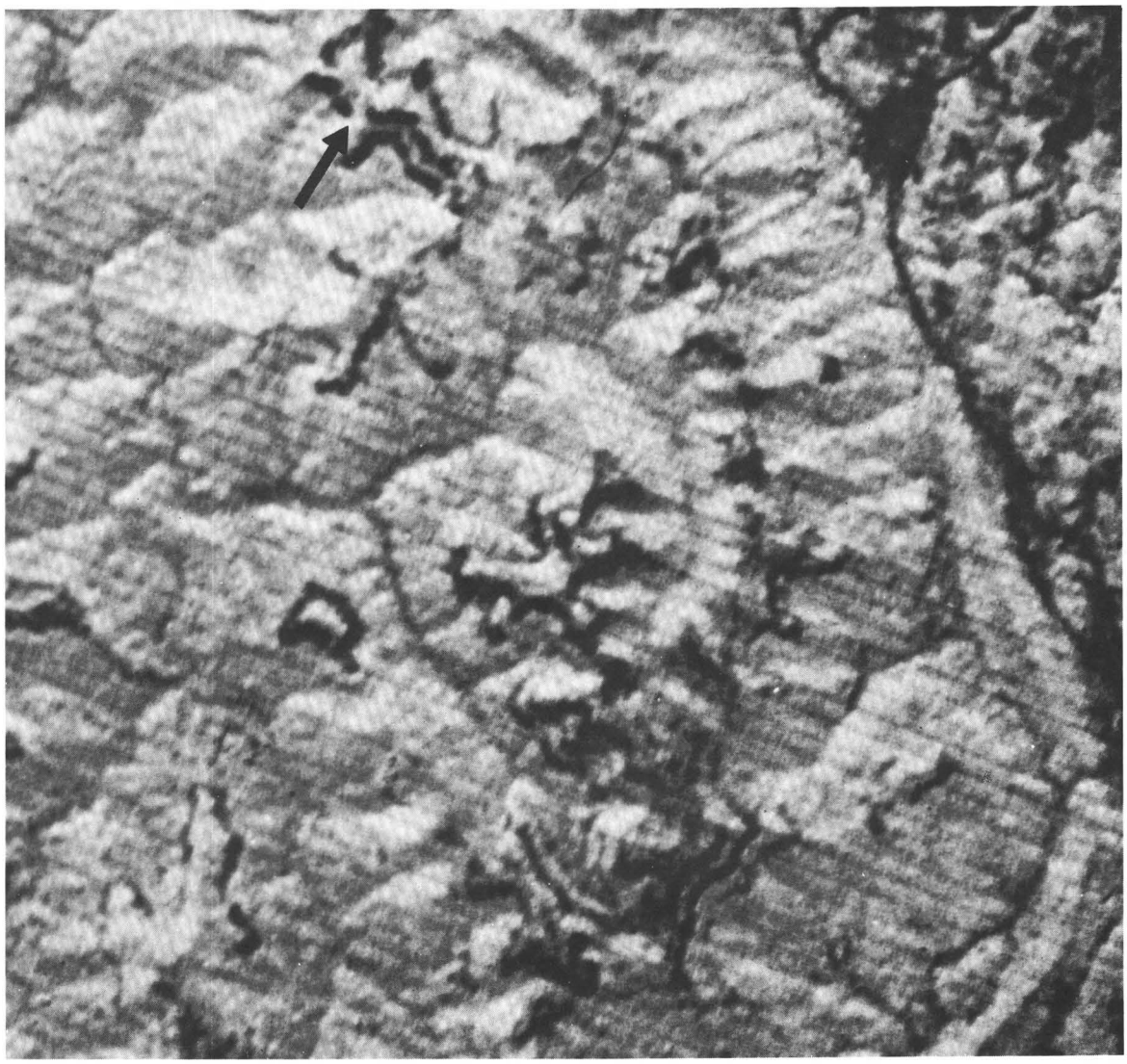

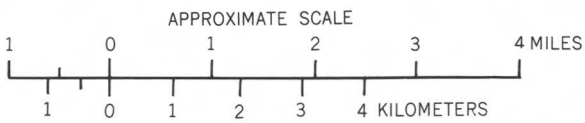


FIGURE 179.—Strip mines on Cumberland Plateau from enlargement of ERTS–1 image acquired on Oct. 15, 1972 (part of 1084–15431, band 5 negative). Dark tones, produced by negative reversal, are enhanced to illustrate cultural landscape features such as strip mines, which are normally shown as light tones on a positive image. Note the degree of strip mining north of the arrow as compared to that in the same area shown in figure 180.

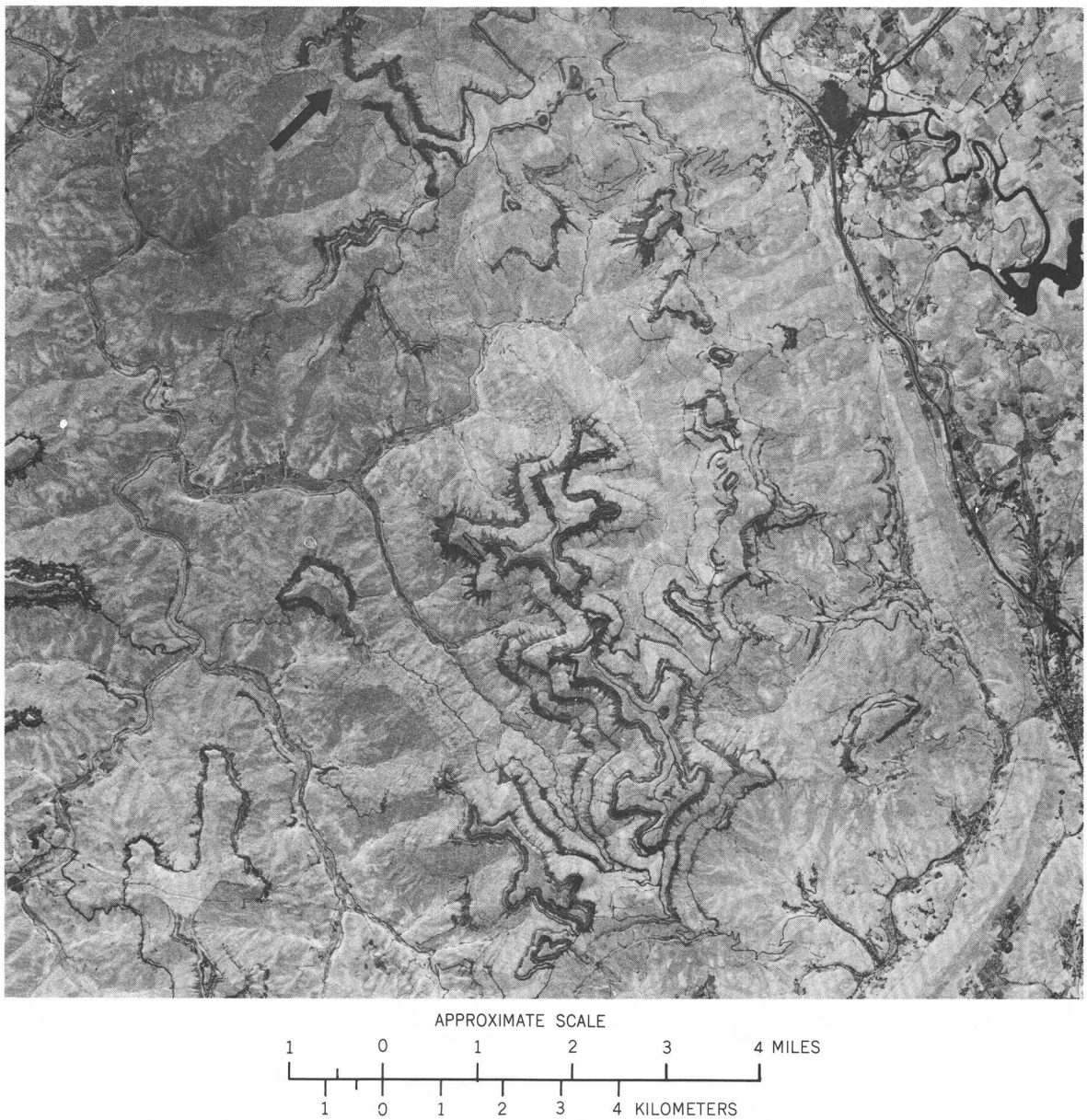


FIGURE 180.—Strip mines on the Cumberland Plateau from NASA high-altitude aerial photography; Mission 197 aerial photograph 26–0063 acquired on Apr. 18, 1972. Note the absence of strip mines north of the arrow as compared with the presence of strip mines for the same location on ERTS–1 image 1084–15431, acquired on Oct. 15, 1972 (fig. 179).

# OIL-WELL FIRE ON ERTS–1 IMAGES

By C. F. Withington, U.S. Geological Survey,
and Roy M. Breckenridge, Wyoming Geological Survey

On Friday, Nov. 30, 1973, a wildcat well being drilled in Converse County, Wyo., blew out, and on December 5 the escaping gas and oil ignited. The first attempts to contain the fire were only partly successful. A shaped nitro-gel explosive was set off over the hole by firefighters on December 19 and damped the fire only slightly. A second shot on December 23 was successful in putting the fire out, but it flared up again the next day. A third attempt on December 26 met with limited success. The well was finally capped 33 days after the blowout, on Jan. 2, 1974. Throughout the period the weather was seasonable—temperatures ranged from just above freezing to −34°C. The well was flowing at an estimated 200 bbl/h the entire time it was uncapped. The oil, being high in paraffin, solidified around the well because of the cold weather and gave a yellowish coating to the area.

The area was imaged by ERTS–1 (fig. 181) at 10:16 a.m. local time on December 20. The oil well and its plume can be distinctly seen on the ERTS image. The plume, a broad black band as much as 0.25 km wide, can be traced for a distance of about 16 km. At this point, the wind coming out of the east-trending valley of Antelope Creek dispersed the plume and blew it in a more easterly direction. This dispersing plume can be traced an additional 30 km.

Bands 4, 5, and 7 (fig. 182) were compared to see which band best indicated the plume. Enlargements of the image to a scale of 1:250,000 determined that band 7 (0.8–1.1 $\mu$m) is most effective in displaying the plume, no doubt because energy at wavelengths of 0.8–1.1 $\mu$m is more capable of penetrating thin cirrus clouds (see Colvocoresses, p. 17, 18, in this paper).

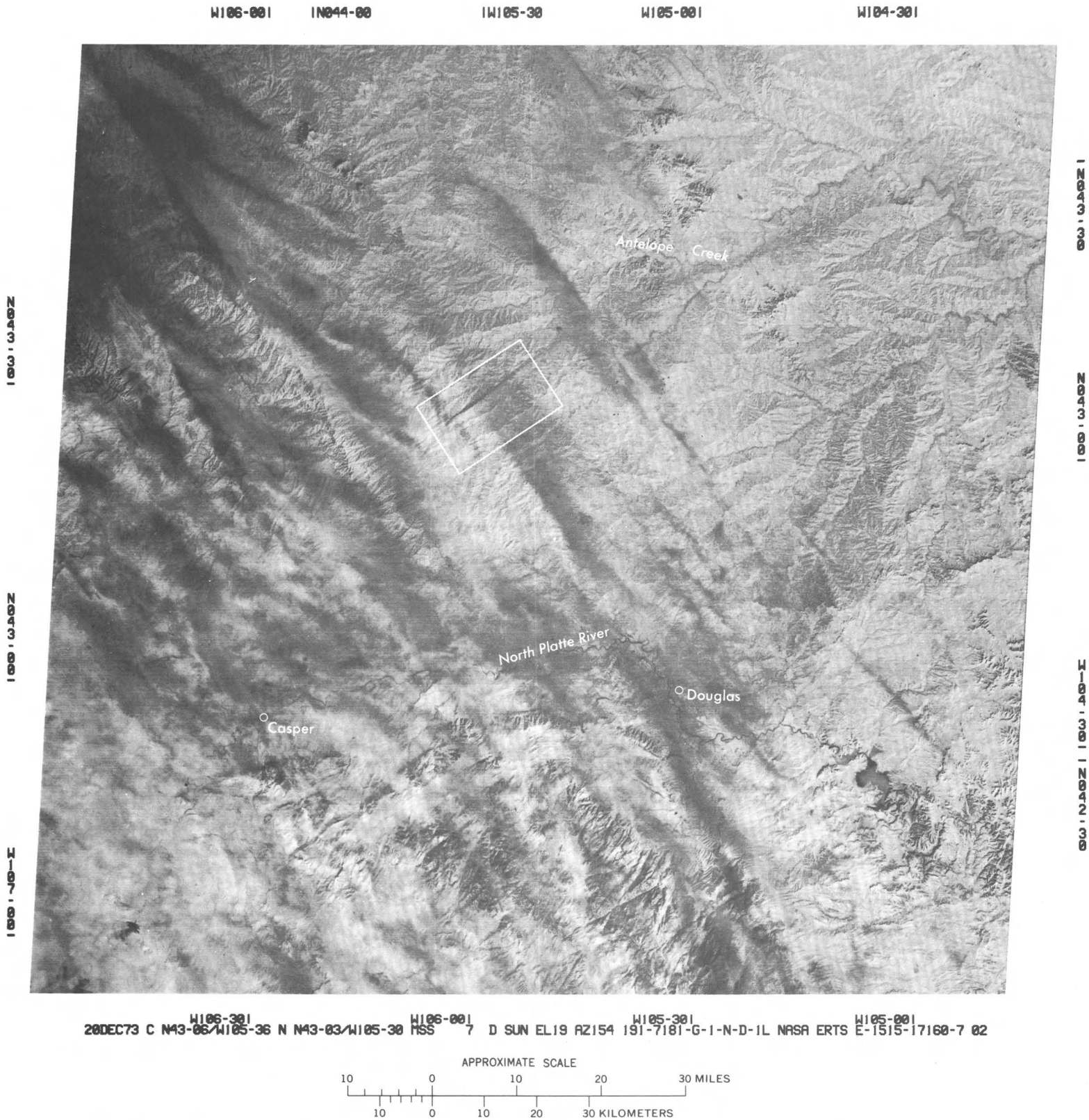


FIGURE 181.—Smoke plume from wildcat oil-well fire, Converse County, Wyo., on ERTS–1 image 1515–17160, band 7, acquired on Dec. 20, 1973. Outline shows approximately the area of figure 182.

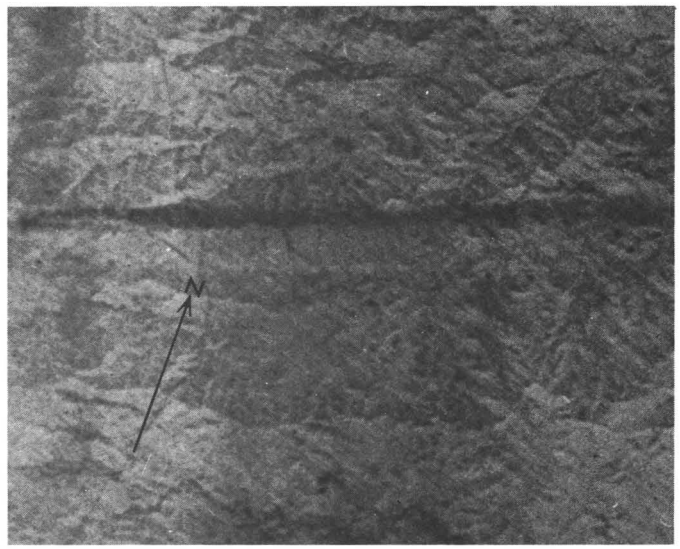


1:250,000 1515 17160 Band 4

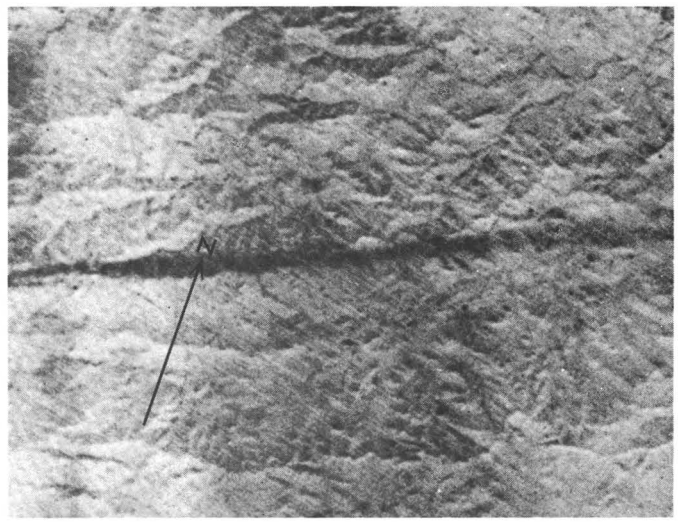


1:250,000 1515 17160 Band 5

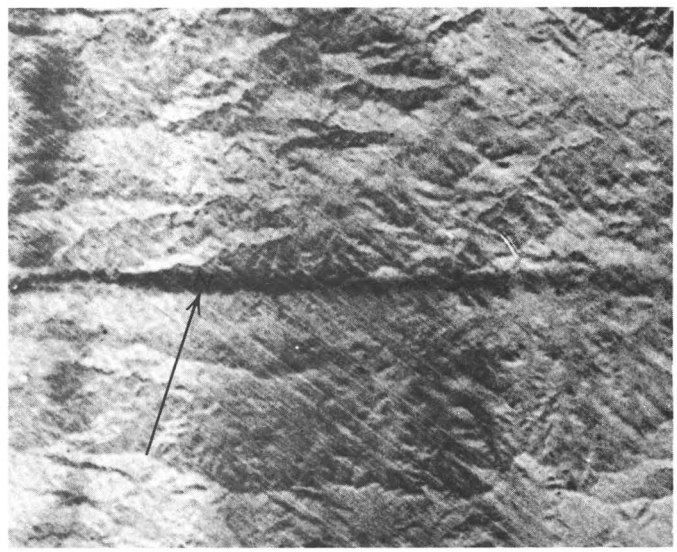

1:250,000 1515 17160 Band 7

APPROXIMATE SCALE

5 0 5 MILES

5 0 5 KILOMETERS

FIGURE 182.—Enlargements of three ERTS–1 images showing comparison of reflectance of smoke plume (part of 1515–17160, bands 4, 5, and 7).

# AIR POLLUTION FROM THE OHIO RIVER AND MONONGAHELA RIVER VALLEYS

By Fred R. Brown and Fred S. Karn,
U.S. Bureau of Mines

The Ohio and Monongahela River valleys south of Pittsburgh, Pa., provide an excellent area for testing the usefulness of ERTS–1 imagery for detecting sources of air pollution due to coal utilization. This area is heavily industrialized and includes many coal-fired power-generating stations.

Figure 183 shows both river systems as shown in an ERTS image dated Jan. 12, 1973. Figure 184 shows a map of the general area covered in the image. Plumes from specific point sources can be easily identified as originating near Morgantown and Captina, W. Va., and near Beverly, Brilliant, and Stratton, Ohio. Coal-fired powerplants of the following sizes are located in these areas.

| *Site* | *Power generated in 1972 (kWh)* | *Approximate population served* |
|---|---|---|
| Morgantown, W. Va. | $7.0\times10^9$ | 160,000 |
| Captina, W. Va. | $11.0\times10^9$ | 520,000 |
| Beverly, Ohio | $8.9\times10^9$ | 420,000 |
| Brilliant, Ohio | $8.2\times10^9$ | 390,000 |
| Stratton, Ohio | $11.1\times10^9$ | 600,000 |

The most prominent feature at several of these locations is a large billowy steam cloud arising from the stations' water-cooling towers. Ground observations reveal that any gaseous or particulate air pollutants emitted from the stacks are often engulfed and obscured by these steam clouds.

The use of the MSS data from ERTS is illustrated in figure 185, which shows the plume from Beverly, Ohio, on Jan. 12, 1973, on all four MSS bands. The images corresponding to the blue-green and red parts of the spectrum (bands 4 and 5) indicate more clearly the physical characteristics of the plume. From these images, the approximate length, width, and altitude of the plume can be calculated. The two infrared images (bands 6 and 7), while partly penetrating the plume, give a more detailed representation of the topography of the region. This difference in sensitivity of the various bands is particularly useful in studying the relationship of water systems located nearby because of the relative increased absorption in the infrared frequencies by bodies of water. This increased absorption provides excellent contrast and facilitates the specific location of the origin of the emissions.

Another specific advantage of the ERTS system in an air-pollution study is the repetitive imaging on an 18-day basis. By continuously providing images of any given area over many days, data are eventually obtained for features in those regions that have relatively few cloud-free days in the year. This advantage is illustrated by figure 186, which contains sections of four ERTS MSS images taken on four different dates. The area is immediately south of Pittsburgh and contains a large coke works. The coke is quenched in open towers that emit plumes of steam, other gaseous emissions, and particulate matter. Changes in the nature and extent of air pollution can be monitored by this repetitive imaging along with data on plant operations and on meteorological conditions.

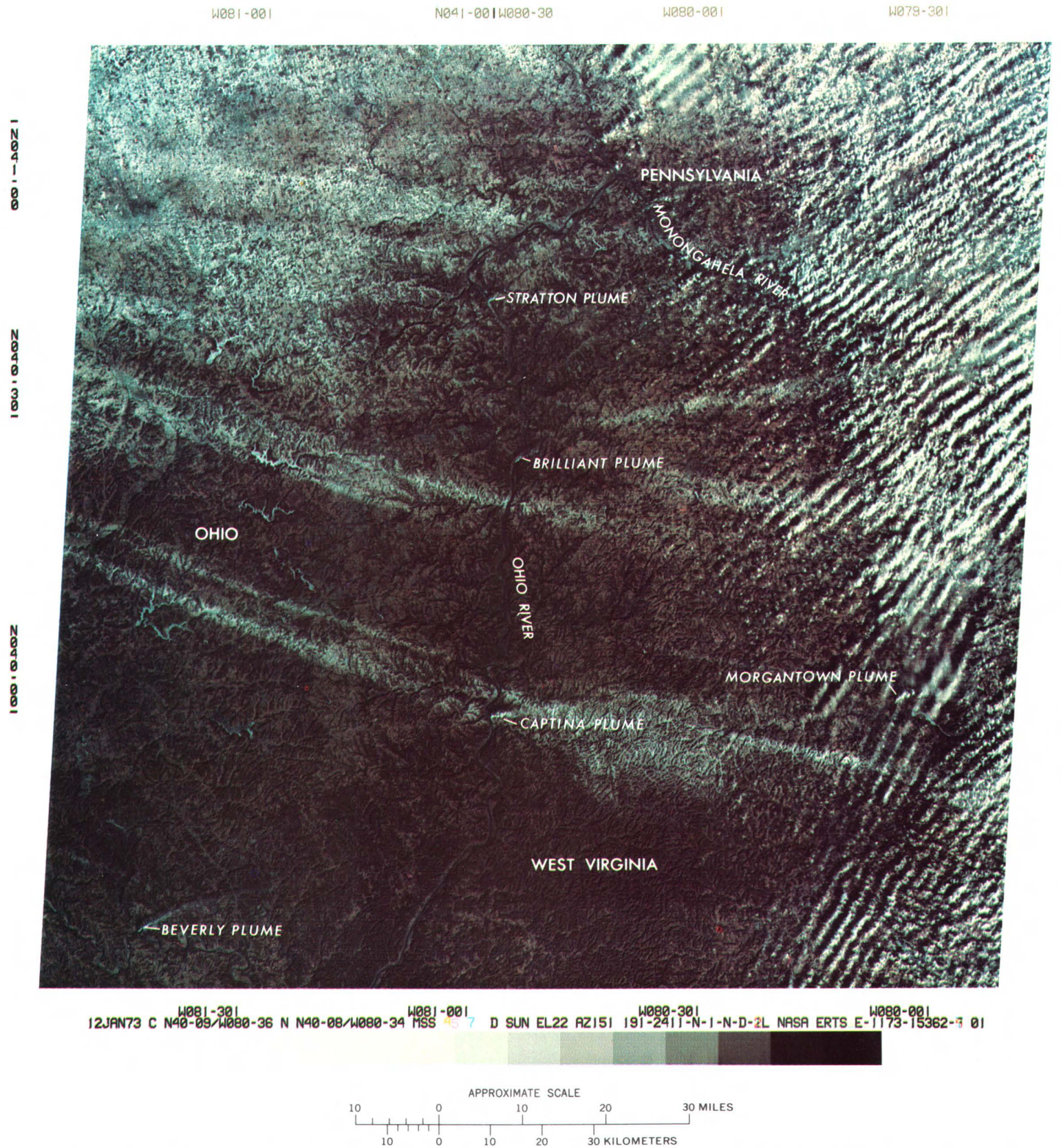


FIGURE 183.—Annotated color composite ERTS–1 image of smoke plumes from power-generating stations in the Ohio River and Monongahela River valleys (1173–15362).

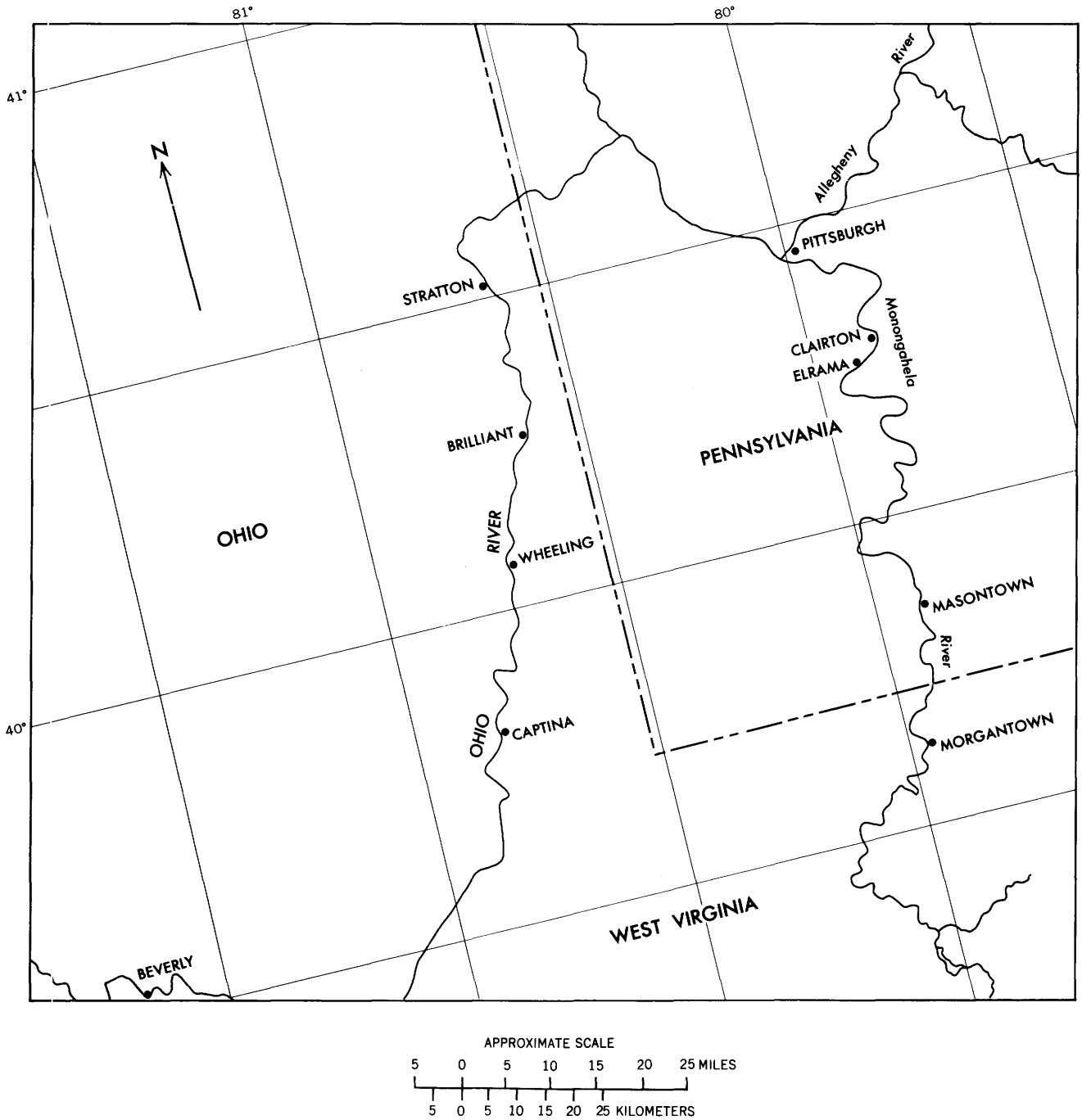


FIGURE 184.—Index map of the Ohio River and Monongahela River valleys (area shown in the image in fig. 183).

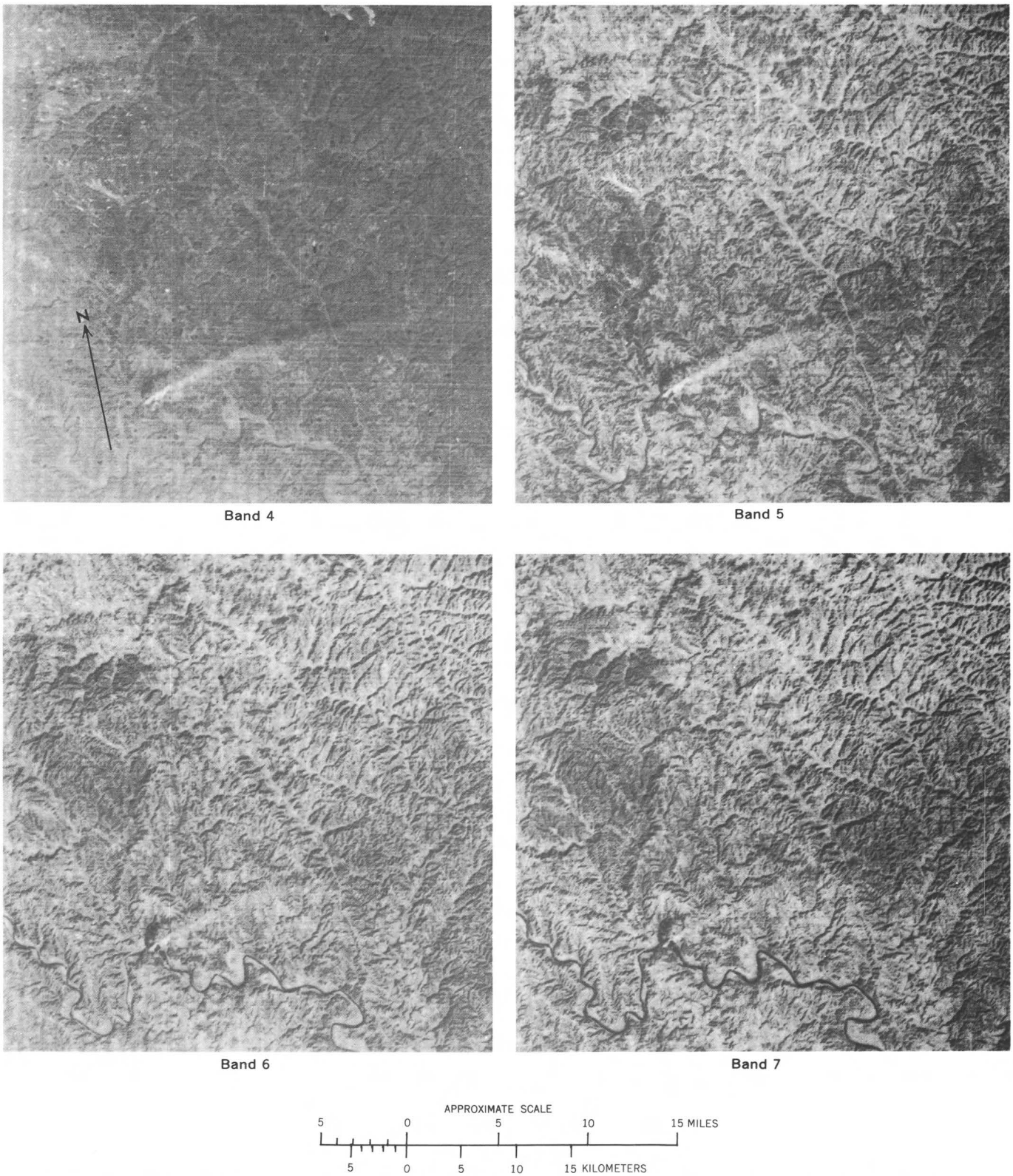


FIGURE 185.—Enlargement of part of the ERTS image of the Beverly, Ohio, area showing smoke plumes on different MSS bands on Jan. 12, 1973 (part of 1173–15362, bands 4–7).

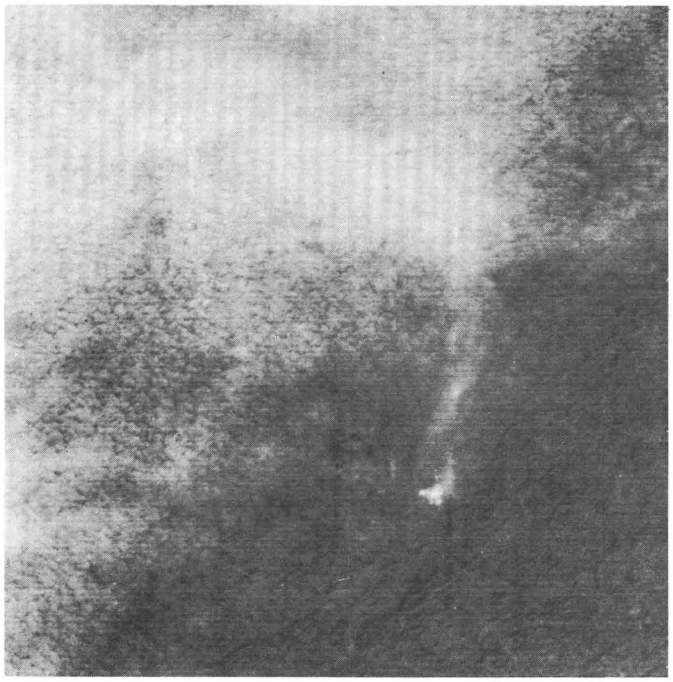

November 18, 1972
ERTS-1 Image, 1118-15305, band 5

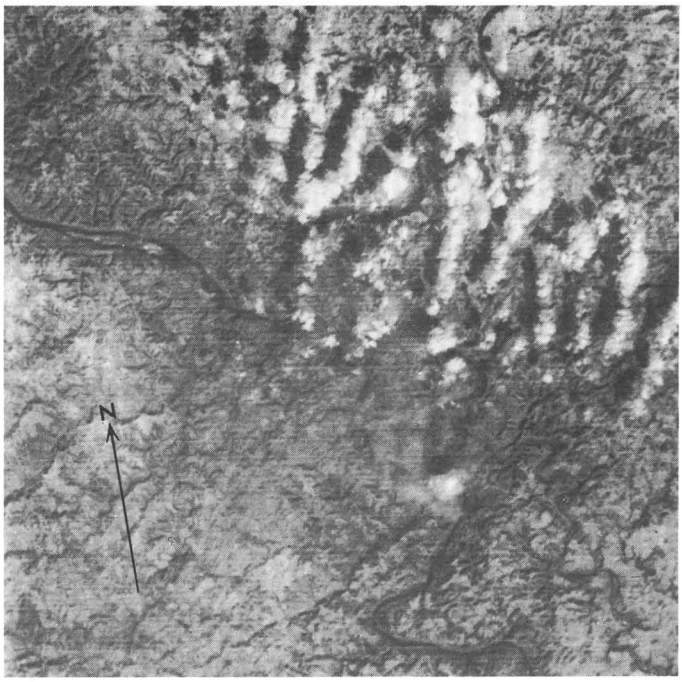


December 7, 1972
ERTS-1 Image, 1137-15364, band 6

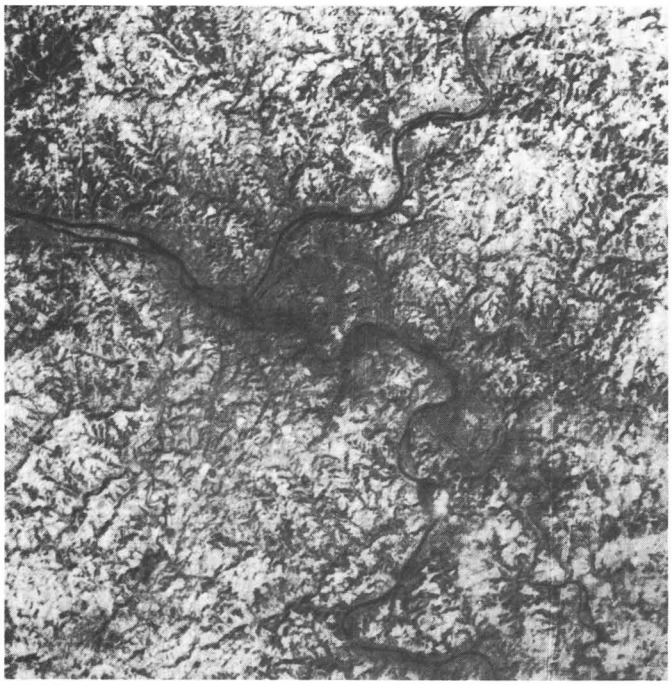

February 17, 1973
ERTS-1 Image, 1209-15365, band 5

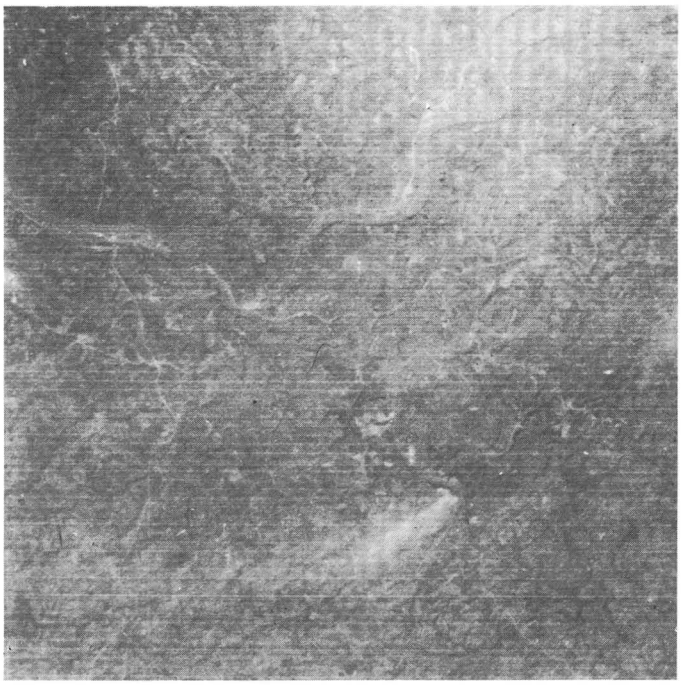

March 24, 1973
ERTS-1 Image, 1244-15312, band 4

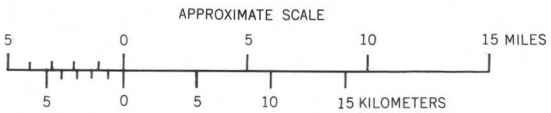


FIGURE 186.—Enlarged parts of four ERTS-1 images showing steam plumes from coke ovens near Pittsburgh, Pa., November 1972 through March 1973 (parts of 1118–15305, band 5; 1137–15364, band 6; 1209–15365, band 5; and 1244–15312, band 4).

# A LAKE MICHIGAN "WHITING"

By Alan E. Strong,
National Oceanic and Atmospheric Administration

Figure 187 is an MSS false-color composite mosaic of Lake Michigan prepared from images acquired on Aug. 21, 1973. Figure 188 is another MSS color composite mosaic that was made by compositing bands 4, 5, and 6 using green, red, and red filters, respectively. Milky water appears to be occurring over nearly the entire surface of Lake Michigan on this date. Virtually all the water color was seen as the light tone in band 4 (fig. 189); band 5 was nearly dark. Reports of milky water have been made over the last few years as pH levels and eutrophication increase. The milky water is believed to have been recently intensified by upwelling that moved nutrient-rich waters to the surface. This enrichment generated massive phytoplankton blooms, raised the pH, and initiated a precipitation of calcium carbonate ($CaCO_3$). Secchi disc readings from University of Michigan research vessels were found to be drastically reduced during these "whitings." Most of the chemical precipitation is occurring beneath the surface to depths of 10 m or more. Deleterious consequences of similar whitings have been clogged municipal water intakes at downwind locations along the Lake Michigan shoreline. The phenomenon has not been observed in Lakes Huron or Superior, where both calcium and pH levels are somewhat lower than those found in Lake Michigan. Similar milky-water periods, however, have been detected by ERTS in Lakes Erie and Ontario.

Within 1 h of this data acquisition by ERTS, the NOAA–2 satellite crossed the Great Lakes area and provided imagery of the upwelling along the entire eastern Lake Michigan shoreline. This upwelling began during the evening of August 20 as the winds over the lake shifted from northwesterly to northeasterly at speeds of 10 to 15 m/s. A marked temperature contrast is evident in the NOAA–2 thermal infrared image and shows water temperatures along the shoreline approaching values of 5°C, contrasting with readings in the lower 20's over the remainder of the Lake Michigan surface water (Strong and others, 1974).

Along the eastern shoreline of the southern basin, sediment can be seen being carried offshore to the south and west. Waves from the north, 1 to 2 m high, are causing considerable erosion of the sand and clay cliffs that are found along this part of the Lake Michigan shoreline. Circulation patterns, not only along the shorelines but in the open lake as well, are nicely revealed by this milky-water phenomenon. An anticyclonic gyre is evident near the center of the southern basin and corresponds to the highest surface temperatures observed by NOAA–2 at this time. Along the Wisconsin shoreline, sinking surface water suppresses much of the whiting. In 1973, the milky water in Lake Michigan was first observed in July and continued well into the fall. This condition was first reported by the University of Michigan in 1966.

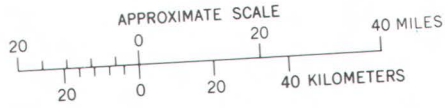


FIGURE 187.—Annotated color composite ERTS–1 image mosaic of Lake Michigan by standard color-combining methods using bands 4, 5, and 7 and yellow, red, and blue light, respectively (1394–16030, 1394–16033, and 1394–16035).

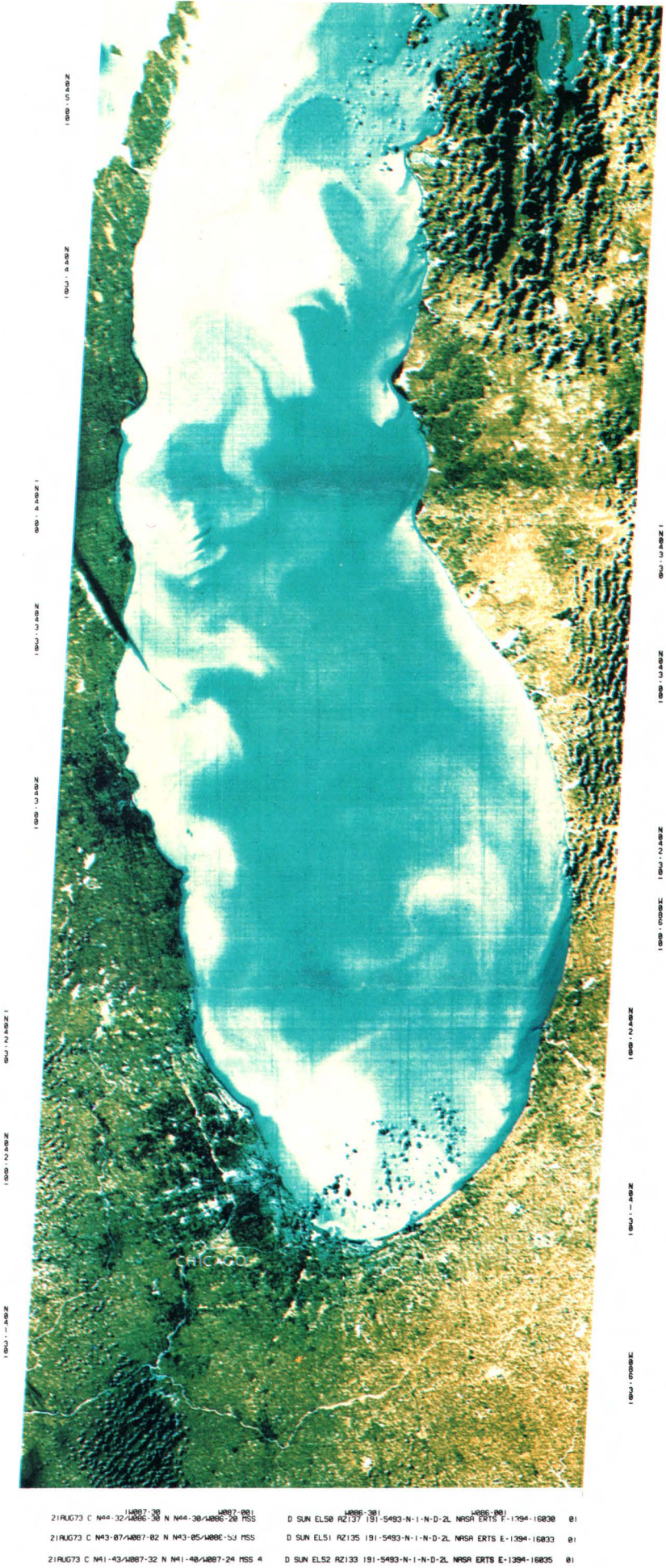


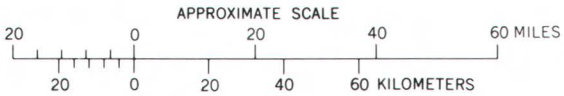


FIGURE 188.—Annotated color composite ERTS–1 image mosaic of Lake Michigan using bands 4, 5, and 6 and green, red, and red light, respectively, to show "whiting" (1394–16030, 1394–16033, and 1394–16035).

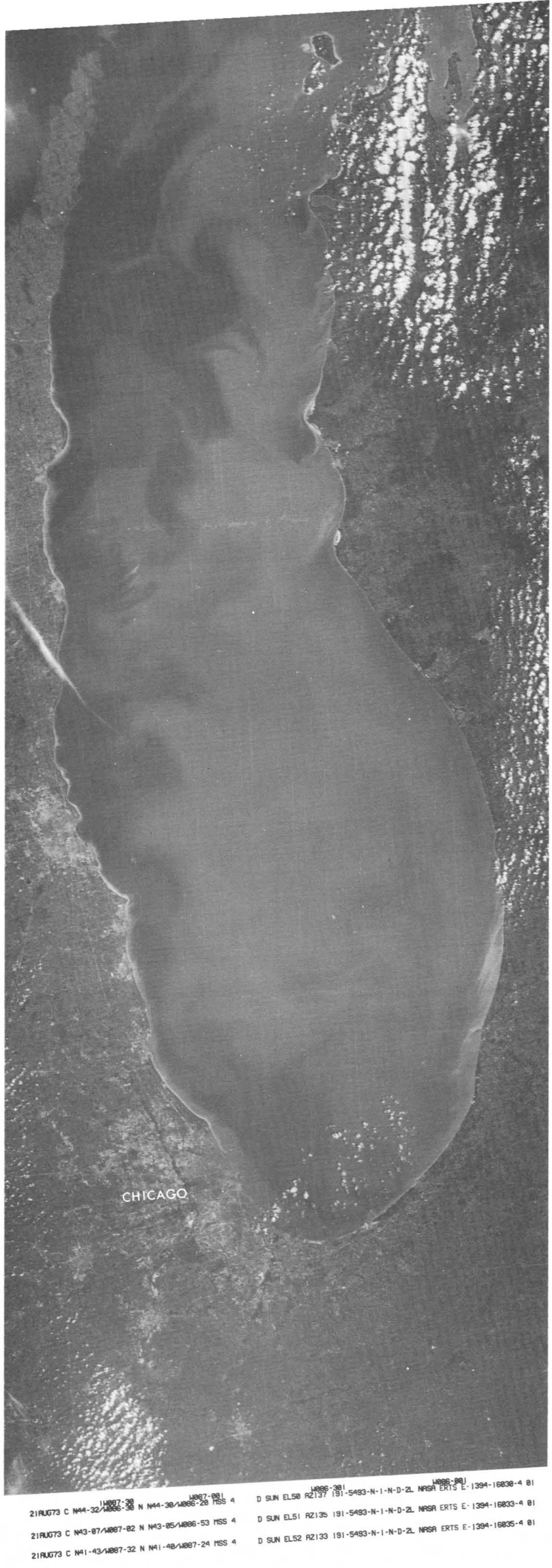


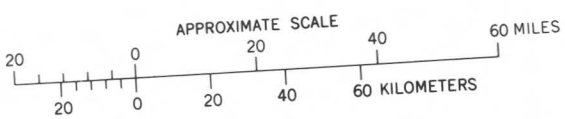


FIGURE 189.—Annotated ERTS–1 image mosaic of band 4 images of Lake Michigan (1394–16030, 1394–16033, and 1394–16035; band 4).

# ALGAL BLOOMS IN UTAH LAKE

By Alan E. Strong,
National Oceanic and Atmospheric Administration

During summer and early fall, when surface waters of lakes reach their maximum temperature, algal blooms are likely to develop. Such a phenomenon, which characterizes eutrophic conditions, has been noticed in ERTS–1 images of Lake Erie and several lakes in the State of Utah. In addition to their biological impact, the concentration of the algae into long streamers provides information on surface circulations. The ERTS–1 image shown here (fig. 190) is of Utah Lake, which has a surface area of about 375 $km^2$ and which is known for its high turbidity and summer algal blooms. Within 1 day of this satellite observation, a limnological cruise on Utah Lake revealed a massive, highly variable bloom of *Aphanizomenon flos-aquae*. Although the algal bloom appears dark to the eye, reflected infrared radiation is quite intense and results in a unique water-surface signature. The color image was made using bands 4, 5, and 7 with blue, green, and red filters, respectively. An anticyclonic gyre is shown in this shallow (about 3 m deep), highly eutrophic lake; the eutrophic state is due to high phosphate content (PO = about 0.5 mg/l). Figure 191, bands 4–7 of ERTS–1 image 1051–17420, shows variation in water penetration at different wavelengths, thereby clearly delineating high turbidity conditions and circulation patterns in bands 4 and 5, sediment and algae in band 6, and only the algal bloom in band 7. Other blooms have been seen and studied in Lake Erie, around the Erie Islands, from ERTS images acquired Sept. 9, 1972, and Oct. 10, 1972 (Strong, 1973).

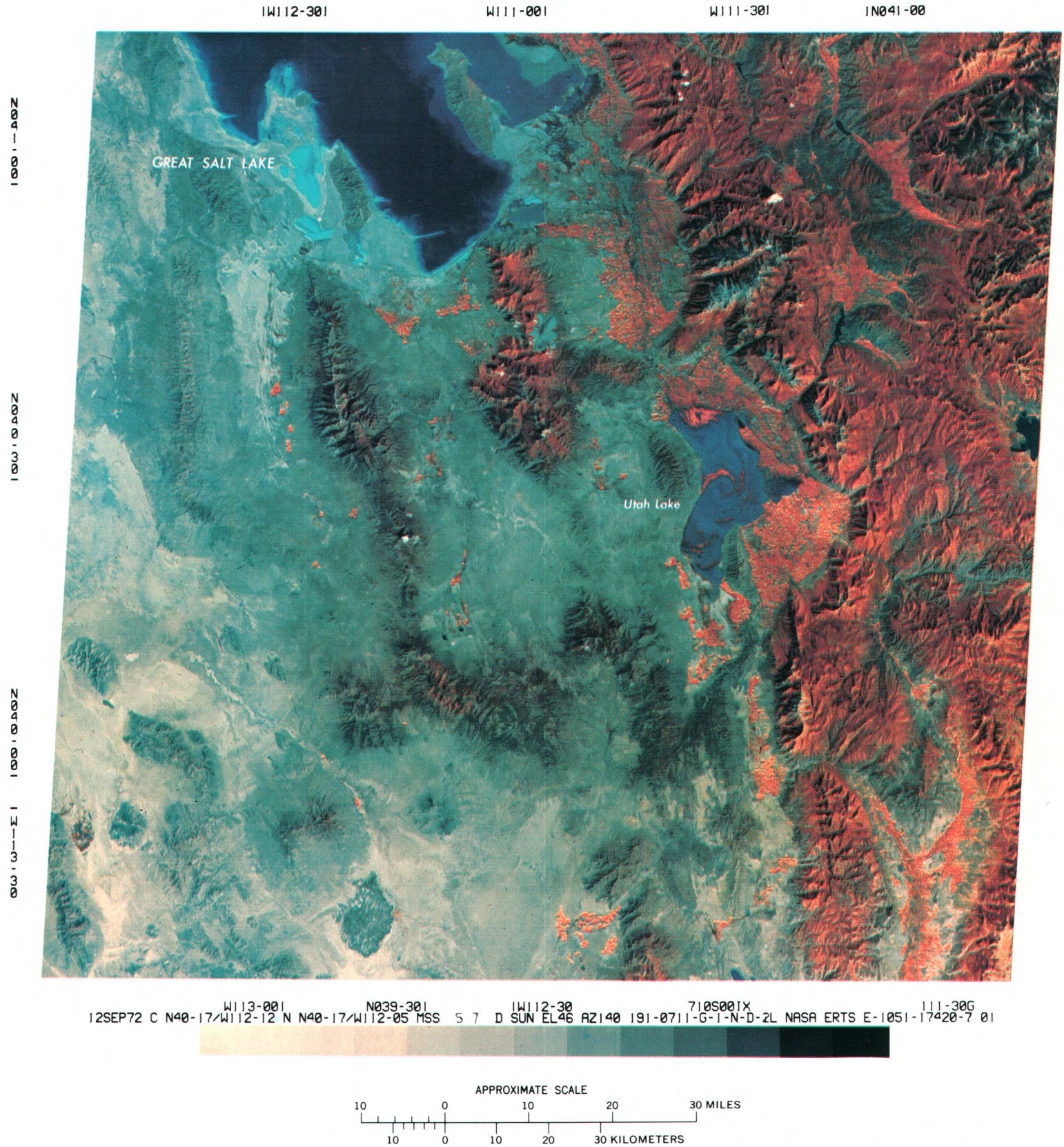


FIGURE 190.—Annotated color composite ERTS–1 image of algal blooms in Utah Lake (1051–17420).

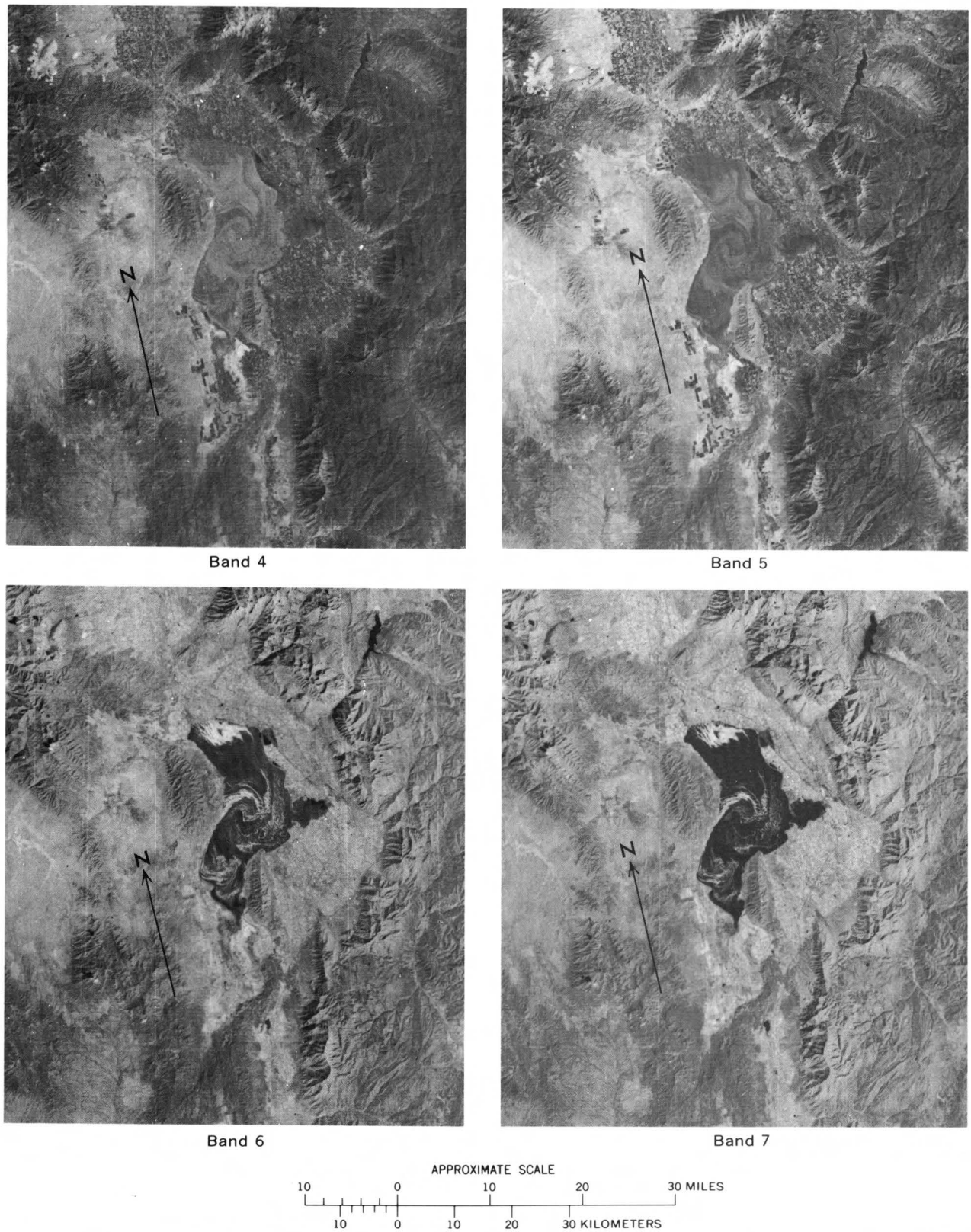


FIGURE 191.—Comparison of a part of ERTS–1 image 1051–17420, bands 4–7, showing algal blooms in Utah Lake. Band 4, penetrates the water to show the greatest amount of turbidity; band 5, high turbidity with more distinct shoreline; band 6, turbidity pattern less distinct, but sediment and algae visible; and band 7, shoreline clearly delineated, slight water penetration, and distinctive pattern of algal bloom.

# WETLAND CLASSIFICATION AND MAPPING ALONG THE SOUTH ATLANTIC COAST

By Virginia Carter, U.S. Geological Survey,
and Richard R. Anderson and John W. McGinness, Jr.
The American University

The wetland-dryland boundary, major vegetation associations, wetland type, and areas modified by man's activity can be identified and delineated on ERTS imagery (Anderson and others, 1972, 1973, 1974). Figure 192, an ERTS band 7 image taken Oct. 12, 1972, of the Charleston area of South Carolina, shows the coastal marshes inland as far as Lake Moultrie. Most of Charleston is on the two large masses of land that jut southward into the Charleston harbor. Inland from the coast along the Wando, Cooper, Ashley, and Stono Rivers, the water becomes progressively less saline, and the vegetation changes accordingly. Because of tidal ebb and flow, broad transitional areas of vegetation exist, and the exact boundaries of wetland types are difficult to place using any mapping method. Figure 193 is a wetland map of the area made from ERTS images taken Oct. 12, 1972, and Mar. 23, 1973, and compiled with a Bausch and Lomb Zoom Transfer Scope at a scale slightly larger than 1:250,000. Figures 194 and 195 are color composites of parts of both of these images and show the seasonal differences.

Three categories of marsh are identified as the water changes from saline to fresh:

1. Salt marsh containing predominantly *Spartina alterniflora* (saltmarsh cordgrass); the following subdominants are present in varying amounts, usually at or near the upper wetland boundary: *Juncus roemarianus* (needlerush), *Salicornia* spp. (glasswort), *Distichlis spicata* (spike-grass), *Spartina patens* (salt-meadow cordgrass), *Borrichia frutescens* (sea oxeye), and *Iva frutescens* (marsh elder).
2. Near-saline to brackish marsh containing predominantly *Juncus roemarianus;* stream channels are bordered by *Spartina alterniflora* at the more saline end and *Spartina cynosuroides* (giant cordgrass) at the fresher end. Subdominants in this area may include *Distichlis spicata*, *Salicornia* spp., *Spartina patens*, *Scirpus* sp. (bulrush, three-square), and *Iva frutescens.*
3. Brackish to fresh marsh containing large stands of *Spartina cynosuroides* along stream margins and *Scirpus americanus* or *S. olneyi* (three-squares) or *Juncus roemarianus* often filling in the remaining area; subdominants include *Scirpus* spp., *Zizania aquatica* (wild rice), and *Juncus* sp. (rush). As the water becomes fresher, *Sagittaria* spp. (arrowhead), *Nuphar advena* (yellow water lily), *Pontederia cordata* (pickerelweed), *Peltandra virginica* (arrowarum), and *Typha* spp. (cattail) become codominants with *Spartina cynosuroides.*

As the water becomes fresher, the species mixture becomes more complex, and the vegetative cover becomes more reflective in the near-infrared. During the growing season the upper wetland boundary in band 7 becomes increasingly difficult to identify farther inland. Supplementing the interpretation with band 5 imagery aids delineation because the marsh shows a gray-level reflectance distinguishable from spoil and agricultural fields (lighter) and water or woods (darker). The best method using black and white imagery, however, is to delineate upper wetland boundaries on band 7 on winter or early spring imagery and to attempt species discrimination using band 7 and 5 imagery taken midway to late in the growing season.

The head of the Cooper River estuary south of Lake Moultrie is split into two branches (A on fig. 193). This area initially presented a complex interpretation problem, because the natural water levels are being affected by events other than tidal. The riverine drainage channel could only be delineated on imagery from Aug. 19, 1972, when tide was very low. Imagery and false-color infrared photography taken at higher tide showed the marsh adjacent to the channel to be flooded, and only the vegetation along the original channel levees had a strong vegetative signature. Before construction of the Santee-Cooper project of the South Carolina Public Service Authority in 1942, the annual freshwater inflow to the Charleston harbor estuary from the Cooper River was 2 $m^3/s$. The project was construction of both a dam and a diversion canal into the Cooper River. The annual inflow is now 42 $m^3/s$, which accounts for flooding of areas adjacent to the river channel. As a result of this project, sedimentation in the navigation channel adjacent to Charleston has increased from about 138,000 to 7,700,000 $m^3/yr$, solid and domestic wastes are trapped in the estuary, and the salinity regime has been drastically altered. A proposed U.S. Army Corps of Engineers project would redirect some of the water, thus altering the estuarine environment again.

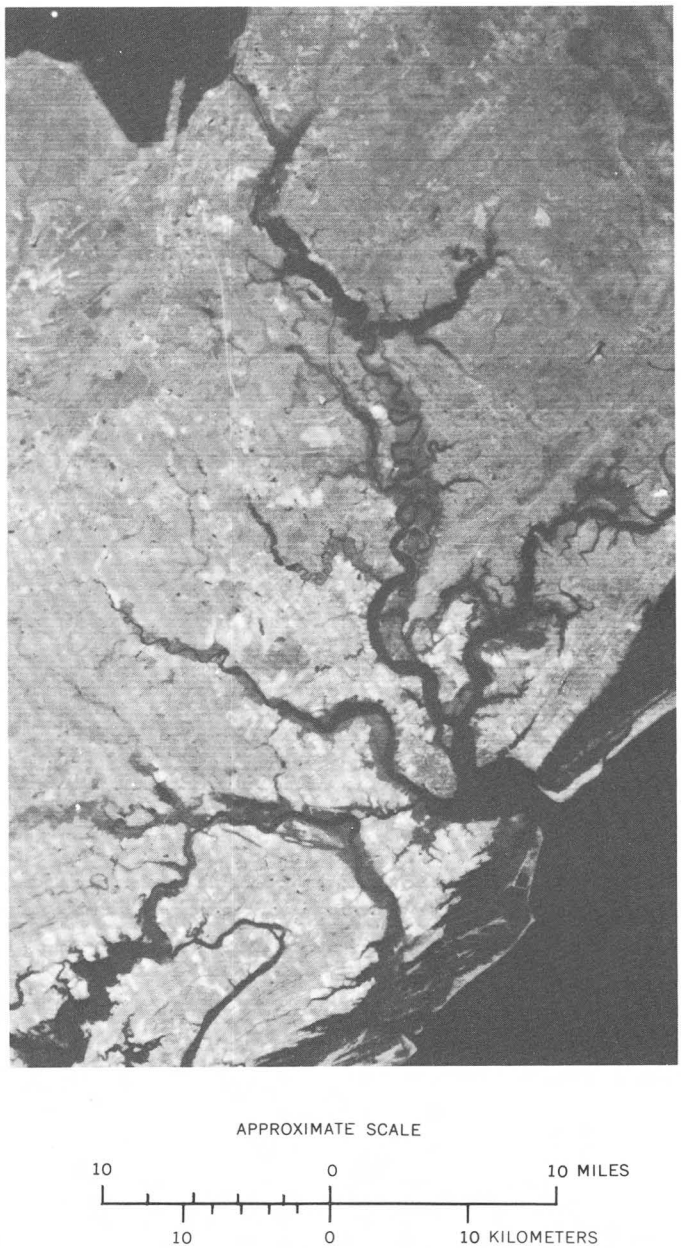


FIGURE 192.—Enlargement of part of ERTS–1 image 1081–15264, band 7, showing the Charleston area of South Carolina.

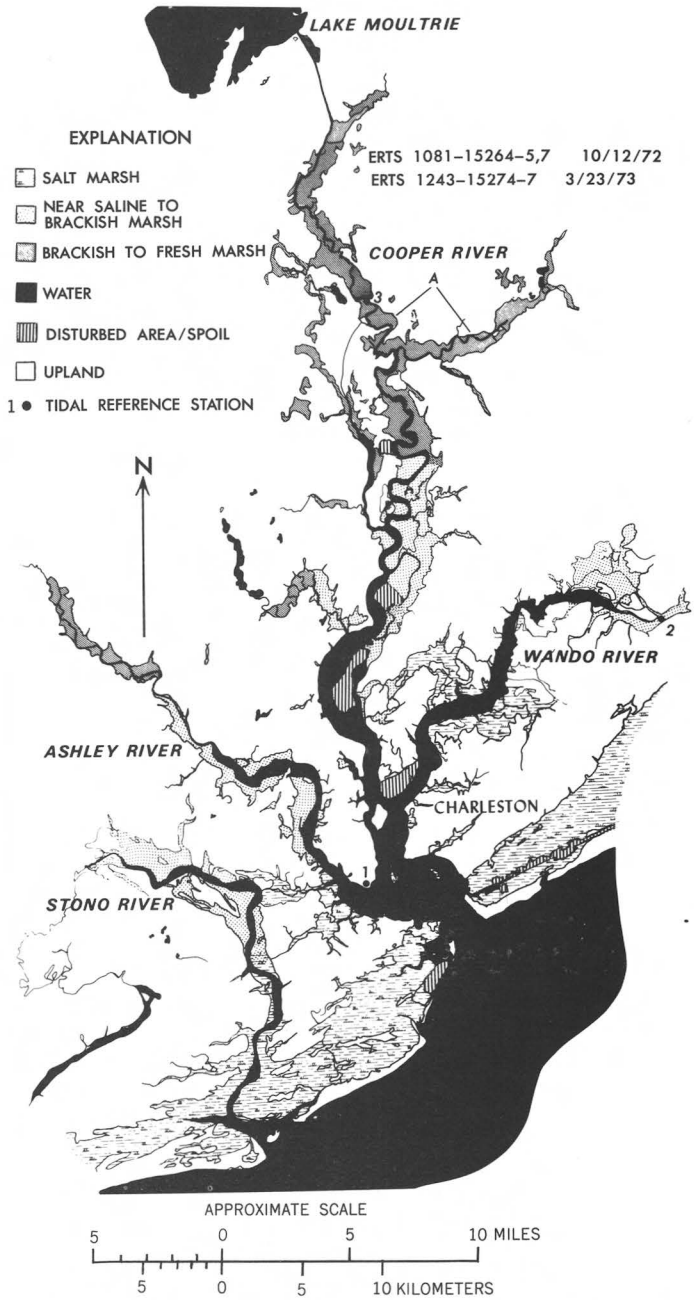


FIGURE 193.—Wetland map of the Charleston, Lake Moultrie, and Cooper River area of South Carolina.

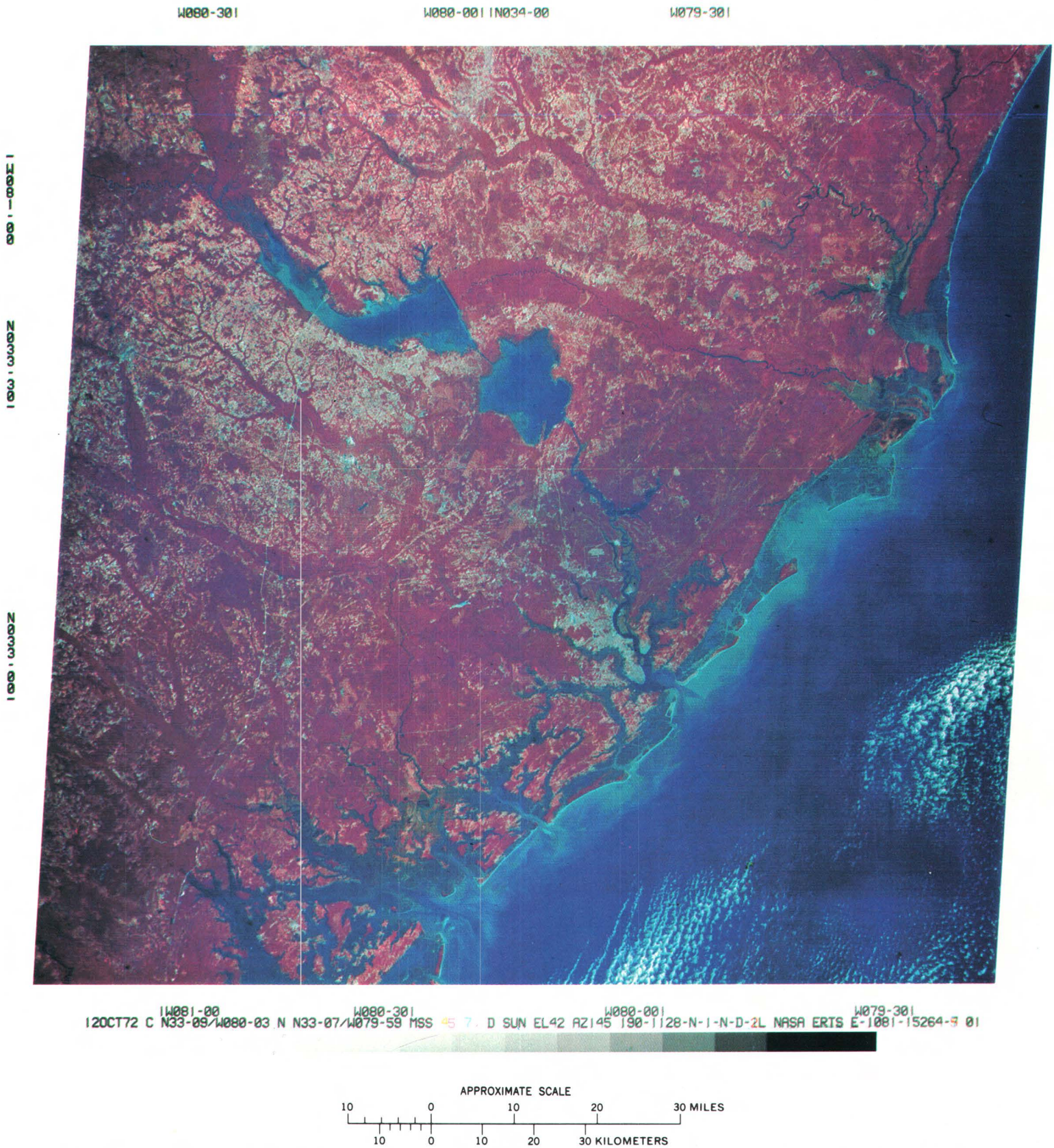


FIGURE 194.—ERTS–1 image of the Charleston area of South Carolina showing wetland vegetation on Oct. 12, 1972 (1081–15264).

FIGURE 195.—ERTS–1 image of the Charleston area of South Carolina showing wetland vegetation on Mar. 23, 1973 (1243–15274).

# COASTAL WETLAND MAPPING IN THE CENTRAL ATLANTIC REGION

By Virginia Carter, U.S. Geological Survey,
and Richard R. Anderson, The American University

Coastal wetlands are among the Nation's most valuable natural resources. The water storage and purification functions of wetlands, as well as the nutrient contribution to aquatic organisms, have been well documented. Wise management of coastal resources includes preservation and maintenance of these healthy wetland ecosystems. In turn, wetland-management decision-making is dependent upon timely and accurate information such as location, size, and value of major wetlands and identification of areas significantly affected by man's activities. ERTS data can supply a relatively low cost and moderately accurate method for mapping these areas. It can also supply repetitive information important for updating maps of coastal areas undergoing rapid change (Anderson and others, 1973).

ERTS imagery (fig. 196) can be used to map wetland plant species and boundaries at scales as large as 1:250,000. Figure 197 is an enlargement of the Oct. 10, 1972, ERTS image (fig. 196) of the Chincoteague salt-marsh complex at the mouth of Chincoteague Bay in the Virginia Eastern Shore. The species composition in these marshes is typical of the central Atlantic salt marshes. Figure 198 is a map of the same area showing five categories: (1) sand/dryland vegetation, (2) water, (3) *Spartina alterniflora* (saltmarsh cordgrass)/*Salicornia* sp. (glasswort) association, (4) *Spartina patens* (salt-meadow cordgrass)/*Distichlis spicata* (spike-grass)/*Iva frutescens* (marsh elder) association, and (5) spoil areas.

The upper wetland boundary is generally sharp except where broad transition zones exist. The marsh/water interface is sometimes difficult to determine in areas interlaced with numerous small tributaries or sparse patches of vegetation. Sand and marsh at the mouth of Chincoteague Bay (A, fig. 198) have accumulated since publication of the U.S. Geological Survey 1:250,000 map in 1946. A recent spoil fill at the tip of Chincoteague Island is designated C. Spoil areas can be easily separated from reflective vegetation by referring to bands 4 and 5 or by using a false-color composite picture, as they are highly reflective in all four bands. Areas labeled D are freshwater impoundments in the Chincoteague National Wildlife Refuge. The area B at the south end of the map is where old spoil banks are partially revegetated. It is quite distinctive in the band 7 image as a light area extending from Wallops Island to the mainland.

FIGURE 196.—Annotated color composite ERTS–1 image of the lower Chesapeake Bay (1079–15140).

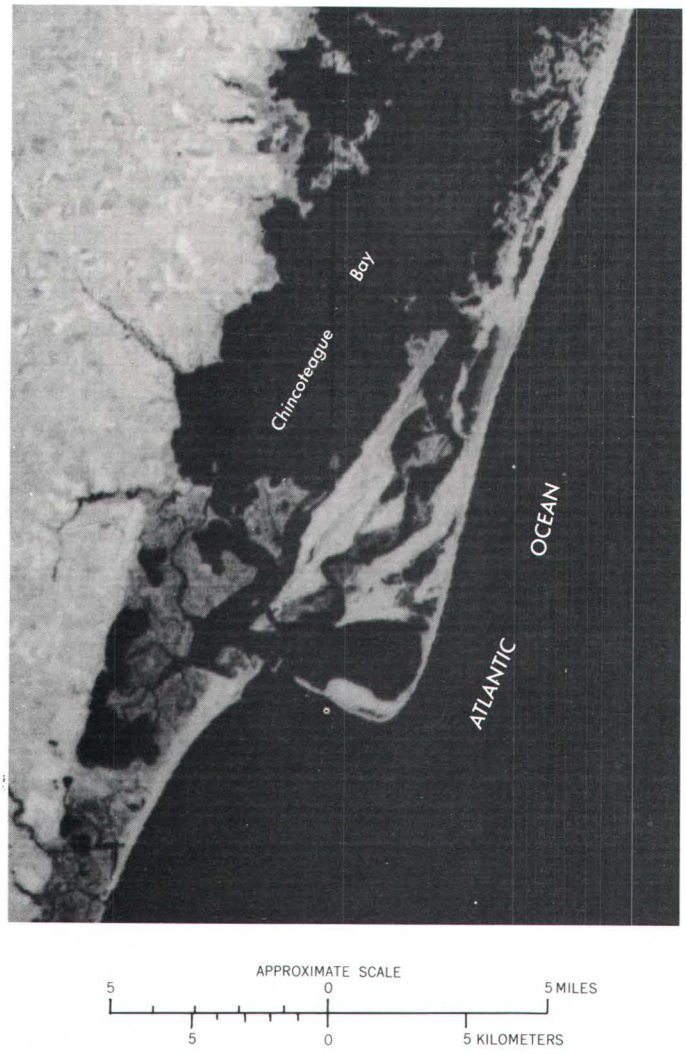


FIGURE 197.—Annotated enlargement of ERTS–1 image of the Chincoteague Bay salt-marsh complex in the Virginia Eastern Shore (part of 1079–15140, band 7).

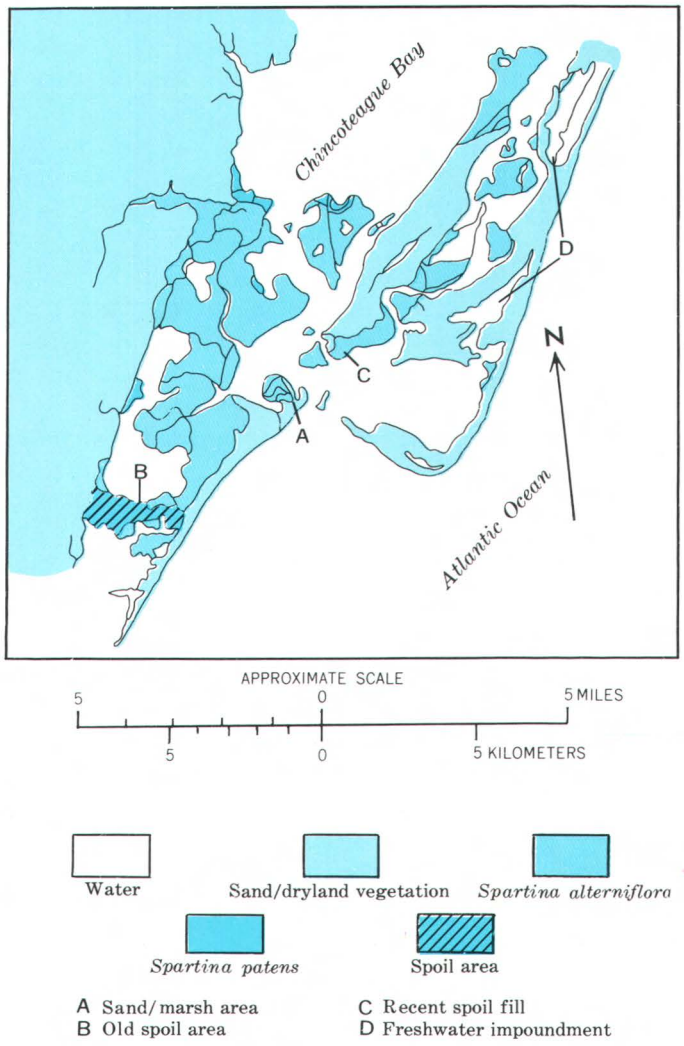


FIGURE 198.—Wetland map of the Chincoteague Bay salt-marsh complex in the Virginia Eastern Shore.

# COMPUTER MAPPING OF COASTAL WETLANDS

By Virginia Carter,
U.S. Geological Survey

ERTS digital data provide maximum spatial and radiometric-reflectance information for satellite mapping in the coastal zone (Carter and Schubert, 1974). Coastal wetlands, such as those located at the mouth of Chincoteague Bay in Virginia, can be mapped at a scale as large as 1:20,000 by computer. Area measurements for different wetland classes can be made by pixel count. Both the maps and the area measurements are of use to resource managers faced with inventory needs and construction-site decisions. Figure 199 is a standard ERTS MSS color composite of the Chincoteague Bay area of the Virginia Eastern Shore on Aug. 30, 1973.

The computer map of the Chincoteague salt-marsh complex (fig. 200) was produced from ERTS digital data from Aug. 30, 1973, using the ERTS ANALYSIS system at Goddard Space Flight Center. The basis for the system is an automatic classification algorithm for vegetation analysis based on the International Biological Programme classification system. A reference table of established coastal wetland classes was used to make the analysis. Six of these classes are identified on this map of the Chincoteague Marsh. These include (1) upland vegetation, (2) open water, (3) spoil, and three wetland vegetation associations—(4) *Spartina alterniflora*, (5) *Spartina patens*, and (6) organic mudflat (sparse vegetation). A fourth wetland association, *Iva frutescens*, could not be identified on the August image but was correctly identified on a similar map made with ERTS digital data from October.

The four major wetland vegetation associations or classes can be defined as follows:

1. *Spartina alterniflora* (saltmarsh cordgrass) association: Included in this category are mixtures of *S. alterniflora* and *Salicornia* spp. (glasswort) and some pure stands of *Salicornia* spp., which seldom exceed 5 $m^2$.
2. *Spartina patens* (salt-meadow cordgrass) association: Included with this species, which grows on slight altitudes in the marsh, is *Distichlis spicata* (spike-grass), which is only occasionally found in pure stands in this area.
3. *Iva frutescens* (marsh elder) association: This shrub grows in slight altitudes in association with *Spartina patens*.
4. Organic mudflat: These are usually covered with a low sparse growth of *Spartina alterniflora*, *Salicornia* spp., or detritus, and have occasional bare spots.

The Chincoteague marsh island, known locally as Wire Narrows Marsh and Black Narrows Marsh, lies 1.5 km west of the town of Chincoteague and is approximately 3 km east-west and 3.5 km north-south. The size of the marsh including interior water as measured from a U.S. Geological Survey 1:24,000 topographic map is 387 ha and as measured from the computer map by pixel count is 386 ha. The identification of wetland classes is extremely accurate in figure 200, except on adjacent Chincoteague Island where some deciduous trees and grasses are misidentified as *Spartina patens*.

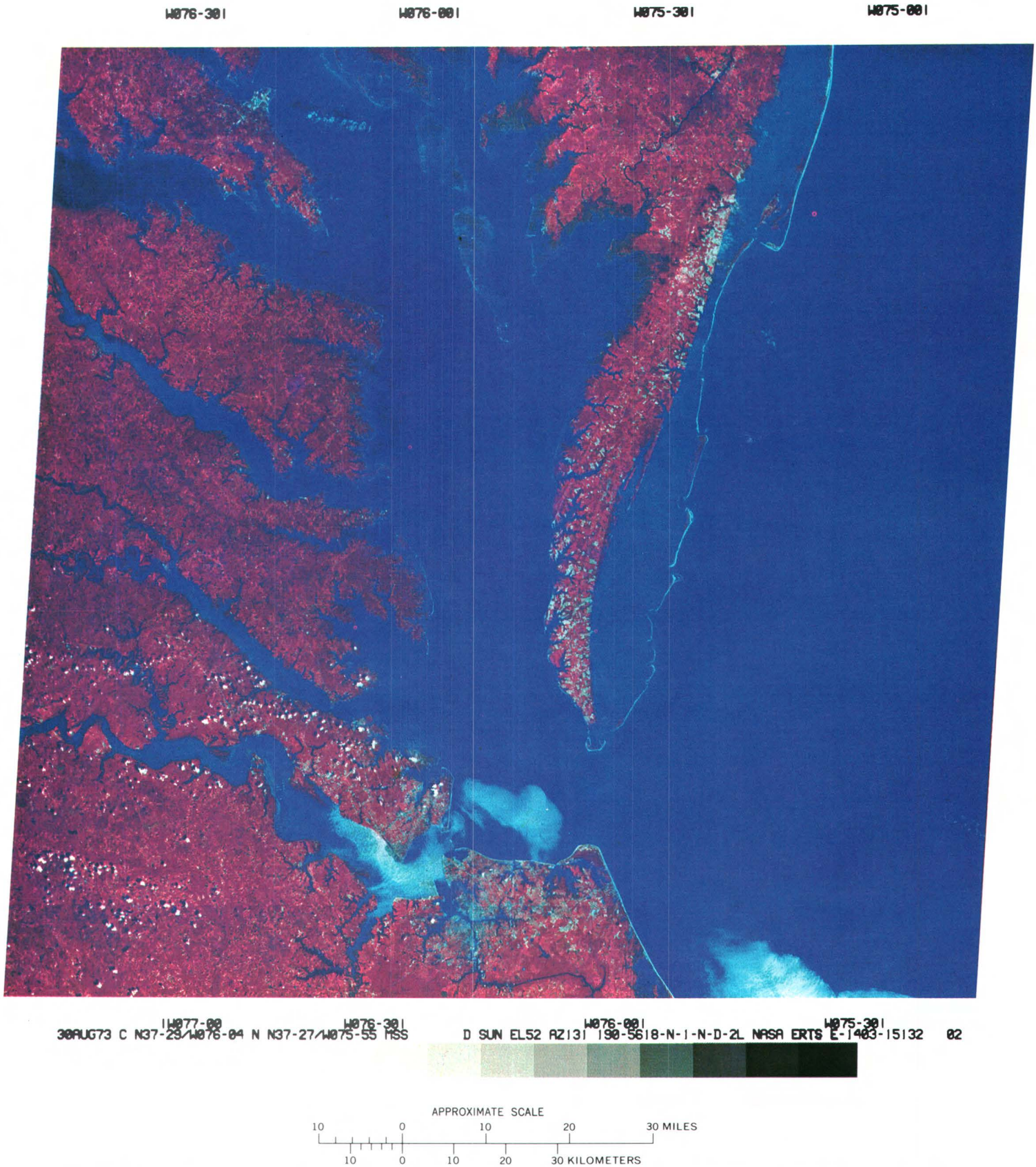


FIGURE 199.—Color composite ERTS–1 image of the Chincoteague Bay area of the Virginia Eastern Shore on Aug. 30, 1973 (1403–15132).

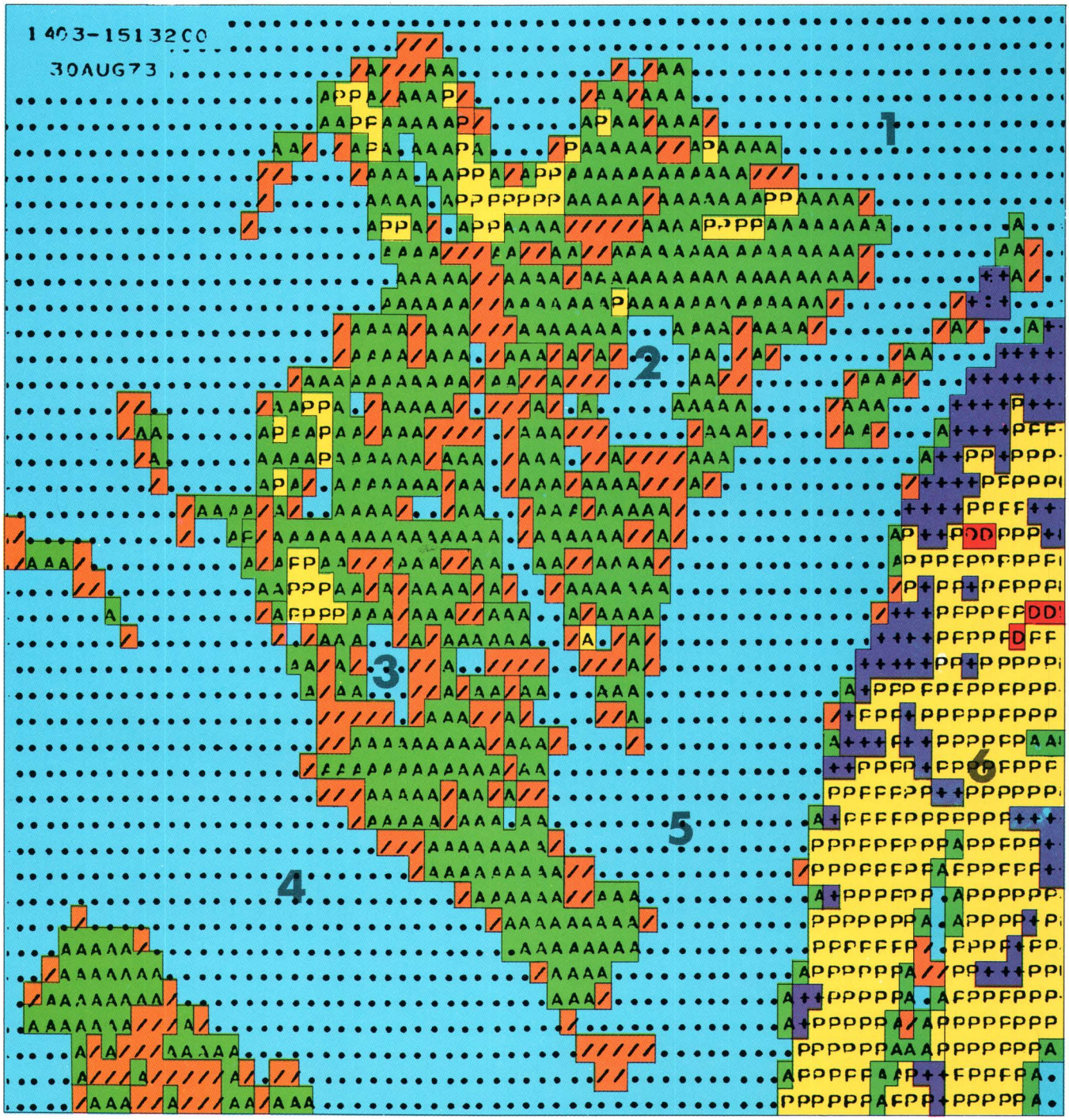


EXPLANATION

- Water
- Organic mud flat
- Spoil
- Spoil
- *Spartina alterniflora*
- *Spartina patens*
- Upland vegetation

APPROXIMATE SCALE

½ 0 ½ MILE

½ 0 ½ KILOMETER

1 *CHINCOTEAGUE BAY*
2 *BLACK NARROWS MARSH*
3 *WIRE NARROWS MARSH*
4 *QUEEN SOUND CHANNEL*
5 *CHINCOTEAGUE CHANNEL*
6 *CHINCOTEAGUE ISLAND*

FIGURE 200.—Computer-processed wetland map of the Chincoteague Bay salt-marsh complex in the Virginia Eastern Shore.

# TIDAL EFFECTS IN COASTAL WETLANDS

By Virginia Carter, U.S. Geological Survey,

and Richard R. Anderson, The American University

ERTS imagery provides a valuable tool for mapping coastal wetlands and interpreting nearshore features. Band 7 is the best single band for coastal wetland mapping; it defines the land-water interface in coastal waters with relatively high turbidity or sediment content more clearly than band 6. The effects of varying tidal stage must be considered in vegetation analysis and boundary determination. Figure 201*A* is the June 3, 1973, image of the Georgia-South Carolina coast. Figure 201*B* is an enlargement of Port Royal Sound, S.C. This image was made at high tide and should be compared with figure 202*A*, which includes an enlargement (fig. 202*B*) from the Apr. 28, 1973, image of Port Royal Sound taken at low tide. The average tidal range in this area is 2 m.

Wetland drainage patterns and mudflats show most clearly on ERTS imagery when the tide is low. Images taken at high tide show only the highest marsh elevations and the tree islands that are surrounded by water. Intermediate tidal stages are most useful for species discrimination because the characteristic density of each vegetation species or association exposes a differing amount of water background, thus creating a different signature. A stepwise analysis of flooding dynamics can be made with a series of ERTS images taken at different tidal stages.

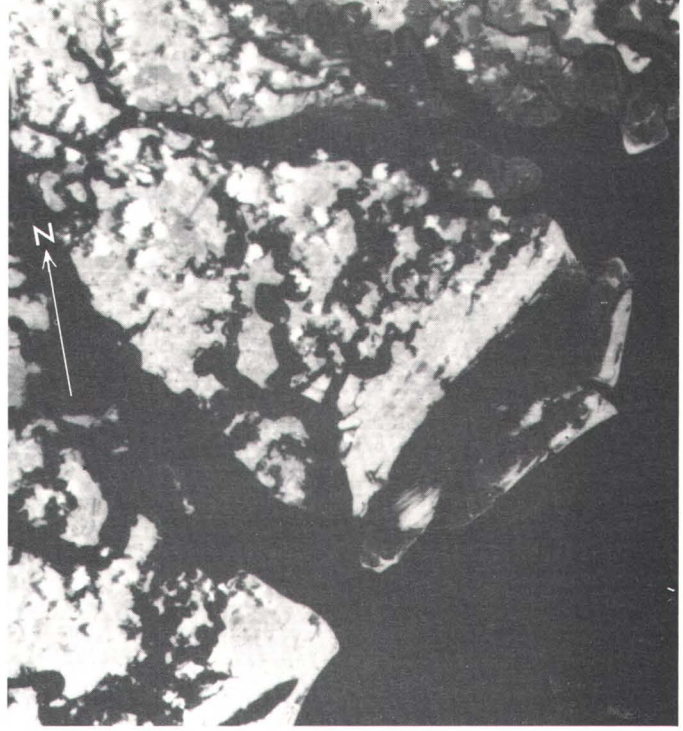


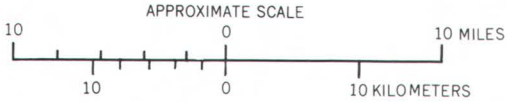


FIGURE 201*A* (below).—Color composite ERTS–1 image of the Georgia-South Carolina coast on June 3, 1973, at high tide (1315–15274).

FIGURE 201*B* (right).—Enlargement of part of ERTS–1 image 1315–15274, band 7, of Port Royal Sound, S.C., at high tide.

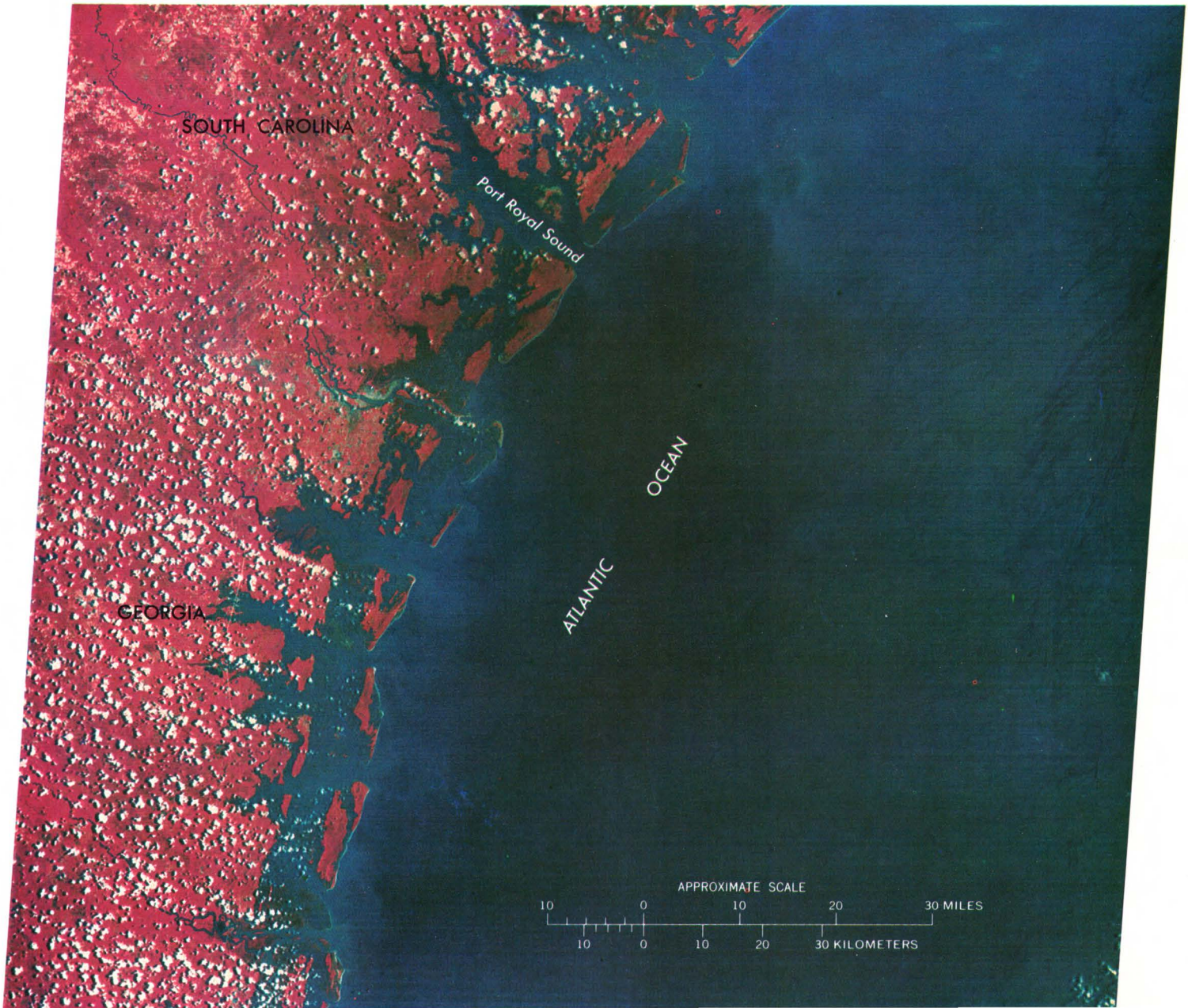

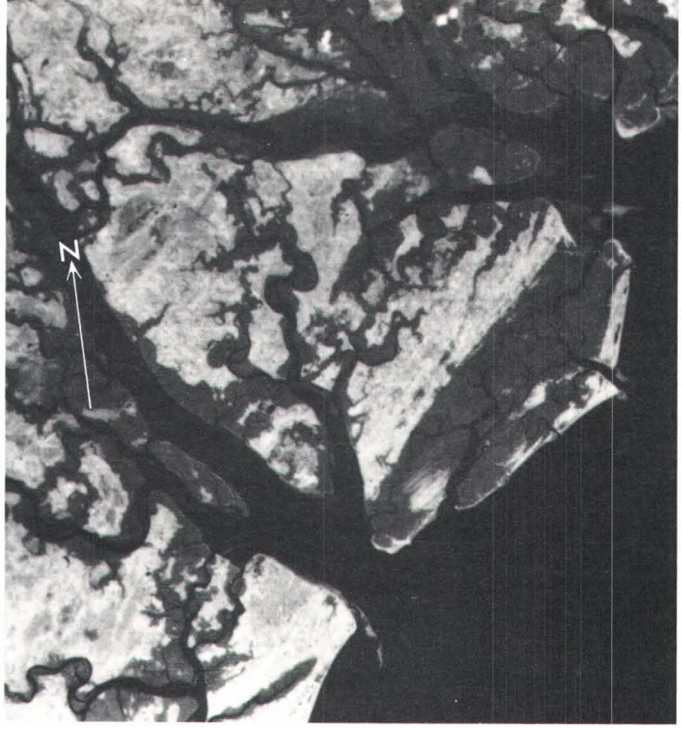


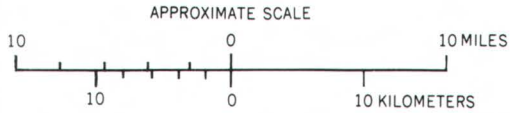


FIGURE 202*A* (below).—Annotated color composite ERTS–1 image of Georgia-South Carolina coast on Apr. 28, 1973, at low tide (1279–15280).

FIGURE 202*B* (left).—Enlargement of part of ERTS–1 image 1279–15280, band 7, of Port Royal Sound, S.C., at low tide.

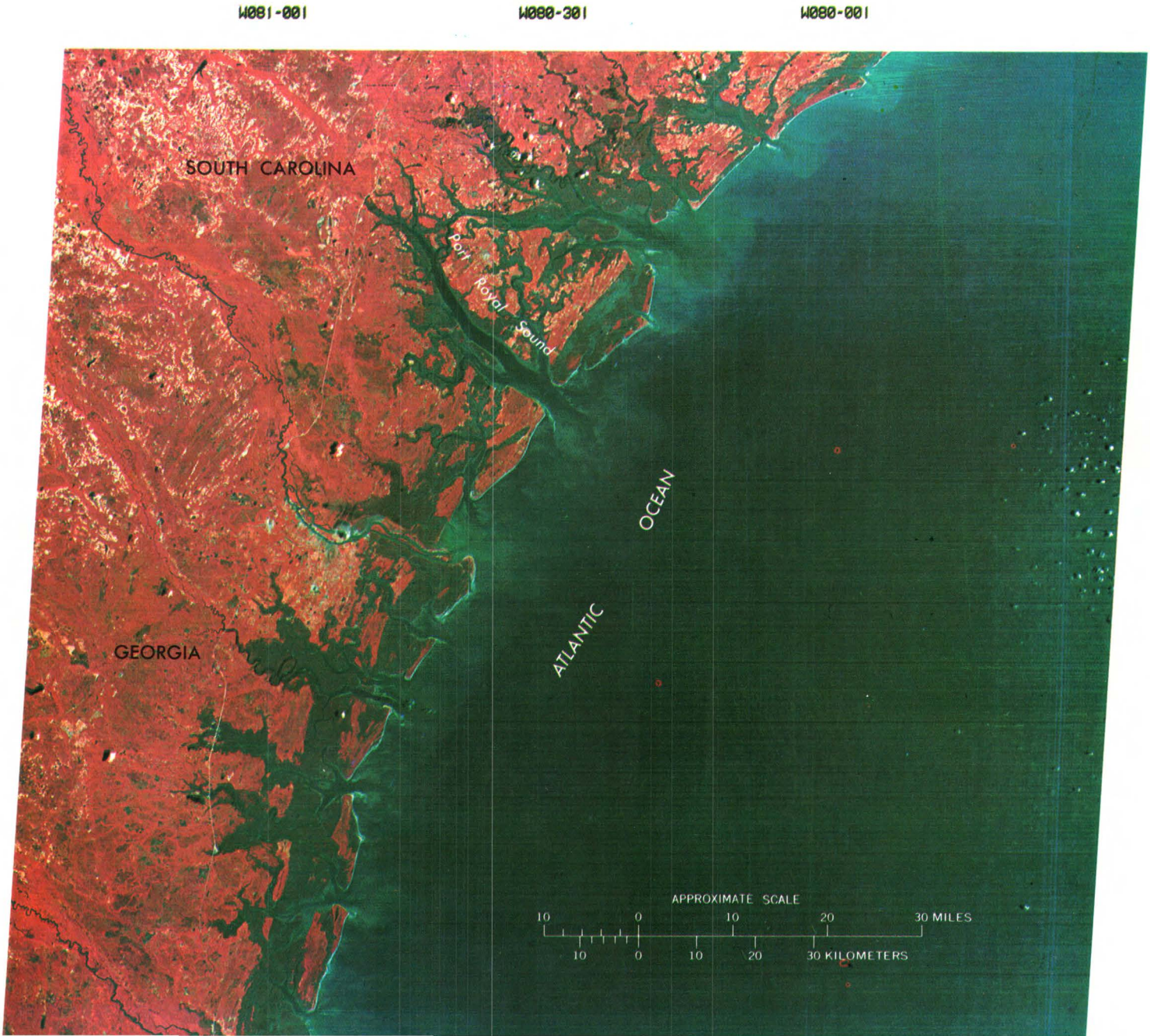

# WETLAND MAPPING IN A LARGE TIDAL BRACKISH-WATER MARSH IN CHESAPEAKE BAY

By Virginia Carter, U.S. Geological Survey,
and John W. McGinness, Jr., and Richard R. Anderson,
The American University

The Chesapeake Bay is one of the largest and most productive estuaries in the world. It is surrounded by tidal marshes, especially along its eastern shore, where human populations are relatively small. Reduction in the number of these wetlands or in wetland primary productivity could reduce the population of finfish, shellfish, and waterfowl in the adjacent bay and shallow ocean. Mapping and monitoring wetland areas of the bay is necessary if proper management and conservation of these valuable natural resources are to be realized.

The Nanticoke Marsh is located at the Nanticoke River entrance to the Chesapeake Bay in Maryland. Figures 203 and 204 include enlargements of band 7 images of the area (figs. 203*B*, 204*B*) acquired on Oct. 10, 1972, and July 7, 1973. The October image shows the marsh at low tide (approximately 6.0 cm above mean low water) near the end of the growing season, when the vegetation has begun to decline. The interior low marsh areas and drainage pattern can be seen clearly because very little water is present. Vegetation patterns are not as distinct because reflectance from vegetation is not optimum at this time of the year. The upper wetland boundary is clearly visible, especially in the northern part of the marsh.

Figure 204*A* was taken at a tidal stage approximately 42.0 cm above mean low water, much higher than that shown in the October image. Interior low marsh areas show little detail and appear as broad dark areas on the band 7 image. Vegetation detail in the higher parts of the marsh is very good; highly reflective marsh vegetation borders creeks and streams and appears as lighter patterns. Vegetation detail in the lower parts of the marsh is obscured because of the increased water background. The upper wetland boundary is not distinct because vegetation in the northern part of the marsh is highly reflective, as is the upland vegetation.

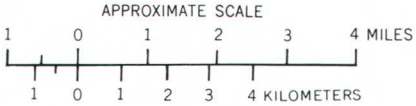


FIGURE 203A (below).—Annotated color composite ERTS–1 image of the Delmarva Peninsula on Oct. 10, 1972 (1079–15133).

FIGURE 203*B* (left).—Part of ERTS image 1079–15133, band 7, showing Nanticoke Marsh on Oct. 10, 1972, at low tide.

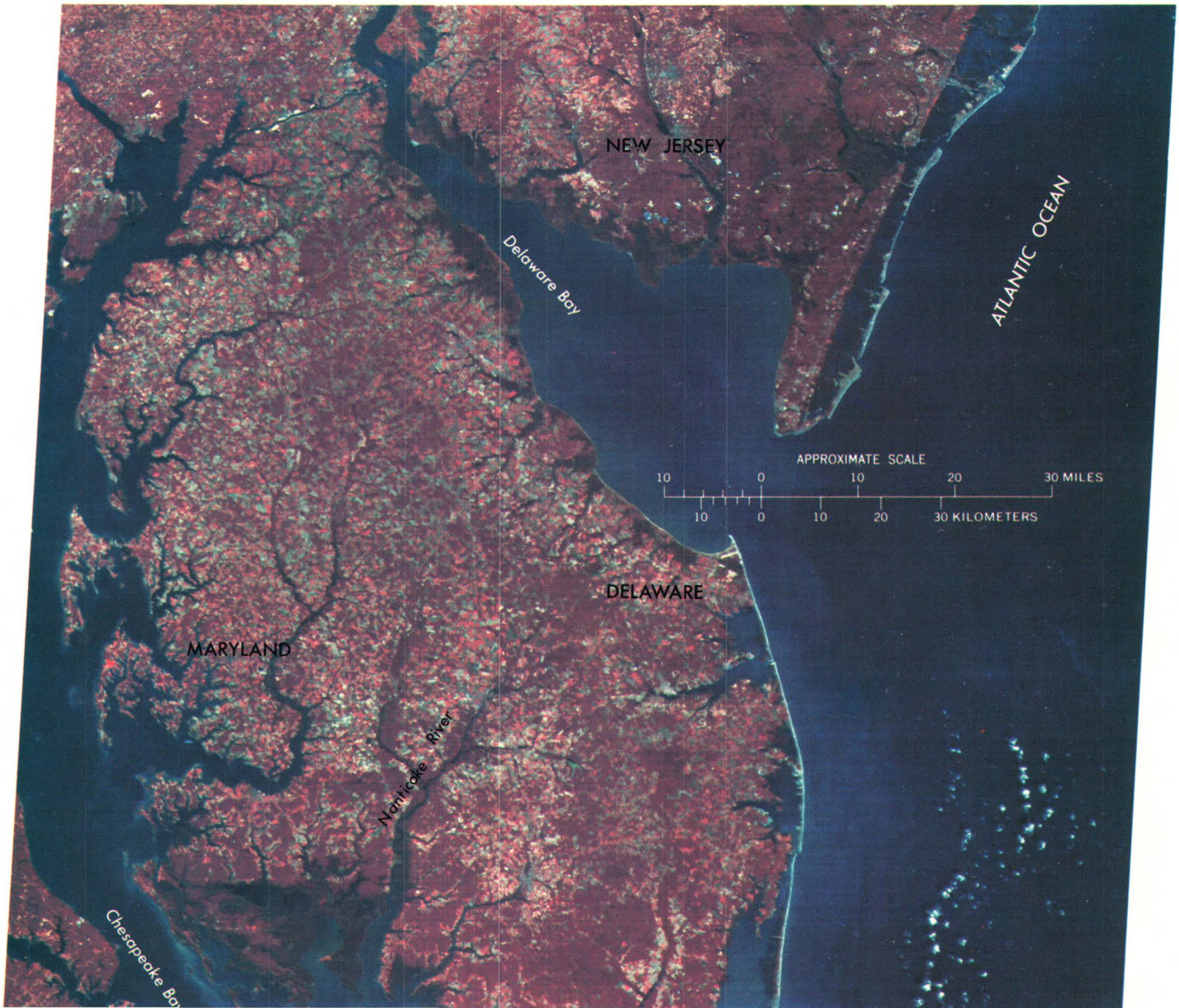

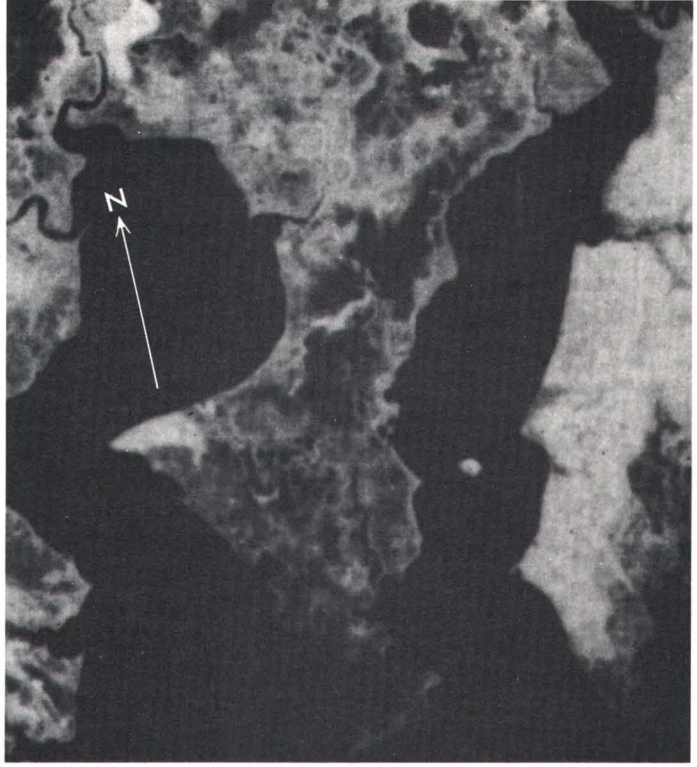


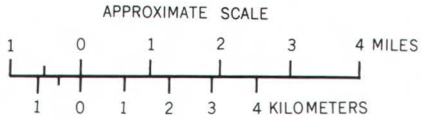


FIGURE 204*A* (below).—Annotated color composite ERTS–1 image of the Delmarva Peninsula on July 7, 1973 (1349–15134).

FIGURE 204*B* (right).—Parts of ERTS image 1349–15134, band 7, showing Nanticoke Marsh on July 7, 1973, when the tide was 42.0 cm above mean low water.

W076-001 W075-301 W075-001

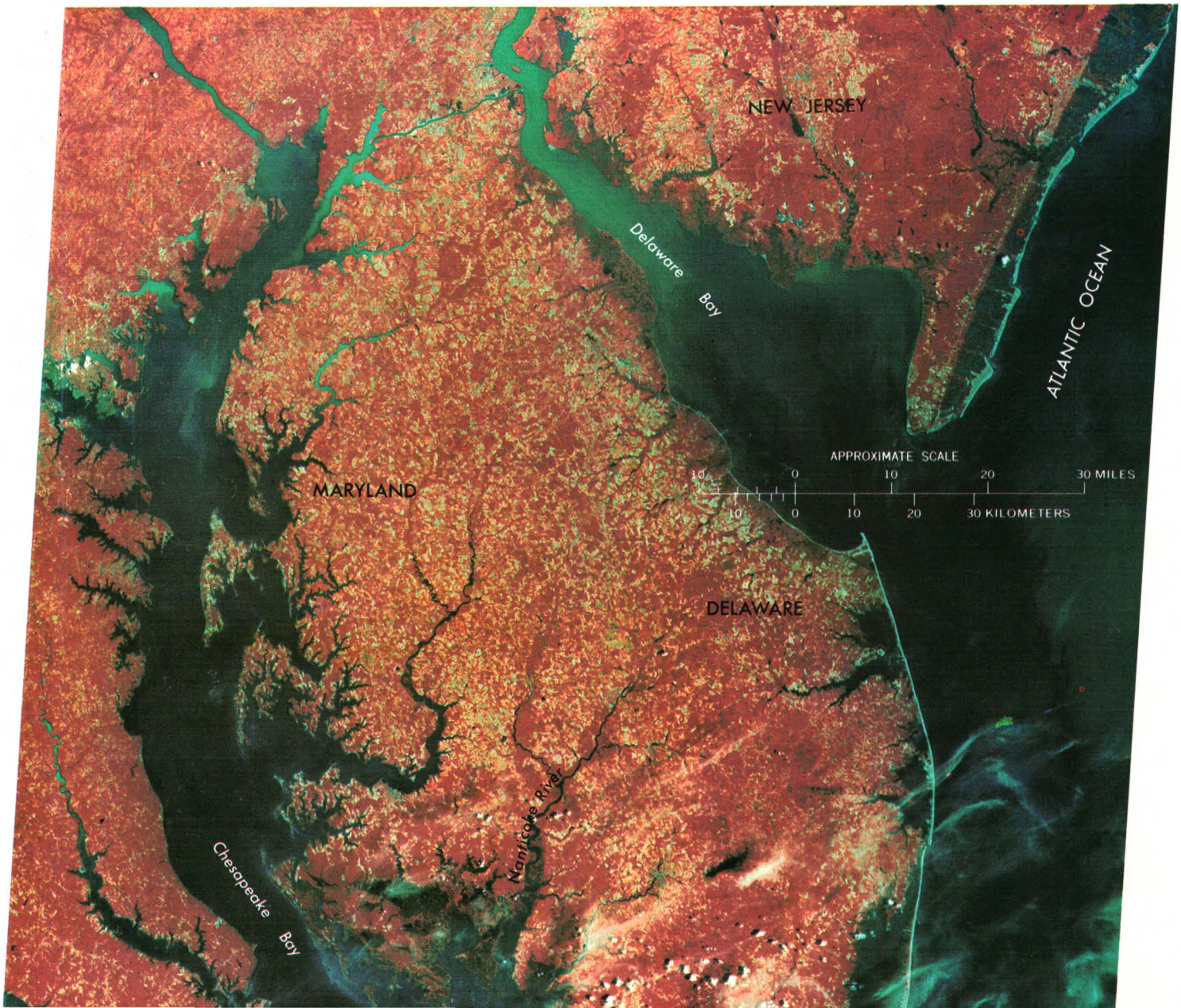

Figure 205 is a wetland map produced from the July 7, 1973, and Aug. 30, 1973, band 7 images. The following general categories can be distinguished: (1) tree island, (2) high marsh, (3) low marsh, (4) low marsh/water, and (5) water. These categories are listed in order of decreasing reflectivity.

Tree islands are upland areas that are the brightest imaging features within the marsh on band 7. The high marsh includes plant species and communities generally found above mean high water and inundated only at flood tides. The vegetation, usually dense and having little background reflectance, is more reflective than other marsh categories. High marsh is made up of varying amounts of *Spartina cynosuroides*, *Spartina patens/Distichlis spicata* association, *Phragmites communis*, *Iva frutescens*, and *Baccharis halimifolia*.

The low marsh covers the greatest area and is composed mostly of large stands of *Juncus roemarianus*. Other species of the low marsh category, *Spartina alterniflora*, *Scirpus* spp., *Distichlis spicata*, and *Salicornia* spp., may be found in homogeneous stands but are predominantly in large mixed plant communities.

The low marsh/water category contains shorter *Juncus* and *Scirpus* stands or areas with sparse plant cover, such as mudflats, which exhibit a very low reflectance because of the water background (Anderson and others, 1973, 1974).

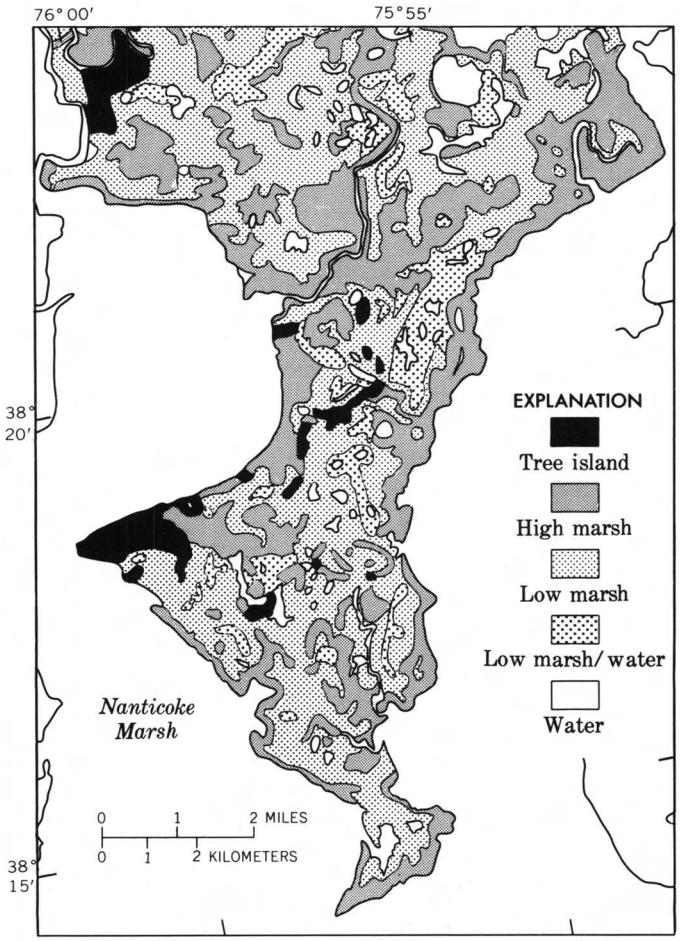


Courtesy of American University

FIGURE 205.—Wetland map of Nanticoke Marsh compiled from ERTS images.

# ENVIRONMENTAL ASSESSMENT OF REMOTE AREAS OF COLOMBIA, SOUTH AMERICA

By William D. Carter,
U.S. Geological Survey

Figure 206 is an ERTS–1 image that shows 34,225 km² of southeastern Colombia, South America. The prominent meandering stream crossing the image from lower left to middle right is the Guaviare River, a major tributary in the southwestern part of the Orinoco River basin. It and the Orinoco flow northeastward; the Orinoco flows into the Atlantic Ocean at Boca Grande, Venezuela. South of this area, rivers flow southeastward into the Negro River and the Amazon River basin. The Eastern Cordillera of the Andes lies west of the area, and Bogotá, Colombia's capital city, is about 290 km to the northwest.

This unusual image dramatically shows man's efforts to conquer, tame, and develop the resources of tropical savanna regions. The red part of the image shows the distribution of natural tropical vegetation. The dark bluish-gray areas are recent manmade burns of savanna grasslands; the brownish-gray areas appear to be older burns that are gradually returning to grasslands for livestock grazing. The blackest patches may be either very recent burns, or possibly wetlands, lakes, or ponds; repetitive views through the year will enable a more accurate identification. The eastern margin of the cleared areas indicates that burning clears the higher ground but leaves the lower parts of the valleys in vegetation (red) and thereby enhances the dendritic stream pattern.

The only major habitation in the scene is San José del Guaviare, shown southeast of the confluence of the Ariari River with the Guaviare River. Note that the Guaviare waters are dark (clear) west of the junction, whereas the Ariari is light blue, indicating shallow, relatively silt-laden water. Part of the Inírida River is seen at the lower right; it also flows eastward and joins the Guaviare a few kilometers west of its junction with the Orinoco on the Venezuela-Colombia border.

The topography of the region is gentle, ranging from nearly flat near the meandering rivers to gently rolling between the rivers.

A part of the U.S. Air Force Operational Navigation Chart L–26 (fig. 207) shows how little was previously known about the region.

This ERTS–1 image has been sent to Colombia for a comprehensive analysis. The area is of interest to the Colombian Government, whose Department of Agriculture has a program to assist ranchers in the savanna region. Perhaps this image will serve as a basis for orderly planning of resource development and preservation of the environment before burning has gone too far.

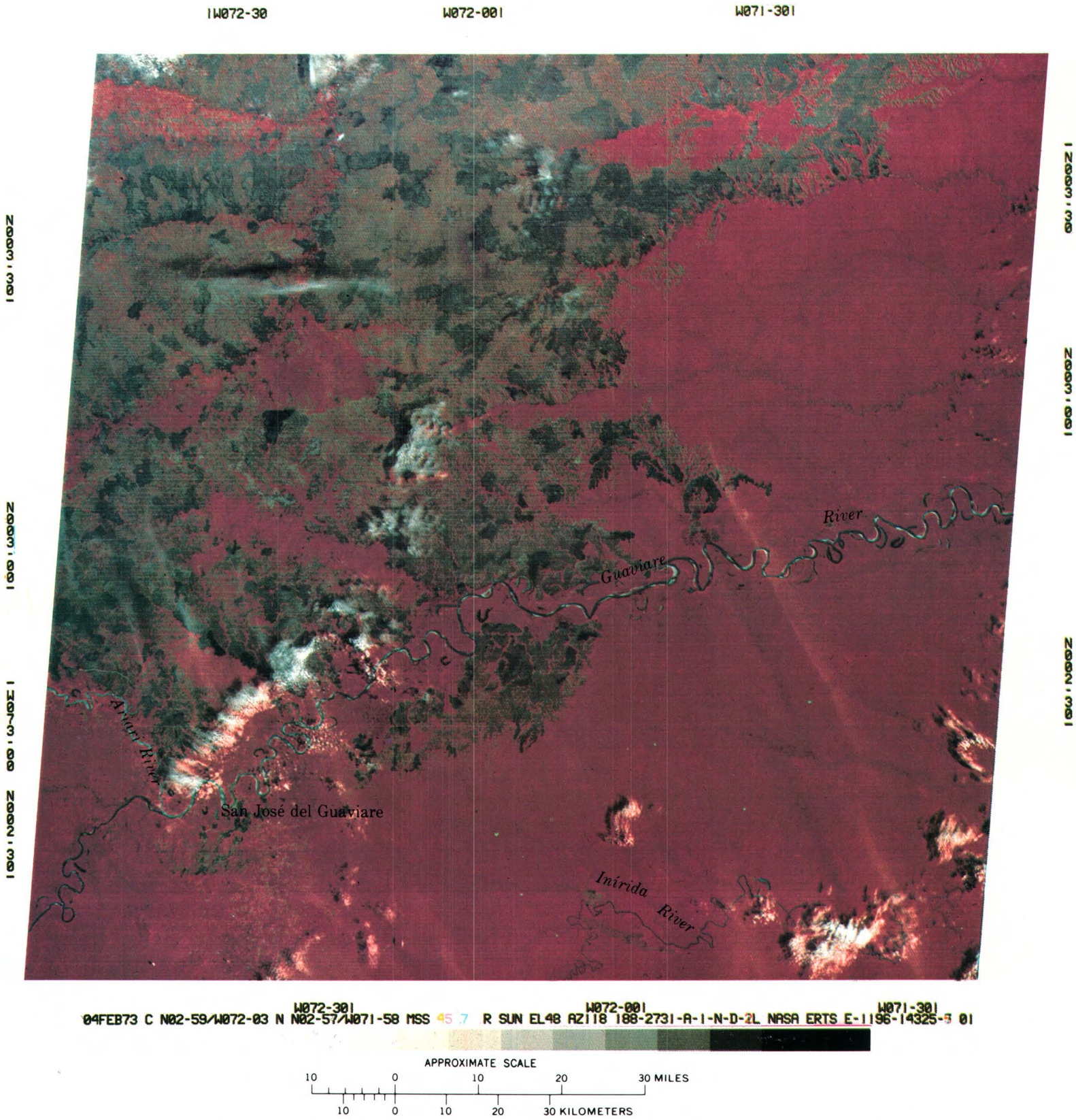


FIGURE 206.—Annotated color composite ERTS–1 image of southeastern Colombia, South America (1196–14325).

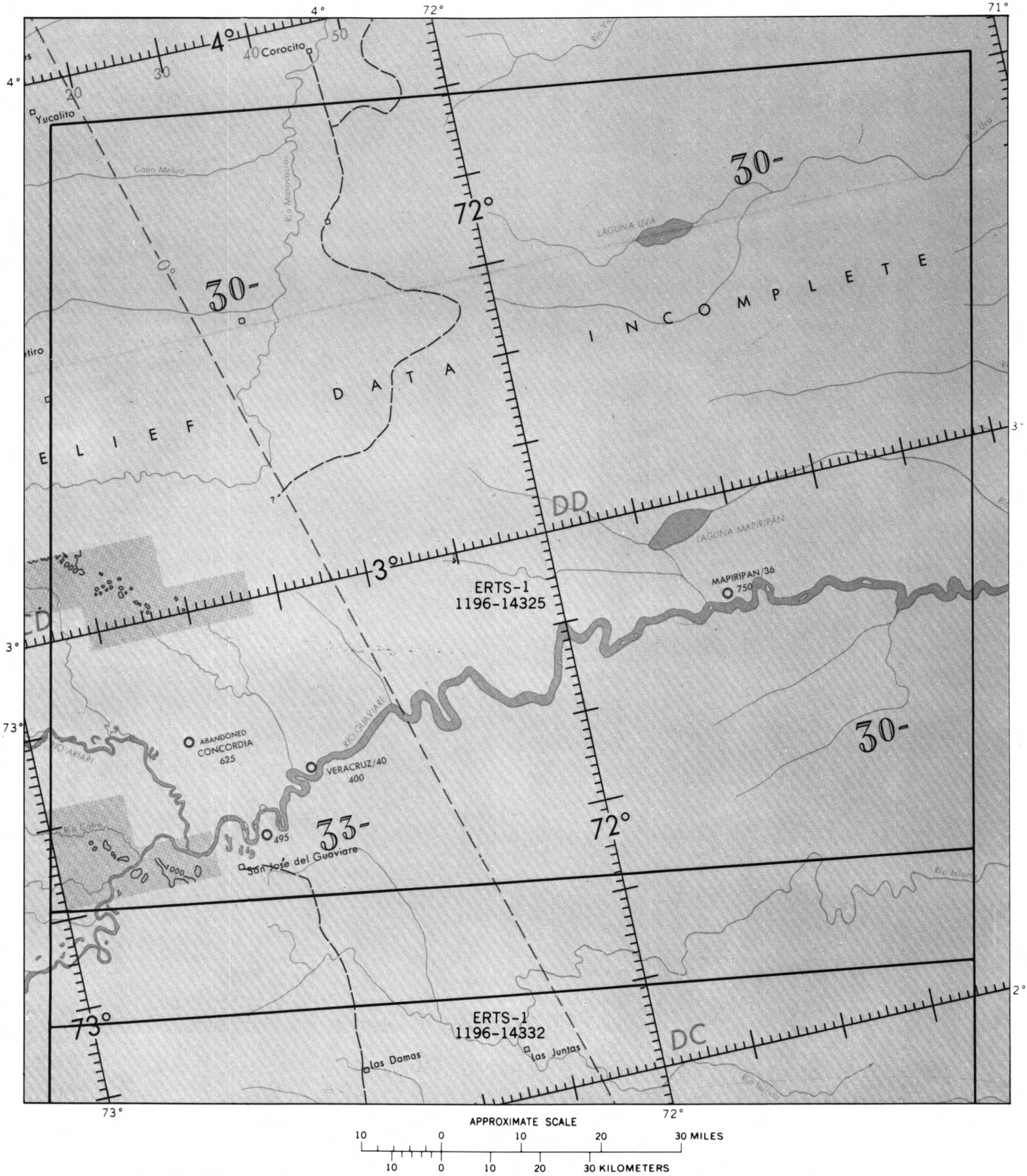


FIGURE 207.—A portion of U.S. Air Force Operational Navigation Chart (ONC L 26) of southeastern Colombia.

# MAN'S IMPACT UPON WETLANDS

By Virginia Carter, U.S. Geological Survey,
and Linda Alsid and Richard R. Anderson,
The American University

To gain ready access to the sea, man historically has centered most of his commerce, industry, and culture along or near coasts and rivers. Eight of our Nation's most populous metropolitan regions are in the coastal zone. This high concentration of population has produced serious impact upon our coastal wetlands; the wetland areas have been consistently developed to maximize their commercial, industrial, and economic values and to reap the tourist dollar.

Man's activities having a direct impact on and resulting in a loss of acreage and viability in coastal wetlands are dredge-and-fill activities for navigation purposes, reclamation for agricultural, residential, and industrial sites, ditching for mosquito control, and indiscriminate dumping of spoil and urban wastes (Anderson and others, 1974). Impoundment and water-level manipulation for wildlife management also has an environmental impact. Figure 208 shows man's influence on the New Jersey coastal wetlands, a result of dredging lagoons and filling for nearshore homesite development (A). The loss of wetlands acreage because of highway construction is evident along the Georgia coast (fig. 209, B). Also depicted in the scene is the Savannah Wildlife Refuge (C) and a large area of spoil deposition adjacent to the Savannah River (D).

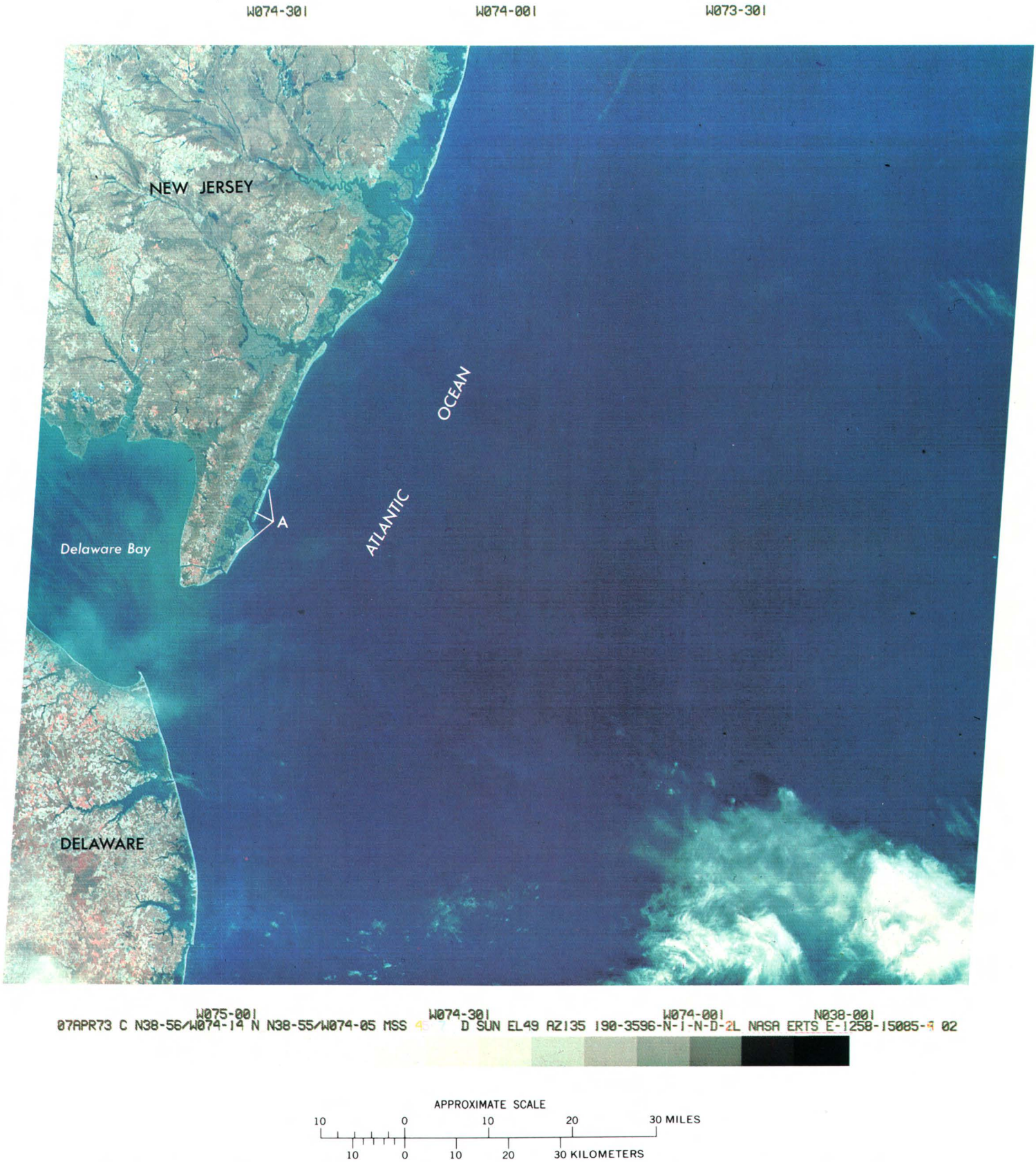


FIGURE 208.—Annotated color composite ERTS–1 image of the New Jersey-Delaware coastal wetlands (1258–15085).

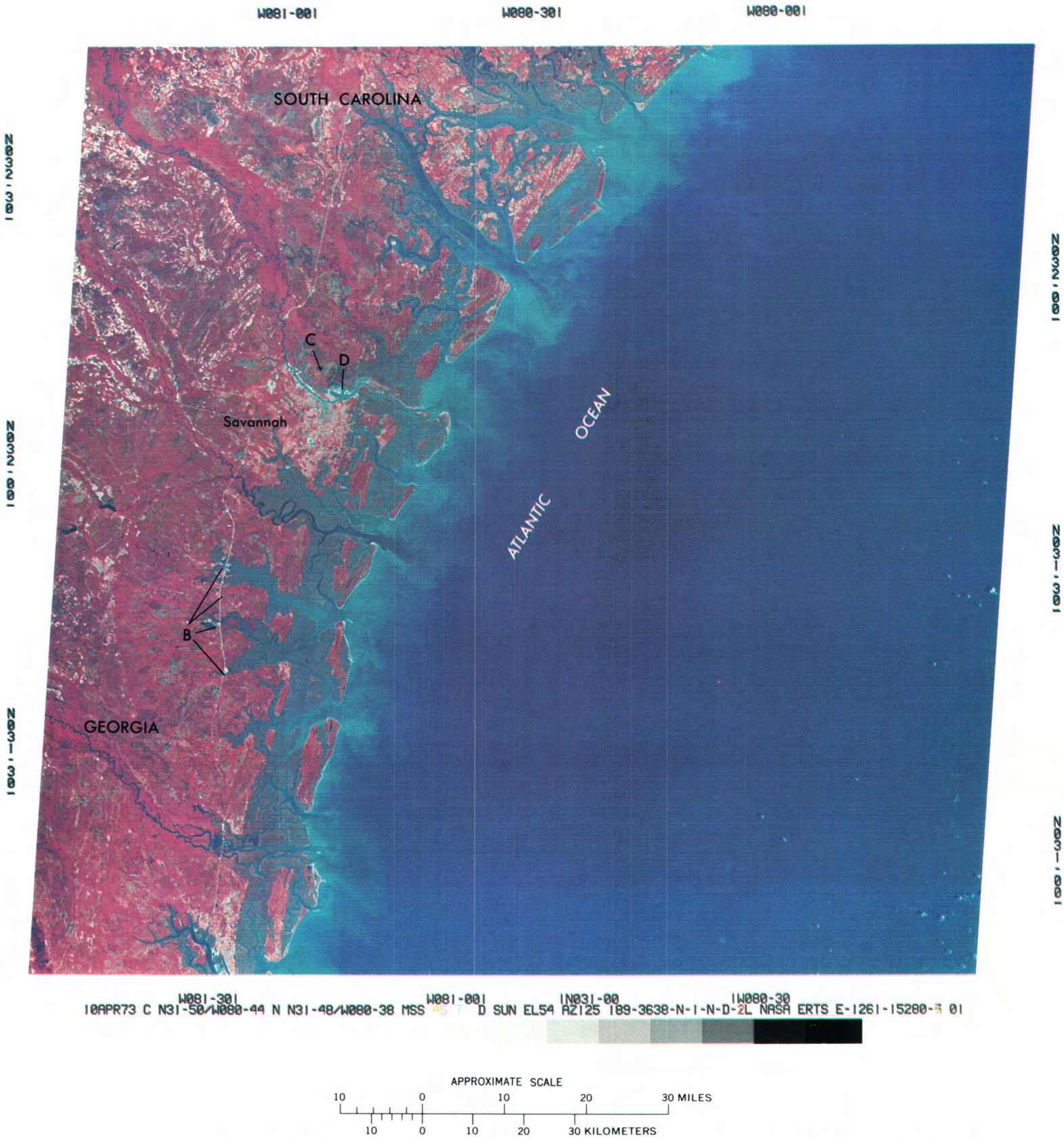


FIGURE 209.—Annotated color composite ERTS–1 image of the Georgia coastal wetlands near Savannah (1261–15280).

# SELECTION OF A ROAD ALINEMENT THROUGH THE GREAT KAVIR IN IRAN

By Daniel B. Krinsley,
U.S. Geological Survey

The Great Kavir in north-central Iran (fig. 210) is a vast desert with extensive salt crusts and swamps underlain by Miocene siltstones and evaporites (Krinsley, 1970, 1972). Access to this difficult terrain is impeded by peripheral mountains and streams that have been incised by recent uplift. The Great Kavir is a serious obstacle to transportation across Iran, and almost all materials produced in northern and central Iran are exchanged by means of trucks moving along the east-west and northwest-southeast road that passes through Teherān. Goods from the north destined for the region immediately south of the Great Kavir must travel more than 900 km around the desert rather than the 200 km that would be required if an all-weather road existed across the desert. Less dramatic but nevertheless significant savings in time and in transportation costs could be achieved with such a road terminating at Nain farther to the southeast (fig. 210). Trucks traveling from Dāmghān to Nain via Teherān cover the 750 km in 9 h; the route across the Great Kavir would be 450 km and require 6 h.

The area of the Great Kavir most suitable for the construction of an all-weather road is shown entirely within one ERTS–1 image. Six false-color composites were prepared from positives of ERTS–1 MSS images taken of this area of the Great Kavir from Sept. 2, 1972, to May 12, 1973. The driest and wettest periods are illustrated in figures 211 and 212, respectively. The route of the existing dry-season road was overlain on each composite, and the seasonal hydrologic conditions along four critical segments were inferred from the ERTS–1 images. Analysis of the ERTS imagery was based on the author's fieldwork east of and along the dry-season road in October 1965 and September 1966, respectively.

The four critical road segments represent areas that are subject to soil saturation or local flooding and thus require special engineering considerations. The road segment from km 25 to 50 is generally trafficable. It is always moist along a narrow drainageway at km 40 (fig. 211) during the dry season, but this area becomes wet by mid-December. Dissolution of the local salt crust parallel to the drainageway suggests saturation of surficial materials. By March, the surface in a slight depression is also wet at km 32. The road from km 25 to 50 can be alined inexpensively to the west, on good natural subgrade, to avoid the two wet areas (fig. 212); culverts will be required along drainageways.

FIGURE 210.—Index map of Iran showing location of the Great Kavir.

The segment from km 60 to 63 is always moist at km 62 during the dry season. This segment is wet by mid-May, and a bridge or raised roadbed would be required at km 62 (fig. 212).

The segment from km 90 to 100 lies in an area principally of salt crusts that have low bearing strengths when dry during September but become untrafficable when moist by mid-December; some dissolution may take place during this period. By early February, both soil and salt crusts are wet, and dissolution of the salt continues. Standing water is present by March 1, and its areal extent has increased by mid-May. This segment is the most difficult and would require both a raised roadbed and a bridge. Although an alinement to the east would avoid the wettest areas, the costs of engineering for the poor subgrade over the increased length of the road (up to 30 km) would be prohibitive (fig. 212).

The segment from km 110 to 116 is always moist at km 113 during the dry season and becomes more moist by mid-December. By March 1, the surface is wet at km 113, and this condition continues into May. This area can be avoided by a short diversion to the west (fig. 212).

The use of ERTS–1 images provides a method for examining areas that are seasonally inaccessible in order to determine hydrologic changes that affect soil conditions and thus their engineering properties. To interpret ERTS–1 images correctly requires some beforehand knowledge of the actual ground conditions, and the eventual determination of the location of any engineering project, such as a road alinement, should be based on extensive records of observation and on-site investigations (Krinsley, 1973).

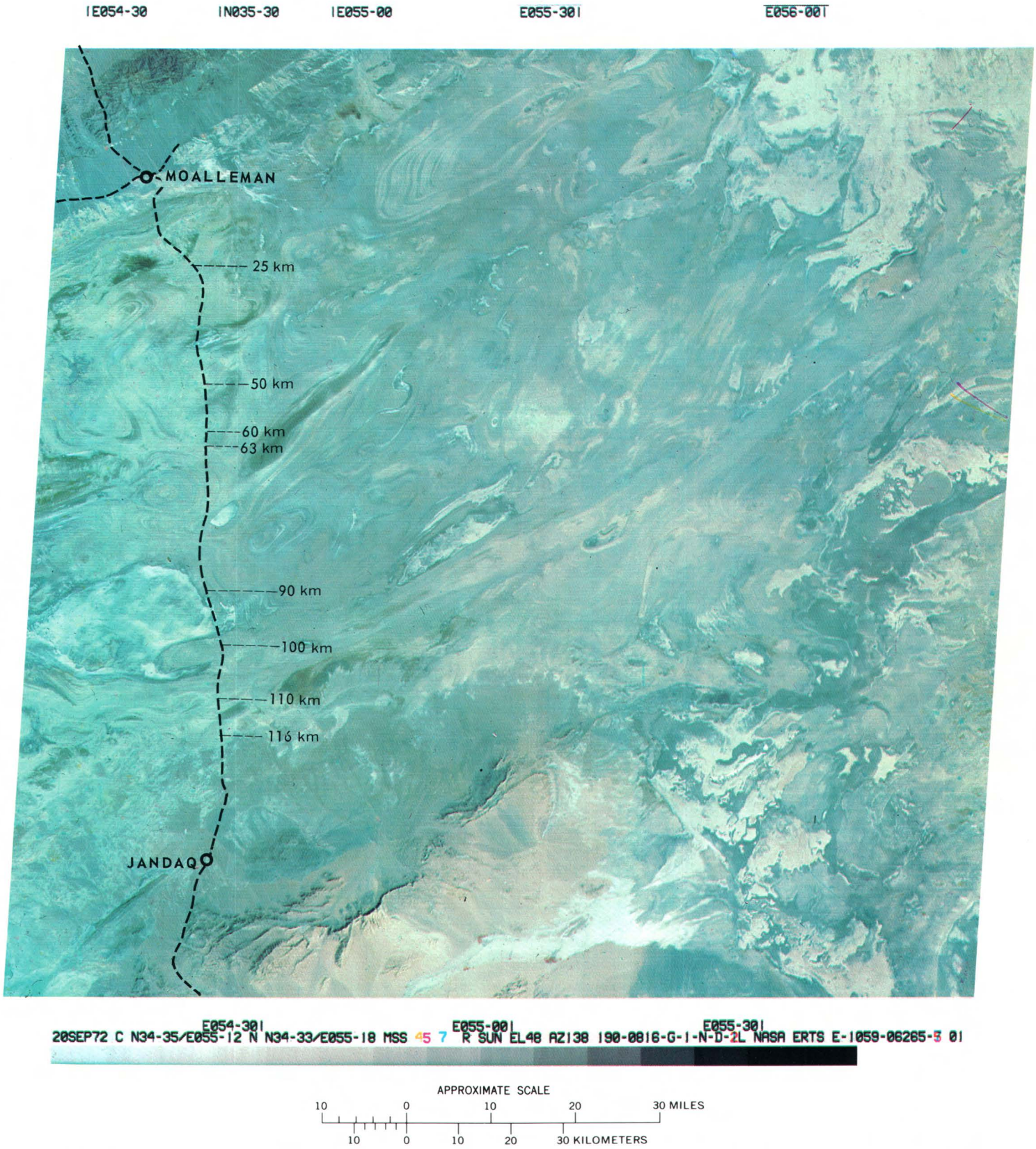


FIGURE 211.—Annotated color composite ERTS–1 image of the Great Kavir in its driest period on Sept. 20, 1972 (1059–06265).

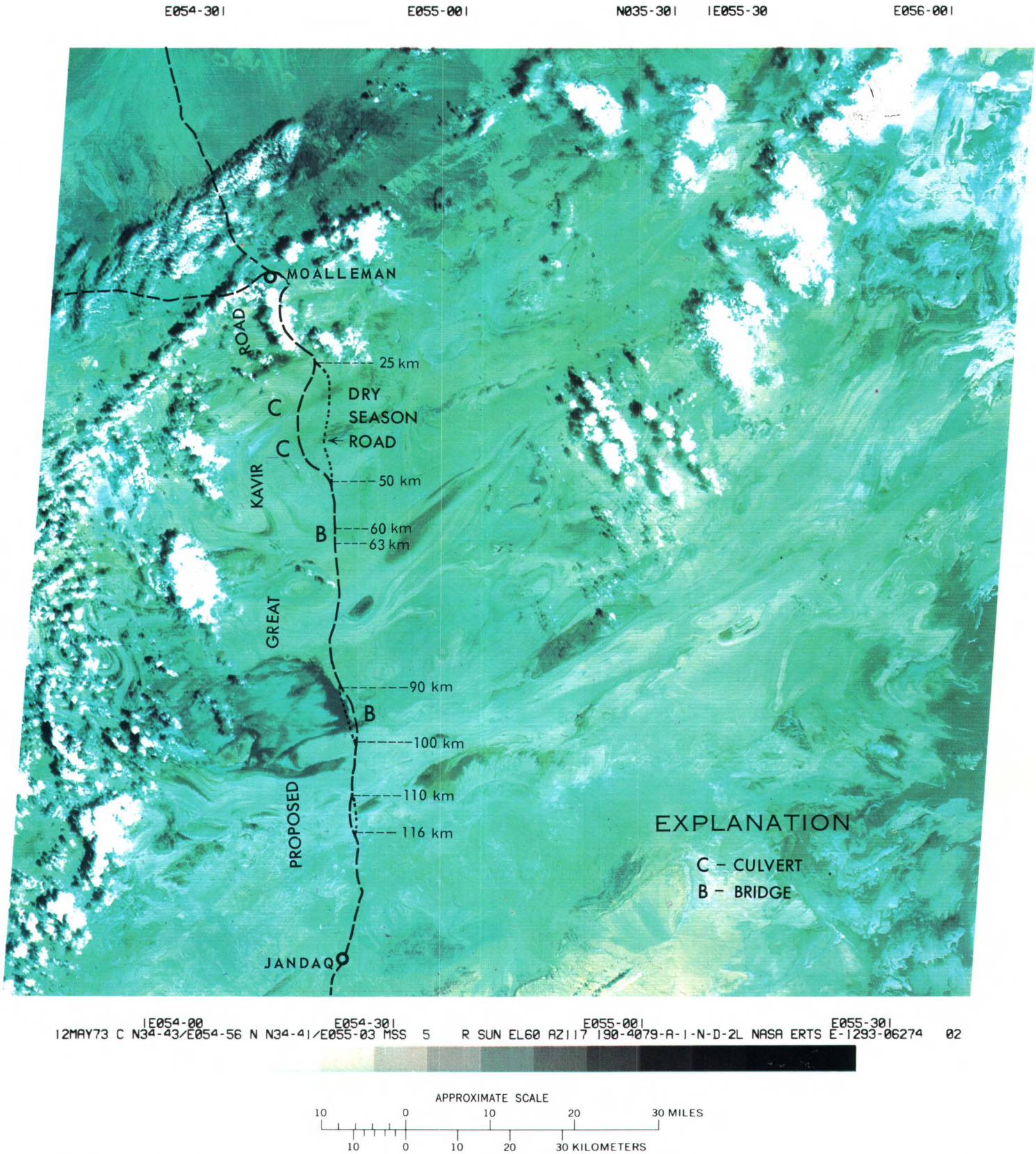


FIGURE 212.—Annotated color composite ERTS–1 image of the Great Kavir in its wettest period on May 12, 1973 (1293–06274).

# TORNADO TRACKS

By Este F. Hollyday, U.S. Geological Survey,
and James G. Cook, U.S. Army Corps of Engineers

Diagonally across the lower left quarter of the ERTS image shown in figure 213 is the track of a tornado that passed through the William B. Bankhead National Forest in Alabama at 9:20 p.m., Apr. 3, 1974. After leveling the town of Guin, Ala. (at the bottom of the image), this tornado felled 20 million board feet of timber within the forest and destroyed one tower of a high-voltage transmission line.

The track of the tornado may be traced continuously for 92 km from a point at the north edge of the forest (near the center of this image) southwest to a point near Sulligent, Ala., which is southwest of Guin (or just off the edge of this image). It is believed to be the longest tornado track ever recorded on satellite imagery. Near the center of the forest, trees were bent or disturbed in a path 1.1 km wide and were uprooted or twisted off in a path 0.6 km wide. Careful examination of the image reveals that the track swings northwest across high ground and swings southeast across stream valleys. The track is wide on high ground and is narrow in the valleys. Ground surveys and low-altitude photography indicate that, although the track is narrow in the valleys, the destruction here is equal to or greater than destruction on the high ground.

The image also shows at least two other tornado tracks that are parallel to the track through the center of the forest. One is near the edge of the forest, 19 km northwest of the main track. The other crosses Lewis Smith Lake near Houston. Ala., 23 km southeast of the main track. These less obvious tracks can be traced for only about 20 km each.

Near the east edge of the southeast quarter of this image is a white condensation trail left by an aircraft, flying at an altitude of 10.4 km, which passed over Boaz, Ala. The gray shadow of this manmade cloud is most obvious on band 7 and occurs 7 km northwest of the trail. The tornado track through the forest was initially believed to be such a condensation trail. The tornado track, however, does not have a parallel shadow. In addition the multispectral nature of the ERTS sensors reveals that the track is bright in band 5 but dull in band 7, as would be expected for stressed vegetation but not for a cloud, which would be bright in all bands. The repetitive nature of ERTS reveals that the track first appeared on imagery for April 10 and on this image for April 28 and the adjacent image for April 29; the condensation trail did not reappear.

Cloud-free imagery from a real-time operational satellite would provide a regional view of areas of tornado destruction. This regional view, together with reports on damage from local agencies, particularly State Civil Defense Offices, would aid the Emergency Operations Planner of the U.S. Army Corps of Engineers in locating areas of possible severe damage, particularly in nonpopulous areas. Damage in these areas could then be assessed jointly by the Corps and the Federal Disaster Assistance Administration. The regional view provided by the imagery would not only aid deployment of reconnaissance aircraft over the most heavily damaged sites but would also be useful in correlating and indexing the resulting aerial photography.

Imagery of tornado tracks could be used to improve interpretations of hydrologic records, especially water levels in artesian wells. The extreme low atmospheric pressures that occur in the path of a tornado reduce the pressure upon the column of water standing in an artesian well without significantly reducing the pressure on the underground reservoir. As a result, water moves into and up the well, resulting momentarily in a very high water level. The highest level on record, therefore, might occur in wells near the tornado track during passage of the storm.

Although much remains to be done in exploring the use of satellite imagery in assessing damage caused by weather-related phenomena such as tornados, hail storms, and hurricanes, this example indicates that ERTS imagery will be a valuable tool. Images should also be of value in assessing the effects of man's attempts to modify weather by cloud seeding and similar procedures.

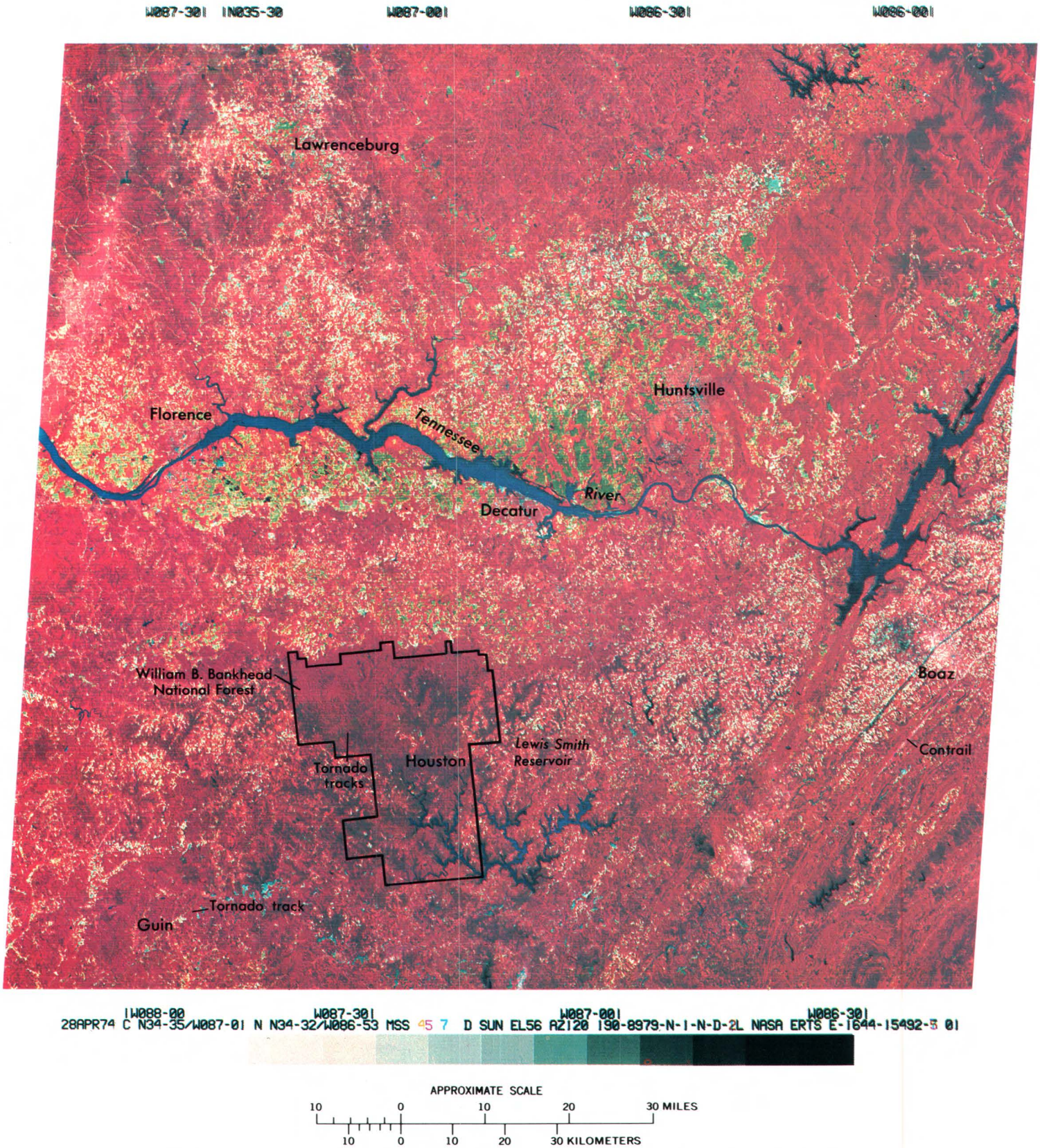


FIGURE 213.—Annotated color composite ERTS–1 image showing tornado tracks in the William B. Bankhead National Forest near Guin, Ala. (1644-15492).

## REFERENCES


Anderson, R. R., Carter, Virginia, and McGinness, J. W., Jr., 1972, Interpretation of wetlands ecology from ERTS–1 [abs.]: NASA Goddard Space Flight Center, Earth Resources Technology Satellite–1 Symposium, Sept. 1972, Proc., p. 147.

——— 1973, Mapping Atlantic coastal marshlands, Maryland, Georgia, using ERTS–1 imagery: NASA Goddard Space Flight Center, Symposium on Significant Results Obtained from the Earth Resources Technology Satellite–1, 2d, New Carrollton, Md., Mar. 1973, Proc., v. 1, sec. A, p. 603–613.

———1974, Applications of ERTS data to coastal wetland ecology with special reference to plant community mapping and typing and impact of man: NASA Goddard Space Flight Center, Symposium on the Earth Resources Technology Satellite–1, 3d, Washington, D.C., Dec. 1973, Proc., v. 1, sec. B, p. 1225–1242.

Carter, Virginia, and Schubert, Jane, 1974, ERTS MSS digital data and field spectral measurements for coastal wetlands analysis: Internat. Symposium on Remote Sensing of Environment, 9th, Ann Arbor, Mich., 1974, Proc., v. 2, p. 1241–1260.

Krinsley, D. B., 1970, A geomorphological and paleoclimatological study of the playas of Iran: U.S. Geol. Survey Interagency Rept. Military–1, 329 p.

———1972, Dynamic processes in the morphogenesis of salt crusts within the Great Kavir, north-central Iran: Internat. Geol. Cong., 24th, Montreal 1972, Proc., sec. 12, p. 167–174.

———1973, Preliminary road alignment through the Great Kavir in Iran by repetitive ERTS–1 coverage [abs.]: NASA Goddard Space Flight Center, ERTS Symposium, 3d, Washington, D.C., 1973, Abs., p. 54.

Rehder, J. B., 1973a, Geographic applications of ERTS–1 data to landscape change: NASA Goddard Space Flight Center, Symposium on Significant Results Obtained from the Earth Resources Technology Satellite–1, 2d, New Carrollton, Md., Mar. 1973, Proc., v. 1, sec. B, p. 955–963.

———1973b, Applications of ERTS–1 data to landscape change: Am. Soc. Photogrammetry, Symposium on Management and Utilization of Remote Sensing Data, Sioux Falls, S. Dak., 1973, Proc., p. 598–609.

Strong, A. E., 1973, ERTS–1 observes algal blooms in Lake Erie and Utah Lake: NASA Goddard Space Flight Center, Symposium on Significant Results Obtained from the Earth Resources Technology Satellite–1, 2d, New Carrollton, Md., Mar. 1973, Proc., v. 1, sec. B, p. 1605–1612.

Strong, A. E., Stumpf, H. G., Hart, J. L., and Pritchard, J. A., 1974, Extensive summer upwelling on Lake Michigan during 1973 as observed by NOAA–2 and ERTS–1 satellites: Internat. Symposium on Remote Sensing of Environment, 9th, Ann Arbor, Mich., 1974, Proc., v. 2, p. 923–932.

# CHAPTER 7.
# APPLICATIONS TO CONSERVATION

## INTRODUCTION

By Richard D. Curnow,
U.S. Fish and Wildlife Service

Modern society has only recently acknowledged the necessity to conserve and manage the resources of the Earth. The exploitation of these finite resources has been frequently accompanied by adverse environmental and socioeconomic effects. Even though some of these effects may be apparent, the causal mechanisms often are little understood. Environmental information commonly has been untimely or insufficient for use in decisionmaking processes of Federal, State, and private institutions, thus hindering the implementation of appropriate conservation and management practices.

Satellite platforms have afforded for the first time the means by which certain types of resource data could be acquired. With the advent of ERTS, land-use planners and managers of natural resources have the capability to reach decisions and implement conservation practices based on timely synoptic data collected over extensive areas.

The continual need for energy, food, and other raw materials has resulted in observable changes in natural and cultural resources on the surface of the Earth that can be evaluated in ERTS data. In the paper by Lyons, Ebert, and Hitchcock (p. 304), the perspective gained in ERTS imagery provided a clearer understanding of the relationships between the cultural features of an ancient Pueblo society and the natural resources upon which that society was dependent.

Williams, in discussing ERTS imagery of Cape Cod and Cape Cod National Seashore (p. 307), emphasizes the accuracy and invaluable synoptic and repetitive characteristics of the data. These features are essential for monitoring large dynamic resources such as coastal marshes or coniferous forests.

A recurring problem in applying remotely sensed data to resource inventories and environmental monitoring is the need for discrimination of increasingly smaller items and the extraction of increasingly more detailed information. Smedes has evaluated the capability of computer analysis of ERTS data applied to land-use planning in Yellowstone National Park (p. 310). Similarly, Gilmer and others discuss computer processing of ERTS data in their study of a migratory-bird breeding habitat (p. 321). These two papers evaluate what appears to be the limit of detail that may be extracted from ERTS imagery. It is through such evaluations that the value of ERTS data for monitoring extremely complex associations of vegetation, land, and water is revealed.

Because of the inaccessibility of many large uninhabited land areas that possess unique ecological value, remote sensors, like those of ERTS, provide a means of rapidly monitoring these resources in a nondisruptive manner. Discussed in the paper by Carter is the use of ERTS data to assess the resource values of the Great Dismal Swamp (p. 316). In a cooperative effort, several agencies were able to use ERTS data as a common source of information about the resources of the swamp.

The authors in this chapter have described examples of the uses of ERTS data and the uses of the tools of remote sensing for conserving natural and cultural resources. I am confident that the applications reported here reflect only a very small aspect of the future involvement that ERTS data will have in meeting the informational needs of resource specialists.

# ARCHAEOLOGICAL ANALYSIS OF IMAGERY OF CHACO CANYON REGION, NEW MEXICO [1]

By Thomas R. Lyons and James I. Ebert, National Park Service,
and Robert K. Hitchcock, University of New Mexico

About a thousand years ago, during the 10th and 11th centuries A.D., in the Chaco Canyon area of northwestern New Mexico (fig. 214), ancient Pueblo Indians, the Anasazi, built an extensive land-route communication system that had many of the physical characteristics of what we today, in a wheel-based civilization, call roads. These prehistoric dirt roadways were as much as 10 m wide and often were curbed with stone masonry. They surmounted cliffs and ledges with cut stairways and masonry ramps, traversed over the depths of ravines on stone causeways, and possessed other features that revealed a high degree of engineering and construction skill.

The existence of a few of the old roadway segments was first recognized in historic times by Navajo occupants of the area who pointed them out to early archaeological investigators in Chaco Canyon. More recently, with the aid of black and white, color, and color-infrared aerial photography and with various kinds of data handling and analyzing equipment, it has been possible to map approximately 320 km of these prehistoric roadways. We can now safely estimate that there existed at least 320 km more that are no longer discernible even on aerial photography.

The structure and magnitude of this purposefully designed regional communication system provide evidence to the archaeological investigator that the character of the social organization responsible for it was far more complex than has heretofore been described.

Many questions about the use or function of these roads arise when it is considered that even though these people were organized in complex ways and possessed a high degree of expertise in the construction of agricultural and architectural facilities, they did not have knowledge of the technologically important wheel nor did they have any large draught animals that could be used in transporting materials over the roads. Also, insofar as we can determine, Anasazi society was not based upon the organization of large numbers of men for labor or military pursuits. What purpose, then, did the road system provide in addition to facilitating communication between communities?

One effort made to obtain answers to this question and that did indeed provide explanatory information was the use of an ERTS–1 image of the San Juan Basin area of northwestern New Mexico (fig. 215). The longest known

[1] This article is Contribution Number 9 of the Chaco Center, National Park Service and University of New Mexico.

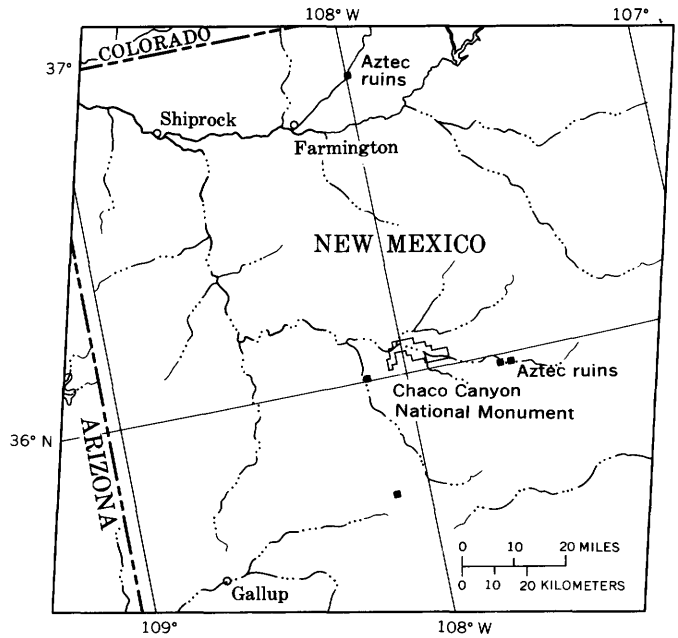


FIGURE 214.—Index map showing location of the Chaco Canyon National Monument, N. Mex.

branches of the roadway system were plotted on this image because it gives an excellent synoptic view of most of the region occupied by Chaco people. The relationship of the great steppe in which Chaco Canyon proper is incised to the adjacent mountain masses and the major river drainage basin is immediately apparent. No attempt was made to locate archaeological sites on the image since the spatial resolution was not adequate for this purpose, but the image did provide a view of the physiographic relationships that were of importance to the early exploiters of this environment.

It was instantly apparent that the major branches of the roadway system led to the following types of potential resources areas: (1) timbered mountain areas where animals could be hunted and wood for building could be collected; (2) river areas where fish could be obtained; and (3) areas where materials could be obtained for use in making pottery, stone tools, and other objects. With the heavy concentration of Anasazi population in the Chaco Canyon region, local resources were no doubt reduced or depleted, thus forcing the Chaco people to exploit an ever-widening area.

A quick review of existing data recovered through excavations in Chaco Canyon supports this explanation. Remains of garfish that occurred prehistorically in the Rio Grande could have been imported over the east or south road extensions. Turkeys apparently were brought in from adjacent highlands to the west and east. Marine shell artifacts and fragments discovered indicate imports from the West Coast and the Gulf of California. Exotic birds were also brought from the south.

We can conclude then that, in addition to other functions, the road system served an economic purpose for the Chaco people, providing access to resources outside their particular sphere of occupation and influence. The Chaco Canyon road system, as suggested by the regional perspective of the ERTS imagery, thus served not only to integrate the various communities in the Chaco region but also to link those communities with areas far outside the canyon.

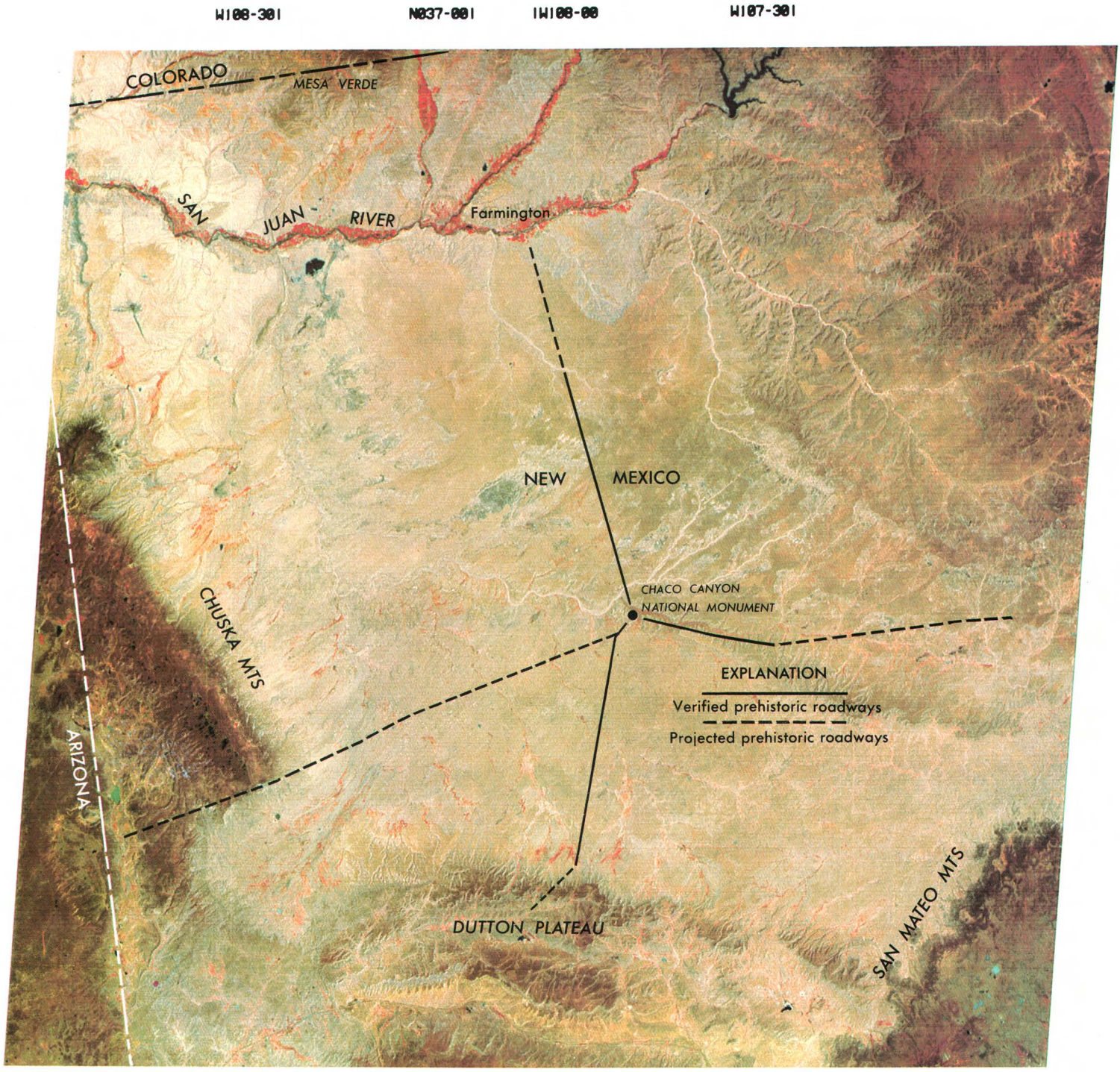


FIGURE 215.—Annotated color composite ERTS–1 image of the Chaco Canyon National Monument, N. Mex. (1317–17210). Solid lines indicate field-verified prehistoric roadways; dashed lines indicate unverified (reported or projected) prehistoric roadways.

# CAPE COD AND THE CAPE COD NATIONAL SEASHORE OF MASSACHUSETTS

By Richard S. Williams, Jr.,
U.S. Geological Survey

The MSS color composite ERTS–1 image in figure 216 shows nearly the full sweep of Cape Cod and its offshore islands: Martha's Vineyard, Nantucket, Monomoy, and other islets (fig. 217). The glacial character of the area is partly revealed by the many bodies of water. Many of the depressions are bogs that have important economic value as the basis for the cranberry industry in this part of Massachusetts. North of the Cape Cod Canal, along the coast, are the sandbars that nearly enclose Plymouth and Duxbury Harbors (Williams, 1973), site of the Pilgrims' final landfall and permanent settlement in 1620.

Cape Cod was given its initial rough outline by the last great Pleistocene ice sheet, the Wisconsinan, which spread south from the north (Davis, 1896). About 10,000 yr ago the ocean began to rise, engulfing the glacial deposits left by the retreating Wisconsinan ice sheet and reworking them with waves and wind (Strahler, 1966). More recently man himself has begun to leave his mark on Cape Cod, the most prominent example being the sinuous Cape Cod Canal that forms an artificial demarcation between Cape Cod and the south shore of southeastern Massachusetts.

The landscape is dotted with kettle ponds, marshes, natural and manmade harbors, sandbars, spits, islands, and islets. It is a region of dynamic geologic processes —the wind, the waves, and the tides all contributing to the erosion of the land and creation of new land. But it is man's capacity to modify the landscape, particularly along coastal areas and coastal wetlands, that often causes unnatural and often unexpected changes that many times result in degradation and despoilation of a unique and irreplaceable natural resource (Chamberlain, 1964).

For all these reasons, Congress in 1961 established the Cape Cod National Seashore, permanently assuring the protection of "one of the last expanses of uninterrupted natural lands along the Atlantic . . . The national seashore will ultimately embrace some 27,000 acres of land" (U.S. Dept. of Interior, 1969). At present it includes the entire outer beach from Provincetown to the tip of Nauset Beach, south of Chatham, and substantial parts of the towns of Provincetown, Truro, Wellfleet, and Orleans (fig. 217). Monomoy Island is protected separately as a wildlife refuge.

ERTS imagery portrays the natural environment in a far more accurate and comprehensive way than any single map could ever do (fig. 217), and it can do it, weather permitting, every 18 days through all the seasonal changes and changes effected by natural processes and by man. Because Cape Cod is a dynamic environment the need exists for frequent and accurate updating of conventional maps of the area. ERTS imagery provides important geologic and hydrologic information necessary for the updating of 1:1,000,000, 1:250,000, and perhaps even 1:125,000 U.S. Geological Survey maps of Cape Cod. Because various types of maps provide an important source of environmental information for resource-management decisions, particularly for preserving the environmental integrity of Cape Cod National Seashore, such maps must be current and accurate. Based on an analysis of MSS images of Cape Cod, the ERTS imagery provides timely environmental information not available from conventional sources (chiefly aerial photography), except at very high cost (Williams and Friedman, 1970). ERTS–1 imagery has the following advantages:

1. Provides synoptic, nearly instantaneous imagery of a large area at different times in the tidal cycle of a coastal area (over several orbital cycles).
2. Provides cyclic and frequent imagery at relatively low cost.
3. Permits the regional planimetric mapping of marshes (wetlands), tidal flats, shoals, sandbars, and harbor channels not normally shown on 1:125,000 and smaller scale maps.
4. Portrays the environment at the correct scale initially, thus avoiding the subjective differences in cartographic representation caused by generalization of features.
5. Provides to resource managers the relevant and current data necessary for wise decisionmaking by periodically recording types of environmental information that can be converted to a map or other form of presentation quickly.

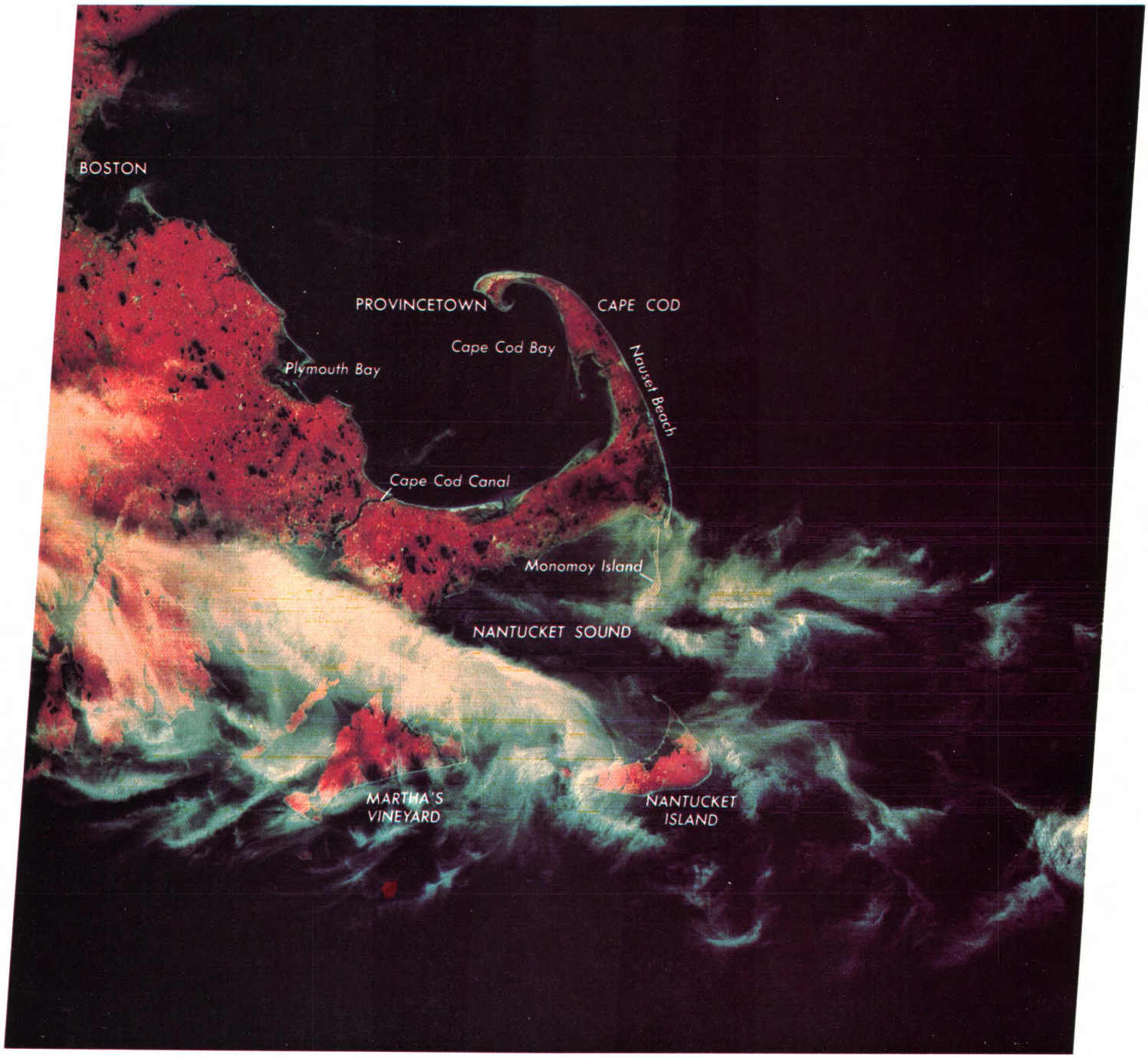


01SEP72 C N41-43/W070-09 N N41-41/W070-02 MSS 5 D SUN EL49 AZ138 191-0556-N-1-N-D-2L NASA ERTS E-1040-14552 1

APPROXIMATE SCALE

10 0 10 20 30 MILES

10 0 10 20 30 KILOMETERS

FIGURE 216.—Annotated color composite ERTS–1 image of the Cape Cod area of Massachusetts (1040–14552) 1½ h before low tide in much of Cape Cod Bay.

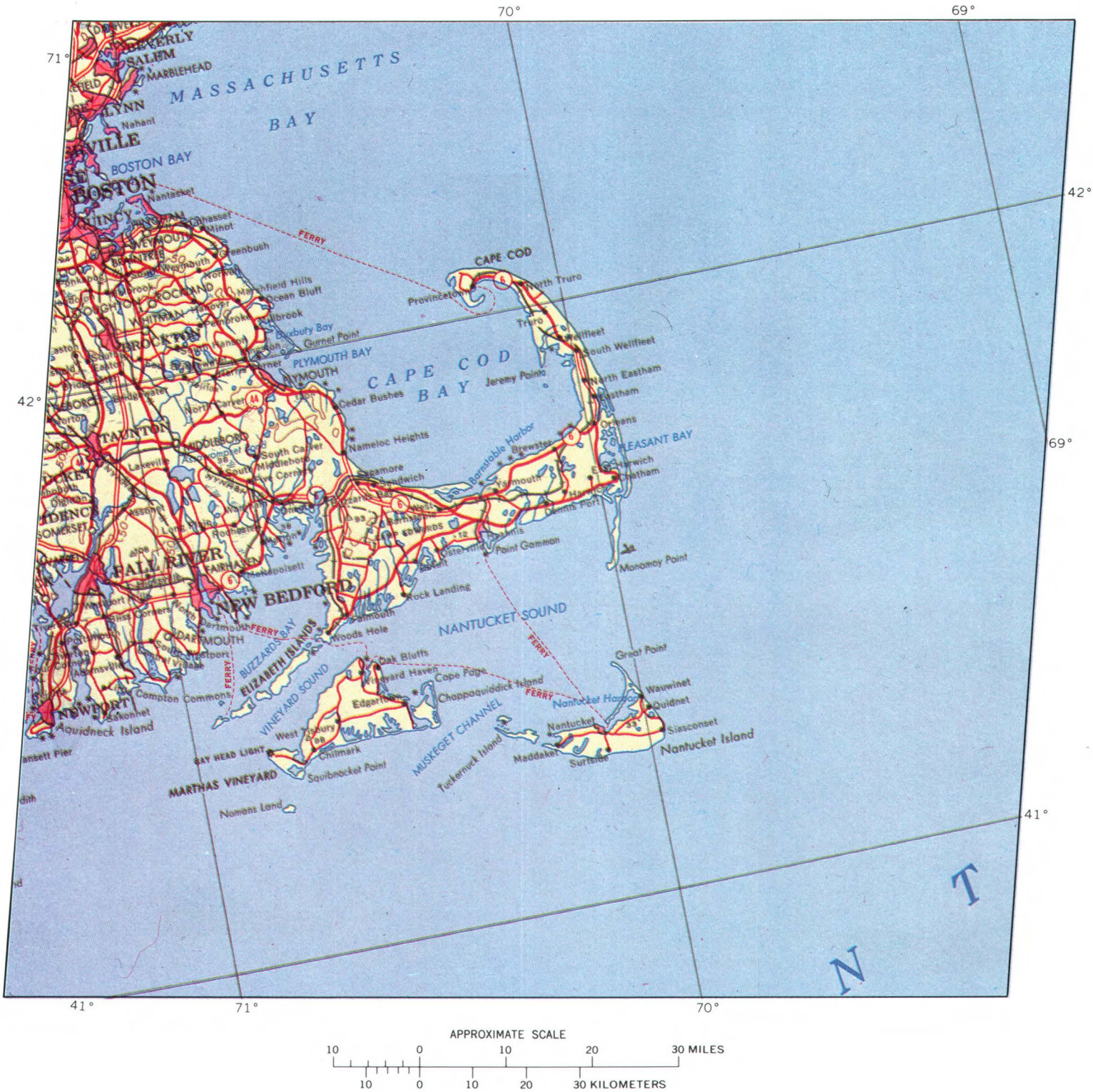


APPROXIMATE SCALE

10 0 10 20 30 MILES

10 0 10 20 30 KILOMETERS

FIGURE 217.—Part of the Boston sheet of the International Map of the World showing the area covered by ERTS–1 image 1040–14552 (fig. 216). [IMW, NK–19, Boston, North America, 1969; compiled by the Army Map Service in 1955 from 1:250,000 maps (1947), 1:506,880 maps (1939), and U.S. Coast and Geodetic Survey Charts (1947 and 1949).]

# LAND-USE PLANNING IN YELLOWSTONE NATIONAL PARK, WYOMING, MONTANA, AND IDAHO

By Harry W. Smedes,
U.S. Geological Survey

Yellowstone National Park (fig. 218) is the oldest national park in the world and the largest in the United States. Established just a little more than a century ago on Mar. 1, 1872, it encompasses nearly 9,000 km² of Wyoming, Montana, and Idaho. The park contains a wide variety of climatic and vegetation zones, wildlife, relief, landforms, and soil and rock types. It is one of the few places in the world where scientists can study the primal "plumbing" system of hot springs and geysers; elsewhere most such systems have been affected by man's intervention and have changed or adjusted in response to that intervention.

The park is on the Pitchstone Plateau, a broad plateau of Quaternary rhyolite bordered on the north, east, and south by an arcuate complex of ridges and dissected highlands of Eocene volcanic rocks and deformed pre-volcanic sedimentary and metamorphic rocks. Yellowstone Lake, about 350 km² in area, dominates the southeastern part of that rhyolite plateau and is one of the largest natural mountain lakes in the United States.

The major part of the rhyolite plateau marks the site of ancient calderas that formed by collapse as a result of the rapid expulsion of large volumes of ash flows, the remnants of which form the fringe of the plateau (Keefer, 1972). Lava subsequently spread across the floors of the calderas to form a coalesced mass of lava domes and flows; the toelike projections of some of these flows can be seen on the Pitchstone Plateau (shown in fig. 218 by arrows at **f**).

Topographic maps, geologic maps, and conventional aerial photographs provide important tools for planning and management of this large, basically primitive area, but ERTS images have provided, for the first time, a comprehensive synoptic picture of the entire park and its environs. In the color composite ERTS image shown in figure 219, the park is in the center. The cloud-free image taken Aug. 7, 1972, documents the condition of the terrain during late summer. (Other images capture the changes in ground cover in response to seasonal changes.) In this false-color composite, verdant vegetation appears red; snow is white; bare rock and soil are light gray and light blue; and water is black. Note that, because it is so muddy, Turbid Lake (2 or 3 km northeast of Yellowstone Lake) is blue (fig. 219).

Before ERTS images became available, the only complete pictorial base of the entire park was a mosaic compiled from more than 80 high-altitude color aerial photographs taken by NASA in 1969 (fig. 220). Three days of flying were required to obtain this relatively cloud free photographic coverage. Even so, large clouds can be seen over the north-central part of the park and along the east-central edge. In contrast, ERTS can provide a synoptic view in a few seconds, in one image.

An investigation was made of the accuracy and usefulness of computerized surface-cover mapping of the entire park and surrounding area using the four-channel MSS data from ERTS–1. Previous studies in the north-central part of the park using low-altitude aircraft MSS data demonstrated the feasibility of accurately mapping a wide variety of terrain classes automatically by computer. Those studies are summarized in a report by Smedes (1971). The ERTS MSS data from which figure 219 was prepared were used to make a similar but more comprehensive computer-produced terrain map of the entire region (CCT's for the Aug. 7, 1972, ERTS image 1015–17404). The resulting map (fig. 221) depicts 12 terrain classes. The few developed areas in the park are mapped as rock because of similar reflectance from building roofs, paved areas, and car and trailer tops. The accuracy of this computer map ranges from 70 to 95 percent.

Because the computer map depicts differences in rock, soils, and vegetation both in forested and nonforested areas, it is more useful than any other existing map for inventorying and monitoring the terrain. The computer map not only shows the location and spatial relations of different classes, but can determine the total area occupied by each terrain class. If computer maps depicting these same 12 terrain classes are produced at given time intervals, such as is possible with the repetitive coverage of ERTS, the changes in the inventory of each class as a function of time may give valuable insights into dynamic Earth processes. For example, one can: (1) determine the specific location as well as the average and maximum extent of surface area burned annually by forest fires, (2) analyze wildlife habitats by identifying dynamic changes in vegetative types used for food and cover, (3) study trends in snowpack accumulation and water levels in lakes, (4) monitor changes in hydrothermal activity as shown by changes in surface thermal deposits and ensuing effects on plant communities, and (5) search for changes that indicate areas of insect-infested trees. In addition, mapping at different seasons should help establish more classes for plant species and rock or soil types.

The National Park Service envisions sometime in the future using a multilayered computer information storage, manipulation, and retrieval system to assist in redirected planning, design, and development and to provide concurrent analysis of the environmental impact of that development. The computer terrain map provides the necessary data on the plant communities and other types of ground cover in a form readily updated and readily entered into a grid or cell information system. In addition to these data, each grid point or cell in the information system could contain digitized information on such attributes as topography, precipitation, wildlife, rock and soil properties, transportation routes, and socioeconomic data.

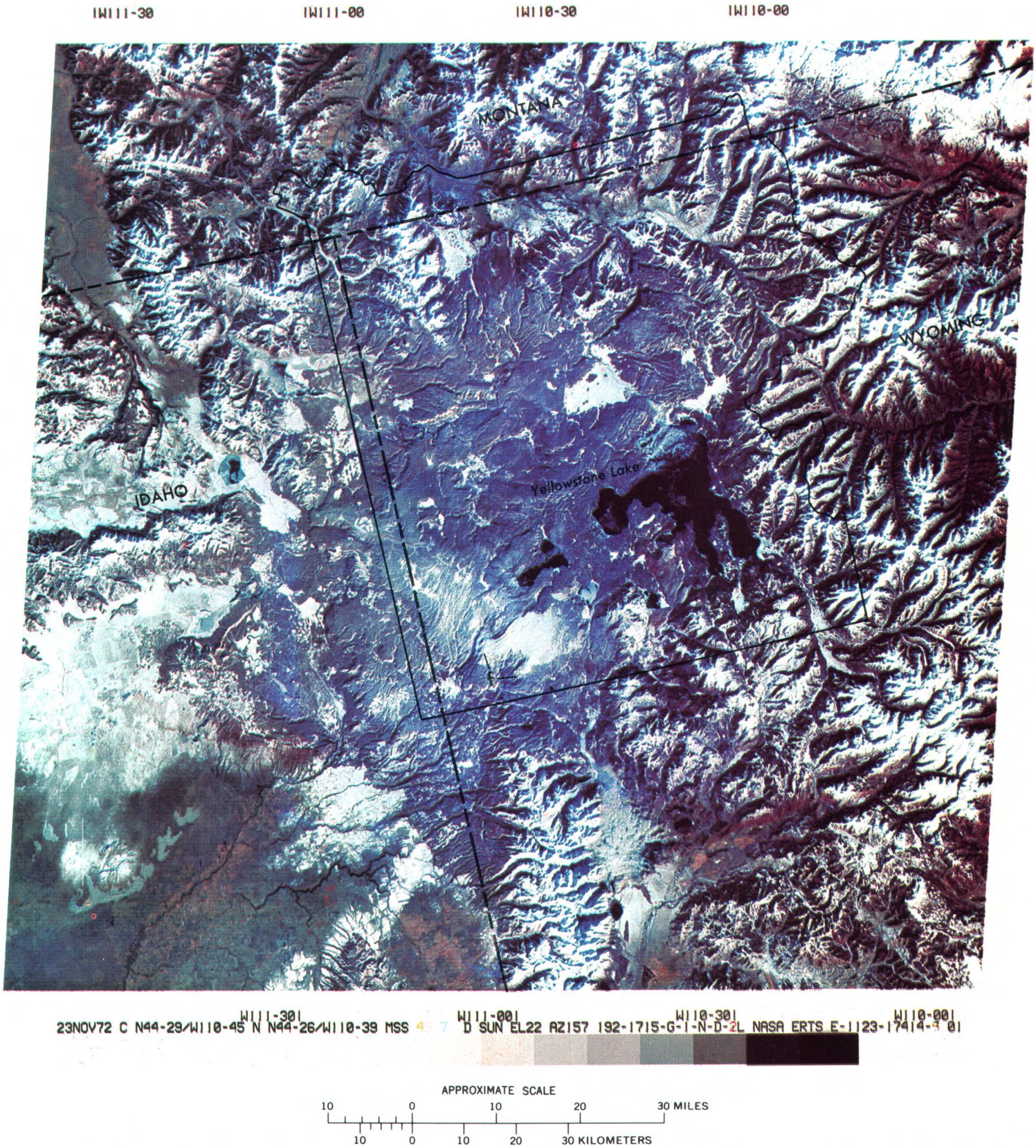


FIGURE 218.—Annotated color composite ERTS–1 image of the Yellowstone National Park and vicinity on Nov. 23, 1972 (1123–17414); toelike projections of flows (f) can be seen on the Pitchstone Plateau.

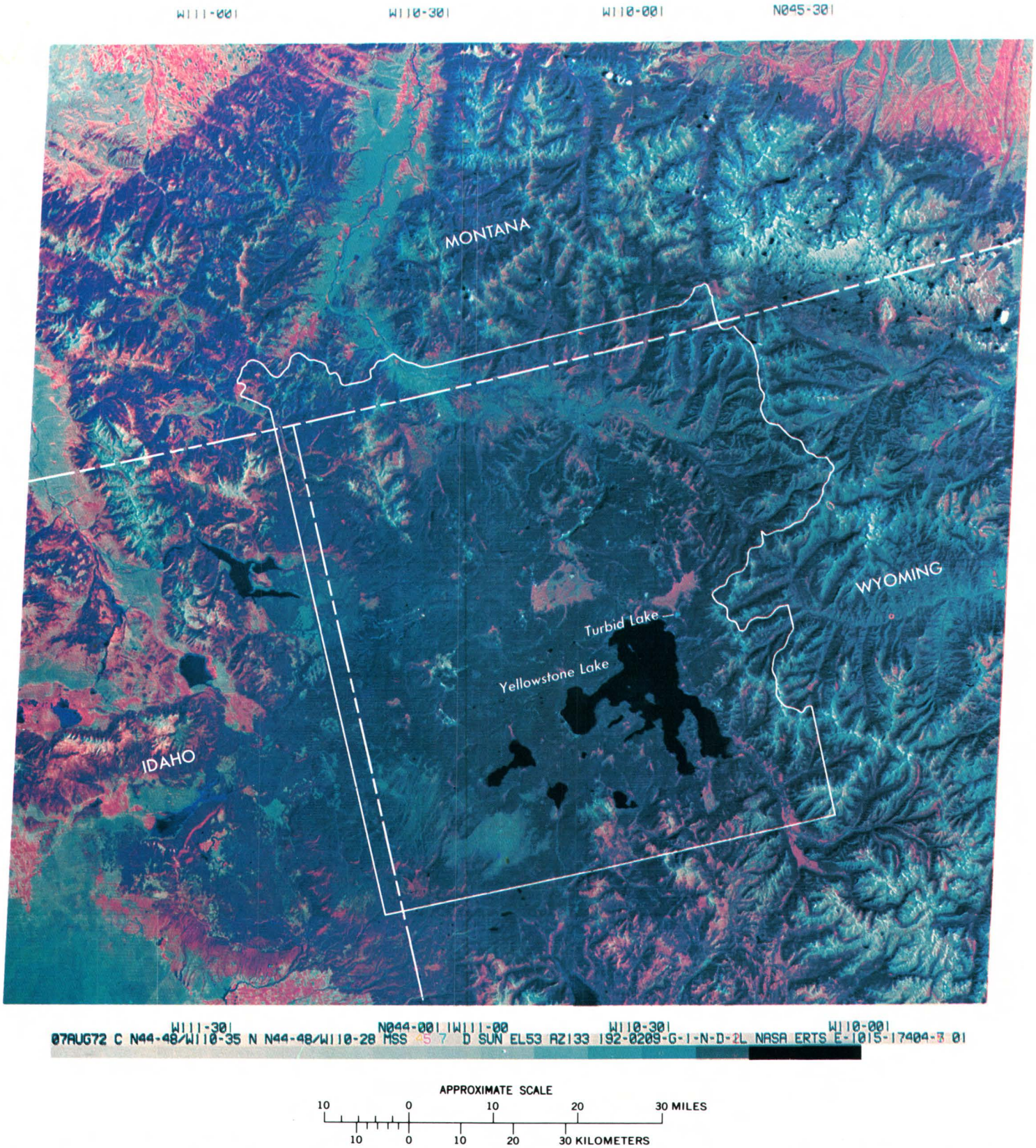


FIGURE 219.—Annotated color composite ERTS–1 image of the Yellowstone National Park (outlined) and vicinity on Aug. 7, 1972 (1015–17404).

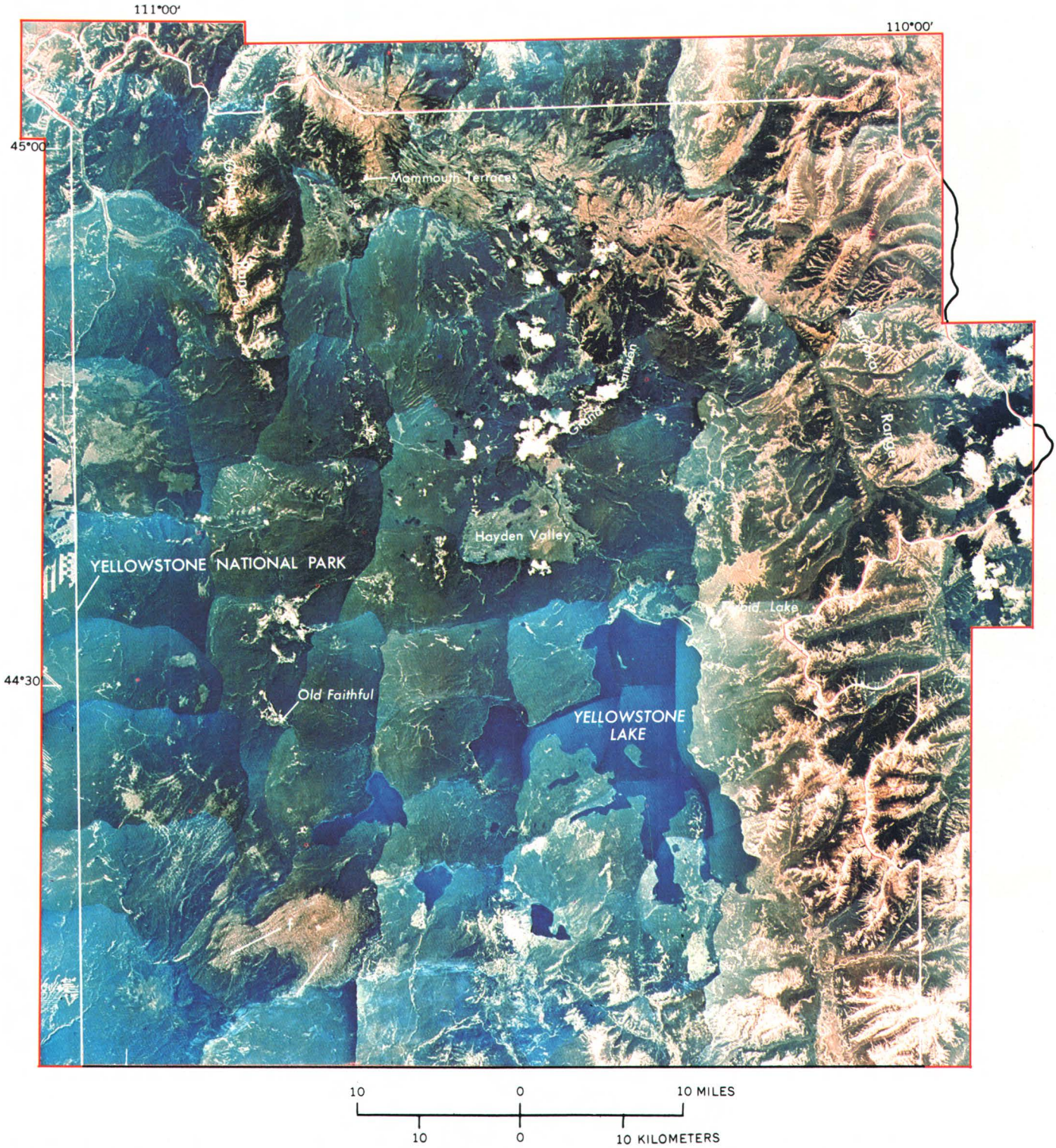


FIGURE 220.—High-altitude color aerial photomosaic of the Yellowstone National Park (1969 NASA aerial photography).

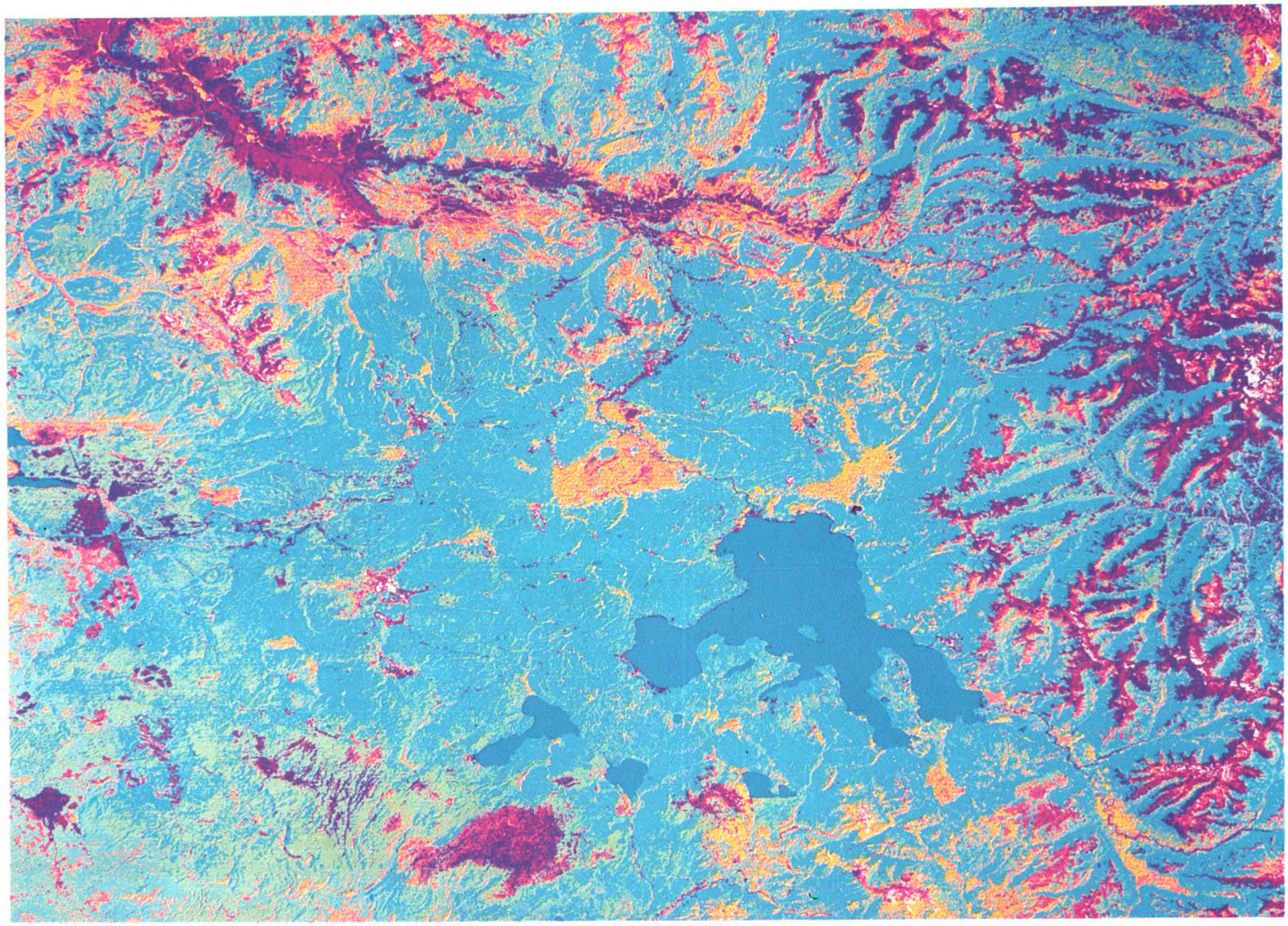

EXPLANATION

- Thermal deposits and hydrothermally altered rocks and soil, travertine, quartzite, and snow
- Dark rock, sand, gravel
- Water
- Coniferous forest with greater than 40 percent canopy cover
- Coniferous forest with 15 to 40 percent canopy, and grass understory
- Coniferous forest with 15 to 40 percent canopy, and light rock understory
- Grassland
- Grass and shrub mixture
- Grassland with 5 to 15 percent cover of conifers
- Sparse vegetation on light rock or soil
- Dominantly light rock and soil
- Shallow water and muddy water

10 0 10 MILES

10 0 10 KILOMETERS

N

FIGURE 221.—Computer-processed terrain map of Yellowstone National Park made from computer compatible tapes for ERTS–1 image 1015–17404.

# THE GREAT DISMAL SWAMP OF VIRGINIA AND NORTH CAROLINA

By Virginia Carter,
U.S. Geological Survey

In 1972 Congress authorized the Department of the Interior to conduct a comprehensive 2-yr study of the Great Dismal Swamp and the Dismal Swamp Canal (Public Law 92–478). The study is designed to determine the desirability and feasibility of protecting and preserving the ecological, scenic, recreational, historical, and other valuable attributes of the Great Dismal Swamp and Canal and to consider the various alternatives for preservation in terms of effectiveness and cost. The study is being coordinated by the U.S. Fish and Wildlife Service. Several Federal agencies are participating in the Great Dismal Swamp study, including the U.S. Geological Survey, which is responsible for water dynamics, mineralogical data, and remote-sensing applications.

On Aug. 31, 1974, President Ford signed the bill creating the Great Dismal Swamp Wildlife Refuge. During the next 3 yr, $7 million will be expended for land acquisition.

The Great Dismal Swamp comprises approximately 850 km$^2$ of wooded swamp and/or forested bog straddling the Virginia-North Carolina border. Because of the large size of the entire swamp and the inaccessibility of many interior parts, remote sensing meets the needs of both the current study and future research and management. It minimizes the extent of the ground work that is needed, allows for more rapid completion of inventory and mapping, enhances the ability to detect changes, and aids in detection of certain areas of special interest that would be likely to escape notice by conventional methods.

The remotely sensed data used include NASA and U.S. Geological Survey aerial photography, ERTS data, and ERTS thematic extractions (Carter and Smith, 1973). These data were applied to: (1) overall study-area selection, (2) location of intensive-study areas, (3) hydrologic studies, (4) vegetation mapping, and (5) field studies, including identification of areas of special interest.

The choice of the study area (fig. 222) by the U.S. Fish and Wildlife Service was made on the basis of both false-color infrared and black and white photographs and required approximately 3 man-weeks. ERTS imagery, on the other hand, later provided a synoptic picture of the entire Great Dismal Swamp and its geographic setting on just one ERTS frame. Figure 223 is an

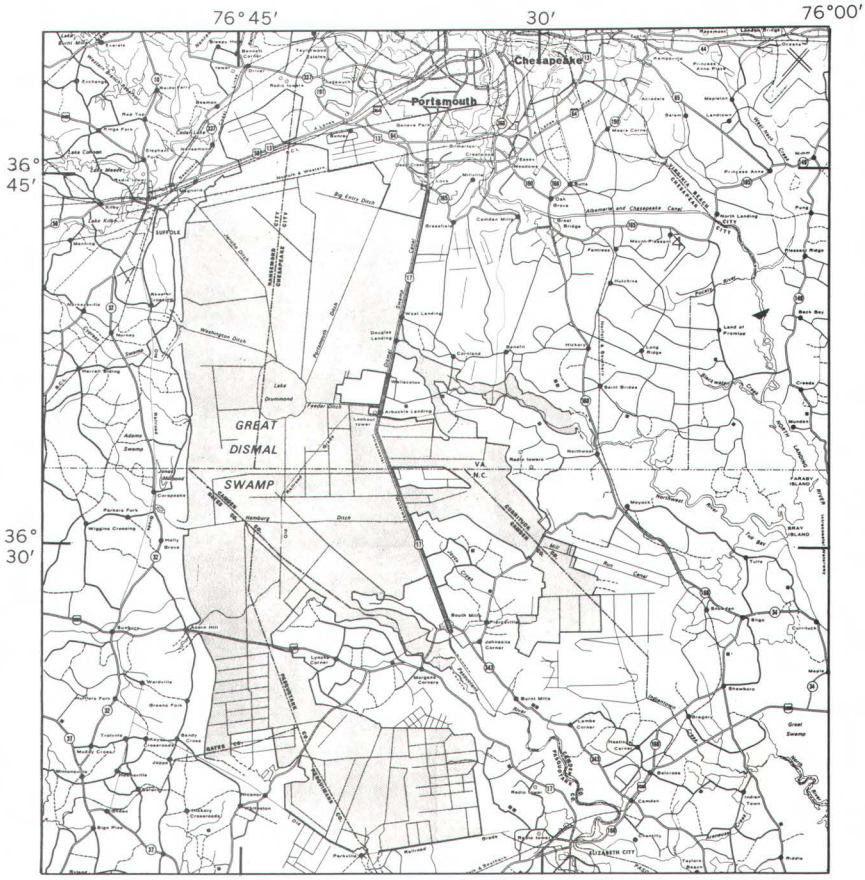


FIGURE 222.—Map of the Great Dismal Swamp study area, Virginia-North Carolina. (Facsimile of a 1973 map prepared by the U.S. Fish and Wildlife Service, from U.S. Geological Survey data, in response to Public Law 92–478.)

FIGURE 223.—Enlargement of part of a color composite ERTS–1 image (fig. 224) showing the Great Dismal Swamp (1205–15150).

enlargement of a part of a color composite ERTS–1 image (fig. 224) taken on Feb. 13, 1973. This image was used to reconfirm the choice of the study area. Comparison of this image with the map of the area (fig. 222) illustrates the utility of ERTS data in determining wetland boundaries. Delineation of the study area from the ERTS image would have reduced the time required for selection from 3 man-weeks to less than 3 man-days, including field checks. Many of the roads, canals, and vegetation associations can be clearly identified on a 1:250,000 enlargement of the ERTS image. Moreover, ERTS imagery can be used to construct a reliable map of similar large wetland areas without the need for either extensive or repetitive fieldwork or low-altitude aircraft coverage.

A preliminary analysis of ERTS digital data from CCT's of the Feb. 13, 1973, Great Dismal Swamp image was made with the General Electric Co. IMAGE 100, an interactive multispectral analysis system that uses a television screen for displaying the results of the analysis. The thematic extractions shown are made by means of multispectral signature analysis. By using the spectral information in each MSS band, a signature can be derived for a selected condition or feature, and all other areas with the same signature can be detected.

Figure 225 is a photograph of the interactive color display screen on which the digital data from part of the ERTS image are combined to give a simulated color-infrared picture of the Great Dismal Swamp. The canals, roads, and centrally located Lake Drummond can be clearly identified. Deciduous trees (blue), evergreen (red), and cultivated land, bare soil, or snow cover (white) can be identified. Figure 226 is a thematic extraction of Atlantic white-cedar, a commercially valuable tree species presently being lumbered in the North Carolina section of the swamp. Figure 227 is a thematic extraction of surface water below deciduous trees. The presence of surface water and maintenance of a high water table during the winter and early spring are essential to the continued survival of the swamp. Figure 228 is a thematic extraction of the drier deciduous areas of the swamp and the clearcut area where some snow remains on the ground. The swamp appears to be moving toward a drier condition, largely because of man's continuing efforts at drainage.

Area measurements of extracted themes can provide useful information to the resource manager. Monitoring the extent of surface water during the winter wet season is very important in assessing the results of water-level manipulation and modification of the hydrologic regime. Updating of tree-cover estimates is necessary periodically. Occasionally very large fires occur during the dry season, and measurements of areal extent of damage are important in plans for revegetation.

FIGURE 224.—Annotated color composite ERTS–1 image of northern Pamlico Sound and the Great Dismal Swamp with a partial snow cover on Feb. 13, 1973 (1205–15150).

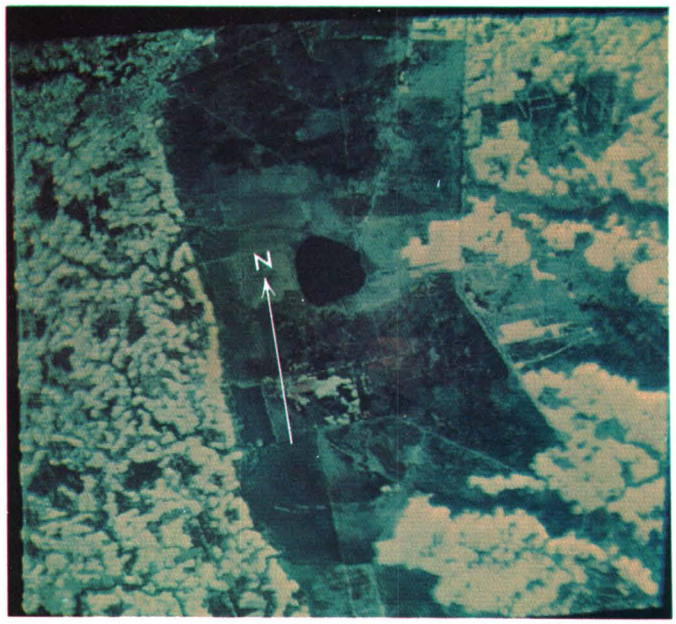


FIGURE 225.—Color digital display of the Great Dismal Swamp in simulated false-color infrared.

FIGURE 226.—Thematic extraction of Atlantic white-cedar in the Great Dismal Swamp.

FIGURE 227.—Thematic extraction of surface water below deciduous trees in the Great Dismal Swamp.

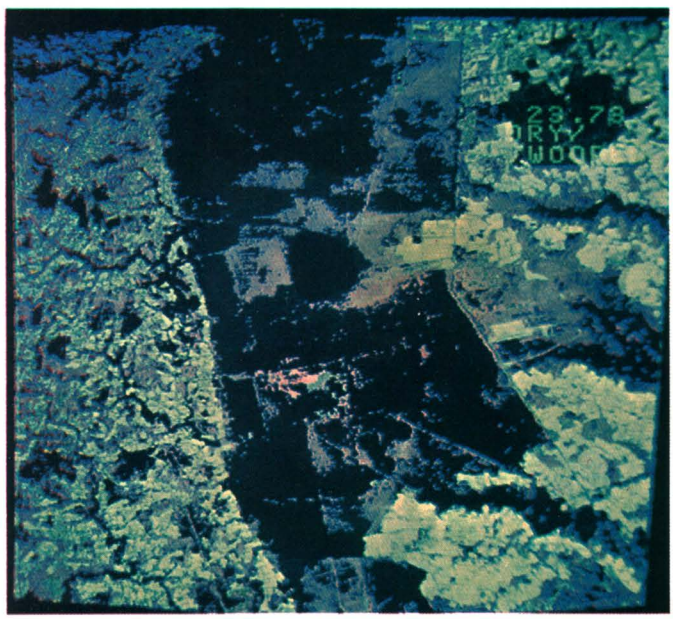

FIGURE 228.—Thematic extraction of drier deciduous areas in the Great Dismal Swamp.

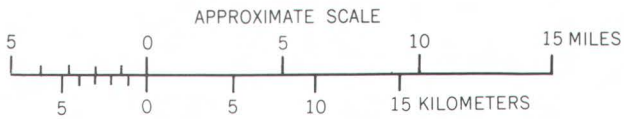

# MONITORING BREEDING HABITAT OF MIGRATORY WATERFOWL

By David S. Gilmer and A. T. Klett, U.S. Fish and Wildlife Service, and Edgar A. Work, Environmental Research Institute of Michigan

Because of their free movement over and between nations and continents, migrating waterfowl, including wild ducks, brant, geese, and swans, are protected by treaties among the United States, Canada, Mexico, and Japan. The agency responsible for coordinating the management of this wildlife resource in the United States is the U.S. Fish and Wildlife Service.

Assessment of breeding habitat is an important part of the management of waterfowl populations. United States and Canadian biologists have suggested that a significant correlation exists between the abundance of wetlands on the breeding grounds and the subsequent size of the continental duck population (Cooch, 1969; Crissey, 1969). The primary duck-breeding range in North America extends over the Dakotas, the southern part of the prairie provinces, northwestern Canada, and parts of Alaska. Because annual variations in habitat quality in these regions greatly influence annual waterfowl population, in order to evaluate habitat conditions, the U.S. Fish and Wildlife Service makes low-level aerial surveys that sample approximately 2.2 million $km^2$ of the breeding range during each spring and summer. Breeding pairs, broods, and wetlands are counted along preestablished survey flight lines. These data are used to estimate future waterfowl population by means of a mathematical model (Geis and others, 1969). This information is needed by resource administrators to establish annual waterfowl-hunting limits and regulations and other management policies.

Biologists have speculated that aerial and satellite remote-sensing and associated data-processing techniques can be used to obtain accurate and rapid counts of wetlands over large areas of the waterfowl-breeding range. Therefore the service began an investigation of the feasibility of using remote-sensing techniques for waterfowl-habitat evaluation in 1968. Biologists at the Northern Prairie Wildlife Research Center in Jamestown, N. Dak., working in cooperation with the Environmental Research Institute of Michigan, Ann Arbor, Mich., conducted a series of tests using an airborne MSS for wetland mapping and land-use studies. The results of these tests demonstrate that airborne remote sensors could be used effectively to obtain regional wetland information and related data on surrounding land use, as well as to evaluate the waterfowl habitat (Burge and Brown, 1970; Nelson and others, 1970).

Evaluation of ERTS MSS data has shown the utility of spaceborne sensors for evaluating waterfowl-breeding habitat (Work and others, 1973, 1974). ERTS test sites were selected in a region in North Dakota that contains some of the best waterfowl-breeding areas in North America. Figure 229 illustrates the coverage provided by three ERTS images obtained during May 1973 and July 1972 and 1973. A part of the Missouri Coteau is included in each frame. The Coteau is a region characterized by stagnation moraine and a nonintegrated drainage system that produces numerous small ponds and lakes. Magnetic tapes derived from telemetered satellite data for portions of

each frame were processed by computer to obtain an enumeration of the wetlands in the image. Comparisons were made to detect seasonal and annual changes. The ERTS image shown in figure 230 is a color composite of a scene obtained on July 7, 1973. Varied land features, such as agricultural fields, and numerous water areas are evident. The ERTS tapes for this image were analyzed on a computer programed to recognize surface water. A 2,389-km² part of the Coteau (enclosed by the dashed line) was selected to demonstrate this recognition capability. Table 2 consists of a size-frequency distribution of all wetlands recognized within the defined area. Additional data provided include the geographic location and size of each wetland; only a partial tabulation is given. Many water areas smaller than 1 ha are not recognized because of the sensor-resolution limitations, but new computer-processing methods and statistical-analysis techniques being evaluated are expected to provide inferential data regarding these small water bodies.

TABLE 2.—*Part of a computer printout for the July 7, 1973, ERTS–1 image (fig. 230) showing size-frequency distribution of surface water and location and size of water bodies*

07JUL73 C N47-22/W098-22 N N47-21/W098-07 1349-16543- SUN EL57 AZ131 192-4866-N D-1-D-1 H ERIM (ERTS DATA)

| | | | | | | | |
|---|---|---|---|---|---|---|---|
| SCENE | N.D. COTEAU | LINES | 1386 THRU 1428 | POINTS | 3 THRU 250 |
| | | LINES | 1429 THRU 1452 | POINTS | 3 THRU 374 |
| | | LINES | 1453 THRU 1499 | POINTS | 3 THRU 498 |
| SCENE AREA= | 923 SQ. MI. | LINES | 1500 THRU 1571 | POINTS | 3 THRU 622 |
| = | 2389 SQ. KM. | LINES | 1572 THRU 2175 | POINTS | 3 THRU 747 |

DISTRIBUTION OF RECOGNIZED WATER BODIES

BY AREA

| AREA (ACRES) | AREA (HECTARES) | FREQUENCY |
|---|---|---|
| .25 TO .50 | .10 TO .20 | 0 |
| .50 TO 1.00 | .20 TO .40 | 0 |
| 1.00 TO 2.00 | .40 TO .81 | 149 |
| 2.00 TO 3.00 | .81 TO 1.21 | 60 |
| 3.00 TO 4.00 | 1.21 TO 1.62 | 47 |
| 4.00 TO 6.00 | 1.62 TO 2.43 | 65 |
| 6.00 TO 8.00 | 2.43 TO 3.24 | 29 |
| 8.00 TO 10.00 | 3.24 TO 4.05 | 21 |
| 10.00 TO 15.00 | 4.05 TO 6.07 | 38 |
| 15.00 TO 20.00 | 6.07 TO 8.09 | 28 |
| 20.00 TO 25.00 | 8.09 TO 10.12 | 10 |
| 25.00 TO 30.00 | 10.12 TO 12.14 | 18 |
| 30.00 TO 40.00 | 12.14 TO 16.19 | 14 |
| 40.00 TO 50.00 | 16.19 TO 20.23 | 11 |
| 50.00 TO 75.00 | 20.23 TO 30.35 | 18 |
| 75.00 TO 100.00 | 30.35 TO 40.47 | 16 |
| 100.00 TO 150.00 | 40.47 TO 60.70 | 13 |
| 150.00 TO 200.00 | 60.70 TO 80.94 | 7 |
| OVER 200.00 | OVER 80.94 | 13 |

TABULATION OF RECOGNIZED WATER BODIES

| LAT | LONG | SCAN LINE | POINT | AREA (ACRES) | AREA (HECTARES) |
|---|---|---|---|---|---|
| 47.3710 | 99.4194 | 1439 | 194 | 20.867 | 8.445 |
| 47.3909 | 99.5535 | 1440 | 13 | 1.098 | .444 |
| 47.3733 | 99.4483 | 1442 | 156 | 1.098 | .444 |
| 47.3637 | 99.4051 | 1446 | 216 | 7.688 | 3.111 |
| 47.3668 | 99.4399 | 1449 | 170 | 1.098 | .444 |
| 47.3320 | 99.2560 | 1458 | 422 | 1.098 | .444 |
| 47.3288 | 99.2353 | 1458 | 450 | 1.098 | .444 |
| 47.3281 | 99.2403 | 1460 | 444 | 4.393 | 1.778 |
| 47.3489 | 99.3953 | 1464 | 236 | 2.196 | .889 |
| 47.3282 | 99.2599 | 1464 | 419 | 2.196 | .889 |
| 47.3190 | 99.2149 | 1467 | 481 | 3.295 | 1.333 |
| 47.3176 | 99.2053 | 1467 | 494 | 2.196 | .889 |
| 47.3268 | 99.2699 | 1468 | 407 | 4.393 | 1.778 |
| 47.3532 | 99.4564 | 1471 | 156 | 1.098 | .444 |
| 47.3194 | 99.2509 | 1474 | 435 | 2.196 | .889 |
| 47.3164 | 99.2458 | 1477 | 443 | 1.098 | .444 |
| 47.3270 | 99.3193 | 1478 | 344 | 3.295 | 1.333 |
| 47.3201 | 99.2742 | 1478 | 405 | 3.295 | 1.333 |
| 47.3168 | 99.2527 | 1478 | 434 | 1.098 | .444 |
| 47.3637 | 99.5683 | 1480 | 8 | 4.393 | 1.778 |
| 47.3109 | 99.2291 | 1481 | 467 | 8.786 | 3.556 |
| 47.3089 | 99.2205 | 1482 | 479 | 3.295 | 1.333 |
| 47.3128 | 99.2606 | 1485 | 426 | 1.098 | .444 |
| 47.3125 | 99.2583 | 1485 | 429 | 2.196 | .889 |
| [illegible] | [illegible] | 1488 | 430 | 1.098 | .444 |
| [illegible] | [illegible] | [illegible] | [illegible] | 9.884 | 4.000 |
| [illegible] | [illegible] | [illegible] | [illegible] | 27.456 | 11.111 |
| [illegible] | [illegible] | [illegible] | [illegible] | [illegible] | 1.778 |
| [illegible] | [illegible] | [illegible] | [illegible] | [illegible] | [illegible] |

The synoptic evaluation of waterfowl breeding habitat using ERTS data can provide the U.S. Fish and Wildlife Service with a powerful tool in the effective management of our important waterfowl resource. Development of an operational system appears to be a realistic goal for the near future.

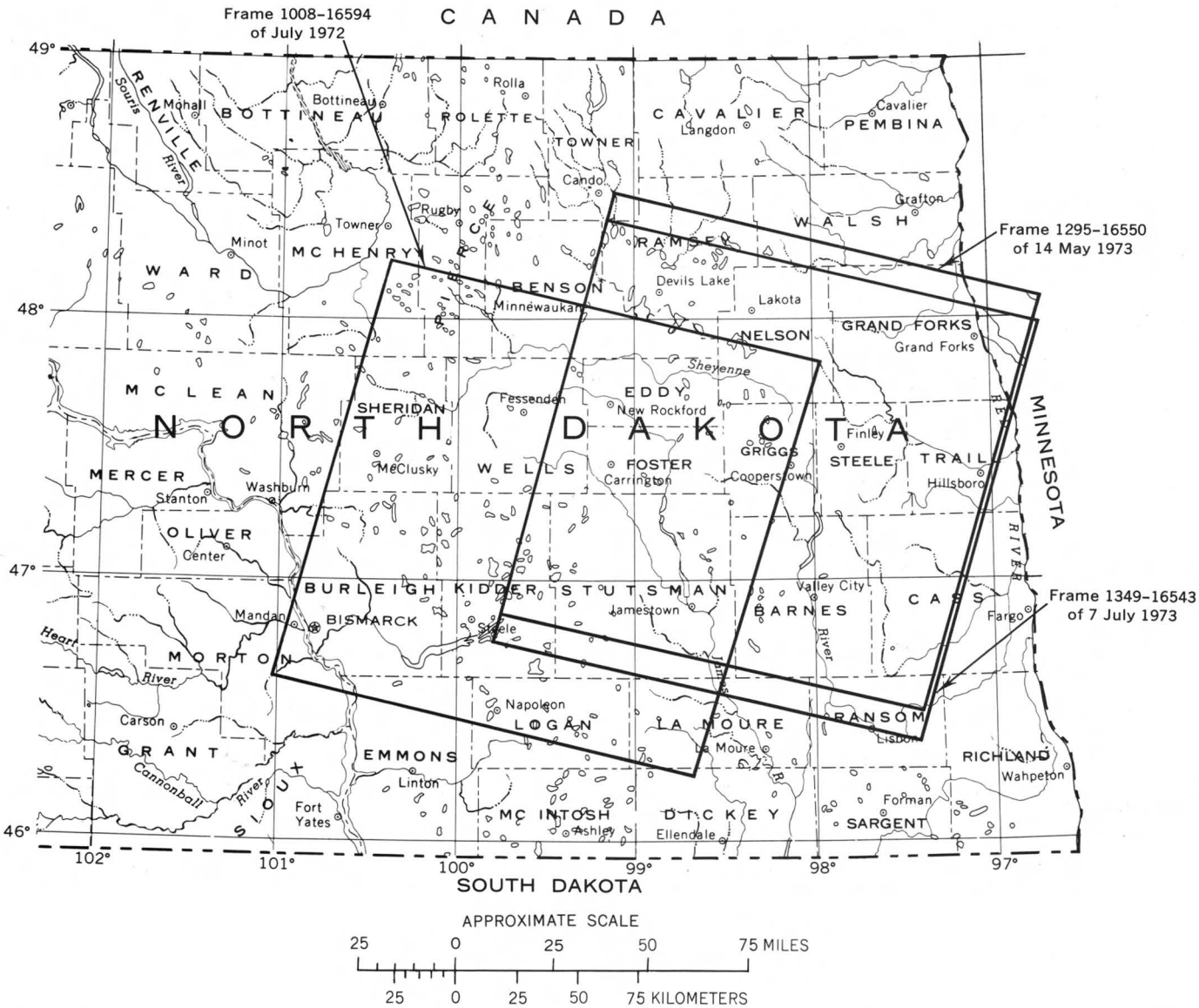


FIGURE 229.—Index map compiled from U.S. Geological Survey data showing coverage provided by three ERTS images in a primary waterfowl-breeding area in North Dakota.

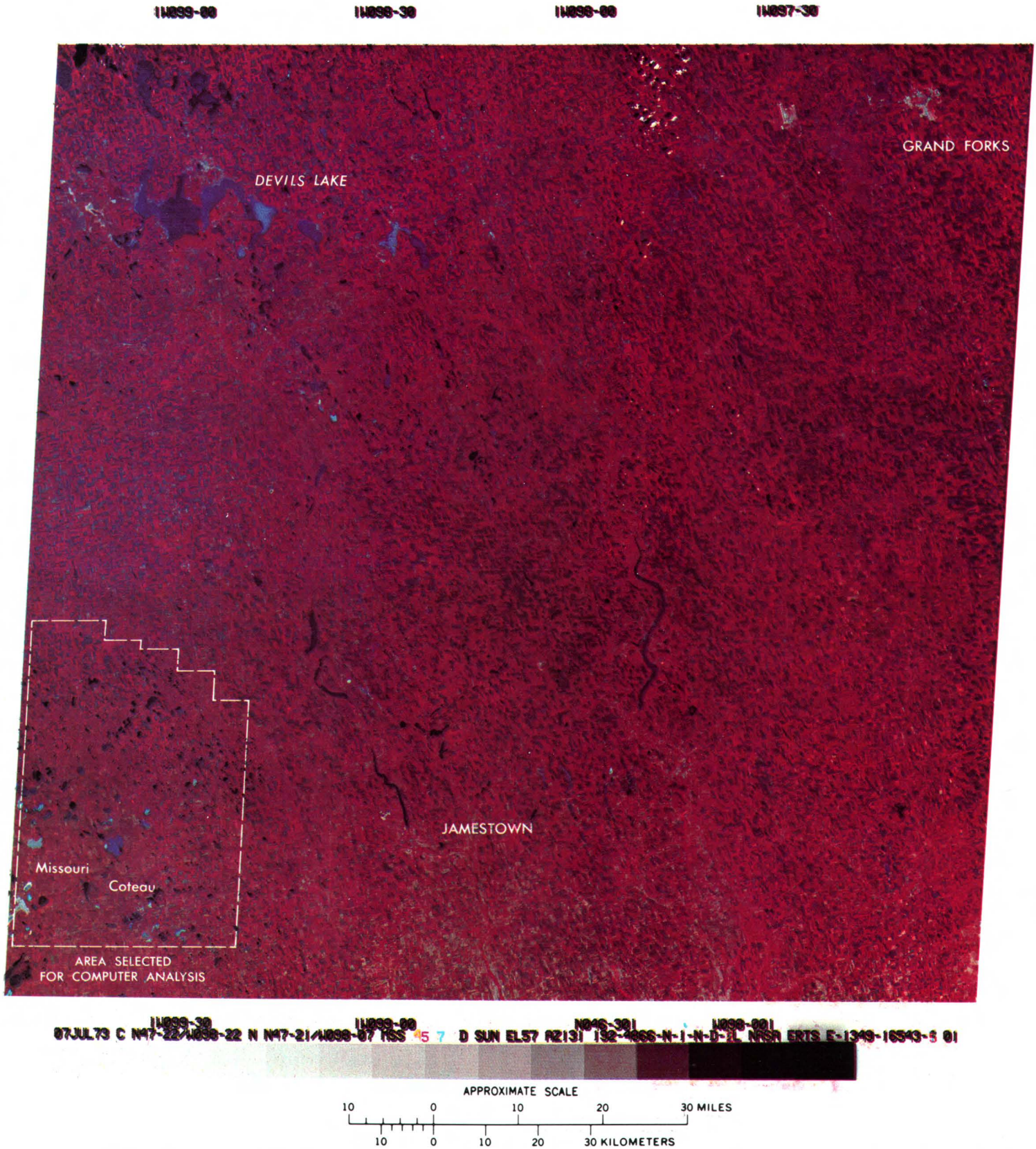


FIGURE 230.—Annotated color composite ERTS–1 image 1349–16543 showing the waterfowl-habitat study area (dashed line) near Jamestown, N. Dak., on July 7, 1973, for which computer recognition of surface water bodies was obtained (table 2).

## REFERENCES


Burge, W. G., and Brown, W. L., 1970, A study of waterfowl habitat in North Dakota using remote sensing techniques: Univ. of Mich., Willow Run Labs., Tech. Rept. 2771–7–F, 61 p.

Carter, Virginia, and Smith, D. G., 1973, Utilization of remotely sensed data in the management of inland wetlands: Am. Soc. Photogrammetry, Symposium on Management and Utilization of Remote Sensing Data, Sioux Falls, S. Dak., 1973, Proc., p. 144–158.

Chamberlain, B. B., 1964, These fragile outposts—a geological look at Cape Cod, Martha's Vineyard, and Nantucket: Garden City, N.Y., The Nat. History Press, 327 p.

Cooch, F. G., 1969, Waterfowl-production habitat requirements: Canadian Wildlife Service Rept. Series, v. 6, p. 5–10.

Crissey, W. F., 1969, Prairie potholes from a continental viewpoint: Canadian Wildlife Service Rept. Series, v. 6, p. 161–171.

Davis, W. M., 1896, The outline of Cape Cod: Am. Acad. Arts and Sci. Proc., v. 31, p. 303–332; also New York, Dover Pub., Geographical Essays, p. 690–724, 1954.

Geis, A. D., Martinson, R. K., and Anderson, D. R., 1969, Establishing hunting regulations and allowable harvest of mallards in the United States: Jour. Wildlife Management, v. 33, no. 4, p. 848–859.

Keefer, W. R., 1972, The geologic story of Yellowstone National Park: U.S. Geol. Survey Bull. 1347, 92 p.

Nelson, H. K., Klett, A. T., and Burge, W. G., 1970, Monitoring migratory bird habitat by remote sensing methods: North Am. Wildlife and Nat. Resource Conf., Trans., v. 35, p. 73–84.

Smedes, H. W., 1971, Automatic computer mapping of terrain: Internat. Workshop on Earth Resources Survey Systems, Proc., v. 2, p. 345–406.

Strahler, A. N., 1966, A geologist's view of Cape Cod: Garden City, N.Y., The Nat. History Press, 115 p.

U.S. Department of the Interior, National Park Service, 1969, Cape Cod National Seashore, Massachusetts: U.S. Govt. Printing Office, 2 p.

Williams, R. S., Jr., 1973, Coastal and submarine features on MSS imagery of southeastern Massachusetts: comparison with conventional maps: NASA Goddard Space Flight Center, Symposium on Significant Results Obtained from the Earth Resources Technology Satellite–1, 2d, New Carrollton, Md., Mar. 1973, Proc., v. 1, sec. B., p. 1413–1422.

Williams, R. S., Jr., and Friedman, J. D., 1970, Geologic mapping applications of coastal aerial photography, Cape Cod, Massachusetts [abs.]: Photogramm. Eng., v. 36, no. 6, p. 597.

Work, E. A., Jr., Gilmer, D. S., and Klett, A. T., 1973, Preliminary evaluation of ERTS–1 for determining numbers and distribution of prairie ponds and lakes: NASA Goddard Space Flight Center, Symposium on Significant Results Obtained from the Earth Resources Technology Satellite–1, 2d, New Carrollton, Md., Mar. 1973, Proc., v. 1, sec. A, p. 801–808.

——— 1974, Utility of ERTS for monitoring the breeding habitat of migratory waterfowl: NASA Goddard Space Flight Center, Symposium on the Earth Resources Technology Satellite–1, 3d, Washington, D.C., Dec. 1973, Proc., v. 1, sec. B, p. 1671–1685.

# CHAPTER 8.
# APPLICATIONS TO OCEANOGRAPHY

## INTRODUCTION

By William J. Campbell,
U.S. Geological Survey

Perhaps in the whole field of geophysical investigations, the most difficult realm in which science is attempting to elucidate the cause and effect of nature is that of the oceans. This is so because the oceans not only cover most of our planet but also both within them and on their surfaces large-scale changes happen in a short time. For example, the wave structure of whole seas can be altered within a few hours by atmospheric forces, and parts of the arctic and antarctic sea-ice canopies move as fast as 50 km/day, and their areal extents undergo seasonal fluctuations of 20 percent and 85 percent, respectively.

The numerical modeling of the physical and biological systems in the oceans is progressing rapidly and promises to give man his first, albeit rough, quantitative understanding of the complex web of oceanic phenomena upon which his very survival may hinge. But as the efforts to make a numerical model of the atmosphere have shown, the use of models is limited not by our lack of an understanding of the physics of the system but by our lack of detailed large-scale sequential data to apply to the models. It is precisely in meeting this profound need that space technology may render its greatest service.

Without a doubt, the most detailed synoptic look at the oceans available to science is that given by ERTS–1. The value of these data is immense, and what follows in this chapter must be considered as simply preliminary and cursory examples of the use that can be made of them.

The following ten papers are grouped into two sets: the first is made up of four papers on the study of turbid water, and the second includes six papers on sea ice.

Carlson has shown how ERTS sequential imagery of suspended-sediment plumes in coastal waters can be used to define the seasonal variation of current direction in nearshore waters (p. 328). These measurements are both difficult and expensive to perform using standard shipboard observations. Furthermore, ERTS imagery gives a truly synoptic view whereas shipboard observations cannot.

Coker and others have shown how ERTS imagery can be used to study the complex current structure of estuaries and the morphological changes of the bottom topography (p. 330). An important environmental finding of their work is that it may be possible, by using ERTS-type imagery and selected

ground information, to distinguish between natural and manmade turbidity in estuaries, information that is essential for assessing the impact of the great numbers of proposed industrial projects to be built on the Nation's estuaries.

Hunter has used ERTS imagery of turbid-water masses off the Texas coast to delineate the complex current patterns of the area (p. 334). He has shown that gyres and turbid plumes can be tracked for periods of several days with high-resolution imagery and that these data can be a valuable complement to data obtained by ships.

Campbell has combined ERTS, Nimbus–5 ESMR, and aircraft imagery of the sea-ice cover of the Beaufort Sea to study both its morphology and dynamics (p. 350). These combined data have given a new picture of this ice cover that could not have been drawn if the measurements were studied separately. The eastern Beaufort Sea is covered with large, round, multiyear ice floes, whereas its western sector and the Chukchi Sea are covered with small, fragmented, predominantly first-year ice.

Campbell has shown how ERTS imagery can be used to track the motion of individual ice floes (p. 337). Such a technique, when applied to a large part of the ice canopy, will give invaluable data to test numerical models of the ice, such as those being developed by AIDJEX.

Campbell has also shown how the complex dynamics of the openings in the sea-ice canopy, leads and polynyas, can be monitored by ERTS (p. 340). The ERTS data, when acquired sequentially over large areas, will prove to be fundamental to thermodynamic studies of the ice cover.

Campbell illustrates how the complex structure and dynamics of the sea-ice shear zone along the Arctic Ocean coasts can be measured by ERTS (p. 346). Considering the intense push to explore this area for oil, long-term monitoring of the Alaskan and Canadian arctic offshore waters with ERTS-type imagery is essential.

Campbell shows that seasonal morphological changes of sea ice can be measured by ERTS (p. 343).

Barnes and Reimnitz show how spring floods along the northern coast of Alaska discharge onto sea ice at their mouths (p. 356); they also describe the effect of sea ice on sedimentological processes as seen in the synoptic view provided by ERTS imagery (p. 360).

# MAPPING SURFACE CURRENT FLOW IN TURBID NEARSHORE WATERS OF THE NORTHEAST PACIFIC

By Paul R. Carlson,
U.S. Geological Survey

ERTS provides an opportunity to study synoptically seasonal differences in current direction in nearshore waters, an area difficult to study by ordinary oceanographic techniques. ERTS MSS imagery shows patterns of suspended sediment that can be used as indicators of the flow direction of the nearshore surface currents (figs. 231, 232). The flow directions are determined by the shapes of the plumes of turbid water, which are elongate in the direction of flow and are especially prominent off the mouths of major rivers. Photographic interpretations of flow directions have been substantiated by the returns of drift drogues dropped off the mouths of the northern and central California rivers at the time of satellite overflights (Carlson and Harden, 1973).

Turbid-water patterns in the nearshore zone around Cape Mendocino, Calif., can be clearly seen on the images for Jan. 6, 1973 (fig. 231), and Apr. 24, 1973 (fig. 232). During the winter and spring rainy season, most of the turbidity is due to large quantities of suspended sediment carried into the ocean by the streams and rivers originating in the California Coast Ranges. For example, the Eel River yields about $30 \times 10^9$ kg/yr of suspended sediment, the highest average annual suspended-sediment yield per square kilometer of drainage basin of any river in the United States (Brown and Ritter, 1971). Other sources of suspended matter and turbidity in the coastal waters are planktonic organisms, coastline erosion and sediment resuspension by storm waves, and waste discharge effluents. During periods of high river discharge, however, the enormous quantities of suspended sediment discharged from the rivers generally mask these other sources.

During January the flow of the coastal currents was generally northerly, but by April it had reversed and was generally southerly. This change in current direction in the nearshore coastal waters corresponds to the seasonal change of current flow observed in the offshore waters. Most of the year the surface flow is southerly (the California Current), but in the winter, owing to seasonal reversal of wind direction, a northerly flowing current surfaces (the Davidson Current) (Schwartzlose and Reid, 1972).

Complex flow directions that appear in both images around Cape Mendocino and Point Delgada may be due to zones of convergence and divergence. These zones apparently are related to oceanographic conditions such as upwelling, to localized wind motions, and/or to topographic features such as coastal irregularities and submarine canyons. The complex current patterns off Humboldt Bay are perhaps manifestations of the tidal circulation in this lagoonal system, and they are complicated further by the discharge plumes of the adjacent Eel and Mad Rivers and the complex submarine and coastal morphology. The January image (fig. 231) was obtained at the time of maximum tidal-flood current in Humboldt Bay. Turbid water, most likely from the Eel River plume, has been carried in the entrance of the bay and into the north channel. The April image (fig. 232) was obtained during ebb-tide conditions (about 2.5 h after maximum ebb) and shows a discrete plume of turbid tidal water outside the entrance to Humboldt Bay.

The 18-day repetitive cycle of ERTS provides opportunities to obtain seasonal coverage of the surface-current directions of nearshore waters along the Pacific coast of North America in spite of the seemingly ever-present cloud cover. Knowledge of the coastal currents is vital in coastal areas for proper planning by land-use commissions, for proper location of sewage effluents by sanitation districts, for proper management of sport and commercial fishing, and for better understanding of ecological conditions.

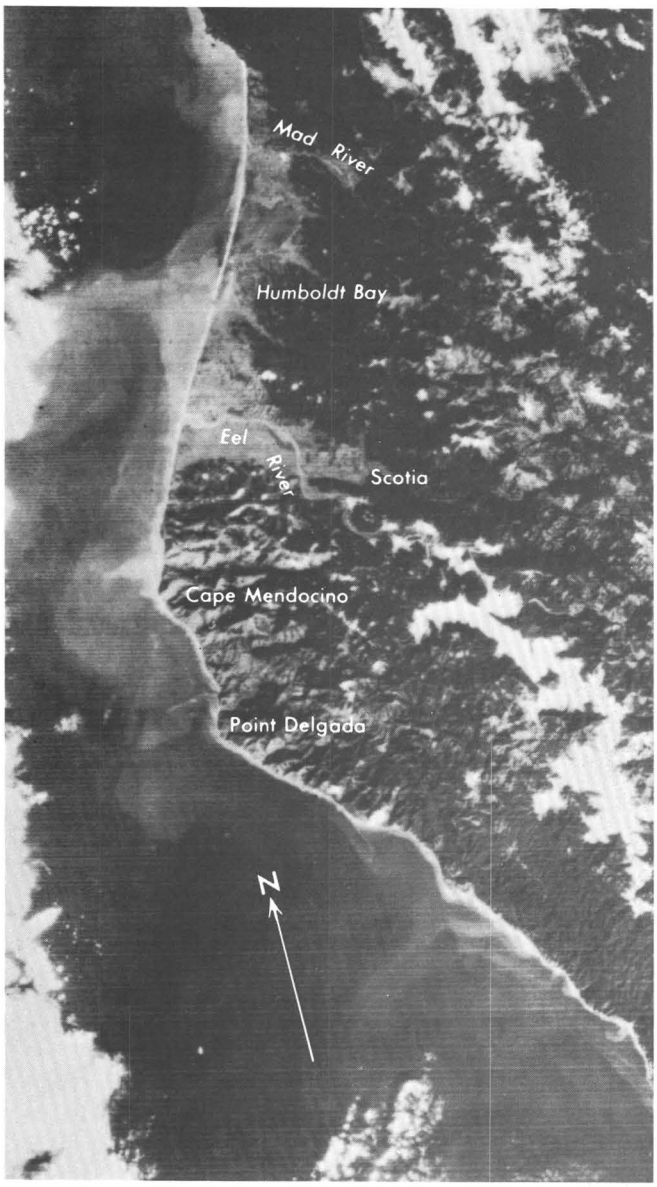


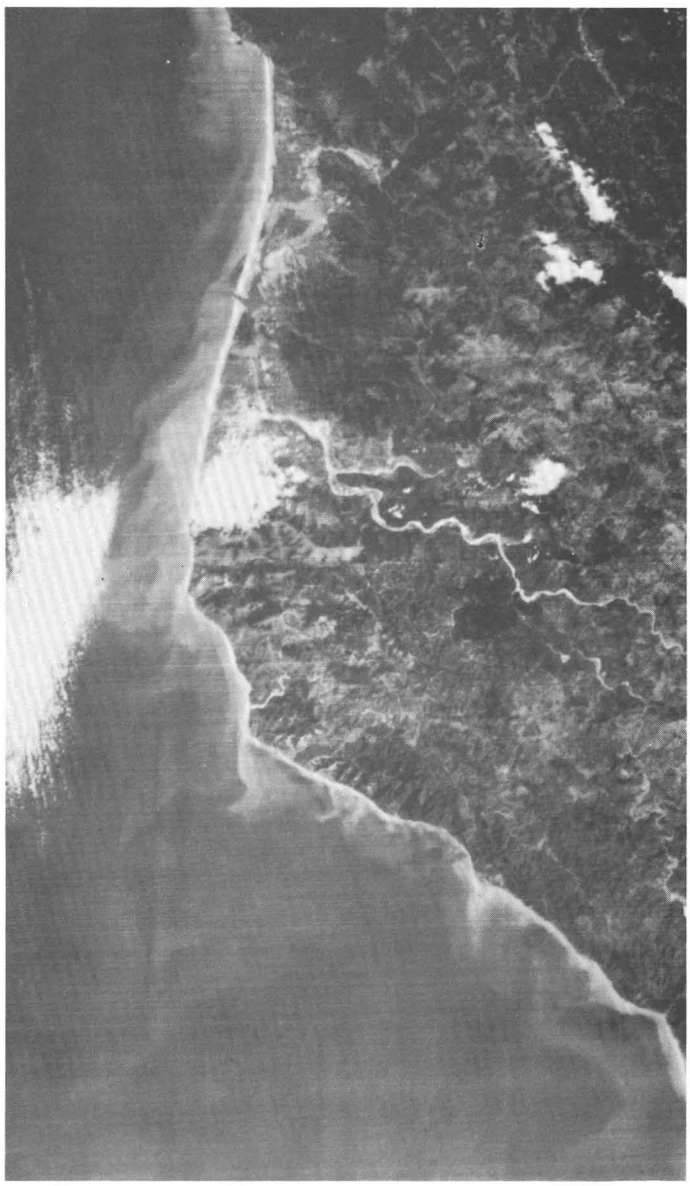

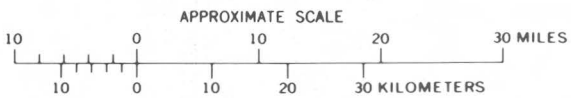


FIGURE 231.—Winter ERTS–1 image of turbid-water plumes along the northern California coast on Jan. 6, 1973 (part of 1167–18283, band 4). White masses at extreme left of image are clouds. The prevailing wind direction for January is from the southeast (NOAA, unpub. data, 1973). The suspended-sediment concentration in the Eel River at Scotia was 122 mg/l on Jan. 5, 1973, at 1610 h (U.S. Geological Survey, unpub. data, 1973).

FIGURE 232.—Spring ERTS–1 image of turbid-water plumes along the northern California coast on Apr. 24, 1973 (part of 1275–18290, band 4). White masses at left edge are clouds. The prevailing wind direction for April is from the north (NOAA, unpub. data, 1973). The suspended-sediment concentration in the Eel River at Scotia was 35 mg/l on Apr. 23, 1973, at 1615 h (U.S. Geological Survey, unpub. data, 1973).

# DETECTION OF TURBIDITY DYNAMICS IN TAMPA BAY, FLORIDA [1]

By A. Eugene Coker, Aaron L. Higer, and Carl R. Goodwin,
U.S. Geological Survey

The Port of Tampa is the 8th largest in the Nation; 32.7 million t of total cargo are handled annually. In terms of export tonnage, the port is fourth in the country—10 million t annually. Through this port passes 50 percent of all the cargo tonnage in the State of Florida. This commerce provides $200 million per year in wages and salaries to workers in the Tampa area, $15 million to $18 million per year to the U.S. Government in the form of customs receipts, and, in addition, $50 million per year to the positive side of the important U.S. balance of payments ledger.

In 1970, Congress authorized the deepening of the Tampa Bay channel (Rivers and Harbors Act of 1970) from 10.4 to 13.4 m. In order to determine the effects of this deepening on circulation, water quality, and biota during and after the construction, the U.S. Geological Survey, in cooperation with the Tampa Port Authority, has collected data and developed a digital-simulation model of the bay.

In addition to data collected using conventional tools, use is being made of data collected from ERTS–1 (fig. 233). RBV multispectral data were collected while a shell-dredging barge was operating in the bay and were used for turbidity recognition and unique spectral signatures representative of type and amount of material in suspension. The processed data integrated with other modeled parameters provide a view of the dynamics of turbid material during dredging periods. A three-dimensional concept of the dynamics of the plume was achieved by superimposing the parts of the plume recognized in each RBV band. This provided a background for automatic computer processing of ERTS data and three-dimensional modeling of turbidity plumes (Coker and others, 1973).

Image identification was made by comparing ERTS–1 transparencies (fig. 233), aerial photographs (fig. 234), maps, and field observations (fig. 235) of the bay with the velocity-vector grid (fig. 236). The relative size and shape of the turbidity plume is shown to the right of figure 237, as recognized in each RBV band. This system operates in three different spectral regions: the green band, 0.475 to 0.575 $\mu$m, band 1; the red band, 0.580 to 0.680 $\mu$m, band 2; and the near-infrared band, 0.690 to 0.830 $\mu$m, band 3.

Organic detritus and clay particles make up most of the suspended particulate matter (turbidity) that results from dredging operations in the waters of Tampa Bay. The water absorbs and reflects sunlight so that the RBV imagery depicts a signature indicative of the turbid condition of the water. The intensity of the reflection registered in the imagery will be modified by quantity and type of material in suspension, stratification, settling depth, type of bottom material, and water-surface roughness. If the water is clear or slightly turbid, the Sun's energy that spans band 3 is mostly absorbed at the surface, and that of bands 2 and 1 will penetrate to progressively greater depths before being absorbed. For this water, the resulting tones on positive black and white images will be almost black for band 3 with progressively lighter, but still dark, tones for bands 2 and 1. The lighter tones are caused by the greater penetration and scattering (less absorption) of light from suspended particulate matter in the water and atmosphere at the shorter wavelengths of bands 2 and 1. Depending upon the span of energy (RBV band), type of particulate matter, stratification, depth of settling, and bottom conditions, the more

[1] Work done in cooperation with the Tampa Port Authority, Tampa, Fla.

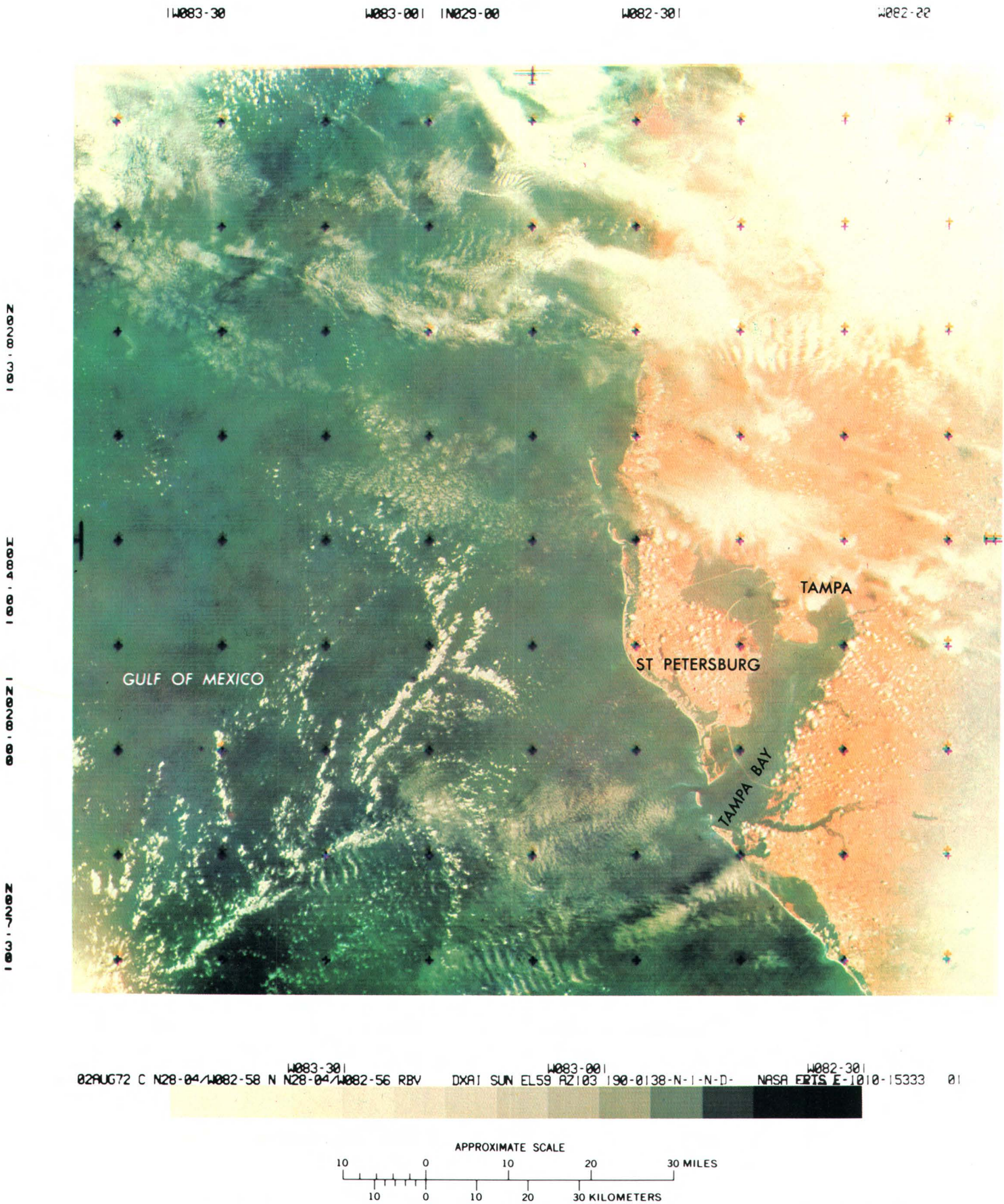


FIGURE 233.—Annotated color composite ERTS–1 RBV image of the Tampa Bay area of Florida (1010–15333).

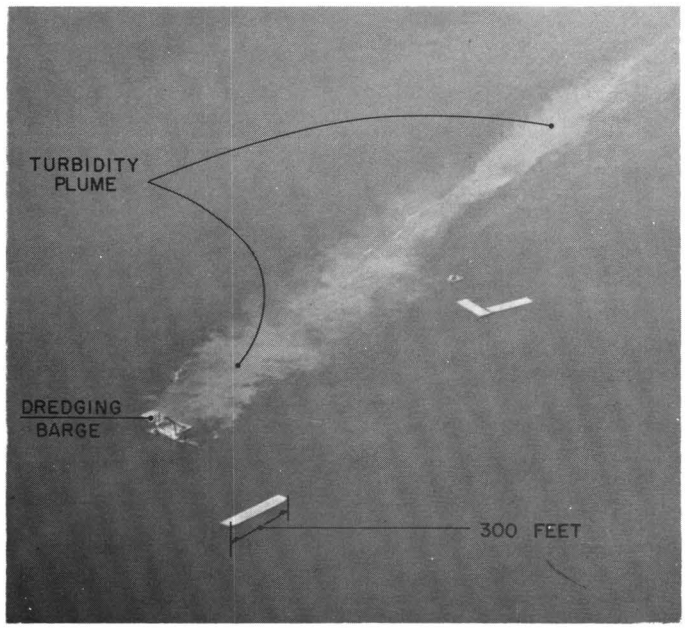


FIGURE 234 (left).—Oblique aerial photograph of shell-dredging operations and turbidity plume. View looking southeast. U.S. Geological Survey photograph by Carl R. Goodwin.

FIGURE 235 (below left).—Sketch map showing observations of turbidity in Tampa Bay.

FIGURE 236 (below right).—Velocity-vector grid of turbidity in Tampa Bay. The barbs indicate current flow direction; the shaft lengths are proportional to current velocity.

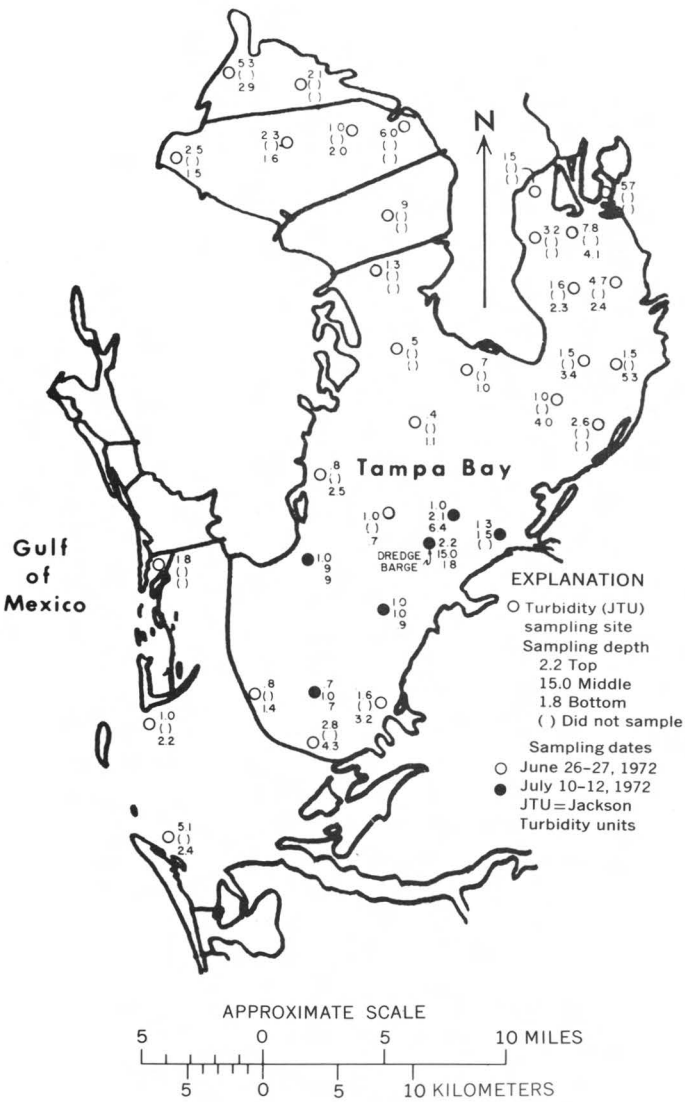


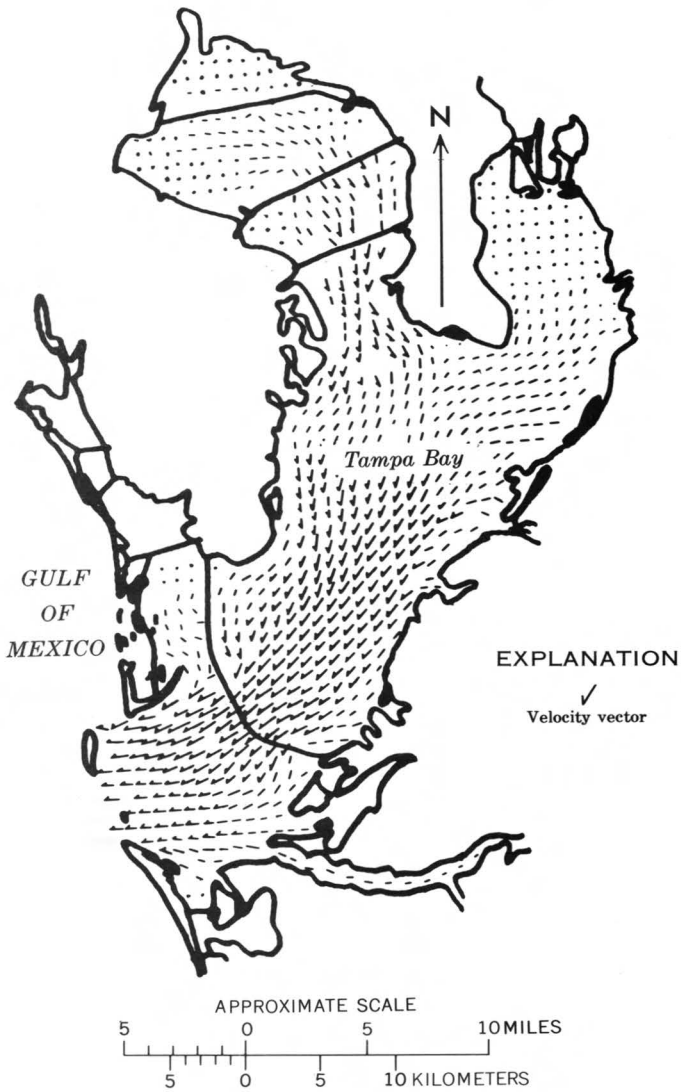

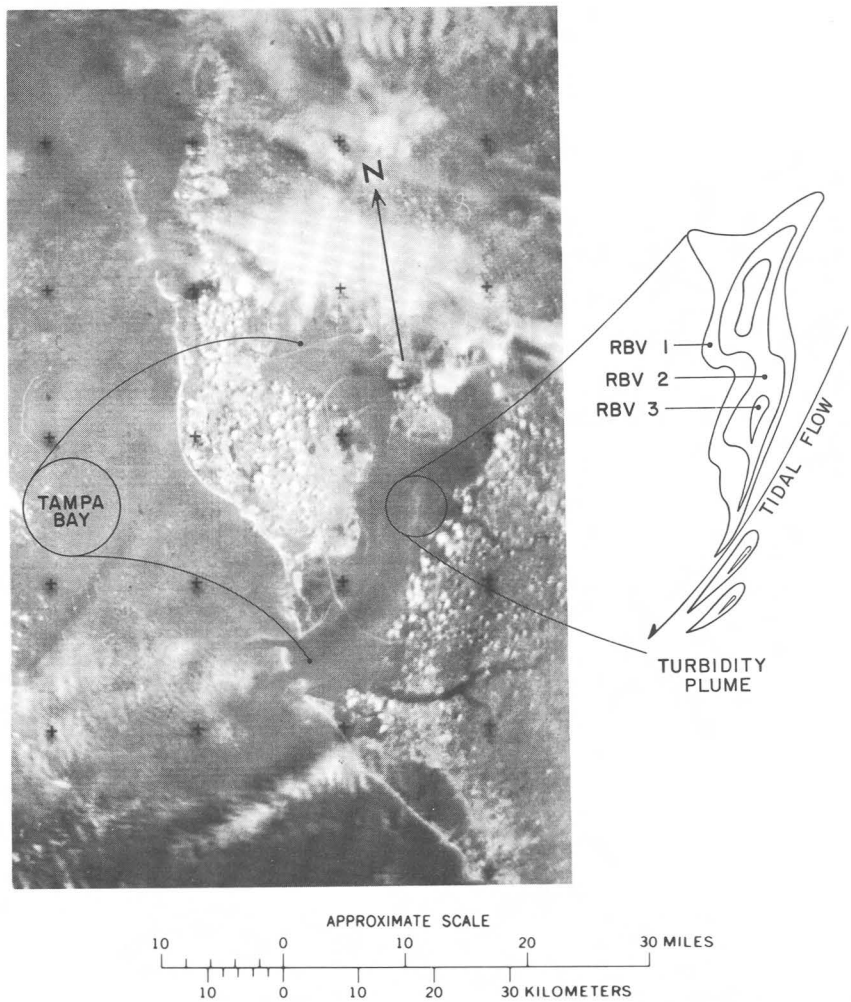


FIGURE 237.—A black and white photograph of RBV bands enhanced by a color-additive viewer and a sketch map of turbidity plume.

turbid waters will be more reflective than the less turbid waters and will appear as lighter gray tones on the imagery.

Assuming that the bay water is slightly turbid (fig. 235), a three-dimensional concept of the shape of the more turbid plume may be demonstrated by superimposing those parts of the plume observed in all three bands (fig. 237). On both band 1 and band 2, positive images, the sediment plume is depicted by lighter gray tones near the center and darker tones of lower reflectance at the outer edges of the plume. The turbidity-plume boundaries in band 1 extend beyond those in bands 2 or 3 and may be areas of deeper settling depths and/or contain less particulate matter in suspension (fig. 237). The energy span of band 3 is mostly absorbed by water at the surface, and only the particulate matter at the surface reflects light. The part of the plume at the surface may be delineated by lighter gray tones in the imagery of this band. This part of the plume may also contain recently suspended material that may be more highly concentrated. The movement of the plume toward the mouth of the bay is in response to ebb-tide conditions at the time of ERTS overpass.

Before ERTS, the extent of dispersion of dredging silt plumes in an area as extensive as Tampa Bay (more than 770 km$^2$) could only be made on a chart by connecting stations having equal turbidity as measured in a massive sampling program, but the positions and number of transects for turbidity sampling did not usually allow complete synoptic coverage showing the dynamic distribution of the turbidity plume. Furthermore, compared with ordinary massive sampling programs, the associated field data needed for correlation with the ERTS imagery may be considerably reduced in number of transects and samples across the bay.

# MOVEMENT OF TURBID-WATER MASSES ALONG THE TEXAS COAST

By Ralph E. Hunter,
U.S. Geological Survey

The dynamic nature of turbid-water masses in the Gulf of Mexico near the Texas coast is well illustrated by the complex patterns in these two ERTS images (figs. 238, 239), taken on successive days in late fall 1973.

Certain features of the system of marine currents over the inner Continental Shelf can be deduced from images such as this. For example, these images show plumes of turbid water from the tidal inlets being deflected by southwestward coastal currents. Plumes formed by river discharge are similarly deflected, but individual river plumes are difficult to identify.

Several fingerlike bands of turbid water not related to tidal inlets or river mouths can be seen projecting obliquely seaward from the nearshore zone of turbid water. Although evidence for the origin of these bands is not obvious in this image, studies of other images suggest that the bands can be related to flow direction in two different ways. Some bands of turbid water are parallel to the current; if the bands in this image are of this type, their orientation indicates that the flow was obliquely seaward. Other bands of turbid water are oblique to the current and are being gradually deformed by current shear; if the fingers in the image were being sheared by a current flowing southwestward parallel to the coast, their orientation indicates that the velocity of the current increased in an offshore direction.

Several gyres can be seen along the shoreward edge of the offshore mass of turbid water in figure 239. Their counterclockwise rotation indicates current shear in a left-lateral sense. Comparison of this image with one overlapping this area on the previous day (fig. 238) suggests that these and other features in the offshore turbid-water mass remained identifiable while drifting during this time. The movement of these features indicates that the current was flowing southwestward approximately parallel to shore and that it ranged in speed from about 0.2 m/s at a distance of 25 to 30 km from shore to about 0.1 m/s at a distance of 50 to 60 km from shore. The greatest speed probably occurred within the zone of clear water at a distance of 15 to 20 km from shore. Zones of rapid flow paralleling the shore, such as the one interpreted as occurring in this image, have been called coastal jets by some oceanographers.

The evidence on current patterns furnished by remote-sensing data in areas of turbid water can be a valuable complement to data obtained from the movement of surface and bottom drifters or drogues and from current meters placed at selected points over extended periods of time.

ERTS–1 imagery has furnished valuable information on the sources, distribution, and movement of suspended sediment in the northwestern Gulf of Mexico; much of this information could hardly be obtained in any other way and certainly could not be obtained over such large areas at such frequent intervals other than by satellites. Measurements of current velocity from single images have proven possible where the place and time of origin of detached plumes from tidal inlets could be inferred, and measurements by time-lapse methods have proven possible in the areas of overlap between images taken on successive days. In addition, the patterns of turbidity variation in the imagery reveal a wealth of detail on current directions and relative velocities (Hunter, 1973).

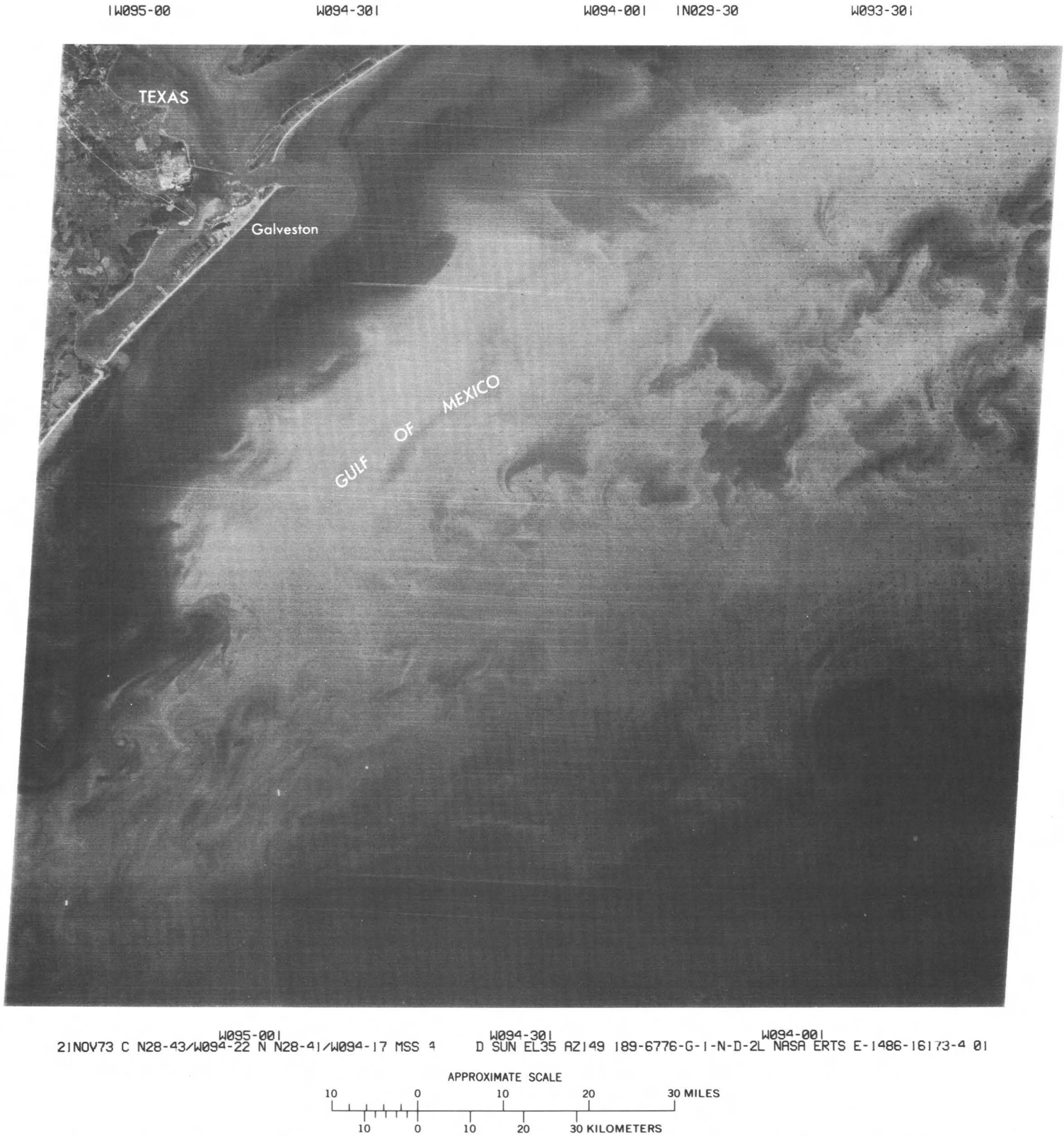


FIGURE 238.—Turbidity patterns in the Gulf of Mexico and Galveston Bay on annotated ERTS–1 image 1486–16173, band 4, on Nov. 21, 1973.

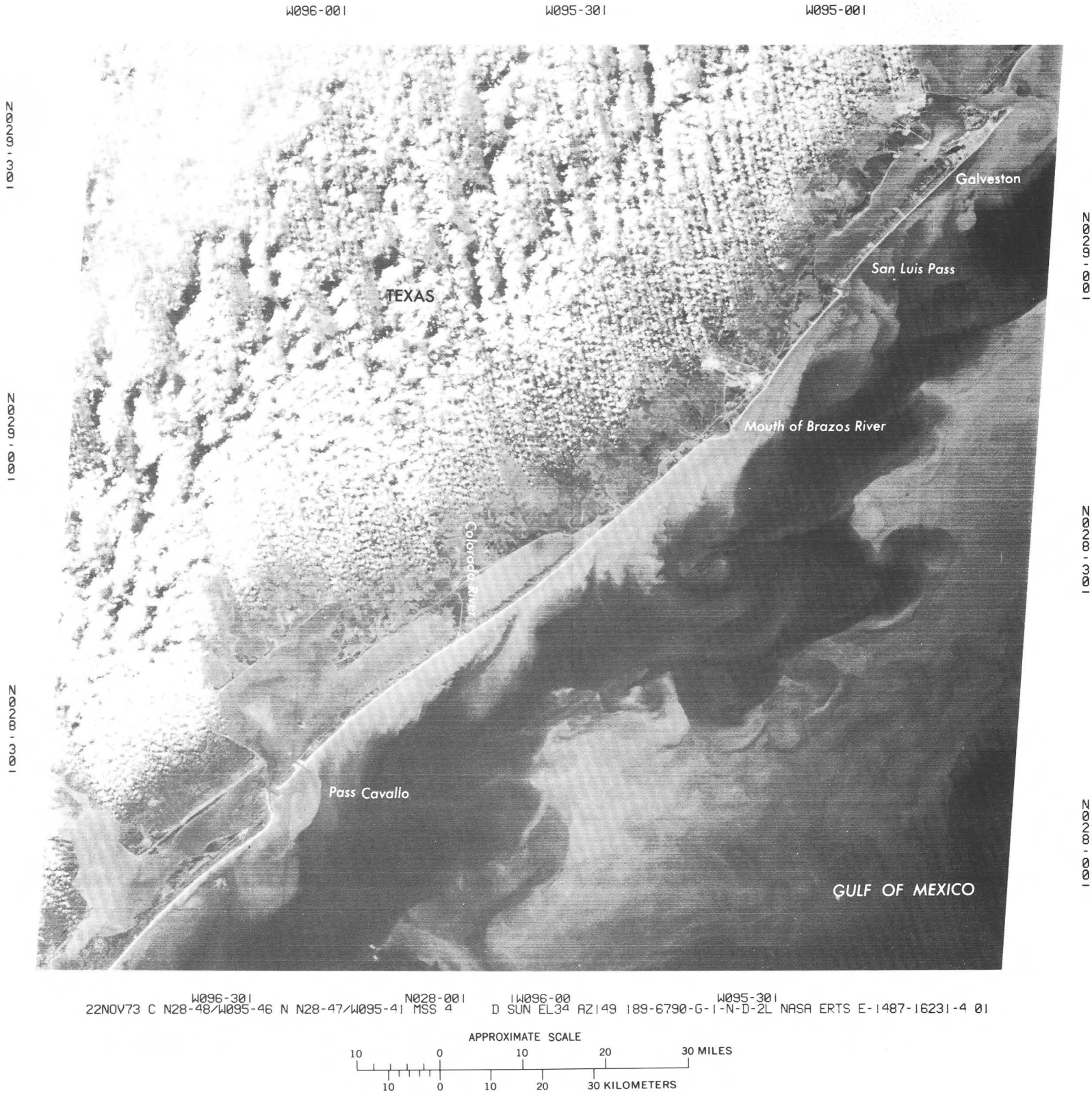


FIGURE 239.—Turbidity patterns along the Texas coast between Galveston and Pass Cavallo on annotated ERTS–1 image 1487–16231, band 4, on Nov. 22, 1973.

# TRACKING ICE FLOES BY SEQUENTIAL ERTS IMAGERY

By William J. Campbell,
U.S. Geological Survey

One of the most difficult measurements in the study of sea ice is to track accurately the trajectory of specific floes. Until very recently the only means of doing this was to have men live on them and make frequent celestial navigational fixes—a very costly, inefficient, and inaccurate approach. Recent experiments by the AIDJEX using unmanned drifting buoys tracked by the Interrogation, Recording, and Location Subsystem on Nimbus–4 have shown that accurate trajectories can be obtained in this way, but the initial cost and emplacement of these buoys are expensive. A recent paper by Campbell and others (1973) has shown how ERTS images can be used to track ice floes, and how images can help interpret data on drifting ice floes obtained from unmanned drift buoys.

In this study two large ice floes in the eastern Beaufort Sea in the Arctic were tracked for the period from Aug. 2 to Sept. 24, 1972, on sequential ERTS imagery of the area. The two floes tracked are shown in figure 240, an ERTS image acquired on Aug. 19, 1972. These were large ice floes measuring 13×28 km (upper right) and 16×27 km (right center), and existed at the edge of the icepack, which was made up of predominantly big floes of about the same size.

The trajectories of these floes, as measured from five sequential ERTS images (Aug. 2 and 19 and Sept. 4, 21, and 24, 1972) are shown in figure 241. The two floes drifted in a similar fashion, and considerable relative strains (relative displacement between two floes) occurred. During the August 19 to September 4 drift, the floes converged with a strain rate of 35 percent (percentage of spatial displacement between floes within a given time interval) in 15 days (2.33 percent per day), and during the September 4 to 21 drift, they diverged with a strain rate of 26 percent in 17 days (1.53 percent per day). Much open water bordered these floes during this period, which allowed the icepack to deform easily, but such large strains have also been observed deep within the arctic ice cover. During the 40 days that these two floes were being observed, only one underwent any weathering; about 20 percent of its area was broken off. Both of these floes were composed of multiyear ice generally 3 to 4 m thick.

These measurements illustrate the extremely dynamic nature of the arctic ice cover. ERTS is providing the first high-resolution imagery that permits sea-ice dynamics and deformation to be accurately measured over wide areas. These data are fundamentally important in the development of numerical models to predict sea-ice dynamics, and if man is ever to operate ships safely in the Arctic Ocean, it will be necessary that such data be acquired on a regular real-time basis.

A recent study by Weeks and Campbell (1973) has suggested the possibility of towing antarctic icebergs to selected sites where they could be used as a water resource. In order to do this, however, it would be necessary to locate and track icebergs of the desired size in the antarctic seas. ERTS imagery has been used by Hult and Ostrander (1973) to study the motion of antarctic icebergs. This study has shown that ERTS is an excellent means of studying antarctic iceberg formation and motion.

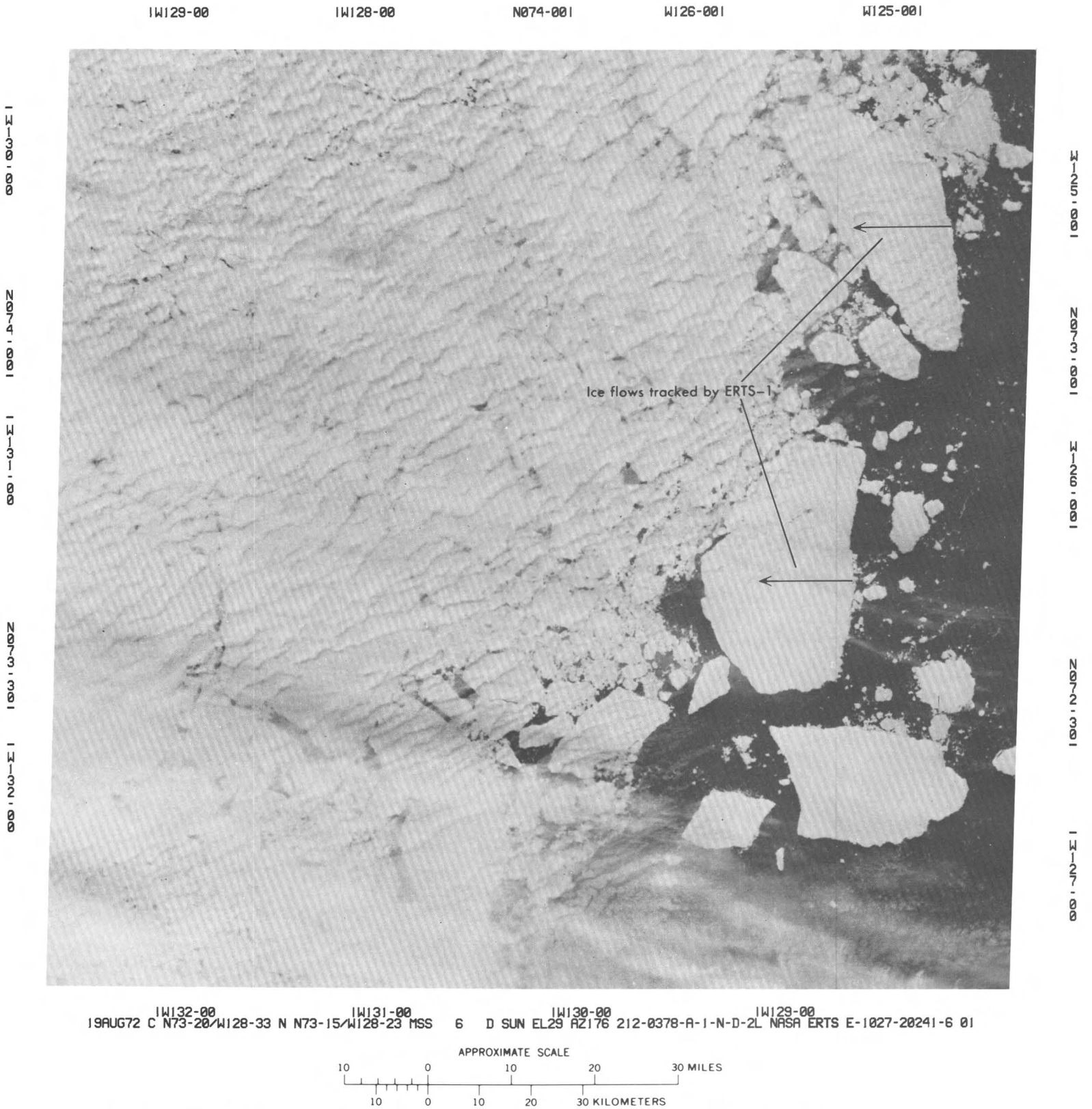


FIGURE 240.—ERTS–1 image of ice floes in the eastern Beaufort Sea on Aug. 19, 1972 (1027–20241, band 6).

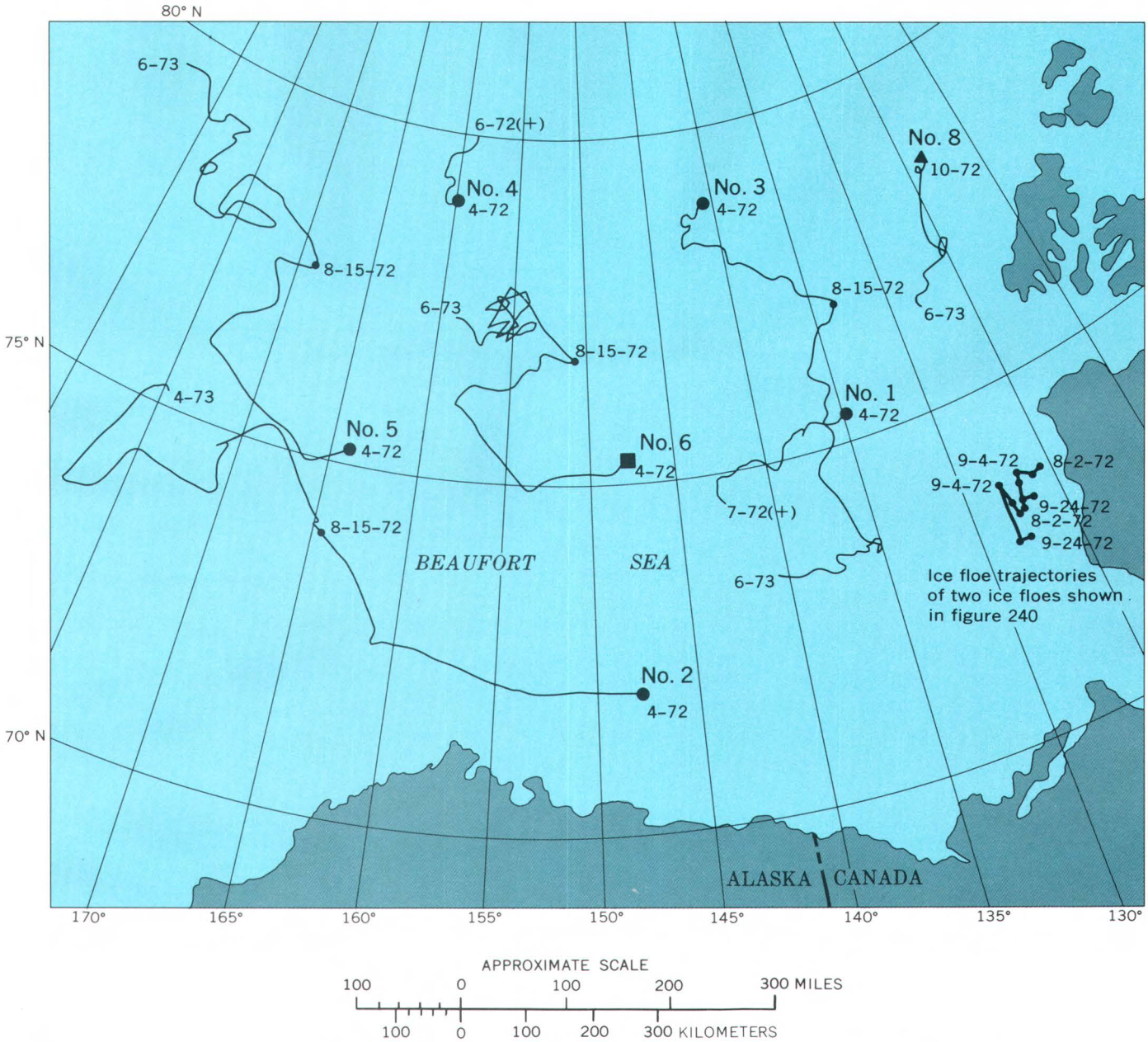


FIGURE 241.—Map showing trajectories of the two ice floes shown in figure 240 (Aug. 2, 1972, 1010–20293; Aug. 19, 1972, 1027–20241; Sept. 4. 1972, 1043–20125; Sept. 21, 1972, 1060–20070; and Sept. 24, 1972, 1063–20241). Other numbers (1–6, 8) and trajectories show movement of unmanned drifting buoys tracked by Nimbus–4.

# ICE LEAD AND POLYNYA DYNAMICS

By William J. Campbell,
U.S. Geological Survey

In order to test any numerical model for the dynamics and thermodynamics of ice-covered oceans, it is necessary to acquire sequential synoptic imagery of the changes in the thickness of the ice cover and its fracturing under the influences of the forces operating upon it: air stress, water drag, internal ice stress, Coriolis force, and gradient current forces. High-resolution imagery is especially important for testing models based on floe-to-floe interactions. The only existing remote-sensing satellite that provides imagery having sufficiently high resolution is ERTS. All the remote-sensing plans for AIDJEX, whose main experiment will take place from the spring of 1975 to the spring of 1976, call for the use of all ERTS imagery obtained of the Arctic Ocean ice cover.

Although ERTS cannot directly measure the thickness of the ice cover, it can be used to distinguish between classes of ice thickness and to monitor changes within each class. In figure 242, a section of the ice cover of the Arctic Ocean deep within the Beaufort Sea is shown. At the time this image was obtained, a light wind was blowing on the surface from the northeast. Large floes of first-year ice or multiyear ice (the whitest ice seen in the image), which vary in thickness from approximately 1.5 to 3 m, can be seen separated by refrozen polynyas filled with gray ice, which is 20 to 40 cm thick. Also, numerous new leads can be seen that are either open or have very thin ice covers (a few centimeters thick) on them. In the center of the image, a large refrozen polynya that runs approximately north-south is composed of two distinct zones of gray ice that have been formed by two separate opening events of the original lead.

Figure 243 shows approximately the same area 1 day later, during which time a moderate wind continued to blow from the northeast. Strong divergence of ice has occurred, and the large polynya has increased in width, the new lead on the eastern side of the polynya having expanded approximately 4 km. Within this polynya, four distinct zones can clearly be seen: (1) a zone of open water immediately adjacent to the eastern edge of the polynya, (2) a zone of thin gray ice formed very recently by the freezing of the grease ice (ice slush), (3) a zone of earlier formed gray ice 20 to 40 cm thick, and (4) a zone of older gray ice 40 to 60 cm thick. A significant internal ice stress has occurred, causing strong deformation in the period between these images, as shown by the recent fracturing of the gray ice in the polynyas.

When ERTS images such as these are combined with surface measurements, as they will be during the main AIDJEX experiment, they will give invaluable information needed to test prediction models for sea-ice dynamics and thermodynamics.

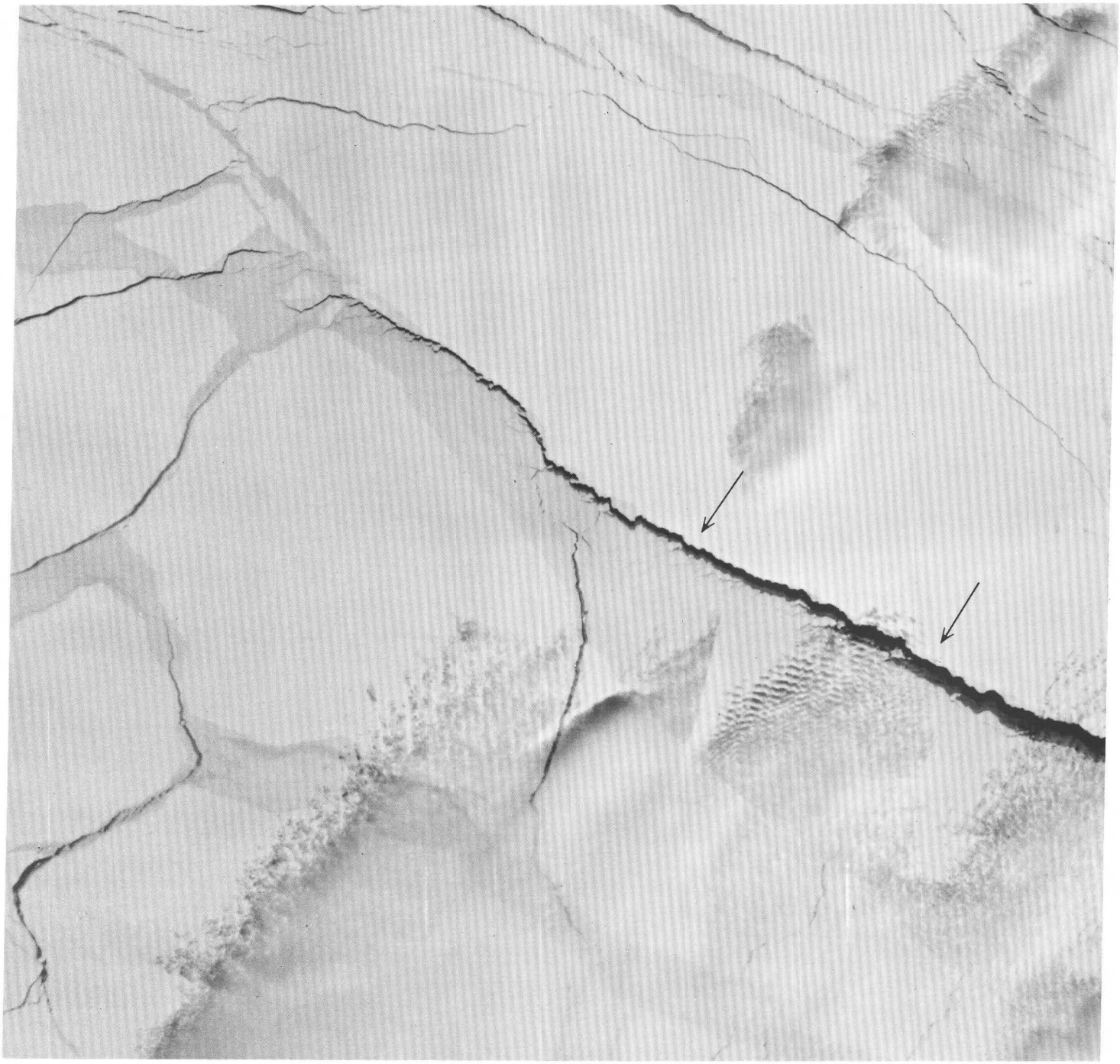


FIGURE 242.—ERTS–1 image of the ice cover in the central Beaufort Sea on Apr. 5, 1973 (1256–21391, band 6); polynya is indicated by arrows.

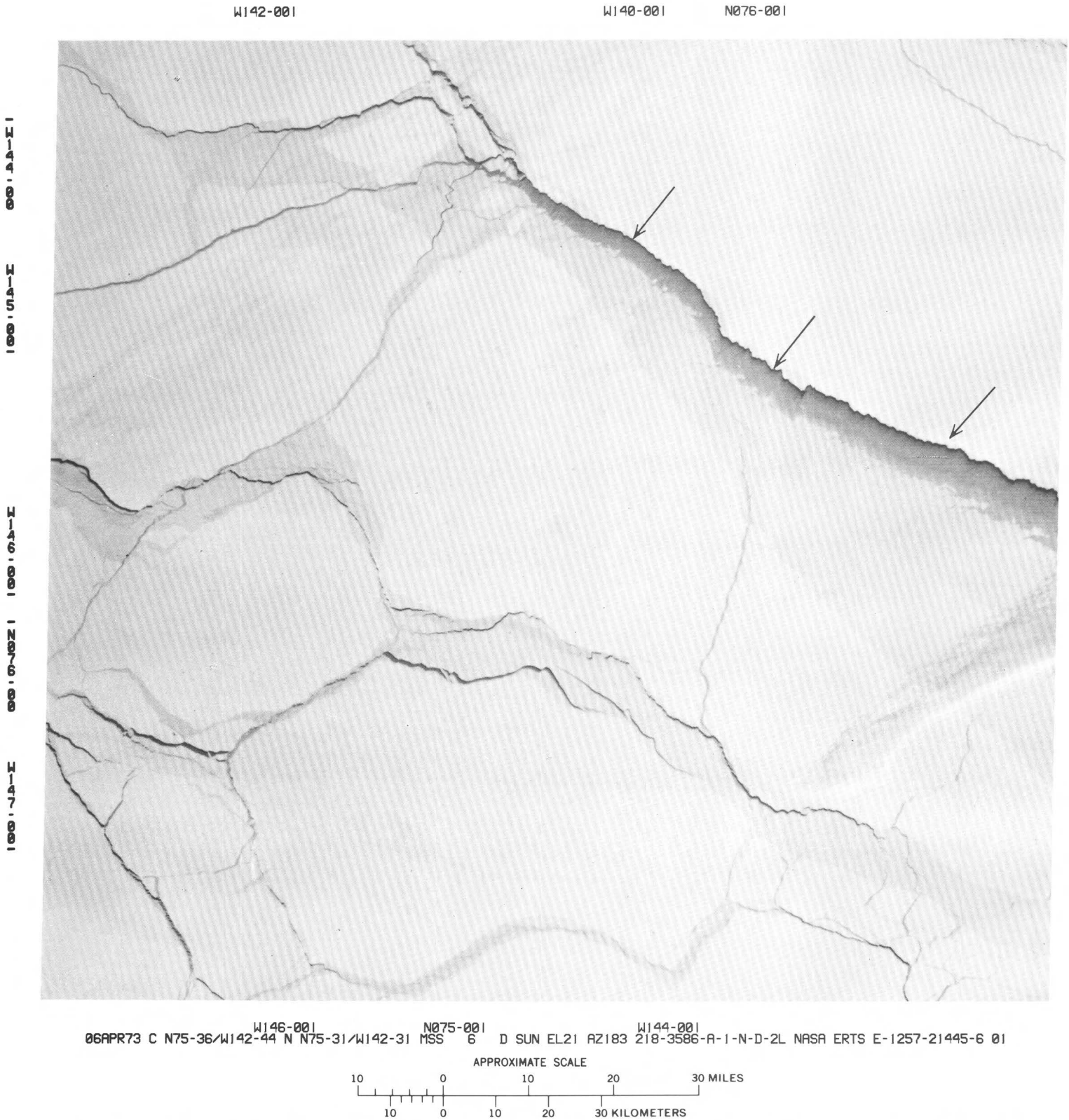


FIGURE 243.— ERTS–1 image of the ice cover in the central Beaufort Sea on Apr. 6, 1973 (1257–21445, band 6), 1 day after figure 242 was imaged; large polynya is indicated by arrows.

# SEASONAL METAMORPHOSIS OF SEA ICE

By William J. Campbell,
U.S. Geological Survey

Not only does sea ice undergo large dynamic and morphologic changes in a short time, it also undergoes significant seasonal changes; especially significant is the change that occurs when winter ice metamorphoses into summer ice. During most of the year, a strong temperature gradient exists in the ice cover that acts as a thin insulating veneer about 3 to 4 m thick. The ice cover separates two fluids at distinctly different temperatures—the sea water having a typical surface temperature of −1.7°C and the surface air temperature during the winter of −30° to −40°C. In the summertime the ice becomes isothermal, and many melt ponds form on its upper surface that are important both for thermodynamic and morphologic reasons. Because they cover from a fifth to a third of the total area of the ice cover at the peak of the summer melt period, the melt ponds are a major item in determining the summertime heat balance of the ice cover. When they refreeze, they form lenses of relatively homogeneous ice with fairly uniform salinity within ice floes having a varying vertical structure.

In figure 244, a very large area of sea ice in the eastern Beaufort Sea is shown before the onset of the summer melt. Five very large ice floes, with approximate dimensions of 40×50 km, are seen to be composed of cemented pieces of very thick ice. The leads and polynyas that appear gray are covered with gray ice from 20 to 40 cm thick, whereas those that appear black probably have no ice on them.

In figure 245, the same area of sea ice is shown 17 days later. During the period between these images, the segment of sea ice has undergone translation within the Beaufort Sea with a net movement to the west of approximately 30 km. Over the entire area of sea ice, numerous melt ponds have now formed. It is difficult to estimate visually the total area covered by the melt ponds, but it is about 20 to 30 percent. (One could make a more accurate estimate by using density-slicing techniques.) It can be seen that by the time of this image, all the gray ice observed earlier had melted, and the entire icefield is now made up of thick ice floes. The large floes visible in the earlier image can clearly be seen to have undergone no weathering, and therefore probably the greater part of the ice seen in these images is multiyear sea ice with an average thickness of 4 m.

Another interesting thing that can be observed by comparing these two figures is that little deformation occurred during the 17 days between observations. The relative positions of all the major floes are the same, and therefore the ice has not been subjected to any strong shearing or stretching deformation.

These images clearly show that the sequential synoptic high-resolution capability of ERTS will provide invaluable data on sea-ice dynamics and morphology on both a day-to-day and a seasonal basis.

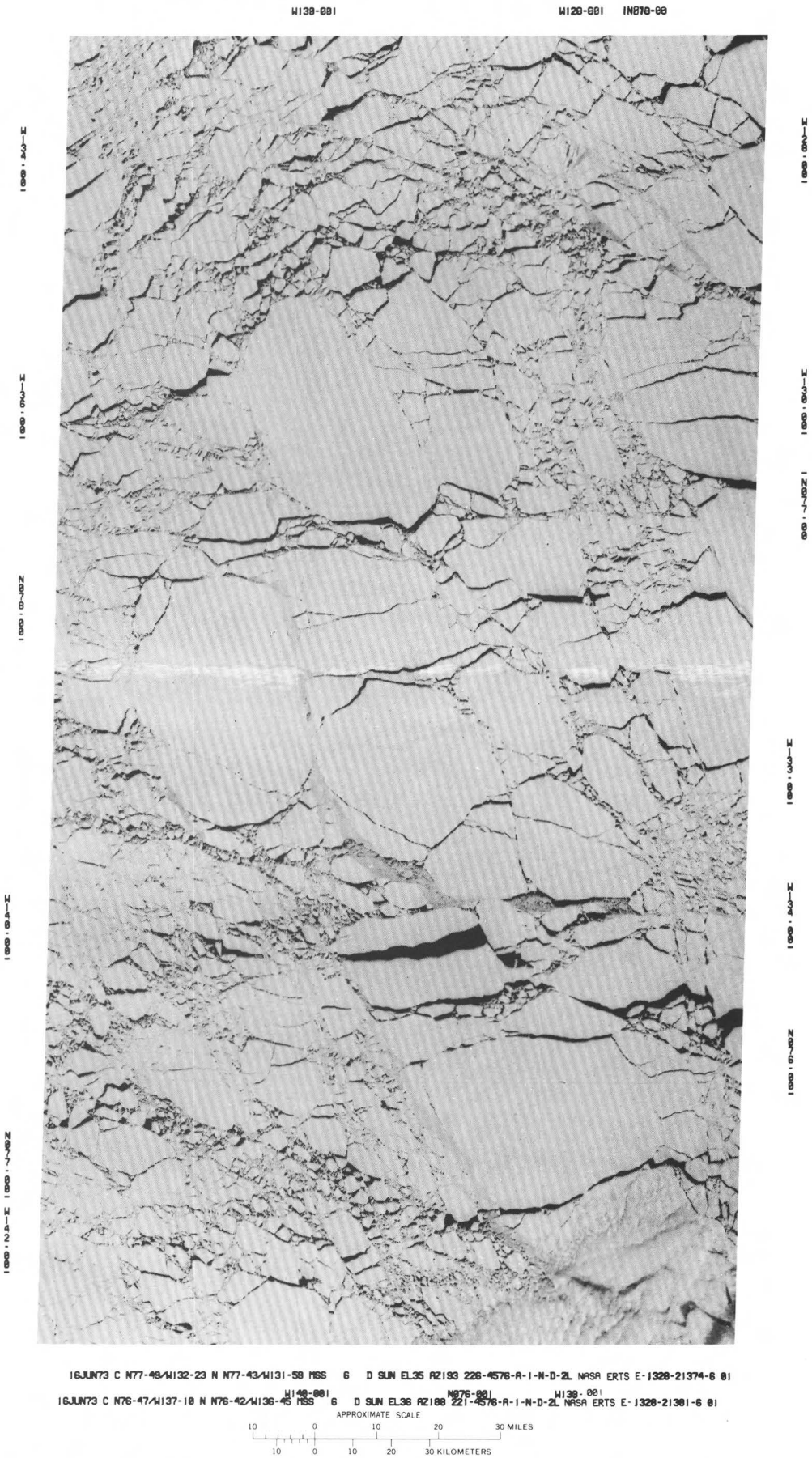


FIGURE 244.—ERTS–1 image mosaic of large ice floes in the eastern Beaufort Sea on June 16, 1973, before onset of the summer melt (1328–21374 and 1328–21381, band 6).

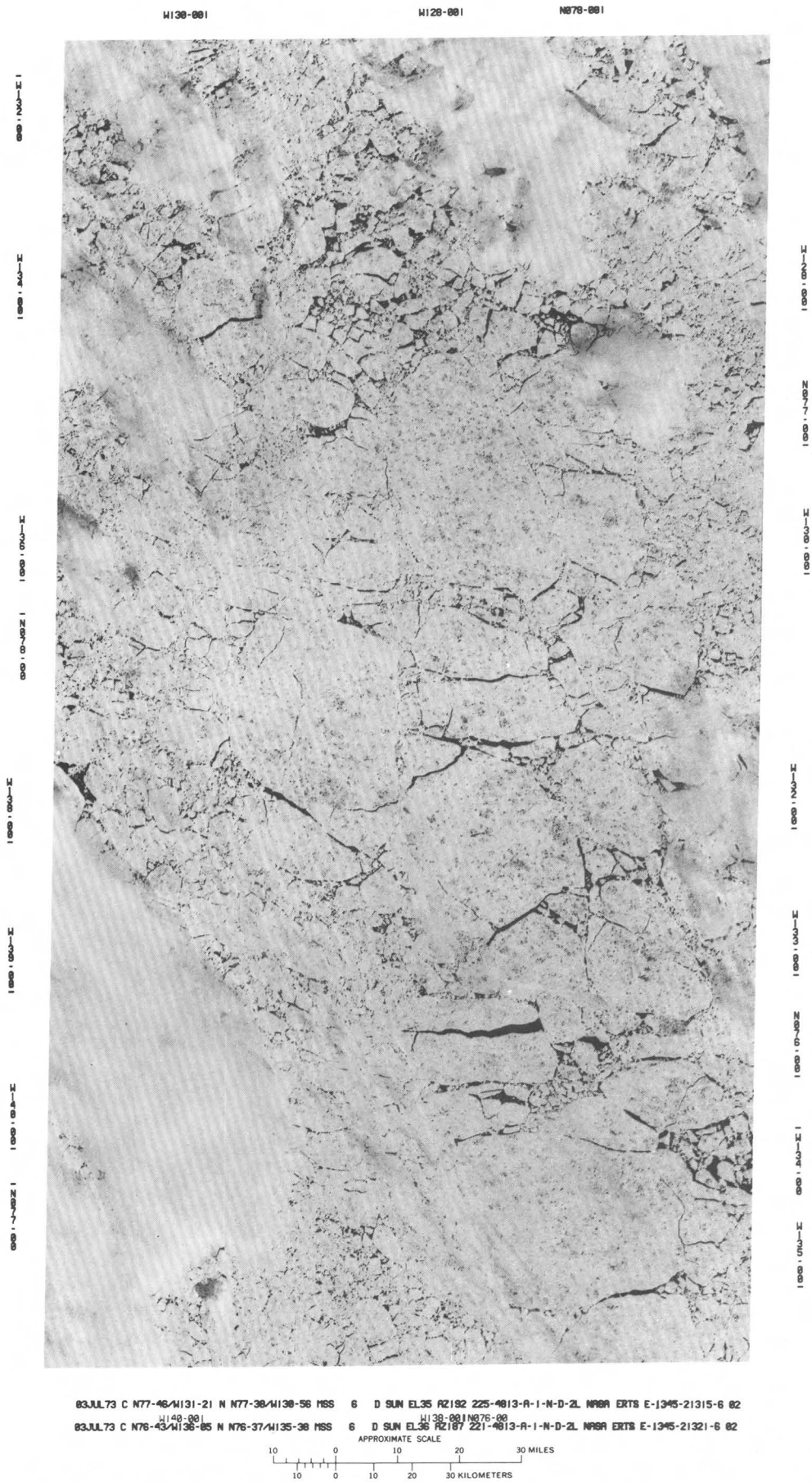


FIGURE 245.—ERTS–1 image mosaic of large ice floes in the eastern Beaufort Sea 17 days after the image in figure 244 (1345–21315 and 1345–21321, band 6).

# DYNAMICS OF ARCTIC ICE-SHEAR ZONES

By William J. Campbell,
U.S. Geological Survey

The arctic ice-shear zone, which borders the northern coast of Alaska and Canada, varies in width from several kilometers to several hundred kilometers and on the average closely corresponds to the width of the Continental Shelf. It is within this shear zone that all the offshore exploration for oil will occur in the foreseeable future. In addition, all proposed arctic shipping must use this same zone. For these reasons, interest in the ice-shear zones in the Beaufort Sea has grown steadily and has resulted in the formation of two international programs to study the morphology and dynamics of arctic sea ice, AIDJEX and the Polar Experiment. Scientists involved in these large-scale studies think that more knowledge of the ice-shear-zone dynamics is of fundamental importance for understanding the dynamics of the ice cover on the interior part of the Arctic Ocean.

ERTS imagery has provided valuable information on the morphology and dynamics of the arctic ice-shear zone. In figure 246, a section of the northwest coast of Banks Island, Northwest Territories, Canada, is shown with its adjacent shear zone. At the time this image was acquired, a strong surface wind was blowing straight off the coast toward the ice, and a recently opened lead can be seen along the entire segment of the coastline. Between the recently opened shore lead and the consolidated pack ice, which is approximately 25 km away, a band of gray ice has formed in the previously opened shore lead. Figure 246, therefore, shows three distinct zones of ice: (1) the shore lead in which frazil ice (groups of needlelike crystals of ice) and grease ice (ice slush) are forming; (2) a zone of recently formed gray ice approximately 20 km wide, which is probably 20 to 30 cm thick; and (3) large consolidated floes of first-year ice, which are probably 1.5 m thick.

In figure 247, the same area is shown approximately 24 h later. The offshore wind continued to blow, and the first-year ice zone is being moved farther offshore, moving about 14 km in 1 day. The gray ice has undergone rafting in several places where the lighter colored bands can be seen running parallel to the shore in the gray-ice zone. The shore lead has remained open along the entire segment of coast, and ice plumes of grease and frazil ice can be seen forming.

Figure 248 shows the same area 17 days later. During this period the first-year ice has been strongly moved to the southwest, and the gray-ice zone is now approximately 40 km wide. At the time this image was obtained, the wind was again blowing offshore, and a recently formed shore lead can be seen. The gray-ice zone by this time was 20 to 30 cm thick, and pieces of shore-fast ice have been stripped off the coast and are adrift in the shore-lead zone. The first-year ice in the northeastern segment of the coast has been pushed strongly against the coast and has undergone heavy fracturing, forming many floes. Thus, the ERTS images clearly show the extremely dynamic nature of the ice-shear zone and its concomitant complex morphological changes.

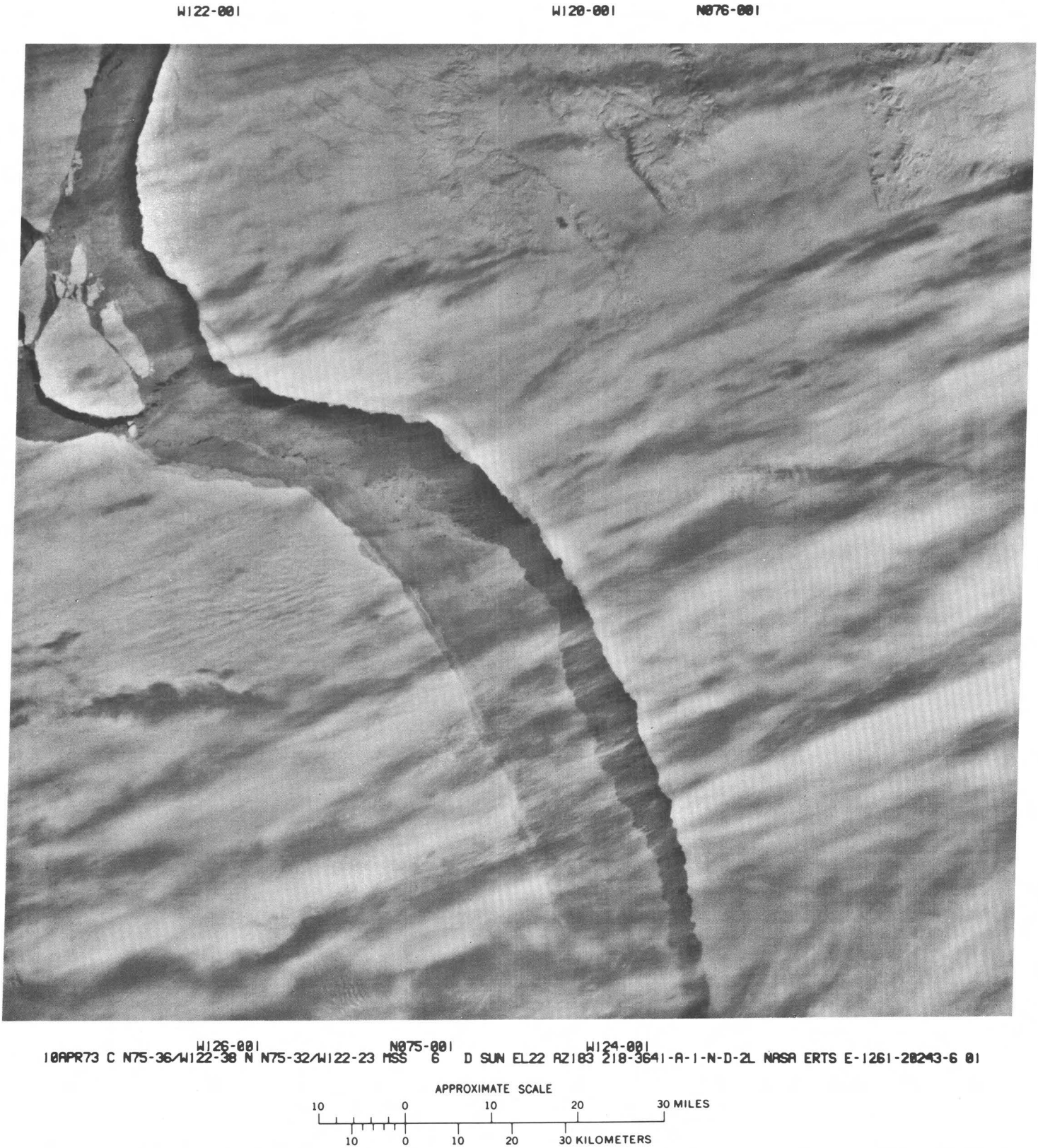


FIGURE 246.—ERTS–1 image of the northwest coast of Banks Island, Northwest Territories, Canada (1261–20243, band 6), Apr. 10, 1973.

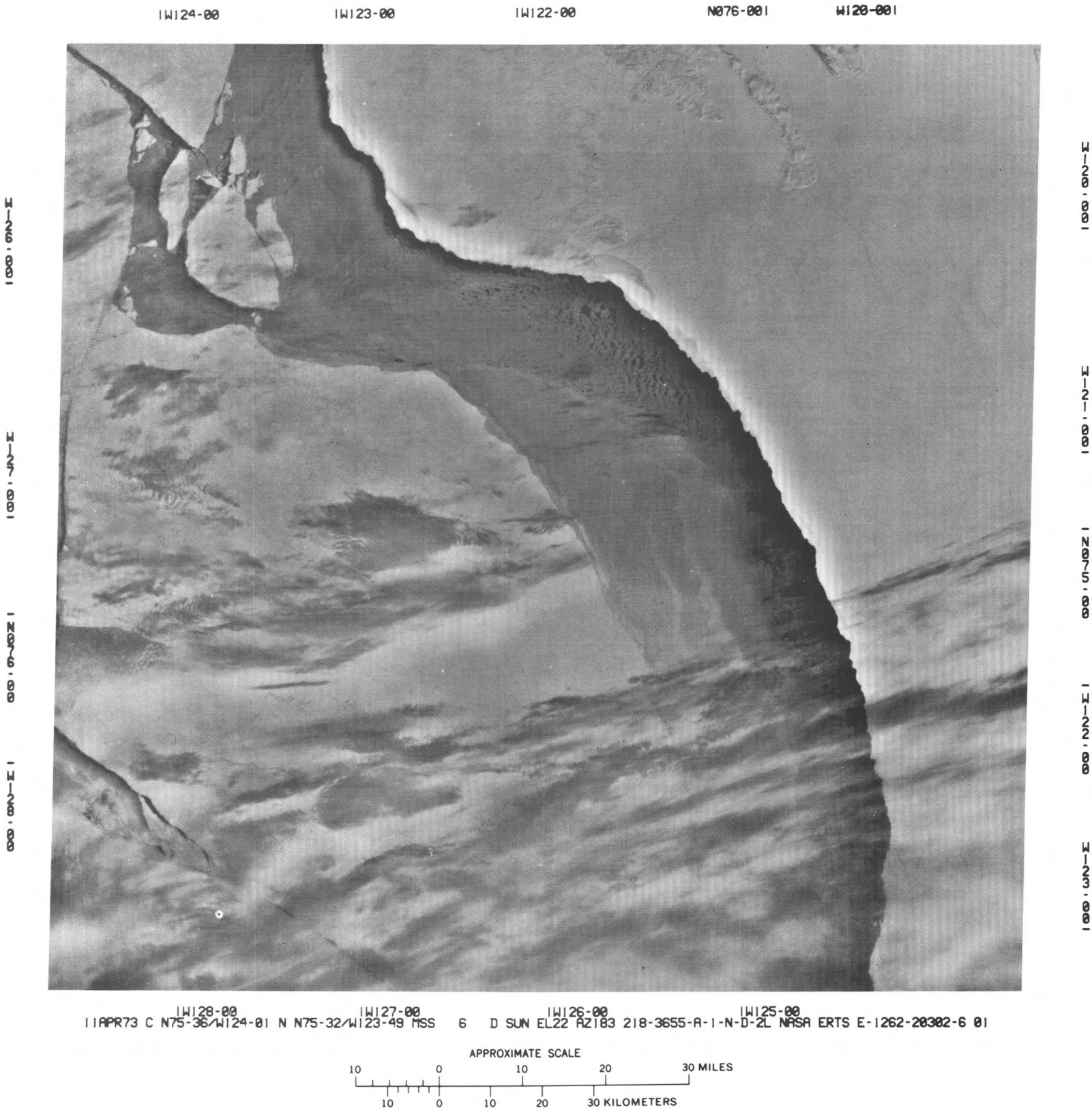


FIGURE 247.—ERTS–1 image of the northwest coast of Banks Island, Northwest Territories, Canada (1262–20302, band 6), 24 h after figure 246 was imaged.

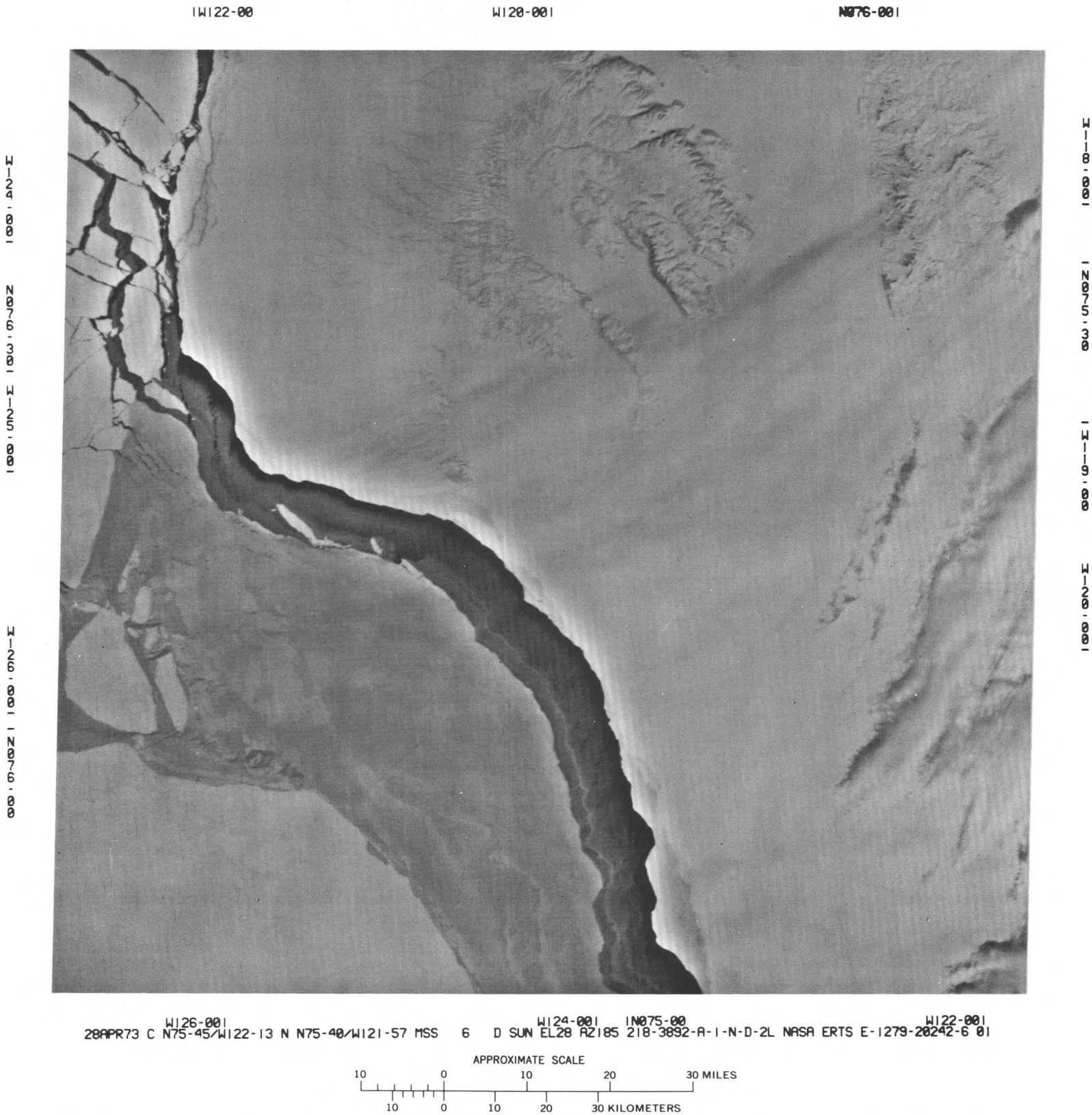


FIGURE 248.—ERTS–1 image of northwest coast of Banks Island, Northwest Territories, Canada (1279–20242, band 6), 17 days after figure 247 was imaged.

# MORPHOLOGY OF BEAUFORT SEA ICE

By William J. Campbell,

U.S. Geological Survey

Sea ice is the most dynamic solid feature on the Earth's surface. At any given moment, sea ice covers approximately 13 percent of the Earth's ocean area. Because of the increased scientific awareness of the important role sea ice plays in determining the polar heat balance, and thus the climate of the Earth, major international research programs such as the AIDJEX and the Polar Experiment have been formed to expand scientific studies of the dynamic and thermodynamic interactions of ocean, ice, and atmosphere.

ERTS imagery has been used by AIDJEX to study the morphology and dynamics of sea ice in the Beaufort Sea. Campbell and others (1973) have shown how a variety of measurements from ERTS–1, Nimbus–4, and Nimbus–5 satellites, when used jointly with data from aircraft and drift stations, show that the morphology of the ice cover of the Beaufort Sea is not uniform and is more complex than hitherto realized. As an example of the use of imagery, on Aug. 22, 1972, ERTS–1 obtained images in both the eastern and western Beaufort Sea. Figure 249 is a mosaic of ERTS imagery of an area 160×480 km in the eastern Beaufort Sea. Large round ice floes cover most of the area, 10 being more than 35 km across and some being as large as 55 km across. These floes can be identified in images obtained a month earlier, and, in the summer period between these observations, the images show that the floes underwent little weathering while moving toward the southwest. The longest sequence of ERTS–1 images covering one section was from Aug. 17 to Sept. 24, 1972, and consisted of five passes over an area just east of that shown in figure 249. The shape and size of the large floes observed in the eastern Beaufort Sea resemble those of major floes shown in microwave images obtained in this area during the 1971 AIDJEX–NASA Remote Sensing Experiment (Gloersen and others, 1973).

Also on Aug. 22, 1972, 200 min after the images comprising figure 249 were obtained, ERTS–1 passed over the western Beaufort Sea and obtained the images shown mosaiced in figure 250. The most striking difference between this mosaic and figure 249 is the complete absence of any big floes. The mean size of the floes in the western area is more than an order of magnitude smaller than those in the eastern area; typical floes are 1 to 2 km across. Also, they are not round but have angular fragmented shapes. It is important to bear in mind that these mosaics show ice floes at the same latitude and are essentially synoptic. The shape and size of these small angular ice floes in the western Beaufort Sea resemble those of ice floes shown in microwave images

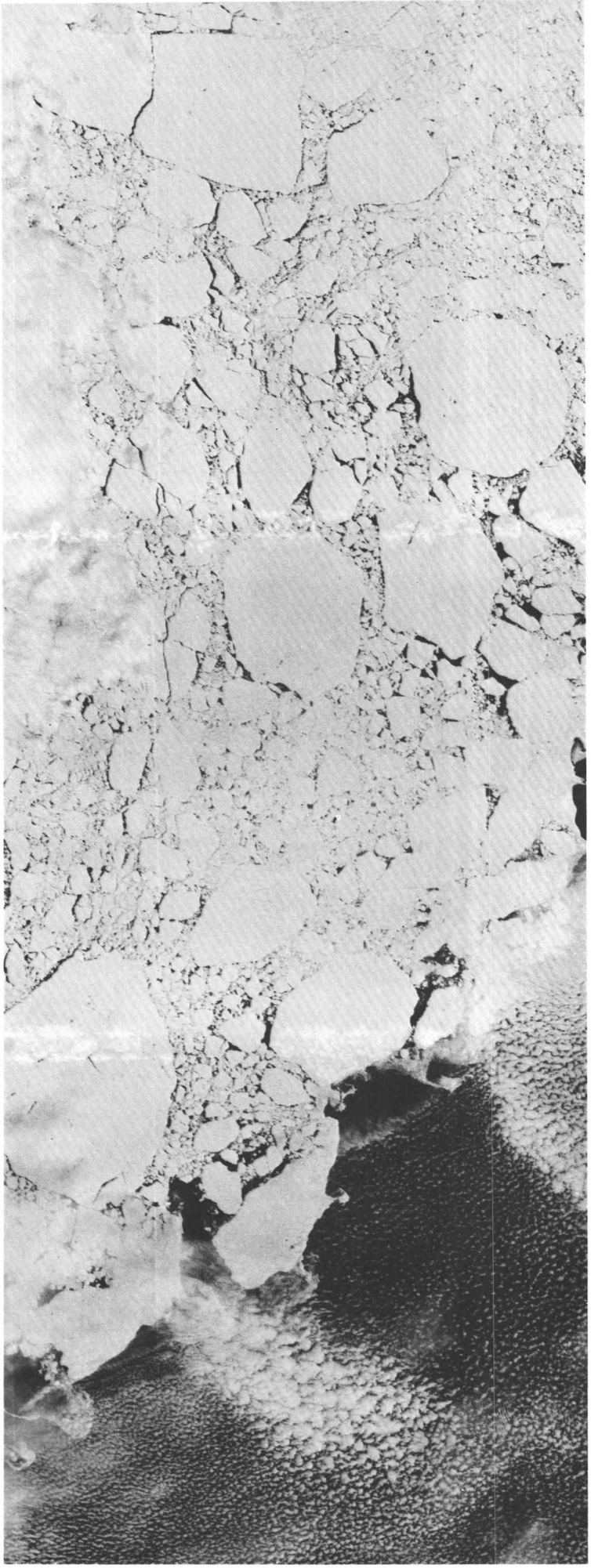

22AUG72 C N74-26/W129-48 N N74-25/W129-43 MSS 6 D SUN EL27 AZ179 215-0420-A-1-N-D-2L NASA ERTS E-1030-20410-6 01

22AUG72 C N73-14/W132-50 N N73-13/W132-46 MSS 6 D SUN EL28 AZ176 212-0420-A-1-N-D-2L NASA ERTS E-1030-20412-6 01

22AUG72 C N71-60/W135-30 N N7 -59/W135-26 MSS 6 D SUN EL29 AZ173 210-0420-A-1-N-D-2L NASA ERTS E-1030-20415-6 01

APPROXIMATE SCALE

FIGURE 249.—ERTS–1 image mosaic of the eastern Beaufort Sea on Aug. 22, 1972 (1030–20410, 1030–20412, and 1030–20415, band 6).

obtained in the same area during the 1972 AIDJEX–NASA Remote Sensing Experiment (Campbell and others, 1973).

Figure 251 shows a mosaic of ERTS–1 images obtained on Sept. 8, 1972; the area is slightly east of that shown in figure 249. From surface measurements of drifting buoys of the AIDJEX-Interrogation, Recording, and Location Subsystem, we know that the ice shown in this image was positioned 95 km to the east on Aug. 22, 1972. The floes in the western part of this mosaic resemble the many small floes visible in figure 250, but in the south-center section a band of larger rounded floes is seen.

Therefore, the ERTS images give us a picture of the southern Beaufort Sea in which the eastern sector is made up of large rounded ice floes, the western sector is made up of small angular floes, and the central sector is made up of small floes and a few larger rounded ones. From the fact that the large rounded floes in the eastern sector were tracked throughout the summer with ERTS images and underwent very little weathering, we can surmise that they were multiyear ice floes having average thicknesses of 3 to 4 m. But we cannot, using ERTS alone, accurately determine the age and type of ice shown in the central and western Beaufort Sea.

The 1971 and 1972 AIDJEX–NASA Remote Sensing Experiments showed that multiyear ice has a "cool" radiometric signature in the 1.55-cm wavelength, whereas first-year ice has a "warm" microwave radiometric signature. The ESMR mounted on the Nimbus–5 satellite is providing synoptic images of microwave emissions at this wavelength over the entire globe, and one of these images of the Arctic on Jan. 11, 1973, is shown in figure 252. If one looks at the Beaufort Sea area in this image, one can see that, according to the ESMR, the ice in the eastern Beaufort Sea has a "cool" radiometric signature (blue) and is therefore multiyear ice. The image also shows that the ice just north of Alaska in the western Beaufort Sea is made up of predominantly first-year sea ice because it has a "warm" (yellow) radiometric signature. Data such as these are fundamentally important if science is to develop predictive numerical models for the arctic ice cover, models which are necessary in order to utilize properly the oil and mineral resources in this highly vulnerable and dynamic region.

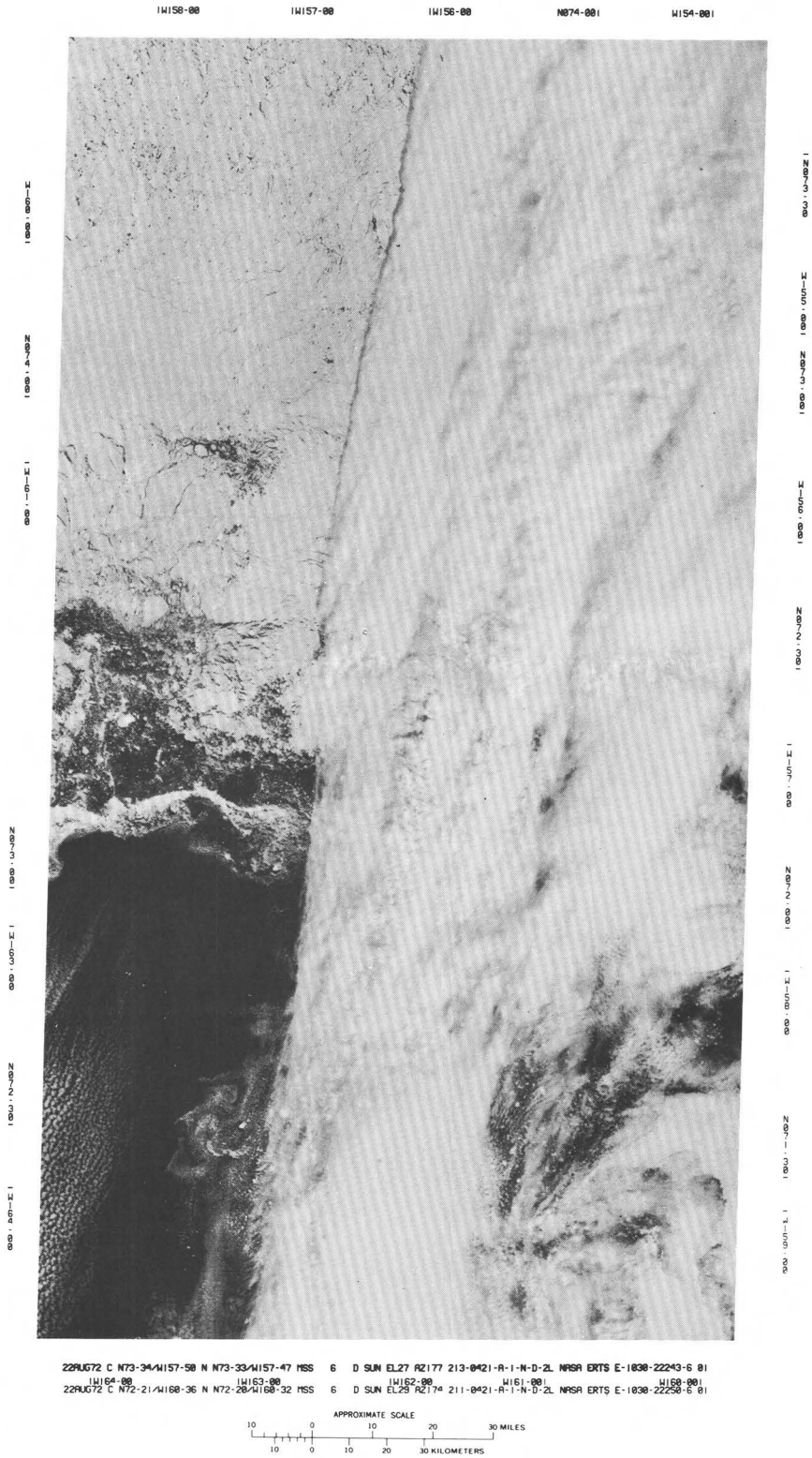


FIGURE 250.—ERTS–1 image mosaic of the western Beaufort Sea on Aug. 22, 1972 (1030–22243 and 1030–22250, band 6).

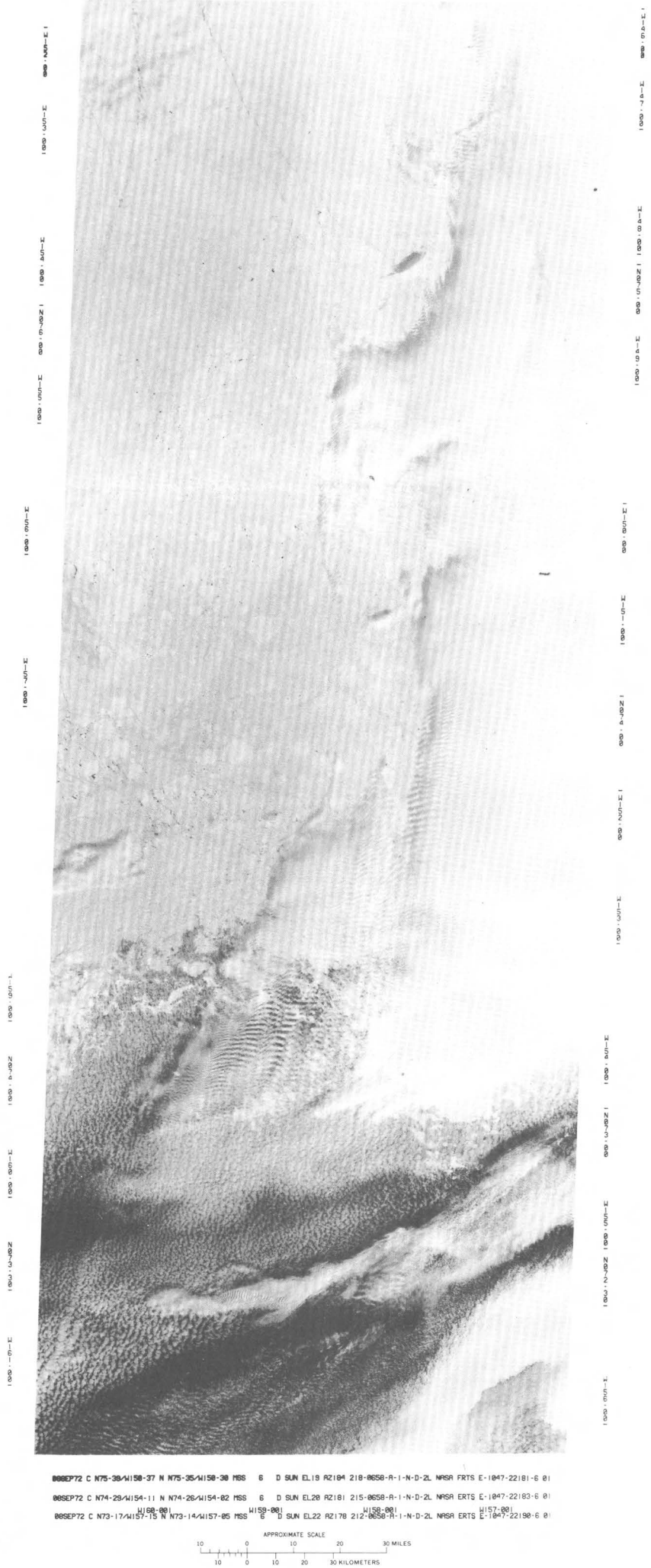


FIGURE 251.—ERTS–1 image mosaic of the eastern Beaufort Sea area on Sept. 8, 1972 (1047–22181, 1047–22183, and 1047–22190, band 6).

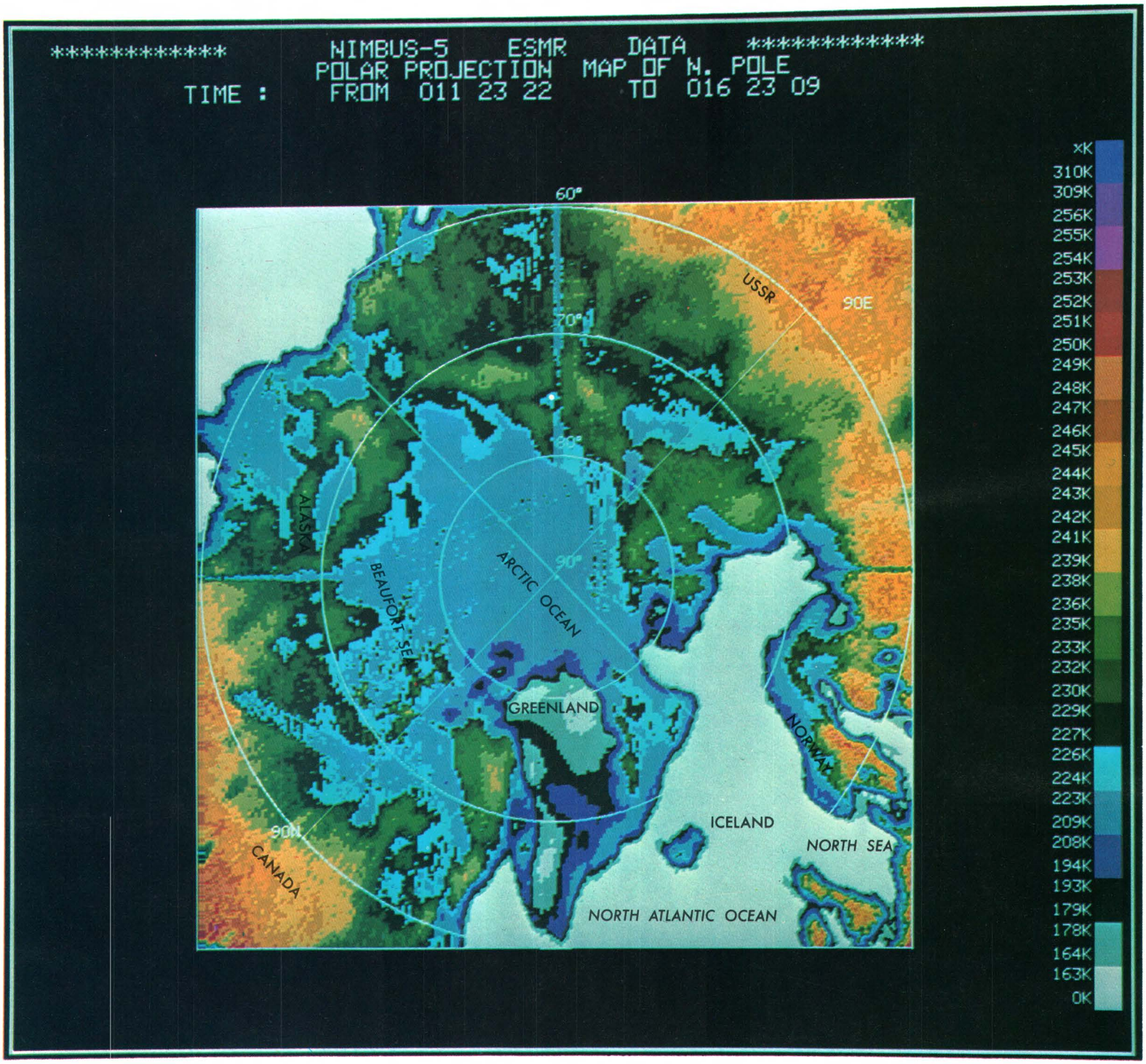


APPROXIMATE SCALE

500 0 500 1000 1500 MILES

500 0 500 1000 1500 KILOMETERS

FIGURE 252.—Polar projection map of the North Pole from Nimbus–5 ESMR data on Jan. 11, 1973. Variations in microwave radiometric temperature are shown in color. The blue and yellow areas are "cool" (multiyear) and "warm" (first-year) sea ice, respectively.

# FLOODING OF SEA ICE BY THE RIVERS OF NORTHERN ALASKA

By Peter W. Barnes and Erk Reimnitz,
U.S. Geological Survey

Three overlapping high-latitude ERTS images show a 4-day sequence of river flooding on the sea ice off the Sagavanirktok River near Prudhoe Bay, Alaska (figs. 253, 254, 255).

The onslaught of catastrophic events has always both threatened and fascinated man, and the spring breakup and initial flow of arctic rivers are such events. On the North Slope of Alaska, rivers flood before the melting and breakup of the sea ice along the coast and thus cause a freshwater overflow, 1 m or more in depth, onto the sea ice in the immediate vicinity of river mouths. Subsequent to the overflow, the floodwaters drain through strudel (drain holes in ice) (Reimnitz and Bruder, 1972). Field studies show that the floodwaters carry very little sediment, because the initial melt involves only the snow overlying the frozen soils and sediments. As the floodwaters drain through strudel in the ice canopy offshore, the sea floor is extensively scoured (Reimnitz and Barnes, 1974). As the season progresses, the ice immediately offshore from the deltas melts because of the influx of warmer river waters. Very little of this freshwater mixes with the offshore and/or underlying seawater, and a large freshwater reservoir is created in this arctic region. Mixing is damped by a weak current structure that results from a small tidal range and the presence of an ice cover that eliminates wind stress.

The development of flooding can be seen on the ERTS images as the expansion of the dark area (freshwater) outside of the delta of the Sagavanirktok River. Flooding of the sea ice by the river apparently started on May 23 and had still not reached its maximum extent 5 days later, although the overflow from the eastern channel was starting to drain. The fact that drainage was occurring is shown in the May 27 image by the lighter color at the western terminus of the overflow. During the period of observation, the area of inundated sea ice increased from approximately 18 $km^2$ to 43 $km^2$. If the area were covered to an average depth of 0.75 m (Barnes and Reimnitz, 1972), this volume represents a freshwater lake on the sea ice of at least $32 \times 10^6$ $m^3$, disregarding drainage and subsequent river flow.

Rapid snowmelt from May 24 through May 27 is indicated by the increased definition of the drilling pads at Prudhoe Bay (fig. 255). The sharp northeast-southwest lineation in the oilfield is due to downwind eolian transport of loose sediment from the roads and pads.

Examination of earlier imagery of the area to the southeast of the Sagavanirktok River and later imagery of the area to the northwest indicates that the rivers of the Alaskan North Slope overflow in sequence from southeast to northwest, apparently in response to the variance of solar insolation at different latitudes.

River flooding of sea ice marks the abrupt change from winter to summer conditions in the Arctic when man's transportation activities must shift from overland to air or water. Thus, knowledge of this phenomenon is essential for the safe utilization of installations on or near deltas, and ERTS imagery provides a tool to determine the variability of the areal extent and intensity of flooding from year to year.

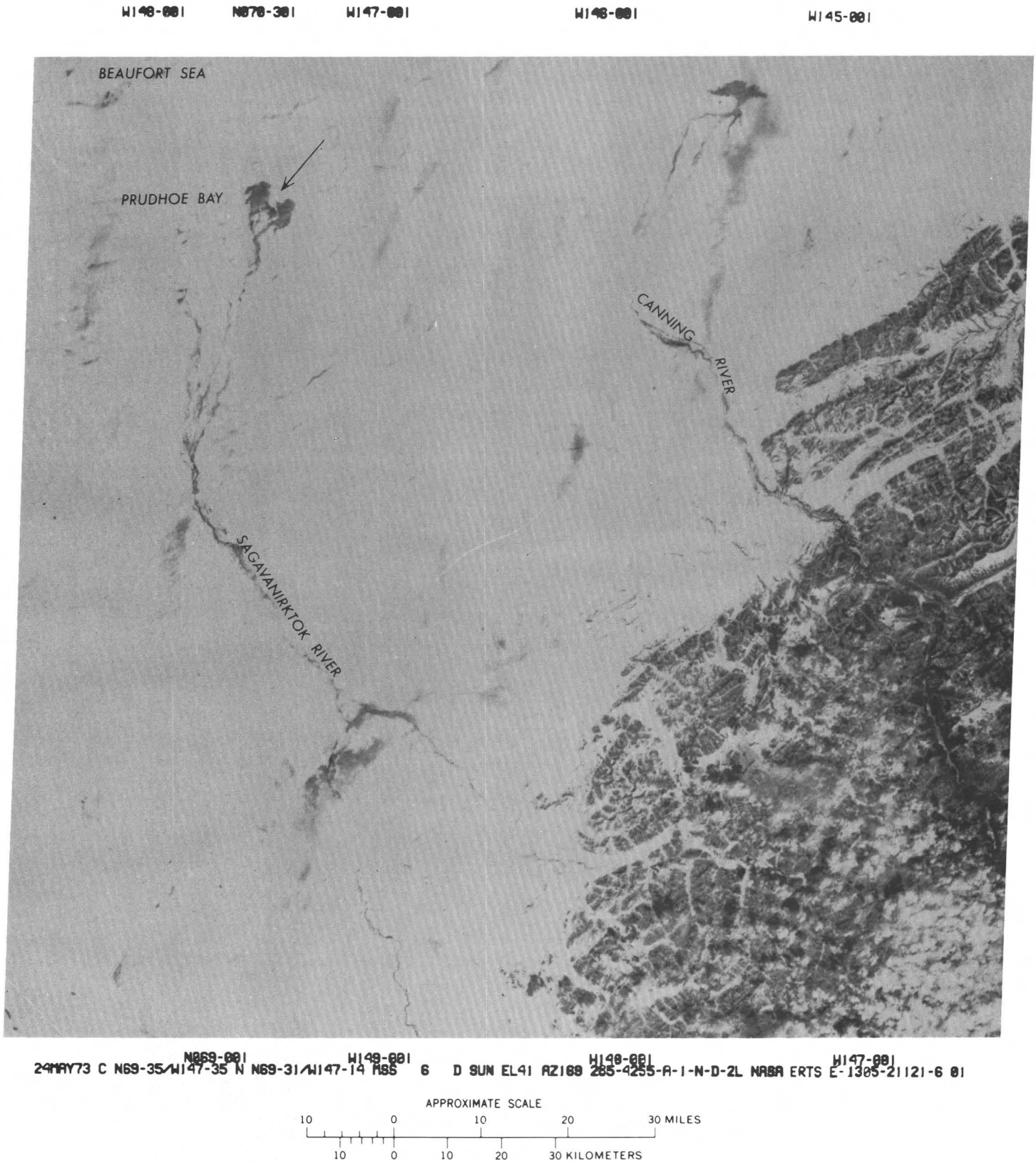


FIGURE 253.—Annotated ERTS–1 image showing an area of river flooding (arrow) on sea ice near Prudhoe Bay, Alaska, on May 24, 1973 (1305–21121, band 6).

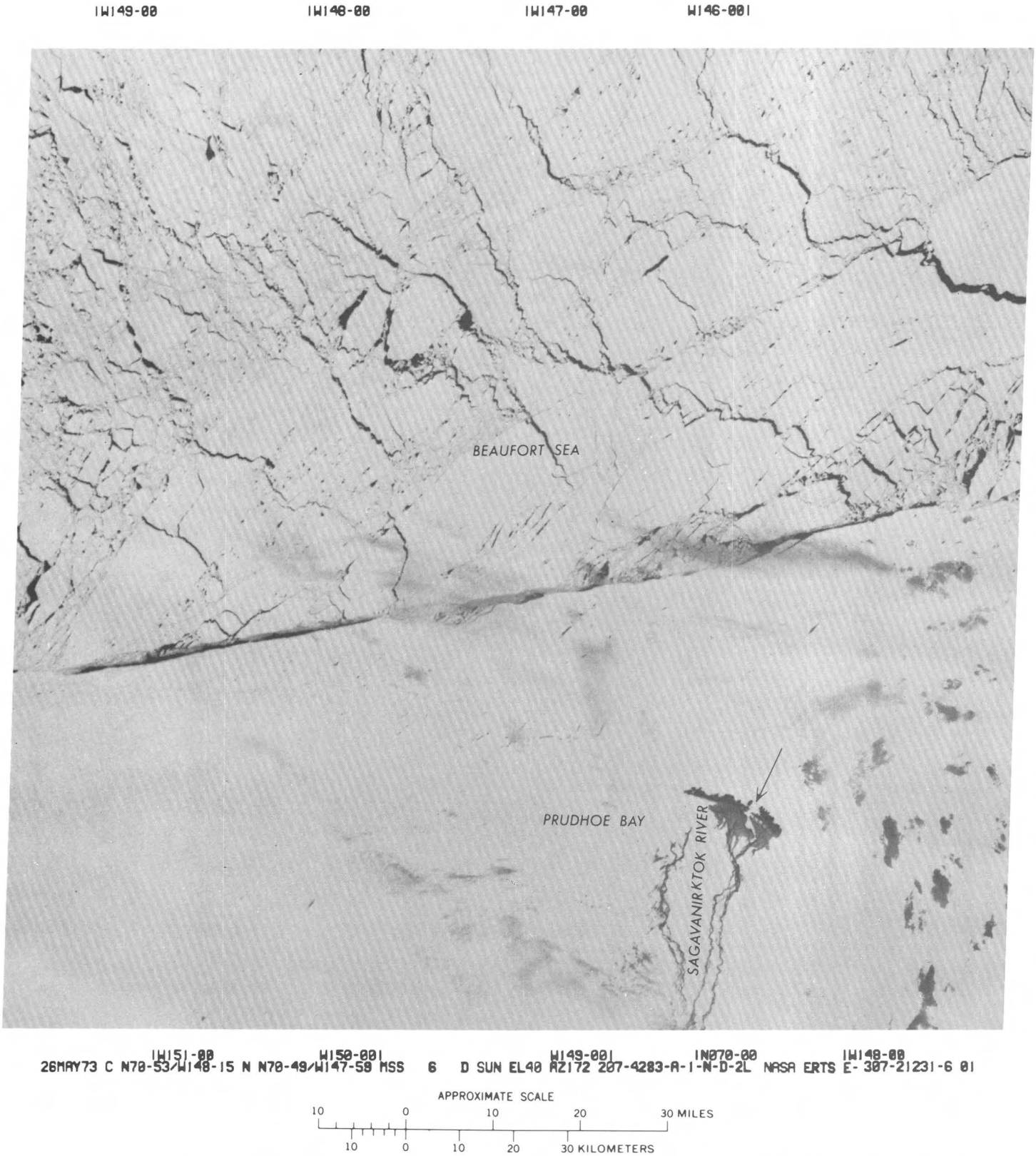


FIGURE 254.—Annotated ERTS–1 image showing an area of river flooding (arrow) on sea ice near Prudhoe Bay, Alaska, on May 26, 1973 (1307–21231, band 6).

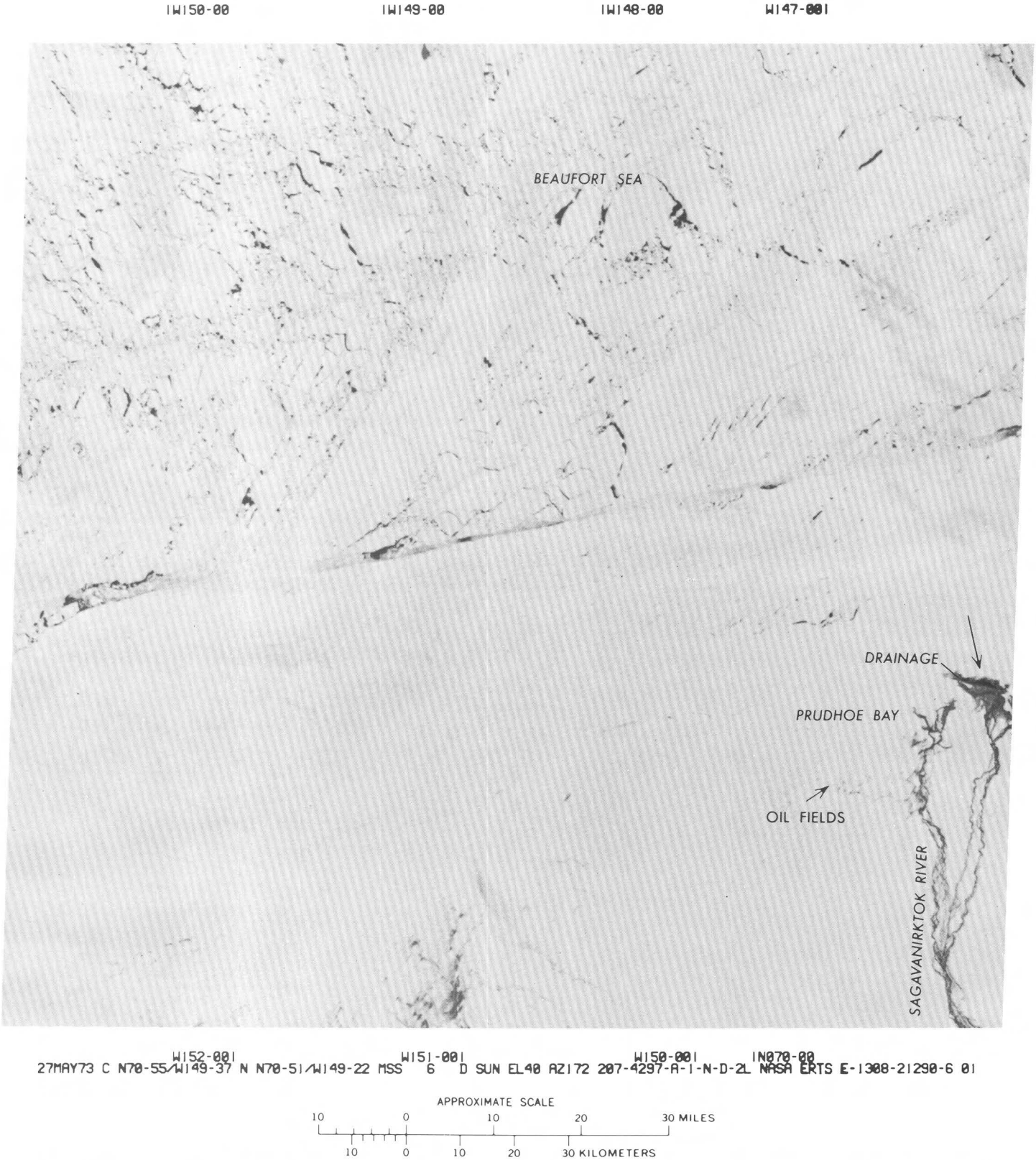


FIGURE 255.—Annotated ERTS–1 image showing an area of river flooding (arrow) on sea ice near Prudhoe Bay, Alaska, on May 27, 1973 (1308–21290, band 6); drilling pads indicated by smaller arrow west of Sagavanirktok River.

# INFLUENCE OF SEA ICE ON SEDIMENTARY PROCESSES OFF NORTHERN ALASKA

By Erk Reimnitz and Peter W. Barnes,
U.S. Geological Survey

The ice cover of the Beaufort Sea has a critical influence on the sedimentary environment of the Continental Shelf north of Alaska. An understanding of this environment is of great scientific interest, for about 25 percent of the world's Continental Shelf areas are seasonally covered by ice today; sea ice was even more widespread during colder periods in the past. Comprehension of this type of environment can be directly applied during future offshore development of the Prudhoe Bay oilfield.

Figure 256 is an ERTS MSS color composite image taken on June 14, 1973, about 2 weeks after the river flooding of the fast ice (sea ice anchored to the coast or bottom) but 3 weeks before the breakup of the ice. With the initiation of river flow, extensive regions of fast ice are inundated by river water that carries some sediment onto the ice (Barnes and Reimnitz, 1972 and this volume; Reimnitz and Bruder, 1972). By the time this ERTS image was taken, most of this water had drained from the ice through strudel (drain holes in ice), producing bottom-scour features on the sea floor (Reimnitz and others, 1974). The outer boundary of the flood of river water can be detected in some areas (arrows). The ice near river mouths has melted (dark-blue area); from later images and ground observations, we can conclude that, at the time of sea-ice breakup, little of the river-supplied sediment remains on the ice to be rafted away from deltas.

The location of the shear line between the fast ice and offshore pack ice has pronounced influence on sedimentological processes of the Continental Shelf. In interpreting ERTS images made during the period from March through June 1973, we find that initially the shear line lies between the 10- and 20-m depth contours along the north coast of Alaska. On the June image (fig. 256) the midwinter location is indicated by a solid line. Seaward of this line is the shear zone in which the ice is intensely deformed and shows a dense pattern of major pressure ridges. Ice movement in this zone occurs mainly during the first half of the winter. Since the keels of many pressure ridges extend to the sea floor, the bottom is ploughed during such movement of ice. Eventually the pressure ridges become so firmly grounded that the ice in the shear zone becomes strongly resistant to further deformation, thereby causing a seaward extension of the fast ice out to 20 to 25 km along a relatively straight coastline. Overlapping ERTS images of late May 1973, taken at a time of strong easterly winds, show that a new shear line has formed (May position plotted as dashed line on fig. 256) with rapidly moving ice to the seaward of the line. Pressure-ridge lineation, which records the deformation of winter ice, is best seen in the right part of the image (fig. 256).

Surveys of the sea-floor bottom made after the sea-ice breakup show sea-floor gouges produced by ice in this zone of major pressure ridges and a remarkably smooth bottom in the area landward of the shear line (Reimnitz and Barnes, 1974). Box cores from the shear zone show that sediments are intensely mixed (Barnes and Reimnitz, 1974). The keels of pressure ridges in the shear zone, where they are in contact with the bottom, may affect water circulation on the Continental Shelf. Obviously the shear zone will be the most hazardous region for any offshore construction.

Our studies of ERTS images indicate that in some areas the shear line migrates seaward during the winter. Whether it initially forms within the same depth range year after year remains to be determined, but in the eastern part of the image in figure 256, where the shear line passes near outlying islands, its location apparently is controlled by bathymetry.

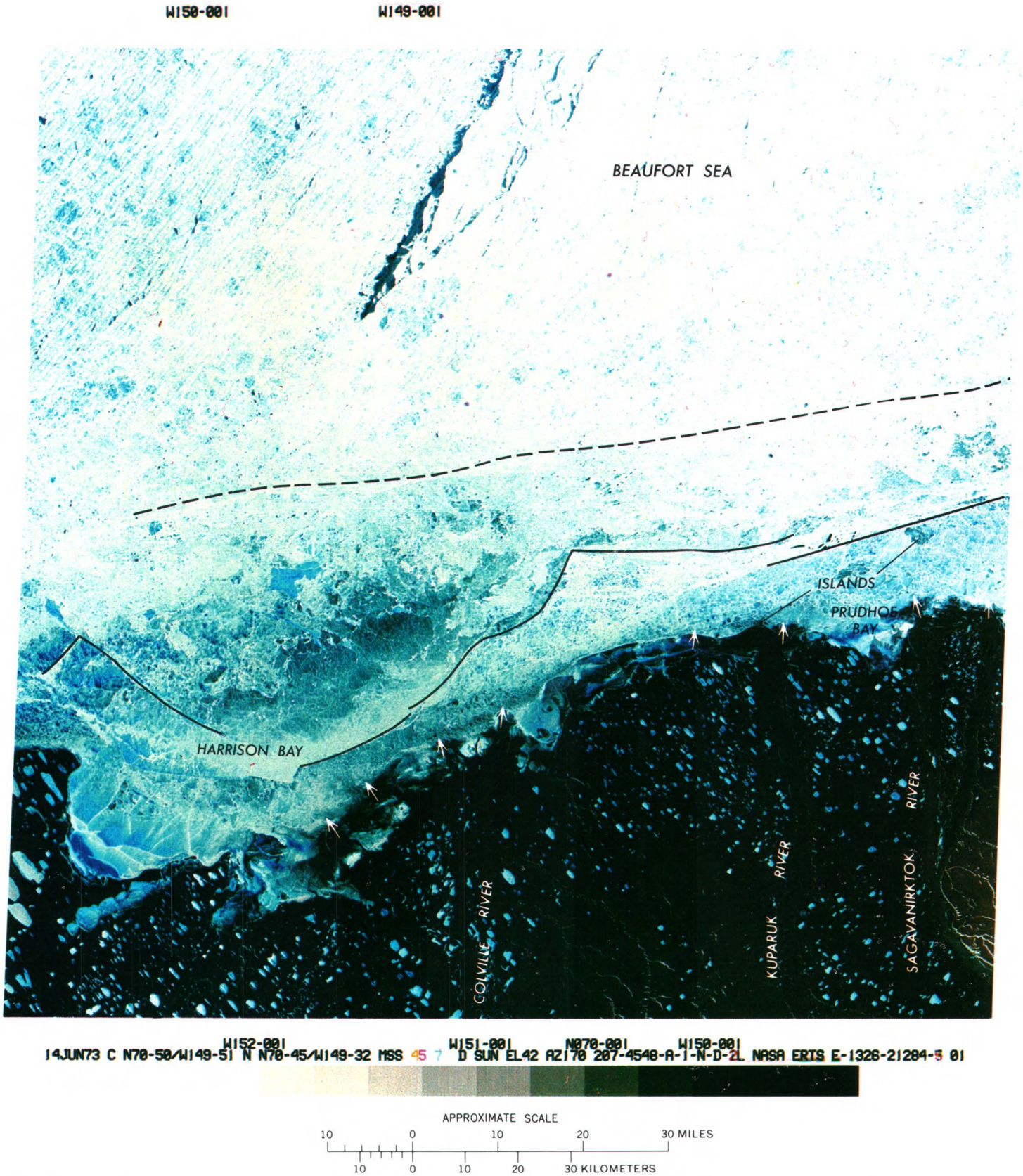


FIGURE 256.—Annotated color composite ERTS–1 image of the Prudhoe Bay area of Alaska on June 14, 1973 (1326–21284). The outer boundary of the flood of river water is indicated by arrows. Location of shear line in midwinter is shown with a solid line, and the new shear line is shown with a dashed line.

## REFERENCES


Barnes, P. W., and Reimnitz, Erk, 1972, River overflow onto the sea ice off the northern coast of Alaska, Spring 1972 [abs.]: Am. Geophys. Union, E⊕S, Trans., v. 53, p. 1020.

——— 1974, Sedimentary processes on arctic shelves off the northern coast of Alaska: Arctic Inst. North America, Symposium on Beaufort Sea Coastal and Shelf Research, San Francisco, Calif., 1974, Proc., p. 439–476.

Brown, W. M., III, and Ritter, J. R., 1971, Sediment transport and turbidity in the Eel River basin, California: U.S. Geol. Survey Water-Supply Paper 1986, 70 p.

Campbell, W. J.; Gloersen, Per; Nordberg, William; and Wilheit, T. T.; 1973, Dynamics and morphology of Beaufort Sea ice determined from satellites, aircraft, and drifting stations: NASA Goddard Space Flight Center, X–650–73–194, 20 p.

Carlson, P. R., and Harden, D. R., 1973, Principal sources and dispersal patterns of suspended particulate matter in nearshore surface waters of the northeast Pacific Ocean, Type I Progress Report to NASA, Period 1 June–15 Aug. 1973: U.S. Dept. Commerce Natl. Tech. Inf. Service E73–11099/WR, 14 p.

Coker, A. E., Higer, A. L., and Goodwin, C. R., 1973, Detection of turbidity dynamics in Tampa Bay, Florida, using multispectral imagery from ERTS–1: NASA Goddard Space Flight Center, Symposium on Significant Results Obtained from the Earth Resources Technology Satellite–1, 2d, New Carrollton, Md., Mar. 1973, Proc., v. 1, sec. B, p. 1715–1726.

Gloersen, Per; Wilheit, T. T.; Chang, T. C.; Nordberg, William; and Campbell, W. J.; 1973, Microwave maps of the polar ice of the Earth: NASA Goddard Space Flight Center, X–652–73–269, 38 p.

Hult, J. L., and Ostrander, N. C., 1973, Applicability of ERTS for surveying Antarctic iceberg resources: The Rand Corp., Final Rept. R–1354–NASA/NSF, 50 p.

Hunter, R. E., 1973, Distribution and movement of suspended sediment in the Gulf of Mexico off the Texas coast: NASA Goddard Space Flight Center, Symposium on Significant Results Obtained from the Earth Resources Technology Satellite–1, 2d, New Carrollton, Md., Mar. 1973, Proc., v. 1, sec. B, p. 1341–1348.

Reimnitz, Erk, and Barnes, P. W., 1974, Sea ice as a geologic agent on the Beaufort Sea shelf of Alaska: Arctic Inst. North America, Symposium on Beaufort Sea Coastal and Shelf Research, San Francisco, Calif., 1974, Proc., p. 301–353.

Reimnitz, Erk, and Bruder, K. F., 1972, River discharge into an ice covered ocean and related sediment dispersal, Beaufort Sea, coast of Alaska: Geol. Soc. America Bull., v. 83, no. 3, p. 861–866.

Reimnitz, Erk, Rodeick, C. A., and Wolf, S. C., 1974, Strudel scour: a unique Arctic marine geologic phenomenon: Jour. Sed. Petrology, v. 44, no. 2, p. 409–420.

Schwartzlose, R. A., and Reid, J. L., 1972, Near-shore circulation in the California Current: Calif. Marine Resources Comm. CalCOFI Rept. 16, p. 57–65.

Weeks, W. F., and Campbell, W. J., 1973, Icebergs as a fresh water source—an appraisal: Jour. Glaciology, v. 12, no. 65, p. 207–234.




☆ U.S. GOVERNMENT PRINTING OFFICE : 1976 O—211-907